

SNLA LIBRARY



* 8 5 2 8 3 3 9 *

SANDIA REPORT

SAND92-1579 • UC-721

Unlimited Release

Printed August 1992

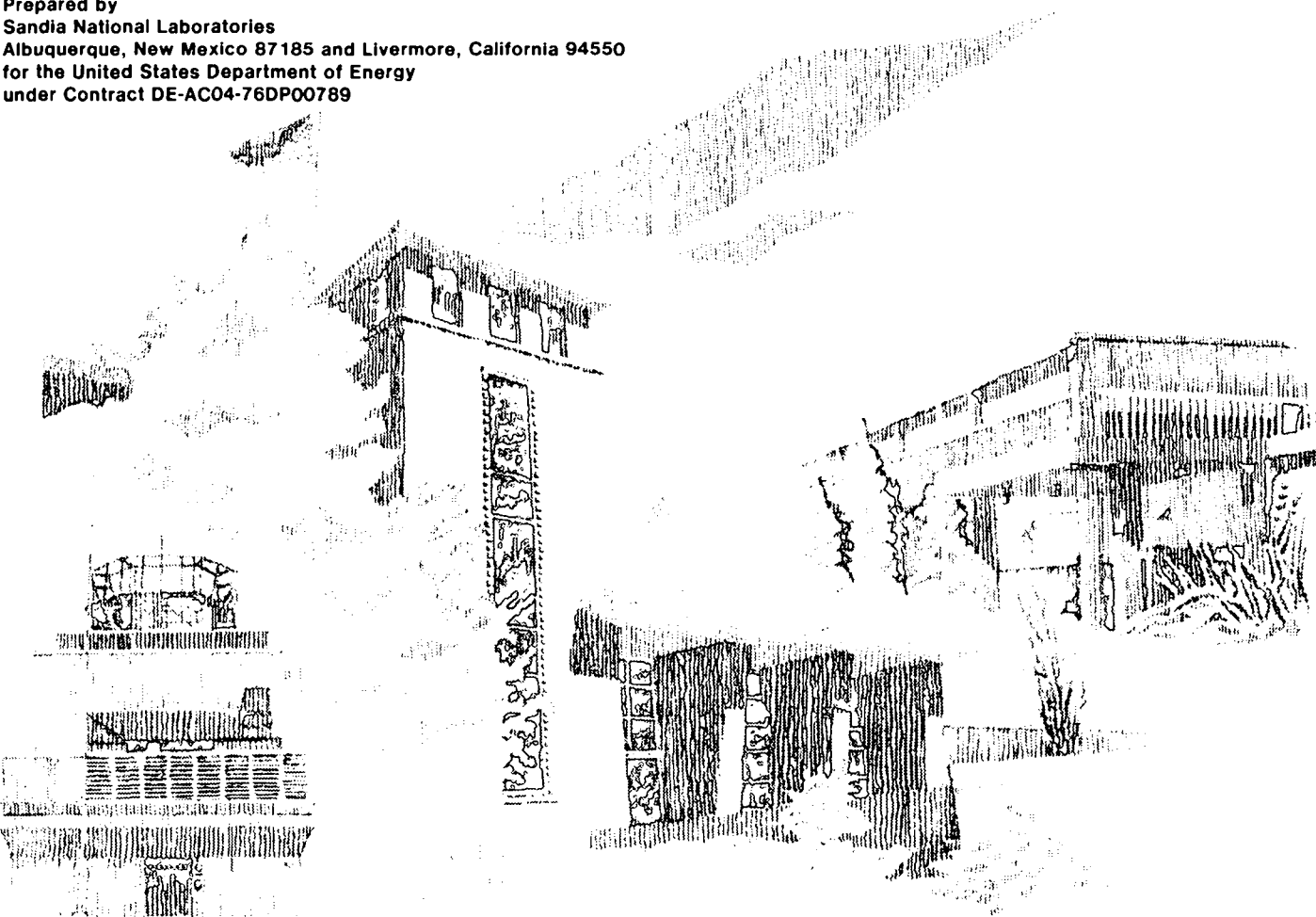
SAND92-1579
0001
UNCLASSIFIED

08/92
480P STAC

Integration of Interpretation Results of Tracer Tests Performed in the Culebra Dolomite at the Waste Isolation Pilot Plant Site

Toya L. Jones, Van A. Kelley, John F. Pickens, David T. Upton,
Richard L. Beauheim, Peter B. Davies

Prepared by
Sandia National Laboratories
Albuquerque, New Mexico 87185 and Livermore, California 94550
for the United States Department of Energy
under Contract DE-AC04-76DP00789



Issued by Sandia National Laboratories, operated for the United States Department of Energy by Sandia Corporation.

NOTICE: This report was prepared as an account of work sponsored by an agency of the United States Government. Neither the United States Government nor any agency thereof, nor any of their employees, nor any of their contractors, subcontractors, or their employees, makes any warranty, express or implied, or assumes any legal liability or responsibility for the accuracy, completeness, or usefulness of any information, apparatus, product, or process disclosed, or represents that its use would not infringe privately owned rights. Reference herein to any specific commercial product, process, or service by trade name, trademark, manufacturer, or otherwise, does not necessarily constitute or imply its endorsement, recommendation, or favoring by the United States Government, any agency thereof or any of their contractors or subcontractors. The views and opinions expressed herein do not necessarily state or reflect those of the United States Government, any agency thereof or any of their contractors.

Printed in the United States of America. This report has been reproduced directly from the best available copy.

Available to DOE and DOE contractors from
Office of Scientific and Technical Information
PO Box 62
Oak Ridge, TN 37831

Prices available from (615) 576-8401, FTS 626-8401

Available to the public from
National Technical Information Service
US Department of Commerce
5285 Port Royal Rd
Springfield, VA 22161

NTIS price codes
Printed copy: A20
Microfiche copy: A01

Integration of Interpretation Results of Tracer Tests Performed in the Culebra Dolomite at the Waste Isolation Pilot Plant Site

Toya L. Jones, Van A. Kelley, John F. Pickens, and David T. Upton
INTERA Inc.
6850 Austin Center Blvd., Suite 300
Austin, TX 78731

Richard L. Beauheim and Peter B. Davies
Fluid Flow and Transport Department
Sandia National Laboratories
Albuquerque, NM 87185

ABSTRACT

Conservative tracer tests have been conducted in the Culebra Dolomite Member of the Rustler Formation at the H-2, H-3, H-4, H-6, and H-11 hydropads for transport scales ranging from approximately 20 to 40 m. Convergent-flow and two-well recirculating tracer tests provide data that is used to quantitatively characterize flow and transport processes. The observed long time period required for initial (detectable) tracer breakthrough (74 to 316 days) in the H-2 and H-4 tracer tests suggest the prevalence of single-porosity, matrix-only transport at these locations. Hydraulic-test responses at these two hydropads also indicate single-porosity, matrix-only conditions. The relatively poor quality of data defining the breakthrough curves from the H-2 and H-4 tracer tests precluded a detailed, quantitative analysis of transport parameter values from these tests. Interpretations of pumping tests and tracer tests at the H-3, H-6, and H-11 hydropads indicated that the Culebra dolomite behaves as a double-porosity (fracture-plus-matrix) medium at these locations. Both the H-3 and H-11 hydropads are located along the offsite transport pathways southeast of the Waste Isolation Pilot Plant waste-panel area. Significant fracture participation in transport is evidenced by rapid initial tracer breakthrough (1 to 21 hrs) on one travel path at each of these hydropads. The H-3, H-6, and H-11 convergent-flow tracer tests were analyzed using the SWIFT II model with the Culebra fracture/matrix system idealized as three, orthogonal, intersecting fracture sets equally spaced in all three directions. Input values and ranges for the assigned transport parameters (effective thickness, well spacing, pumping rate, free-water diffusion coefficient, longitudinal dispersivity, and matrix porosity) were specified based on field measurements, laboratory measurements on Culebra core, and scientific judgement. Measurement and/or calculated uncertainties were also defined for the assigned parameters. Two approaches were used to model double-porosity transport. The first approach assumed that differences in tracer breakthrough behavior at a single hydropad were caused by differences (heterogeneity) in matrix-block length (fracture spacing) between different travel paths. The second approach assumed that differences in tracer breakthrough behavior were caused by horizontal anisotropy in the flow field. Interpretations based on the heterogeneous-analysis approach yielded matrix-block lengths ranging from 0.11 to 1.23 m and fracture porosities ranging from 5.0×10^{-4} to 1.0×10^{-3} . Interpretations based on the anisotropic-analysis approach yielded matrix-block lengths ranging from 0.15 to 0.48 m, fracture porosities ranging from 1.0×10^{-3} to 3.0×10^{-3} , and anisotropy ratios ranging from 3:1 to 7:1. Sensitivity analyses were conducted to provide insight into the relative impact of varying individual transport parameters and to provide estimates of fitted-parameter uncertainty. These analyses yielded minimum and maximum matrix-block lengths for all hydropads that ranged from 0.02 to 3.22 m. Sensitivity analyses also showed that neither single-porosity, fracture-only transport nor single-porosity, matrix-only transport can reproduce the observed transport behavior at the H-3, H-6, and H-11 hydropads.

ACKNOWLEDGEMENTS

The authors wish to thank George Saulnier, Jr., Wayne Stensrud, Banda RamaRao, Elaine Gorham, Craig Novak, Mark Reeves, and Chin-Fu Tsang for helpful discussions and/or review comments.

CONTENTS

1.0	INTRODUCTION	1- 1
2.0	SITE CHARACTERIZATION	2- 1
2.1	Regional Geology	2- 1
2.2	Regional Hydrogeology	2- 5
2.3	Post-Depositional Alteration of the Rustler Formation	2-13
2.4	Characterization of the Culebra Dolomite	2-19
3.0	TRACER-TEST INTERPRETATION METHODOLOGY	3- 1
3.1	Transport Conceptualizations for the Culebra	3- 1
3.1.1	Characterization of Fractures in the Culebra	3- 1
3.1.2	Single- and Double-Porosity Transport Conceptualizations ..	3- 4
3.1.3	Other Transport Conceptualizations	3- 9
3.2	SWIFT II Code Description	3-11
3.3	Model Verification of SWIFT II	3-13
3.4	Methodology for Heterogeneous and Anisotropic Tracer-Test Analyses	3-14
3.4.1	Heterogeneous-Analysis Approach	3-18
3.4.2	Anisotropic-Analysis Approach	3-19
3.4.3	Tracer-Input Conceptualization	3-20
3.4.4	Implementation of Heterogeneous- and Anisotropic-Analysis Approaches in SWIFT II	3-28
4.0	TRACERS UTILIZED IN WIPP-SITE TRACER TESTS	4- 1
4.1	Organic Anions	4- 1
4.2	Inorganic Anions	4- 5
4.3	Noncharged Halogenated Hydrocarbons	4- 6
5.0	CULEBRA AND TRACER-TEST-SITE TRANSPORT PARAMETERS .	5- 1
5.1	Assigned Transport Parameters	5- 1
5.1.1	Culebra Effective Thickness	5- 2
5.1.2	Well Spacing	5- 8
5.1.3	Pumping Rate	5-14
5.1.4	Free-Water Diffusion Coefficients	5-15
5.1.5	Longitudinal Dispersivity	5-15
5.1.6	Matrix Porosity	5-23
5.1.7	Matrix Tortuosity	5-29
5.2	Fitted Transport Parameters	5-37
5.2.1	Fracture Porosity	5-37
5.2.2	Matrix-Block Length	5-39
5.2.3	Anisotropy	5-40

CONTENTS (Continued)

5.3	Identification of Independent Parameter Groups	5-45
6.0	H-2 HYDROPAD TRACER TESTS	6- 1
6.1	Well Configurations	6- 1
6.2	Local Hydrogeology	6- 5
6.3	Tracer-Test History	6- 5
6.3.1	Test Equipment	6- 8
6.3.2	Pumping and Tracer-Injection History	6-12
6.3.3	Observed Tracer Breakthrough	6-14
6.4	Previous Interpretation of the Tracer Tests	6-14
6.5	Suitability of Tracer Tests for Further Analysis	6-17
6.6	Summary of Results for H-2	6-20
7.0	H-3 HYDROPAD TRACER TEST	7- 1
7.1	Well Configurations	7- 1
7.2	Local Hydrogeology	7- 4
7.3	Tracer-Test History	7- 8
7.3.1	Pumping and Tracer-Injection History	7- 8
7.3.2	Test Equipment	7-11
7.3.3	Observed Tracer Breakthrough	7-15
7.4	Analysis of Tracer-Breakthrough Curves	7-17
7.4.1	Heterogeneous-Analysis Approach	7-17
7.4.1.1	Previous Interpretation of the Convergent-Flow Tracer Test Conducted at the H-3 Hydropad Using the Heterogeneous-Analysis Approach	7-18
7.4.1.2	Current Interpretation of the Convergent-Flow Tracer Test Conducted at the H-3 Hydropad Using the Heterogeneous-Analysis Approach	7-18
7.4.2	Anisotropic-Analysis Approach	7-22
7.5	Sensitivity Analyses	7-28
7.5.1	Effect of Tortuosity	7-29
7.5.2	Effect of Longitudinal Dispersivity	7-29
7.5.3	Effect of Fracture Porosity	7-31
7.5.4	Effect of Matrix Porosity	7-34
7.5.5	Effect of Matrix-Block Length	7-36
7.5.6	Effect of Effective Culebra Thickness	7-39
7.5.7	Effect of Anisotropy in Horizontal Transmissivity	7-42
7.5.8	Determination of Maximum and Minimum Matrix-Block Lengths	7-49
7.6	Summary of Results for H-3	7-52

CONTENTS (Continued)

8.0	H-4 HYDROPAD TRACER TEST	8- 1
8.1	Well Configurations	8- 1
8.2	Local Hydrogeology	8- 4
8.3	Tracer-Test History	8- 6
8.3.1	Pumping and Tracer-Injection History	8- 6
8.3.2	Test Equipment	8- 9
8.3.3	Observed Tracer Breakthrough	8-13
8.4	Previous Interpretation of the Convergent-Flow Tracer Test	8-17
8.5	Suitability of Tracer Test for Further Analysis	8-19
8.6	Summary of Results for H-4	8-20
9.0	H-6 HYDROPAD TRACER TESTS	9- 1
9.1	Well Configurations	9- 1
9.2	Local Hydrogeology	9- 4
9.3	History of the Seven Tracer Tests and Selection of Tracer Tests for Interpretation	9- 6
9.3.1	Two-Well Recirculating Tracer Tests	9- 7
9.3.1.1	Tracer Test Histories	9- 7
9.3.1.2	Suitability of Tracer Tests for Analysis	9-10
9.3.2	Convergent-Flow Tracer Tests	9-12
9.3.2.1	Pumping and Tracer-Injection History	9-13
9.3.2.2	Suitability of Tracer Tests for Analysis	9-24
9.3.2.3	Test Equipment for Analyzed Tests	9-27
9.3.2.4	Observed Tracer Breakthroughs for Analyzed Tests	9-29
9.4	Analysis of Tracer-Breakthrough Curves for Convergent-Flow Tracer Test #1	9-32
9.4.1	Heterogeneous-Analysis Approach	9-32
9.4.2	Anisotropic-Analysis Approach	9-35
9.5	Analysis of Tracer-Breakthrough Curve for Convergent-Flow Tracer Test #2	9-37
9.6	Sensitivity Analyses	9-40
9.6.1	Effect of Matrix-Block Length	9-44
9.6.2	Effect of Anisotropy Ratio	9-47
9.6.3	Determination of Maximum and Minimum Matrix-Block Lengths	9-47
9.7	Summary of Results for H-6	9-53
10.0	H-11 HYDROPAD TRACER TEST	10- 1
10.1	Well Configurations	10- 1
10.2	Local Hydrogeology	10- 4

CONTENTS (Continued)

10.3	Tracer-Test History	10-10
10.3.1	Pumping and Tracer-Injection History	10-10
10.3.2	Test Equipment	10-11
10.3.3	Observed Tracer Breakthrough	10-19
10.4	Analysis of Tracer-Breakthrough Curves	10-21
10.4.1	Heterogeneous-Analysis Approach	10-21
10.4.2	Anisotropic-Analysis Approach	10-27
10.5	Sensitivity Analyses	10-30
10.5.1	Effect of Matrix-Block Length	10-30
10.5.2	Effect of Anisotropy Ratio	10-32
10.5.3	Determination of Maximum and Minimum Matrix-Block Lengths	10-33
10.6	Summary of Results for H-11	10-36
11.0	COMPARISON OF SINGLE- AND DOUBLE-POROSITY TRANSPORT CONCEPTUALIZATIONS FOR THE H-3, H-6, AND H-11 TRACER TESTS	11- 1
12.0	SUMMARY AND CONCLUSIONS	12- 1
12.1	Summary	12- 1
12.2	Conclusions	12-11
12.3	Implications for Regional-Scale Transport Calculations	12-15
13.0	REFERENCES	13- 1
APPENDIX A	REVIEW OF CHEMICAL AND BIOLOGICAL ACTIVITY OF FLUORINATED ACIDS USED AS TRACERS	A- 1
APPENDIX B	TABULATED TRACER-CONCENTRATION DATA FROM TWO-WELL RECIRCULATING TRACER TEST #2 CONDUCTED AT THE H-2 HYDROPAD	B- 1
APPENDIX C	TABULATED TRACER-CONCENTRATION DATA FROM THE CONVERGENT-FLOW TRACER TEST CONDUCTED AT THE H-3 HYDROPAD	C- 1
APPENDIX D	TABULATED TRACER-CONCENTRATION DATA FROM THE CONVERGENT-FLOW TRACER TEST CONDUCTED AT THE H-4 HYDROPAD	D- 1

CONTENTS (Continued)

APPENDIX E-1	TABULATED TRACER-CONCENTRATION DATA FROM TWO-WELL RECIRCULATING TRACER TEST #1 AT THE H-6 HYDROPAD	E1- 1
APPENDIX E-2	TABULATED TRACER-CONCENTRATION DATA FROM TWO-WELL RECIRCULATING TRACER TEST #2 AT THE H-6 HYDROPAD	E2- 1
APPENDIX F-1	TABULATED TRACER-CONCENTRATION DATA FROM CONVERGENT-FLOW TRACER TEST #1 CONDUCTED AT THE H-6 HYDROPAD	F1- 1
APPENDIX F-2	TABULATED TRACER-CONCENTRATION DATA FROM CONVERGENT-FLOW TRACER TEST #2 CONDUCTED AT THE H-6 HYDROPAD	F2- 1
APPENDIX F-3	TABULATED TRACER-CONCENTRATION DATA FROM CONVERGENT-FLOW TRACER TEST #3 CONDUCTED AT THE H-6 HYDROPAD	F3- 1
APPENDIX F-4	TABULATED TRACER-CONCENTRATION DATA FROM CONVERGENT-FLOW TRACER TEST #4 CONDUCTED AT THE H-6 HYDROPAD	F4- 1
APPENDIX F-5	TABULATED TRACER-CONCENTRATION DATA FROM CONVERGENT-FLOW TRACER TEST #5 CONDUCTED AT THE H-6 HYDROPAD	F5- 1
APPENDIX G	TABULATED TRACER-CONCENTRATION DATA FROM THE CONVERGENT-FLOW TRACER TEST CONDUCTED AT THE H-11 HYDROPAD	G- 1

Tables

4-1.	Tracers Used for Evaluation of Culebra Transport Parameters	4- 2
4-2.	Free-Water Diffusion Coefficients for Organic Anion Tracers Used at the WIPP Site	4- 4

Tables (Continued)

5-1.	Ground-Surface and Culebra Dolomite Elevations for WIPP-Area Boreholes	5- 3
5-2.	Summary of Base-Case Transport Parameters, Range of Measured or Estimated Values, Measurement or Calculation Uncertainty, and Range of Potential Values for Assigned Parameters	5- 9
5-3.	Summary of Porosities Determined Using Boyle's Law Technique on Culebra Core Samples	5-24
5-4.	Summary of Average and Range of Porosities for Core from the H-2, H-3, H-4, H-6, and H-11 Hydropads	5-27
5-5.	Summary of Formation-Factor and Tortuosity Values	5-31
5-6.	Results from Diffusion Studies Performed on the Culebra Dolomite by Sandia National Laboratories	5-33
5-7.	Summary of Literature Values of Anisotropy Ratios at the WIPP Site . . .	5-44
6-1.	UTM Coordinates, Ground-Surface Elevations, and Top-of-Casing Elevations for the H-2 Hydropad Wells	6- 3
6-2.	Summary of Pumping and Tracer-Injection Information for the Two-Well Recirculating Tracer Tests Conducted at the H-2 Hydropad	6-13
7-1.	UTM Coordinates, Ground-Surface Elevations, and Top-of-Casing Elevations for the H-3 Hydropad Wells	7- 3
7-2.	Summary of Pumping and Tracer-Injection Information for the Convergent-Flow Tracer Test Conducted at the H-3 Hydropad	7-10
7-3.	Transport Parameters Used by Kelley and Pickens (1986) in Their Interpretations of the H-3 Convergent-Flow Tracer Test	7-19
7-4.	Transport Parameters Used in the Interpretations of the H-3 Convergent-Flow Tracer Test	7-23
7-5.	Transport Parameters Used in the Analysis of Sensitivity to Assumed Effective Culebra Thickness of 2 m	7-40
7-6.	Transport Parameters Used in the Sensitivity Analysis to Determine the Maximum and Minimum Matrix-Block Lengths at the H-3 Hydropad	7-50
8-1.	UTM Coordinates, Ground-Surface Elevations, and Top-of-Casing Elevations for the H-4 Hydropad Wells	8- 3
8-2.	Summary of Pumping and Tracer-Injection Information for the Convergent-Flow Tracer Test Conducted at the H-4 Hydropad	8- 8
9-1.	UTM Coordinates, Ground-Surface Elevations, and Top-of-Casing Elevations for the H-6 Hydropad Wells	9- 3
9-2.	Summary of Pumping and Tracer-Injection Information for the Two-Well Recirculating Tracer Tests Conducted at the H-6 Hydropad	9- 8

Tables (Continued)

9-3.	Summary of Pumping and Tracer-Injection Information for the Convergent-Flow Tracer Tests Conducted at the H-6 Hydropad	9- 14
9-4.	Transport Parameters Used in the Interpretations of H-6 Convergent-Flow Tracer Test #1	9- 34
9-5.	Transport Parameters Used in the Interpretation of H-6 Convergent-Flow Tracer Test #2	9- 42
9-6.	Transport Parameters Used in the Sensitivity Analysis to Determine the Maximum and Minimum Matrix-Block Lengths at the H-6 Hydropad	9- 50
10-1.	UTM Coordinates, Ground-Surface Elevations, and Top-of-Casing Elevations for the H-11 Hydropad Wells	10- 3
10-2.	Summary of Pumping and Tracer-Injection Information for the Convergent-Flow Tracer Test Conducted at the H-11 Hydropad	10- 13
10-3.	Depths of the Packers and Tracer-Injection Ports in the Three Tracer-Addition Wells for the H-11 Convergent-Flow Tracer Test	10- 17
10-4.	Transport Parameters Used in the Interpretations of the H-11 Convergent-Flow Tracer Test	10- 23
10-5.	Transport Parameters Used in the Sensitivity Analysis to Determine the Maximum and Minimum Matrix-Block Lengths at the H-11 Hydropad	10- 38
11-1.	Transport Parameters for Attempted Single-Porosity Interpretations of the H-3 Convergent-Flow Tracer Test	11- 3
11-2.	Transport Parameters for Attempted Single-Porosity Interpretations of H-6 Convergent-Flow Tracer Test #1	11- 7
11-3.	Transport Parameters for Attempted Single-Porosity Interpretations of the H-11 Convergent-Flow Tracer Test	11- 11
12-1.	Summary of Best-Fit, Double-Porosity, Fitted Parameters from Interpretation of the Tracer Tests at the H-3, H-6, and H-11 Hydropads	12- 5
12-2.	Best-Fit, Minimum, and Maximum Matrix-Block Lengths for the H-3, H-6, and H-11 Hydropads	12- 9
12-3.	Summary of Transmissivities, Fracture Porosities, and Matrix-Block Lengths for the H-3, H-6, and H-11 Hydropads	12- 16

Figures

1-1.	Location of the Waste Isolation Pilot Plant (WIPP) site in southeastern New Mexico	1- 2
1-2.	WIPP-area boreholes	1- 3

Figures (Continued)

2-1.	Geologic column representative of WIPP area	2- 2
2-2.	Generalized geologic cross section	2- 3
2-3.	Center-of-Culebra elevations in the model area	2- 7
2-4.	Calibrated log ₁₀ transmissivities in the Culebra	2- 8
2-5.	Culebra freshwater-head contour surface	2- 9
2-6.	Kriged Culebra formation-fluid densities	2-10
2-7.	Identification of pathways within the Culebra dolomite from release points above the corners and center of the waste-storage area	2-11
2-8.	The occurrence of halite beds within the Rustler Formation	2-15
2-9.	Stratigraphic cross section of the Rustler Formation west to east across the WIPP site	2-16
2-10.	Schematic diagram of the map units in the Culebra dolomite in the Air-Intake Shaft	2-20
3-1.	Schematic of various conceptualizations for analysis of convergent-flow or two-well recirculating tracer tests, (a) single-porosity porous medium, (b) single-porosity fracture only, (c) multiple-permeability, single-porosity porous medium, (d) multiple-permeability, single-porosity fracture only, (e) double-porosity porous medium, (f) multiple-permeability, double- porosity porous medium	3- 5
3-2.	Idealization of fracture sets	3-12
3-3.	Comparison of analytic and SWIFT II results for double-porosity solute transport using prismatic matrix blocks	3-15
3-4.	Comparison of analytic and SWIFT II results for double-porosity solute transport using spherical matrix blocks	3-16
3-5.	Ideal representation of tracer-labeled region surrounding the tracer- addition well immediately after injection	3-22
3-6.	Schematic representation of the modeled region, (a) cross section, (b) plan view	3-24
3-7.	Relationship between actual input-tracer-mass geometry and the model space discretization	3-25
3-8.	Tracer-input function as applied to the actual model space discretization .	3-27
3-9.	Conceptualization of volumetric flow rate input into SWIFT II	3-30
5-1.	Schematic tracer-breakthrough curve at the pumping well for a radial- convergent tracer test with pulse injection	5-17
5-2.	Scale of observation versus longitudinal dispersivity for the saturated zone: reliability classification	5-20
5-3.	Comparison between tortuosity determined from electrical-resistivity measurements and diffusion experiments plotted as a function of porosity .	5-35

Figures (Continued)

5-4.	Summary of anisotropy calculations for the 1984 pumping tests at the H-11 hydropad	5-42
5-5.	Reported anisotropy at the WIPP site	5-43
6-1.	Plan view of the wells at the H-2 hydropad showing distances between wells at the center of the Culebra	6- 2
6-2.	Results of core examination of the Culebra dolomite from borehole H-2b	6- 6
6-3.	Results of core examination of the Culebra dolomite from borehole H-2b2	6- 7
6-4.	Downhole-equipment configuration for two-well recirculating tracer test #1 at the H-2 hydropad	6- 9
6-5.	Downhole-equipment configuration for two-well recirculating tracer test #2 at the H-2 hydropad	6-10
6-6.	Surface tracer-injection system for the two-well recirculating tracer tests conducted at the H-2 hydropad	6-11
6-7.	Observed PFB data recovered from H-2c during two-well recirculating tracer test #2 after having been injected into H-2c during two-well recirculating tracer test #1	6-15
6-8.	Observed SCN data for two-well recirculating tracer test #2 conducted at the H-2 hydropad	6-16
7-1.	Plan view of the wells at the H-3 hydropad showing distances between wells at the center of the Culebra	7- 2
7-2.	Results of core examination of the Culebra dolomite from borehole H-3b2	7- 5
7-3.	Results of core examination of the Culebra dolomite from borehole H-3b3	7- 6
7-4.	Pumping rate at well H-3b3 during the convergent-flow tracer test conducted at the H-3 hydropad	7- 9
7-5.	Downhole-equipment configurations for the tracer test at the H-3 hydropad	7-12
7-6.	Pressure data for the H-3 hydropad wells during the convergent-flow tracer test	7-14
7-7.	Observed m-TFMB and PFB data for the convergent-flow tracer test conducted at the H-3 hydropad	7-16
7-8.	Observed and best-fit simulated breakthrough curves for the H-3 convergent-flow tracer test using the heterogeneous-analysis approach . . .	7-21
7-9.	Mass distribution in the fractures and matrix and mass recovered at the pumping well for the best-fit heterogeneous simulation of the tracer-breakthrough curves for the H-3 hydropad	7-24

Figures (Continued)

7-10.	Observed and best-fit simulated breakthrough curves for the H-3 convergent-flow tracer test using the anisotropic-analysis approach	7-26
7-11.	Mass distribution in the fractures and matrix and mass recovered at the pumping well for the best-fit anisotropic simulation of the tracer-breakthrough curves for the H-3 hydropad	7-27
7-12.	Sensitivity to tortuosity for the H-3 convergent-flow tracer test	7-30
7-13.	Sensitivity to longitudinal dispersivity for the H-3 convergent-flow tracer test	7-32
7-14.	Sensitivity to fracture porosity for the H-3 convergent-flow tracer test	7-33
7-15.	Sensitivity to matrix porosity for the H-3 convergent-flow tracer test	7-35
7-16.	Sensitivity to matrix-block length for the H-3 convergent-flow tracer test	7-37
7-17.	Demonstration of different parameter combinations on independent-parameter group τ'	7-38
7-18.	Observed and best-fit simulated breakthrough curves for the H-3 convergent-flow tracer test using the heterogeneous-analysis approach and an assumed effective Culebra thickness of 2 m	7-41
7-19.	Observed and best-fit simulated breakthrough curves for the H-3 convergent-flow tracer test using the anisotropic-analysis approach and an assumed effective Culebra thickness of 2 m	7-43
7-20.	Sensitivity to horizontal anisotropy ($T_x:T_y$) for the H-3 convergent-flow tracer test	7-45
7-21.	Sensitivity to principal T_x orientation for the H-3 convergent-flow tracer test	7-47
7-22.	Sensitivity to variation in $T_x:T_y$ and principal T_x orientation for the H-3 convergent-flow tracer test	7-48
7-23.	Sensitivity recalibration to observed tracer breakthrough at the H-3 hydropad to obtain maximum matrix-block lengths	7-51
7-24.	Sensitivity recalibration to observed tracer breakthrough at the H-3 hydropad to obtain minimum matrix-block lengths	7-53
8-1.	Plan view of the wells at the H-4 hydropad showing distances between wells at the center of the Culebra	8- 2
8-2.	Results of core examination of the Culebra dolomite from borehole H-4b	8- 5
8-3.	Pumping rate at well H-4c during the convergent-flow tracer test conducted at the H-4 hydropad	8- 7
8-4.	Downhole-equipment configurations for the tracer test at the H-4 hydropad	8-10
8-5.	Pressure data for the H-4 hydropad wells during the convergent-flow tracer test	8-12

Figures (Continued)

8-6.	Observed PFB and p-FB data for the convergent-flow tracer test conducted at the H-4 hydropad	8- 14
8-7.	Observed m-TFMB and SCN data for the convergent-flow tracer test conducted at the H-4 hydropad	8- 15
9-1.	Plan view of the wells at the H-6 hydropad showing distances between wells at the center of the Culebra	9- 2
9-2.	Results of core examination of the Culebra dolomite from borehole H-6b	9- 5
9-3.	Observed PFB and SCN data for two-well recirculating tracer test #1 conducted at the H-6 hydropad	9- 9
9-4.	Observed m-TFMB and p-FB data for two-well recirculating tracer test #2 conducted at the H-6 hydropad	9-11
9-5.	Pumping rate at well H-6c during convergent-flow tracer tests #1 and #2 conducted at the H-6 hydropad	9-17
9-6.	Observed PFB, m-TFMB, m-FB, and o-FB data for convergent-flow tracer test #1 conducted at the H-6 hydropad	9-19
9-7.	Observed p-FB data for convergent-flow tracer test #2 conducted at the H-6 hydropad	9-20
9-8.	Observed p-FB data for convergent-flow tracer test #3 conducted at the H-6 hydropad	9-22
9-9.	Observed PFB and SCN data for convergent-flow tracer test #4 conducted at the H-6 hydropad	9-23
9-10.	Observed m-TFMB, SCN, and p-FB data for convergent-flow tracer test #5 conducted at the H-6 hydropad	9-25
9-11.	Downhole-equipment configurations for convergent-flow tracer tests #1 and #2 at the H-6 hydropad	9-28
9-12.	Pressure data for the H-6 hydropad wells during convergent-flow tracer tests #1 and #2	9-30
9-13.	Observed and best-fit simulated breakthrough curves for H-6 convergent-flow tracer test #1 using the heterogeneous-analysis approach	9-33
9-14.	Mass distribution in the fractures and matrix and mass recovered at the pumping well for the best-fit heterogeneous simulation of the test #1 tracer-breakthrough curves for the H-6 hydropad	9-36
9-15.	Observed and best-fit simulated breakthrough curves for H-6 convergent-flow tracer test #1 using the anisotropic-analysis approach	9-38
9-16.	Mass distribution in the fractures and matrix and mass recovered at the pumping well for the best-fit anisotropic simulation of the test #1 tracer-breakthrough curves for the H-6 hydropad	9-39
9-17.	Observed and best-fit simulated breakthrough curve for H-6 convergent-flow tracer test #2 using the heterogeneous-analysis approach	9-41

Figures (Continued)

9-18.	Mass distribution in the fractures and matrix and mass recovered at the pumping well for the best-fit heterogeneous simulation of the test #2 tracer-breakthrough curve for the H-6 hydropad	9-43
9-19.	Sensitivity to matrix-block length for H-6 convergent-flow tracer test #1 . .	9-45
9-20.	Sensitivity to matrix-block length for H-6 convergent-flow tracer test #2 . .	9-46
9-21.	Sensitivity to horizontal anisotropy ($T_x:T_y$) for H-6 convergent-flow tracer test #1	9-48
9-22.	Sensitivity recalibration to observed tracer breakthrough at the H-6 hydropad to obtain maximum matrix-block lengths	9-51
9-23.	Sensitivity recalibration to observed tracer breakthrough at the H-6 hydropad to obtain minimum matrix-block lengths	9-52
10-1.	Plan view of the wells at the H-11 hydropad showing distances between wells at the center of the Culebra	10- 2
10-2.	Results of core examination of the Culebra dolomite from borehole H-11b1	10- 5
10-3.	Results of core examination of the Culebra dolomite from borehole H-11b2	10- 6
10-4.	Results of core examination of the Culebra dolomite from borehole H-11b3	10- 7
10-5.	Results of core examination of the Culebra dolomite from borehole H-11b4	10- 8
10-6.	Pumping rate at well H-11b1 during the convergent-flow tracer test conducted at the H-11 hydropad	10-12
10-7.	Downhole-equipment configuration for pumping well H-11b1 during the convergent-flow tracer test conducted at the H-11 hydropad	10-14
10-8.	Schematic illustration of the tracer-injection system used in H-11b2, H-11b3, and H-11b4 during the convergent-flow tracer test conducted at the H-11 hydropad	10-16
10-9.	Pressure data for the H-11 hydropad wells during the convergent-flow tracer test	10-18
10-10.	Observed m-TFMB, PFB, and o-TFMB data for the convergent-flow tracer test conducted at the H-11 hydropad	10-20
10-11.	Observed and best-fit simulated breakthrough curves for the H-11 convergent-flow tracer test using the heterogeneous-analysis approach . . .	10-22
10-12.	Mass distribution in the fractures and matrix and mass recovered at the pumping well for the best-fit heterogeneous simulation of the tracer-breakthrough curves for the H-11 hydropad	10-26
10-13.	Observed and best-fit simulated breakthrough curves for the H-11 convergent-flow tracer test using the anisotropic-analysis approach	10-28

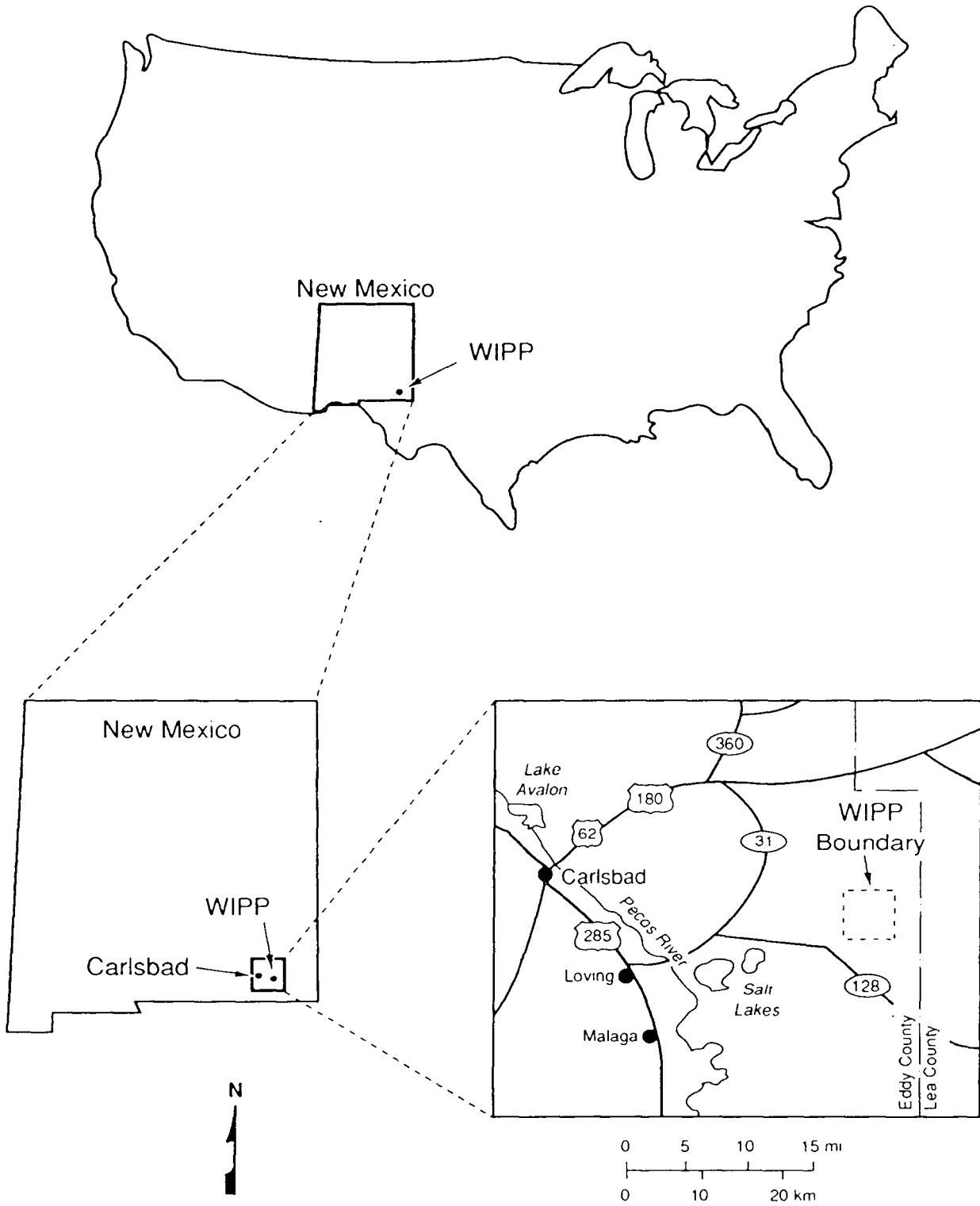
Figures (Continued)

10-14.	Mass distribution in the fractures and matrix and mass recovered at the pumping well for the best-fit anisotropic simulation of the tracer-breakthrough curves for the H-11 hydropad	10-29
10-15.	Sensitivity to matrix-block length for the H-11 convergent-flow tracer test	10-31
10-16.	Sensitivity to horizontal anisotropy ($T_x:T_y$) for the H-11 convergent-flow tracer test	10-34
10-17.	Sensitivity recalibration to observed tracer breakthrough at the H-11 hydropad to obtain maximum matrix-block lengths	10-35
10-18.	Sensitivity recalibration to observed tracer breakthrough at the H-11 hydropad to obtain minimum matrix-block lengths	10-37
11-1.	Single-porosity, fracture-system simulation of the m-TFMB breakthrough curve at the H-3 hydropad	11- 2
11-2.	Single-porosity, matrix-system simulations of the m-TFMB and PFB breakthrough curves at the H-3 hydropad	11- 5
11-3.	Single-porosity, fracture-system simulation of the PFB breakthrough curve at the H-6 hydropad	11- 6
11-4.	Single-porosity, matrix-system simulations of the PFB and m-TFMB breakthrough curves at the H-6 hydropad	11- 8
11-5.	Single-porosity, fracture-system simulation of the m-TFMB breakthrough curve at the H-11 hydropad	11-10
11-6.	Single-porosity, matrix system simulations of the m-TFMB, PFB, and o-TFMB breakthrough curves at the H-11 hydropad	11-12
12-1.	Summary of ranges of best-fit, maximum, and minimum matrix-block lengths for the H-3, H-6, and H-11 hydropads using the heterogeneous-analysis approach	12-10
12-2.	Transient calibrated \log_{10} transmissivities within the WIPP-site boundary	12-18

1.0 INTRODUCTION

Site-characterization, data interpretation, and modeling efforts have been conducted for the Waste Isolation Pilot Plant (WIPP), a U.S. Department of Energy facility, in southeastern New Mexico (Figure 1-1) as part of the evaluation of the suitability of the bedded salt of the Salado Formation for isolation of defense transuranic wastes. The Culebra Dolomite Member of the Rustler Formation is the most transmissive and laterally continuous hydrogeologic unit above the Salado Formation and is considered to be the principal offsite pathway for radionuclide transport in the subsurface, should a breach of the repository occur. The potential importance of this offsite pathway has motivated the design and implementation of tests to characterize the solute-transport properties of the Culebra dolomite. On a regional scale, long-term pumping tests have been performed and analyzed to provide information concerning the broad hydrologic flow characteristics of the Culebra dolomite. At the local (or hydropad) scale, conservative (i.e., nonreactive) tracer tests have been performed to characterize the solute-transport properties of the Culebra dolomite. Sandia National Laboratories (SNL) coordinates the site-characterization, experimental, and performance-assessment studies on behalf of the Department of Energy. The tracer-test interpretations presented in this report were performed by INTERA Inc. under contract to SNL. The tracer tests and their interpretation provide data for use in performance-assessment calculations of site suitability for waste isolation. In particular, transport parameters determined from these tests are used as input for offsite solute-transport simulations.

Conservative tracer tests have been completed in the Culebra dolomite at the H-2, H-3, H-4, H-6, and H-11 hydropads (Figure 1-2) during the period 1983 to 1988. A hydropad is a location with three to four wells located within tens of meters of each other. Two types of tracer tests have been performed at the WIPP site: convergent-flow and two-well recirculating tracer tests. Convergent-flow tracer tests were performed by pumping one well at a hydropad at a constant rate to establish a steady flow field, injecting a slug of



IRI-6330-3-3

Figure 1-1. Location of the Waste Isolation Pilot Plant (WIPP) site in southeastern New Mexico.

tracer-labelled water at each of one or more additional wells at the hydropad, and monitoring the breakthrough of each tracer at the pumping well. The two-well recirculating tracer tests involved establishing a steady flow field by pumping one well and injecting the pumped fluid into a second well, adding tracer to the injection well for a finite period, and monitoring the tracer breakthrough at the pumping well. Preliminary interpretations of the tracer tests at the H-2 hydropad and at the H-3 and H-4 hydropads have been reported in Hydro Geo Chem (1986) and Kelley and Pickens (1986), respectively. The present report summarizes the previous interpretations noted above and provides an integration of results and interpretations of all tracer tests completed in the Culebra to date.

The tracer-test analyses used the SWIFT II finite-difference code and compared model results to measured breakthrough curves. Simulations were conducted iteratively by varying parameters influencing transport within estimated bounds until the simulated breakthrough curves agreed favorably with the measured breakthrough curves. Sensitivity studies were conducted to examine the cause-and-effect relationship of varying individual parameters, to characterize uncertainty in the interpreted parameters, and to test alternative models.

The objectives of this report are to:

- Evaluate all tracer data available from the WIPP site;
- Develop an approach for interpreting the tracer test results that is consistent with geologic and hydrologic data;
- Develop values and uncertainty ranges for assigned input transport parameters for test interpretations;
- Analyze tests to obtain process information, fitted parameter values, and uncertainty in fitted parameters; and

- Evaluate implications of the tracer-test results for regional-scale transport calculations.

The report is organized into sections that describe geologic and hydrogeologic characterization of the Culebra dolomite at the WIPP site, conceptual models for tracer-test interpretation and analysis methodology selected, tracers utilized at the WIPP site, base-case and ranges of Culebra transport parameters, individual tracer tests and their interpretation including sensitivity analyses, comparison of results from single- and double-porosity conceptualizations, and summary and conclusions including implications for regional-scale transport simulations.

2.0 SITE CHARACTERIZATION

This section presents the regional geology, regional hydrogeology, and regional dissolution in the Rustler Formation based primarily on discussion and information in LaVenue et al. (1990).

2.1 Regional Geology

The WIPP site lies within the geologic region known as the Delaware Basin and specifically within the geographic region known as Los Medaños. Both the Delaware Basin and Los Medaños region occur within the southern section of the Pecos River portion of the Great Plains Physiographic Province. Los Medaños is a region of gently sloping terrain which rises eastward from the Pecos River to the western caprock of the Llano Estacado, located approximately 40 km to the northeast of the WIPP site (Mercer, 1983).

The formations which crop out in and around the WIPP site range in age from Permian to Quaternary as shown in the geologic column of Figure 2-1. The Delaware Mountain Group represents the basin facies of Permian Guadalupian age and is composed of a sequence of fine-grained clastic rocks. In the WIPP area, the Delaware Mountain Group consists of the Brushy Canyon, Cherry Canyon, and Bell Canyon Formations. The Bell Canyon consists of interbedded sandstone and shale, which represent the fore-reef facies of a massive Permian reef known as the Capitan Limestone. The Ochoan Series rocks overlie the Guadalupian Series and contain a thick evaporitic sequence that accumulated in the Delaware Basin during late Permian time. The Castile Formation is the basal formation of the Ochoan Series and is composed principally of anhydrite and halite with some carbonates and sandstones. Overlying the Castile is the Salado Formation, which contains the WIPP repository (Figure 2-2). The Salado is composed of thick beds of halite

SYSTEM	SERIES	GROUP	FORMATION	MEMBER
RECENT	RECENT		SURFICIAL DEPOSITS	
QUATERNARY	PLEISTOCENE		MESCALERO CALICHE	
			GATUÑA	
TRIASSIC		DOCKUM	UNDIVIDED	
PERMIAN	OCHOAN		DEWEY LAKE RED BEDS	
			RUSTLER	Forty-niner
				Magenta
				Tamarisk
				Culebra
				Unnamed
			SALADO	Upper
	McNutt			
	Lower			
	CASTILE			
	GUADALUPIAN	DELAWARE MOUNTAIN	BELL CANYON	
			CHERRY CANYON	
			BRUSHY CANYON	

Figure 2-1. Geologic column representative of WIPP area.

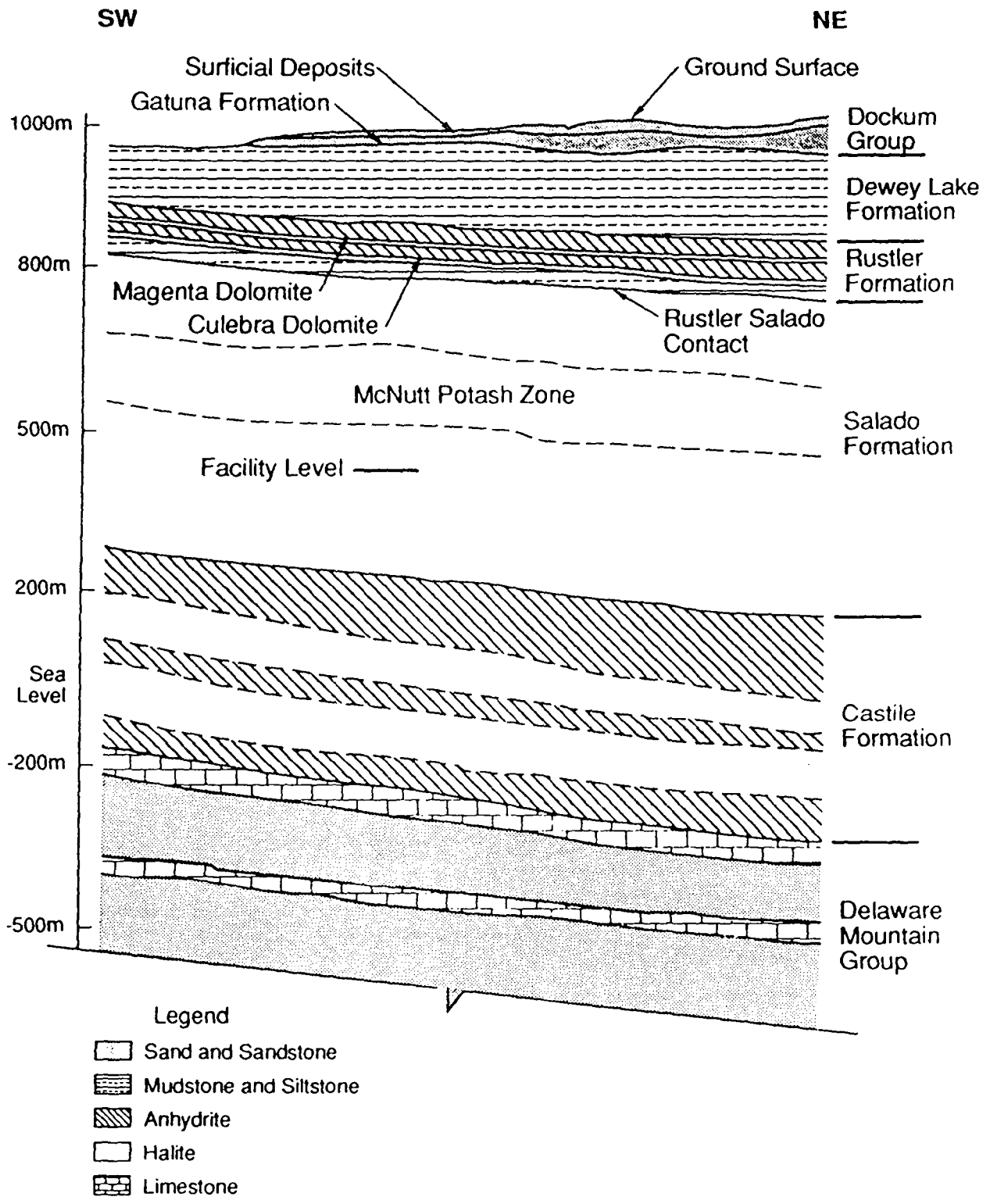


Figure 2-2. Generalized geologic cross section (after Deal et al., 1991).

interbedded with anhydrite, polyhalite, dolomite, and clay. More complete descriptions of the Salado Formation are found in Jones (1975) and Jones et al. (1973).

Overlying the Salado Formation is the Rustler Formation, which is the most water-transmissive formation in the area (Mercer, 1983). The Rustler Formation has been divided into five separate members based upon lithology (Vine, 1963). They are, in ascending order: (1) an unnamed lower member composed of massive siltstone overlain by beds of halite, siltstone, and anhydrite; (2) the Culebra Dolomite Member; (3) the Tamarisk Member, composed of two zones of massive to bedded anhydrite separated by a sequence of halite and siltstones; (4) the Magenta Dolomite Member; and (5) the Forty-niner Member, composed of two anhydrite zones separated by a silty-halite unit, as in the Tamarisk. The Rustler Formation lithology presented above represents the lithological succession encountered in borehole P-18, which Snyder (1985) believes to be a complete unaltered section. The Rustler lithology varies across the model area due to differences in depositional facies and locally to post-depositional dissolution of halite (Section 2.3).

The Rustler Formation is conformably overlain by the Upper Permian Dewey Lake Red Beds, a series of interbedded siltstones and sandstones. These beds have abundant horizontal to subhorizontal fractures that are generally gypsum filled (Holt and Powers, 1990a).

In the eastern portion of the WIPP site, the Dewey Lake Red Beds are unconformably overlain by a Triassic clastic sequence deposited in a transitional depositional complex of fluvial, deltaic, and lacustrine environments. These units are collectively referred to as the Dockum Group.

Overlying the Dockum Group, where present, and the Dewey Lake Red Beds in the WIPP-site area is a sequence of poorly sorted continental deposits of Quaternary age. These are, in ascending order, the Gatuña Formation, the Mescalero caliche, and recent alluvium and other surficial deposits. The Gatuña Formation consists of a sequence of

pale reddish-brown terrestrial sandstones and conglomerates that were laid down after a maximum cycle of erosion within the Pecos River Valley during a much more humid pluvial time (Bachman, 1980). Izette and Wilcox (1982) dated an ash bed in the upper portion of the Gatuña as middle Pleistocene (600,000 yrs before present) by mineralogy and fission-track dating.

Overlying the Gatuña Formation is the Mescalero caliche, which is a pedogenic caliche formed in the C horizon of a paleosol during a tectonically and climatically stable period following the deposition of the Gatuña Formation (Bachman, 1980). The Mescalero caliche has been dated as being Pleistocene (510,000-410,000 yrs before present) through uranium-series disequilibrium techniques (Bachman, 1980). Overlying the caliche is a series of Holocene surficial deposits that consist of sheetlike deposits of surface sand, sand soil, and sand dunes.

2.2 Regional Hydrogeology

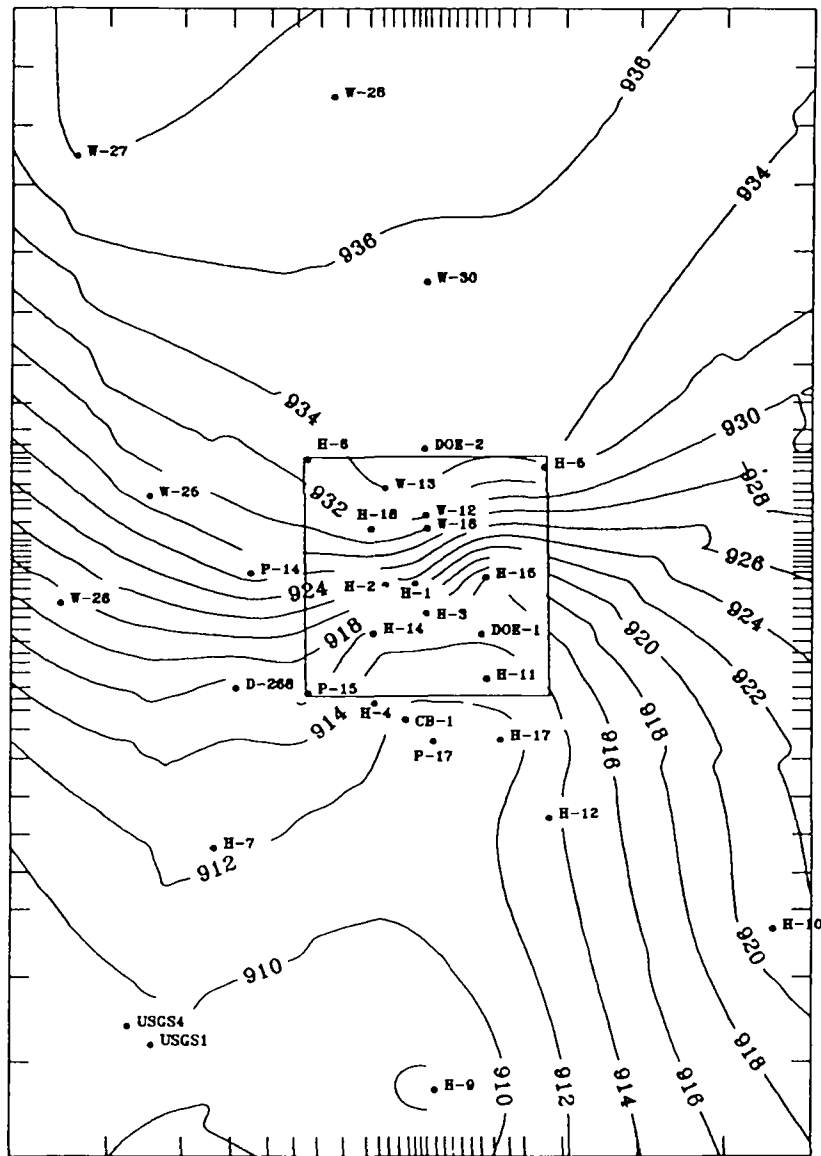
The discussion of the regional hydrogeology in this report is limited to the Rustler Formation and its contact with the Salado Formation. The hydrogeology of the individual hydrostratigraphic units is discussed in ascending order from the Rustler-Salado contact.

The Rustler-Salado contact is transmissive in some areas around the WIPP site (Mercer, 1983). In Nash Draw and areas immediately west of the WIPP site, the contact exists as a dissolution residue capable of transmitting water. Robinson and Lang (1938) referred to this residuum making up the contact as a "brine aquifer." As one moves eastward from Nash Draw toward Livingston Ridge (Figure 1-2), dissolution in the uppermost Salado, at the Rustler-Salado contact, and within the unnamed lower member of the Rustler Formation decreases and the transmissivity of this interval decreases. Transmissivities for the Rustler-Salado contact range from 2×10^{-10} to 9×10^{-6} m²/s in Nash Draw and from 3×10^{-11} to 5×10^{-8} m²/s eastward from Livingston Ridge (Mercer, 1983).

At well DOE-2, Beauheim (1986) attempted a slug test on the unnamed lower member and the Rustler-Salado contact and found that the permeability in this interval was too low to be tested effectively. In the Waste-Handling Shaft located at about the center of the WIPP site, no water inflows from this interval were observed during excavation and shaft mapping (Holt and Powers, 1984). At H-16, Beauheim (1987a) performed drill-stem tests on a 34-m interval including the unnamed-lower-member siltstone and the Rustler-Salado contact, and reported the transmissivity of this interval to be about $3 \times 10^{-10} \text{ m}^2/\text{s}$.

The Culebra dolomite is considered to be the most transmissive laterally continuous hydrogeologic unit in the WIPP-site area. The data base for the Culebra and a listing of data sources are presented in Cauffman et al. (1990), which includes data for transmissivity, storativity, formation-fluid density, borehole locations, ground-surface and Culebra elevations, and undisturbed and transient equivalent freshwater heads. This data base was used in the development of a calibrated ground-water flow model by LaVenue et al. (1990). LaVenue et al. (1990) present kriged surfaces for the Culebra-center elevations (Figure 2-3), combined steady-state and transient calibrated transmissivity distribution (Figure 2-4), undisturbed freshwater heads (Figure 2-5), and formation-fluid densities (Figure 2-6). The Culebra has higher elevations in the western part of the WIPP region and lower elevations in the east and southeast. Within the model area presented in LaVenue et al. (1990), transmissivities range from 1×10^{-10} to $1 \times 10^{-3} \text{ m}^2/\text{s}$ (Figure 2-4). Transmissivities tend to decrease from west to east with locally high transmissivities around and southward from the DOE-1 and H-11 boreholes. Hydraulic gradients in the Culebra at the WIPP site generally range from 1×10^{-3} to $4 \times 10^{-3} \text{ m/m}$, based on the equivalent freshwater head distribution for undisturbed conditions (Figure 2-5). As a general trend, total dissolved solids in Culebra ground waters increase from west to east across the WIPP site and the model area (Figure 2-6).

The offsite travel paths within the Culebra from release points located above the corners and center of the waste-storage-panel region are illustrated in Figure 2-7. These pathways were determined using a particle-tracking code in conjunction with the Darcy-



● Observation Well
 Freshwater Heads in m amsl
 Contour Interval: 2m

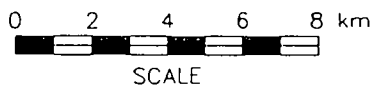
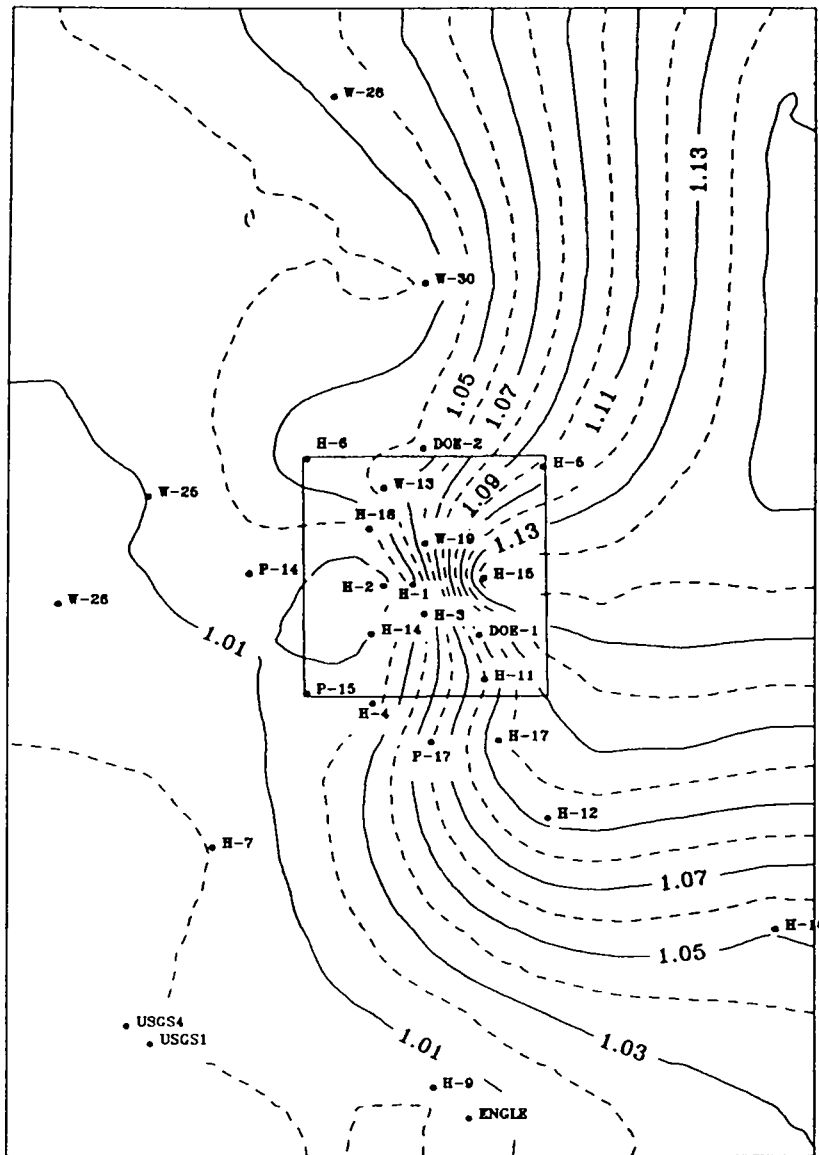


Figure 2-5. Culebra freshwater-head contour surface (from LaVenue et al., 1990).



• H-8

• Observation Well

Formation-Water Densities in g/cm^3

Contour Interval: 0.01 g/cm^3

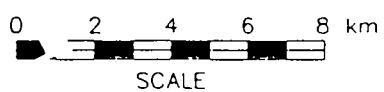
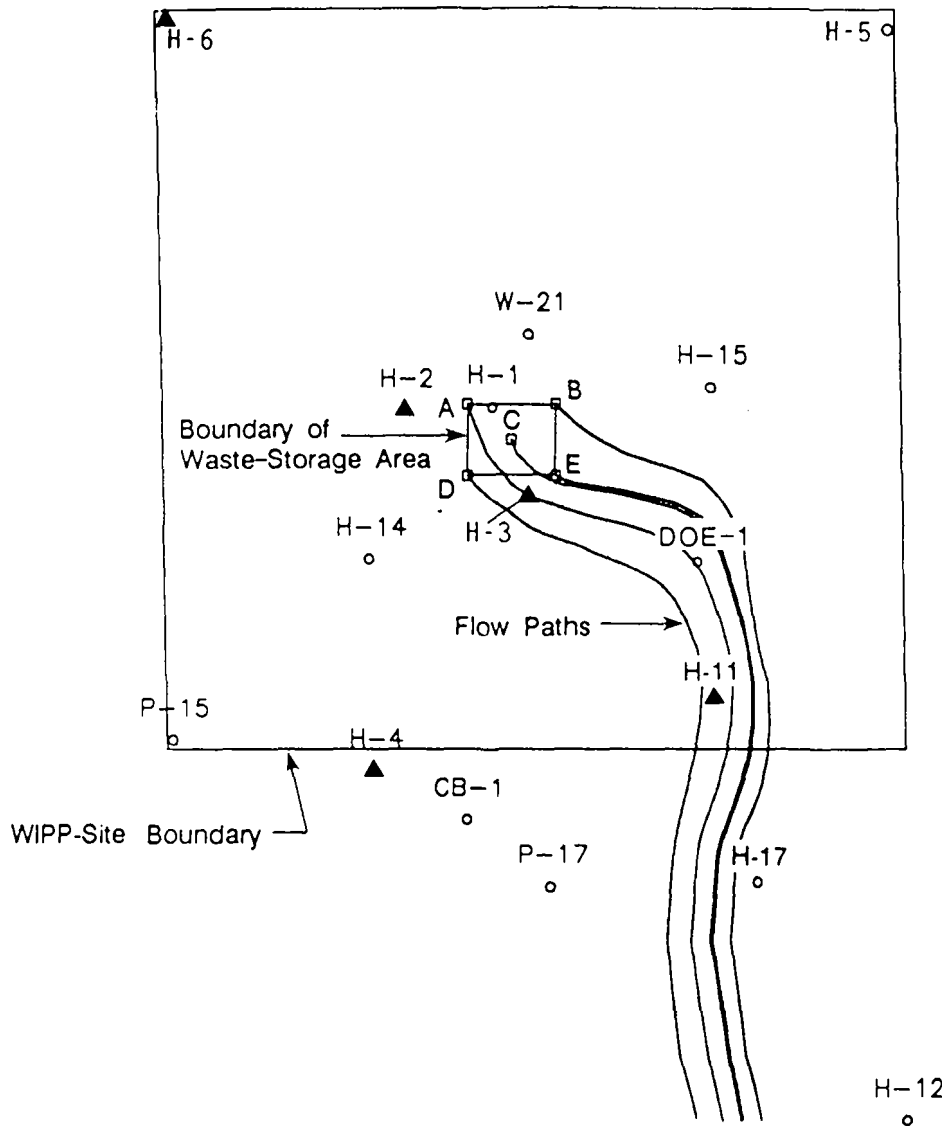


Figure 2-6. Kriged Culebra formation-fluid densities (from LaVenue et al., 1990).



Calculated Particle Travel Times (yrs)

<u>Particle</u>	<u>WIPP Boundary</u>
A	12,800
B	21,000
C	14,200
D	12,100
E	12,400

LEGEND


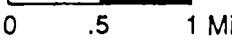
- 0 1 2 Kilometers

 0 .5 1 Miles

- WIPP-Site Observation Wells or Hydropads
 - ▲ Tracer-Test Hydropad Locations

Figure 2-7. Identification of pathways within the Culebra dolomite from release points above the corners and center of the waste-storage area (after Reeves et al., 1991).

velocity distribution for the undisturbed flow field calibrated by LaVenue et al. (1990). The calculated particle travel times from the five release points to the WIPP-site boundary are tabulated on Figure 2-7. By definition, particle travel times are calculated using the Darcy-velocity distribution and a selected porosity. The particle travel times shown on Figure 2-7 are based on an assumed total (fracture-plus-matrix) porosity of 0.1615 (0.16 matrix porosity plus 0.0015 fracture porosity). Figure 2-7 illustrates that the H-3 and H-11 hydropads, where tracer tests have been performed, are located along the expected offsite pathway in the Culebra from release points that originate above the waste-storage panels.

The Tamarisk Member of the Rustler separates the Culebra dolomite from the Magenta, and is composed of a sequence of halite and siltstones sandwiched between upper and lower anhydrites. The Tamarisk siltstone sequence has been tested at wells H-14 and H-16 (Beauheim, 1987a) and at DOE-2 (Beauheim, 1986). In all cases, the hydraulic testing was unsuccessful due to the extremely low permeability of the unit. Mercer (1983) reported that in a few cases argillaceous zones within the Tamarisk Member have produced water at rates equivalent to the Magenta upon testing.

Ground water in the Magenta dolomite generally flows from the north toward the west-southwest (Mercer, 1983). In most areas east of Nash Draw, and east and south of the H-6 hydropad, the Magenta exists as a confined system with low transmissivity (less than or equal to $2 \times 10^{-7} \text{ m}^2/\text{s}$) (Mercer, 1983; Beauheim, 1987a; Beauheim et al., 1991). The difference between Magenta and Culebra hydraulic potentials generally increases eastward, with the Magenta having higher potentials. In areas of Nash Draw, the Magenta is generally at water-table conditions and may be in hydraulic connection with other units in the Rustler Formation due to the absence of Rustler halite within the Nash Draw area. In other parts of Nash Draw, the Magenta is unsaturated. Magenta transmissivities of $4 \times 10^{-4} \text{ m}^2/\text{s}$ have been reported at WIPP-25 in Nash Draw (Mercer, 1983).

The uppermost member of the Rustler Formation, the Forty-niner, has claystones which are more transmissive than those in the Tamarisk Member. At well H-14, Beauheim

(1987a) performed drill-stem tests upon the Forty-niner and determined that transmissivities were approximately an order of magnitude higher than in the Magenta at H-14. The average value of transmissivity calculated for the Forty-niner at H-14 was $6 \times 10^{-8} \text{ m}^2/\text{s}$ as opposed to $6 \times 10^{-9} \text{ m}^2/\text{s}$ for the Magenta. Beauheim (1986) also tested the Forty-niner claystone in well DOE-2. Here again, he calculated slightly higher transmissivities for the Forty-niner claystone than for the Magenta. The average of the two transmissivities of the Forty-niner reported by Beauheim (1986) for DOE-2 is $7.3 \times 10^{-9} \text{ m}^2/\text{s}$. Drill-stem tests of the Forty-niner claystone at H-16 provided a transmissivity estimate of about $6 \times 10^{-9} \text{ m}^2/\text{s}$, lower than that of the Magenta at H-16 (Beauheim, 1987a). At H-3d, Beauheim et al. (1991) obtained a transmissivity estimate of about $4 \times 10^{-9} \text{ m}^2/\text{s}$ from a pulse test and a slug test on the Forty-niner claystone.

2.3 Post-Depositional Alteration of the Rustler Formation

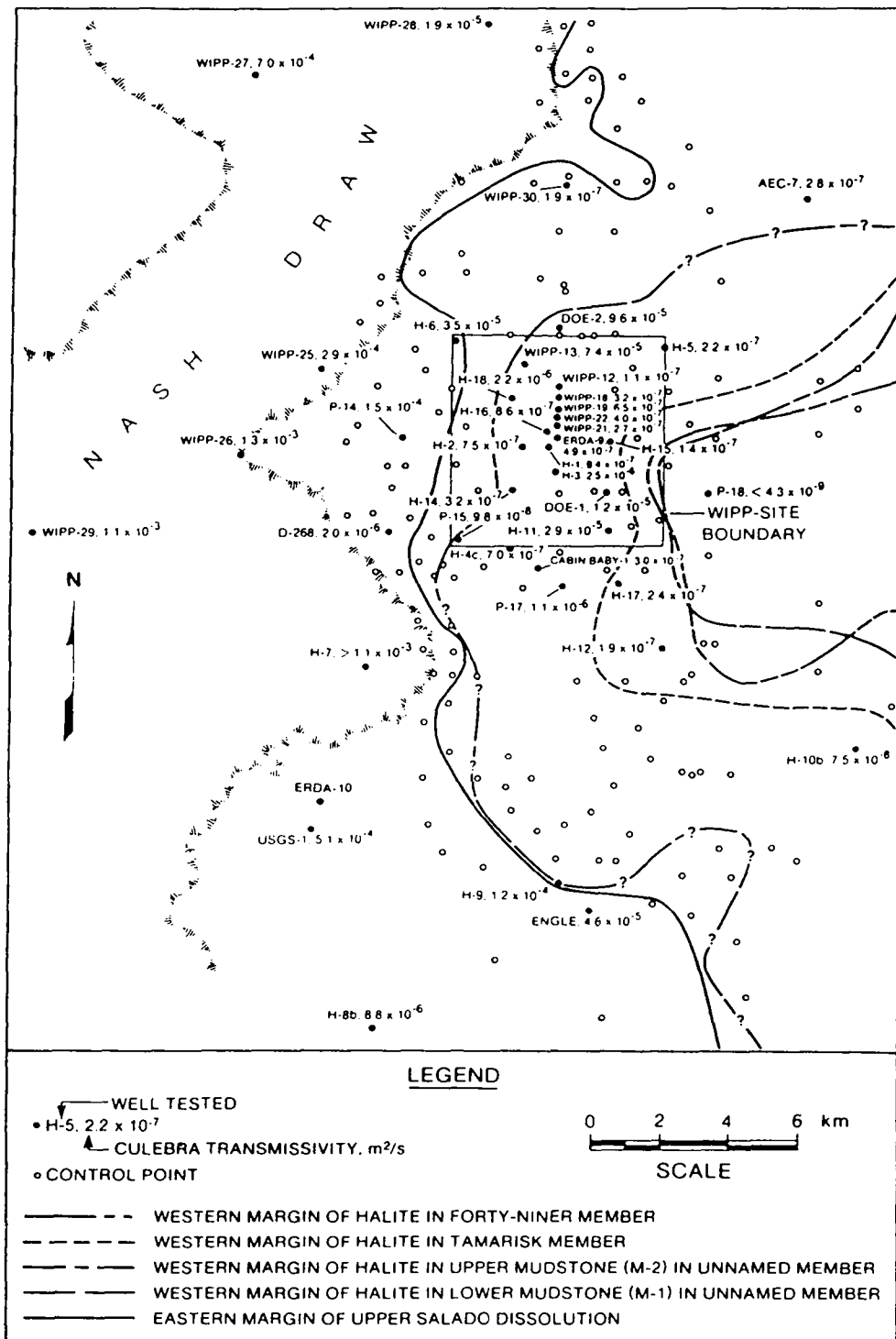
The primary processes that have affected the Rustler Formation since its deposition are dissolution and erosion. Bachman (1980) identified three types of dissolution occurring in the Delaware Basin: local, regional, and deep-seated. Of these, regional dissolution is the type that has the most potential to dictate or alter the flow characteristics of the Rustler Formation underlying the WIPP site. Regional dissolution occurs when chemically unsaturated water penetrates to permeable beds, where it migrates laterally, dissolving the soluble units it contacts. On a regional scale, the consequence of such dissolution appears to be removal of highly soluble rock types, such as halite, combined with displacement and fracturing of overlying rocks.

Bachman (1987) observed evidence for dissolution within the upper Salado Formation and/or the Rustler Formation both at the surface within Nash Draw, and in the subsurface at the WIPP site. Nash Draw, located immediately west of the WIPP site (Figure 1-2), is a topographic depression resulting from both dissolution and erosion. In Nash Draw, members of the Rustler and the upper Salado are actively undergoing

dissolution and locally contain caves, sinks, and tunnels typical of karst morphology in evaporitic terrane.

Snyder (1985) cites evidence for the presence of an eastward-migrating dissolution front within the Rustler Formation at the WIPP site. In his study, Snyder (1985) concludes that the regional dissolution was greatest in the west, in Nash Draw, and decreased eastward, as evidenced by an increase in the number and thickness of halite beds and a corresponding thickening of the Rustler Formation (Figure 2-8). The stratigraphic level of the uppermost occurrence of salt is in the upper Rustler along the eastern margin of the WIPP site. Moving westward toward Nash Draw, the uppermost salt is found in progressively deeper horizons of the Rustler. Snyder (1985) believes that, as a general trend, the eastward advancement of the dissolution front is greatest in the upper Rustler and decreases toward the Rustler-Salado contact. As the halite units are dissolved, insoluble residues remain, forming beds of mudstone, siltstone, and chaotic breccia with a clay matrix. As can be seen in a cross section taken between boreholes P-6, H-3, DOE-1, and P-18 (Figure 2-9), halite beds tend to thin and grade into argillaceous zones westward toward Nash Draw.

Lowenstein (1987) conducted a detailed analysis on core from wells DOE-2, WIPP-19, H-11, and H-12 to distinguish between syndepositional features and post-depositional alteration features within the Rustler. He correlated structures, both syndepositional and post-depositional, over the study area and concluded that facies changes were not responsible for the westward decrease in halite within the Rustler in the study area. Lowenstein (1987) found evidence of late-stage alteration involving physical processes such as small-scale brecciation, slumping, fracturing, and faulting, as well as chemical processes such as rehydration of anhydrite to gypsum, precipitation of gypsum, and dissolution of halite, anhydrite, and gypsum. He attributed the late-stage alteration to the introduction into the Culebra of waters undersaturated with respect to halite and gypsum, which progressively invaded underlying and overlying units. Thus, the study of Lowenstein (1987) supports the theory of post-depositional dissolution of salt in the Rustler.



TRI-6330-94-0

Figure 2-8. The occurrence of halite beds within the Rustler Formation (from Lappin et al., 1989).

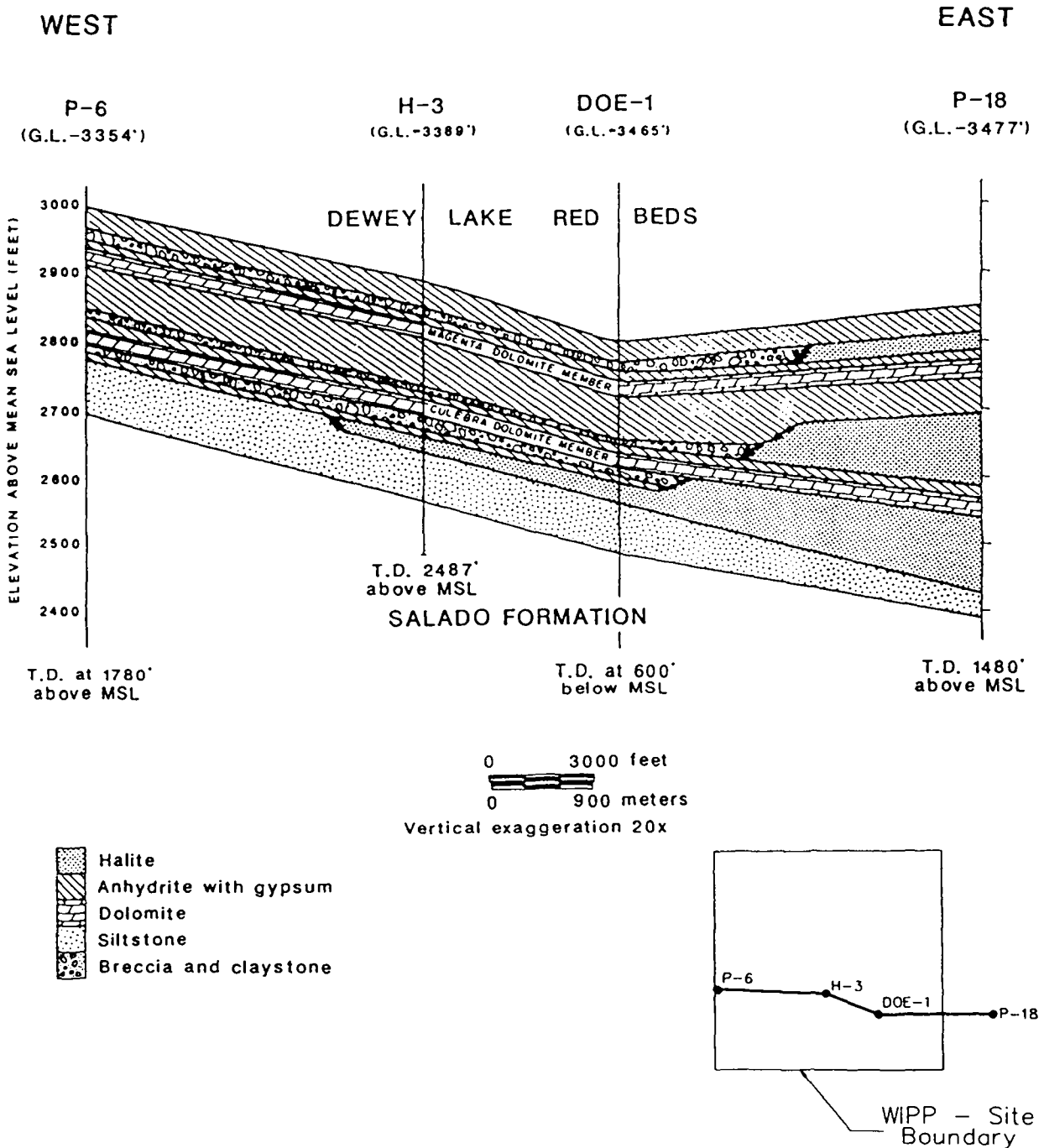


Figure 2-9. Stratigraphic cross section of the Rustler Formation west to east across the WIPP site (after Chaturvedi and Channell, 1985).

While dissolution may have been an active process within the Rustler and/or the Salado in the past, whether or not this dissolution is still active is uncertain. Within the last 1.8 million yrs (Pleistocene), the climate in southeastern New Mexico has varied between periods of cold, moist continental glaciation and relatively warm, arid periods (Bachman, 1987). In middle Pleistocene time, approximately 500,000 yrs before present, southeastern New Mexico received precipitation well in excess of evapotranspiration. This period was followed by several hundred thousand years of a drier climate. In late Pleistocene time (approximately 75,000 to 10,000 yrs before present), rainfall was more prevalent than today and temperatures were lower (Bachman, 1987). Bachman thinks that most of the dissolution in the Rustler predates, or occurred during, middle Pleistocene (Gatuña) time. However, he suggests that dissolution is ongoing in Nash Draw and areas very close to Livingston Ridge (Figure 1-2). The interpretation of radiocarbon data (Lambert, 1987) and stable isotopes (Lambert and Harvey, 1987; Lambert, 1987) has suggested that recharge and subsequent dissolution of the Rustler ended after the more pluvial late Pleistocene (20,000 to 10,000 yrs before present).

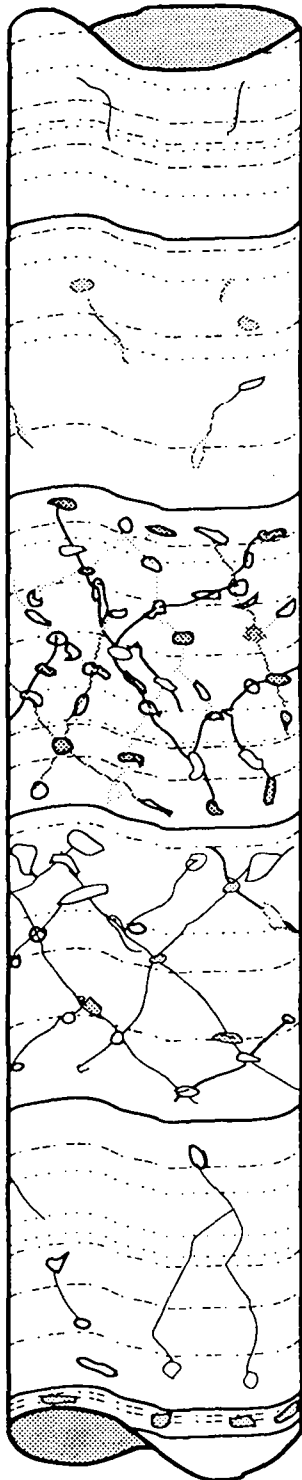
Although many investigators agree with the interpretation that a dissolution zone exists in the Rustler Formation at the WIPP site (Cooper and Glanzman, 1971; Powers et al., 1978; Mercer, 1983; Chaturvedi and Rehfeldt, 1984; Bachman, 1985; Snyder, 1985; Lowenstein, 1987), other investigators oppose this concept and think that the westward decrease of halite within the Rustler simply represents depositional limits (Powers and Holt, 1984; Holt and Powers, 1988; Beauheim and Holt, 1990). Holt and Powers (1984, 1986, 1990b) performed detailed mapping in the Waste-Handling, Exhaust, and Air-Intake Shafts at the WIPP site and reported no post-depositional features, such as upward stoping and collapse above supposedly dissolved units, in any of the stratigraphic horizons. In addition, they found pronounced primary sedimentary features in several zones that had previously been identified as dissolution residues in several boreholes near the shafts (Holt and Powers, 1984).

Holt and Powers (1988) expanded their earlier work by analyzing geophysical logs and re-examining Rustler cores from the WIPP-site area. This study presented a detailed depositional model for the Rustler Formation ranging from shallow lagoons and subtidal environments to shallow saline pans and environments marginal to the saline pan. Holt and Powers (1988) propose that part of the Rustler formed when fresher water transgressed over the Salado, depositing clastics, carbonates, or subaqueous sulfates. As transgressing water evaporated, halite was deposited, forming lenticular units with the thickest part south and east of the WIPP site, in the depocenter. Halite in the halite and mudstone units at small to large scales was dissolved syndepositionally. After a transgression, and in some cases continuing after overlying sediments were deposited, halite was subjected to dissolution by less saline water. This dissolution would cause deformation and slumping in the overlying sediment. When the water table in the margins was lowered by subsidence or evaporation, halite was dissolved by meteoric water in the vadose zone and redeposited in the depocenter. Thus, the present-day distribution of halite in the Rustler at the WIPP site may reflect only original depositional variations coupled with syndepositional dissolution, and not late-stage dissolution as recent as Pleistocene time.

Significant erosion has occurred at the WIPP site since Permian time. The present-day thickness of the Permian Dewey Lake Red Beds ranges from 165 m east of the WIPP site at P-18 to 105 m west of the WIPP site at P-14 (Figure 1-2). Mercer (1983) attributes the difference in Dewey Lake thickness across the WIPP site to erosion. Similarly, the Triassic Dockum Group is 173 m thick at H-10, 66 m thick at H-5, 3 m thick at ERDA-9, and entirely absent over the western portion of the WIPP site. The Miocene-age Ogallala Formation has been entirely eroded over the WIPP site. Erosion of these units has reduced the overburden stress on underlying units, potentially allowing fractures to open.

2.4 Characterization of the Culebra Dolomite

The WIPP shafts are the only locations where complete exposures of the Culebra unaltered by surface weathering have been available for observation and description. Holt and Powers (1990b) describe the Culebra dolomite at the WIPP Air-Intake Shaft as "an argillaceous dolomicrite containing abundant open and gypsum-filled porosity." They divided the 7.3-m-thick Culebra into six map units (Figure 2-10). The upper 1.1 m (unit 1) consists of thinly laminated and bedded argillaceous dolomite with no vugs and few fractures. The underlying unit 2, 1.4 m thick, consists of microcrystalline, argillaceous dolomite that is thinly laminated to thinly bedded. Large vugs are rare, and most of those that exist are unfilled. Most of the fractures present are filled with gypsum. The underlying 1.7 m (unit 3a) consists of extensively fractured dolomite that produced more water into the shaft than the other map units. The dolomite is laminated to thin bedded, and its texture is dominated by abundant vugs. The vugs are as large as 7.6 cm in diameter. Most of the vugs are partially to completely filled with clay, although some are filled with gypsum and others are open. Half of the abundant subvertical to vertical fractures are filled with gypsum and half are open. Fractures 5 to 10 cm long interconnect all vugs. Map unit 3b is 1.5 m thick. It is laminated and contains abundant vugs that decrease in size downward. Most of the vugs are open or are filled with clay. Few vugs contain gypsum. Subvertical fracturing between vugs is extensive. Holt and Powers (1990b) describe units 3a and 3b as packbreccias due to the extensive fracturing between vugs. The underlying 1.5 m (unit 3c) consists of thinly laminated to very thinly bedded dolomite. Fractures and large vugs are less abundant than in the overlying units. The lower 0.15 m of the Culebra (unit 4) consists of laminated, locally brecciated dolomite. The Culebra is underlain by a mudstone unit 1.7 m thick. The contact between the Culebra and this mudstone undulates by as much as 0.8 m in the Air-Intake Shaft. Except for the degree of fracturing, the amounts and types of vugs and fracture fillings, and individual unit thicknesses, which vary with location, this description of the Culebra from the Air-Intake Shaft is representative of the Culebra over the entire WIPP site.



Unit 1 - Thinly laminated and argillaceous dolomite; no vugs and few fractures.

Unit 2 - Thinly laminated and thinly bedded, microcrystalline, argillaceous dolomite; few vugs; most fractures gypsum filled.

Unit 3a - Laminated to thinly bedded dolomite; abundant vugs; extensive subvertical to vertical fracturing; about half of fractures gypsum filled and rest are open; fractures interconnect all vugs.

Unit 3b - Laminated dolomite; abundant vugs that decrease in size downward; extensive subvertical facturing between vugs.

Unit 3c - Thinly laminated to very thinly bedded dolomite; less abundant fracturing and vugs.

Unit 4 - Locally brecciated dolomite with undulations.

TRI-6344-834-0

Figure 2-10. Schematic diagram of the map units in the Culebra dolomite in the Air-Intake Shaft.

Based upon observations of outcrops, core, and shaft exposures, fracturing within the Culebra appears to be ubiquitous over the WIPP site. However, the fracturing is not hydraulically significant at all locations. Fractures tend to be closed or filled with gypsum in the northeastern (H-5, H-15, WIPP-12), central (H-1, H-2, ERDA-9, WIPP-21), and southwestern (H-4, H-14, P-15) portions of the WIPP site. At these locations, fractures appear to have little effect on either ground-water flow or solute transport. Where fractures are open and fillings are absent or have been dissolved, such as in the northwest (H-6, WIPP-13, DOE-2) and southeast (H-3, H-11, DOE-1) portions of the WIPP site, fractures significantly enhance ground-water flow and solute transport.

The fracturing and development of secondary porosity within the Culebra are thought by some investigators to be a product of late-stage alteration and dissolution of the Rustler Formation (Mercer, 1983; Chaturvedi and Channell, 1985; Snyder, 1985; Bachman, 1985; Lowenstein, 1987). By this theory, halite dissolution caused foundering and collapse of the more competent dolomitic members, resulting in fracturing that increased their transmissivities. This theory implies that the Culebra should be fractured and transmissive everywhere that halite is missing from the unnamed lower member of the Rustler. However, as shown on Figure 2-8, halite is absent from the mudstone (M-2) directly underlying the Culebra over the entire WIPP site and from the lower mudstone (M-1) in the unnamed lower member over most of the WIPP site, and yet the transmissivity of the Culebra varies over three orders of magnitude over the same area. The dissolution model also implies that the Culebra should be well-connected hydraulically to overlying and underlying units by fractures created during subsidence and collapse. Evidence for vertical communication between Rustler members is lacking, however, even at locations such as H-3 and H-6 where fracturing is significant in the Culebra.

Beauheim and Holt (1990) concur with the opinion that dissolution of Rustler evaporites and the upper Salado in and around Nash Draw has resulted in collapse and fracturing of the Culebra. However, they see little evidence for post-depositional dissolution of Rustler halite at the WIPP site except along halite depositional margins. They attribute

most fracturing in other locations to stress relief from unloading caused by erosion of overburden. The stress relief may have activated pre-existing planes of weakness, such as syndepositional faults or slumps and bedding planes. The effects of the erosional unloading may have been amplified by deformation of the pliable mudstone underlying the Culebra. Fracturing in the Culebra may also be related to dissolution of vug and fracture fillings. After formation, some Culebra fractures and vugs were filled by precipitation of gypsum and/or anhydrite from solution. These fracture and vug fillings may have been locally dissolved by influxes of relatively fresh water into the Culebra during the Cenozoic. Dissolution of these fillings may have structurally weakened the Culebra, resulting in increased fracturing at those locations.

In summary, the Culebra is a laminated to thinly bedded dolomite containing abundant vugs. Fractures are also abundant in the Culebra, and typically interconnect vugs. Vugs and fractures may be open, or they may be partially or completely filled with clay, gypsum, or anhydrite. Fracturing of the Culebra dolomite may, depending on location, be related to Salado dissolution, Rustler dissolution, erosional unloading, and/or dissolution of pore-filling material. Whatever the exact cause(s) of fracturing in the Culebra may be at a particular location, the factor controlling the present-day significance of fractures with respect to ground-water flow and transport is the presence or absence of fracture-infilling material.

3.0 TRACER-TEST INTERPRETATION METHODOLOGY

This section discusses characterization of fracturing in the Culebra, fracture/matrix interactions during hydraulic and tracer tests, single- and double-porosity transport conceptualizations, verification of the transport model SWIFT II, and the methodology used for tracer-test analyses.

3.1 Transport Conceptualizations for the Culebra

The following subsections describe the physical characteristics of the Culebra pertinent to transport and a variety of conceptual models that may be appropriate as the basis for transport simulations.

3.1.1 Characterization of Fractures in the Culebra

As described in Section 2.4, the Culebra is a vuggy, fractured dolomite. Depending on location, the fractures within the Culebra may be open or closed (healed), and they may or may not contain clay or gypsum filling. The presence or absence of infilling material in the fractures has a strong influence on the local flow and transport properties of the Culebra. Information on the characteristics of fractures within the Culebra at the WIPP site comes from:

- examination of core from boreholes;
- mapping of exposed Culebra in the shafts;
- interpretation of hydropad-scale hydraulic tests; and
- interpretation of hydropad-scale tracer tests.

At least two factors should be considered when reviewing fracture data based on core descriptions. First, there may be mechanical destruction of the in-situ physical character of the rock due to the process of coring. For example, the fracture surfaces and near-fracture matrix material may disintegrate and/or the core may break into a larger number of pieces due to the mechanical stresses of the drilling operation. Second, due to poor core recovery in incompetent or highly fractured zones, fracture frequency or the presence of fractures may be underestimated.

For all of the hydropads investigated by tracer tests, examination of the core revealed the presence of fractures. The fractures present in core from the H-2 and H-4 hydropads are generally gypsum filled and the fractures present in core from the H-3, H-6, and H-11 hydropads generally vary from open to gypsum filled. Further information on core descriptions of the Culebra is presented in later sections describing the tracer tests at these hydropads.

Beauheim and Holt (1990) summarized fracture-characterization studies based on visual examination of core and three shafts at the center of the WIPP site. They report:

"Culebra cores yield little information concerning the degree of fracturing due to variable core recovery and zones of poor recovery. Culebra descriptions from three shafts at the WIPP show that the majority of the fractures at the WIPP site [shafts] are subvertical and occur within a very vuggy zone near the base of the Culebra (Holt and Powers, 1984, 1986, 1990[b]). These fractures usually extend from vug to vug (Holt and Powers, 1990[b]). This zone can be recognized within Culebra cores as a zone of poor or no recovery. Horizontal fractures, parallel to bedding planes, occur throughout the Culebra in core and the WIPP shafts (Holt and Powers, 1984, 1986, 1990[b]). High-angle subvertical fractures are commonly intersected in core near the upper part of the Culebra and may be vertically persistent for several feet. As these nearly

vertical fractures are common, the density of these fractures must be relatively high, at least locally."

The shafts are located north of the H-3 hydropad and northeast of the H-2 hydropad. Culebra transmissivity at the location of the shafts is similar to that occurring at the H-2 hydropad and about one order of magnitude less than that occurring at the H-3 hydropad. Considering the much higher transmissivity present at the H-3 hydropad, fracturing at that hydropad is potentially more extensive than at the shaft locations, more open fractures may be present, or a combination of both.

In addition to being fractured, the Culebra dolomite contains a relatively large matrix porosity. Measurements of porosity on Culebra core yield values of 3 to 30 percent with an average of 15 percent. The presence of large porosities creates the potential for significant interaction between fractures and matrix during flow and transport. A fractured porous medium in which both fractures and matrix components are hydraulically active is commonly referred to as a double-porosity medium.

Interpretations of pumping tests conducted at the H-3 hydropad in 1984 and 1985 indicate that the Culebra dolomite behaves as a double-porosity medium at that location and that "H-3b1 and H-3b3 appear to be very well connected by fractures" (Beauheim, 1987b). Based on the hydraulic responses from the H-11 multipad/tracer test, Beauheim (1989) concluded that the Culebra is a "double-porosity medium" at the H-11 site and that the area between H-3 and H-11 contains hydrologically significant fractures as well. Beauheim (1987c) reports that the Culebra dolomite is also a fractured system around the H-6 hydropad. Hydraulic testing at the H-2 and H-4 hydropads has shown no indication of double-porosity behavior; the test responses are well represented by single-porosity, porous-medium models. The following general conclusions can be drawn from the examination of core and analysis of pumping tests at the WIPP site: (1) cores collected at locations with estimated transmissivities of about 10^{-6} m²/s or greater contain abundant open fractures and

(2) at these same locations, pumping tests yield hydraulic responses in the Culebra that are characteristic of a double-porosity medium.

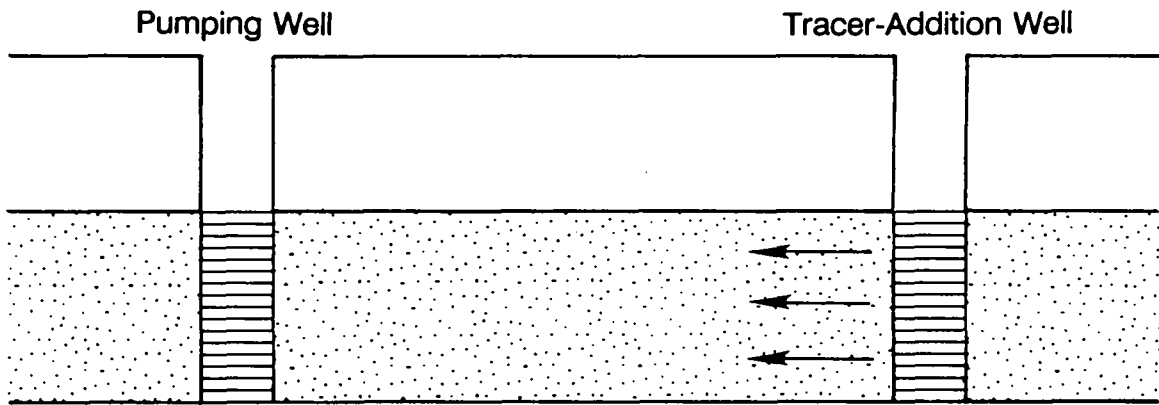
Breakthrough curves obtained from convergent-flow tracer tests conducted at the H-3, H-6, and H-11 hydropads indicate rapid transport along one of the flow paths tested at each of these hydropads. Interpretations of these tracer tests were performed using a double-porosity conceptualization for the Culebra dolomite and yielded good fits between the observed and simulated data. The rapid transport that occurred on at least one flow path at each hydropad and the good fits obtained for the double-porosity conceptualization provide evidence that transport has occurred through a fracture system and that diffusion of tracer into the adjacent matrix has occurred. Significant quantities of the tracers would be expected to diffuse from the fractures to the matrix because of the relatively high matrix porosities (0.10 to 0.30) measured on Culebra core samples from these hydropads. A complete discussion of interpretations of the convergent-flow tracer tests is provided in later sections of this report.

In summary, both the presence of open fractures and their importance to both hydrologic responses and solute transport have been identified for the H-3, H-6, and H-11 hydropads. Fractures do not appear to be of hydraulic or transport significance for the H-2 and H-4 hydropads.

3.1.2 Single- and Double-Porosity Transport Conceptualizations

Various conceptualizations for describing single- and double-porosity solute transport in the Culebra dolomite have been considered (Figure 3-1). Figures 3-1a and 3-1b illustrate transport in a homogeneous system consisting of either a nonfractured porous medium or a system of fractures only. If one considers vertical heterogeneity, these cases may be generalized to the layered or multipermeability single-porosity scenarios shown in Figures 3-1c and 3-1d. For locations exhibiting double-porosity behavior, Figures 3-1e and

(a) Single-porosity porous medium



(b) Single-porosity fracture only

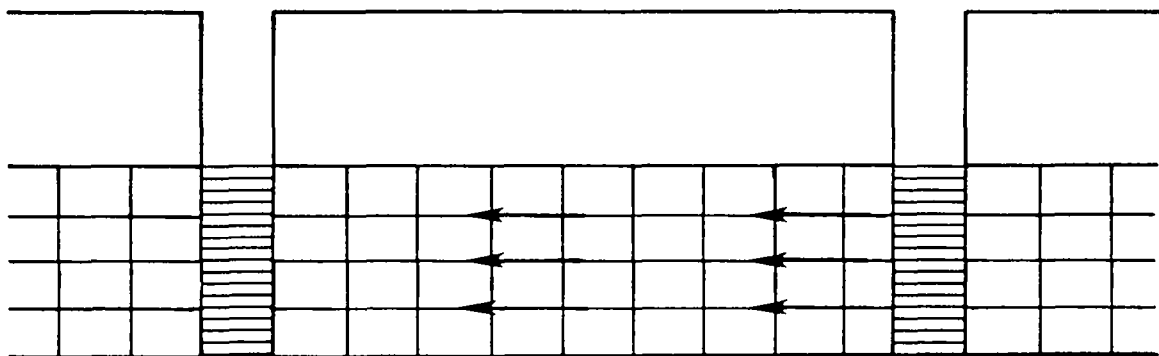
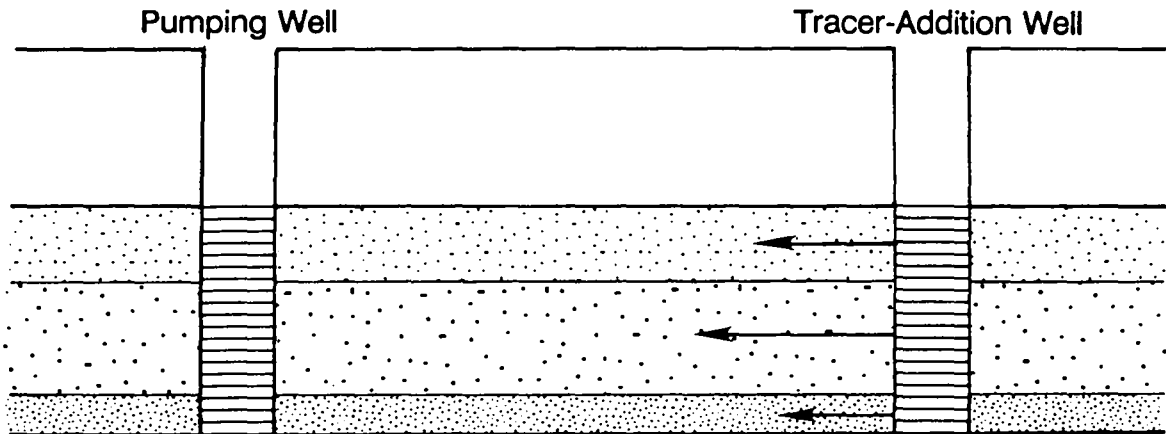


Figure 3-1. Schematic of various conceptualizations for analysis of convergent-flow or two-well recirculating tracer tests, (a) single-porosity porous medium, (b) single-porosity fracture only.

(c) Multiple-permeability, single-porosity porous medium



(d) Multiple-permeability, single-porosity fracture only

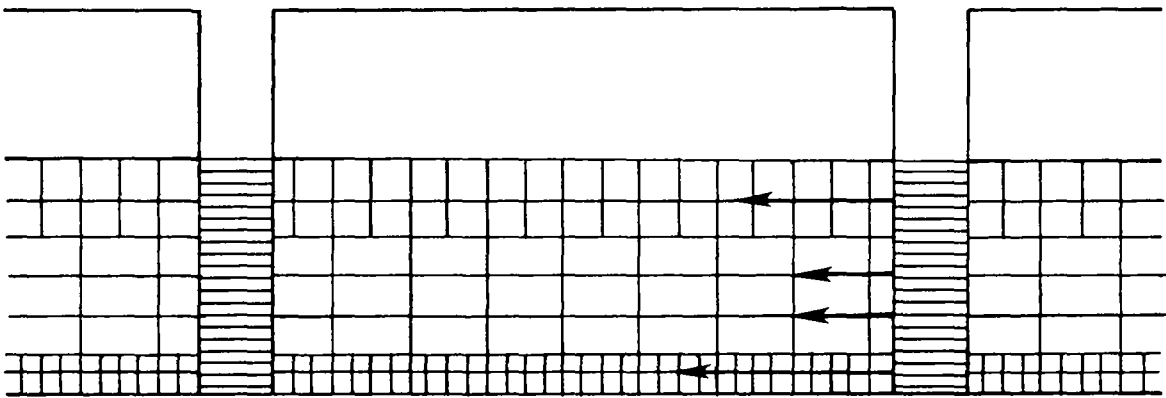
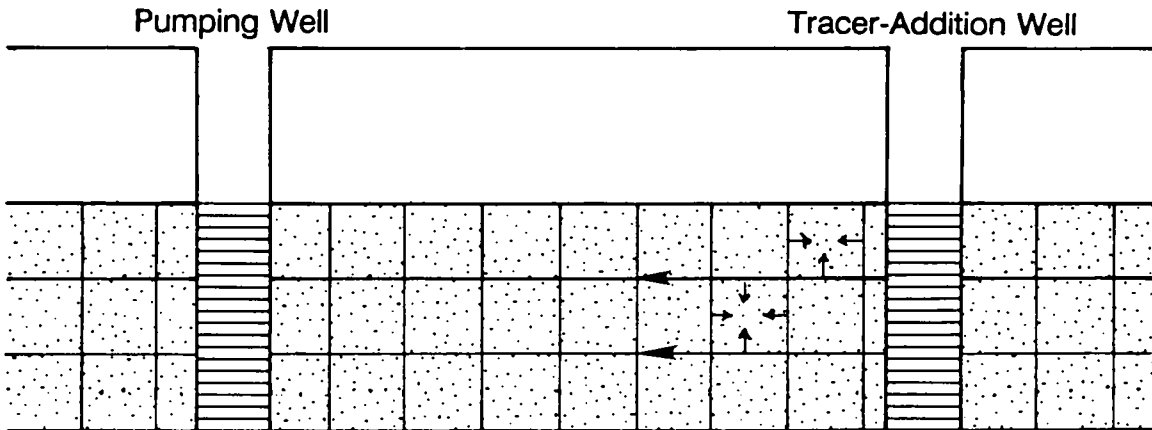


Figure 3-1. Schematic of various conceptualizations for analysis of convergent-flow or two-well recirculating tracer tests, (c) multiple-permeability, single-porosity porous medium, (d) multiple-permeability, single-porosity fracture only.

(e) Double-porosity porous medium



(f) Multiple-permeability, double-porosity porous medium

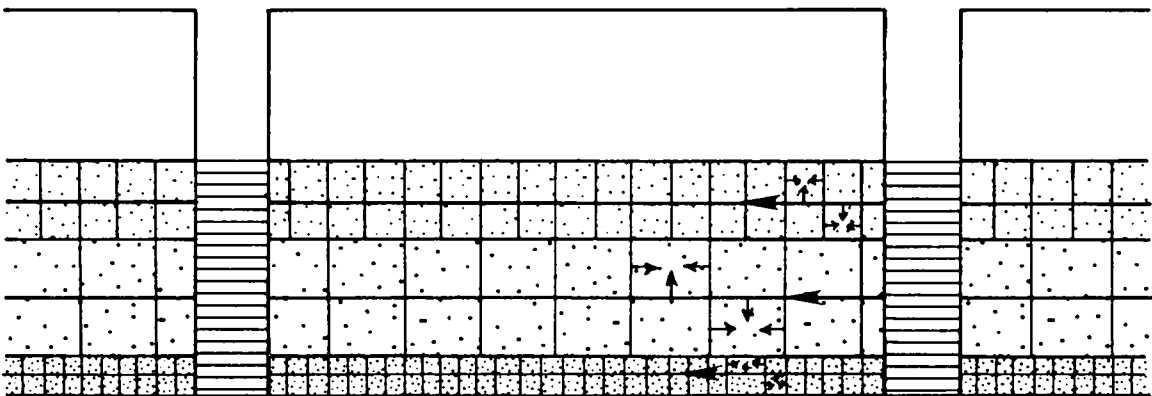


Figure 3-1. Schematic of various conceptualizations for analysis of convergent-flow or two-well recirculating tracer tests, (e) double-porosity porous medium, (f) multiple-permeability, double-porosity porous medium.

3-1f illustrate cases corresponding to homogeneous and multipermeability systems, respectively. Although not shown in Figure 3-1, variations of these conceptualizations exhibiting horizontal heterogeneity in addition to vertical heterogeneity are also possible.

The Culebra is known to be heterogeneous over its vertical and horizontal extent based on examination of core from WIPP boreholes, mapping of WIPP shafts, and examination of Culebra outcrops west of the WIPP site. While the limited data on core permeabilities (Kelley and Saulnier, 1990) give some evidence of variations in intergranular permeability, it does not provide data on variations in permeability when fractures are present. In general, data are lacking to define adequately the horizontal and vertical heterogeneity of the Culebra at a hydropad. For this reason, the interpretations of the tracer tests assumed the Culebra to be homogeneous vertically and between a tracer-addition well and the pumping well of a tracer test. Thus, the multipermeability conceptualizations as shown in Figures 3-1c, 3-1d, and 3-1f were not considered.

Open fractures in core, double-porosity behavior during hydraulic testing, and rapid tracer transport along at least one flow path have been identified at the H-3, H-6, and H-11 hydropads. For this reason, interpretation of the tracer tests at these locations using a double-porosity approach was considered most appropriate. In addition, because of the high matrix porosities determined from samples of the Culebra cores (Section 5.1.6) diffusive losses of solutes from the fractures to the matrix is expected to be an important process during these tracer tests. The double-porosity conceptualization assuming homogeneity at the hydropad scale as shown in Figure 3-1e was selected for interpretation of the H-3, H-6, and H-11 tracer tests. As discussed earlier, sufficient data are not available to directly estimate horizontal and vertical heterogeneity. The rapid tracer transport on one path and the slower transport with a much lower peak concentration on one or more additional paths at each hydropad suggests that either heterogeneity in fracturing or anisotropy (horizontal) in the transmissivity field may exist. The absence of multiple peaks in the observed tracer-breakthrough curves could be possibly the consequence of relative homogeneity in the fracturing and aperture distribution. Simulations were also performed

to investigate suitability of single-porosity, porous-medium and single-porosity, fracture-only conceptualizations (Figures 3-1a and 3-1b, respectively) for interpreting the H-3, H-6, and H-11 tracer tests (Section 11).

For the H-2 and H-4 hydropads, core observations indicate predominantly closed or gypsum-filled fractures, hydraulic-test responses show no indication of double-porosity behavior, and tracer tests revealed slow tracer transport along all flow paths. Thus, a single-porosity, matrix-only system appears to be the most appropriate conceptualization for these hydropads.

3.1.3 Other Transport Conceptualizations

As discussed in Section 3.1.1, there is strong evidence to support the presence of fractures in the Culebra at the H-3, H-6, and H-11 hydropads where tracer tests have been performed. The double-porosity interpretation approach discussed in Section 3.1.2 assumes that transport occurs in a homogeneous system consisting of three intersecting sets of parallel fractures with a constant aperture and that the solute diffuses from/to the fractures to/from the adjacent matrix blocks. An alternative transport conceptualization that consists of fractures with variable apertures has been published in the literature (Tsang and Tsang, 1987; Moreno et al., 1988; Tsang et al., 1988; Shapiro and Nicholas, 1989; Moreno et al., 1990; Abelin et al., 1991; Johns and Roberts, 1991; Moreno and Tsang, 1991). This conceptualization is referred to as a variable-aperture channel model. The apertures of a fracture are assumed to vary spatially in the fracture plane with the bulk of the flow in the fracture occurring in preferred flow paths or "channels." The above-referenced studies consider transport to occur in the fractures only, with the exception of Johns and Roberts (1991) which also consider diffusive solute interaction between the fractures and matrix.

Johns and Roberts (1991) idealized this conceptualization as a fracture plane of varying apertures consisting of regions of constant, but markedly different, aperture with the

large-aperture regions representing the high-flow-rate fracture channels and the small-aperture regions representing zones in which fluid is immobile or moves at very low flow rates. Slowing of the solute front occurs as a result of mass transfer by lateral diffusion and dispersion from the fracture channels into the more stagnant regions. They considered longitudinal advection in the large-aperture region, longitudinal advection in the small-aperture region, lateral diffusion and dispersion across the large-aperture region, lateral diffusion and dispersion across the small-aperture region, lateral diffusion and dispersion between the large-aperture channel and the small-aperture region contacting the channel, diffusion into the rock matrix from both regions, and equilibrium sorption in the rock matrix. They did not include longitudinal dispersion in the fracture based on their review of Tang et al. (1981) that indicated that longitudinal dispersion has little effect on transport in fractures with high flow velocities.

The variable-aperture-channel-model conceptualization has been demonstrated to yield breakthrough curves for converging-flow tracer tests with a sharp leading edge and a long trailing tail (e.g., Tsang et al., 1988; Shapiro and Nicholas, 1989). This breakthrough-curve behavior is quite similar to the observed breakthrough curves for at least one of the flow paths for the tracer tests performed at the H-3, H-6, and H-11 hydropads. Therefore, it is expected that the Culebra breakthrough curves could be fit successfully using a variable-aperture channel model. Tsang et al. (1988) characterize the apertures along the flow channels by an aperture density distribution and a spatial correlation length. They found that the tracer-breakthrough-curve shape has a rapid rise and a long tail even though their model does not include matrix diffusion. They state that the system must be statistically homogeneous to predict a tracer-breakthrough curve. Channel-model interpretation approaches have not been attempted in this report. The interpretation conceptualization presented in this report for the Culebra tracer tests is the double-porosity conceptualization as outlined in Section 3.1.2.

3.2 SWIFT II Code Description

The tracer tests conducted at the WIPP site have been interpreted using the SWIFT II (Sandia Waste Isolation, Flow, and Transport Code) code. SWIFT II was selected because it is versatile and has been extensively verified against analytical results. SWIFT II is supported by comprehensive documentation and an extensive testing history. Reeves et al. (1986a) discuss the theory and implementation of the code and the basic limitations of the methodology. A guide to the input data is provided by Reeves et al. (1986b). Comparisons of the results from SWIFT II to analytical solutions appear in Finley and Reeves (1981), Reeves et al. (1986c), and Ward et al. (1984).

SWIFT II is a fully transient three-dimensional, finite-difference code that solves the coupled equations for single-phase flow and transport in porous and fractured (double-porosity) geologic media. The processes that SWIFT II is capable of simulating include fluid flow, heat transport, dominant-species miscible displacement (brine), and trace-species miscible displacement (radionuclide chains or other contaminants). The first three processes are coupled via porosity, fluid density, viscosity, and enthalpy. Together they provide the Darcy-velocity field required to model solute transport. SWIFT II can be used in a transient or steady-state mode and is capable of modeling confined or unconfined (including partially saturated) flow systems. The model can be used with either Cartesian or cylindrical coordinate systems. The latter system is restricted to two-dimensional, r-z simulations. SWIFT II also includes the capability of modeling heterogeneous and/or anisotropic conditions.

The inherent complexity of simulating transport in fractured porous media requires the assignment of specific characteristics to both the fracture and matrix subsystems. Based upon the conceptualization of the fracture network, the fracture/matrix system can be represented with SWIFT II as a system of parallel, not-intersecting fractures or as a system of three orthogonal, intersecting fracture sets with equal spacing in all directions (Figure 3-2).

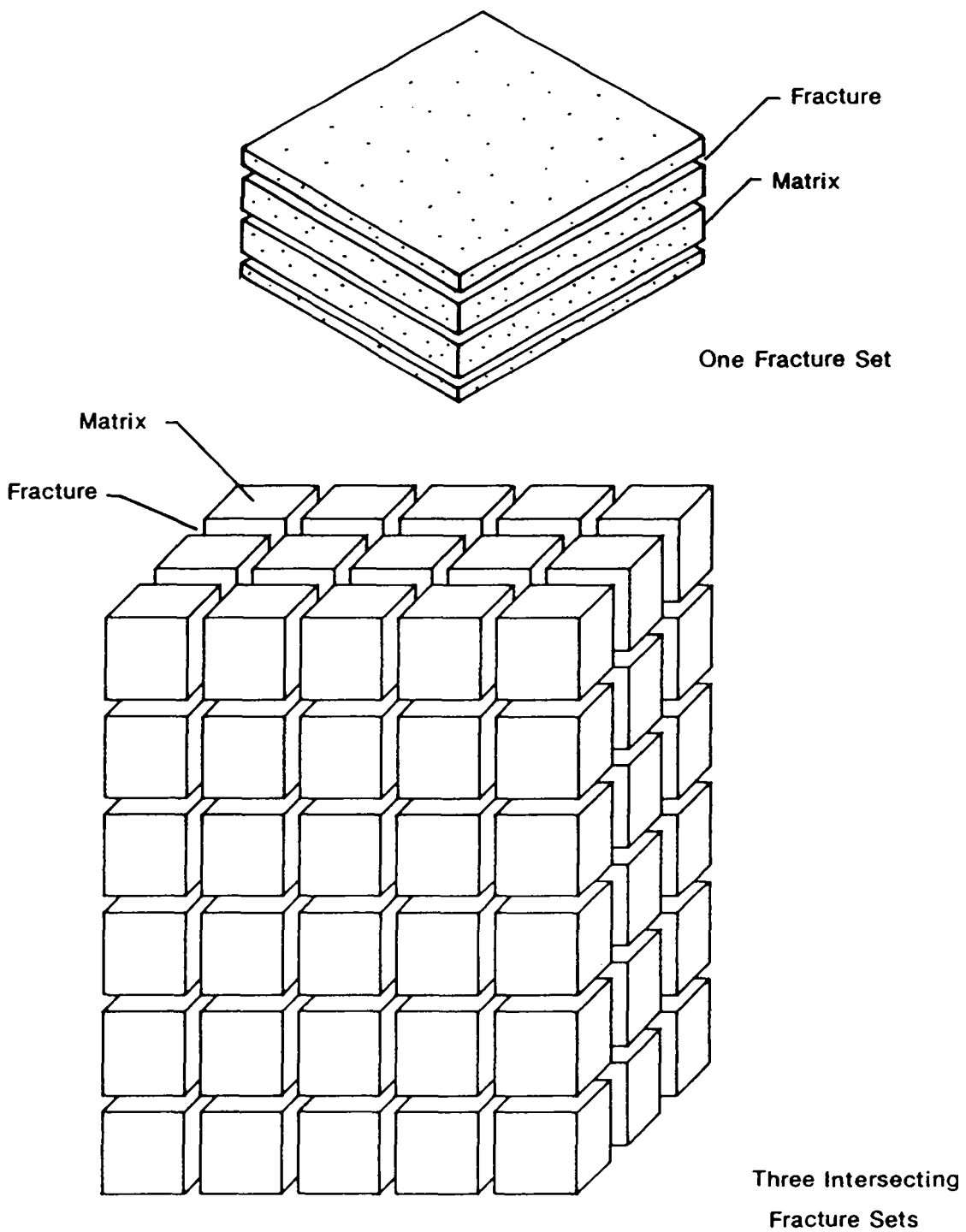


Figure 3-2. Idealization of fracture sets (from Reeves et al., 1986a).

3.3 Model Verification of SWIFT II

Model verification is a demonstration that the numerical formulation and solution of the system of differential equations representing the modeled processes are accurate. SWIFT II is one of the most extensively verified codes in use in the ground-water modeling discipline. It has been developed and maintained under quality assurance requirements, consistent with 10 CFR 50, Appendix B (U.S. Nuclear Regulatory Commission, 1977) and ANSI/ASME NQA-1 (American Society of Mechanical Engineers, 1986). The verification test cases are described in Finley and Reeves (1981) and Ward et al. (1984). SWIFT II has been verified against analytic solutions for various types of test cases including flow, heat, and solute transport with one-dimensional, two-dimensional, or radial geometries. These published verification examples, while extensive, do not include solute transport in a double-porosity medium using a radial injection or pumping geometry. Because the interpretation of the tracer tests required use of this option in SWIFT II, verification against analytical solutions of double-porosity radial transport was conducted.

Two analytic solutions for double-porosity solute transport were identified to verify the applicability of the SWIFT II code to problems similar to the convergent-flow tracer tests described in the present study. In both analytic solutions, advection and dispersion are limited to the fracture subsystem while only diffusion occurs in the matrix subsystem. These conceptualizations are consistent with the present study. Consequently, the fracture subsystem serves in a transport capacity and the matrix subsystem serves in a mass-storage capacity.

In the SWIFT II model (Reeves et al., 1986a), prismatic matrix blocks (representing parallel, non-intersecting fractures) and spherical matrix blocks (representing three orthogonal, intersecting fracture sets) may be employed. Prisms are given a dimension equal to one half of the fracture spacing, whereas spheres are given a radius equal to one half of the fracture spacing, which is assumed to be equal in all three directions.

Detailed discussions of the analytic examples can be found in Chen (1986) (prismatic matrix blocks) and Moench (1987) (spherical matrix blocks). Based upon the stated assumptions and information provided in each of the examples, data-input files were constructed and used as input to SWIFT II. Output resulting from the SWIFT II simulations was compared to the published results of the analytic examples. As demonstrated in Figures 3-3 and 3-4, the output obtained from SWIFT II compares favorably to the analytical data provided in Chen (1986) and Moench (1987), respectively.

3.4 Methodology for Heterogeneous and Anisotropic Tracer-Test Analyses

The modeling methodology used to interpret the convergent-flow tracer tests is divided into two phases. The first phase is done outside of SWIFT II as a pre-processor and models tracer injection at the tracer-addition wells from the surface to the formation. This phase characterizes the tracer-input function and provides the initial tracer-mass distribution for the numerical transport calculations. The second phase is the numerical modeling conducted using SWIFT II. The numerical model takes advantage of the fact that lateral-concentration differences in the convergent-flow field need not be preserved at the pumping well and models the system with a radial grid. Guvanasen and Guvanasen (1987) developed an approximate semianalytical solution for analysis of convergent-flow tracer tests in single-porosity systems with tracer-volume and chaser-volume injection conditions identical to those used for the WIPP-site tracer tests. They demonstrated theoretically that "...it can be seen that effects due to lateral dispersion do not appear at the pumping well. The solution is equivalent to that of an axisymmetric problem with a square pulse of initial concentration..." Their conclusion is significant in that it provides a theoretical justification for the simplified radial-transport conceptualization presented here for interpreting the WIPP-site convergent-flow tracer tests.

The double-porosity model selected for use is a continuum model rather than a discrete model type. The continuum model was chosen because discrete or distributed

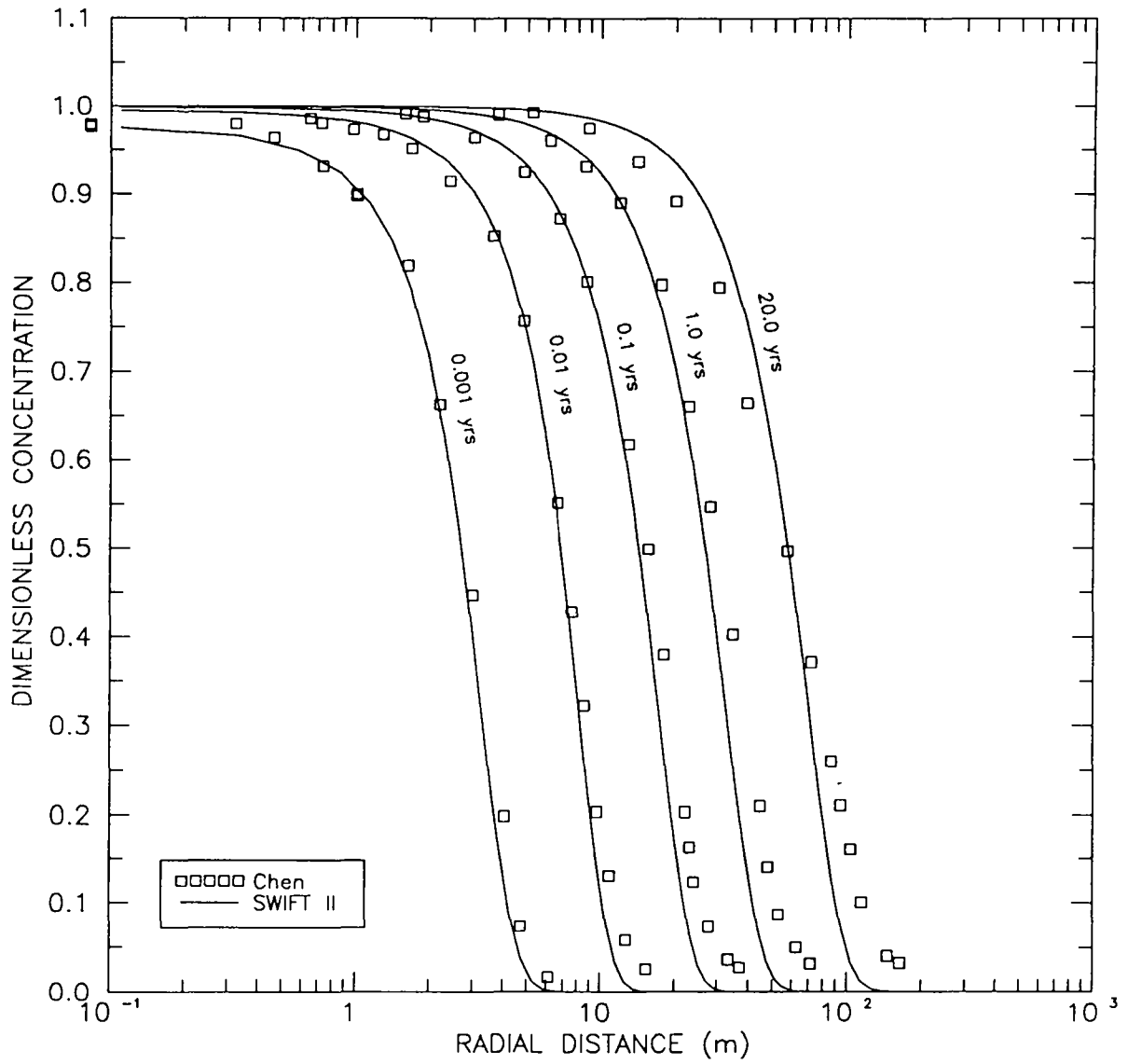


Figure 3-3. Comparison of analytic and SWIFT II results for double-porosity solute transport using prismatic matrix blocks.

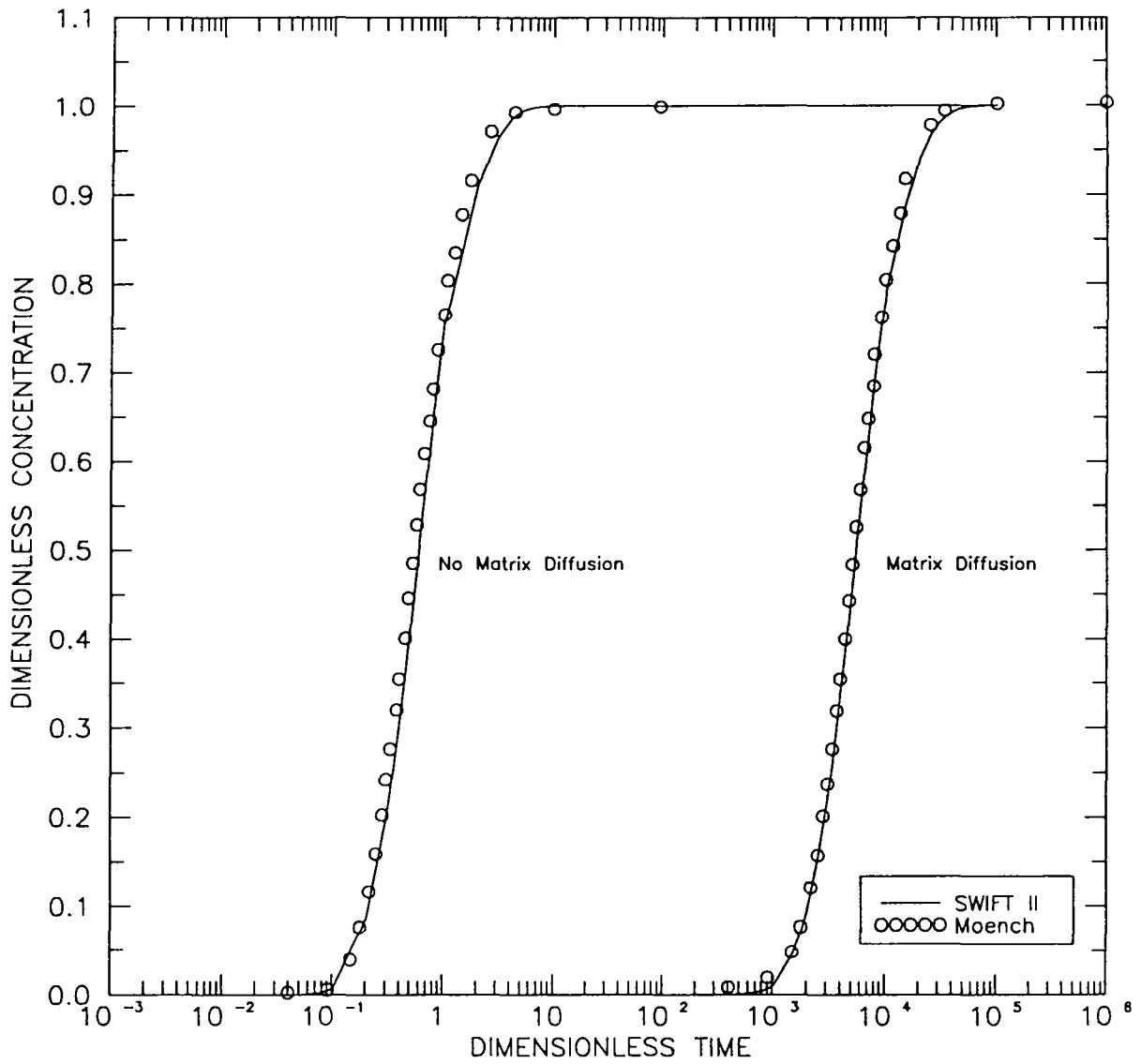


Figure 3-4. Comparison of analytic and SWIFT II results for double-porosity solute transport using spherical matrix blocks.

fracture characteristics are unknown. Although assumptions required for the application of continuum double-porosity models are restrictive theoretically and may be hard to satisfy over small scales of transport, the use of continuum models is often necessitated by the lack of sufficient data for discrete formulations.

Although the tracer tests selected for analysis in this study were those for which it could be demonstrated that the tracer behaved conservatively (i.e., no detectable sorption or degradation), the breakthrough curves show significant differences between flow paths at individual WIPP-hydropad locations. Assuming conservative tracers and no large source-function differences, the differences in the tracer-breakthrough curves at a hydropad are attributed to differences in the travel times and matrix diffusion occurring along the different flow paths as a result of differences in the rock and/or flow field. The interpretation methodology employed for the study assumed that the primary factors causing differences in the breakthrough curves were different rock characteristics along different flow paths (i.e., heterogeneity) and anisotropy in the horizontal transmissivity field. Two different cases were considered for analysis. For the first case, differences in the tracer-breakthrough curves at a hydropad were attributed entirely to heterogeneity, while in the second case they were attributed entirely to anisotropy in the horizontal transmissivity.

For the first case, referred to as the heterogeneous-analysis approach, the differences in the breakthrough curves observed at a single hydropad are assumed to be the result of flow-path heterogeneity. It is assumed that this heterogeneity can be described by differences in the amount of surface area available for matrix diffusion between the flow paths. Within SWIFT II, this surface area is defined by specifying the type of matrix blocks (prismatic or spherical for one or three fracture sets, respectively) and the matrix-block length (or fracture spacing).

The second case is referred to as the anisotropic-analysis approach. This approach assumes that the breakthrough-curve differences are the result of anisotropy in the horizontal transmissivity. This anisotropy causes differences in the flow velocity along

different flow paths resulting in differences in the time available for matrix diffusion to occur along different paths.

The existence of different matrix-block lengths on each of the transport paths is considered possible based on the observed heterogeneity in fracturing over distances of meters to tens of meters horizontally at the Culebra outcrops southwest of the WIPP site. The interpreted block sizes from the heterogeneous-analysis approach are somewhat uncertain because the same average flow rate was assumed for each transport path. Alternatively, the anisotropic-analysis approach allows estimation of a different flow rate on each transport path while fitting to a horizontal-anisotropy ratio and principal-transmissivity direction and to a single matrix-block length.

The matrix-block lengths determined from both analysis approaches represent effective fracture spacings. The conceptualization for the simulations assumes an idealized set of three intersecting fractures rather than the more realistic case of locally limited fracture continuity. Therefore, the matrix-block lengths determined through interpretation of the tracer tests may reflect the total surface area available for diffusion of tracer mass from the fractures to the matrix and not the actual geometry of the fracture system.

3.4.1 Heterogeneous-Analysis Approach

Analysis of the tracer tests requires calibration of the simulated results to the observed tracer-breakthrough curves. For the heterogeneous case, the calibration parameters are fracture porosity and matrix-block length. The remaining transport parameters are held at constant values thought to be consistent with the current physical and conceptual understanding of the Culebra. A detailed discussion of each of the transport parameters is provided in Section 5.0. The heterogeneous-analysis approach assumes that the rapid arrival of a tracer at the pumping well for one of the transport paths is a result of predominately fracture transport along that path. Therefore, fracture porosity is used as

a fitting parameter in the analysis of the rapid-transport breakthrough curve. The other fitting parameter with the heterogeneous-analysis approach is the matrix-block length. Using the rapid-transport tracer-breakthrough curve, fracture porosity is adjusted until a good fit to the rising limb and the time of the peak concentration is obtained. Matrix-block length is then adjusted to fit the magnitude of the peak concentration and the trailing limb of the observed curve. The heterogeneous-analysis approach assumes that fracture porosity is an appropriate fitting parameter for the rapid-transport breakthrough curve but not for the slow-transport breakthrough curve which exhibits transport that is dominated by matrix diffusion. As a result, the fracture porosity determined through calibration of the rapid-transport breakthrough curve is also used in the analysis of the slow-transport breakthrough curve. With fracture porosity assigned, the only fitting parameter for analysis of the slow-transport breakthrough curve is matrix-block length. In summary, the heterogeneous-analysis approach first calibrates to the breakthrough curve for the rapid-transport path using fracture porosity and matrix-block length as fitting parameters. The breakthrough curve for the slow-transport path is then assigned the same fracture porosity and fit with matrix-block length only.

3.4.2 Anisotropic-Analysis Approach

The calibration parameters for the anisotropic-analysis approach are horizontal anisotropy, in the form of the anisotropy ratio ($T_x:T_y$); principal-transmissivity direction (T_x direction); and matrix-block length. Fracture porosity was determined using a relationship based on the theoretical plug-flow travel time between the tracer-addition well and the pumping well in a convergent-flow tracer test (see Section 5.2.1). The remaining transport parameters were held constant at values considered to be consistent with the current physical and conceptual understanding of the Culebra. The transport parameters are discussed in detail in Section 5.0. The objective of the anisotropic simulations was to determine a single anisotropy, principal-transmissivity direction, and matrix-block length that would give simulated breakthrough curves that matched the observed concentrations for all

travel paths at a given hydropad. As with the heterogeneous-analysis approach, the anisotropic-analysis approach assumes that the rapid arrival of a tracer at the pumping well is the result of fracture-dominated flow and that the slow arrival of a tracer is the result of matrix-diffusion-dominated transport. For the anisotropic-analysis approach, anisotropy ratio, principal-transmissivity direction, and matrix-block length were simultaneously adjusted until one combination of these parameters yielded simulated breakthrough curves that matched all observed breakthrough curves at the pumping well. The criteria for determination of the anisotropy ratio, principal-transmissivity direction, and matrix-block length was the observed difference in the shape of the observed breakthrough curves. A complete discussion of how anisotropy is integrated into the simulation input parameters is provided in Section 3.4.4.

3.4.3 Tracer-Input Conceptualization

The initial steps in developing input for interpreting the tracer tests were to (1) calculate the initial tracer-pulse distribution and allocate it into the radial-model grid and (2) determine the volumetric flux through the tracer pulse as it is controlled by the approach chosen for analysis (heterogeneous or anisotropic). This and the following sections describe the conceptualization of the tracer-input function and the implementation of anisotropy in the form of a modified volumetric flux through the tracer pulse.

Analysis of the tracer tests considered the tracer-injection phase independently from tracer transport between the tracer-addition and pumping wells. Calculation of the tracer-concentration distribution in the Culebra immediately after tracer injection was done to determine the initial conditions for the SWIFT II transport calculations. This treatment is supported by the relatively short time period during which tracer injection occurred compared to the time at which the peak tracer concentration was observed at the pumping well. Tracer injection consisted of two parts, injection of an initial tracer-labeled fluid volume followed by the injection of a non-labeled chaser volume. The function of the

chaser volume was to displace the tracer volume from the wellbore system into the formation. Assuming that the fluid injected into the tracer-addition well moves through the injection tubing, wellbore, and formation under plug-flow conditions, tracer would not enter the formation until one system volume (SV) of fluid had been injected into the wellbore. The wellbore-system volume is defined as the fluid volume from the point of tracer addition at the surface to the base of the Culebra. If the tracer-labeled volume (V_t) is followed by a chaser volume (V_c) and V_c is greater than SV, then the initial concentration distribution about the injection well will be in the form of two concentric circles between which the tracer-labeled fluid exists. This conceptualization assumes plug flow, neglects the radially converging flow to the pumping well and past the injection well during tracer injection, neglects anisotropy effects, and neglects matrix diffusion during tracer injection.

The tracer pulse is defined to exist between the radius r_i defining the inner radius and the radius r_o defining the outer radius (Figure 3-5). The outer radius of the initial tracer-input zone contains within it the total displaced volume which is defined as the difference between the total injected volume and the system volume ($V_t + V_c - SV$). The outer and inner radii of the tracer-labeled region in the Culebra are calculated by:

$$r_o = \left(\frac{V_t + V_c - SV}{b \pi \phi} \right)^{1/2} \quad (3-1)$$

$$r_i = \left(\frac{V_c - SV}{b \pi \phi} \right)^{1/2} \quad (3-2)$$

where:

b = aquifer thickness, and

ϕ = fracture porosity.

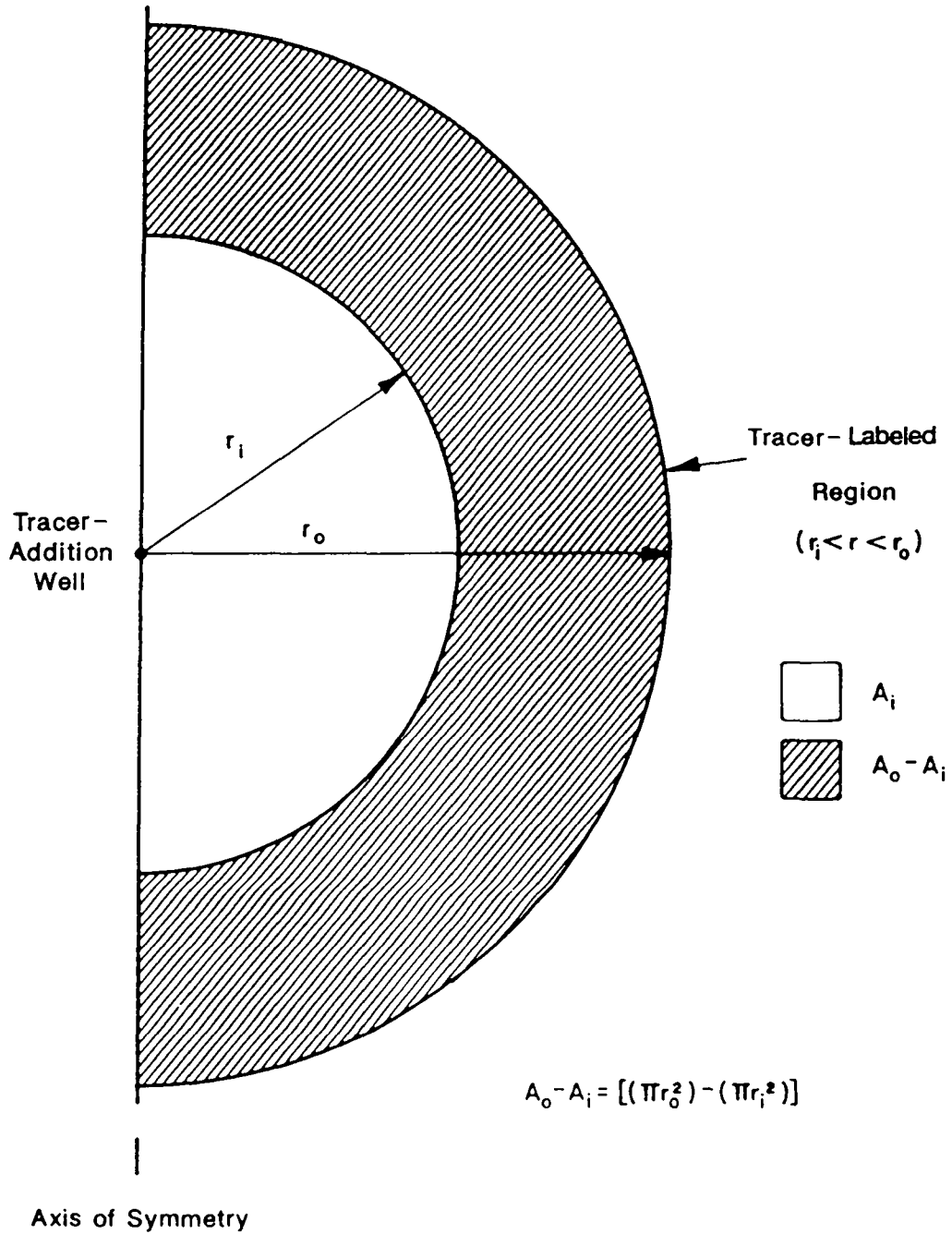


Figure 3-5. Ideal representation of tracer-labeled region surrounding the tracer-addition well immediately after injection (after Kelley and Pickens, 1986).

The inner volume between the well radius and the inner radius of the tracer-input zone (numerator in Equation 3-2) is defined by the volumetric difference between the total displaced volume and the tracer-labeled volume. The relationship between the inner and outer radii and the tracer-addition well is illustrated in Figure 3-5. Due to the assumed radial symmetry of the input zone centered on the tracer-addition well, any line projected through the tracer-addition well is an axis of bilateral symmetry. Therefore, only one half of the input region is illustrated for discussion purposes.

The tracer-input zone is modeled as a series of concentric rings centered on the pumping well (Figure 3-6). The model grid blocks that intersect the tracer-input zone will either intersect only portions of the outer circle or will intersect portions of both the inner and outer circles. For example, in Figure 3-7 model element n_3 intersects regions circumscribed by r_i and r_o while model element n_5 only intersects regions of the outer circle described by r_o . Only one half of the tracer-input zone, model grid blocks n_1 through n_5 , is shown in Figure 3-7 due to symmetry.

Since the distribution of the tracer immediately after tracer injection acts as the initial condition for the numerical model, the distribution of mass within the tracer-input zone must be calculated and initialized into the radial grid used by the model. The allocation of mass between the SWIFT II grid blocks is done based upon volumetric relationships. Theoretically, the input mass should reside in a ring of finite volume with inner boundary equal to r_i and outer boundary equal to r_o and of some finite vertical dimension. Since the thickness of the input zone (i.e., the Culebra) is considered a constant at the tracer-addition well, areal relationships instead of volumetric relationships can be used to calculate the allocation of mass. The amount of mass distributed within a given grid block (n) is based upon the area of the tracer-labeled pulse in that block divided by the total area of the tracer-labeled pulse. Model element n_3 in Figure 3-7 intersects a portion of the inner-circle area (between the tracer-addition well and r_i) and also a larger area of the outer circle (between r_i and r_o). The area within r_i is considered devoid of tracer-input mass. For each model element, the intersected area of the tracer-labeled region

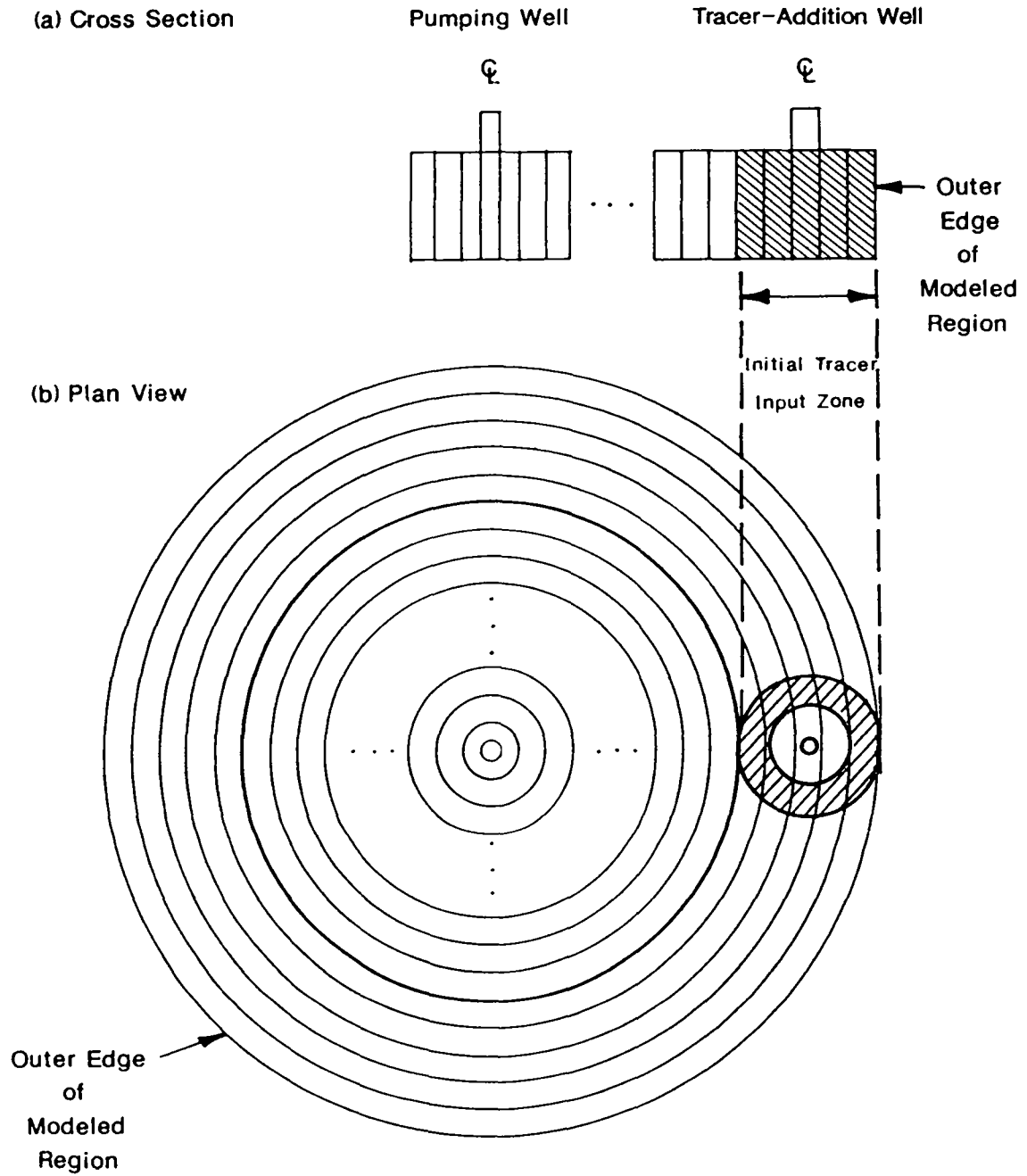


Figure 3-6. Schematic representation of the modeled region, (a) cross section, (b) plan view (after Kelley and Pickens, 1986).

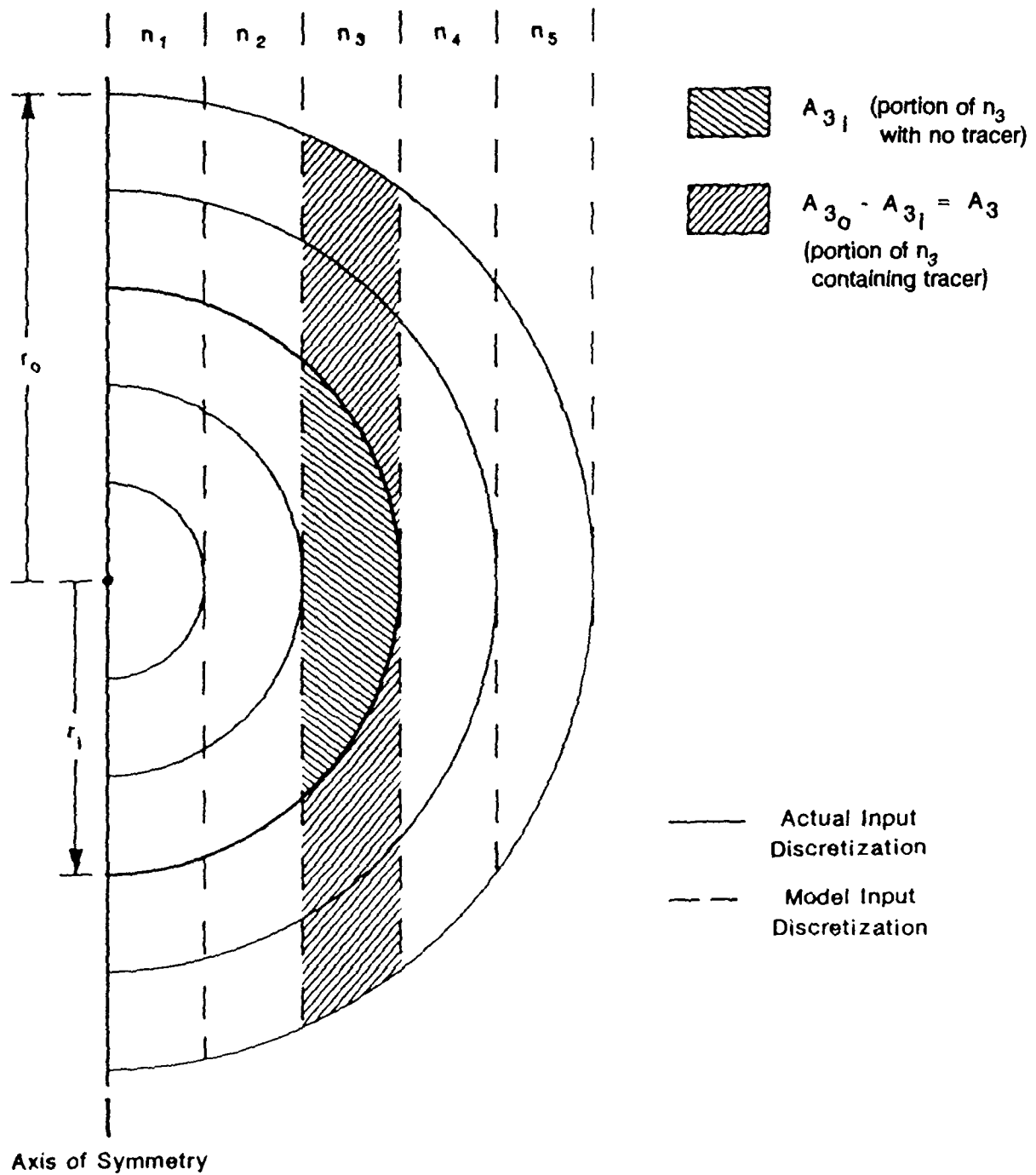


Figure 3-7. Relationship between actual input-tracer-mass geometry and the model space discretization (after Kelley and Pickens, 1986).

($r_i < r < r_o$) can be calculated and designated A_n . In the case of model element n_3 (Figure 3-7), A_3 would be equal to $A_{3(o)} - A_{3(i)}$. The appropriate mass for each model element is calculated assuming perfect mixing in the zone defined by r_o and r_i with the relationship:

$$M_n = \frac{A_n}{A_o - A_i} \cdot M_{inj} \quad (3-3)$$

where:

- M_n = mass allocated to block n,
- A_n = area of the tracer-labeled region intersected by element n,
- A_o = tracer-labeled area defined by the outside radius,
- A_i = tracer-labeled area defined by the inside radius, and
- M_{inj} = tracer mass injected.

Figure 3-8 schematically illustrates the initial mass distribution as a function of grid block. This initial distribution is symmetric about the injection origin and tends to be mass deficient in the middle which is representative of the original two-dimensional ring of the tracer plume immediately after injection. The two-dimensional initial tracer distribution is modeled with a radial one-dimensional grid which distributes the mass laterally and integrates the mass over 2π radians at the pumping well.

Guvanasen and Guvanasen (1987) investigated the impact of the ring-shaped initial tracer distribution for a convergent-flow tracer test in a single-porosity confined aquifer. They used a semi-analytical method to model both the injection phase for the tracer-addition well and the transport phase using the injection-phase calculations for initial conditions. They used a particle-tracking method to determine the initial distribution of tracer and then used an analytical solution which solved the radially converging transport problem. The primary difference between their method and the method employed here is

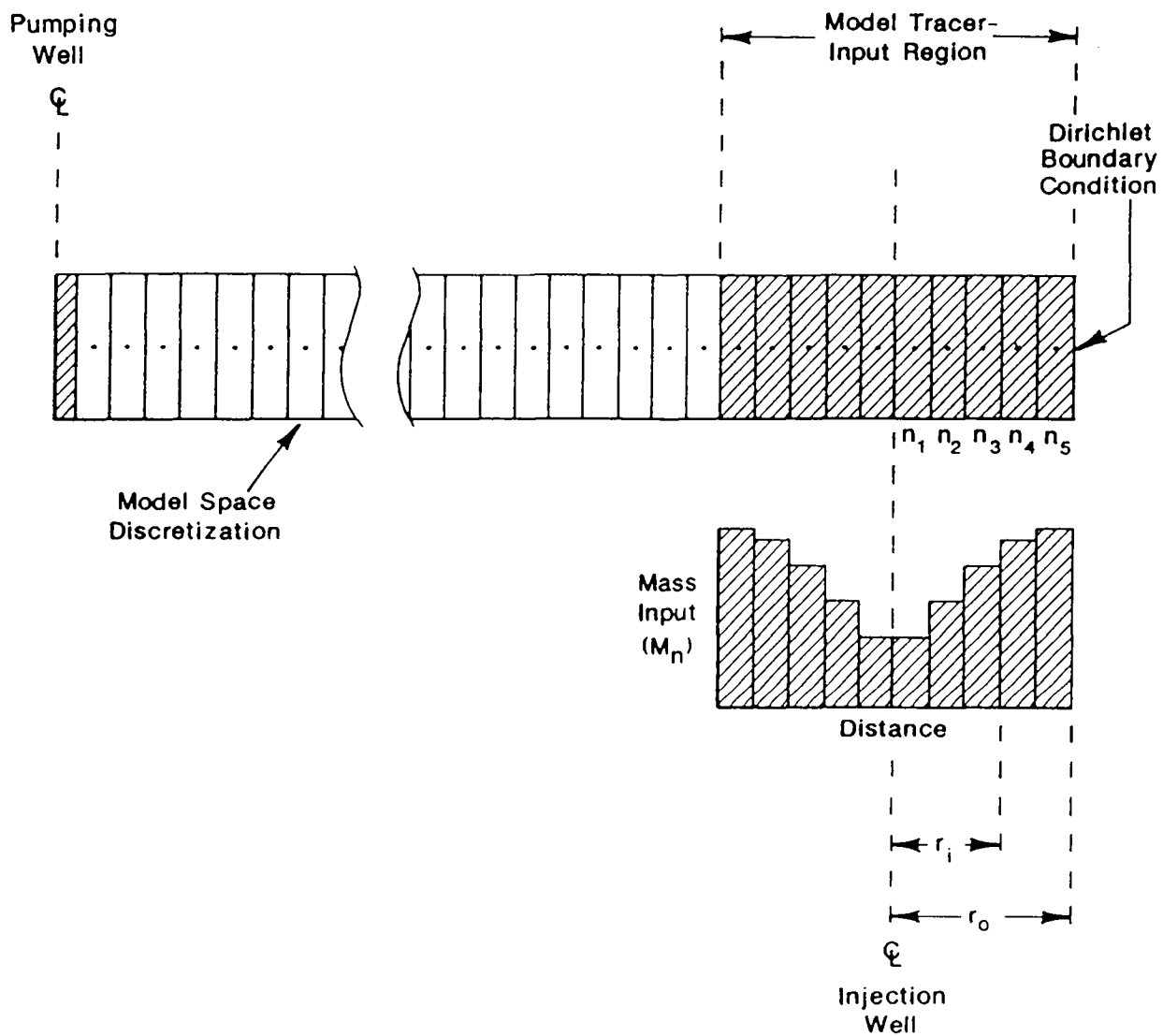


Figure 3-8. Tracer-input function as applied to the actual model space discretization (from Kelley and Pickens, 1986).

that they did not neglect the converging-flow-field velocities superimposed on the injection phase. Guvanasen and Guvanasen (1987) defined geometric parameters which governed the shape of the tracer plume immediately after injection and then employed their semi-analytic method to determine the effect of these geometric parameters upon the observed breakthrough at the pumping well. They found that the initial tracer distribution could lead to double-peaked breakthroughs for small dispersivities. The effect of the shape of the initial tracer distribution on the breakthrough curve at the pumping well was eliminated as longitudinal dispersivity was increased because of the increased spreading or dispersion. It is expected that in a double-porosity medium the effect of the shape of the initial tracer distribution on the pumping-well breakthrough curve would be further reduced due to matrix diffusion.

3.4.4 Implementation of Heterogeneous- and Anisotropic-Analysis Approaches in SWIFT II

The anisotropic-analysis approach assumes that the differences in tracer-breakthrough curves are the result of anisotropy in the horizontal transmissivity. Implementation of this approach uses a one-dimensional radial model and separately simulates the observed breakthrough curves for each different travel path. Since the simulations were one-dimensional and examined only one flow path at a time, direct input of an anisotropy ratio and a principal-transmissivity direction was not possible. The technique used to implement anisotropy into the radial model was to adjust the volumetric flow rate at the pumping well. The following discussion explains the relationship between the anisotropy ratio and principal-transmissivity direction and the volumetric flow rate. For both the heterogeneous- and anisotropic-analysis approaches, observed drawdowns/pressures and interpreted transmissivities play no role in the analysis.

The tracer tests are all modeled using a radial system with a pumping or tracer-pumping well located at the center and a tracer-addition well near the outer edge of the

model (Figure 3-6). The hydraulic gradient imposed by the convergent-flow field is considered much greater in magnitude than the ambient regional hydraulic gradient, and therefore, the latter is not considered in the analyses. The modeled region represents a cylindrical volume of the aquifer which is defined by the limits of the injected-tracer pulse immediately after injection.

Figure 3-9 shows a radial isotropic-transmissivity field where potential functions are perfect circles surrounding a sink located at the origin and an analogous anisotropic-transmissivity field where potential functions are ellipses. The anisotropic flow system can be transformed into an equivalent isotropic system by change of coordinates (de Marsily, 1986). Any ray emanating from the origin of these fields is a stream function (ψ) and can be defined as:

$$\psi = \frac{Q}{2\pi} \beta \quad (3-4)$$

where:

Q = pumping rate at the pumping well, and

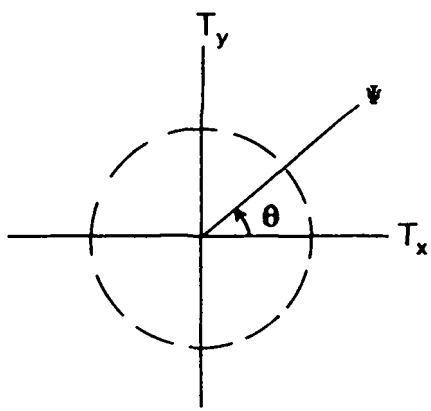
β = a geometric factor for transforming the angle of deviation of the stream function from the principal axis in the transformed coordinate system back to the natural coordinate system.

For the isotropic-conductivity field:

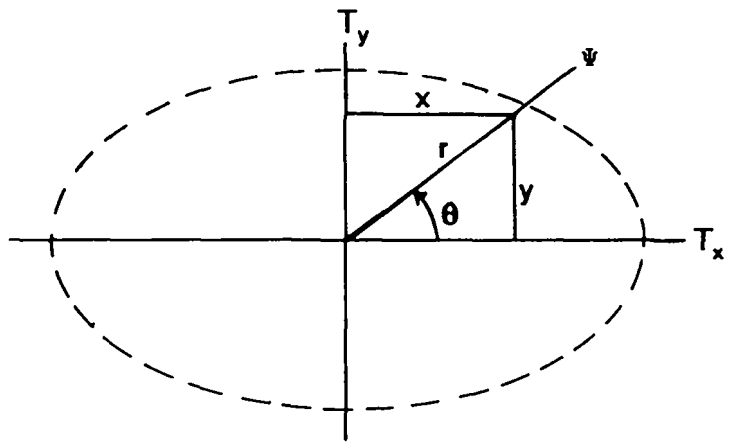
$$\beta = \theta \quad (3-5)$$

where:

θ = angle of deviation of the stream function from the principal axis.



ISOTROPIC



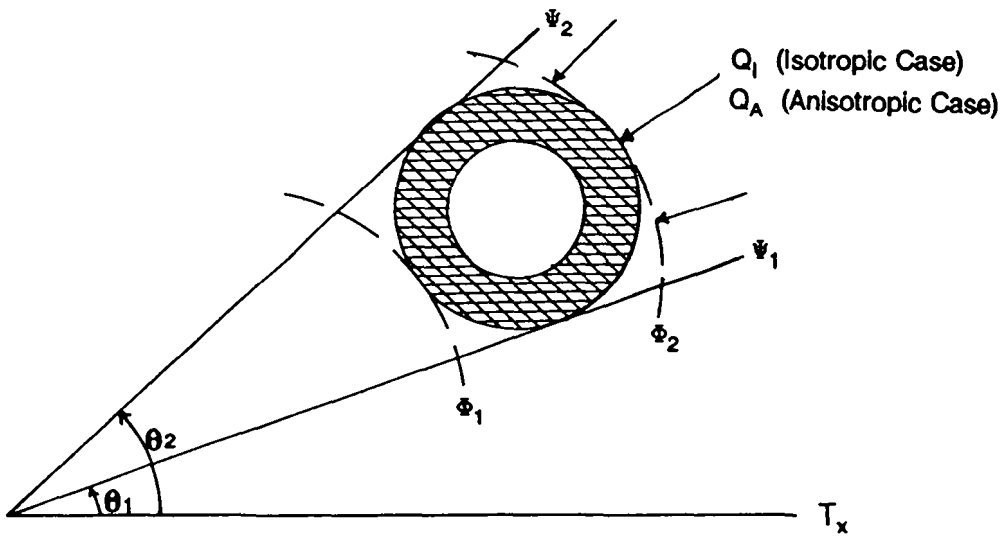
ANISOTROPIC

$$\psi = \frac{Q}{2\pi} \beta$$

$$\beta = \theta$$

$$\beta = \tan^{-1} \left[\left(\frac{T_x}{T_y} \right)^{\frac{1}{2}} \tan \theta \right]$$

$$\tan \theta = \frac{y}{x}$$



 Tracer-labeled pulse

Figure 3-9. Conceptualization of volumetric flow rate input into SWIFT II.

The equation describing the volumetric flow rate that passes through the injected tracer pulse in an isotropic, two-dimensional system is:

$$Q_I = \int_{\theta_1}^{\theta_2} \psi(\theta) d\theta = \frac{Q}{2\pi} (\theta_2 - \theta_1) = \Delta\theta \frac{Q}{2\pi} \quad (3-6)$$

The partial flow rate Q_I is schematically shown in Figure 3-9. For the isotropic, one-dimensional model used in the tracer-test interpretations, $\Delta\theta$ is equal to 2π . Therefore, the volumetric flow rate entered into the SWIFT II model is equal to the pumping rate at the pumping well.

For the anisotropic-conductivity field:

$$\beta = \tan^{-1} \left[\left(\frac{T_x}{T_y} \right)^{1/2} \tan \theta \right] \quad (3-7)$$

where:

T_x/T_y = anisotropy ratio,

θ = angle of deviation of the stream function from the principal axis, and

$\tan \theta$ = y/x (as defined in Figure 3-9).

Therefore, the partial volumetric flow rate passing through the injected-tracer pulse in an anisotropic, two-dimensional system is equal to:

$$\begin{aligned}
Q_A &= \int_{\theta_1}^{\theta_2} \psi(\theta) \, d\theta \\
&= \frac{Q}{2\pi} \left(\tan^{-1} \left[\left(\frac{T_x}{T_y} \right)^{1/2} \tan \theta_2 \right] - \tan^{-1} \left[\left(\frac{T_x}{T_y} \right)^{1/2} \tan \theta_1 \right] \right)
\end{aligned} \tag{3-8}$$

The two-dimensional flow rate given in Equation 3-8 is modified for the one-dimensional anisotropic system by:

$$Q_m = \frac{Q_A}{Q_1} Q \tag{3-9}$$

Therefore, the modified pumping rate at the pumping well (Q_m) used in the one-dimensional anisotropic model is:

$$Q_m = Q \left(\frac{\tan^{-1} \left[\left(\frac{T_x}{T_y} \right)^{1/2} \tan \theta_2 \right] - \tan^{-1} \left[\left(\frac{T_x}{T_y} \right)^{1/2} \tan \theta_1 \right]}{\Delta\theta} \right) \tag{3-10}$$

The purpose of the flow rate developed in Equation 3-10 is to introduce the effect of an anisotropic transmissivity field into the tracer-test interpretation.

Since the modified pumping rate entered into the anisotropic model (Q_m) is non-physical, the input mass flux must be corrected to maintain the correct input concentration.

The actual input mass flux is multiplied by a correction factor, F, to obtain the modified input mass flux. The correction factor is given by:

$$F = \frac{Q_m}{Q} \quad (3-11)$$

Using the modified flow rate calculated with Equation 3-10 and the correction factor calculated with Equation 3-11, the tracer concentration input into the model is identical to the concentration actually injected during the tracer test.

4.0 TRACERS UTILIZED IN WIPP-SITE TRACER TESTS

Tracers that have been used for evaluation of the transport characteristics of the Culebra at the WIPP site are summarized in Table 4-1. These tracers can be divided into three classes: organic anions, inorganic anions, and noncharged halogenated hydrocarbons.

4.1 Organic Anions

The organic anion tracers used in WIPP-site tracer tests (Table 4-1) are anhydrous fluorinated organic acids derived from benzoic acid and are referred to as halogenated aromatic acids. These tracers have no background levels in natural waters, are detectable at very low concentration levels with proven analytical methods, and tend to be very stable (i.e., nonreactive) species. The long-term chemical stability of halogenated aromatic acids is considered very good (Stetzenbach and Stetzenbach, Appendix A). The greater the number of halogen atoms bound to the aromatic compound, the greater the stability of the compound. This is especially true if the halogen is fluorine because carbon-fluorine bonds are the shortest and, therefore, the strongest of the carbon-halogen bonds. The results of a 30-day stability study conducted by Thompson and Stetzenbach (1980) indicate that of the WIPP tracers considered (o-FB, m-FB, p-FB, benzoate, PFB, and m-TFMB), benzoate was the least stable, reducing to zero concentration by the middle of the study period, and m-TFMB and PFB were the most stable, sustaining a constant concentration during the entire study period.

For the organic-anion tracers, reactivity in the subsurface is limited to adsorption and biodegradation (Stetzenbach and Stetzenbach, Appendix A). PFB has been tested extensively, both in the field and laboratory, and has not shown evidence of sorption or degradation (Bowman, 1984; Bowman and Rice, 1986). m-TFMB has also been tested

Table 4-1. Tracers Used for Evaluation of Culebra Transport Parameters

<u>Tracer</u>	<u>Abbreviation or Chemical Formula</u>	<u>Hydropad(s) Where Used</u>
pentafluorobenzoate ^a	PFB	H-2, H-3, H-4, H-6, H-11
meta-trifluoromethylbenzoate ^a	m-TFMB	H-3, H-4, H-6, H-11
ortho-trifluoromethylbenzoate ^a	o-TFMB	H-11
para-fluorobenzoate ^a	p-FB	H-4, H-6
ortho-fluorobenzoate ^a	o-FB	H-6
meta-fluorobenzoate ^a	m-FB	H-6
benzoate ^a		H-2
thiocyanate ^b	SCN	H-2, H-4, H-6
tetrachloromethane ^c	CCl ₄	H-2
trichlorofluoromethane ^c	CCl ₃ F	H-2
dichlorodifluoromethane ^c	CCl ₂ F ₂	H-2
difluorochlorobromomethane ^c	CF ₂ ClBr (BCF)	H-2

^a Fluorinated organic anions derived from benzoic acid.
^b Inorganic anion derived from sodium thiocyanate.
^c Noncharged halogenated hydrocarbons.

extensively and shows no signs of sorption. Experiments carried out at the University of Arizona have shown m-TFMB to be resistant to degradation for at least six months and PFB resistant for at least two years (Stetzenbach and Stetzenbach, Appendix A). In a 30-day study, Bowman (1984) found that m-TFMB may not be conservative under aerobic field conditions. Barackman (1986) conducted experiments to determine the biodegradability of PFB, o-TFMB, and m-TFMB in water that had been in contact with fluorinated benzoic acids and benzoate for four years. His results indicate no degradation of the three compounds after 30 days. Experimental results reported by Thompson and Stetzenbach (1980) indicate that o-FB, m-FB, and p-FB significantly degrade in 31, <30, and 13 days, respectively. In field notes recorded by Hydro Geo Chem, the conclusion is drawn that of the tracers p-FB, PFB, m-TFMB, o-FB, and m-FB, only p-FB, PFB, and m-TFMB showed no signs of degradation during the H-2, H-3, H-4, and H-6 tracer tests. However, given a long enough residence period most organics, including PFB and m-TFMB, could be susceptible to biodegradation by the indigenous microbial populations present within the Culebra. Hydro Geo Chem states in field notes that the tracers o-FB and m-FB showed signs of degradation in laboratory stability test in time periods of days to tens of days.

Free-water diffusion coefficients for the organic-anion tracers have been reported by Walter (1982). The Nernst expression and data from laboratory experiments conducted to determine the limiting ionic conductances of the tracer species were used to calculate the values of the free-water diffusion coefficients. The calculated values are provided in Table 4-2.

Klaus Stetzenbach, Director of the Physical Science Division at the Harry Reid Center for Environmental Studies at the University of Nevada, Las Vegas estimates that the molecular size of m-TFMB, PFB, and o-TFMB is on the order of 1×10^{-9} m. Mercury-intrusion porosimetry performed on 25 Culebra core samples yielded median pore-throat diameters that varied from 1.5×10^{-7} to 1.2×10^{-6} m with an arithmetic average value of 6.3×10^{-7} m (Kelley and Saulnier, 1990). The high-pressure mercury-injection tests provided quantitative estimates of the distribution of pore-throat diameters ranging down to as low

Table 4-2. Free-Water Diffusion Coefficients for Organic Anion Tracers Used at the WIPP Site

Tracer	Abbreviation	Free-Water Diffusion Coefficient ^a (m ² /s)
pentafluorobenzoate	PFB	7.2 x 10 ⁻¹⁰
meta-trifluoromethylbenzoate	m-TFMB	7.4 x 10 ⁻¹⁰
ortho-trifluoromethylbenzoate	o-TFMB	7.4 x 10 ⁻¹⁰
para-fluorobenzoate	p-FB	9.3 x 10 ⁻¹⁰
ortho-fluorobenzoate	o-FB	8.1 x 10 ⁻¹⁰
meta-fluorobenzoate	m-FB	8.0 x 10 ⁻¹⁰
benzoate		8.2 x 10 ⁻¹⁰

^a Values from Walter, 1982

as 8×10^{-9} m. For the 25 samples tested, the average percent mercury saturation was 95.4 corresponding to the 8×10^{-9} m pore-throat diameter. Thus, the molecular size of the organic tracers is sufficiently small in comparison to the pore-throat diameters in the Culebra that accessibility of the pores should not be a problem during diffusion.

4.2 Inorganic Anions

The only inorganic anion tracer used during tracer testing at the WIPP site is thiocyanate (SCN). The chemical behavior of SCN is similar to that of halide ions, and therefore, SCN is expected to behave in a conservative manner. Contradicting this expectation are the results of Bowman (1984) which indicate that greater than five percent of the SCN used in a 30-day soil tracer test was lost due to chemical or biological degradation. Stetzenbach and Stetzenbach (Appendix A) state that recovery of SCN is rarely 100 percent and that at least 5 percent of the SCN injected during a tracer test can be expected to be lost. This loss is a result of chemisorption in aquifers containing high levels of bacteria and bacterial activity in soils having been in contact with vegetation and manmade chemicals. In addition, Stetzenbach and Stetzenbach (Appendix A) believe that "thiocyanate is not a good long-term tracer because of the chemisorption problems." Hydro Geo Chem report in field notes that SCN results from the tracer tests conducted at the WIPP site show signs of degradation. Laboratory stability tests show that SCN degrades in time periods of days to tens of days as described in field notes recorded by Hydro Geo Chem. Repeated use of SCN as a tracer or using SCN during long tests appears to enable microbiota within the Culebra to acquire the capability to metabolize and otherwise decompose SCN as it moves through the formation (Hydro Geo Chem, 1986). For example, only 0.2 percent of the SCN injected during the long-term tracer test conducted at the H-4 hydropad was recovered in comparison to 37 percent recovery of m-TFMB which was injected at the same time and mass as SCN. During the H-6 convergent-flow tracer tests, SCN appeared to have behaved nonconservatively compared to p-FB, PFB, and m-TFMB. Comparison of the cumulative percent mass recovery of PFB and SCN for a dual-tracer

injection during a convergent-flow tracer test at the H-6 hydropad indicates that the tracers behaved identically for time periods less than 50 hours after tracer injection but quite differently thereafter. The lower concentrations of SCN relative to PFB can be explained by degradation of SCN after 50 hours.

4.3 Noncharged Halogenated Hydrocarbons

Halomethanes were selected for use during the recirculation tests conducted at the H-2 hydropad because their chemical stability is excellent. Unfortunately, they are difficult to handle because of their volatility and precise analysis for their concentration is difficult. In addition, they were found by Russell and Thompson (1981) to sorb to aquifer matrix. Although the halomethanes listed in Table 4-1 were injected into the Culebra interval during the H-2 recirculating tracer test, no effort was made to analyze samples for their content (Hydro Geo Chem, 1986). Hydro Geo Chem (1986) concluded that halomethanes were not appropriate tracers for use in subsequent tracer tests conducted at the WIPP site.

5.0 CULEBRA AND TRACER-TEST-SITE TRANSPORT PARAMETERS

This section discusses and summarizes the data base available for characterizing the transport properties of the Culebra at the hydropads where tracer tests have been performed and, to the extent possible, regionally. In addition, the range of measured or estimated values for each transport parameter is presented along with the measurement and/or calculated uncertainty in the parameter and the potential range for the parameter at each hydropad where tracer tests have been performed. Potential ranges of values were defined for use in sensitivity investigations.

Interpretation of the tracer tests was accomplished through calibration of the model to the observed breakthrough curves. For the calibration process, values were assigned to the parameters Culebra effective thickness, well spacing, pumping rate, free-water diffusion coefficient, longitudinal dispersivity, matrix porosity, and matrix tortuosity. These parameters are referred to as the assigned transport parameters. Fitting of the simulated breakthrough curves to the observed breakthroughs was achieved by adjusting the fracture porosity and matrix-block length for the heterogeneous-analysis approach and the anisotropy ratio, principal-transmissivity direction, and matrix-block length for the anisotropic-analysis approach. The parameters fracture porosity, matrix-block length, anisotropy ratio, and principal-transmissivity direction are referred to as the fitted transport parameters.

5.1 Assigned Transport Parameters

Values were assigned to the transport parameters Culebra effective thickness, well spacing, pumping rate, free-water diffusion coefficient, longitudinal dispersivity, matrix porosity, and matrix tortuosity for the tracer-test interpretations. Selection of the

parameters for which values would be assigned was based upon the availability of measured and/or literature values.

5.1.1 Culebra Effective Thickness

The Culebra elevations, depths below ground surface, and thicknesses for WIPP-area boreholes are presented in Table 5-1. The data sources are summarized in Cauffman et al. (1990). The Culebra thickness from boreholes in the WIPP-site region ranges from 5.5 m (H-2b1 and H-2c) to 11.3 m (H-7). For the hydropads where tracer tests were performed, the Culebra thickness is reported to be 5.5 to 6.7 m at H-2, 7.0 to 7.3 m at H-3, 7.3 to 7.9 m at H-4, 7.0 m at H-6, and 7.0 to 7.9 m at H-11.

Results of an ^{131}I tracer survey conducted across the Culebra perforations in H-3b1 suggest that the entire thickness of the Culebra did not accept fluid equally from the borehole (Mercer and Orr, 1979). A total of 1703 L of traced fluid was injected into the borehole at pump-in rates of approximately 0.5 L/s. The survey indicated the majority of fluid was lost to a 3.4-m section of the 8.5-m perforated interval. No additional data are available to define vertical heterogeneity at H-3 or any of the other hydropads where tracer tests have been performed.

The base-case value for the effective thickness of the Culebra was taken as the average of the Culebra thicknesses determined for the hydropad boreholes. The base-case values for the hydropads with tracer tests were 6.1 m for H-2, 7.2 m for H-3, 7.7 m for H-4, 7.0 m for H-6, and 7.6 m for H-11. The minimum effective thickness for flow in the Culebra is considered to be approximately 2 m. The ranges in Culebra effective thickness considered by the tracer-test interpretations were taken to be 2 m to the largest thickness measured at each hydropad. The greatest thicknesses were 6.7, 7.3, 7.9, 7.0, and 7.9 m at the H-2, H-3, H-4, H-6, and H-11 hydropads, respectively.

Table 5-1. Ground-Surface and Culebra Dolomite Elevations for WIPP-Area Boreholes
(from Cauffman et al., 1990)

WELL	REFERENCE ELEVATION m amsl ^a	CULEBRA DEPTH m bgs ^b			CULEBRA ELEVATION m amsl ^a			CULEBRA THICKNESS m
		Top	Center	Bottom	Top	Center	Bottom	
H-1	1035.68	206.04	209.55	213.06	829.64	826.13	822.62	7.01
H-2a	1029.55	189.89	193.24	196.60	839.66	836.31	832.95	6.71
H-2b1	1029.50	190.20	192.94	195.68	839.30	836.56	833.82	5.49
H-2b2	1029.49	189.89	193.24	196.60	839.60	836.25	832.90	6.71
H-2c	1029.52	190.20	192.94	195.68	839.32	836.58	833.84	5.49
H-3b1	1033.04	204.22	207.87	211.53	828.82	825.17	821.51	7.32
H-3b2	1033.07	206.04	209.70	213.36	827.03	823.37	819.71	7.32
H-3b3	1032.71	205.13	208.64	212.14	827.58	824.07	820.57	7.01
H-4a	1015.84	151.18	154.84	158.50	864.66	861.01	857.35	7.32
H-4b	1015.80	149.35	153.31	157.28	866.45	862.48	858.52	7.92
H-4c	1016.04	149.35	153.31	157.28	866.69	862.73	858.76	7.92
H-5a	1068.49	273.41	276.91	280.42	795.09	791.58	788.08	7.01
H-5b	1068.44	273.41	276.91	280.42	795.03	791.53	788.02	7.01
H-5c	1068.56	274.02	277.83	281.64	794.55	790.74	786.93	7.62
H-6a	1020.24	184.10	187.60	191.11	836.15	832.64	829.14	7.01
H-6b	1020.34	184.10	187.60	191.11	836.24	832.73	829.23	7.01
H-6c	1020.45	184.10	187.60	191.11	836.35	832.84	829.34	7.01
H-7b1	964.25	72.24	77.88	83.52	892.01	886.37	880.73	11.28
H-7b2	964.35	72.24	77.88	83.52	892.11	886.47	880.83	11.28
H-7c	964.21	72.24	77.88	83.52	891.97	886.33	880.69	11.28
H-8b	1046.34	179.22	183.18	187.15	867.12	863.16	859.19	7.92
H-8c	1046.14	179.22	183.18	187.15	866.92	862.96	858.99	7.92
H-9a	1038.16	197.21	201.78	206.35	840.95	836.38	831.81	9.14
H-9b	1038.21	197.21	201.78	206.35	841.00	836.43	831.86	9.14
H-9c	1038.31	197.21	201.78	206.35	841.10	836.53	831.96	9.14

Table 5-1. Ground-Surface and Culebra Dolomite Elevations for WIPP-Area Boreholes
(cont'd) (from Cauffman et al., 1990)

WELL	REFERENCE ELEVATION m amsl ^a	CULEBRA DEPTH m bgs ^b			CULEBRA ELEVATION m amsl ^a			CULEBRA THICKNESS m
		Top	Center	Bottom	Top	Center	Bottom	
H-10b	1124.32	414.53	419.25	423.98	709.79	705.07	700.34	9.45
H-10c	1124.14	414.53	419.25	423.98	709.61	704.89	700.16	9.45
H-11b1	1039.68	222.50	226.47	230.43	817.18	813.21	809.25	7.92
H-11b2	1039.75	223.42	227.08	230.73	816.33	812.67	809.02	7.32
H-11b3	1039.99	223.72	227.53	231.34	816.27	812.46	808.65	7.62
H-11b4	1039.32	220.37	223.88	227.38	818.95	815.45	811.94	7.01
H-12	1044.24	250.85	254.97	259.08	793.39	789.27	785.16	8.23
H-14	1019.70	166.12	170.23	174.35	853.58	849.47	845.35	8.23
H-15	1060.77	262.43	265.79	269.14	798.34	794.98	791.63	6.71
H-16	1039.25	214.12	217.46	220.80	825.13	821.79	818.45	6.68
H-17	1031.45	215.13	219.03	222.93	816.32	812.42	808.52	7.80
H-18	1040.39	209.89	213.58	217.26	830.50	826.82	823.13	7.37
DOE-1	1056.16	249.94	253.44	256.95	806.23	802.72	799.22	7.01
DOE-2	1041.89	251.16	254.51	257.86	790.73	787.38	784.03	6.71
P-1	1019.50	163.98	168.10	172.21	855.52	851.40	847.29	8.23
P-2	1060.00	261.21	265.18	269.14	798.79	794.82	790.86	7.92
P-3	1031.00	195.68	199.19	202.69	835.32	831.81	828.31	7.01
P-4	1048.90	236.22	240.33	244.45	812.68	808.57	804.45	8.23
P-5	1058.20	245.06	248.56	252.07	813.14	809.64	806.13	7.01
P-6	1022.20	163.68	167.18	170.69	858.52	855.02	851.51	7.01
P-7	1015.50	151.18	155.14	159.11	864.32	860.36	856.39	7.92

Table 5-1. Ground-Surface and Culebra Dolomite Elevations for WIPP-Area Boreholes
(cont'd) (from Cauffman et al., 1990)

WELL	REFERENCE ELEVATION m amsl ^a	CULEBRA DEPTH m bgs ^b			CULEBRA ELEVATION m amsl ^a			CULEBRA THICKNESS m
		Top	Center	Bottom	Top	Center	Bottom	
P-8	1016.90	171.60	175.41	179.22	845.30	841.49	837.68	7.62
P-9	1038.90	223.72	227.23	230.73	815.18	811.67	808.17	7.01
P-10	1069.40	283.77	287.73	291.69	785.63	781.67	777.71	7.92
P-11	1068.60	277.98	281.94	285.90	790.62	786.66	782.70	7.92
P-12	1029.00	192.94	196.44	199.95	836.06	832.56	829.05	7.01
P-13	1019.70	184.10	187.60	191.11	835.60	832.10	828.59	7.01
P-14	1024.05	174.65	178.00	181.36	849.40	846.05	842.69	6.71
P-15	1008.82	125.88	129.24	132.59	882.94	879.58	876.23	6.71
P-16	1012.80	152.40	155.91	159.41	860.40	856.89	853.39	7.01
P-17	1016.74	170.08	173.89	177.70	846.66	842.85	839.04	7.62
P-18	1059.88	277.98	282.24	286.51	781.90	777.64	773.37	8.53
P-19	1080.90	294.74	299.31	303.89	786.16	781.59	777.01	9.14
P-20	1082.90	290.47	294.44	298.40	792.43	788.46	784.50	7.92
P-21	1069.90	274.02	277.83	281.64	795.88	792.07	788.26	7.62
WIPP-11	1044.25	257.25	260.76	264.26	787.00	783.49	779.99	7.01
WIPP-12	1058.05	246.89	250.70	254.51	811.16	807.35	803.54	7.62
WIPP-13	1037.96	213.66	217.17	220.68	824.30	820.79	817.28	7.01
WIPP-18	1053.51	239.88	243.08	246.28	813.63	810.43	807.23	6.40
WIPP-19	1046.40	230.43	233.93	237.44	815.97	812.47	808.96	7.01

Table 5-1. Ground-Surface and Culebra Dolomite Elevations for WIPP-Area Boreholes
(cont'd) (from Cauffman et al., 1990)

WELL	REFERENCE ELEVATION m amsl ^a	CULEBRA DEPTH m bgs ^b			CULEBRA ELEVATION m amsl ^a			CULEBRA THICKNESS m
		Top	Center	Bottom	Top	Center	Bottom	
WIPP-21	1041.53	222.20	225.86	229.51	819.33	815.68	812.02	7.32
WIPP-22	1044.18	226.16	229.51	232.87	818.02	814.67	811.31	6.71
WIPP-25	979.16	136.25	140.06	143.87	842.91	839.10	835.29	7.62
WIPP-26	960.65	56.69	60.20	63.70	903.95	900.45	896.94	7.01
WIPP-27	968.40	89.00	92.96	96.93	879.40	875.43	871.47	7.92
WIPP-28	1020.05	128.02	131.98	135.94	892.03	888.07	884.11	7.92
WIPP-29	907.37	3.66	8.23	12.80	903.72	899.14	894.57	9.14
WIPP-30	1044.70	192.33	195.68	199.03	852.37	849.01	845.66	6.71
ERDA-6	1079.05	216.41	220.22	224.03	862.64	858.83	855.02	7.62
ERDA-9	1039.00	214.58	218.08	221.59	824.42	820.92	817.41	7.01
ERDA-10	1027.50	145.08	149.35	153.62	882.42	878.15	873.88	8.53
CB-1	1014.15	153.31	157.28	161.24	860.84	856.88	852.91	7.92
ENGLE	1042.00	200.86	204.22	207.57	841.14	837.78	834.43	6.71
USGS-1	1044.12	157.58	162.46	167.33	886.54	881.66	876.79	9.75
USGS-4	1040.22	142.88	148.03	153.18	897.34	892.19	887.04	10.30
USGS-6	1036.32	151.79	156.97	162.15	884.53	879.35	874.17	10.36
USGS-7	1036.93	156.67	161.4	166.12	880.26	875.54	870.81	9.45
USGS-8	1039.52	140.21	145.39	150.57	899.31	894.13	888.95	10.36
D-268	999.30	112.47	115.98	119.48	886.83	883.33	879.82	7.01

Table 5-1. Ground-Surface and Culebra Dolomite Elevations for WIPP-Area Boreholes
(cont'd) (from Cauffman et al., 1990)

WELL	REFERENCE ELEVATION m amsl ^a	CULEBRA DEPTH m bgs ^b			CULEBRA ELEVATION m amsl ^a			CULEBRA THICKNESS m
		Top	Center	Bottom	Top	Center	Bottom	
AEC-7	1114.73	265.18	269.14	273.10	849.55	845.59	841.63	7.92
AEC-8	1076.60	253.90	257.86	261.82	822.70	818.74	814.78	7.92
FFG-107	987.6	99.70	103.66	107.62	887.90	883.94	879.98	7.92
FFG-153	917.1	7.50	11.35	15.20	909.60	905.75	901.90	7.7
FFG-165	935.7	22.90	28.54	34.18	912.80	907.16	901.52	11.3
FFG-181	1016.5	86.00	89.96	93.92	930.50	926.54	922.58	7.92
FFG-188	979.0	133.71	137.56	141.41	845.29	841.44	837.59	7.7
FFG-225	1138.3	534.80	538.76	542.72	603.50	599.54	595.58	7.92
FFG-236	1101.2	418.50	422.46	426.42	682.70	678.74	674.78	7.92
FFG-244	1120.0	398.70	402.66	406.62	721.30	717.34	713.38	7.92
FFG-426	996.1	69.20	73.16	77.12	926.90	922.94	918.98	7.92
1 DANF	989.4	24.38	28.19	32.00	965.02	961.21	957.40	7.62
1 DUNC	1011.9	39.62	42.67	45.72	972.28	969.23	966.18	6.10

^a amsl abbreviates above mean sea level

^b bgs abbreviates below ground surface

Interpretations of geophysical logs generally report Culebra top and bottom to the nearest foot resulting in an uncertainty in Culebra thickness of about ± 0.3 m. Geophysical logs were not conducted in H-6a and H-6b. The thickness of the Culebra in these wells has been estimated to be equal to the Culebra thickness at H-6c. An error of ± 0.3 m in the estimated Culebra thickness at H-6a and H-6b was assumed for interpretation purposes. This error is consistent with the differences in Culebra thickness in the three wells at the H-3 hydropad and wells H-11b1, H-11b2, and H-11b3 at the H-11 hydropad. Incorporating these sources of error, the uncertainty assumed for the upper value of the Culebra thickness was ± 0.3 m for all wells at the H-2, H-3, H-4, and H-11 hydropads, ± 0.6 m for H-6a and H-6b, and ± 0.3 m for H-6c. The resulting maximum ranges for the potential effective thicknesses of the Culebra at the H-2, H-3, H-4, H-6, and H-11 hydropads were 2 to 7.0 m, 2 to 7.6 m, 2 to 8.2 m, 2 to 7.6 m, and 2 to 8.2 m, respectively. The range of measured thicknesses, the thickness uncertainties, and the ranges of potential values for the effective thickness of the Culebra are summarized in Table 5-2.

5.1.2 Well Spacing

Analysis of the tracer tests requires knowledge of the distances from the tracer-addition wells to the pumping well at the depth of the Culebra center. These distances were determined based on borehole surface locations and borehole-deviation surveys. The borehole-deviation surveys for the wells at the H-2, H-3, H-4, and H-6 hydropads and the original three wells at the H-11 hydropad are summarized in Saulnier et al. (1987). The deviation survey for H-11b4 is presented in Stensrud et al. (1988). The distances from the tracer-addition wells to the pumping wells at the H-2, H-3, H-4, H-6, and H-11 hydropads are summarized in Table 5-2.

The uncertainties in the well spacings include uncertainties in the surface locations of the boreholes and uncertainties in the borehole-deviation surveys. Measurements of distances between the centers of the wells at a hydropad using a steel tape are judged to be

Table 5-2. Summary of Base-Case Transport Parameters, Range of Measured or Estimated Values, Measurement or Calculation Uncertainty, and Range of Potential Values for Assigned Parameters

PARAMETER	BASE-CASE VALUE	RANGE OF MEASURED OR ESTIMATED VALUES	MEASUREMENT OR CALCULATION UNCERTAINTY		RANGE OF POTENTIAL VALUES* FOR SENSITIVITY ANALYSES
			LOW END	HIGH END	
Culebra Effective Thickness					
H-2	6.1 m	5.5 to 6.7 m (measured)	±0.3 m		2 to 7.0 m
H-3	7.2 m	7.0 to 7.3 m (measured)	±0.3 m		2 to 7.6 m
H-4	7.7 m	7.3 to 7.9 m (measured)	±0.3 m		2 to 8.2 m
H-6	7.0 m	7.0 m (measured)	±0.6 m for H-6a and H-6b ±0.3 m for H-6c		2 to 7.6 m
H-11	7.6 m	7.0 to 7.9 m (measured)	±0.3 m		2 to 8.2 m
Well Spacing					
H-2b1 to H-2c	23.2 m		±0.44 m		22.8 to 23.6 m
H-3b1 to H-3b3	30.7 m		±0.44 m		30.3 to 31.1 m
H-3b2 to H-3b3	26.8 m		±0.44 m		26.4 to 27.2 m
H-4a to H-4c	29.5 m		±2.84 m		26.7 to 32.3 m
H-4b to H-4c	31.0 m		±1.04 m		30.0 to 32.0 m
H-6b to H-6c	29.9 m		±1.04 m		28.9 to 30.9 m

Table 5-2. Summary of Base-Case Transport Parameters, Range of Measured or Estimated Values, Measurement or Calculation Uncertainty, and Range of Potential Values for Assigned Parameters (cont'd)

PARAMETER	BASE-CASE VALUE	RANGE OF MEASURED OR ESTIMATED VALUES	MEASUREMENT OR CALCULATION UNCERTAINTY		RANGE OF POTENTIAL VALUES ^a FOR SENSITIVITY ANALYSES
			LOW END	HIGH END	
Well Spacing (cont.)					
H-6a to H-6c	29.9 m			±1.24 m	28.7 to 31.1 m
H-11b3 to H-11b1	20.9 m			±0.44 m	20.5 to 21.3 m
H-11b2 to H-11b1	21.4 m			±0.44 m	21.0 to 21.8 m
H-11b4 to H-11b1	43.1 m			±0.44 m	42.7 to 43.5 m
Pumping Rate					
H-2 Test #1	0.019 L/s			±0.001 L/s	0.018 to 0.020 L/s
H-2 Test #2	0.016 to 0.024 L/s			±0.001 L/s	0.015 to 0.025 L/s
H-3	0.19 L/s			±0.005 L/s	0.185 to 0.195 L/s
H-4	0.017 to 0.033 L/s			±0.001 L/s	0.016 to 0.034 L/s
H-6	1.04 L/s			±0.025 L/s	1.015 to 1.065 L/s
H-11	0.38 L/s			-0.0025 to +0.0075 L/s	0.3775 to 0.3875 L/s
Free-Water Diffusion Coefficient					
PFB	$7.2 \times 10^{-10} \text{ m}^2/\text{s}$			$\pm 5.0 \times 10^{-11} \text{ m}^2/\text{s}$	$6.7 \times 10^{-10} \text{ to } 7.7 \times 10^{-10} \text{ m}^2/\text{s}$
m-TFMB	$7.4 \times 10^{-10} \text{ m}^2/\text{s}$			$\pm 5.2 \times 10^{-11} \text{ m}^2/\text{s}$	$6.9 \times 10^{-10} \text{ to } 7.9 \times 10^{-10} \text{ m}^2/\text{s}$

Table 5-2. Summary of Base-Case Transport Parameters, Range of Measured or Estimated Values, Measurement or Calculation Uncertainty, and Range of Potential Values for Assigned Parameters
(cont'd)

PARAMETER	BASE-CASE VALUE	RANGE OF MEASURED OR ESTIMATED VALUES	MEASUREMENT OR CALCULATION UNCERTAINTY		RANGE OF POTENTIAL VALUES ^a FOR SENSITIVITY ANALYSES
			LOW END	HIGH END	
Free-Water Diffusion Coefficient (cont.)					
o-TFMB	$7.4 \times 10^{-10} \text{ m}^2/\text{s}$		$\pm 5.2 \times 10^{-11} \text{ m}^2/\text{s}$		6.9×10^{-10} to $7.9 \times 10^{-10} \text{ m}^2/\text{s}$
p-FB	$9.3 \times 10^{-10} \text{ m}^2/\text{s}$		$\pm 6.5 \times 10^{-11} \text{ m}^2/\text{s}$		8.6×10^{-10} to $1.0 \times 10^{-9} \text{ m}^2/\text{s}$
Longitudinal Dispersivity					
H-2	1.5 m				0.5 to 3.0 m
H-3	1.5 m	0.8 to 2.0 m (calculated)	-1.0 m	+1.5 m	0.5 to 3.0 m
H-4	1.5 m				0.5 to 3.0 m
H-6	1.5 m	1.2 to 2.0 m (calculated)	-1.0 m	+1.5 m	0.5 to 3.0 m
H-11	1.5 m	1.7 to 2.1 m (calculated)	-1.0 m	+1.5 m	0.5 to 3.0 m
Matrix Porosity^b					
H-2	0.13	0.082 to 0.154 (measured)	-0.016	+0.046	0.08 to 0.30
H-3	0.20	0.168 to 0.244 (measured)	-0.016	+0.046	0.08 to 0.30

Table 5-2. Summary of Base-Case Transport Parameters, Range of Measured or Estimated Values, Measurement or Calculation Uncertainty, and Range of Potential Values for Assigned Parameters
(cont'd)

PARAMETER	BASE-CASE VALUE	RANGE OF MEASURED OR ESTIMATED VALUES	MEASUREMENT OR CALCULATION UNCERTAINTY		RANGE OF POTENTIAL VALUES ^a FOR SENSITIVITY ANALYSES
			LOW END	HIGH END	
Matrix Porosity^b (cont.)					
H-4	0.25	0.208 to 0.297 (measured)	-0.016	+0.046	0.08 to 0.30
H-6	0.16	0.107 to 0.255 (measured)	-0.016	+0.046	0.08 to 0.30
H-11	0.16	0.099 to 0.303 (measured)	-0.016	+0.046	0.08 to 0.30
Matrix Tortuosity					
H-2	0.15	0.029 to 0.331 (measured from 11 borehole locations)	-0.002	+0.049	0.027 to 0.380
H-3	0.15	0.029 to 0.331 (measured from 11 borehole locations)	-0.002	+0.049	0.027 to 0.380
H-4	0.15	0.029 to 0.331 (measured from 11 borehole locations)	-0.002	+0.049	0.027 to 0.380
H-6	0.15	0.029 to 0.331 (measured from 11 borehole locations)	-0.002	+0.049	0.027 to 0.380

Table 5-2. Summary of Base-Case Transport Parameters, Range of Measured or Estimated Values, Measurement or Calculation Uncertainty, and Range of Potential Values for Assigned Parameters
(cont'd)

PARAMETER	BASE-CASE VALUE	RANGE OF MEASURED OR ESTIMATED VALUES	MEASUREMENT OR CALCULATION UNCERTAINTY		RANGE OF POTENTIAL VALUES ^a FOR SENSITIVITY ANALYSES
			LOW END	HIGH END	
Matrix Tortuosity (cont.)					
H-11	0.11	0.029 to 0.331 (measured from 11 borehole locations)	-0.002	+0.049	0.027 to 0.380

^a The range of potential values defines the high- and low-end transport-parameter values used in sensitivity simulations.

^b Measurement uncertainty was added to matrix-porosity range of average porosity at each hydropad or borehole location to yield range of potential values.

within ± 0.04 m. Borehole-deviation surveys were conducted with a rate-integrating north-seeking gyroscope at the H-2, H-3, and H-11 hydropads and with a conventional two-degree-of-freedom gyroscope at the H-4 and H-6 hydropads. The company that conducted the surveys at the H-2, H-3, and H-11 hydropads and that uses both types of gyroscopes estimates that the accuracy in the rate-integrating north-seeking gyroscope is 0.15 m per 305 m (6 inches per 1000 ft), the accuracy in the conventional gyroscope is 0.3 to 0.6 m per 305 m (1 to 2 ft per 1000 ft), and the accuracy in the wireline is 0.15 m per 305 m (6 inches per 1000 ft). These accuracies correspond to uncertainties in the borehole-deviation surveys of ± 0.2 m at the H-2, H-3, and H-11 hydropads and ± 0.5 m at the H-4 and H-6 hydropads. Additional uncertainties in the borehole deviation of H-4a and H-6a derive from the deviation surveys having been conducted to depths 27.7 and 26.8 m shallower, respectively, than the Culebra center thus, requiring extrapolation of the available deviation data to the center of the Culebra. These uncertainties are judged to be twice the extrapolated deviations or about ± 1.8 m at H-4a and about ± 0.2 m at H-6a. The ranges of potential values for the well spacings at the H-2, H-3, H-4, H-6, and H-11 hydropads are summarized in Table 5-2.

5.1.3 Pumping Rate

The flow rates through the recirculating system at the H-2 hydropad were 0.019 L/s during test #1 and 0.016 to 0.024 L/s during test #2. The pumping rates measured during the tracer tests were averaged to obtain base-case rates of 0.19 L/s at H-3, 0.017 to 0.033 L/s at H-4, 1.04 L/s at H-6, and 0.38 L/s at H-11. Because numerous pump stoppages of unknown duration occurred during the H-2 and H-4 tracer tests, an uncertainty of about five percent of the average pumping rate or 0.001 L/s was assumed. At H-3, the flow rate was calculated using a container and a stop watch. At rates measured during the H-3 tracer test, an error of 1.5 sec over a time period of one minute, or ± 0.005 L/s, was assumed. At H-6, the measured flow rates averaged about five times higher than the rates during the H-3 test. Therefore, an uncertainty five times higher than that for H-3 was

assumed for H-6. Flow rates during the H-11 tracer test were measured by two methods. The rates used in the tracer-test interpretations were measured using a Precision totalizing flow meter and averaged about 0.005 L/s lower than the rates measured with a calibrated standpipe. The uncertainty in the totalizing flow meter rates was judged to be half as much as the difference between the two flow-rate measurements, or ± 0.0025 L/s. The total uncertainty in the flow rates during the H-11 test was assumed to be -0.0025 to $+0.0075$ L/s. The measurement uncertainties and ranges of potential values for the flow rates during the H-2, H-3, H-4, H-6, and H-11 tracer tests are summarized in Table 5-2.

5.1.4 Free-Water Diffusion Coefficients

The free-water diffusion coefficients for the organic-anion tracers were reported by Walter (1982) and are summarized in Section 4.0. The technique used to determine those values is discussed in Section 4.1. Walter (1982) reports an error in the calculated free-water diffusion coefficients of approximately seven percent. The calculated uncertainties and ranges of potential free-water diffusion coefficient values for the tracers analyzed at the H-3, H-6, and H-11 hydropads are presented in Table 5-2.

5.1.5 Longitudinal Dispersivity

Welty and Gelhar (1989) presented a theoretical analysis for a convergent-flow tracer test with a pulse input at a tracer-addition well. Their analysis accounts for the radially varying velocity field. Using the assumption that longitudinal dispersivity divided by the distance between the pumping- and tracer-addition wells is much less than unity, they developed the following relation to estimate longitudinal dispersivity:

$$\alpha_L = \frac{3r \left(\frac{\Delta t}{t_m} \right)^2}{64} \quad (5-1)$$

where:

- α_L = longitudinal dispersivity,
- r = distance between tracer-addition and pumping wells,
- t_m = arrival time of the peak concentration,
- Δt = twice the time from concentration $e^{-1}c_m$ to concentration c_m ,
- c_m = peak concentration.

Figure 5-1 schematically depicts the definitions of t_m and Δt .

Using Equation 5-1, a longitudinal dispersivity of 1.9 m was calculated based on the m-TFMB breakthrough curve at the H-3 hydropad. The peak concentration used for this calculation was the third highest m-TFMB concentration measured at the pumping well. As discussed in Section 7.4.1.2, the two highest points could not be matched while maintaining a reasonable fit to the remaining m-TFMB data. Therefore, they were not considered to be representative of the trend in the m-TFMB breakthrough curve. However, if the highest measured m-TFMB concentration was used to calculate a longitudinal dispersivity, a value of 1.0 m would be obtained. The longitudinal dispersivities calculated at the H-6 hydropad were 1.7 m from the PFB breakthrough curve of test #1 and 1.8 m from the p-FB breakthrough curve of test #2. At the H-11 hydropad, a dispersivity of 1.9 m was calculated from the m-TFMB breakthrough curve.

The range of potential values for longitudinal dispersivity was calculated based on the potential range of the individual parameters in Equation 5-1. Equation 5-1 requires the time and magnitude of the peak concentration. The degree of error in the analytic method used to determine tracer concentrations is assigned a value of ± 2.5 percent. This

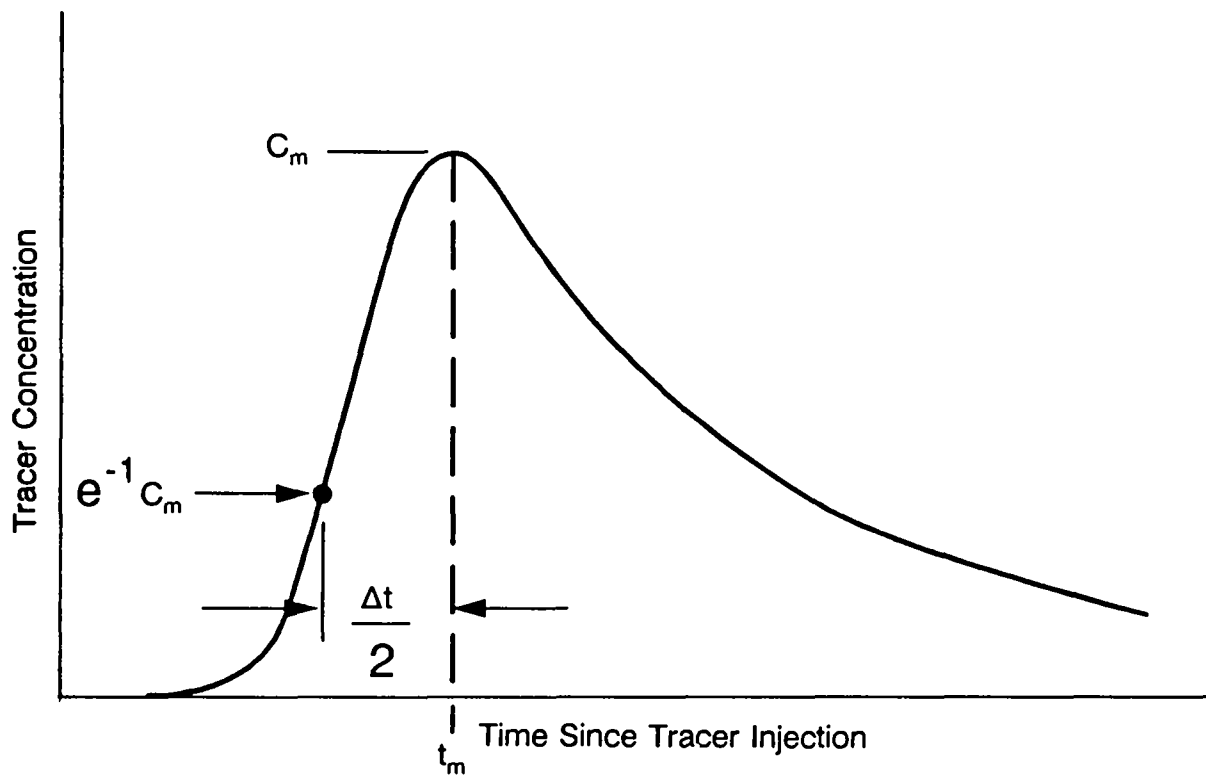


Figure 5-1. Schematic tracer-breakthrough curve at the pumping well for a radial-convergent tracer test with pulse injection.

uncertainty, based on analysis of duplicate samples collected at the H-11 hydropad, was assumed for the H-3 and H-6 measured concentrations as well as the H-11 measured concentrations. The uncertainty in the peak-concentration arrival time consists of two components. The first component is the error in the estimated plug-flow time for tracer to travel down the injection well to the Culebra center and up the pumping well to the sampling point. This error is assumed to be on the order of ± 25 percent for an error of ± 0.026 days for H-3, ± 0.006 days for H-6, and ± 0.012 days for H-11. The second component is the potential error from inability to define the peak concentration precisely due to the sampling frequency. The second source of error was incorporated by assuming the peak concentration could have occurred from as early as midway between the peak concentration and the previous sample time to midway between the peak concentration and the following sample time. These times were -0.90 to $+0.15$ days for H-3, -0.10 to $+0.07$ days for H-6 test #1, ± 0.02 days for H-6 test #2, and ± 0.01 days for H-11. Also required by Equation 5-1 is the distance from the tracer-addition well to the pumping well. The base-case and range for these distances at H-3, H-6, and H-11 are discussed in Section 5.1.2. Incorporating the potential errors in measured concentration, peak-concentration arrival time, and well spacing discussed above, the potential ranges in longitudinal dispersivity are 0.8 to 2.0 m at H-3, 1.2 to 2.0 m at H-6, and 1.7 to 2.1 m at H-11.

Equation 5-1 was applied only to the breakthrough curves exhibiting fracture-dominated transport because we are interested in obtaining estimates of dispersivity representing dispersion during transport in the fracture system. The shape of the breakthrough curve used to calculate the dispersivity from Equation 5-1, however, is dependent on diffusive losses to the matrix. Diffusive losses would be expected to result in some widening of the breakthrough curve, thus dispersivities estimated using Equation 5-1 may be on the high side. Therefore, a value of 1.5 m was selected for the base-case longitudinal dispersivity which is less than the calculated values of 1.7 to 1.9 m from the H-3, H-6, and H-11 hydropads.

In an attempt to incorporate uncertainty in longitudinal dispersivity due to errors in peak-concentration arrival time and well spacing and due to limitations in the use of Equation 5-1 as discussed above, longitudinal dispersivity is assumed to range from a factor of three less than to a factor of two greater than the base-case value of 1.5 m. Thus, the range of potential values of longitudinal dispersivity considered for simulation purposes is from 0.5 to 3.0 m. The calculated longitudinal dispersivities at the H-3, H-6, and H-11 hydropads, the uncertainties in the calculated values based on errors in peak-concentration arrival times and well spacings, and the ranges of potential dispersivities are summarized in Table 5-2. Further discussion of dispersivities reported in the literature and relationships between longitudinal dispersivity and transport scale is given below.

A review of the literature for various tracer-test scales and contaminant-plume sizes (e.g., Lallemand-Barres and Peaudecerf, 1978; Pickens and Grisak, 1981a; Gelhar et al., 1985) suggests that the magnitude of dispersivity increases with increasing scale of the tracer test or contamination plume. The most comprehensive review of dispersivity values is presented by Gelhar et al. (1985). For scales of observation ranging from 0.75 m to 100 km, they reported longitudinal dispersivities from 0.01 to 5500 m. From an evaluation of the test configuration, tracer monitoring, and data-analysis method for each site, they concluded that only five sites in their survey had produced highly reliable dispersivity data. Furthermore, they noted that the high-reliability data subset indicated that "the dispersivity initially increases with the scale of observation" and "it is not clear whether the dispersivity increases indefinitely with scale or reaches an asymptotic value as is assumed in classical modelling and predicted by recent stochastic theories." A plot of longitudinal dispersivity versus scale of observation from Gelhar et al. (1985) is presented in Figure 5-2.

Pickens and Grisak (1981b) presented an evaluation of two tracer tests with transport scales of 1 to 32.5 m and found that the ratio of apparent dispersivity to transport distance varies from 0.05 to 0.10. They presented an approach which allowed dispersivity to vary temporally as a function of the median travel distance of the solute from an input source. For the tracer tests conducted at the WIPP site, transport distances between tracer-addition

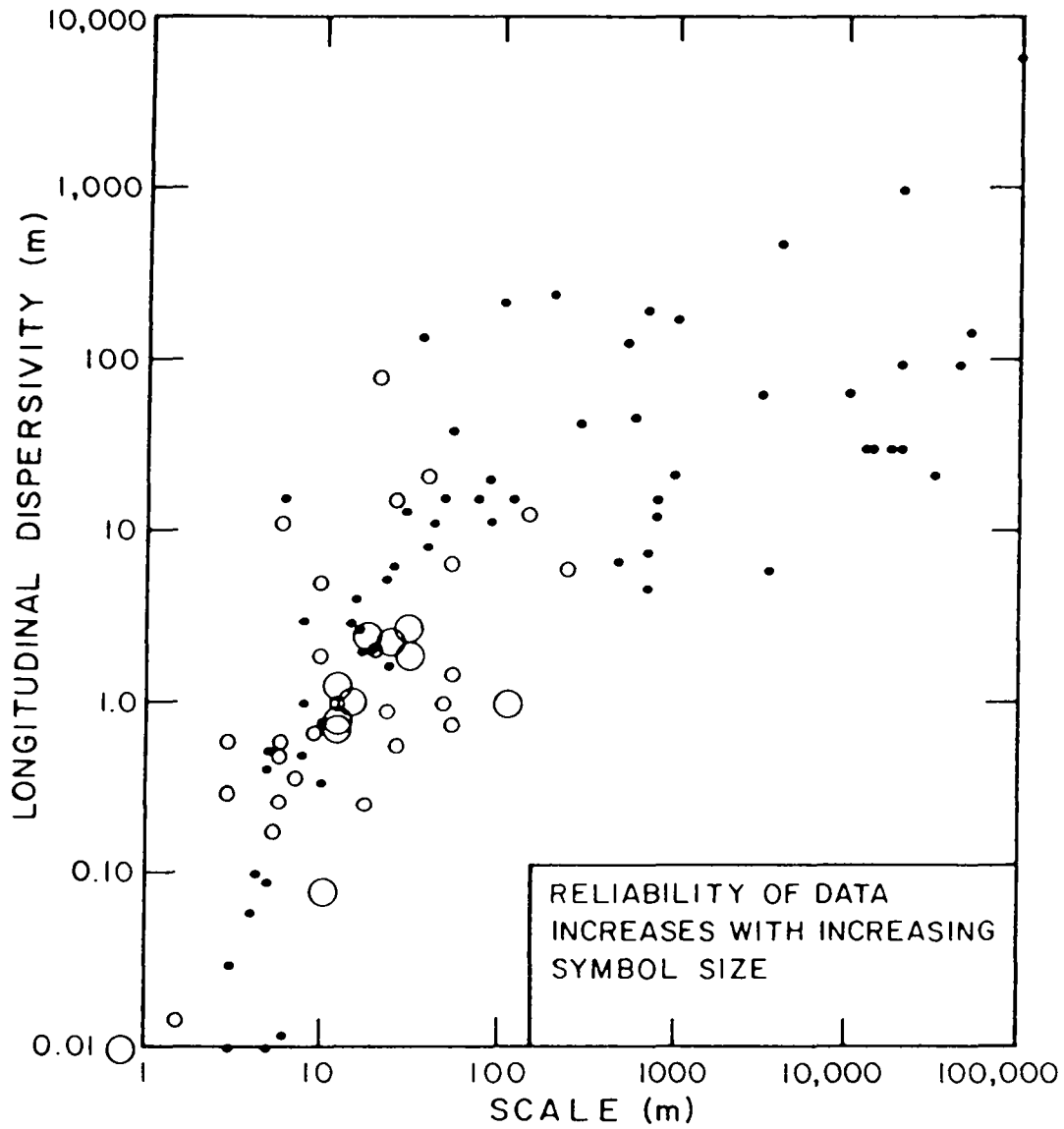


Figure 5-2. Scale of observation versus longitudinal dispersivity for the saturated zone: reliability classification (from Gelhar et al., 1985).

and pumping wells at Culebra depth vary from 26.8 to 30.7 m at the H-3 hydropad, are 29.9 m at the H-6 hydropad, and vary from 20.9 to 43.1 m at the H-11 hydropad. For a typical hydropad transport scale of about 30 m, the relationship reported above by Pickens and Grisak (1981b) yields a dispersivity range of 1.5 to 3.0 m. Considering the similarity in transport scale for the H-2 and H-4 hydropads to the H-3, H-6, and H-11 hydropads, identical base-case (1.5 m) and range values (0.5 to 3.0 m) were selected for H-2 and H-4.

Neuman (1990) interpreted the dispersivity scale effect as representing a continuous hierarchy of log hydraulic-conductivity fields. He found that both porous and fractured media appeared to follow the same idealized scaling rule for both flow and transport and that data suggest that transport-model calibration using hydraulic-conductivity measurements "has the effect of filtering out the large-scale modes from the hierarchy." He evaluated over 130 longitudinal dispersivities from laboratory and field-tracer studies in porous and fractured media recorded by Lallemand-Barres and Peaudecerf (1978), Pickens and Grisak (1981a), Gelhar et al. (1985), Arya (1986), and Arya et al. (1988). Dispersivities ranged from less than 1 mm to more than 1 km corresponding to site scales of less than 10 cm to more than 100 km. Neuman (1990) fit a regression line to a logarithmic plot of apparent longitudinal dispersivities α_{aL} versus the scale of the study L_s , as given by the aforementioned authors, for $L_s < 3500$ m and excluding numerical-model calibration results. This line can be expressed

$$\alpha_{aL} = 0.0175L_s^{1.46} \quad (5-2)$$

with a regression coefficient $R^2 = 0.74$. In addition, he fit two separate regression lines to data with $L_s \leq 100$ m and $L_s \geq 100$ m as follows:

$$\alpha_{aL} = 0.0169L_s^{1.53} \quad , \text{ for } L_s \leq 100 \text{ m} \quad (5-3)$$

with a regression coefficient $R^2 = 0.71$, and

$$\alpha_{aL} = 0.32L_s^{0.83} \quad , \text{ for } L_s \geq 100 \text{ m} \quad (5-4)$$

with a regression coefficient $R^2 = 0.44$.

Using the relationship presented by Neuman (1990) for apparent dispersivity as a function of scale of study for $L_s \leq 100$ m, one can calculate a dispersivity of about 3 m for the transport scale of 30 m typical of the H-3, H-6, and H-11 hydropads. This estimated dispersivity may be on the high side for reasons discussed below.

Many of the field cases for longitudinal-dispersivity values and corresponding transport scales presented in Gelhar et al. (1985) and Neuman (1990) were for sites and interpretations with poor reliability. Factors causing uncertainty in the reported dispersivities and which, in some cases, yield large apparent dispersivities include:

- permeability testing and water-quality or tracer sampling over long borehole intervals when transport is over shorter intervals;
- uncertainties in the injection intervals of the introduced tracers;
- nonconservative transport of some of the tracers (e.g., tracer degradation or sorption);
- poor or inadequate definition of the flow regime;
- test interpretations using a single-porosity analysis when the flow system is actually a double-porosity medium; and
- test interpretation in one or two dimensions when the data should have been analyzed in two or three dimensions, respectively.

Gelhar et al. (1985) suggest that ... "High-quality dispersivities were those for which the dimensionality of the solute plume, the solute measurements, and the data analyses are consistent." Because of the limitations listed above for literature values for longitudinal dispersivity, selecting a range at a transport scale of 30 m from Figure 5-2 would be inappropriate in defining a dispersivity range for the tracer tests conducted in the Culebra. The Culebra tracer tests utilized carefully controlled tracer-input conditions, carefully controlled flow regimes, interpretations using a double-porosity analysis where indicated by the tracer-transport behavior, and analysis of only those breakthrough curves where the tracers are considered to have behaved conservatively. In summary, the range for longitudinal dispersivity shown in Figure 5-2 for a transport scale of 30 m exceeds by far what is reasonable for the Culebra at the hydropads at the WIPP site. The range of 0.5 to 3.0 m discussed earlier is considered most representative for sensitivity analyses of the tracer tests.

5.1.6 Matrix Porosity

Laboratory matrix-porosity determinations have been performed on 79 core samples from the Culebra at 15 borehole or hydropad locations at and surrounding the WIPP site (Table 5-3). Factors affecting core selection for laboratory porosity determinations included availability of core samples and competency of the core samples for analysis. Not all boreholes have core available. In addition, core recovery during drilling was very poor at some locations (e.g., approximately 10 and 40 percent at H-3b2 and H-3b3, respectively).

The number of samples, average porosity, and range of matrix porosities for the H-2, H-3, H-4, H-6, and H-11 hydropads are summarized in Table 5-4. These averages are based on a limited number of samples ranging from two to ten at each hydropad. For the double-porosity transport interpretations of the tracer tests performed at the H-3, H-6, and H-11 hydropads, a matrix porosity of 0.20 was selected for the H-3 hydropad and a matrix porosity of 0.16 was selected for the H-6 and the H-11 hydropads.

Table 5-3. Summary of Porosities Determined Using Boyle's Law Technique on Culebra Core Samples (after Kelley and Saulnier, 1990)

<u>Borehole Number</u>	<u>Sample Number</u>	<u>Porosity</u>	<u>Average Hydropad or Borehole Porosity</u>
H-2a	H-2a-1	0.116	0.125
	H-2a-2	0.131 ^a	0.125
H-2b	1-1	0.141	0.125
	2-1/3-1	0.154 ^b	0.125
	1-2	0.118	0.125
	2-2/3-2	0.103 ^b	0.125
H-2b1	H-2b1-1	0.082	0.125
	H-2b1-1F	0.105	0.125
	H-2b1-2	0.142 ^a	0.125
	H-2b1-3	0.153	0.125
H-3b2	1-3	0.188	0.198
	1-4	0.168	0.198
H-3b3	2-3/3-3	0.180 ^b	0.198
	2-4/3-4V	0.202 ^b	0.198
	1-6/3-6V	0.244	0.198
	2-5/3-5	0.205 ^b	0.198
H-4b	1-9	0.297	0.253
	2-6/3-6V	0.208 ^b	0.253
H-5b	H-5b-1a	0.128 ^a	0.178
	H-5b-1b	0.155	0.178
	H-5b-2	0.228	0.178
	H-5b-2F	0.248	0.178
	H-5b-3	0.133	0.178
H-6b	2-7	0.108	0.147
	2-8	0.116	0.147
	1-7	0.107	0.147
	1-8/3-8V	0.255	0.147

Table 5-3. Summary of Porosities Determined Using Boyle's Law Technique on Culebra Core Samples (after Kelley and Saulnier, 1990)

<u>Borehole Number</u>	<u>Sample Number</u>	<u>Porosity</u>	<u>Average Hydropad or Borehole Porosity</u>
H-7b1	H-7b1-1	0.177	0.169
	H-7b1-1F	0.149	0.169
	H-7b1-2a	0.206 ^a	0.169
	H-7b1-2b	0.278	0.169
H-7b2	H-7b2-1	0.159 ^a	0.169
	H-7b2-2	0.118	0.169
H-7c	H-7c-1a	0.130 ^a	0.169
	H-7c-1b	0.165	0.169
	H-7c-1F	0.138	0.169
H-10b	H-10b1	0.089 ^a	0.096
	H-10b2	0.115	0.096
	H-10b2F	0.066	0.096
	H-10b3	0.112	0.096
H-11	H-11-1	0.155	0.162
	H-11-2	0.105 ^a	0.162
	H-11-2F	0.104	0.162
	H-11-b3-1	0.303	0.162
	H-11-b3-1F	0.223	0.162
	H-11-b3-2	0.099	0.162
	H-11-b3-2F	0.123	0.162
	H-11-b3-3	0.130	0.162
	H-11-b3-4	0.152 ^a	0.162
H-11-b3-4F	0.224	0.162	
WIPP-12	W-12-1a	0.028	0.107
	W-12-1b	0.114 ^a	0.107
	W-12-2	0.126 ^a	0.107
	W-12-2F	0.135	0.107
	W-12-3	0.134	0.107

Table 5-3. Summary of Porosities Determined Using Boyle's Law Technique on Culebra Core Samples (after Kelley and Saulnier, 1990)

<u>Borehole Number</u>	<u>Sample Number</u>	<u>Porosity</u>	<u>Average Hydropad or Borehole Porosity</u>
WIPP-13	W-13-1	0.143	0.180
	W-13-2	0.219	0.180
	W-13-2F	0.260	0.180
	W-13-3a	0.179 ^a	0.180
	W-13-3b	0.097	0.180
WIPP-25	W-25-1	0.115	0.115
WIPP-26	W-26-1	0.124	0.122
	W-26-1F	0.112	0.122
	W-26-2	0.126	0.122
	W-26-3	0.127 ^a	0.122
WIPP-28	W-28-1a	0.142	0.162
	W-28-1b	0.130 ^a	0.162
	W-28-2	0.187	0.162
	W-28-3	0.170	0.162
	W-28-3F	0.179	0.162
WIPP-30	W-30-1	0.128	0.165
	W-30-2	0.150	0.165
	W-30-3a	0.176	0.165
	W-30-3b	0.149 ^a	0.165
	W-30-3F	0.149	0.165
	W-30-4	0.239 ^a	0.165
AEC-8	AEC-8-1	0.079	0.103
	AEC-8-1F	0.122	0.103
	AEC-8-2	0.109	0.103

^a Represents an average value from porosity determinations from Terra Tek Laboratories and K&A Laboratories.

^b Represents an average of porosity values determined using sample bulk volume estimated from measured sample dimensions and from fluid displacement.

Number of samples = 79
 Average porosity = 0.153
 Standard deviation = 0.053
 Range for all samples = 0.028 - 0.303
 Range for average hydropad or borehole porosities = 0.10 - 0.25

Table 5-4. Summary of Average and Range of Porosities for Core from the H-2, H-3, H-4, H-6, and H-11 Hydropads

<u>Hydropad</u>	<u>Number of Samples</u>	<u>Average Matrix Porosity</u>	<u>Range of Matrix Porosity</u>
H-2	10	0.125	0.082 - 0.154
H-3	6	0.198	0.168 - 0.244
H-4	2	0.253	0.208 - 0.297
H-6	4	0.147	0.107 - 0.255
H-11	10	0.162	0.099 - 0.303

Interpretation of the tracer tests using a double-porosity conceptualization requires an effective matrix porosity over the entire thickness of interest. An estimate of the range of representative values for effective matrix porosity for the entire Culebra thickness at a specific hydropad was determined by averaging the measured matrix porosities at each hydropad or borehole location (Table 5-3). Individual matrix-porosity measurements at point locations within the Culebra were not considered to be representative of effective matrix porosity for the full Culebra thickness for simulation purposes. The average matrix porosity from 15 hydropad or borehole locations ranged from a low of 0.10 at H-10 to a high of 0.25 at H-4. Therefore, the representative measured range is assumed to be 0.10 to 0.25. Uncertainty resulting from measurement technique and analyzing laboratory is discussed below.

Detailed core descriptions and full details on experimental techniques and results for matrix porosity are presented in Kelley and Saulnier (1990). The porosities of all samples were determined by the Boyle's Law technique using helium or air with the bulk volume of the sample determined by the caliper method and volumetric relationships. For six samples, two helium porosities were determined by one laboratory using two different methods to calculate the sample bulk volume. The porosities from bulk volume measurements by caliper and volumetric relationships were 0.046 lower to 0.016 higher than the porosities from bulk volume determination by the fluid displacement technique. Porosity determination for 30 samples was conducted by one laboratory using both the Boyle's Law technique and the water-resaturation technique. The porosities determined using the two techniques were very consistent with the Boyle's Law porosities ranging from 0.006 lower to 0.003 higher than the resaturation porosities. For 18 samples, a Boyle's Law porosity was measured by two different laboratories. The porosities were similar in magnitude with values from one laboratory ranging from 0.022 lower to 0.003 higher than the porosities measured by the second laboratory. In so much as porosities were not exactly reproducible by a second laboratory or using a different method, some uncertainty exists in the measured porosities. The value assigned for this uncertainty was selected as the largest difference observed between laboratories or between methods. This approach indicates that the

porosities considered for tracer-test interpretations could be 0.046 too low to 0.016 too high. Adding this uncertainty to the range of average matrix porosity for 15 borehole or hydropad locations across the WIPP site (0.10 to 0.30) yields a potential range for the effective matrix porosity of 0.08 to 0.30 for the full Culebra thickness. The range of measured porosities at the H-2, H-3, H-4, H-6, and H-11 hydropads, the uncertainty in the measured matrix porosities, and the range of potential effective matrix porosities for the full Culebra thickness for interpretation purposes are summarized in Table 5-2.

5.1.7 Matrix Tortuosity

The effective diffusion coefficient within the matrix blocks is defined for use in the SWIFT II model by the relation:

$$E' = \theta' \phi' D' \quad (5-5)$$

where:

E' = effective diffusion coefficient in the porous medium,

θ' = matrix tortuosity,

ϕ' = matrix porosity, and

D' = free-water diffusion coefficient.

and the prime indicates matrix values.

Bear (1972) defines tortuosity as:

$$\theta' = (L/L_c)^2 \quad (5-6)$$

where:

L = sample length, and

L_e = actual tortuous flowpath length that a fluid particle would take passing through a sample of length L .

Tortuosity, with magnitude $0 < \theta' < 1$, is a measure of the tortuous nature of the interconnected pore space through which the solute is diffusing. Smaller tortuosities indicate longer diffusional path lengths and, therefore, greater resistance to diffusion.

Generally, values for tortuosity are determined by either of two indirect methods: electrical-resistivity measurements and diffusion experiments. Electrical-resistivity measurements were carried out using core plugs from a number of borehole and hydropad locations at the WIPP site. Full details on experimental techniques and results are presented in Kelley and Saulnier (1990). The electrical resistivity of a saturated porous medium is directly related to the resistivity of the fluid that saturates the porous medium. The constant of proportionality relating the resistivity of the formation and its saturating fluid is called the formation factor ($F \geq 1.0$) and is equal to:

$$F = R_b / R_w \quad (5-7)$$

where R_b is equal to the resistivity of the porous media saturated with fluid of resistivity R_w . Klinkenberg (1951) deduced that, from a theoretical viewpoint, the factors that impede electrical conductance through a porous medium are the same factors that impede diffusion of a conservative solute. Based upon the conclusion of Klinkenberg (1951) that diffusion should be analogous to conduction in a porous medium, an equation relating formation factor, porosity, and tortuosity can be developed as follows:

$$\theta' = 1/(F\phi') \quad (5-8)$$

The formation factors and calculated tortuosities from 15 core samples from 11 borehole or hydropad locations at the WIPP site are shown in Table 5-5 (Kelley and

Table 5-5. Summary of Formation-Factor and Tortuosity Values (after Kelley and Saulnier, 1990)

<u>Sample Number</u>	<u>Helium Porosity</u>	<u>Formation Factor</u>	<u>Tortuosity^a</u>
AEC-8-1F	0.122	90.09	0.091
H-2b1-1F	0.105	326.77	0.029
H-5b-2F	0.248	12.2	0.331
H-7b1-1F	0.149	73.49	0.091
H-7C-1F	0.138	79.61	0.091
H-10b-2F	0.066	406.78	0.037
H-11-2F	0.104	94.82	0.101
H-11b3-1F	0.223	36.35	0.123
H-11b3-2F	0.123	101.93	0.080
H-11b3-4F	0.224	32.74	0.136
W-12-2F	0.135	47.3	0.157
W-13-2F	0.26	13.26	0.290
W-26-1F	0.112	68.77	0.130
W-28-3F	0.179	26.3	0.212
W-30-3F	0.149	31.49	0.213

^a Tortuosities are calculated from formation factors determined from electrical-resistivity measurements.

Number of samples = 15
 Average tortuosity = 0.141
 Range = 0.029 to 0.331

Saulnier, 1990). Calculated tortuosities range from about 0.03 to 0.33 with an arithmetic average of 0.14.

Diffusion experiments have been performed at Sandia National Laboratories on three samples of the Culebra dolomite (Dykhuisen and Casey, 1989). Eight different diffusion experiments were performed on three different samples from three different locations. Four experiments were performed on a rock sample of the Culebra dolomite from core recovered from WIPP-19 (sample WIPP-19). Three experiments were performed on one sample of the Culebra dolomite using a slab of the Culebra dolomite from the WIPP-site Exhaust Shaft (sample ESM-143-2). One experiment was performed on a rock sample of the Culebra dolomite from the WIPP-site Air-Intake Shaft (sample A1S-SNL-16). Porosities and tortuosities were determined from analysis of the concentration data yielded by the diffusion experiments using methods described in Katsube et al. (1986) and Dykhuisen and Casey (1989). (These are denoted diffusion porosities and diffusion tortuosities in the following text.) Table 5-6 summarizes the results of these diffusion experiments. For the diffusion experiments, two samples were tested with multiple tracers and one sample with a single tracer. For calculating mean values from the diffusion data, rock samples with more than one diffusion experiment using different tracers were averaged to give an average diffusion tortuosity and diffusion porosity for that rock sample. The single tracer and average multiple-tracer values were then averaged to arrive at a mean value for the three rock samples used in the diffusion experiments. This procedure incorporates the variation within one sample, yet prevents any one tracer result from dominating the mean value.

The results of the diffusion experiments on the three samples indicated a diffusion-tortuosity range of 0.03 to 0.17, with a mean value of 0.10. The diffusion porosity ranged from 0.01 to 0.13, with a mean value of 0.06. The mean diffusion tortuosity of 0.10 is about a third less than the mean tortuosity of 0.14 calculated from electrical-resistivity measurements on samples reported in Kelley and Saulnier (1990). This result is not surprising, given that the measured porosities of the samples used in the diffusion experiment are generally much less than the porosities of the samples from which the

Table 5-6. Results from Diffusion Studies Performed on the Culebra Dolomite by Sandia National Laboratories (after Kelley and Saulnier, 1990)

<u>Sample Number</u>	<u>Sample Name</u>	<u>Date Reported</u>	<u>Tracer Ion</u>	<u>D_o (cm²/s)</u>	<u>Sample Vol (cm³)</u>	<u>Helium Porosity</u>	<u>Diffusion Porosity</u>	<u>Tortuosity</u>	<u>Diffusion Formation Factor</u>
1	WIPP-19	3/23/88	22 Na	7.50E-06	19.68	0.1550	0.040	0.043	577
	WIPP-19	3/23/88	3 H	1.31E-05	19.68	0.1550	0.060	0.025	409
	WIPP-19	3/23/88	129 I	1.00E-05	19.68	0.1550	0.020	0.104	625
	WIPP-19	3/23/88	22 Na	7.50E-06	19.68	0.1550	0.040	0.066	395
2	ESM-143-2	6/23/88	129 I	1.00E-05	41.61	0.0975	0.012	0.088	150
	ESM-143-2	6/23/88	22 Na	7.50E-06	41.61	0.0975	0.011	0.093	714
	ESM-143-2	11/21/88	3 H	1.31E-05	41.61	0.0975	0.040	0.033	437
3	AIS-SNL-16	6/30/89	3 H	1.31E-05	0.35	0.1950	0.130	0.170	44

Note: D_o = free-water diffusion coefficient.

The data were taken from Dykhuizen and Casey (1989).

electrical-resistivity formation factors were calculated. As shown in Figure 5-3, there is an apparent direct relationship between matrix porosity and tortuosity. Because of the limited number of samples, no conclusions or correlations can be developed between the tortuosity results of the diffusion experiments and the results derived from electrical-resistivity calculations.

Figure 5-3 combines the results from the electrical-resistivity calculations and the diffusion experiments. The diffusion tortuosities are plotted as a function of both diffusion porosity (open symbols) and helium porosity (filled symbols). All experiments on the same sample are indicated by the same symbol to indicate the experimental uncertainty in the results for that sample. Figure 5-3 shows that the variability in results for a given sample is high but the results from the diffusion experiments generally fall within the scatter of the values derived from electrical-resistivity measurements. The data presented in Table 5-6 show that the diffusion porosity is generally less than the porosity determined by the Boyle's Law technique using helium. Dykhuizen and Casey (1989) indicate that this difference is due to the inadequacies of simple versions of Fick's First Law of Diffusion for solutes in a porous medium. Also, heterogeneity can contribute significant differences in porosity over distances of several centimeters using various subsamples of a given rock sample (Kelley and Saulnier, 1990).

Because tortuosity shows a general trend of being directly proportional to porosity (Table 5-5) and the diffusion experiments tended to be performed on core with lower porosities, it was decided to select the results from the electrical-resistivity measurements to estimate tortuosities that would be representative for the wider porosity range that is representative of the Culebra. The tortuosities based on electrical-resistivity measurements from 11 borehole or hydro pad locations had an arithmetic average value of 0.141 and a range from about 0.03 to 0.33. For the four samples analyzed for the H-11 hydro pad, an average tortuosity of 0.110 is calculated with a corresponding average porosity of 0.169 for these same samples. For the double-porosity transport interpretations of the tracer tests performed at the H-3, H-6, and H-11 hydro pads, a matrix tortuosity of 0.15 was selected for

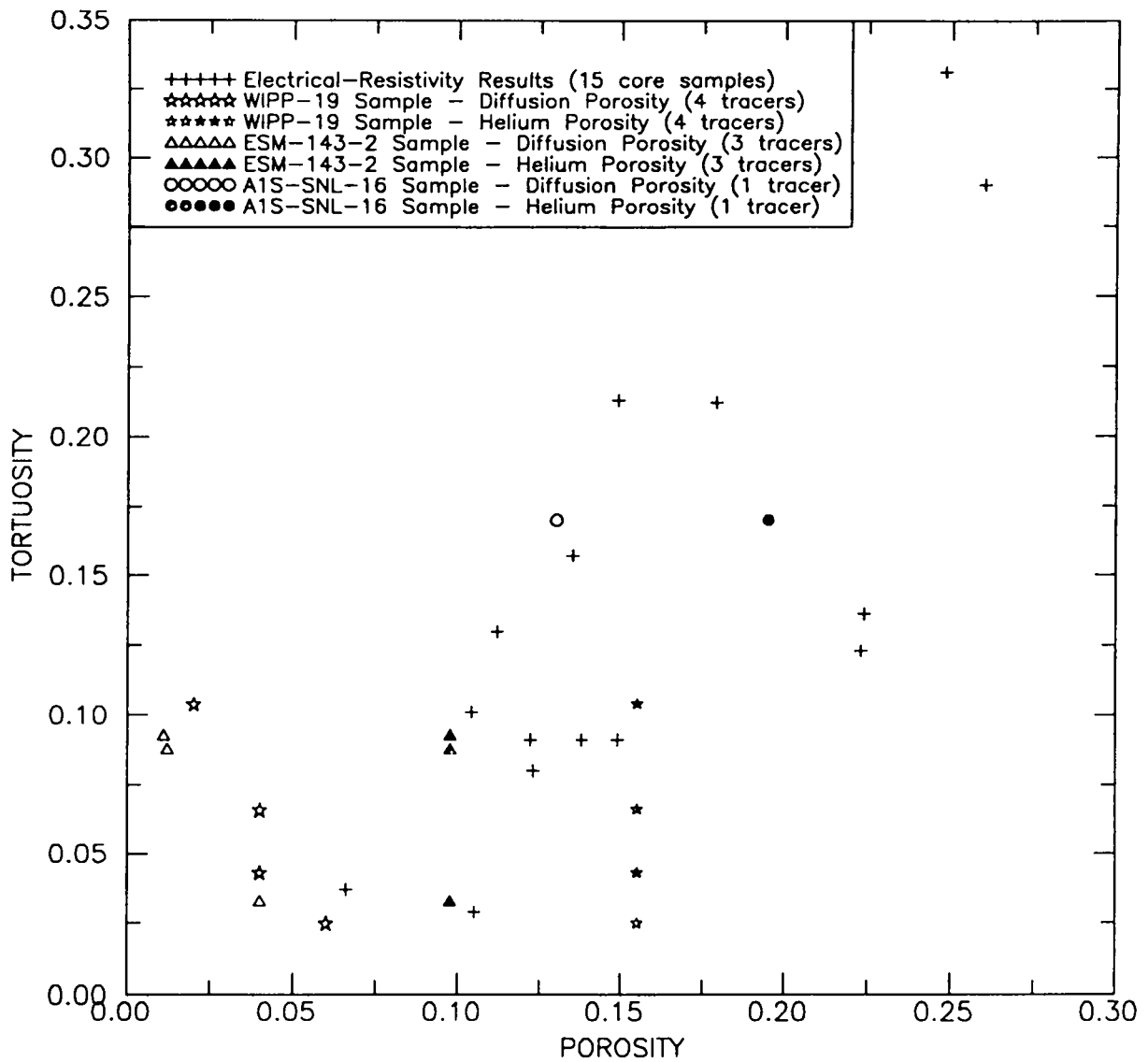


Figure 5-3. Comparison between tortuosity determined from electrical-resistivity measurements and diffusion experiments plotted as a function of porosity (after Kelley and Saulnier, 1990).

the H-3 and H-6 hydropads and 0.11 for the H-11 hydropad. The matrix tortuosity of 0.15 is slightly higher than the arithmetic-average value for the core samples but is consistent with the base-case value that has been used in previous transport studies for the Culebra dolomite by Reeves et al. (1987, 1991) and Lappin et al. (1989, 1990). A single tortuosity of 0.029 was measured for a core sample from the H-2 hydropad. Because of only one measurement for the H-2 hydropad and a lack of data for the H-4 hydropad, a tortuosity of 0.15 was selected as reasonable for these two hydropads.

Equation 5-8 shows that matrix tortuosity is calculated from formation factor and matrix porosity. Therefore, the uncertainty in tortuosity results in part from the uncertainty in formation factor and porosity. To drive matrix tortuosity to the lowest potential value, the formation factor and porosity of 326.77 and 0.105, respectively, used to determine the lowest calculated tortuosity of 0.029 must be increased based on the uncertainty in their value. The laboratory that conducted the formation factor measurements estimated an uncertainty in the experimental determination of formation factor of ± 1 percent. For a formation factor of 326.77, the uncertainty is 3.27. The average error in porosity for measurements near 0.105 is 0.008. Increasing formation factor by 3.27 and matrix porosity by 0.008 yields a value of 0.027 for the lowest potential matrix tortuosity. The formation factor and matrix porosity used in the calculation of the highest tortuosity of 0.331 were 12.2 and 0.248, respectively. For matrix-porosity values on the order of 0.248, the error in the measured matrix porosity is about 0.03. The error in the formation factor of 12.2 is 0.12. Decreasing the matrix porosity of 0.248 by 0.03 and decreasing the formation factor of 12.2 by 0.12 yields a maximum potential matrix tortuosity of 0.380.

In summary, the range of tortuosity calculated from measured porosities and formation factors is 0.029 to 0.331. The uncertainty in this range is -0.002 at the low end and +0.049 at the high end based on the uncertainty in the measured matrix porosity and formation factor used to calculate the lowest and highest tortuosities. These uncertainties yield a potential range in matrix tortuosity of 0.027 to 0.38 (Table 5-2). Uncertainty associated with the degree to which electrical methods are representative to determine

diffusion tortuosity cannot be determined. However, the potential range in matrix tortuosity of 0.027 to 0.380 for the full Culebra thickness at a tracer-test site is considered to be sufficiently broad so as to include any additional uncertainty related to this aspect.

5.2 Fitted Transport Parameters

Interpretations of the tracer tests used fracture porosity, matrix-block length, anisotropy in the horizontal transmissivity, and principal-transmissivity direction to fit the simulated breakthrough curves to the observed breakthrough curves. These parameters were selected for fitting purposes because no measured values nor reliable literature values are available.

5.2.1 Fracture Porosity

Estimates of fracture porosity can be obtained by interpreting tracer tests conducted at sites exhibiting double-porosity transport behavior. Of the tracer tests performed at the WIPP site, the tests conducted at the H-3, H-6, and H-11 hydropads appear to demonstrate fracture-transport behavior, as evidenced by the rapid tracer breakthrough that occurs on at least one flow path between tracer-addition and pumping wells at each of these hydropads. The transport behavior of tracers at the H-2 and H-4 hydropads does not exhibit any indication of the presence of fracturing.

Based on the theoretical plug-flow travel time between the tracer-addition well and the pumping well in a convergent-flow tracer test, an initial estimate of fracture porosity can be calculated using the relationship:

$$\phi = Qt_p / \pi r^2 b \quad (5-9)$$

where:

- ϕ = fracture porosity,
- Q = discharge rate at the pumping well,
- t_p = time to reach the peak concentration at the pumping well after injection of a pulse of tracer at a tracer-addition well,
- r = distance between the tracer-addition and pumping wells, and
- b = aquifer thickness.

The time to reach the peak concentration is used for this estimate because this time is assumed to be representative of the average transport rate between the tracer-addition and pumping wells. Although the time to reach the peak concentration also depends on hydraulic anisotropy, longitudinal dispersivity, and diffusive losses to the matrix, this approach provides a first estimate of fracture porosity for calibration of the tracer-breakthrough curves.

The calculated fracture porosities for the flow paths exhibiting the strongest fracture-transport behavior are 2.0×10^{-3} , 3.1×10^{-3} , and 1.0×10^{-3} for the H-3, H-6, and H-11 hydropads, respectively, assuming full Culebra thickness during transport. These initial estimates of fracture porosity at each of these hydropads are based on the assumption of an isotropic fracture distribution, which may not be valid for some portions of the Culebra dolomite. Fracture porosity was used as a fitting parameter for the heterogeneous-analysis approach to double-porosity transport interpretations.

The range of initial estimates of fracture porosity can be calculated from Equation 5-9 using the end-member values for pumping rate, peak-concentration arrival time, well spacing, and Culebra thickness. The potential ranges of values for pumping rate are discussed in Section 5.1.3, for well spacing in Section 5.1.2, and for Culebra thickness in Section 5.1.1. The error in the time of the peak concentration is discussed in Section 5.1.5. Using the maximum pumping rate and peak-concentration arrival time and the minimum well spacing and Culebra thickness, a maximum initial estimate for the

fracture porosity can be calculated. Taking the parameters to the opposite extremes yields the minimum initial estimate for the fracture porosity. The range in initial estimates for the fracture porosity at H-3, H-6, and H-11 are 1.8×10^{-3} to 7.7×10^{-3} , 2.5×10^{-3} to 1.2×10^{-2} , and 8.7×10^{-4} to 4.3×10^{-3} , respectively. These ranges are consistent with generic values reported by Van Golf-Racht (1982). He reports a range of 1×10^{-4} to 2×10^{-2} for a fissure network, where fissures are defined as fractures with narrow openings and limited extent generally within individual layers. While he does not cite sources for the data, it is assumed that they are based on his experience and review of the literature.

Development of a range in fracture porosity provided a guideline for selecting an initial value for use in the simulations. Further refinement of fracture porosity was governed by the difference between the simulated and observed breakthrough curves. Since Equation 5-9 gives only an estimate of the fracture porosity, the values most representative of each hydropad were determined by using fracture porosity as a fitting parameter.

5.2.2 Matrix-Block Length

Little quantitative data are available concerning the geometry and continuity of fractures in the Culebra. Examination of core from the WIPP-site boreholes has revealed that both high-angle and horizontal fractures are present, and that fractures vary from being open, to partially or fully filled with gypsum. Mapping at the WIPP-site shafts has indicated that the fractures are associated with discrete levels within the Culebra. Examination of a Culebra outcrop near the WIPP site shows significant fracturing both horizontally and vertically. However, the enhanced weathering and differential vertical movements at the outcrop have likely caused fracturing to be much more extensive than within the Culebra at the H-3, H-6, and H-11 hydropads.

The range of matrix-block sizes for the Culebra is difficult to estimate based on examination of the hydropad-specific core because of the limited amount of core recovered

from the various boreholes. Conceptually, solute transport at the hydropad scale likely takes place through a network of fracture sets intersecting in three dimensions. For modeling purposes using SWIFT II, three orthogonal fracture sets are assumed and the fracture spacing is assumed to be equal in all three dimensions. Based on the combination of core information and shaft-mapping results, initial matrix-block sizes of 10 cm to several meters were selected.

Assigning base-case values for the assigned transport parameters and fitting the observed breakthrough curves using fracture porosity and matrix-block length yielded best-fit values for matrix-block length. In addition to determining best-fit values, uncertainty in the interpreted matrix-block length values was determined through sensitivity recalibrations using end-member values as constraints for the assigned transport parameters.

5.2.3 Anisotropy

Hydraulic tests for anisotropy of the horizontal-transmissivity tensor have been performed at three locations at the WIPP site. These locations were the H-4 hydropad, the H-5 hydropad, and the H-6 hydropad. In addition, pumping tests conducted at the H-3 and H-11 hydropads have been examined in an effort to determine anisotropy at those two sites. These five hydropads consist of three wells completed to the Culebra and arranged in a triangular array. (H-11b4 had not been drilled at the time the pumping test used for analysis of anisotropy at the H-11 hydropad was conducted.) The traditional four-well methods for determining the principal components of the transmissivity tensor (Papadopulos, 1965; Hantush, 1966) were modified by Neuman et al. (1984) to require only three wells. The three-well technique requires individually pumping two or more wells at the site and observing the drawdowns in all three wells. Using the method presented in Neuman et al. (1984), Gonzalez (1983) analyzed the anisotropy tests conducted at the H-4, H-5, and H-6 hydropads and presented an anisotropy ratio of 2.7:1 and a principal direction of N76°W

at the H-4 hydropad, an anisotropy ratio and principal direction of 2.4:1 and N25°W, respectively, at the H-5 hydropad, and 2.1:1 for the anisotropy ratio and N29°W for the principal direction at the H-6 hydropad. Using the three-well method for determining horizontal anisotropy, Neuman et al. (1984) analyzed the anisotropy test conducted at the H-6 hydropad and concluded that the anisotropy ratio at the location is 1.91:1 and the principal direction of transmissivity is N29.6°W.

Saulnier (1987) analyzed pumping tests conducted at the H-11 hydropad in 1984 using the method of Hantush (1966) to evaluate whether any local anisotropy in hydraulic properties could be demonstrated at that site. Saulnier (1987) concluded that the anisotropy ratio at the H-11 hydropad is 1.6:1 and that the average direction of the principal transmissivity is oriented N84.2°E (Figure 5-4). Six sets of maximum and minimum anisotropy values were calculated by Saulnier (1987) because pumping tests were performed at each of the three H-11 wells and each test was monitored at two observation wells. Figure 5-4 indicates an approximately 80-degree range in the direction of the principal transmissivity from the various calculated anisotropies for the H-11 hydropad.

Analyses of pumping tests performed at the H-3 hydropad were inconclusive in determining whether the horizontal transmissivity is anisotropic at that location (Beauheim, 1986).

Figure 5-5 summarizes the information currently available on horizontal anisotropy from hydraulic testing at the WIPP site. The relative positions of the wells at each hydropad are shown schematically with a solid line representing the flow path during the test that exhibited rapid transport and the dotted line representing paths that exhibited slower transport. The anisotropy ratios presented in Gonzalez (1983), Neuman et al. (1984), and Saulnier (1987) are summarized in Table 5-7 and were considered to be initial estimates in the anisotropic-analysis approach to interpreting the tracer-test results. The anisotropy

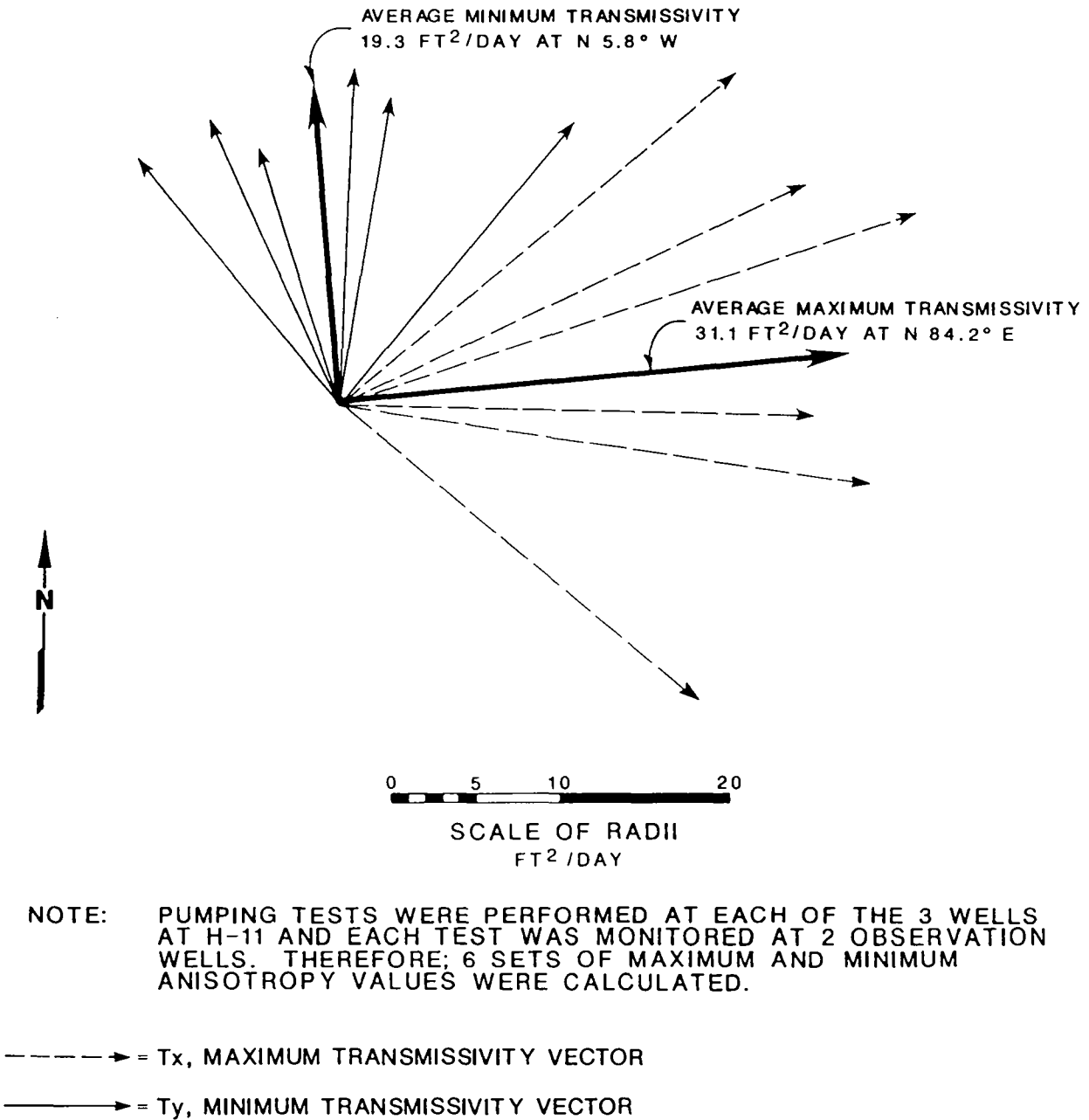
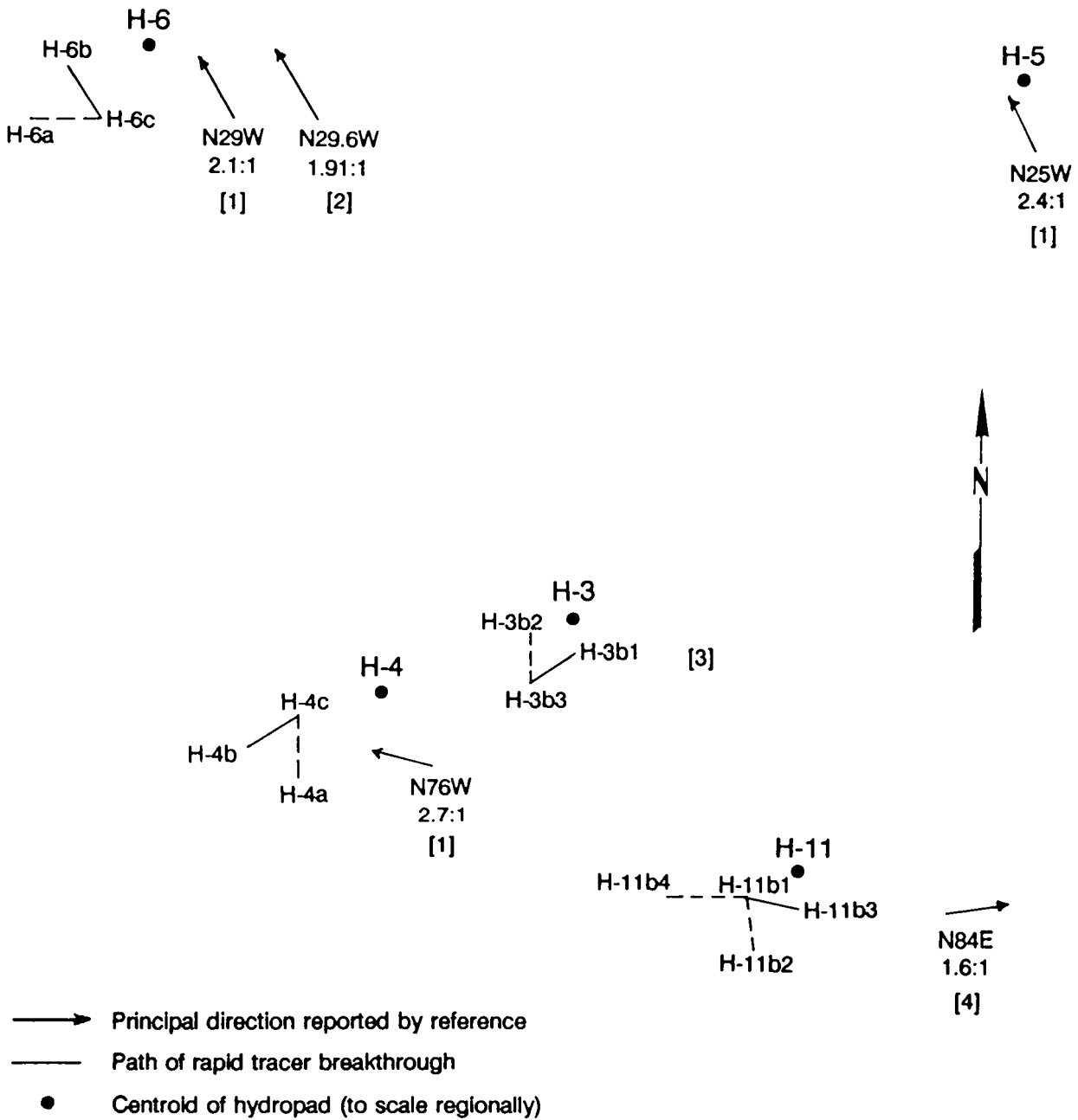


Figure 5-4. Summary of anisotropy calculations for the 1984 pumping tests at the H-11 hydropad (after Saulnier, 1987).



REFERENCES:

- [1] Gonzalez (1983)
- [2] Neuman et al. (1984)
- [3] Beauheim (1987b): Anisotropy in horizontal conductivity was inconclusive.
- [4] Saulnier (1987)

Figure 5-5. Reported anisotropy at the WIPP site.

Table 5-7. Summary of Literature Values of Anisotropy Ratios at the WIPP Site.

<u>Hydropad</u>	<u>Anisotropy Ratio</u>	<u>Principal Direction</u>	<u>Reference</u>
H-4	2.7:1	N76° W	Gonzalez (1983)
H-5	2.4:1	N25° W	Gonzalez (1983)
H-6	2.1:1	N29° W	Gonzalez (1983)
H-6	1.91:1	N29.6° W	Neuman et al. (1984)
H-11	1.6:1	N84.2° E	Saulnier (1987)

determined from hydraulic testing is expected to be different than that interpreted from fitting of the tracer-breakthrough curves because of the different scales tested. The tracer tests are evaluating only the flow-path length between the tracer-addition and pumping wells (about 21 to 43 m) whereas the hydraulic tests are hydraulically stressing the Culebra to much larger distances (to 100's or 1000's of meters). Sensitivity analyses were conducted to illustrate the effect of varying the anisotropy ratio and principal direction on the calculated breakthrough curves.

5.3 Identification of Independent Parameter Groups

Using an analytical analysis of tracer migration, this section identifies four independent parameters or parameter groups. An understanding of such parameter groups is important to a sensitivity analysis, particularly whenever a parameter group contains several natural parameters within its definition. In such a case, the sensitivity for one natural parameter of an independent-parameter group may be obtained easily from the sensitivity of another member of the same group. Thus, a knowledge of the independent parameters simplifies the understanding of sensitivity results. It may also be used to minimize the number of simulations since any combination of values of parameters in an independent-parameter group that yields the same calculated value for the group when all other parameters remain constant will produce an identical simulated breakthrough curve.

The development of the independent parameters, or parameter groups, is provided in Reeves et al. (1991). Two independent parameters refer only to the fractures: interstitial ground-water velocity and longitudinal dispersivity. Interstitial ground-water velocity in the fractures is given by:

$$v = \frac{u}{\phi} \quad (5-10)$$

where:

- v = interstitial ground-water velocity,
- u = fracture flux, and
- ϕ = fracture porosity.

Longitudinal dispersivity enters the dispersion coefficient as:

$$E = \alpha_L v \quad (5-11)$$

where:

- E = dispersion coefficient,
- α_L = longitudinal dispersivity, and
- v = interstitial ground-water velocity.

Two independent-parameter groupings refer to the matrix (matrix parameters are indicated by the prime). The storage-enhancement parameter describes the factor by which storage capacity is increased relative to the capacity of the fracture system alone. Storage enhancement is given by:

$$\kappa' = \frac{\phi + \phi'}{\phi} \quad (5-12)$$

where:

- κ' = storage enhancement,
- ϕ = fracture porosity, and
- ϕ' = matrix porosity.

The second matrix-parameter group is the characteristic matrix-diffusion time given by:

$$\tau' = \frac{L'^2}{\theta' D'} \quad (5-13)$$

where:

τ' = characteristic matrix-diffusion time,

L' = one half of the matrix-block length,

θ' = matrix tortuosity, and

D' = free-water diffusion coefficient.

Physically, the characteristic matrix-diffusion time represents the time required for diffusion to penetrate from the fracture-matrix interface to the center of the matrix block, and for the concentration at that point to reach approximately 68 percent of its value at the fracture-matrix interface.

A key characteristic of the independent parameter groups is that if the group value is maintained, the values for the individual parameters within the group can be changed and the simulated results would not be altered. For example, changes in one individual parameter on the right-hand side of Equation 5-13 can be directly compensated by adjusting any other individual parameter on the right-hand side. As long as the group value on the left-hand side remains constant, the simulation results will remain unchanged, assuming that all other parameters are held constant.

Equations 5-10 and 5-11 present independent-parameter groups for the fractures and Equations 5-12 and 5-13 present independent-parameter groups for the matrix. Notice that fracture porosity appears in both the equation for interstitial velocity and in the equation for storage enhancement. Therefore, any change in fracture porosity must be accompanied by a change in fracture flux and matrix porosity in order to have no effect on the simulated results. A demonstration of the role of independent-parameter groups, through examination of the characteristic diffusion time, is presented for the H-3 hydropad.

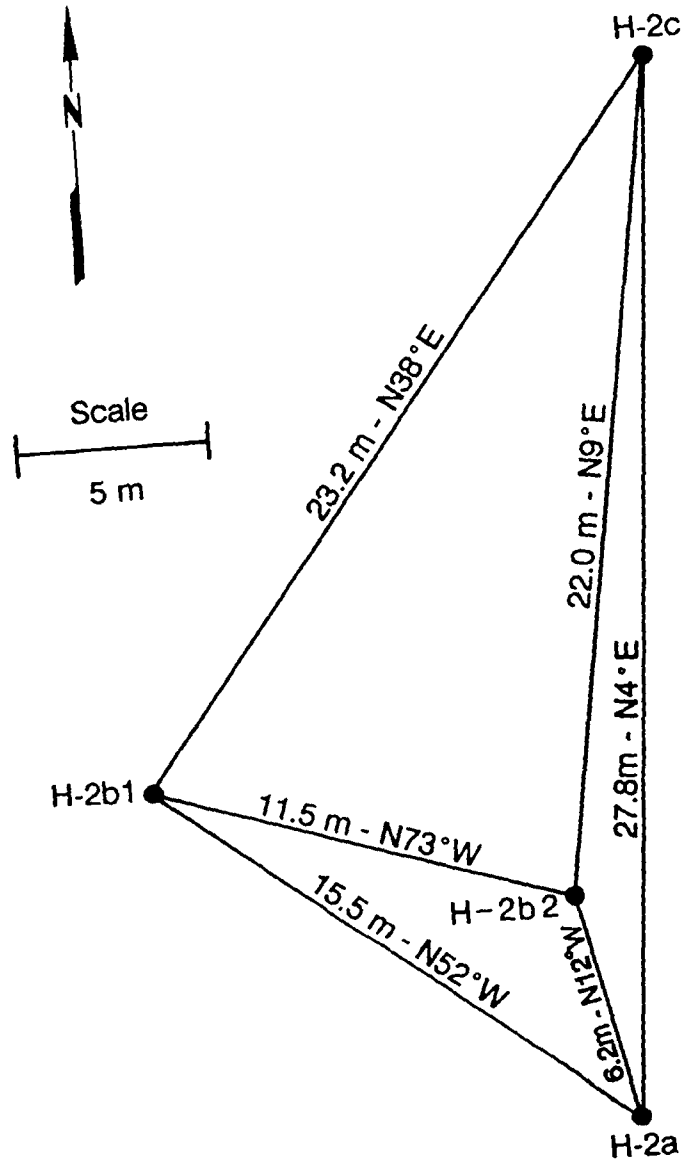
6.0 H-2 HYDROPAD TRACER TESTS

Two recirculating-tracer tests performed at the H-2 hydropad between February 1980 and April 1981 were the first multiwell tracer tests conducted at the WIPP site. The first test began in February 1980 and terminated in June 1980 due to pumping and tracer-injection equipment failure. The second test was conducted between July 1980 and April 1981. The following sections discuss the well configurations, hydropad hydrogeology, tracer-test history, previous interpretation of the H-2 tracer tests presented in Hydro Geo Chem (1986), suitability of the tests for further analysis, and a summary of the tracer-test results.

6.1 Well Configurations

The H-2 hydropad is located in the west-central portion of the WIPP site, approximately two kilometers from the center of the site (Figure 1-2). It consists of four wells, H-2a, H-2b1, H-2b2, and H-2c (Figure 6-1). At the time the recirculating tracer tests were conducted at the site, the H-2 hydropad consisted of three wells, H-2a, H-2b (later renamed and hereafter called H-2b1), and H-2c with only H-2b1 and H-2c completed to the Culebra. All of the hydropad wells are located in Section 29, Township 22 south, and Range 31 east. The Universal Transverse Mercator (UTM) coordinates, ground-surface elevations, and top-of-casing elevations for the H-2 hydropad wells are summarized in Table 6-1. Figure 6-1 illustrates the relative positions of the wells at the depth of the Culebra dolomite.

In mid-February 1977, H-2a was drilled to the top of the Magenta dolomite at a depth of 156.4 m below ground surface (BGS), cased with 16.83-cm (6-5/8-inch) casing, cemented and then cored through the Magenta. The borehole was deepened through the



NOTE:

The Culebra interval was completed in wells H-2a and H-2b2 in 1983.
 H-2b1 is also referred to as H-2b.
 The borehole deviation survey did not extend to the center of the Culebra dolomite in borehole H-2b2.

Figure 6-1. Plan view of the wells at the H-2 hydropad showing distances between wells at the center of the Culebra.

Table 6-1. UTM Coordinates, Ground-Surface Elevations, and Top-of-Casing Elevations for the H-2 Hydropad Wells

<u>Well</u>	<u>UTM Coordinates</u>		<u>Ground-Surface Elevation (m amsl)</u>	<u>Top-of-Casing Elevation (m amsl)</u>
	<u>m East</u>	<u>m North</u>		
H-2a	612,663	3,581,641	1029.55	1029.64
H-2b1	612,651	3,581,651	1029.50	1029.75
H-2b2	612,661	3,581,649	1029.49	1029.71
H-2c	612,666	3,581,668	1029.52	1029.74

Culebra dolomite to a depth of 204.9 m BGS in July 1983. In April and May 1984, H-2a was re-entered and cleaned, then 11.43-cm (4-1/2-inch) casing was set and cemented to the top of the Culebra. A lead-coned packer with an attached well screen and bottom cap was installed across the Culebra at this time. H-2a was not completed to the Culebra at the time the two-well recirculating tracer tests were conducted.

In February 1977, H-2b1 was drilled to 185.6 m BGS, cased with 16.83-cm (6-5/8-inch) casing, and cemented. The borehole was then cored through the Culebra interval to a total depth of 201.5 m BGS. H-2b1 was perforated across the Magenta interval and converted to a dual-completion borehole in April and May 1977. The bottom 15.9 m of the borehole is open hole with a diameter of 12.1 cm.

H-2b2 was completed in July 1983. The well was originally drilled to the top of the Culebra, cased, and cemented. The well was then cored through the Culebra interval to a total depth of 201.2 m BGS. In April 1984, the borehole was re-entered, cleaned, and a lead-coned packer with an attached well screen and bottom cap was installed across the Culebra dolomite. H-2b2 had not been drilled at the time the two-well recirculating tracer tests were conducted.

H-2c was originally drilled in February and March 1977 to the top of the Rustler-Salado contact, cased with 16.83-cm (6-5/8-inch) casing, and cemented. The borehole was then cored through the Rustler-Salado contact to a total depth of 242.4 m BGS. The casing was perforated using three 1.27-cm (0.5-inch) shots per 0.3 m across the Culebra interval (190.20 to 198.73 m) at this time and a production-injection packer (PIP) was installed in the borehole to allow monitoring of both the Culebra and Rustler-Salado contact intervals.

6.2 Local Hydrogeology

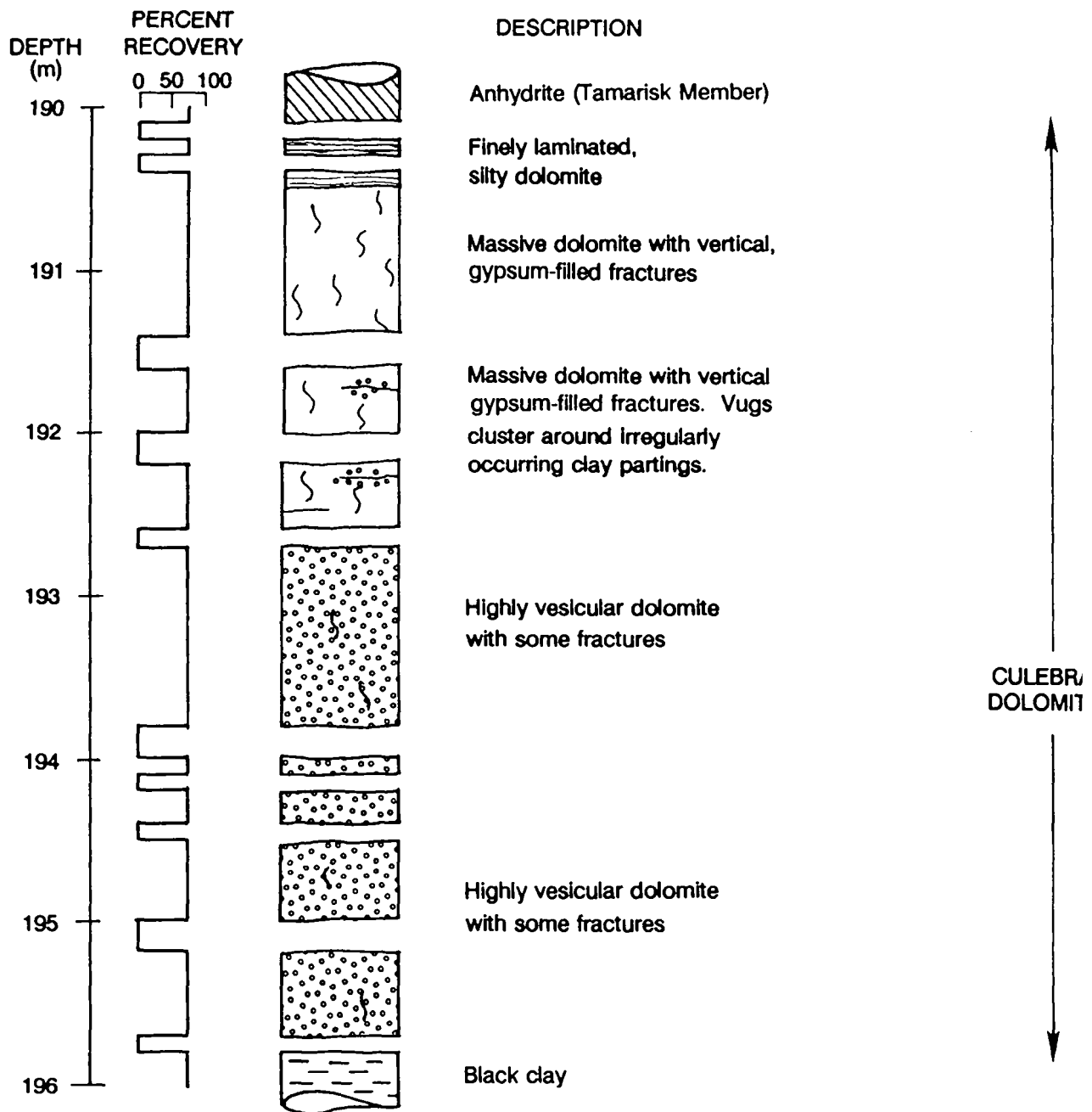
The Culebra dolomite is approximately 6 m thick at the H-2 hydropad and ranges from very dense to vesicular. The Culebra interval was cored in wells H-2b1 and H-2b2. Core recovery from H-2b1 was about 75 percent and from H-2b2 was about 50 percent. Figures 6-2 and 6-3 present results of examination of the core located in the Department of Energy Core Library at the WIPP site. At H-2b1, the upper portion of the Culebra is dense dolomite with gypsum-filled fractures and the lower portion is extremely vesicular dolomite. The majority of the Culebra is a finely laminated, vesicular dolomite with vugs clustered around organic bands in H-2b2. The results of porosity and permeability measurements on the core recovered at the H-2 hydropad are reported in Kelley and Saulnier (1990). Gas permeabilities range from 8.0×10^{-18} to 1.2×10^{-15} m² and porosities range from 0.082 to 0.154.

Pumping tests, drill-stem tests (DSTs), and slug tests have been performed at the H-2 hydropad in an effort to determine the hydraulic properties of the Culebra dolomite at that location. These tests are discussed in Mercer (1983), Gonzalez (1983), and Seward (1982). From these tests, Cauffman et al. (1990) estimated an average transmissivity of 6.3×10^{-7} m²/s at the H-2 hydropad.

Hydraulic tests have determined that horizontal transmissivity is anisotropic in the Culebra dolomite at some locations at the WIPP site. Unfortunately, the types of tests needed to determine anisotropy have not been performed at the H-2 hydropad.

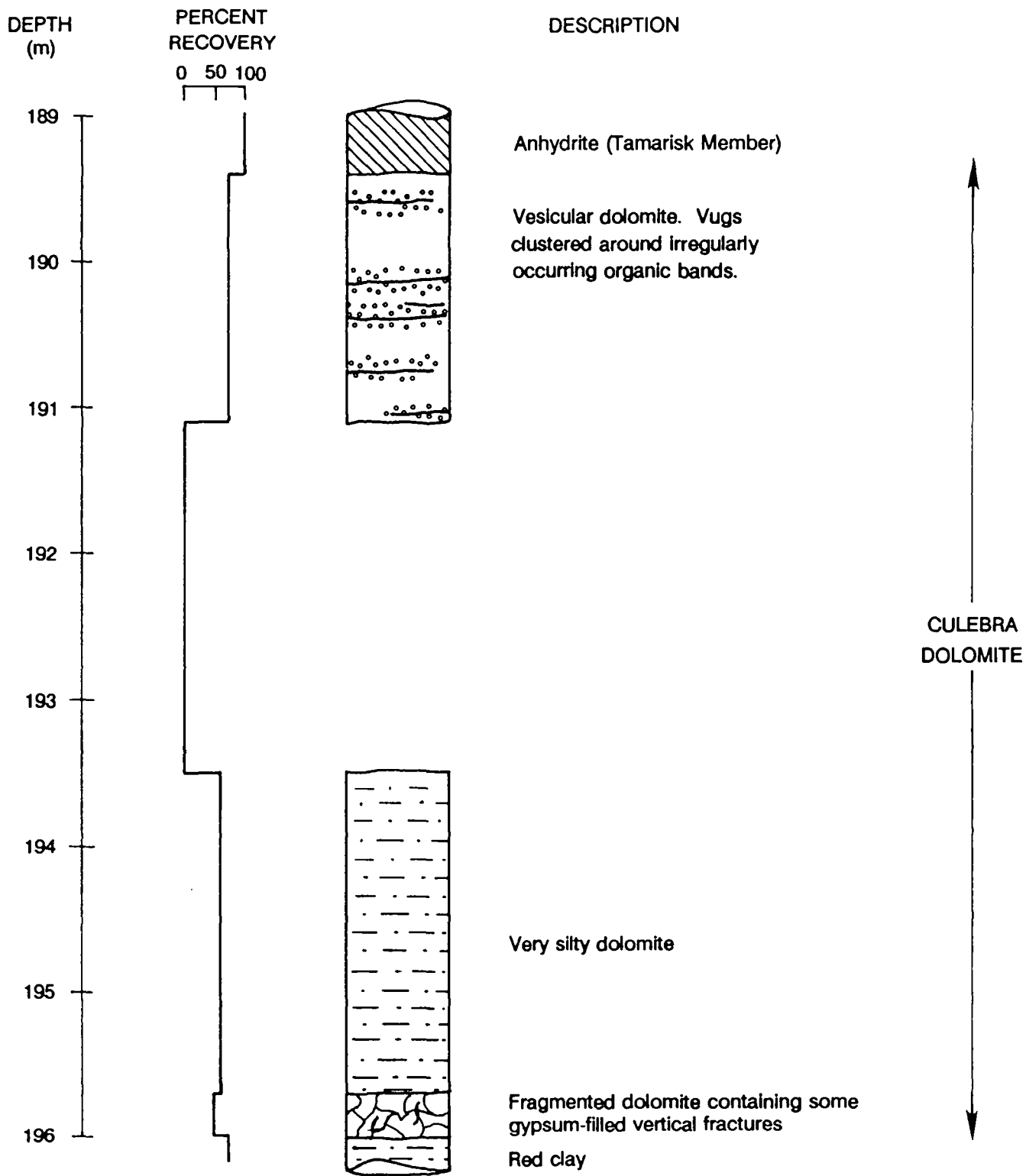
6.3 Tracer-Test History

Two two-well recirculating tracer tests were conducted at the H-2 hydropad between February 1980 and April 1981. These tests consisted of withdrawing fluid from one well, adding a tracer to the fluid, and injecting the fluid into the second well in a continuous



NOTE: Depths here correspond to depths reported on the core.

Figure 6-2. Results of core examination of the Culebra dolomite from borehole H-2b.



NOTE: Depths here correspond to depths reported on the core.

Figure 6-3. Results of core examination of the Culebra dolomite from borehole H-2b2.

recirculation loop. For the first test, the withdrawal well was H-2b1 and the injection well was H-2c. The withdrawal and injection wells for the second test were H-2c and H-2b1, respectively. Full details on the H-2 tracer tests are reported in Hydro Geo Chem (1985).

6.3.1 Test Equipment

The configuration of wells H-2b1 and H-2c during test #1 is illustrated in Figure 6-4 and during test #2 in Figure 6-5. In H-2b1, a PIP was installed to isolate the Culebra interval. The depth of this PIP was 182.9 m during test #1 and 184.4 m during test #2. The Culebra was isolated in H-2c with a bridge packer set below the Culebra at a depth of 197.5 m and a PIP set above the Culebra at a depth of 186.8 m for test #1 and at a depth of 188.4 m for test #2. A 3.81-cm (1-1/2-inch) galvanized pipe connected the PIP in H-2c to the surface. The remainder of the discussion of the test equipment applies to both recirculating tests. Fluid was pumped from the withdrawal well using a pump jack with a positive-displacement cylinder set on the feed-through tubing below the PIP. Fluid removed from the withdrawal well was recirculated and injected into the fluid-addition well through a 1.905-cm (3/4-inch) pipe train. This pipe was connected to 1.27-cm (1/2-inch) tubing, which extended to the Culebra, in the injection well. During test #2, the filter in the injection line was replaced with a combination filter and settling tank.

A pump located at the surface of the injection well was used to maintain a constant rate of tracer injection. Volatile tracers were injected from a pressure tank located at the surface of the injection well. A diagram of the tracer-injection system is provided in Figure 6-6. Fluid samples were collected at the pumping well from a faucet located at the pumping head. Samples collected for analysis of anionic tracers were stored in 30-mL plastic scintillation counting bottles. Samples collected for analysis of volatile tracers were stored in 30-mL glass melt-seal vials. High-performance liquid chromatography (HPLC) with ultraviolet detection was used to analyze samples for anionic tracer concentrations.

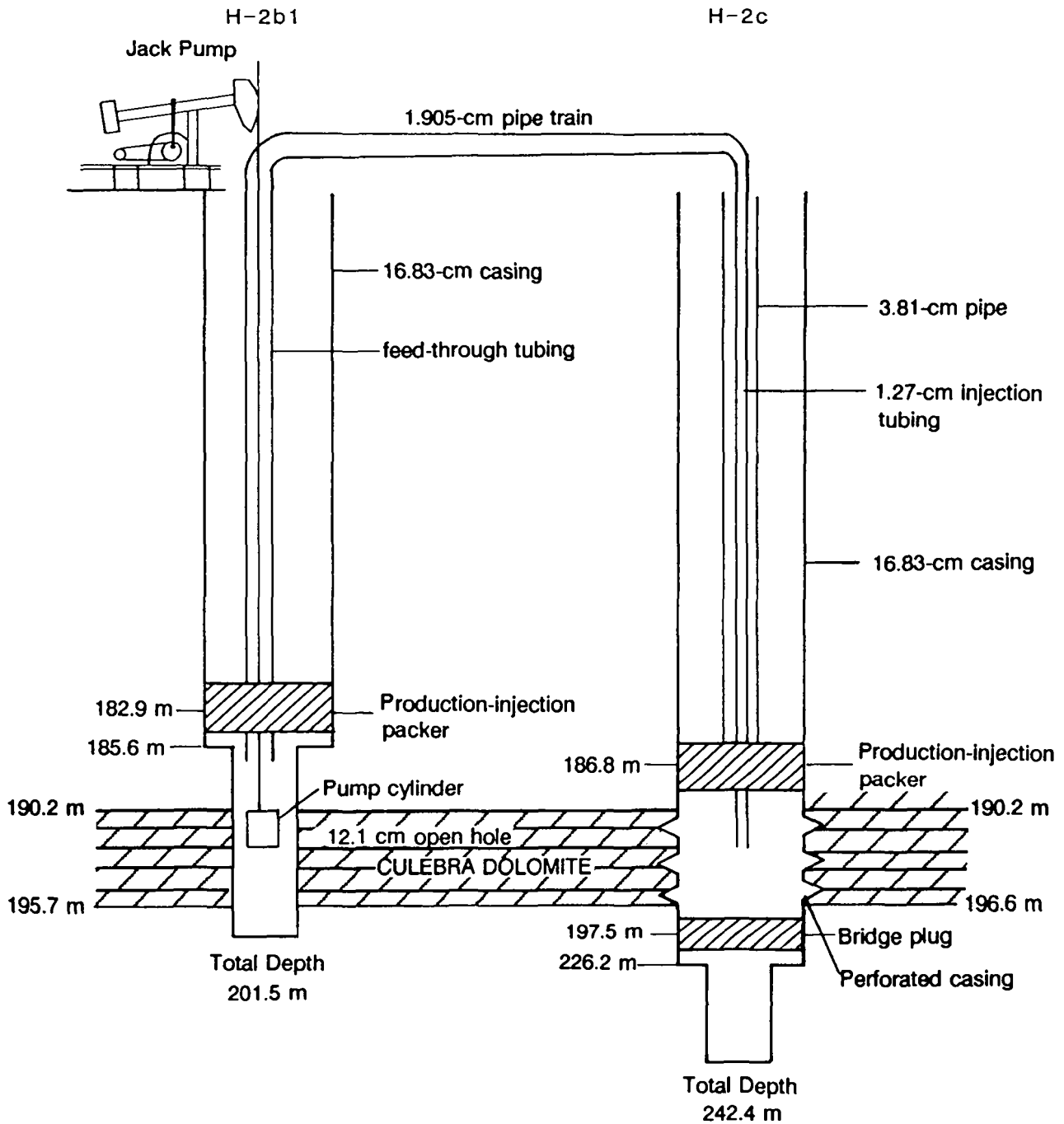


Figure 6-4. Downhole-equipment configuration for two-well recirculating tracer test #1 at the H-2 hydropad.

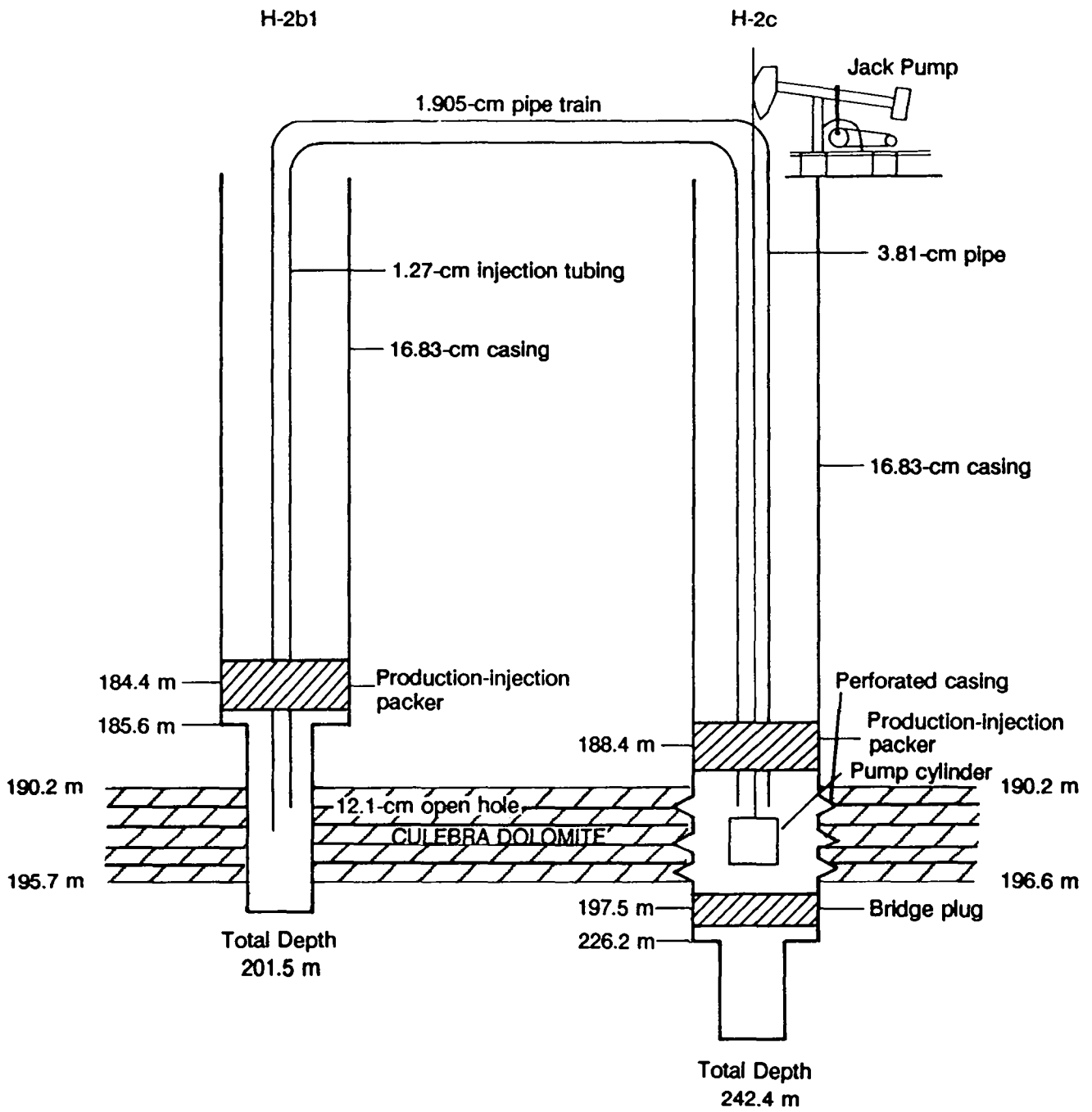


Figure 6-5. Downhole-equipment configuration for two-well recirculating tracer test #2 at the H-2 hydropad.

INJECTION SCHEMATIC

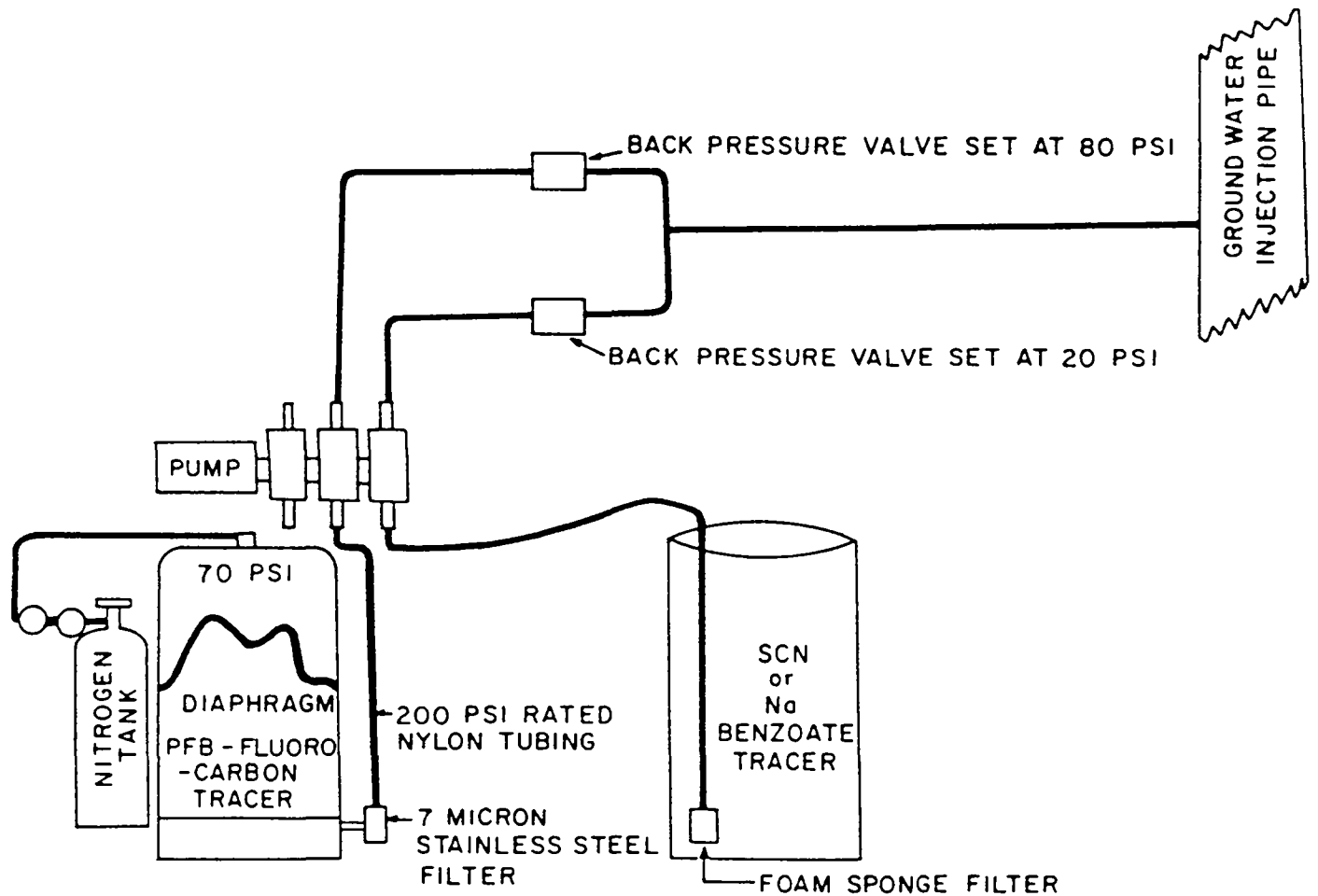


Figure 6-6. Surface tracer-injection system for the two-well recirculating tracer tests conducted at the H-2 hydropad (from Hydro Geo Chem, 1985).

Qualitative determinations of the concentrations of the volatile tracers were conducted at the H-2 site. Laboratory analyses of samples for volatile-tracer concentrations were not conducted. Further discussion of the test equipment and tracer-analysis techniques can be found in Hydro Geo Chem (1985, 1986).

6.3.2 Pumping and Tracer-Injection History

Pumping for test #1 began in H-2b1 on February, 13, 1980. Injection of the anionic tracers benzoate and pentafluorobenzoate (PFB) and the halocarbon tracers CCl_4 , CFCl_3 , and CF_2Cl_2 into H-2c began at 23:30 on February 22, 1980. Flow through the system at the start of tracer injection was about 0.019 L/s. Injection of the tracers continued until the tracer-injection line ruptured sometime between 12:00 on February 24, 1980 and 12:00 on February 25, 1980. The pump at H-2b1 continued to operate at a rate of about 0.019 L/s until it was shut down for maintenance on March 20, 1980. An attempt was made to continue the test by resuming pumping on March 27, 1980. When the pump was restarted, large amounts of sediment were produced from H-2b1. These sediments clogged the injection system and well H-2c. Intermittent pumping of H-2b1 was continued until June 18, 1980, on which date pumping was stopped and the test was terminated. At that time, PFB had not yet been detected in fluid samples collected at withdrawal well H-2b1. Table 6-2 summarizes the pumping and tracer-injection information for test #1. During test #2, tracer analyses for PFB were performed on water samples taken from pumping well H-2c.

Test #2 began on July 7, 1980 with the initiation of pumping at H-2c. The pumping rate ranged from 0.016 L/s to 0.024 L/s during the test. Tracer injection began on July 10, 1980 and ended on August 7, 1980. The tracers thiocyanate (SCN) and difluorochlorobromomethane (BCF) were injected into H-2b1 at rates of about 3.17×10^{-5} and 1.25×10^{-5} L/s, respectively. Pumping at H-2c was terminated on April 7, 1981. Pumping and tracer-injection information for test #2 are summarized in Table 6-2.

Table 6-2. Summary of Pumping and Tracer-Injection Information for the Two-Well Recirculating Tracer Tests Conducted at the H-2 Hydropad

	H-2b1		H-2c
TEST #1			
Well Type	Pumping		Injection
Flow Rate Through System	0.019 L/s		
Date Pumping Began	02/13/80		
Date Pumping Ended ^a	06/18/80		
Tracers Injected			benzoate, PFB, CCl ₄ , CFCI ₃ , CF ₂ Cl ₂
Date and Time Tracer Injection Began			23:30 on 02/22/80
Date and Time Tracer Injection Ended			between 12:00 on 02/24/80 and 12:00 on 02/25/80
TEST #2			
Well Type	Injection		Pumping
Date Pumping Began			07/07/80
Date Pumping Ended			04/07/81
Discharge Rate			0.016 to 0.024 L/s
Tracers Injected	SCN	BCF	
Date Tracers Injected	07/10/80 to 08/07/80		
Average Tracer-Injection Rates	3.17x10 ⁻⁵ L/s	1.25x10 ⁻⁵ L/s	
^a Pumping was continuous from 02/13/80 to 03/20/80 and intermittent from 03/27/80 to 06/18/80.			

6.3.3 Observed Tracer Breakthrough

Test #1 was terminated before any tracer was detected in fluid samples collected at the withdrawal well. Therefore, tracer-breakthrough curves do not exist for that test. Samples collected during test #2 were analyzed for SCN, which was injected as part of test #2, and also for PFB, which had been injected during test #1 into the well that served as the test #2 withdrawal well. A plot of PFB concentration as a function of time since pumping began for test #2 is provided in Figure 6-7. The SCN breakthrough curve is illustrated in Figure 6-8. The concentration data reported by Hydro Geo Chem (1985) for the two tracers are presented in Appendix B.

The tracer SCN was first detected at the withdrawal well approximately 74 days after it had been injected into H-2b1. The peak concentration of SCN occurred about 171 days later. Only 15 samples collected after observation of the peak concentration of SCN were analyzed. Thus, the falling limb of the SCN breakthrough curve is ill defined (Figure 6-8). The tracer BCF was also injected during test #2, but no data for that tracer were reported by Hydro Geo Chem (1985).

6.4 Previous Interpretation of the Tracer Tests

A previous interpretation of the two-well recirculating tracer tests conducted at the H-2 hydropad is presented in Hydro Geo Chem (1986). Through examination of the PFB breakthrough curve they concluded that the Peclet number, defined as average path length divided by dispersivity, is 13. They also reported that quantitative evaluation of formation properties from the PFB breakthrough curve (Figure 6-7) was not possible for three reasons:

- No analytical or semianalytical solution existed with which to model the operating conditions that yielded the observed PFB data;

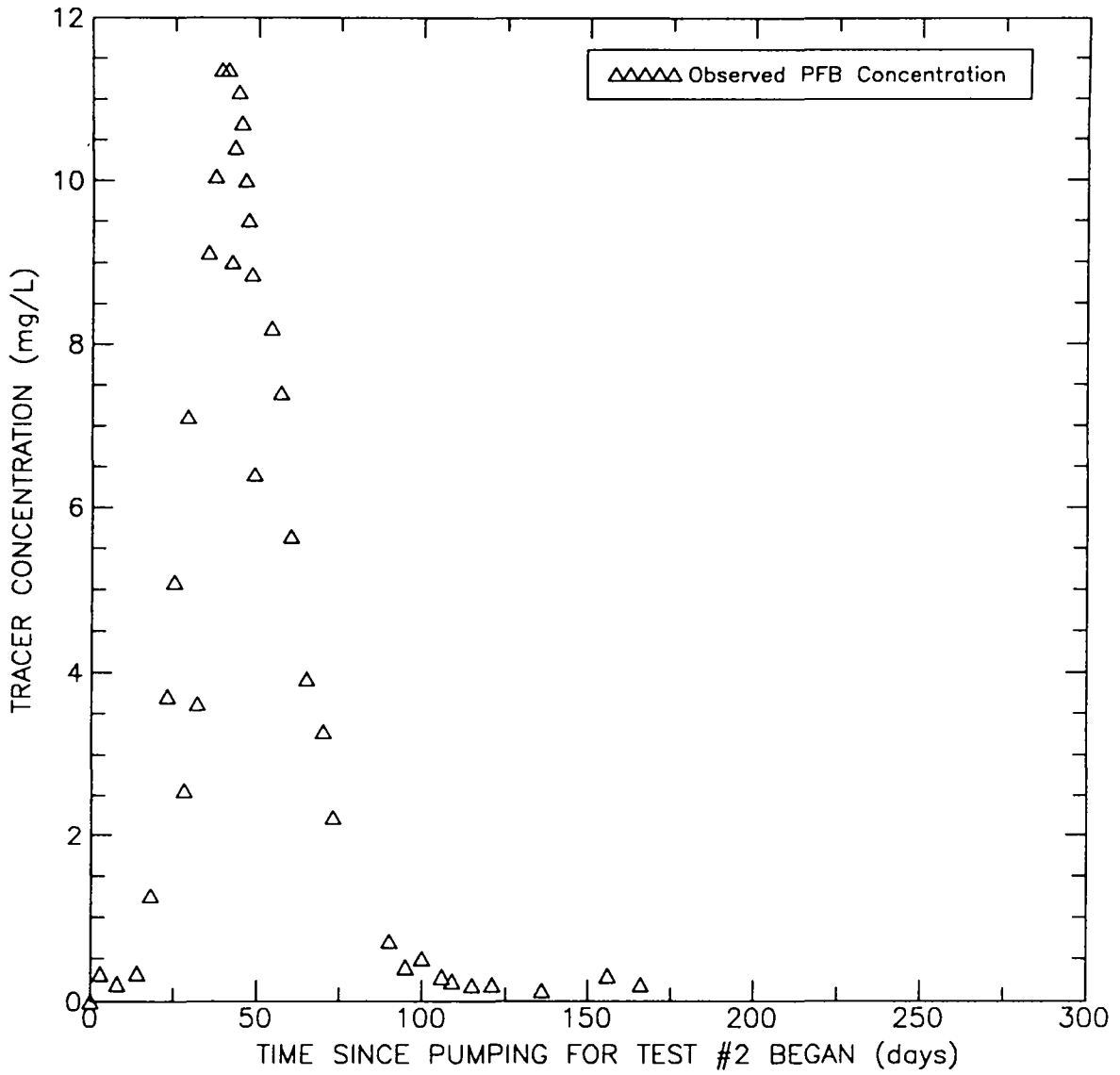


Figure 6-7. Observed PFB data recovered from H-2c during two-well recirculating tracer test #2 after having been injected into H-2c during two-well recirculating tracer test #1.

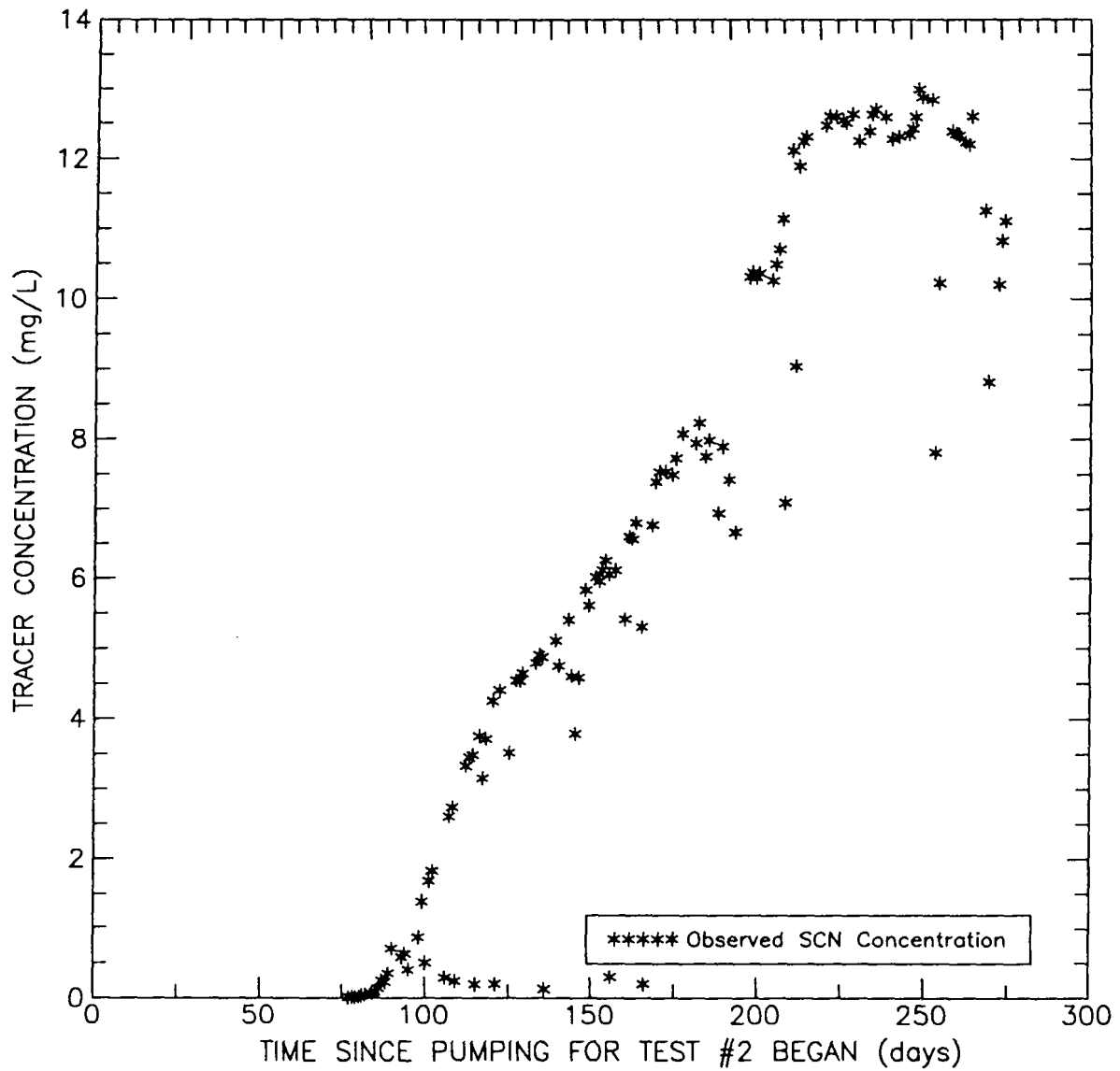


Figure 6-8. Observed SCN data for two-well recirculating tracer test #2 conducted at the H-2 hydropad.

- The pumping history of H-2b1 and H-2c was very complicated due to pump shutdowns for repairs and well cleaning to remove sediments; and
- The duration of PFB injection was unknown due to the rupture of the injection line at an unknown time.

Hydro Geo Chem (1986) interpreted the SCN breakthrough curve (Figure 6-8) using the model developed by Grove and Beetem (1971) which assumes a one-dimensional, single-porosity, homogeneous porous medium. They reported a poor comparison between the model and observed breakthrough curve and stated that the differences were probably the result of one or more of the following factors: local heterogeneities in the Culebra, possible tracer degradation, and double-porosity transport with diffusion between the fractures and matrix. Matching to the general overall shape of the SCN data, they estimated a range of 0.17 to 0.19 for effective porosity and a range of 4.9 to 5.5 m for dispersivity. Matching to the early portion of the SCN breakthrough curve, they estimated an effective porosity of 0.11 to 0.12. They questioned the meaning of the dispersivity values based on the Fickian-model assumptions used in the Grove and Beetem model. They suggested that much of the apparent dispersion is better explained by local-scale aquifer heterogeneities that result in path-line divergence beyond that expected for a homogeneous, isotropic aquifer.

6.5 Suitability of Tracer Tests for Further Analysis

The two tests were evaluated for their suitability for further detailed analysis to determine Culebra transport parameters representative of the H-2 hydropad. Test #1 suffered from a number of equipment and well problems including:

- Rupture of the tracer-injection line at sometime between 1.5 and 2.5 days after the start of tracer injection resulting in a loss of the remaining tracer solution;

- Shut down of the pump for an extended period (1 week) for maintenance at about 1 month after the start of the test;
- When the pump was restarted after the maintenance period, large amounts of sediment were produced from H-2b1 resulting in clogging of the injection system and well H-2c; and
- Pumping continued intermittently until about four months after the start of the test at which time the test was terminated.

No tracers were detected in fluid samples collected from the withdrawal well during test #1. Because of effects of the equipment-related difficulties and the lack of tracer breakthrough, test #1 is not considered useful for detailed quantitative interpretation for transport parameters.

Qualitative interpretation of test #1 with respect to the presence of single-porosity (matrix) or double-porosity transport was conducted as follows. The plug-flow travel time between wells in a two-well recirculating tracer test can be estimated using the relation (Webster et al., 1970):

$$t_m = \pi \phi b d^2 / 3Q \quad (6-1)$$

where:

- t_m = plug-flow travel time between wells,
- ϕ = porosity,
- b = aquifer thickness,
- d = distance between the two wells, and
- Q = pumping and injection rate.

For test #1, the Culobra thickness between H-2c and H-2b1 is 5.5 m, the distance between wells is 23.2 m, and the average flow rate is 0.019 L/s. For comparison, the plug-flow travel time between wells is calculated at 236 days assuming an average matrix porosity of 0.125 (Table 5-3) for the H-2 hydropad and is calculated at 1.9 to 5.7 days assuming fracture porosities of 1×10^{-3} to 3×10^{-3} (representative of range for H-3, H-6, and H-11 hydropads). The total duration for test #1 was 125 days, although pumping was intermittent during some periods. No tracers were detected at the pumping well before the end of the test. Comparison of the plug-flow transit time for a fractured system (1.9 to 5.7 days) with the test duration (125 days) suggests that significant transport through fractures did not occur during test #1. Larger estimated fracture porosities which would result in longer transit times are unlikely considering the relatively low transmissivity at the H-2 hydropad.

Fluid samples obtained from withdrawal well H-2c during test #2 were analyzed for PFB which had been injected during test #1. The resultant observed data are presented in Figure 6-7. After injection into H-2c during test #1, PFB traveled toward pumping well H-2b1. The PFB tracer was then pumped back to and recovered from H-2c during test #2. The relative symmetry and lack of late-time tailing of the PFB breakthrough curve provides further evidence for no double-porosity transport. Because of the problems listed earlier for test #1 and the reversed roles of the pumping and injection wells for test #2, the operating conditions are considered too uncertain and complex to warrant further quantitative analysis of the PFB breakthrough curve.

Although two tracers (SCN and BCF) were injected during test #2, only data for one tracer (SCN) were reported (Hydro Geo Chem, 1985). SCN was injected on July 10, 1980 and was first detected at the withdrawal well about 74 days later on September 22, 1980. The peak concentration of SCN did not occur until March 12, 1981 and the test was terminated on April 7, 1981. Stetzenbach and Stetzenbach (Appendix A) state that the recovery of SCN is seldom 100 percent and at least 5 percent of the SCN injected during a tracer test can be expected to be lost. They list causes of SCN loss as chemisorption in aquifers that do not have high bacteria levels and bacterial activity in media that have been

in contact with manmade chemicals and vegetation. Stetzenbach and Stetzenbach (Appendix A) believe that "thiocyanate is not a good long-term tracer because of the chemisorption problem." Given the long duration of recirculating test #2, the concentration results are considered unreliable and were not analyzed. Hydro Geo Chem reports in field notes that, in laboratory stability tests, SCN shows signs of degradation in time periods of days to tens of days. Further evidence of significant degradation problems for SCN is provided from examination of the tracer-breakthrough results from the H-4 hydropad. For the H-4 convergent-flow tracer test, the peak concentration for SCN was a factor of about 1,800 lower than for m-TFMB even though the same tracer mass was injected for each tracer at the same tracer-addition well.

Test #2 was operated for 275 days with flow rates from 0.016 to 0.024 L/s with an average of about 0.018 L/s. For porous-medium assumptions, the plug-flow travel time between wells is 219 days based on Equation 6-1. Considering that dispersion effects will result in earlier arrival of the tracer, examination of the SCN breakthrough curve for the 275-day test suggests that transport in a single-porosity (matrix) system is likely occurring. No further quantitative interpretation of the SCN breakthrough curve beyond that reported by Hydro Geo Chem (1986) was performed. Their interpreted effective porosity of 0.11 to 0.12 for matching the early portion of the breakthrough curve compares well with the average value of 0.125 obtained from laboratory determinations on ten core samples from the H-2 hydropad.

6.6 Summary of Results for H-2

Two two-well recirculating tracer tests were performed at the H-2 hydropad. The first test could not be quantitatively interpreted because of equipment problems. The SCN breakthrough curve from the second test was interpreted by Hydro Geo Chem (1986) to yield effective-porosity estimates from 0.11 to 0.19 and dispersivity estimates from 4.9 to 5.5 m. Due to the long duration of test #2, biodegradation of SCN may have occurred

resulting in a more gradual breakthrough of tracer at the pumping well. Interpretation of such a curve, without incorporating biodegradation effects, yields higher apparent dispersivities. Therefore, the dispersivities reported by Hydro Geo Chem (1986) are considered to be uncertain.

Calculations were performed to estimate the plug-flow travel time between wells for tests #1 and #2 for both fracture-flow and porous-medium conditions. The data suggest that transport through fractures was not important. Single-porosity (matrix) transport is considered to be the most representative conceptualization for the H-2 hydropad.

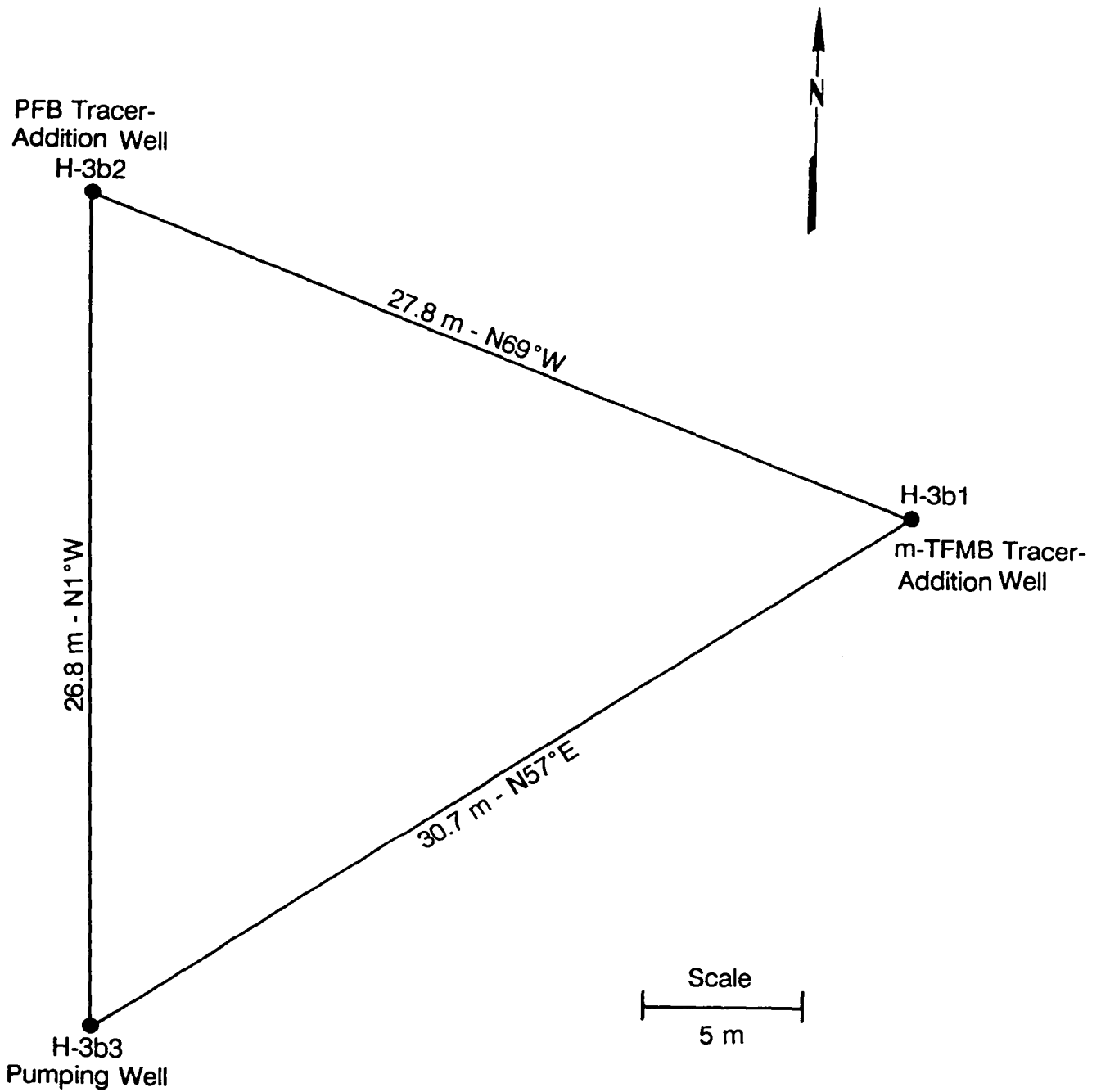
7.0 H-3 HYDROPAD TRACER TEST

Pumping and tracer tests were conducted at the H-3 hydropad from April 18, 1984 to June 12, 1984. Initial pumping was used to develop well H-3b3 and a later pumping test was intended to provide information about the anisotropy in horizontal transmissivity of the Culebra at the H-3 hydropad location. After the pumping test, H-3b3 became the pumping well for a convergent-flow tracer test with tracers injected into the two other hydropad wells, H-3b1 and H-3b2. The following sections briefly describe the well configurations, hydropad hydrogeology, tracer-test history, and previous interpretation of the H-3 tracer tests. This chapter also presents the current analysis of the tracer test, sensitivity analyses, and summarizes the tracer-test results.

7.1 Well Configurations

The H-3 hydropad is located in the south-central portion of the WIPP site, approximately 1.2 km south of the center of the site (Figure 1-2), and consists of three wells, H-3 (later renamed and hereafter called H-3b1), H-3b2, and H-3b3, completed in the Rustler Formation. The wells are arranged in an approximate equilateral triangle with approximately 28-m sides (Figure 7-1). The three wells are located in Section 29, Township 22 south, and Range 31 east. The UTM coordinates, ground-surface elevations, and top-of-casing elevations for the H-3 hydropad wells are summarized in Table 7-1. The relative positions of the wells at the depth of the Culebra dolomite are illustrated in Figure 7-1.

Well H-3b1, completed on August 12, 1976, was drilled under the direction of the United States Geological Survey (Mercer and Orr, 1979). The well has a total depth of 274.9 m BGS and is cased with 16.83-cm (6-5/8-inch) steel casing to a depth of 273.4 m BGS. The casing from 171.3 to 179.8 m BGS adjacent to the Magenta dolomite



NOTE: The borehole-deviation survey did not extend to the center of the Culebra dolomite in boreholes H-3b2 and H-3b3.

Figure 7-1. Plan view of the wells at the H-3 hydropad showing distances between wells at the center of the Culebra.

Table 7-1. UTM Coordinates, Ground-Surface Elevations, and Top-of-Casing Elevations for the H-3 Hydropad Wells

<u>Well</u>	<u>UTM Coordinates</u>		<u>Ground-Surface Elevation (m amsl)</u>	<u>Top-of-Casing Elevation (m amsl)</u>
	<u>m East</u>	<u>m North</u>		
H-3b1	613,729	3,580,895	1033.10	1033.47
H-3b2	613,701	3,580,906	1033.10	1033.28
H-3b3	613,705	3,580,876	1033.10	1032.87

was perforated using 84 jet shots 1.27 cm (0.5 inches) in diameter. At the Culebra dolomite from 204.2 to 211.5 m BGS, the casing was perforated using 84 jet shots 1.27 cm in diameter. The casing at the Rustler-Salado contact from 247.8 to 255.1 m BGS was perforated using 72 jet shots 1.27 cm in diameter. A bridge plug is located in the borehole at a depth of 243.5 m BGS to separate the Culebra and Rustler-Salado contact zone. The ground waters of the Magenta and Culebra dolomites are separated by a PIP located 201.2 m BGS.

In 1983, the triangular array of wells at the H-3 hydropad was completed with the drilling of wells H-3b2 and H-3b3 (Hydro Geo Chem, 1985). Well H-3b2 was initially drilled to a depth of approximately 205.1 m and cased with 13.97-cm (5-1/2-inch) steel casing. In order to access the Culebra interval, H-3b2 was deepened to 221.0 m BGS. The lower portion of the well is open hole with a diameter of 12.1 cm. Well H-3b3 was drilled to a total depth of approximately 222.5 m and cased with 13.97-cm (5-1/2-inch) steel casing to a depth of 204.4 m (Hydro Geo Chem, 1985). The 18.1 m below the casing is open hole with a diameter of 12.1 cm.

7.2 Local Hydrogeology

At the H-3 hydropad, the Culebra dolomite is approximately 7 m in thickness and ranges from strongly indurated dolomite to easily friable siltstone. The Culebra interval was cored in wells H-3b2 and H-3b3. Core recovery was very poor (Figures 7-2 and 7-3) suggesting a high degree of fracturing, vugs, and/or poor induration due to a high silt content. Approximately 10 percent of the Culebra interval was recovered in H-3b2 and approximately 40 percent in H-3b3. Much of the core was available only as rubble. Both vugs and fractures are evident in the core, some of which are filled with gypsum. Figures 7-2 and 7-3 were generated based on an examination of the respective borehole cores located in the Department of Energy Core Library at the WIPP site and on core photographs taken by Sandia National Laboratories at the time of coring. Core samples

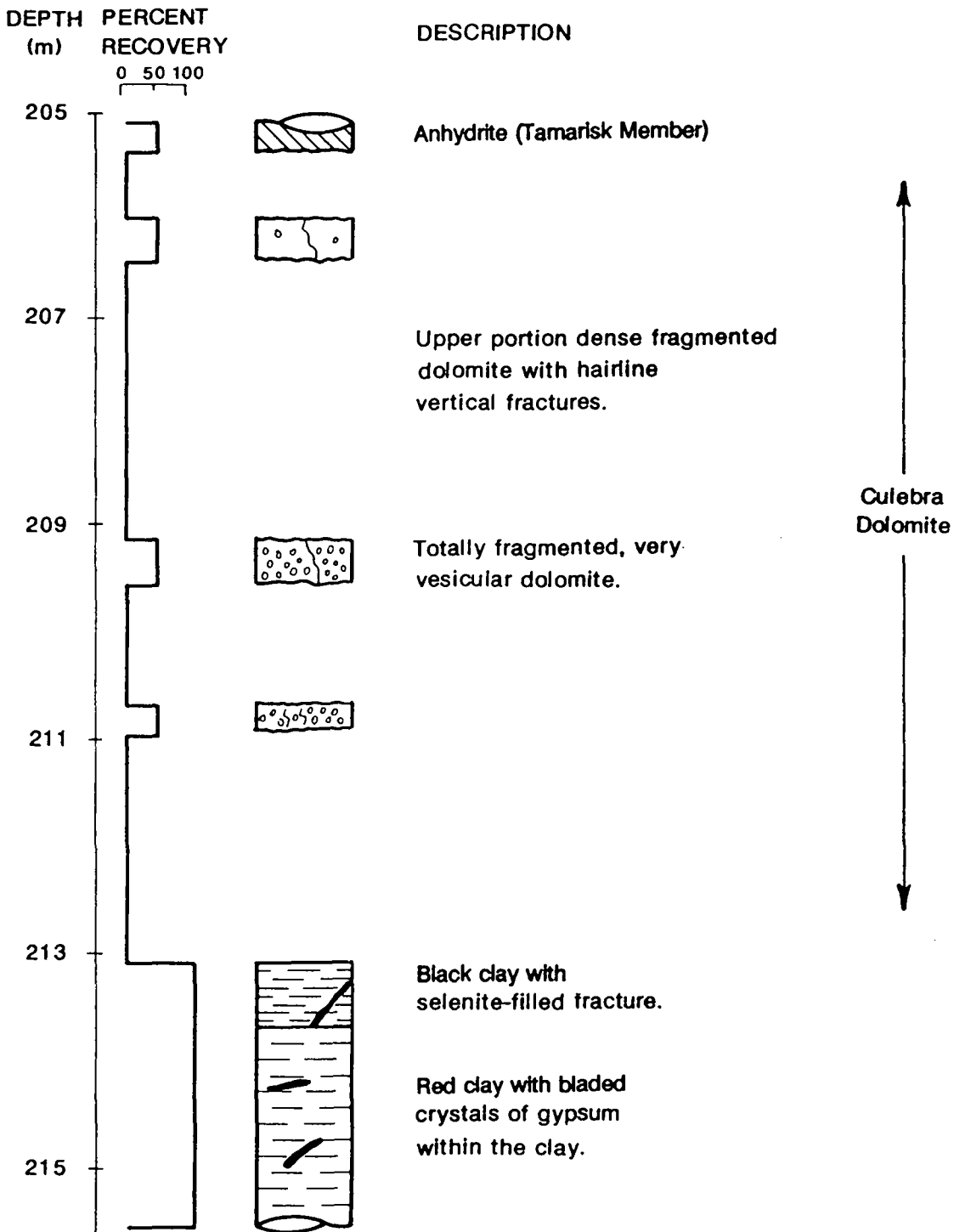


Figure 7-2. Results of core examination of the Culebra dolomite from borehole H-3b2 (after Kelley and Pickens, 1986).

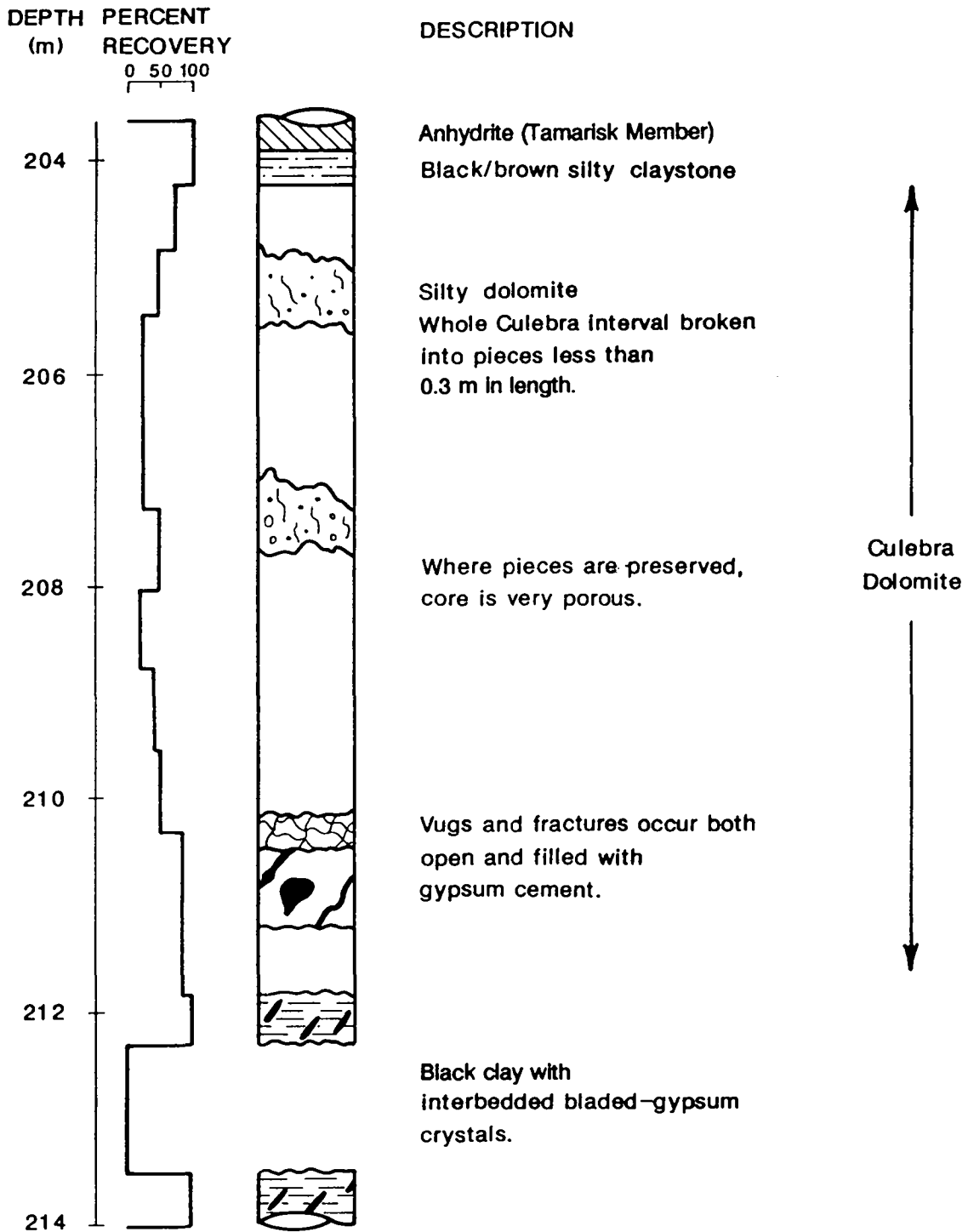


Figure 7-3. Results of core examination of the Culebra dolomite from borehole H-3b3 (after Kelley and Pickens, 1986).

revealed that (1) both horizontal and vertical fractures are present, (2) greater than 50 percent of the fractures present are open, and (3) the core is very porous. The largest piece of core recovered at the H-3 hydropad was 0.3 m in length. The results of physical measurements (i.e., permeability and porosity) on samples of the core from the H-3 hydropad are reported in Kelley and Saulnier (1990). Gas permeabilities range from less than 9.9×10^{-18} to 9.9×10^{-15} m² and porosities range from 0.168 to 0.244.

Pumping tests, slug tests, and DSTs have been performed at the H-3 hydropad in an effort to determine the hydraulic properties of the Culebra dolomite at that location (Beauheim, 1987b; Mercer, 1983; Seward, 1982). Cauffman et al. (1990) used data obtained from the pumping tests (Beauheim, 1987b) to determine an average transmissivity of 2.5×10^{-6} m²/s at the H-3 hydropad.

Beauheim (1987b) analyzed two pumping tests conducted at the H-3 hydropad. For the first test, conducted in 1984, H-3b3 was pumped at a rate of 0.25 L/s for 15 days. The second test was performed in 1985 with H-3b2 as the pumping well. This test lasted 63 days and had an average pumping rate of 0.3 L/s. Both pumping wells responded with typical double-porosity pressure responses. Beauheim (1987b) analyzed these tests using the log-log double-porosity type curves generated by Bourdet and Gringarten (1980) and pressure-derivative techniques (Bourdet et al., 1989). He concluded that the Culebra was a double-porosity medium at the H-3 hydropad and that direct fracture connections exist between wells. However, based on differences in the responses at H-3b1 and H-3b2 to pumping-rate fluctuations in H-3b3, Beauheim (1987b) concluded that a more direct fracture connection might exist between H-3b3 and H-3b1 than between H-3b3 and H-3b2.

Interpretation of hydraulic-test results has determined that horizontal transmissivity is anisotropic in the Culebra dolomite at some locations at the WIPP site. Analysis of pumping tests performed at the H-3 hydropad are inconclusive in determining anisotropy at that location (Beauheim, 1987b).

7.3 Tracer-Test History

The following sections briefly discuss the pumping and tracer-injection history, the test equipment, and the characteristics of the observed tracer-breakthrough curves for the H-3 tracer test. Detailed descriptions of the test equipment, test histories and annotated plots and tabulations of the pressure responses in the wells, quality of the pumped water, and tracer concentrations are presented in Hydro Geo Chem (1985) and INTERA (1986).

7.3.1 Pumping and Tracer-Injection History

From April 18, 1984 to June 12, 1984, a series of pumping activities was conducted at the H-3 hydropad. These activities included well-development pumping, a pumping test designed to provide a portion of the data needed to evaluate the anisotropy in transmissivity at the H-3 hydropad, and the pumping period for the convergent-flow tracer test. During this time period the pumping well was H-3b3. The pumping test began at 10:30 on April 23, 1984 with the pump operating at a rate of 0.25 L/s. This rate was maintained until 14:50 on May 7, 1984, at which time the rate was reduced to 0.19 L/s in preparation for the convergent-flow tracer test. The pumping rate was held at approximately 0.19 L/s during the tracer test. Pumping ended at 12:04 on June 12, 1984 after approximately 910 m³ of water had been pumped from the Culebra dolomite at well H-3b3. The pumping record, based on periodic measurements of the pumping rate, is presented in Figure 7-4 for the duration of the tracer test. Pumping information for the tracer test is summarized in Table 7-2.

The convergent-flow tracer test began on May 9, 1984 with the injection of tracers into wells H-3b1 and H-3b2. One kilogram of the tracer meta-trifluoromethylbenzoate (m-TFMB) mixed with 76 L of formation fluid was injected into H-3b1. This tracer-labeled volume was followed by the injection of 303 L of formation fluid. The total injection time was approximately 1 hr and 35 min from 13:55 to 15:30 and the total volume injected was

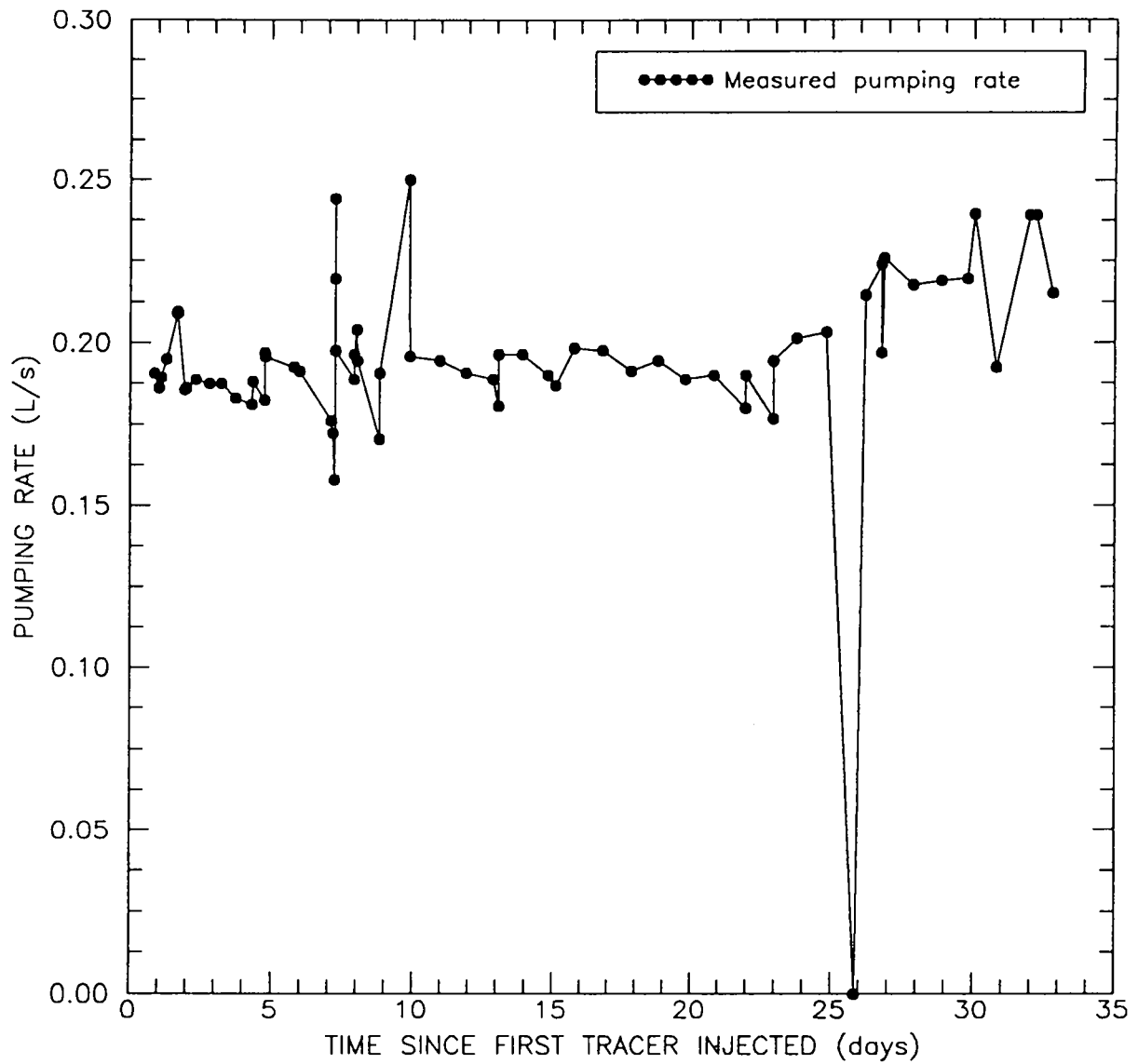


Figure 7-4. Pumping rate at well H-3b3 during the convergent-flow tracer test conducted at the H-3 hydropad.

Table 7-2. Summary of Pumping and Tracer-Injection Information for the Convergent-Flow Tracer Test Conducted at the H-3 Hydropad

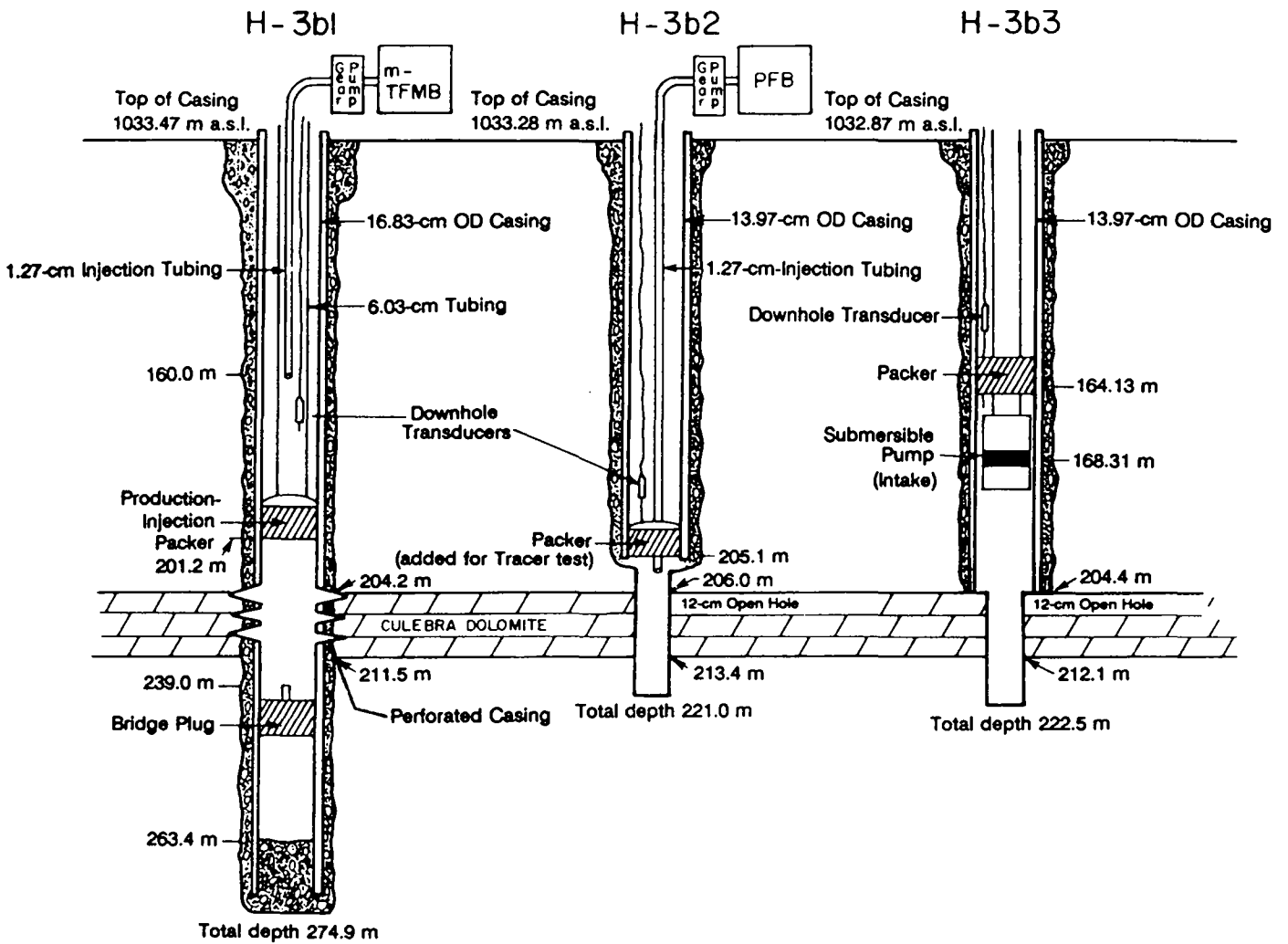
	<u>H-3b1</u>	<u>H-3b2</u>	<u>H-3b3</u>
Well Type	Tracer Injection	Tracer Injection	Pumping
Average Pumping Rate			0.19 L/s
Time Pumping Began			10:30
Date Pumping Began			04/23/84
Time Pumping Ended			12:04
Date Pumping Ended			06/12/84
Tracer Injected	m-TFMB	PFB	
Mass Injected	1.0 kg	1.0 kg	
Time Tracer Injected	13:55 to 15:30	12:45 to 13:45	
Date Tracer Injected	05/09/84	05/09/84	
Tracer Volume	76 L	38 L	
Chaser Volume	303 L	189 L	
Downhole System Volume	258 L	98 L	

379 L, 121 L greater than the downhole-system volume of 258 L. The tracer pentafluorobenzoate (PFB) was injected into well H-3b2. The tracer-labeled volume consisted of 1 kg of PFB mixed with 38 L of formation water. A volume of 189 L of formation fluid was injected immediately after tracer injection. The total injection period was from 12:45 to 13:45, approximately 1 hr. The total injected volume (227 L) was approximately 129 L greater than the downhole-system volume of 98 L. Tracer-injection information for the tracer test is summarized in Table 7-2. Full details on the H-3 hydropad tracer tests are reported in Hydro Geo Chem (1985).

7.3.2 Test Equipment

The configuration of the three H-3 hydropad wells during the pumping and tracer-test sequence is illustrated in Figure 7-5. In H-3b3, a submersible pump was installed below an air-inflatable sliding-end packer. A discharge line extended through the packer to the ground surface. A feed-through plug attached to the packer accommodated a three-phase electrical cable and the transducer access tube to the test interval. Fluid pressure in the borehole was measured with a pressure transducer. The transducer, and its associated electric cable, were strapped to the discharge pipe. Nylon tubing passing through the packer feed-through assembly allowed access to the test interval for the transducer.

In well H-3b1, a PIP was installed above the Culebra interval. Fluid pressure in the borehole was measured using a pressure transducer. The transducer was lowered on the transducer cable into the 6.03-cm (2-3/8-inch) tubing which accessed the Culebra interval through the PIP. A 1.27-cm polyethylene tube was lowered inside the 6.03-cm tubing string to a depth of 160 m below top of casing (BTC). At that depth, the 1.27-cm tube encountered an obstruction which prevented positioning of the tube at a greater depth.



All depths measured below ground surface.

Figure 7-5 Downhole-equipment configurations for the tracer test at the H-3 hydropad (after Kelley and Pickens, 1986).

A packer and feed-through plug were also used in H-3b2. Fluid pressure was measured in the borehole using a pressure transducer. During the pumping test, the transducer was lowered into the open hole on the transducer cable. The transducer was later strapped to the packer tubing, as described for H-3b3, for the period of the tracer test. A 1.27-cm polyethylene tube was installed from ground surface to the packer feed-through plug to allow tracer injection into the zone below the packer.

A microcomputer-controlled data-acquisition system (DAS) was utilized to monitor the transducers measuring pressures in the Culebra intervals of the three hydropad wells. Water levels in H-3b1 and H-3b2 were also monitored using an electric water-level sounder. The pressure data for the three H-3 hydropad wells are shown in Figure 7-6 and are tabulated as water levels in INTERA (1986).

The two tracers were mixed in separate containers on site. A gear pump was used to pump the tracers through the 1.27-cm polyethylene tubing and into the respective borehole. Water samples were collected from the pump discharge line using an automatic sampler. A portion of the water from the pump discharge line entered a reservoir at ground surface. Personnel collecting samples during the test estimated a fluid residence time of less than 30 sec in the discharge reservoir. Samples for the automatic sampler were pumped from the discharge reservoir through tygon tubing using a peristaltic pump. The tygon tubing leading from the reservoir to the sample containers was blown free of fluid after each sample was collected. The net effect of any droplets left in the tubing between samples was negligible due to the size of the collected samples (750 mL). Therefore, cross-sample contamination is considered to be minimal. Samples were collected manually during periods when the automatic sampler malfunctioned. Fluid collected by the automatic sampler was transferred to 50-mL polyethylene bottles prior to daily shipment to a laboratory for analysis. The fluid samples were analyzed to determine the concentration of each fluorobenzoate tracer by HPLC using analytical techniques described in Hydro Geo Chem (1985) and Stetzenbach et al. (1982).

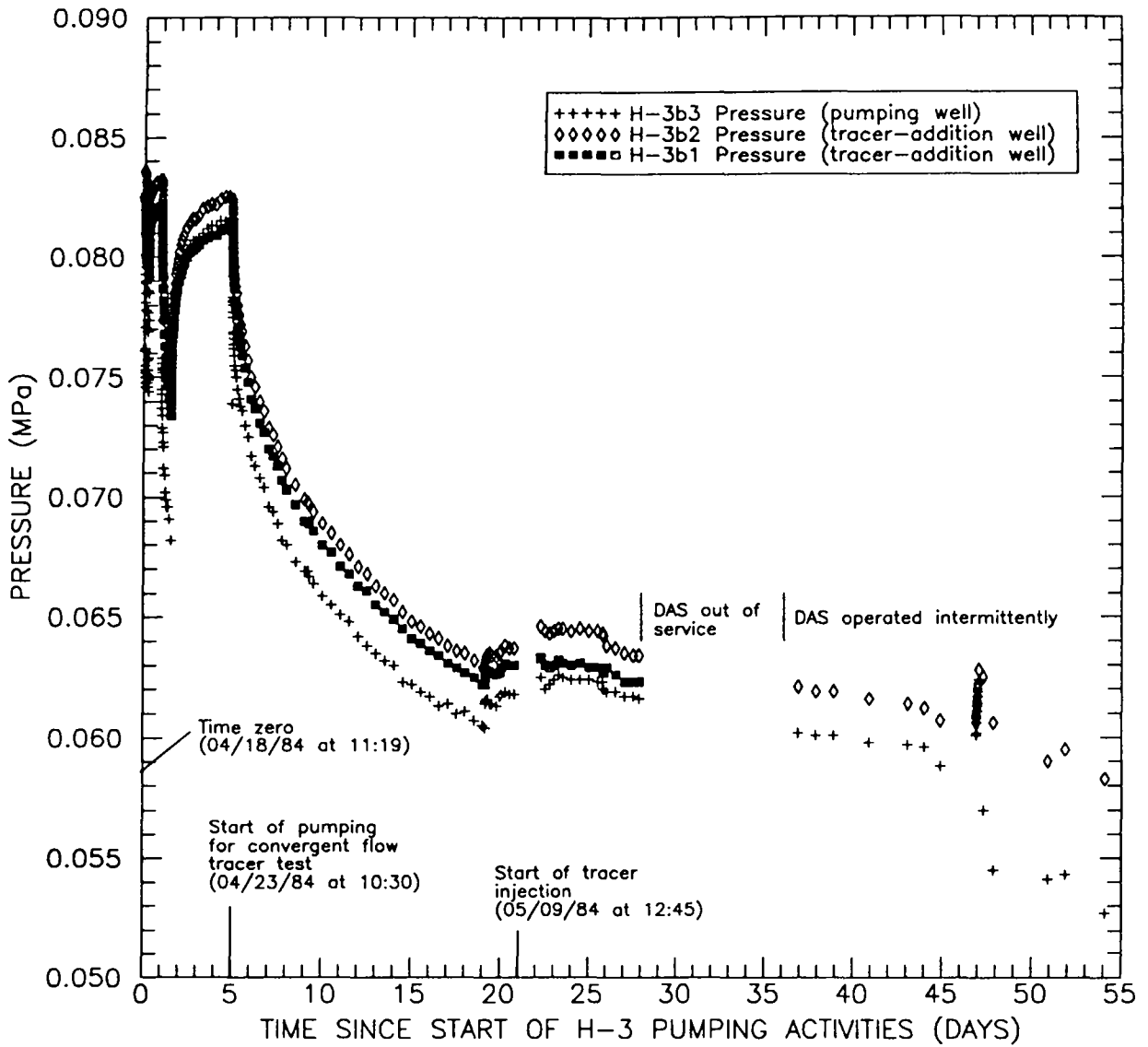


Figure 7-6. Pressure data for the H-3 hydropad wells during the convergent-flow tracer test.

7.3.3 Observed Tracer Breakthrough

The breakthrough curves obtained for m-TFMB and PFB from water samples collected at the pumping well are illustrated in Figure 7-7. The concentration data reported by Hydro Geo Chem (1985) and the corrected travel times are presented in Appendix C. The times are corrected to account for the time required for the tracer to travel from the injection point down to the Culebra center in the injection well and to account for the time required for tracer travel from the Culebra up the pumping well to the sampling point. The time corrections are noted in Appendix C.

The tracer m-TFMB was first detected at the pumping well about 21 hrs (corrected time) after it was injected. The peak concentration of m-TFMB occurred about 61 hrs (corrected time) after injection. Integration of the m-TFMB breakthrough curve yields an estimate of approximately 54 percent tracer recovery. The corrected times of first detection and peak concentration for the tracer PFB are approximately 94 and 552 hrs, respectively. Only two samples were collected after the peak concentration of PFB was observed. The concentration of these samples was about 12 percent lower than the peak concentration. Because of insufficient samples, the falling limb of the PFB breakthrough curve can not be accurately defined. The percent recovery of PFB at the pumping well, calculated by integrating the breakthrough curve, is approximately 15 percent. The peak concentration of PFB is about a factor of eight lower than the peak concentration of m-TFMB. The peak concentration of PFB occurred a factor of nine later than the peak concentration of m-TFMB. The shape of the observed breakthrough curves suggests that a more direct connection exists between H-3b1 and H-3b3 than between H-3b2 and H-3b3. This observation is consistent with the conclusion of Beauheim (1987b) that a more direct fracture connection might exist between H-3b3 and H-3b1 than between H-3b3 and H-3b2.

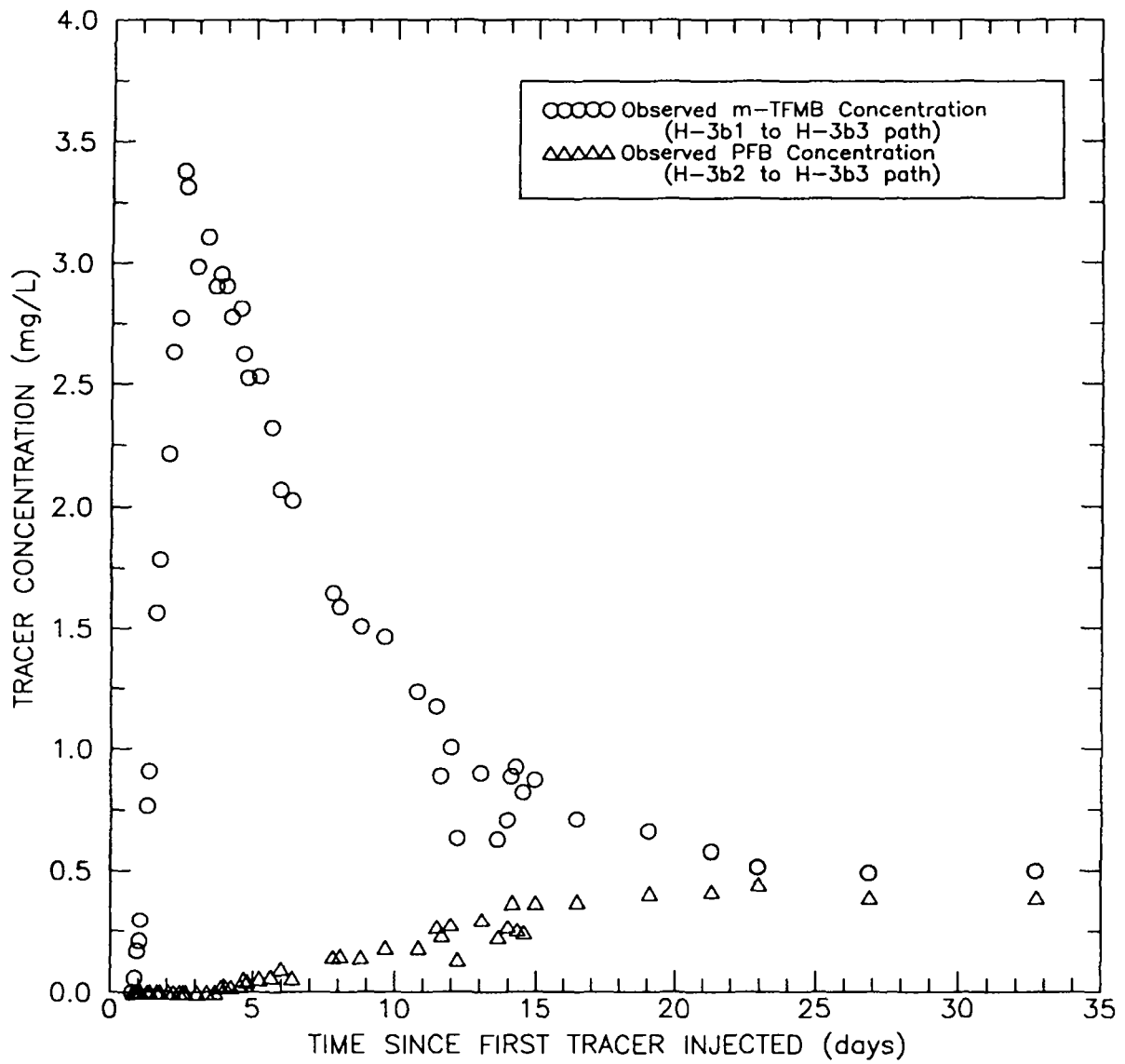


Figure 7-7. Observed m-TFMB and PFB data for the convergent-flow tracer test conducted at the H-3 hydropad.

7.4 Analysis of Tracer-Breakthrough Curves

Major differences can be seen in the breakthrough curves of m-TFMB and PFB (Figure 7-7). For m-TFMB, the peak concentration occurs shortly after the start of the tracer test and the breakthrough curve peaks sharply and tails significantly. The PFB breakthrough curve, on the other hand, is very broad and has a much lower peak concentration. Interpretation of the H-3 tracer-test results considered two approaches to explain the difference in the shapes of the two breakthrough curves. The first approach assumed that the difference is a result of heterogeneity between the two flow paths. The heterogeneity considered was matrix-block length (fracture spacing), which provides differences in the amount of surface area available for matrix diffusion. The second approach assumed that anisotropy in the horizontal transmissivity between the flow paths can explain the different tracer-breakthrough characteristics. The existence of anisotropy implies that directional fracture/matrix properties are present at the hydropad and that preferred fracture orientations result in more direct transport between H-3b1 and H-3b3 than between H-3b2 and H-3b3. The methodologies for the heterogeneous and anisotropic simulations are discussed in detail in Section 3.4. The actual solute-transport system likely exhibits a combination of heterogeneity and anisotropy. For simplicity, however, this analysis investigated only the two idealized cases.

7.4.1 Heterogeneous-Analysis Approach

The method used to calibrate the simulated results to the observed tracer-breakthrough curves using the heterogeneous-analysis approach is discussed in Section 3.4.1. The following sections present a previous analysis and the current interpretation of the convergent-flow tracer test conducted at the H-3 hydropad.

7.4.1.1 PREVIOUS INTERPRETATION OF THE CONVERGENT-FLOW TRACER TEST CONDUCTED AT THE H-3 HYDROPAD USING THE HETEROGENEOUS-ANALYSIS APPROACH

A previous interpretation of the convergent-flow tracer test conducted at the H-3 hydropad is presented in Kelley and Pickens (1986). The methodology used for those interpretations was identical to that described for the heterogeneous-analysis approach in Section 3.4.1. Although Kelley and Pickens (1986) do not explicitly describe their analysis approach as the heterogeneous-analysis approach, the discussion in Section 3.4.1 is directly applicable to their interpretations. Values used by Kelley and Pickens (1986) for the assigned parameters are summarized in Table 7-3. At the time of their interpretation, site-specific data for Culebra tortuosity were not available and, therefore, literature values were used. The two literature values selected were 0.15 and 0.45. Subsequent determinations of tortuosity from Culebra core indicate that only the value of 0.15 was relevant to WIPP conditions. Kelley and Pickens (1986) report a fracture porosity of 1.9×10^{-3} for the H-3 hydropad, matrix-block lengths of 1.2 and 2.1 m for tortuosities of 0.15 and 0.45, respectively, for the H-3b1 to H-3b3 path, and matrix-block lengths of 0.25 and 0.44 m for tortuosities of 0.15 and 0.45, respectively, for the H-3b2 to H-3b3 path.

7.4.1.2 CURRENT INTERPRETATION OF THE CONVERGENT-FLOW TRACER TEST CONDUCTED AT THE H-3 HYDROPAD USING THE HETEROGENEOUS-ANALYSIS APPROACH

On the figures illustrating the current test interpretations, the transport parameters used in the simulations are reported exactly as they appeared in the model input. Reporting parameters to a large number of significant digits on the figures does not imply a high degree of certainty in the value; it does, however, provided the reader with the parameter value required to reproduce the simulated results. Because the parameters are not known to a high degree of certainty, some values reported in the tables and text are rounded to a smaller number of significant digits.

Table 7-3. Transport Parameters Used by Kelley and Pickens (1986) in Their Interpretations of the H-3 Convergent-Flow Tracer Test

Parameter	Value	
Pumping Rate	0.19 L/s	
Culebra Thickness	7.0 m	
Well Spacings	30.7 m	H-3b1 to H-3b3
	26.8 m	H-3b2 to H-3b3
Free-Water Diffusion Coefficients	$7.4 \times 10^{-10} \text{ m}^2/\text{s}$	m-TFMB
	$7.2 \times 10^{-10} \text{ m}^2/\text{s}$	PFB
Longitudinal Dispersivities	3.0 m	H-3b1 to H-3b3 path
	1.5 m	H-3b2 to H-3b3 path
Tortuosities	0.15 and 0.45	
Matrix Porosity	0.2	

Figure 7-8 shows the observed and the best-fit simulated breakthrough curves for m-TFMB. The fracture porosity and matrix-block length used to generate this simulated curve were 1.2×10^{-3} and 1.23 m, respectively. Notice in Figure 7-8 that the simulated curve does not match the two highest observed m-TFMB concentrations. It was not possible to match those concentrations while maintaining a reasonable fit to the remainder of the m-TFMB breakthrough curve. The simulated-breakthrough curve indicated about 63 percent recovery of m-TFMB at the pumping well as compared to an estimate of 54 percent recovery based on the observed tracer-breakthrough curve. Using the fracture porosity determined through calibration of the m-TFMB breakthrough curve, the matrix-block length giving the closest match between the observed and simulated PFB concentrations was 0.23 m (Figure 7-8). Simulated recovery of PFB at the pumping well was about 12 percent, which is slightly lower than the recovery of 15 percent estimated from the observed tracer-breakthrough curve.

For the fracture porosity of 1.2×10^{-3} used in the heterogeneous simulations, the inner and outer radii of the tracer-input zones (shown schematically in Figures 3-5 and 3-8) were 1.29 and 2.15 m, respectively, for H-3b1 and 1.80 and 2.10 m, respectively, for H-3b2. Simulation of the m-TFMB breakthrough curve used 102 grid blocks ranging in size from 0.30 to 0.43 m between the pumping well and the outer edge of the initial-tracer mass. The tracer mass was input over 10 blocks. For the PFB breakthrough curve, 94 grid blocks ranging in size from 0.30 to 0.34 m were used with initial-tracer mass in 14 grid blocks. All simulations discussed in this report discretized the matrix with 35 nodes between the fracture/matrix interface and the center of the matrix block.

The larger matrix-block length determined for the path from H-3b1 to H-3b3 (1.23 m) indicates more widely spaced fractures with less surface area available for matrix diffusion. The results of tracer migration through a medium of this type are rapid transport with less mass lost to the matrix during a given time period. For the path from H-3b2 to H-3b3, the heterogeneous analysis yielded a smaller matrix-block length (0.23 m). This smaller value represents narrower fracture spacing and more surface area for matrix

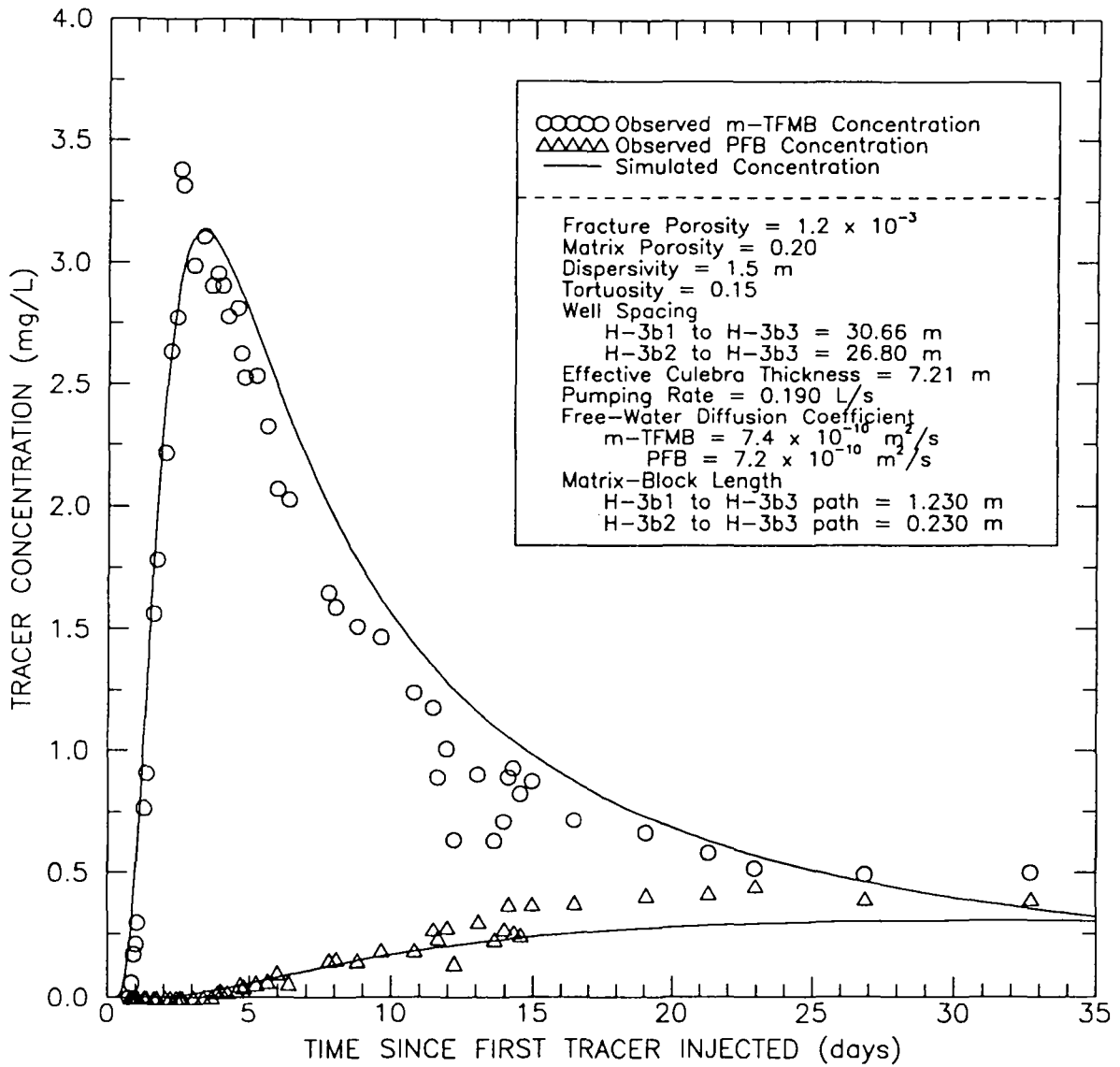


Figure 7-8. Observed and best-fit simulated breakthrough curves for the H-3 convergent-flow tracer test using the heterogeneous-analysis approach.

diffusion. Consequently, tracer migration through a medium with smaller matrix blocks results in more mass lost to the matrix, resulting in lower concentrations at the observation point, and slower transport times. The input parameters used in the best-fit, heterogeneous simulations are summarized in Table 7-4.

Comparison of the mass distribution in the fractures and matrix and mass recovery at the pumping well for the two travel paths provides insight into the significance of diffusive solute losses (Figure 7-9). Due to losses to both the matrix and the pumping well, the mass of m-TFMB in the fractures rapidly declines in the first several days of the tracer test. Large diffusive losses to the matrix, on the other hand, explain the rapid decline in PFB mass in the fractures along the slow path. At the end of the tracer test, the bulk of the unrecovered tracers (37 percent for m-TFMB and 88 percent for PFB) is located in the matrix (Figure 7-9).

The matrix-block lengths of 1.23 and 0.23 m for the m-TFMB and PFB breakthrough curves from the current interpretation compare closely with the values of 1.2 and 0.25 m, respectively, reported in the previous interpretation by Kelley and Pickens (1986) for a tortuosity of 0.15. The minor differences are a consequence of changes in the assigned values for longitudinal dispersivity and Culebra thickness and the fitted value for fracture porosity.

7.4.2 Anisotropic-Analysis Approach

The fitting parameters for the anisotropic simulations are horizontal anisotropy and matrix-block length. The objective of the anisotropic simulations was to determine a single anisotropy and matrix-block length that, for both tracers, would give simulated breakthrough curves that match the observed concentrations. Anisotropy includes the ratio of T_x to T_y and the orientation of the T_x direction. A complete discussion of how anisotropy is integrated into the simulation input parameters is provided in Section 3.4.2. The first

Table 7-4. Transport Parameters Used in the Interpretations of the H-3 Convergent-Flow Tracer Test

Parameter	Heterogeneous-Analysis Approach		Anisotropic-Analysis Approach	
Culebra Thickness	7.2 m			
Well Spacings	30.7 m		H-3b1 to H-3b3	
	26.8 m		H-3b2 to H-3b3	
Free-Water Diffusion Coefficients	$7.4 \times 10^{-10} \text{ m}^2/\text{s}$		m-TFMB	
	$7.2 \times 10^{-10} \text{ m}^2/\text{s}$		PFB	
Longitudinal Dispersivity	1.5 m			
Tortuosity	0.15			
Matrix Porosity	0.20			
Fracture Porosity	1.2×10^{-3}		2.0×10^{-3}	
Matrix-Block Lengths	1.23 m	H-3b1 to H-3b3	0.48 m	H-3b1 to H-3b3
	0.23 m	H-3b2 to H-3b3	0.48 m	H-3b2 to H-3b3
Anisotropy Ratio	1:1		6:1	
Principal-Transmissivity Direction	na		N57° E (parallel to the H-3b1 to H-3b3 path)	

na means not applicable

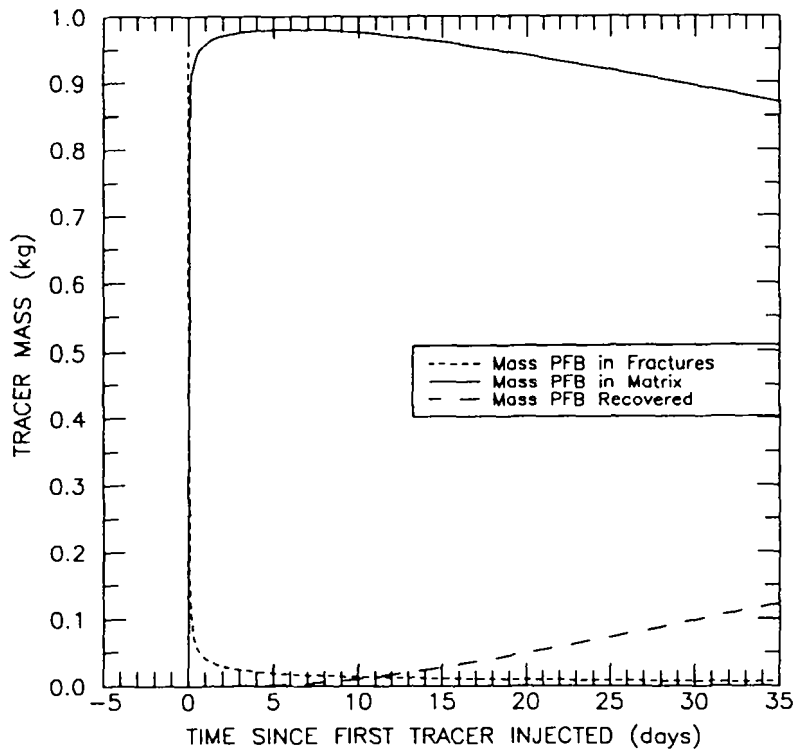
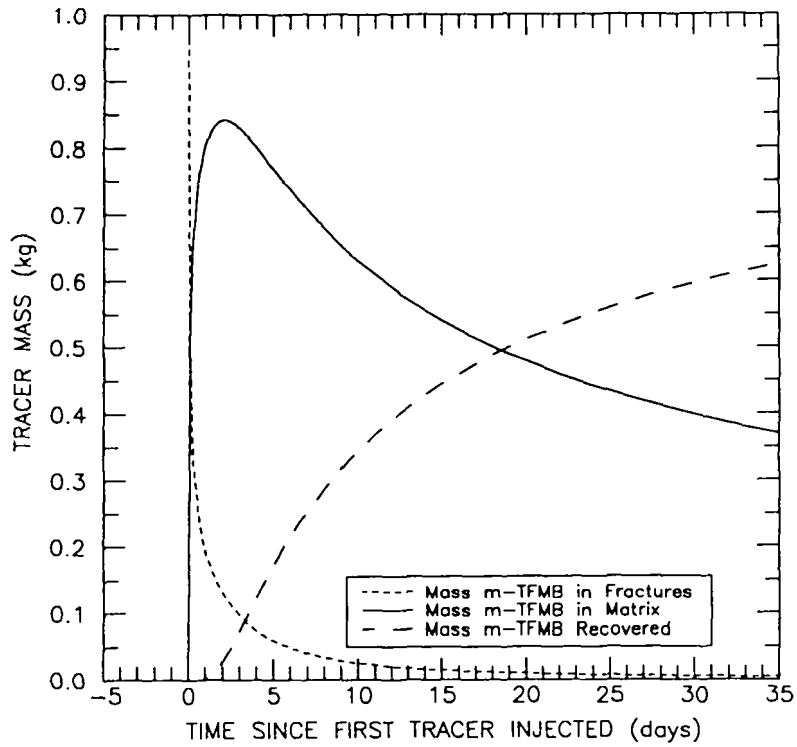


Figure 7-9. Mass distribution in the fractures and matrix and mass recovered at the pumping well for the best-fit heterogeneous simulation of the tracer-breakthrough curves for the H-3 hydropad.

estimate for the fracture porosity of 2.0×10^{-3} , calculated using Equation 5-9, was used in the anisotropy simulations. This fracture porosity yields inner and outer radii for the tracer-input zones (shown schematically in Figures 3-5 and 3-8) of 0.99 and 1.65 m, respectively, for H-3b1 and 1.44 and 1.68 m, respectively, for H-3b2. The paths from H-3b1 to H-3b3 and H-3b2 to H-3b3 were discretized into 104 and 96 grid blocks, respectively. The grid-block sizes ranged from 0.24 to 0.34 m. Initial mass was distributed over 10 grid blocks at H-3b1 and over 14 grid blocks at H-3b2.

The fracture porosities for the heterogeneous and anisotropic approaches were 1.2×10^{-3} and 2.0×10^{-3} , respectively. Fracture porosity is an important parameter with respect to matching the time of the peak concentration on the rapid-transport path. Since the fluid flux rate on the rapid-transport path is higher for the anisotropic case as compared to the heterogeneous case, this explains the larger fracture porosity required for the anisotropic case as compared to the heterogeneous case.

The observed concentrations were best fit using a $T_x:T_y$ of 6:1, a preferred T_x direction of N57° E (parallel to the H-3b1 to H-3b3 path), and a matrix-block length of 0.48 m. Figure 7-10 compares the observed and simulated breakthrough curves for both tracers. As can be seen in the figure, the observed tracer concentrations can be closely matched using the anisotropy approach. Table 7-4 summarizes the input parameters utilized in the best-fit, anisotropic simulations.

The significance of diffusive solute losses can be examined by comparing the mass distribution in the fractures and matrix and the mass recovered at the pumping well for the two travel paths (Figure 7-11). For the fast path, the mass of m-TFMB in the fractures exhibits a rapid decline in the first several days of the test in response to both losses to the matrix and losses to the pumping well. In contrast, the very rapid decline in PFB mass in the fractures along the slow path is the result of large diffusive losses to the matrix. It can be seen from Figure 7-11 that the bulk of the tracer mass remaining in the Culebra at the end of the tracer test (approximately 36 percent for m-TFMB and 87 percent for PFB) is

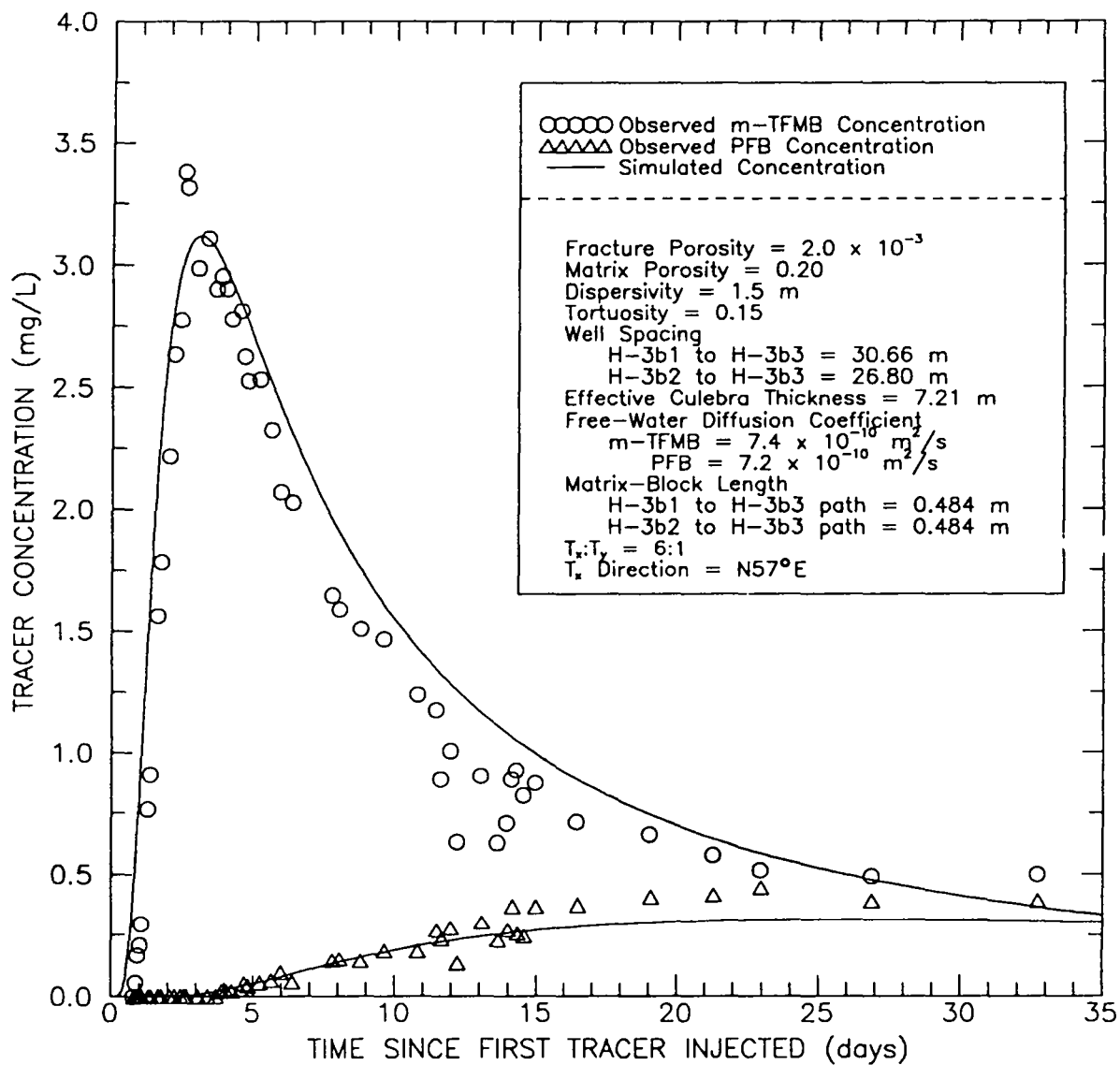


Figure 7-10. Observed and best-fit simulated breakthrough curves for the H-3 convergent-flow tracer test using the anisotropic-analysis approach.

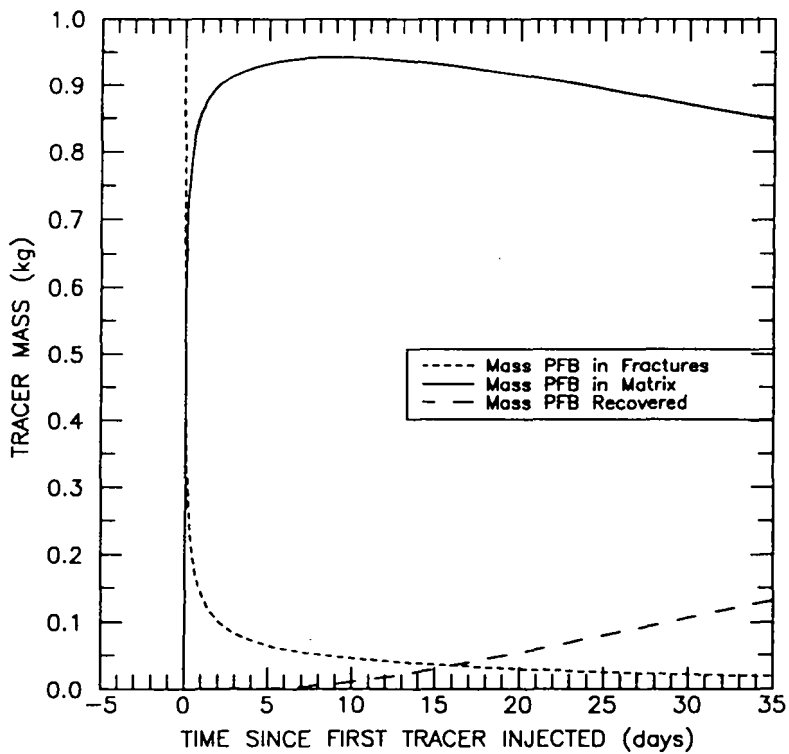
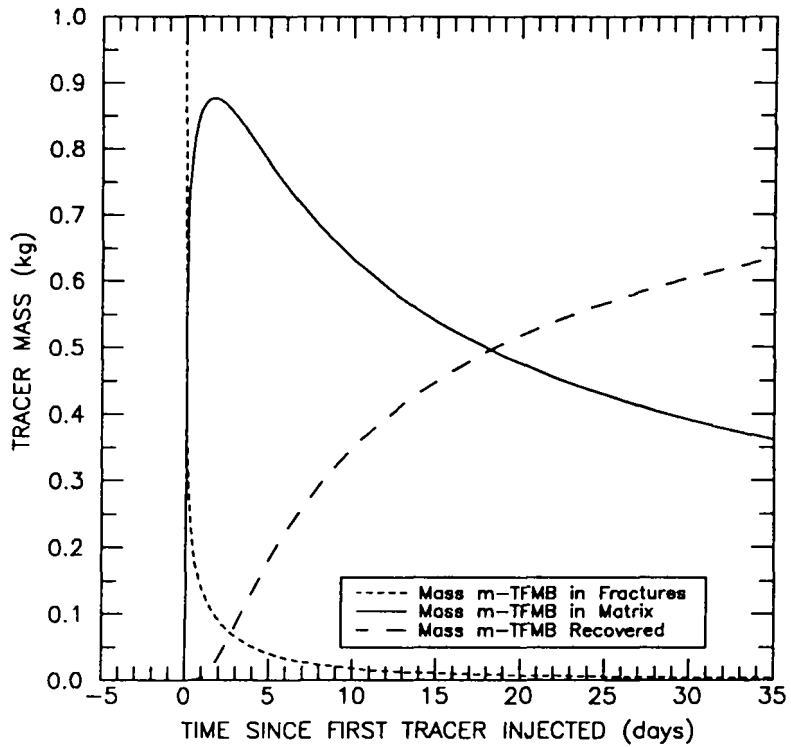


Figure 7-11. Mass distribution in the fractures and matrix and mass recovered at the pumping well for the best-fit anisotropic simulation of the tracer-breakthrough curves for the H-3 hydropad.

located in the matrix. Comparing Figures 7-9 and 7-11 for the heterogeneous- and anisotropic-analysis approaches, respectively, shows that the distribution of mass between fracture and matrix is similar using either approach.

7.5 Sensitivity Analyses

Domenico (1972) defined a model as "a representation of reality that attempts to explain the behavior of some aspect of it and is always less complex than the real system it represents." When applying a model to a real system, such as the Culebra dolomite, one must be cognizant of the model's ideal behavior. Assuming one is using the correct conceptual model of the real system, knowledge of ideal behavior lends a rational method of checking for inconsistent data and inadequate testing methods. Additionally, a sensitivity analysis allows the cause-and-effect relationship between input and output parameters to be characterized, thus providing a rationale to guide test interpretations.

A detailed sensitivity analysis was conducted for the H-3 tracer-breakthrough curves to provide a basis for examining input-parameter cause-and-effect relationships. Simulations conducted to determine the sensitivity of the model results to tortuosity, longitudinal dispersivity, fracture porosity, matrix porosity, and matrix-block length varied one input parameter from the best-fit, anisotropic simulations (Table 7-4) while all others were held constant. Additional sensitivities of this type were presented in Kelley and Pickens (1986).

A sensitivity study/analysis on effective Culebra thickness included recalibration of the numerical model for both the heterogeneous- and anisotropic-analysis approaches using an effective thickness of 2 m. To examine the effect of anisotropy in the horizontal direction, the model was recalibrated to the m-TFMB breakthrough curve using different combinations of anisotropy ratio and principal-transmissivity direction. The predicted PFB breakthrough curve with the recalibrated model was then compared to the observed PFB breakthrough curve.

A sensitivity analysis was also conducted to determine maximum and minimum estimates of the matrix-block lengths at the H-3 hydropad. These maximum and minimum estimates provide insight into the uncertainty in matrix-block length, which is a fitted parameter. The heterogeneous-analysis approach was used for this sensitivity because it yields an upper and lower bound on the interpreted matrix-block length for an individual hydropad location. In order to determine the maximum and minimum matrix-block lengths, the assigned transport parameters were based on the ranges summarized in Section 5.0. All sensitivity analyses examine the fast path from H-3b1 to H-3b3 (m-TFMB breakthrough curve) as well as the slow path from H-3b2 to H-3b3 (PFB breakthrough curve).

7.5.1 Effect of Tortuosity

Tortuosity directly affects the magnitude of the effective solute-diffusion coefficient in the matrix (Equation 5-5). Tortuosity values and ranges are discussed in Section 5.1.7. The sensitivity analysis compared simulations using tortuosities of 0.027 and 0.38 to the base-case simulation which used a value of 0.15. The results of the sensitivity to tortuosity are illustrated in Figure 7-12. Increasing the tortuosity results in increased diffusive losses from the fractures to the matrix. This higher solute flux to the matrix leads to a decreased peak concentration at the pumping well and a delay in the time to reach the peak concentration. The late-time gradual decrease in tracer concentration after the peak concentration is reached, the "tailing effect", is also increased with an increase in tortuosity. The opposite effects are true for a decrease in tortuosity. Travel along both the fast and slow path was very sensitive to the tortuosities investigated here.

7.5.2 Effect of Longitudinal Dispersivity

The base-case longitudinal dispersivity is 1.5 m or about 5 percent of the travel distance between the tracer-addition wells and the pumping well. For the sensitivity

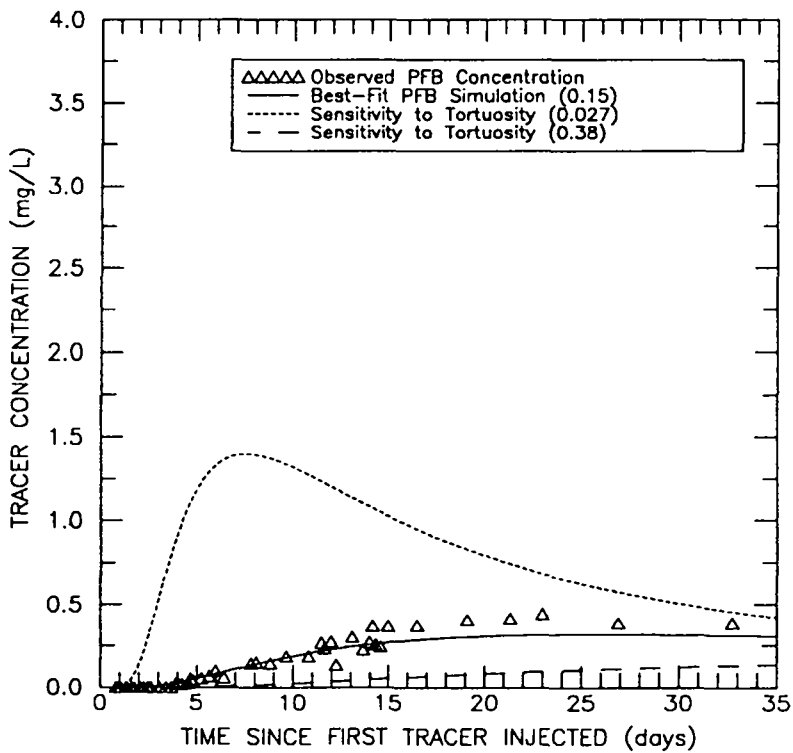
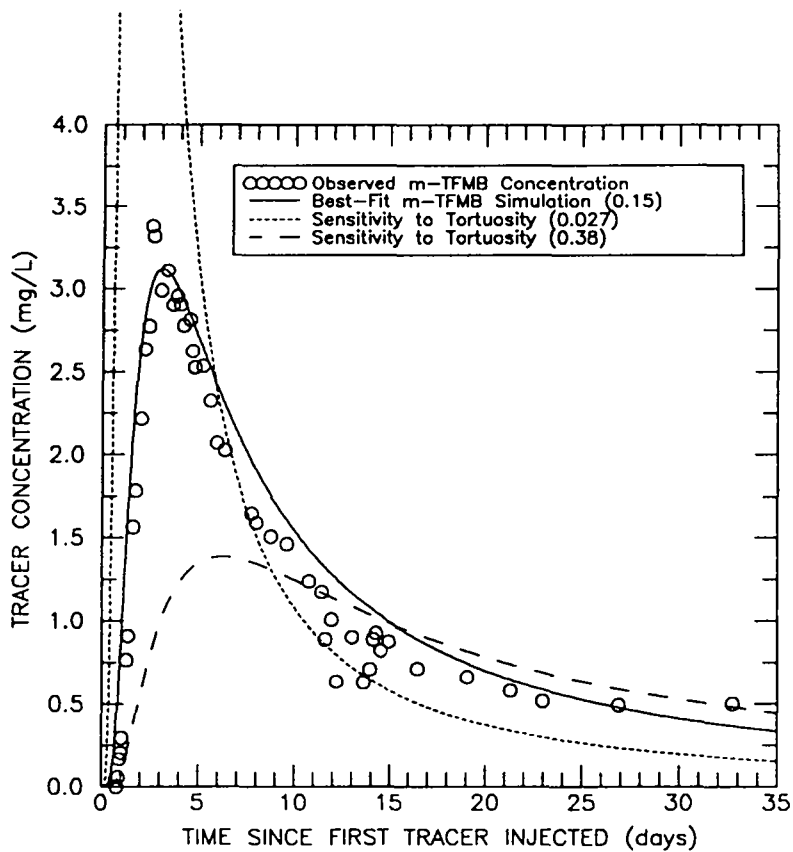


Figure 7-12. Sensitivity to tortuosity for the H-3 convergent-flow tracer test.

analysis, longitudinal dispersivity was reduced to 0.5 m and increased to 3.0 m (see Section 5.1.5). The effects of varying longitudinal dispersivity are illustrated in Figure 7-13. For the fracture-controlled fast path, increasing dispersivity increased the peak concentration and decreased the arrival time of the peak; decreasing dispersivity also increased the peak concentration but increased the peak-concentration arrival time. By increasing the dispersivity in the fractures, the tracer moves more rapidly to the pumping well, resulting in less mass loss to the matrix and a higher peak concentration and tailing. A decrease in dispersivity along the fracture-controlled path causes a reduction in the influence of hydrodynamic dispersive transport and a corresponding later arrival of the peak concentration at the pumping well. This effect also yielded a higher peak concentration.

The slow path from H-3b2 to H-3b3 appears less controlled by direct fracture transport and, therefore, diffusive losses are more significant. For this path, increasing dispersivity decreases the amount of mass lost to the matrix. As a result, the breakthrough curve peaks earlier and has a higher peak concentration. Reducing the dispersivity increases diffusive losses to the matrix which yields a breakthrough curve that peaks later and has a lower peak concentration.

7.5.3 Effect of Fracture Porosity

In a double-porosity system, the fractures are the principal transport medium whereas the matrix represents the bulk of the storage capability. An increase in fracture porosity results in a corresponding decrease in ground-water velocity within the fracture system under the same pumping rate. Fracture porosities considered in the sensitivity analysis were 3.0×10^{-3} and 1.0×10^{-3} which are above and below, respectively, the base-case fracture porosity of 2.0×10^{-3} . Results of the sensitivity simulations are presented in Figure 7-14. As fracture porosity increases, mass breakthrough is delayed and the maximum observed concentration is decreased. The lower ground-water velocity resulting from a higher fracture porosity increases the residence time in the fractures, thus allowing greater diffusive losses

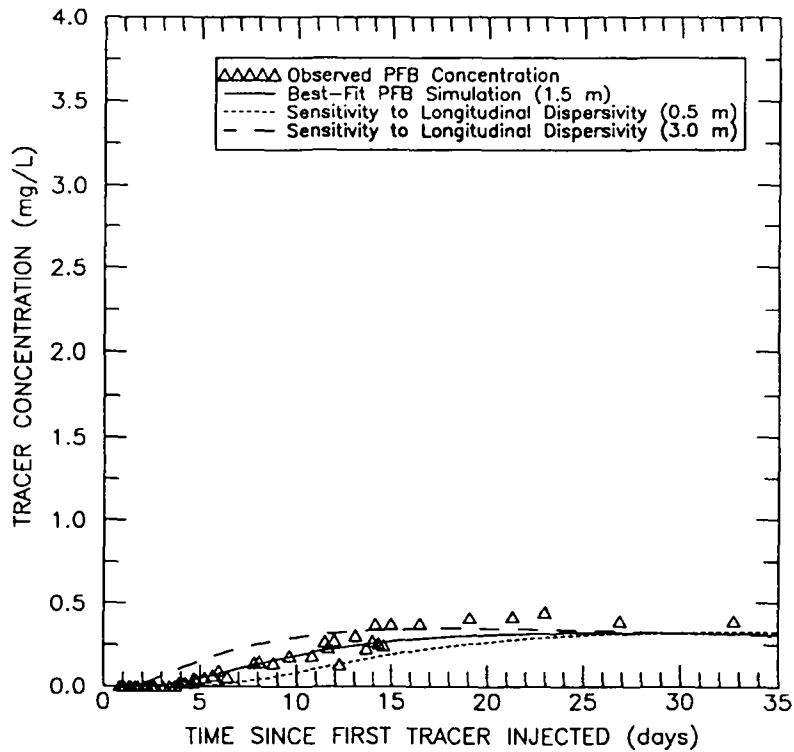
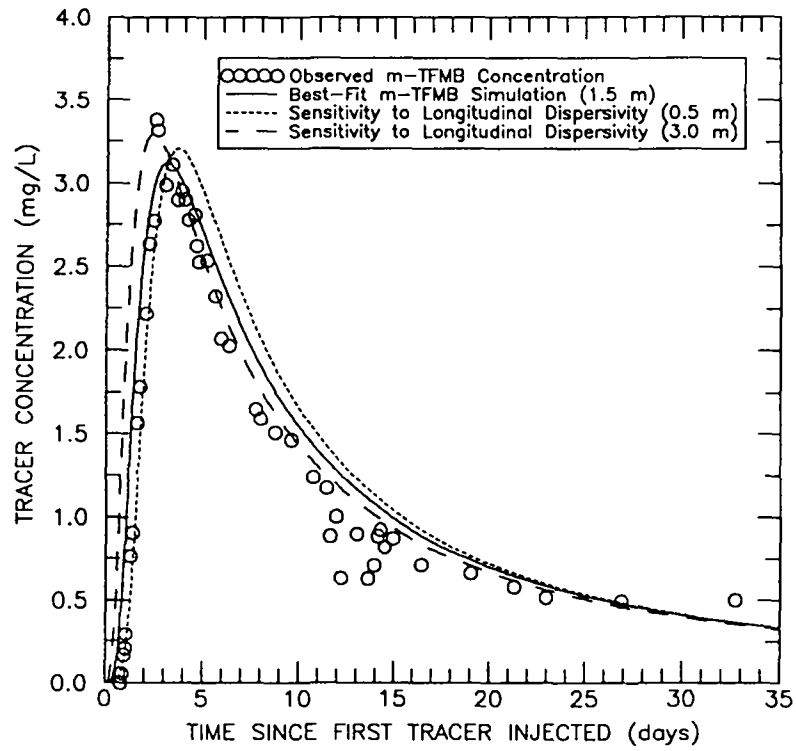


Figure 7-13. Sensitivity to longitudinal dispersivity for the H-3 convergent-flow tracer test.

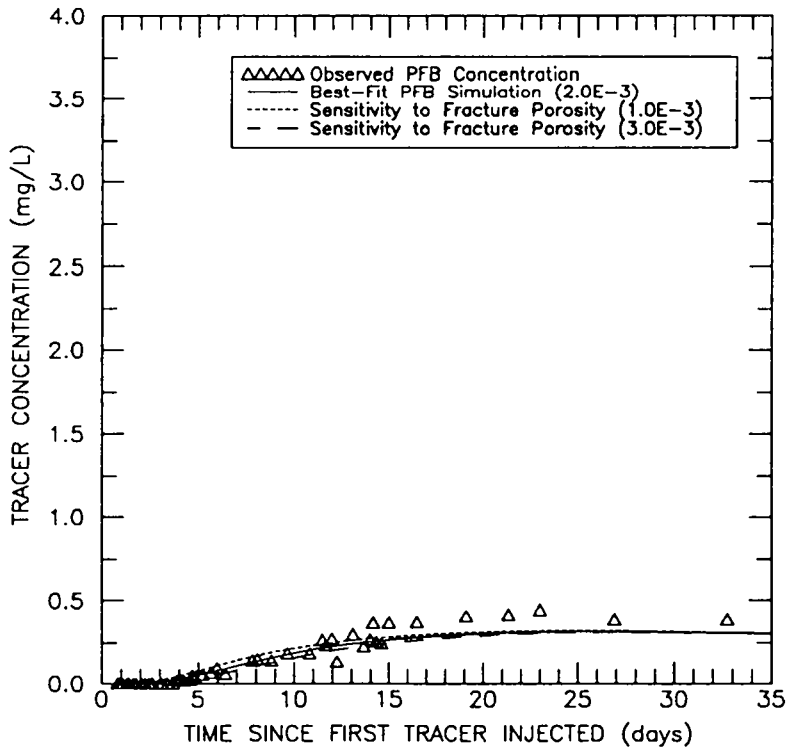
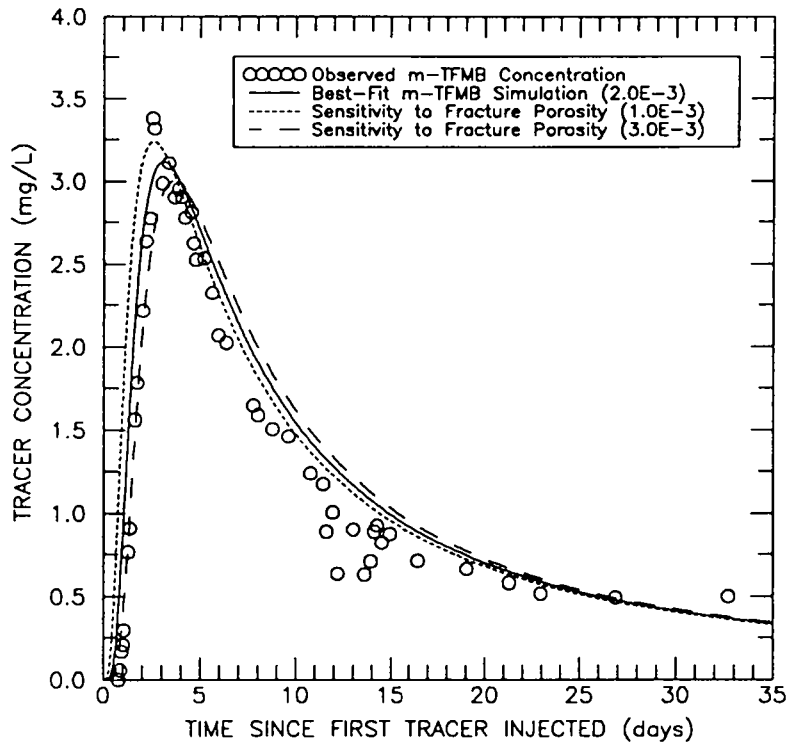


Figure 7-14. Sensitivity to fracture porosity for the H-3 convergent-flow tracer test.

to the matrix. The opposite effects occur when the fracture porosity is decreased. The effect of fracture porosity on breakthrough concentration was more evident along the apparent fracture-dominated transport path from H-3b1 to H-3b3. Along the slow path from H-3b2 to H-3b3, the breakthrough curve is not very sensitive to the fracture porosities considered here.

7.5.4 Effect of Matrix Porosity

The effective solute diffusion coefficient in the matrix is directly affected by the matrix porosity (Equation 5-5). In addition, the magnitude of the matrix porosity directly affects the solute-storage capacity of the matrix. The base-case matrix porosity (0.20) was selected based on the results of hydropad-specific porosity measurements taken on two core samples recovered in well H-3b2 and on four core samples recovered in well H-3b3. Table 5-2 summarizes the range of potential values for average borehole or hydropad porosity for the WIPP site. The porosities given in this summary range from a low of 0.08 to a high of 0.30. For the investigation of breakthrough sensitivity to matrix porosity, the end members of this range were considered.

Figure 7-15 illustrates the effect of matrix porosity on tracer breakthrough. Increasing the matrix porosity yielded later mass breakthrough, decreased maximum concentration, and increased tailing because the higher matrix porosity allowed greater mass loss to the matrix. The effect of matrix porosity on the peak-concentration arrival time is greater for the slow path than for the fast path. This is because transport along the slow path involves greater matrix participation than transport along the fast path.

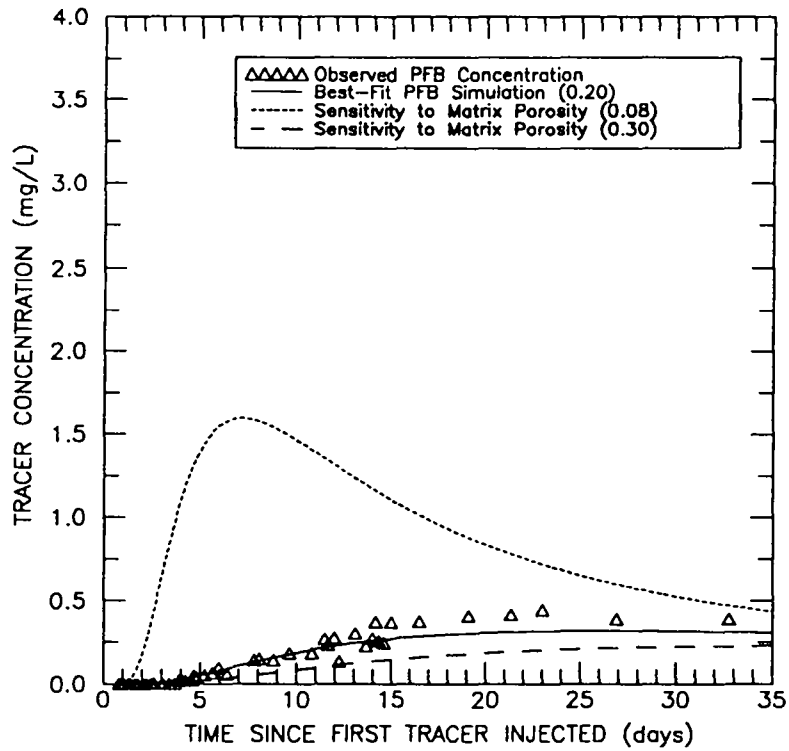
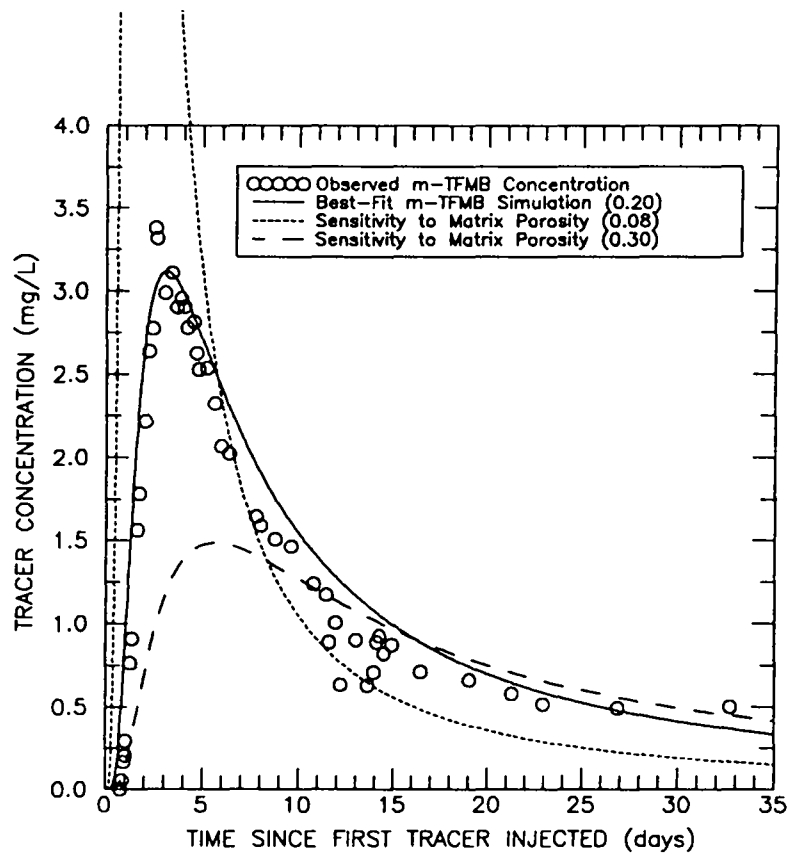


Figure 7-15. Sensitivity to matrix porosity for the H-3 convergent-flow tracer test.

7.5.5 Effect of Matrix-Block Length

Two matrix-block lengths corresponding to values that are 5 percent above (0.508 m) and below (0.460 m) the best-fit value of 0.484 m, determined for the anisotropic-analysis approach, were considered in this sensitivity study/analysis. Selection of sensitivity values that differed from the base-case value by only 5 percent provided the opportunity to observe the degree to which the fractured-dominated transport path is sensitive to a small changes (0.024 m) in the matrix-block length. The results of the sensitivity to matrix-block length are illustrate in Figure 7-16. As matrix-block length decreases, the matrix surface area to volume ratio increases and, for a given fracture porosity, the number of fractures increases resulting in a decrease in the fracture aperture. Both of these effects result in greater diffusion of solute from the fracture to the matrix. As a result, the peak concentration is reduced, the peak-concentration arrival time is delayed, and tailing is increased. The opposite is true for an increase in the matrix-block length. The effect of matrix-block length on the simulated results is greatest for the path with the least fracture/matrix interaction (i.e., the fracture-dominated path from H-3b1 to H-3b3).

As discussed in Section 5.3, matrix-block length is a parameter in the independent-parameter group τ' which defines the characteristic diffusion time. Results that leave the left-hand side of Equation 5-13 unchanged will be invariant to changes in the parameters half matrix-block length L' , matrix tortuosity θ' , and free-water diffusivity D' . This effect is demonstrated in Figure 7-17. The characteristic matrix-diffusion time for each simulation was 16.7 yrs, however, the parameters used to calculate that value were different. The values used for the half matrix-block length, the tortuosity, and the free-water diffusion coefficient were 0.24 m, 0.15, and $7.4 \times 10^{-10} \text{ m}^2/\text{s}$, respectively, for simulation 1, 0.39 m, 0.38, and $7.4 \times 10^{-10} \text{ m}^2/\text{s}$, respectively, for simulation 2, and 0.10 m, 0.027, and $7.4 \times 10^{-10} \text{ m}^2/\text{s}$, respectively, for simulation 3. The tortuosity values selected for this demonstration correspond to the lowest and highest tortuosities determined for Culebra core (Section 5.1.7). By selecting tortuosity values in this way, a subsequent result from this exercise was the definition of matrix-block lengths that correlate to the minimum and

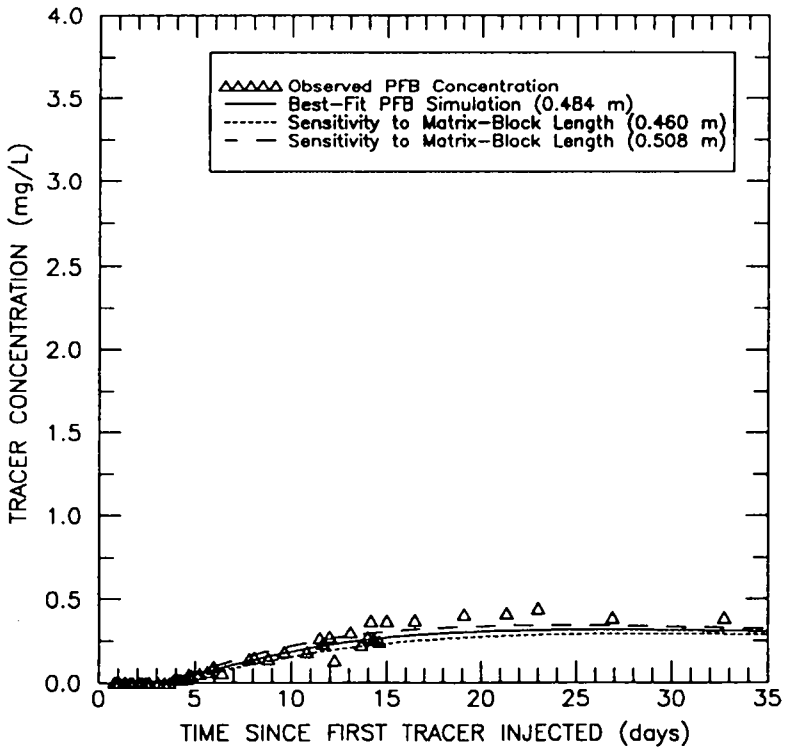
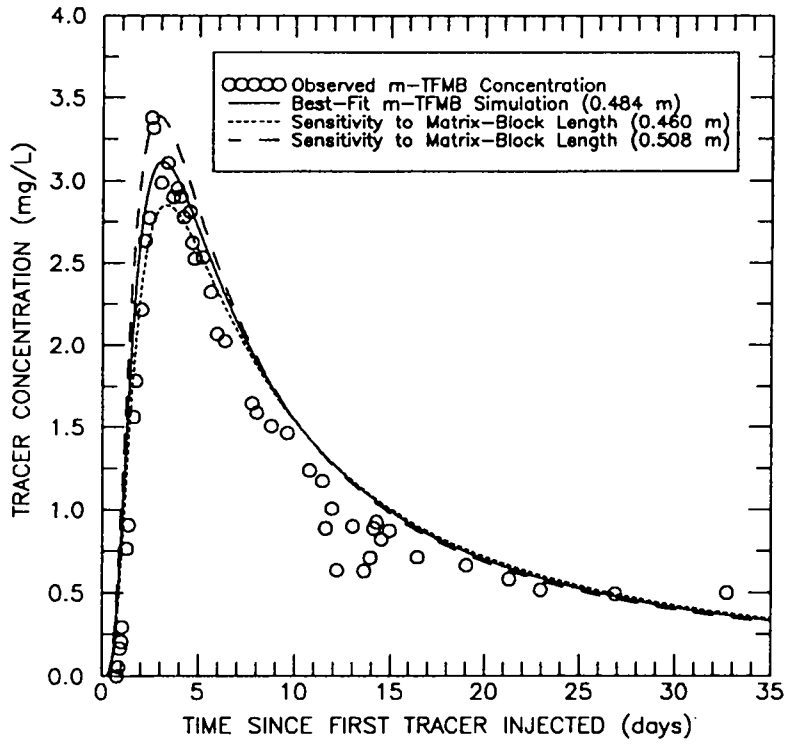


Figure 7-16. Sensitivity to matrix-block length for the H-3 convergent-flow tracer test.

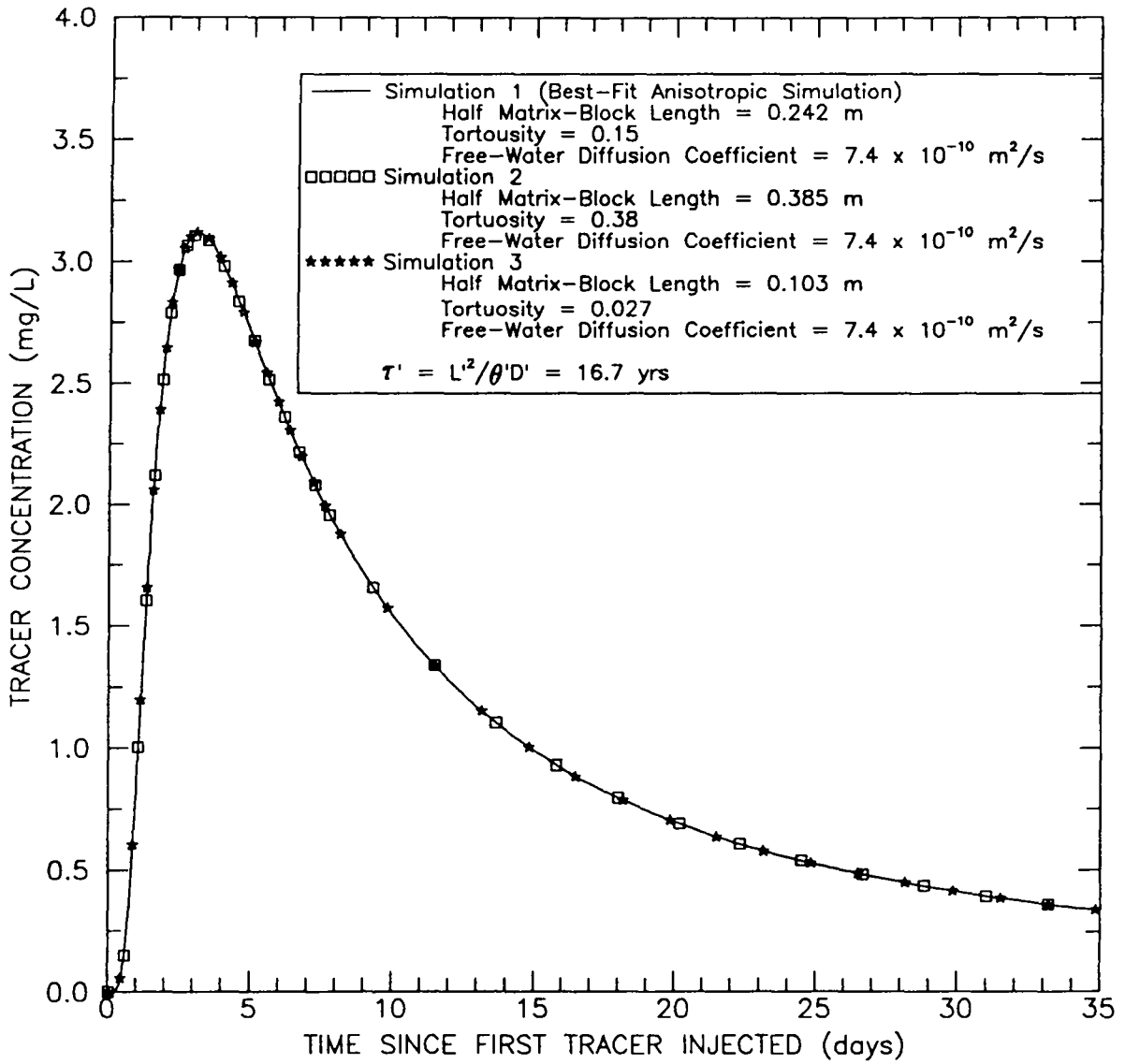


Figure 7-17. Demonstration of different parameter combinations on independent-parameter group τ' .

maximum WIPP specific tortuosities. Since the free-water diffusion coefficient has a relatively narrow potential range (Section 5.1.4), its value was held constant.

7.5.6 Effect of Effective Culebra Thickness

The approach used to investigate the sensitivity to effective Culebra thickness differed from the approach used in the sensitivities discussed to this point. The purposes of this sensitivity study/analysis was to determine the matrix-block length required to fit the observed data for an assumed effective Culebra thickness of 2 m. To achieve this goal, the Culebra thickness was reduced to 2 m and the m-TFMB and PFB breakthrough curves were recalibrated using the heterogeneous-analysis approach and the anisotropic-analysis approach.

For the heterogeneous-analysis approach, a fracture porosity of 3.8×10^{-3} best fit the arrival time of the peak m-TFMB concentration. This fracture porosity yields inner and outer radii for the tracer-input zones (shown schematically in Figures 3-5 and 3-8) of 1.35 and 2.25 m, respectively for H-3b1 and 1.98 and 2.31 m, respectively, for H-3b2. Initial mass was distributed over 10 grid blocks at H-3b1 and over 14 grid blocks at H-3b2. The paths from H-3b1 to H-3b3 and H-3b2 to H-3b3 were discretized into 102 and 93 grid blocks, respectively. The input parameters used in the recalibrations for an effective Culebra thickness of 2 m are summarized in Table 7-5. In order to calibrate the model using an effective Culebra thickness of 2 m, the matrix porosity was increased from the base-case value (0.20) to the maximum value measured in Culebra core (0.30). Without this modification to the matrix porosity, the observed breakthrough data could not be fit. Figure 7-18 shows the observed and the best-fit simulated breakthrough curves for m-TFMB and PFB using a matrix-block length of 0.50 m for the path from H-3b1 to H-3b3 and a matrix-block length of 0.09 m for the H-3b2 to H-3b3 path. The matrix-block lengths determined for an effective Culebra thickness of 2 m were smaller than those determined

Table 7-5. Transport Parameters Used in the Analysis of Sensitivity to Assumed Effective Culebra Thickness of 2 m

Parameter	Heterogeneous-Analysis Approach		Anisotropic-Analysis Approach	
Culebra Thickness	2 m			
Well Spacings	30.7 m		H-3b1 to H-3b3	
	26.8 m		H-3b2 to H-3b3	
Free-Water Diffusion Coefficients	$7.4 \times 10^{-10} \text{ m}^2/\text{s}$		m-TFMB	
	$7.2 \times 10^{-10} \text{ m}^2/\text{s}$		PFB	
Longitudinal Dispersivity	1.5 m			
Tortuosity	0.15			
Matrix Porosity	0.30			
Fracture Porosity	3.8×10^{-3}		7.2×10^{-3}	
Matrix-Block Lengths	0.50 m	H-3b1 to H-3b3	0.19 m	H-3b1 to H-3b3
	0.09 m	H-3b2 to H-3b3	0.19 m	H-3b2 to H-3b3
Anisotropy Ratio	1:1		6:1	
Principal-Transmissivity Direction	na		N57° E (parallel to the H-3b1 to H-3b3 path)	
<hr/> na means not applicable				

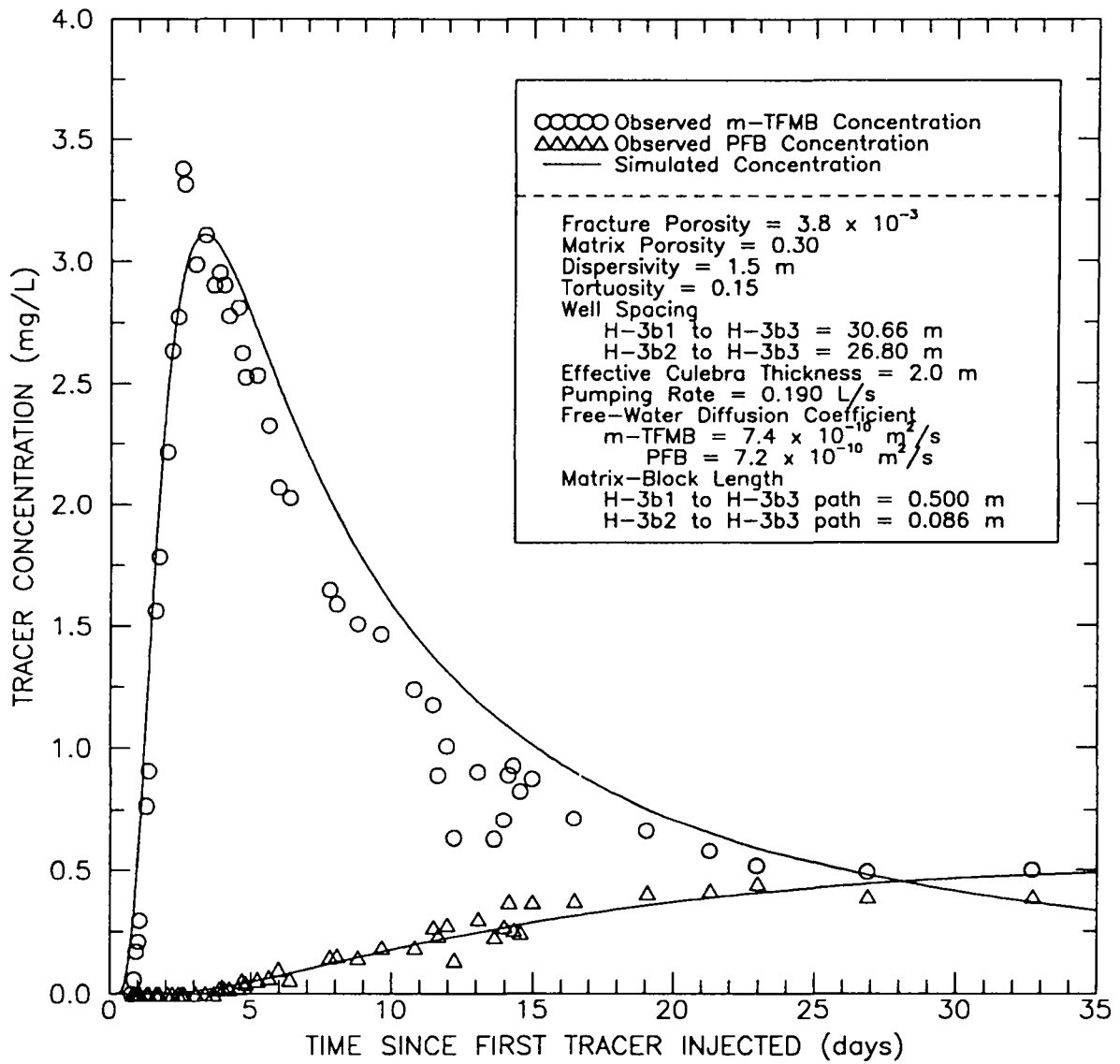


Figure 7-18. Observed and best-fit simulated breakthrough curves for the H-3 convergent-flow tracer test using the heterogeneous-analysis approach and an assumed effective Culebra thickness of 2 m.

for an effective Culebra thickness of 7.2 m. The difference was a factor of 2.5 for the path from H-3b1 to H-3b3 and a factor of 2.6 for the H-3b2 to H-3b3 path.

The fracture porosity yielding the closest match to the peak m-TFMB concentration using the anisotropic-analysis approach was 7.2×10^{-3} . For this fracture porosity, the inner and outer radii for the tracer-input zones (shown schematically in Figures 3-5 and 3-8) were 0.99 and 1.65 m, respectively, for H-3b1 and 1.44 and 1.68 m, respectively, for H-3b2. Initial mass was distributed over 10 grid blocks at H-3b1 and the path from H-3b1 to H-3b3 was discretized with 104 grid blocks. The path from H-3b2 to H-3b3 was discretized using 95 grid blocks. Initial mass was distributed over 14 grid blocks at H-3b2. The observed and best-fit simulated breakthrough curves using the anisotropic-analysis approach are shown in Figure 7-19. The observed data was matched using an anisotropy ratio of 6:1, a principal-transmissivity direction of N57° E, and a matrix-block length of 0.19 m. The anisotropy ratio and principal direction determined here are identical to those determined using an effective Culebra thickness of 7.2 m. The difference between the results using different values for effective Culebra thickness was in the interpreted value for matrix-block length. For a thickness of 7.2 m, a matrix-block length of 0.48 m was determined (Section 7.4.2) which is a factor of 2.5 greater than the length of 0.19 m determined for a thickness of 2 m.

7.5.7 Effect of Anisotropy in Horizontal Transmissivity

The sensitivity analysis to anisotropy in the horizontal transmissivity examined the anisotropy ratio and principal-transmissivity direction separately. In addition to a detailed discussion of the results of these two sensitivity analyses, the effect of varying both $T_x:T_y$ and the T_x direction simultaneously is discussed. The approach for this sensitivity was similar to that for the sensitivity to effective Culebra thickness in that the model was recalibrated to the m-TFMB breakthrough curve. The PFB breakthrough curve was then simulated and compared to the observed-concentration data using the anisotropy parameters which best fit the observed m-TFMB concentrations.

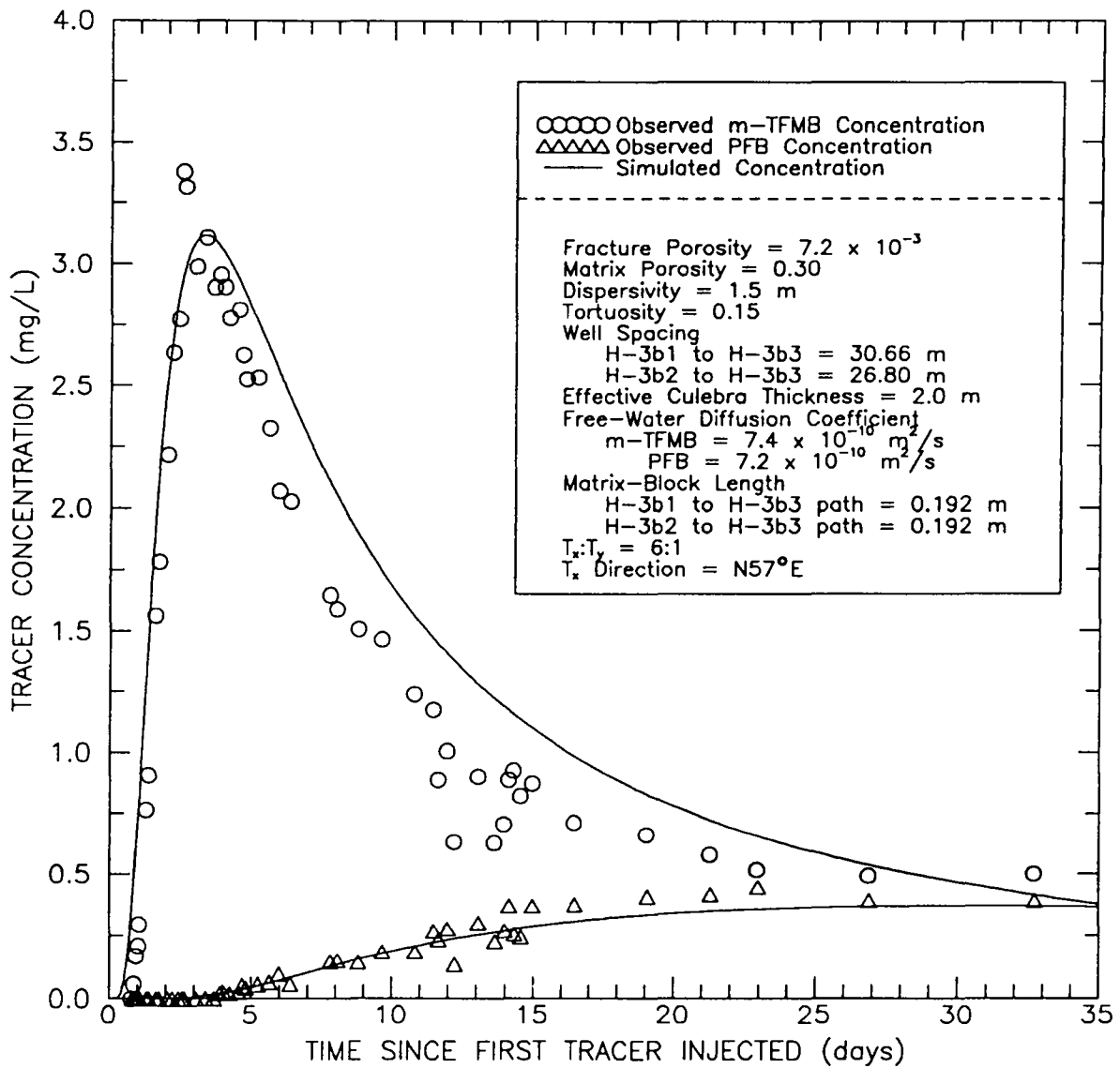


Figure 7-19. Observed and best-fit simulated breakthrough curves for the H-3 convergent-flow tracer test using the anisotropic-analysis approach and an assumed effective Culebra thickness of 2 m.

The purpose of the sensitivity study/analysis to anisotropy ratio was to determine whether both breakthrough curves could be matched with a $T_x:T_y$ of 3:1 rather than the best-fit value of 6:1. An anisotropic ratio of 3:1 was chosen for the sensitivity because it was close to the anisotropy ratios previously determined for the WIPP site based on hydraulic testing (Neuman et al., 1984; Gonzalez, 1983; and Saulnier, 1987). To achieve this goal, $T_x:T_y$ was reduced to 3:1, the principal T_x direction was maintained at N57°E, and the m-TFMB breakthrough was recalibrated by adjusting the matrix-block length until a match between the observed and simulated data was obtained. Therefore, both the best-fit simulation, with $T_x:T_y$ equal to 6:1 and matrix-block length equal to 0.48 m, and the sensitivity simulation, with $T_x:T_y$ equal to 3:1 and matrix-block length equal to 0.70 m, closely match the observed m-TFMB data (Figure 7-20). After recalibration of the m-TFMB curve, the PFB breakthrough curve was simulated using the same anisotropy ratio (3:1) and the same matrix-block length (0.70 m). Figure 7-20 illustrates that the m-TFMB and PFB breakthrough curves cannot both be matched with a $T_x:T_y$ of 3:1 and T_x direction of N57°E.

Two points of interest concerning this sensitivity need to be addressed. First, as the ratio of T_x to T_y is reduced, the matrix-block length needed to match the m-TFMB breakthrough curve must be increased. This effect occurs because a reduced anisotropy ratio reflects a reduction in the magnitude of T_x . Therefore, ground-water velocities are slower along the fast flow path resulting in greater diffusion into the matrix. To counterbalance this increase, the surface area available for diffusion must be reduced by increasing the matrix-block length. The second point relates to the sensitivity approach. This sensitivity illustrates that the m-TFMB curve, considered by itself, can be closely matched with two different anisotropy ratios. If the approach had been to recalibrate to the PFB breakthrough curve first and then, using the recalibrated matrix-block length, simulate the m-TFMB curve, a close match would have been obtained for the PFB curve but not for the m-TFMB curve. In other words, this sensitivity is not meant to prove that the PFB breakthrough curve cannot be adequately simulated with an anisotropy ratio of 3:1. Instead,

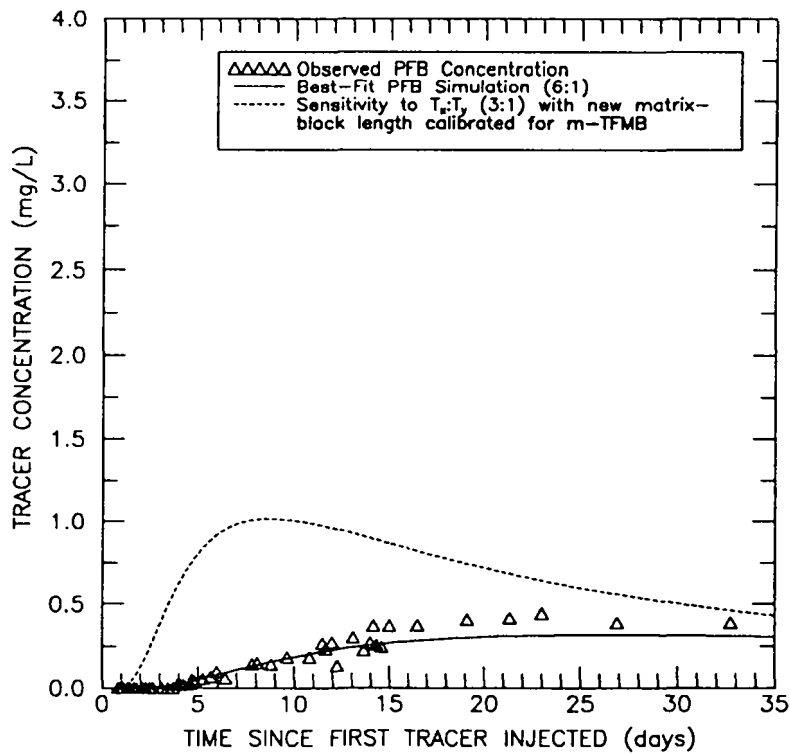
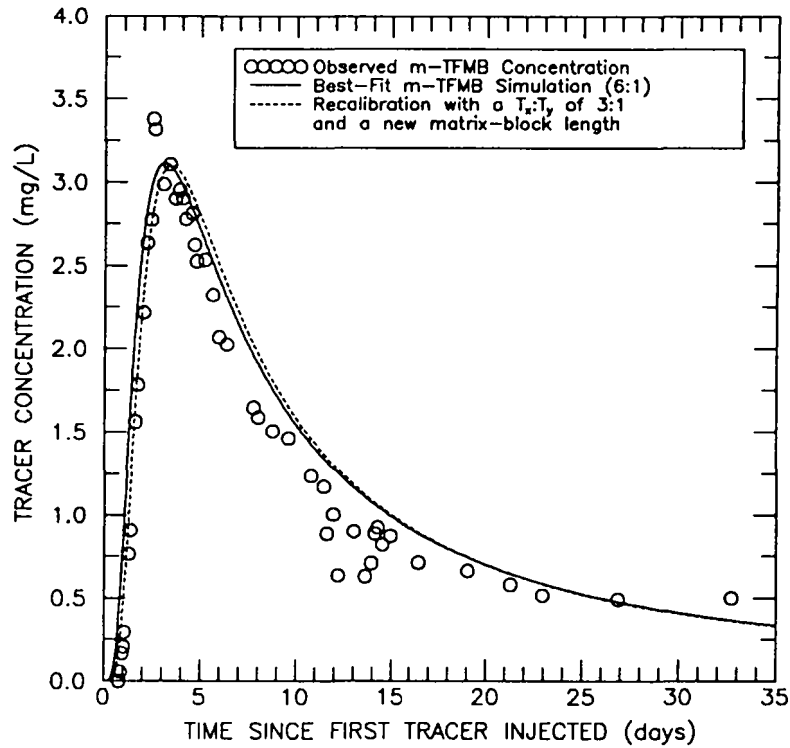


Figure 7-20. Sensitivity to horizontal anisotropy ($T_x:T_y$) for the H-3 convergent-flow tracer test.

it demonstrates that both breakthrough curves cannot be fit simultaneously with an anisotropy ratio of 3:1 and a single matrix-block length.

The approach for the T_x -orientation sensitivity study/analysis was the same as for the sensitivity to anisotropy ratio, but instead of varying $T_x:T_y$, the orientation of the T_x direction was varied. The base-case orientation was $N57^\circ E$ (parallel to the H-3b1 to H-3b3). For this sensitivity, orientations of $N77^\circ E$ (20 degrees clockwise from the H-3b1 to H-3b3 path) and $N37^\circ E$ (20 degrees counter-clockwise from the H-3b1 to H-3b3 path) were considered in combination with a $T_x:T_y$ value of 6:1. The results of the sensitivity are shown in Figure 7-21. Notice on the figure that, for the rapid-transport path, the sensitivity simulations are identical. This is because the anisotropy ellipse is symmetrical about the rapid-transport path (Section 3.4). Note, however, that the slow-path breakthrough curves could not be matched with the two T_x orientations considered here together with an anisotropy ratio of 6:1.

Many combinations of $T_x:T_y$ and T_x direction were tried in an attempt to match the observed H-3 tracer-test data with any combination other than the best-fit values of 6:1 and $N57^\circ E$. The values of anisotropy ratio considered varied from one to 15 and the values of principal orientation considered varied from $N37^\circ E$ to $N77^\circ E$. It was concluded that a better match between the observed and simulated breakthrough curves could not be obtained. Use of an anisotropy ratio of 5:1 and a principal direction of $N67^\circ E$ yielded a close match to the m-TFMB breakthrough curve and a reasonable match to the PFB breakthrough curve. Comparison of this simulation to the best-fit simulation (Figure 7-22), illustrates that the best-fit simulation of the PFB breakthrough curve more closely matches the observed data during the first 15 days of the tracer test and under predicts the concentrations during the final 20 days of the test. The sensitivity simulation, on the other hand, overpredicts the concentrations until about day 15 and then closely matches the observed data. In conclusion, values for the anisotropy parameters other than the best-fit values can provide reasonable fits to the observed data, but the values resulting in a closer

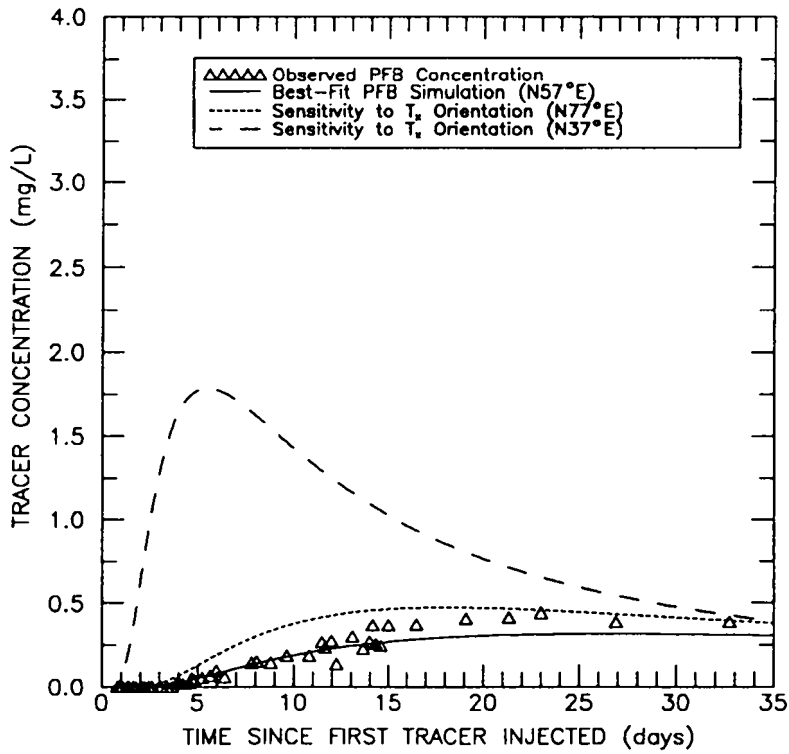
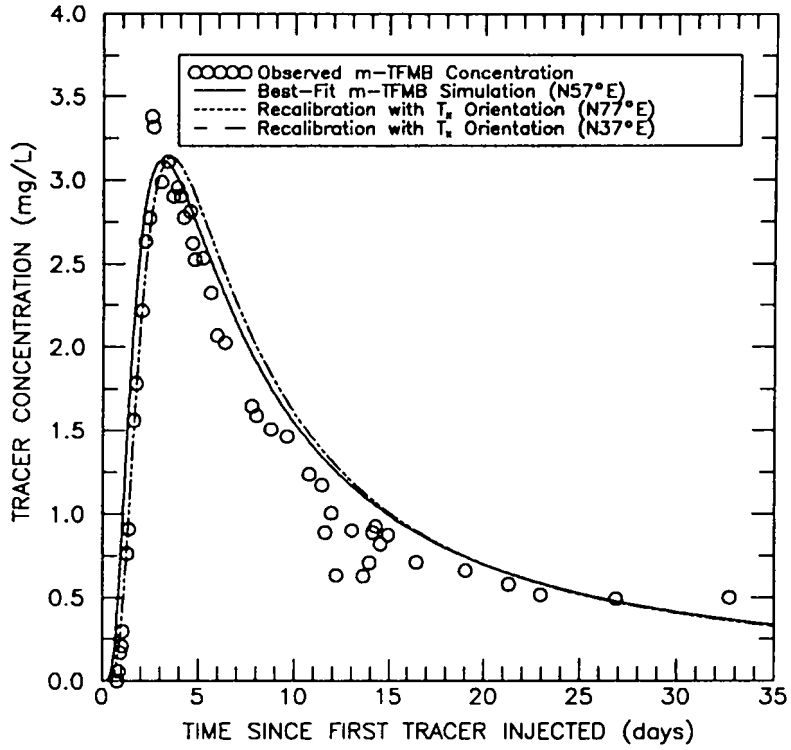


Figure 7-21. Sensitivity to principal T_x orientation for the H-3 convergent-flow tracer test.

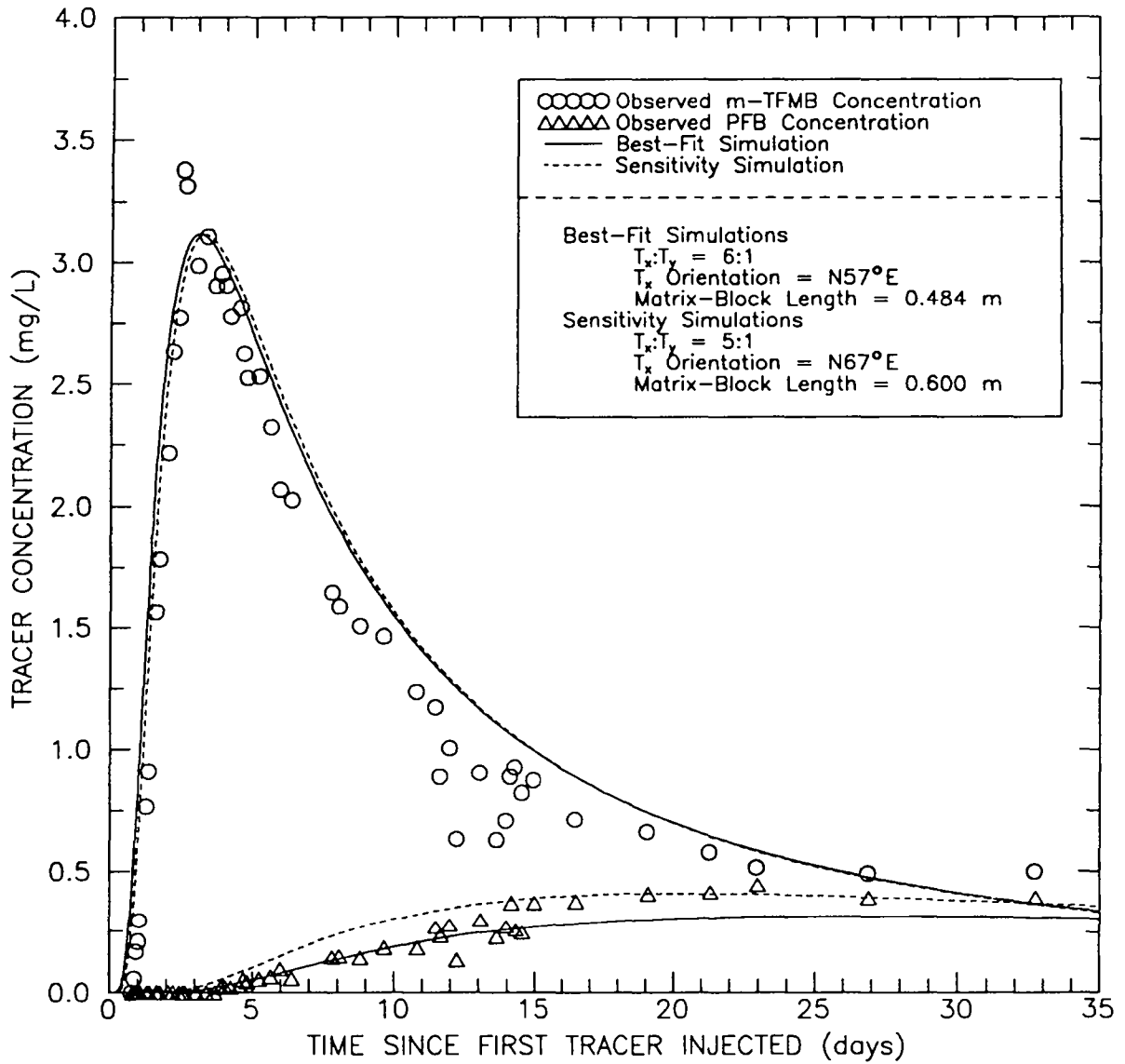


Figure 7-22. Sensitivity to variation in $T_x:T_y$ and principal T_x orientation for the H-3 convergent-flow tracer test.

match between the observed and simulated breakthrough curves are an anisotropy ratio of 6:1 and a principal T_x orientation of N57° E.

7.5.8 Determination of Maximum and Minimum Matrix-Block Lengths

A sensitivity analysis was conducted for the H-3 tracer test to determine maximum and minimum matrix-block lengths for the two travel paths to further characterize the uncertainty in this important fitting parameter. A maximum matrix-block length of 3.22 m was interpreted from calibration to the m-TFMB breakthrough curve for the H-3 hydropad using fracture porosity and matrix-block length as the fitting parameters and assigning maximum values for tortuosity, matrix porosity, well spacing, effective Culebra thickness, and free-water diffusion coefficient and minimum values for pumping rate and longitudinal dispersivity. The parameters used for this simulation are summarized in Table 7-6. Assigning model-input parameters in this way resulted in maximum diffusive losses from the fractures to the matrix. To counteract this higher solute flux to the matrix and the associated decrease in peak concentration and delay in peak-concentration arrival time, a significant increase in the matrix-block length (i.e., decrease in the surface area available for matrix diffusion) and a decrease in the fracture porosity to 6.5×10^{-4} was required to fit the m-TFMB breakthrough curve. The maximum matrix-block length of 3.22 m determined here is a factor of 2.6 higher than the base-case length of 1.23 m for the H-3b1 to H-3b3 travel path. Using these parameters and fitting to the PFB breakthrough curve yielded a matrix-block length of 0.75 m, which is a factor of 3.3 higher than the base-case length of 0.23 m for the H-3b2 to H-3b3 path. A comparison of the simulated and observed breakthrough curves for this sensitivity study/analysis is provided in Figure 7-23.

If diffusive losses from the fracture to the matrix are minimized through parameter assignment, the reduction in peak concentration and delay in peak-concentration arrival time required to match the observed data can be achieved by significantly decreasing the matrix-block length thus increasing the surface area available for matrix diffusion. Using minimum

Table 7-6. Transport Parameters Used in the Sensitivity Analysis to Determine the Maximum and Minimum Matrix-Block Lengths at the H-3 Hydropad

Parameter	Sensitivity Analysis to Determine Maximum Matrix-Block Length		Sensitivity Analysis to Determine Minimum Matrix-Block Length	
Effective-Culebra Thickness	7.62 m		2.0 m	
Well Spacings	31.1 m	H-3b1 to H-3b3	30.3 m	H-3b1 to H-3b3
	27.2 m	H-3b2 to H-3b3	26.4 m	H-3b2 to H-3b3
Free-Water Diffusion Coefficients	m-TFMB	$7.9 \times 10^{-10} \text{ m}^2/\text{s}$	m-TFMB	$6.9 \times 10^{-10} \text{ m}^2/\text{s}$
	PFB	$7.7 \times 10^{-10} \text{ m}^2/\text{s}$	PFB	$6.7 \times 10^{-10} \text{ m}^2/\text{s}$
Longitudinal Dispersivity	0.5 m		3.0 m	
Tortuosity	0.38		0.027	
Matrix Porosity	0.30		0.30	
Fracture Porosity	6.5×10^{-4}		7.0×10^{-3}	
Matrix-Block Length	3.22 m	H-3b1 to H-3b3	0.20 m	H-3b1 to H-3b3
	0.75 m	H-3b2 to H-3b3	0.03 m	H-3b2 to H-3b3

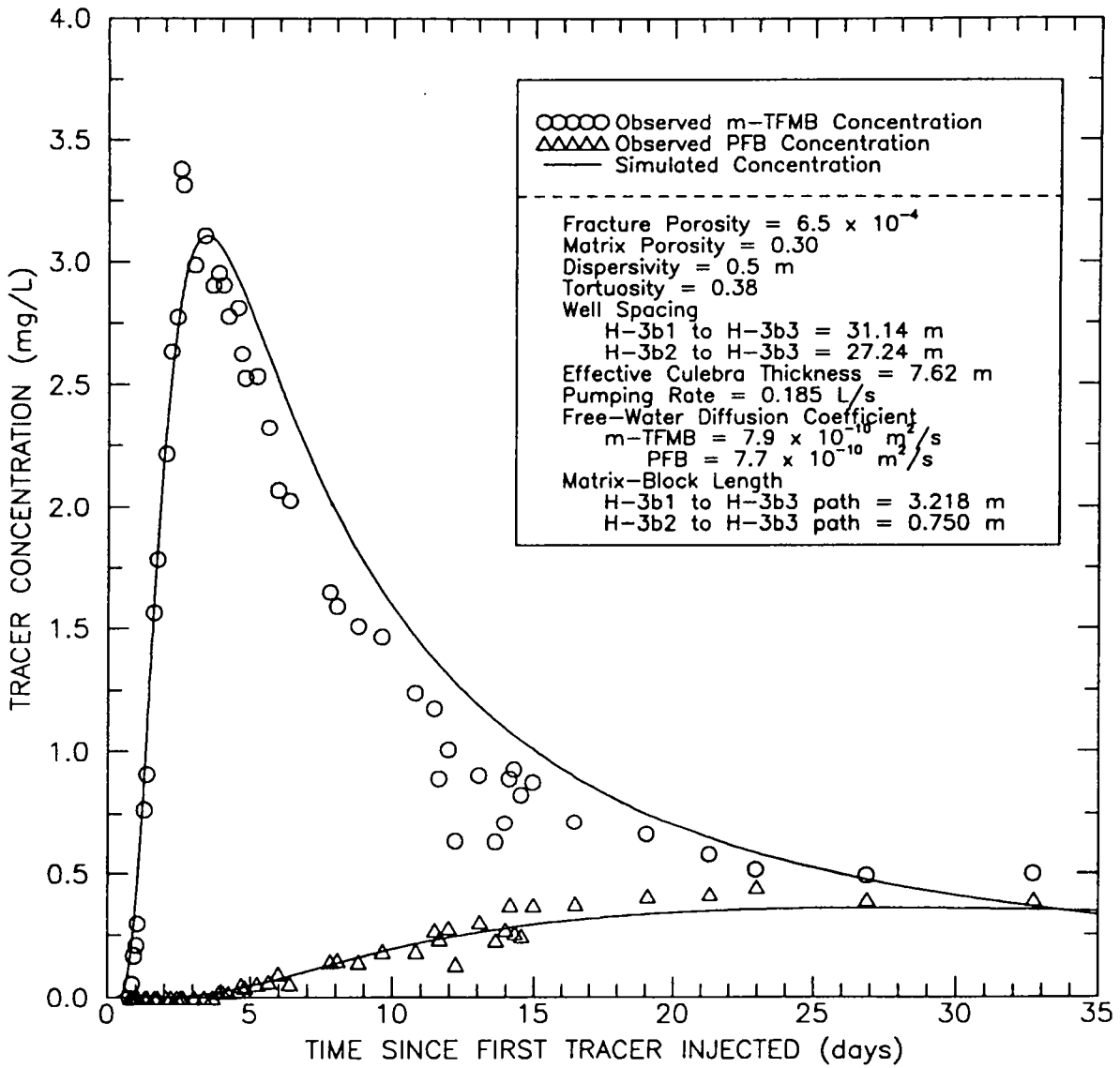


Figure 7-23. Sensitivity recalibration to observed tracer breakthrough at the H-3 hydropad to obtain maximum matrix-block lengths.

values for tortuosity, matrix porosity, well spacing, effective Culebra thickness, and free-water diffusion coefficient and maximum values for pumping rate and longitudinal dispersivity resulted in a match to the m-TFMB breakthrough curve using a fracture porosity of 5.7×10^{-3} and a matrix-block length of 0.05 m. However, this parameter set was unable to match the PFB breakthrough curve. Therefore, a minimum matrix-block length could not be defined for the H-3b2 to H-3b3 path using those extreme values. By increasing the matrix porosity from its minimum value of 0.08 to its maximum value of 0.30, a good match between the simulated and observed PFB data could be obtained. Figure 7-24 presents a recalibration to the m-TFMB and PFB breakthrough curves to define minimum matrix-block lengths at the H-3 hydropad. The parameter values for these simulations are summarized on the figure and in Table 7-6. The best-fit fracture porosity was 7.0×10^{-3} and the matrix-block lengths which yielded good matches between the observed and simulated data were 0.20 m for the path from H-3b1 to H-3b3 and 0.03 m for the path from H-3b2 to H-3b3. The minimum matrix-block lengths are a factor of 6.1 and 7.7 lower than the base-case, heterogeneous-analysis lengths for the fast and slow paths, respectively.

7.6 Summary of Results for H-3

The observed breakthrough curves from the H-3 convergent-flow tracer test differ significantly for the two transport paths. For m-TFMB, which traveled from H-3b1 to H-3b3, the observed concentrations rise rapidly, peak sharply, and tail significantly. The observed concentrations for PFB, which traveled a path from H-3b2 to H-3b3, rose gradually and did not produce a well-defined peak. Due to a lack of data, the degree of tailing for the PFB curve cannot be assessed. Two approaches were identified to explain the difference in the shapes of the breakthrough curves. The first approach assumed that the difference could be explained by heterogeneity, in the form of different matrix-block lengths, between the flow paths. The second approach assumed the flow field was homogeneous and that anisotropy in horizontal transmissivity could explain the difference.

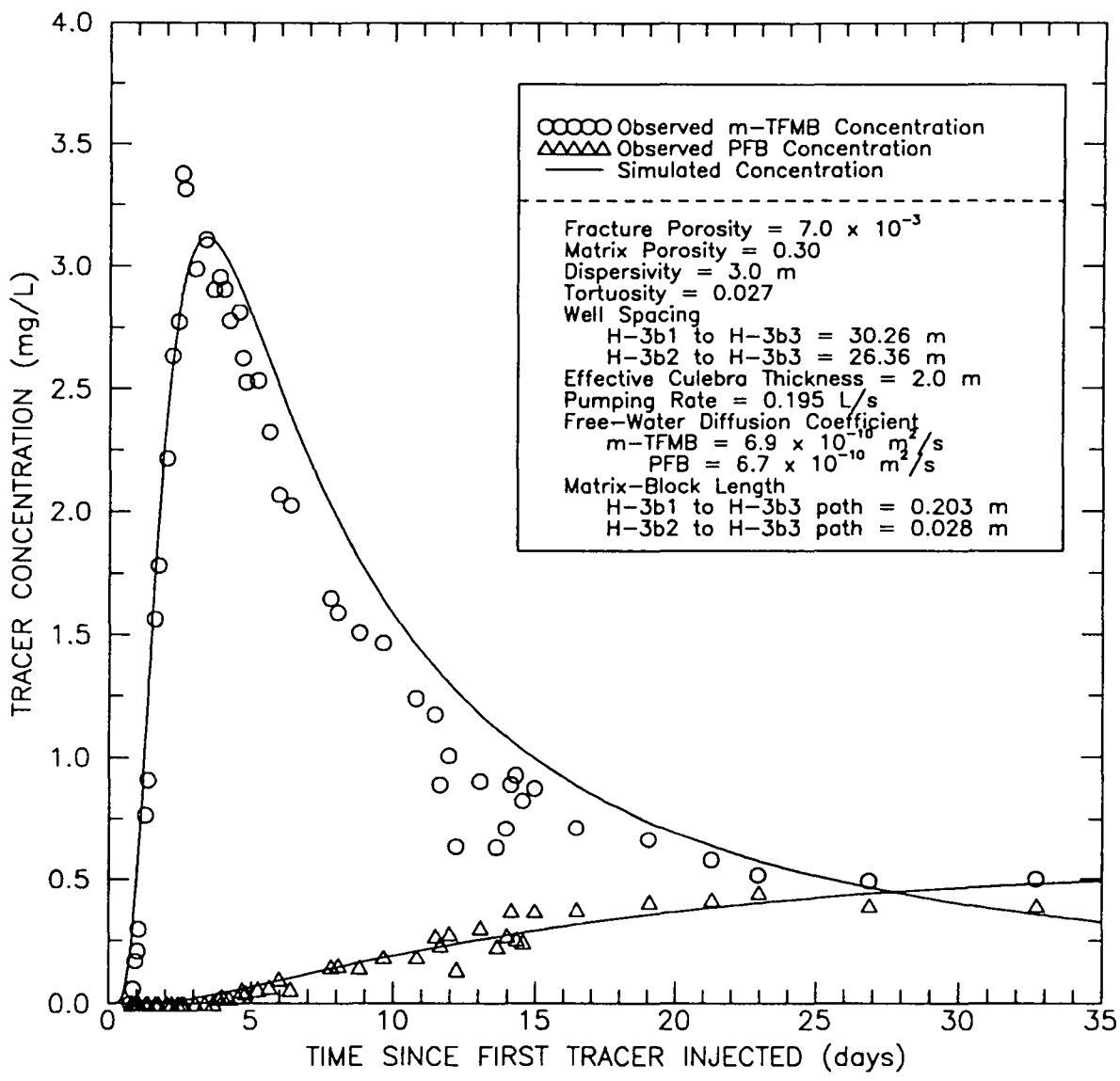


Figure 7-24. Sensitivity recalibration to observed tracer breakthrough at the H-3 hydropad to obtain minimum matrix-block lengths.

For the heterogeneous-analysis approach, matrix-block lengths of 1.23 and 0.23 m were determined for the H-3b1 to H-3b3 path and the H-3b2 to H-3b3 path, respectively. The larger block size along the path from H-3b1 to H-3b3 reflects more widely spaced fractures and less matrix surface area. Consequently, tracer diffusion into the matrix is less along that path resulting in a breakthrough curve that peaks rapidly, has a high peak concentration, and has high mass recovery. The opposite is true along the path with the smaller matrix-block length. Since flow along the fast path was dominated by fracture transport, the model was calibrated to the m-TFMB breakthrough curve which determined a value of 1.2×10^{-3} for the fracture porosity. The heterogeneous approach, because it forces matrix diffusion alone to account for the differences in the breakthrough curves, is considered to provide both an upper and lower bound on the interpreted matrix-block length.

For the anisotropic-analysis approach, both tracer-breakthrough curves were closely matched with an anisotropy ratio of 6:1, a T_x direction of N57° E (parallel to the H-3b1 to H-3b3 path), and a matrix-block length of 0.48 m. The matrix-block length determined with the anisotropy approach is bounded by the two lengths (1.23 and 0.23 m) determined with the heterogeneous approach. The anisotropy approach forces anisotropic flow alone to account for the difference in the H-3 breakthrough curves.

The fits to the observed data obtained by the heterogeneous simulations were neither better nor worse than the fits obtained by the anisotropic simulations. Therefore, it could not be determined which approach is better for modeling the H-3 tracer-test results.

Sensitivity analyses were conducted to determine the effect of matrix tortuosity, longitudinal dispersivity, fracture porosity, matrix porosity, matrix-block length, anisotropy ratio, and T_x orientation on the simulated breakthrough curves. Additional sensitivities involved recalibration of the model for an assumed effective Culebra thickness of 2 m and model recalibration to identify maximum and minimum matrix-block lengths at the H-3 hydropad.

Increasing matrix tortuosity resulted in a decrease in the peak concentration at the pumping well and a delay in the time to reach the peak concentration due to an increase in diffusive losses from the fractures to the matrix. The opposite was true for a decrease in the matrix tortuosity. Travel along both the fast and slow transport paths was very sensitivity to the tortuosities of 0.027 and 0.38 investigated.

Sensitivity to longitudinal dispersivity investigated values of 0.5 and 3.0 m. For the fracture-controlled transport path, increasing dispersivity resulted in more rapid breakthrough at the pumping well and a higher peak concentration. Later arrival of the peak concentration at the pumping well and a higher peak concentration were observed when longitudinal dispersivity was decreased. For the slow path, increasing dispersivity resulted in earlier peak of the breakthrough curve and a higher peak concentration. The opposite was true when dispersivity was decreased.

Ground-water velocity is inversely proportional to fracture porosity. An increase in the fracture porosity resulted in lower velocities which yielded later tracer breakthrough and lower peak concentrations because the lower velocities allowed more time for matrix diffusion to occur. The effect of fracture porosity on breakthrough concentration was more evident along the apparent fracture-dominated transport path.

Increasing matrix porosity yielded later mass breakthrough, decreased maximum concentration, and increased tailing because the higher matrix porosity allowed greater mass loss to the matrix.

Decreasing the matrix-block length increased diffusion of solute from the fractures to the matrix resulting in reduced peak concentrations, delayed peak-concentration arrival times, and increased tailing. Matrix-block length was determined to be a more sensitive parameter for the path with less matrix participation.

The sensitivities to anisotropy ratio and T_x orientation indicated that values other than the best-fit values can provide reasonable fits to the observed data, but the values resulting in a closer match between the observed and simulated breakthrough curves are an anisotropy ratio of 6:1 and a principal T_x direction of N57° E.

The model was recalibrated to the observed data using an effective Culebra thickness of 2 m. For the heterogeneous-analysis approach, the results yielded a fracture porosity of 3.8×10^{-3} and matrix-block lengths of 0.50 and 0.09 m for the H-3b1 to H-3b3 path and the H-3b2 and H-3b3 path, respectively. Those block lengths are a factor of 2.5 and 2.6 smaller than the values of 1.23 and 0.23 m yielded by the best-fit heterogeneous simulations for the H-3b1 to H-3b3 and H-3b2 to H-3b3 paths, respectively. The fitting parameters determined using the anisotropic-analysis approach were a fracture porosity of 7.2×10^{-3} , a matrix-block length of 0.19 m for both transport paths, an anisotropy ratio of 6:1, and a principal-transmissivity direction of N57° E. Comparison of these results to the results from the best-fit anisotropic simulation shows identical anisotropy ratios and principal-transmissivity directions, a fracture porosity a factor of 3.6 larger, and a matrix-block length a factor of 2.5 smaller.

The sensitivity analysis conducted to determine the maximum and minimum matrix-block lengths for the H-3 hydropad yielded a high-end value of 3.22 m and a low-end value of 0.03 m. Because the assigned parameters used in the sensitivity analysis included parameter uncertainty, the maximum and minimum matrix-block lengths can be viewed as a measure of uncertainty in that fitted parameter.

8.0 H-4 HYDROPAD TRACER TEST

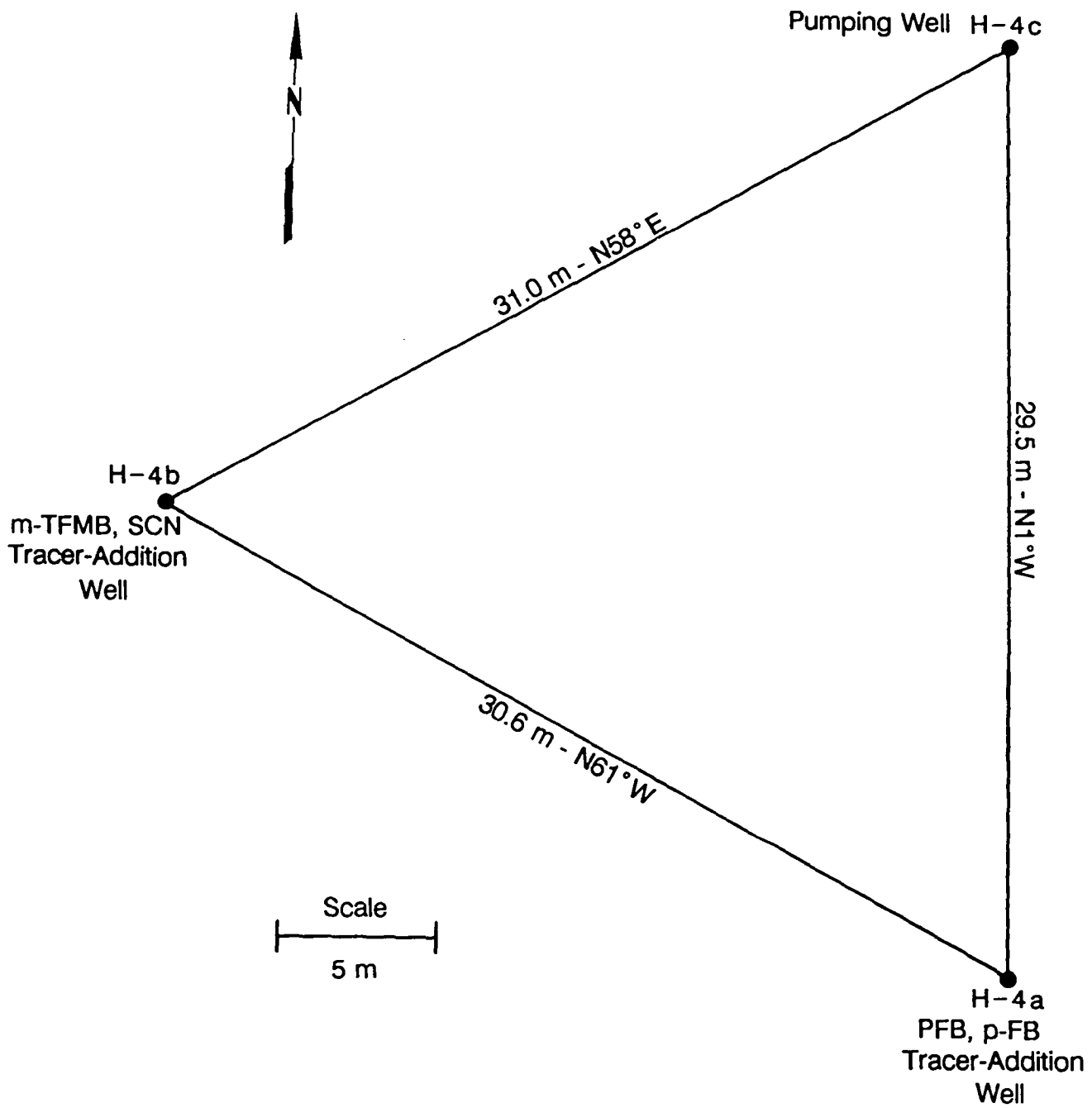
A long-term convergent-flow tracer test was conducted at the H-4 hydropad from October 1982 to October 1984. The following sections briefly describe the well configurations, hydropad hydrology, tracer-test history, previous interpretations of the tracer test, suitability of the test for further analysis, and a summary of the tracer-test results.

8.1 Well Configurations

The H-4 hydropad, located approximately four kilometers southwest of the center of the WIPP site (Figure 1-2), consists of three wells, H-4a, H-4b, and H-4c, arranged in an approximate equilateral triangle with approximately 30-m sides (Figure 8-1). The wells at the H-4 hydropad are completed to the Culebra Dolomite Member of the Rustler Formation. All three H-4 wells are located in Section 5, Township 23 south, and Range 31 east and have UTM coordinates, ground-surface elevations, and top-of-casing elevations as summarized in Table 8-1. Figure 8-1 illustrates the relative positions of the wells at the depth of the Culebra dolomite.

H-4a was initially completed on May 22, 1978 to a depth of 126.49 m BGS under the direction of the U.S. Geological Survey (Mercer et al., 1981). From February 2 to February 4, 1981, Sandia National Laboratories directed the deepening of the well through the Culebra to a total depth of 162.15 m BGS. H-4a is cased with 13.97-cm (5-1/2-inch) steel casing to a depth of 110.95 m BGS and is open hole from that depth to the total depth of 162.15 m BGS. The open-hole section of the borehole has a diameter of 12.1 cm.

H-4b was completed through the Culebra to a total depth of 161.24 m BGS on May 15, 1978 (Mercer et al., 1981). From ground surface to 145.08 m BGS the borehole



NOTE: The borehole-deviation survey did not extend to the center of the Culebra dolomite in borehole H-4a.

Figure 8-1. Plan view of the wells at the H-4 hydropad showing distances between wells at the center of the Culebra.

Table 8-1. UTM Coordinates, Ground-Surface Elevations, and Top-of-Casing Elevations for the H-4 Hydropad Wells

Well	UTM Coordinates		Ground-Surface Elevation (m amsl)	Top-of-Casing Elevation (m amsl)
	m East	m North		
H-4a	612,407	3,578,469	1015.84	1016.12
H-4b	612,380	3,578,483	1015.80	1016.01
H-4c	612,406	3,578,499	1016.04	1016.22

is cased with 13.97-cm steel casing and from 145.08 m BGS to the total depth of 161.24 m BGS it is open hole with a diameter of 12.1 cm.

On May 8, 1978, H-4c was completed to a total depth of 201.47 m BGS (Mercer et al., 1981). The borehole is cased with 13.97-cm steel casing to a depth of 185.78 m BGS. The casing is perforated with four shots per 0.3 m across the Culebra interval from 151.18 to 158.50 m. From 185.78 to 201.47 m BGS the well is a 12.1-cm diameter open borehole.

8.2 Local Hydrogeology

At the H-4 hydropad, the Culebra dolomite is 7.9 m thick and is locally fractured. Core from H-4b is preserved in very small pieces which generally contain gypsum-filled or closed fractures. Open fractures are rare in the recovered H-4b core. The largest intact piece of recovered core is 0.13 m in length. Core recovery at H-4b was approximately 10 to 15 percent. The results of an examination of the core located in the Department of Energy Core Library at the WIPP site and an examination of core photographs taken by Sandia National Laboratories at the time of coring are presented in Figure 8-2. Kelley and Saulnier (1990) present the results of permeability and porosity measurements taken on samples from H-4b. Gas permeabilities were 5.2×10^{-14} and 5.2×10^{-15} m² and porosities were 0.208 and 0.297.

Based on hydropad-scale (tens of meters) interference pumping tests, Cauffman et al. (1990) estimate an average transmissivity of 1.0×10^{-6} m²/s at the H-4 hydropad. Large-scale pumping tests stressed the Culebra over an area greater than the scale of interest in the tracer-test analysis. Therefore, data obtained from this type of test were not used to define the transmissivity of the Culebra at the hydropad scale.

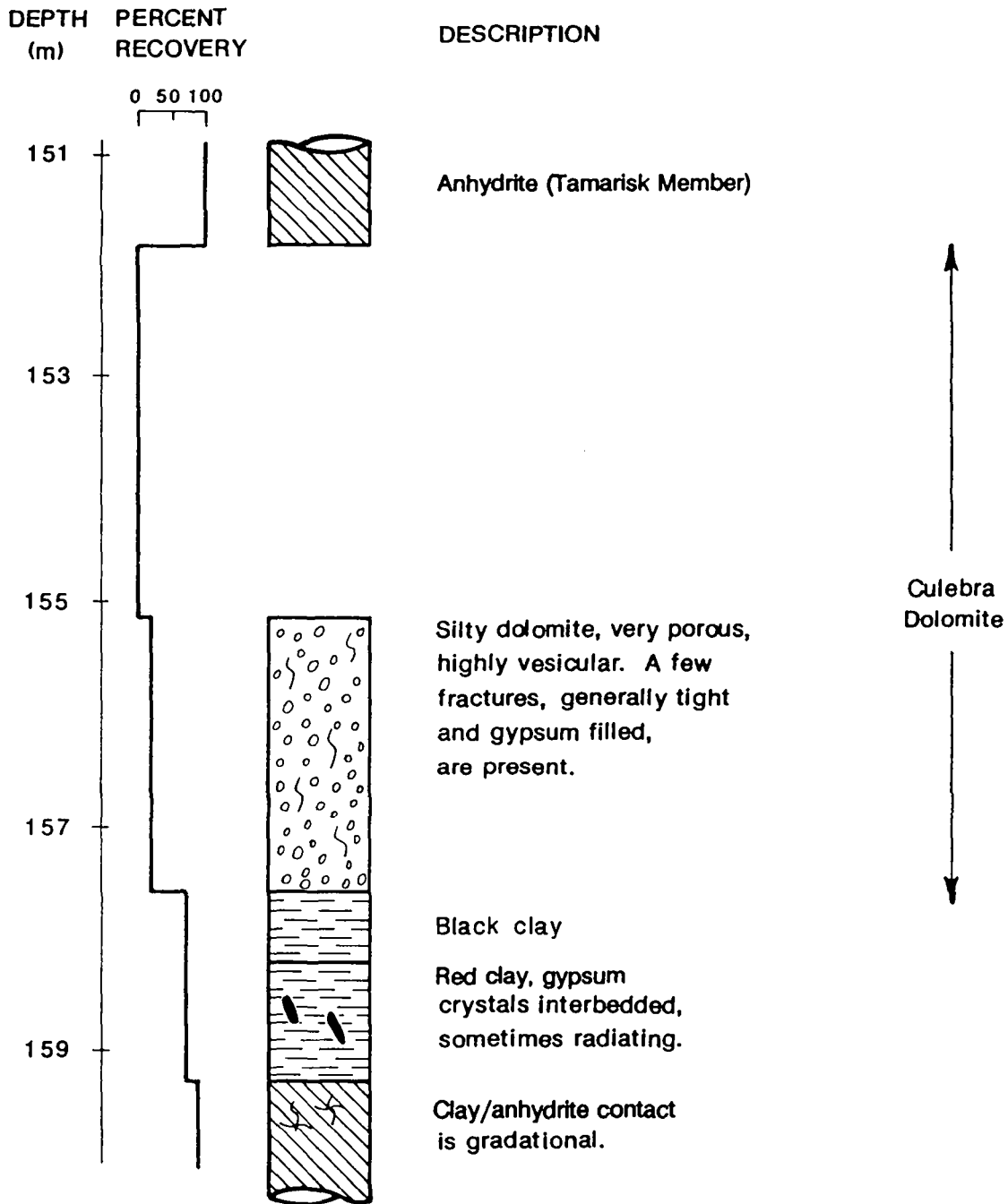


Figure 8-2. Results of core examination of the Culebra dolomite from borehole H-4b (after Kelley and Pickens, 1986).

Interpretations of hydraulic tests conducted at the H-4 hydropad have determined that horizontal permeability is anisotropic at that location. The method used to analyze the hydraulic tests for anisotropy requires three wells with sequential pumping from at least two of the wells and monitoring of the drawdown in all the wells (Gonzalez, 1983). An anisotropy ratio of 2.7:1 and a principal direction of N76°W are reported in Gonzalez (1983) for the H-4 hydropad.

8.3 Tracer-Test History

The following sections briefly describe the pumping and tracer-injection history, the test equipment, and the characteristics of the observed breakthrough curves. Detailed descriptions of the test equipment and test histories are presented in Hydro Geo Chem (1985).

8.3.1 Pumping and Tracer-Injection History

The pumping well for the H-4 convergent-flow tracer test was H-4c. The pumping period for the tracer test lasted from October 24, 1982 to October 15, 1984, approximately 722 days. The pumping record, based on discharge records reported periodically in the field notebook, is presented in Figure 8-3. During the first 230 days of the test (October 24, 1982 to June 10, 1983) the pumping rate averaged the designed rate of 1.7×10^{-2} L/s. After 230 days no tracers had been detected at the pumping well and the pumping rate was doubled to an average rate of 3.3×10^{-2} L/s for the remainder of the test (June 10, 1983 to October 15, 1984). Pumping was discontinued a number of times during the test due to electrical and mechanical failures which affected the pump jack (Figure 8-3). The pumping information for the H-4 tracer test is summarized in Table 8-2.

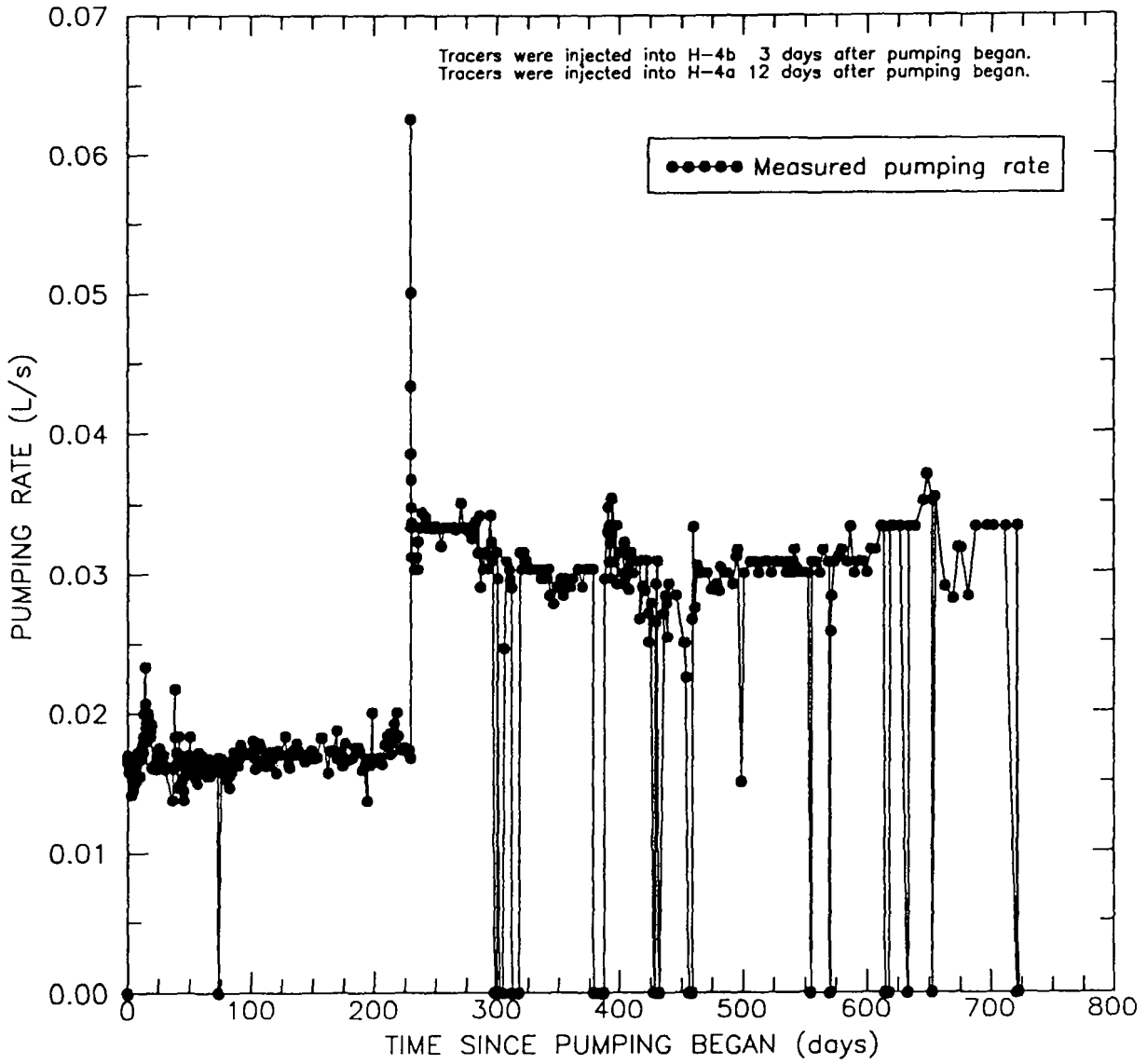


Figure 8-3. Pumping rate at well H-4c during the convergent-flow tracer test conducted at the H-4 hydropad.

Table 8-2. Summary of Pumping and Tracer-Injection Information for the Convergent-Flow Tracer Test Conducted at the H-4 Hydropad

Well Type	H-4a		H-4b		H-4c
	Tracer Injection		Tracer Injection		Pumping
Average Pumping Rate					0.017 L/s ^a 0.033 L/s ^b
Time Pumping Began					08:10
Date Pumping Began					10/24/82
Time Pumping Ended					08:35
Date Pumping Ended					10/15/84
Tracers Injected	p-FB	PFB	m-TFMB	SCN	
Mass Injected	2 kg	1 kg	1 kg	1 kg	
Time Tracers Injected	12:00 to 12:30		07:53 to 08:20		
Date Tracers Injected	11/05/82		10/27/82		
Tracer Volume	200 L		114 L	100 L	
Chaser Volume	227 L		189 L		
Downhole System Volume	122 L		158 L		

^a Average pumping rate from October 24, 1982 to June 10, 1983.

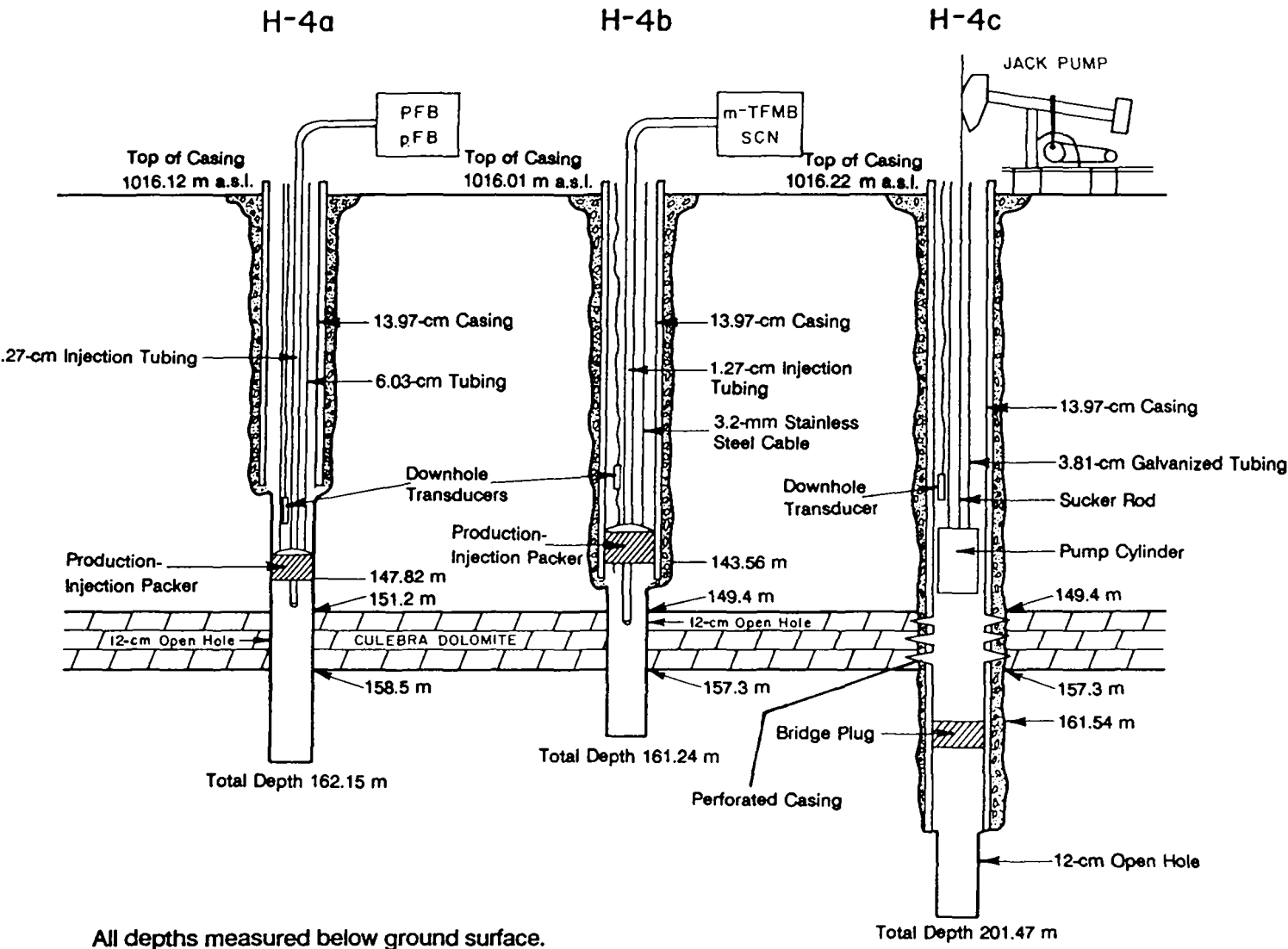
^b Average pumping rate from June 10, 1983 to October 15, 1984.

The tracers m-TFMB and SCN were injected into H-4b from 07:53 to 08:20 on October 27, 1982. The tracer-labeled volumes consisted of 1 kg of m-TFMB mixed with 114 L of formation fluid and 1 kg of SCN mixed with approximately 100 L of formation fluid. The chaser volume consisted of 189 L of formation fluid. The total volume of fluid injected into H-4b was approximately 245 L greater than the downhole system volume. One kilogram of PFB and 2 kg of para-fluorobenzoate (p-FB) were mixed together with 200 L of formation fluid and injected into H-4a from 12:00 to 12:30 on November 5, 1982. A 227-L chaser volume was injected after the well had been allowed to recover for about 3.5 hours. The downhole system volume in H-4a was approximately 305 L less than the total volume of fluid injected into the well. Table 8-2 summarizes the tracer-injection information. Full details on the H-4 tracer tests are reported in Hydro Geo Chem (1985).

8.3.2 Test Equipment

Figure 8-4 shows the downhole configuration of the three wells during the convergent-flow tracer test conducted at the H-4 hydropad. In H-4a, a PIP was set between the Magenta and Culebra intervals at a depth of about 147.82 m. The packer had 6.03-cm (2-3/8-inch) tubing attached to allow surface access to the isolated Culebra. The 1.27-cm tracer-injection tubing was lowered inside this 6.03-cm tubing. To keep the injection tubing completely extended downhole and to prevent it from pinching, a 1.27-cm diameter, 0.9- to 1.5-m length of perforated stainless steel tubing was attached to the end of the injection tubing. A pressure transducer was lowered on a transducer cable into the 6.03-cm tubing to monitor fluid pressures in the well.

A feed-through packer system, lowered to a depth of 143.56 m, was used in H-4b to minimize the system volume by isolating the test interval from the wellbore fluid in the annular space above the packer. The packer feed-through assembly was suspended in the wellbore by 3.2-mm stainless-steel braided cable. The packer consisted of a 11.4-cm rubber element mounted on a 7.6-cm mandrel. The element was attached to the mandrel with two



All depths measured below ground surface.

Figure 8-4. Downhole-equipment configurations for the tracer test at the H-4 hydropad (after Kelley and Pickens, 1986).

1.3-cm banding clamps at each end of the packer. The feed through for the packer was a 3.17-cm (1.25-inch) pipe reduced to a 1.27-cm (0.5-inch) union-tube fitting. Tracer was injected through 1.27-cm tubing running through the packer feed-through pipe and extending about 3.0 to 4.6 m below the bottom of the packer. As in well H-4a, a 0.9- to 1.5-m piece of perforated stainless-steel tubing was attached at the end of the injection tubing. Fluid pressures in the well were measured with a pressure transducer mounted above the packer. The transducer was hydraulically connected to the Culebra interval with an access tube through the packer feed-through assembly.

The pump used in pumping well H-4c was a pump jack with a positive-displacement cylinder set in open casing. Discharge from the pump was carried to the surface through a 3.81-cm (1.5-inch) galvanized pipe. The galvanized discharge pipe extended an additional 15 m on the surface and was then coupled to a 2.54-cm (1-inch) polyvinyl chloride (PVC) pipe which entered the protective housing for the automatic water sampler. The transducer in H-4c was mounted above the pump cylinder and its conductor cable was strapped to the discharge pipe. The pumping rate was periodically measured by timing the filling of a graduated volumetric cylinder. Flow was regulated during the test by regulating the number of strokes per unit time of the positive-displacement pump system.

Fluid pressures in the H-4 wells were measured during the tracer test with a microcomputer-controlled DAS. The DAS used downhole pressure transducers in each of the wells to monitor pressure changes. Water levels in H-4a and H-4b were monitored periodically using an electrical water-level sounder. The long duration of the tracer test and economic factors forced discontinuation of the use of the electronic DAS for pressure monitoring on August 3, 1983 (about 9 months after testing began). Pressure data for the three H-4 hydropad wells are shown in Figure 8-5.

The tracer-labeled volumes were prepared for injection on site. Tracer and chaser volumes were injected into the tracer-addition wells, under gravity-feed conditions, through 1.27-cm injection tubing. Water samples from H-4c were initially collected from the pump

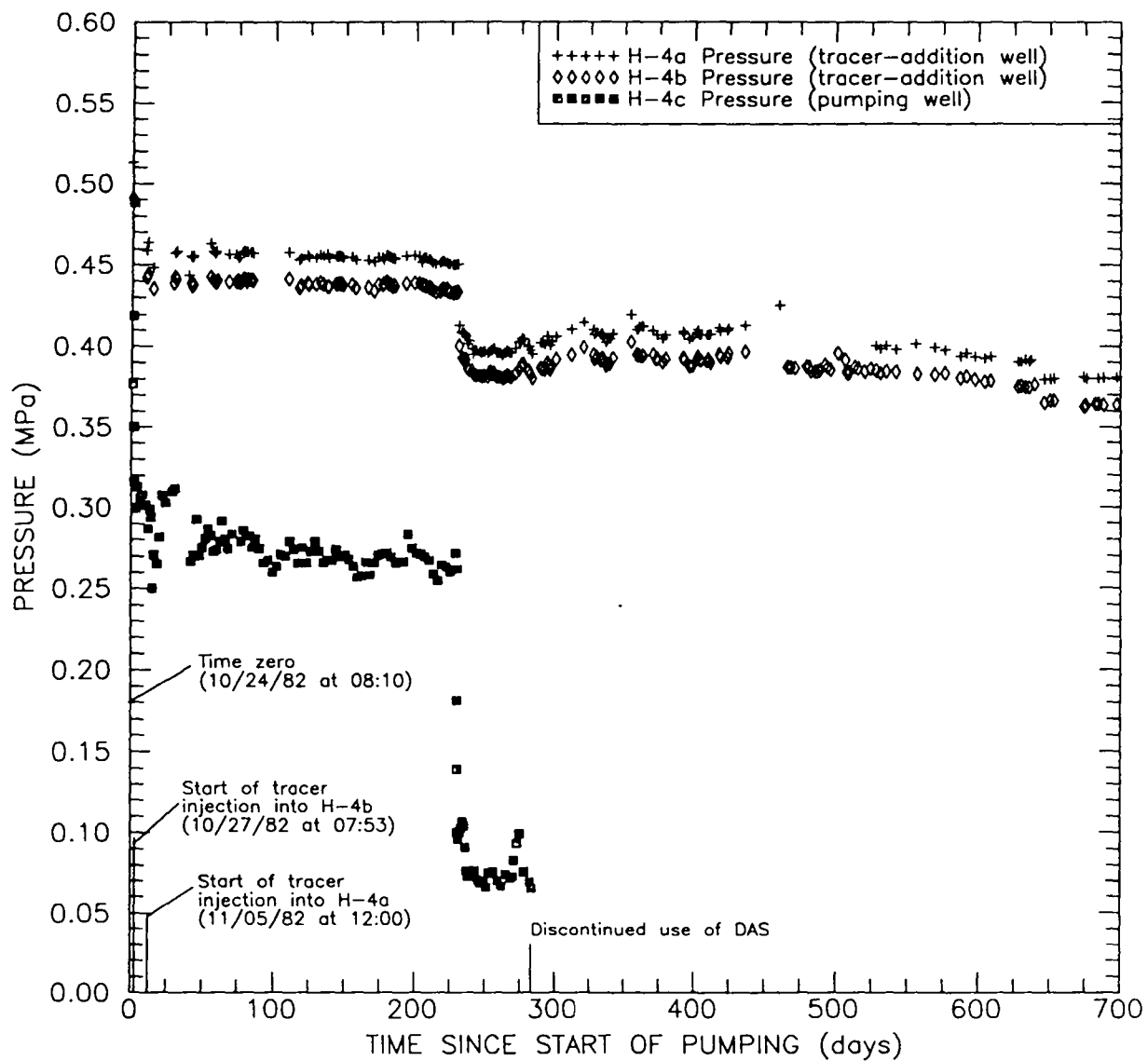


Figure 8-5. Pressure data for the H-4 hydropad wells during the convergent-flow tracer test.

discharge line using an automatic water sampler. After April 4, 1983, all samples were collected manually directly from the pump-discharge line. Samples were transferred from the collection container to 50-mL polyethylene bottles and refrigerated prior to shipment to a laboratory for analysis. None of the fluid samples collected with the automatic sampler contained tracer at detectable concentrations. The tracer samples were analyzed to determine tracer concentration by HPLC utilizing the analytical techniques described in Hydro Geo Chem (1985) and Stetzenbach et al. (1982).

8.3.3 Observed Tracer Breakthrough

The breakthrough curves obtained for PFB and p-FB (injected into H-4a) and for m-TFMB and SCN (injected into H-4b) from water samples collected from the pumping well (H-4c) are illustrated in Figures 8-6 and 8-7. All of the breakthrough curves exhibit erratic variations in the concentration level. Tracers PFB and p-FB are plotted separately but with identical concentration scales in Figure 8-6. Tracers m-TFMB and SCN are plotted separately in Figure 8-7 but with different concentration scales because of the much lower concentrations obtained for SCN. Appendix D contains the concentration data reported by Hydro Geo Chem (1985) and the corrected travel times. Hydro Geo Chem (1985) reports that the apparent breakthrough of PFB, p-FB, and m-TFMB early in the tracer test "is thought to be an artifact due to contamination of the samples from spillage of tracer in the box containing the sample bottles."

From later sampling, the tracer m-TFMB was next detected about 262 days after it was injected. The peak concentration of m-TFMB occurred 388 days after injection. Integration of the observed m-TFMB breakthrough curve yields an estimate of about 37 percent recovery. The observed data for m-TFMB were very erratic with the samples immediately before and after the sample with the peak concentration being 58 and 18 percent, respectively, of the peak concentration. The times of first detection and peak concentration for SCN were 270 and 316 days, respectively. The observed data for SCN

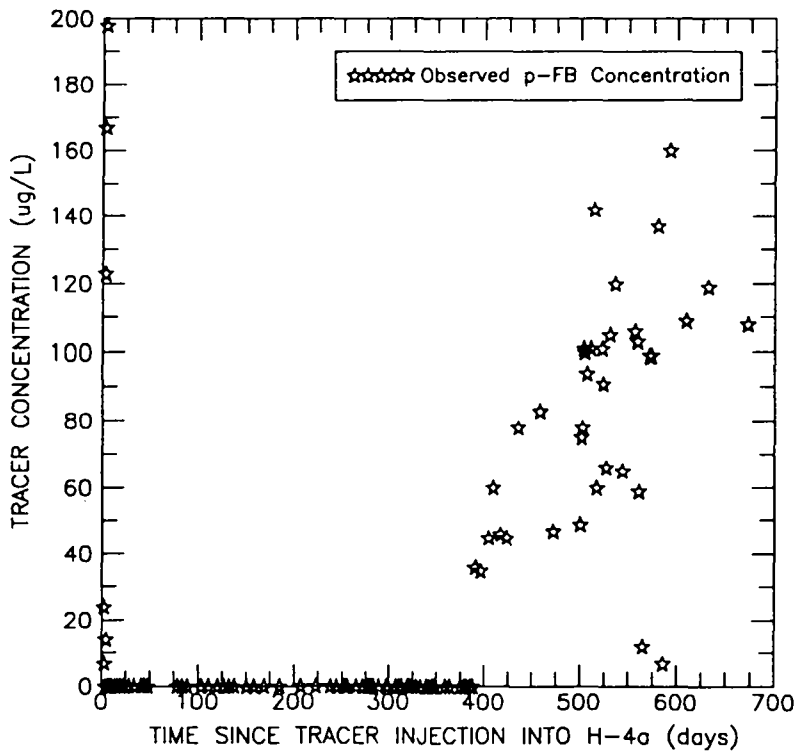
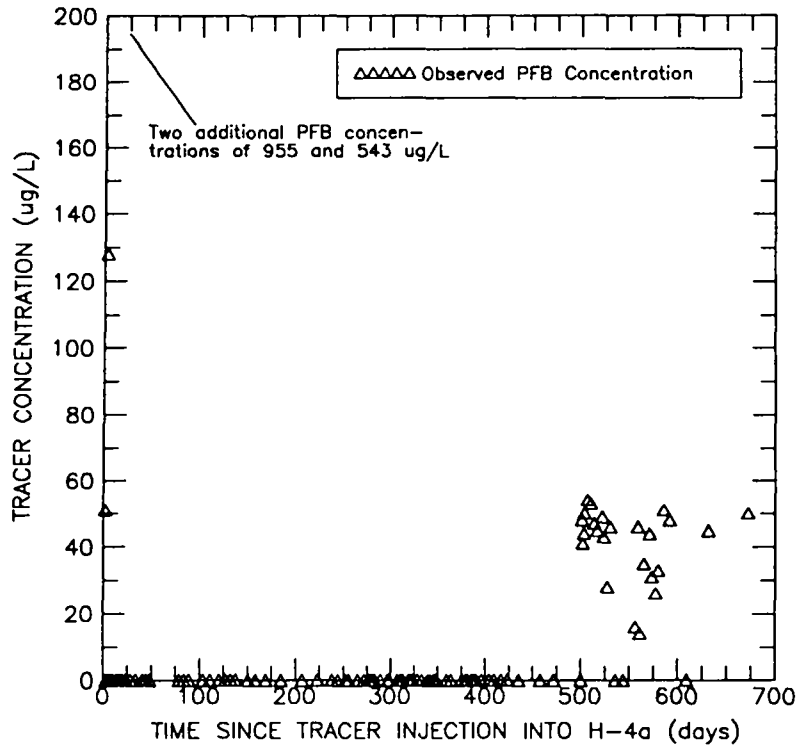


Figure 8-6. Observed PFB and p-FB data for the convergent-flow tracer test conducted at the H-4 hydropad.

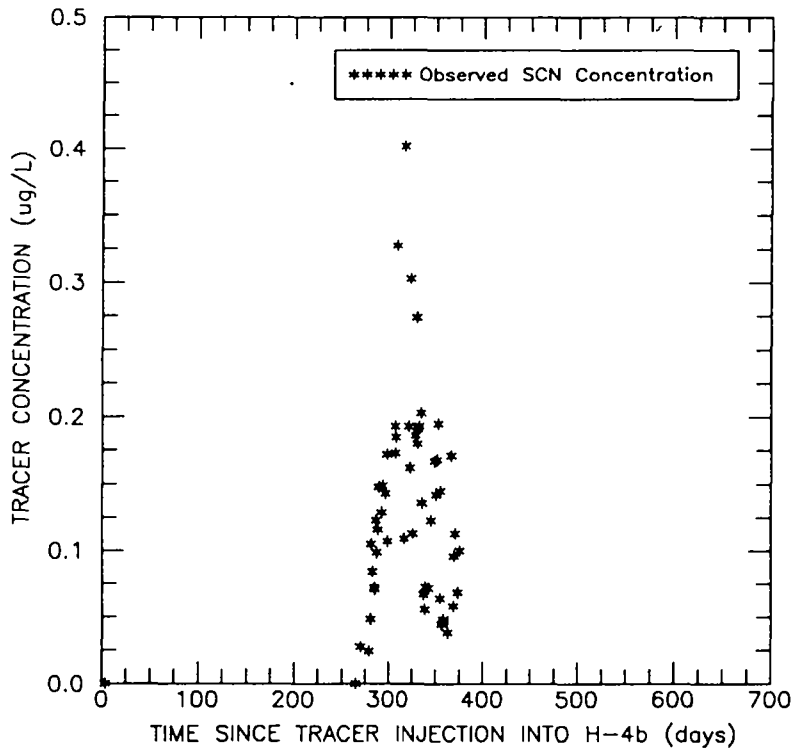
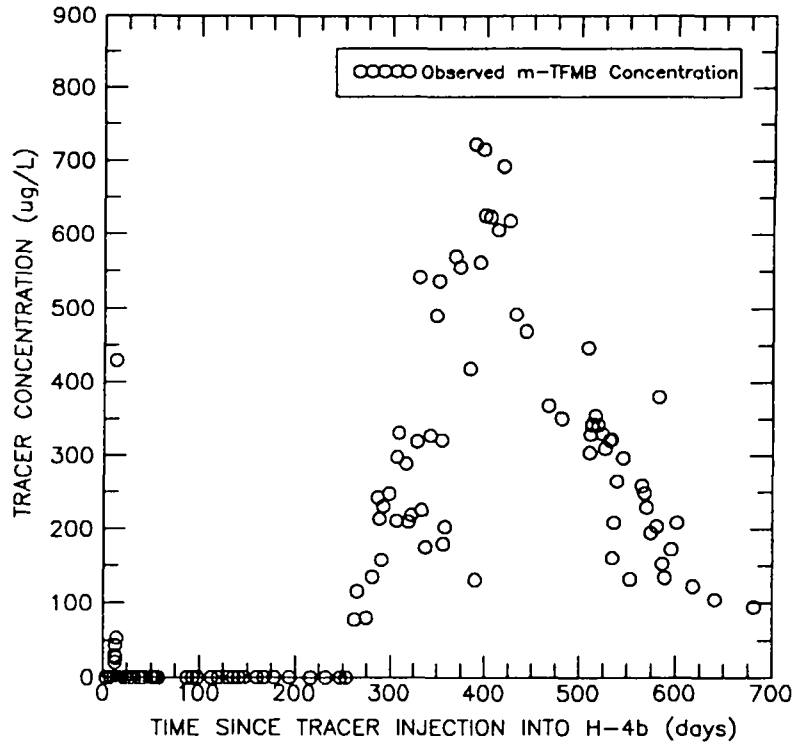


Figure 8-7. Observed m-TFMB and SCN data for the convergent-flow tracer test conducted at the H-4 hydropad.

were very erratic with concentrations varying by as much as 70 percent between samples. The water sample with the peak SCN concentration was collected after a sample with a concentration 27 percent lower than the peak concentration and prior to a sample with a concentration 48 percent lower than the peak value. The erratic behavior of the observed breakthrough curve suggests that the analytical accuracy may be uncertain at the parts-per-billion concentrations measured for SCN. Only through pre-column enrichment techniques could a breakthrough curve for SCN be defined. Approximately 0.2 percent of the SCN injected into H-4b was recovered at H-4c during the tracer test. The maximum m-TFMB concentration was a factor of about 1800 greater than the maximum SCN concentration. The very large difference in peak concentration for m-TFMB and SCN suggests that there has been substantial degradation of SCN during transport. The peak concentration of SCN occurred a factor of about 1.2 sooner than the peak concentration of m-TFMB. However, because of the potential difficulty in analytical accuracy of the SCN, comparison of the apparent arrival times of peak SCN and m-TFMB concentrations may not be appropriate.

The two tracers injected into H-4a were first detected at the pumping well 390 days (p-FB) and 501 days (PFB) after injection. The breakthrough curves were erratic in behavior and did not exhibit well-defined peaks. The apparent peak concentration of p-FB occurred 592 days after injection and the apparent peak concentration of PFB occurred 507 days after injection, only 140 hrs after it was first detected. The mass recoveries for p-FB and PFB were 3.5 and 2.2 percent, respectively. Correcting for the difference in the amounts of mass of each tracer injected, the peak concentration of p-FB was about 1.5 times greater and arrived a factor of 1.2 later than the peak concentration of PFB. Because the peak concentrations for the p-FB and PFB breakthrough curves are poorly defined, comparison of the apparent peak-concentration arrival times may not be appropriate.

8.4 Previous Interpretation of the Convergent-Flow Tracer Test

A previous interpretation of the convergent-flow tracer test conducted at the H-4 hydropad is presented in Kelley and Pickens (1986). From a review of the Culebra data base for the H-4 hydropad, they concluded that there was no evidence of double-porosity transport. This information base included:

- lack of open fractures identified in core samples;
- observation of relatively long transport times between the tracer-addition wells and the pumping well; and
- hydraulic testing at H-4c indicated single-porosity (matrix) behavior (Beauheim, 1987a).

Kelley and Pickens (1986) considered three conceptualizations in characterizing solute transport in the Culebra at the H-4 hydropad. The first conceptual model was a single-porosity conceptualization in which there exists only a primary (matrix) porosity. In this system, solute transport is a function of porosity and dispersivity, if one considers aquifer thickness and pumping rate to be constant and known.

The second transport conceptualization was a double-permeability system. In this system there exists a primary medium (matrix) and a secondary medium (aquifer). Transport from the injection well to the pumping well by advection and dispersion takes place only through a more transmissive aquifer (or multiple aquifers) of smaller dimensions than the full Culebra thickness. In addition, diffusion of the tracer mass occurs into the less transmissive matrix units bounding the aquifer or aquifers vertically. In this system, solute transport is a function of the aquifer porosity, matrix porosity, longitudinal dispersivity, aquifer thickness, and the effective molecular-diffusion coefficient.

The third solute-transport conceptualization was the double-porosity system. Solute transport for this case is a function of matrix porosity, matrix tortuosity, longitudinal dispersivity, free-water diffusion coefficient, fracture porosity, and matrix-block length.

Kelley and Pickens (1986) examined each of the breakthrough curves as to their suitability for interpretation of transport parameters. The leading edges of the p-FB and PFB breakthrough curves for the H-4a to H-4c flow path were abrupt in shape which is unexpected for natural systems (Figure 8-6). The PFB data can be characterized as a poor-quality breakthrough curve. In addition to having an abrupt shape, the data shows no peak and zero concentrations after tracer breakthrough. The transport of tracer SCN on the H-4b to H-4c flow path was not analyzed because it did not appear to behave conservatively with only 0.2 percent of the input tracer mass (1 kg) recovered at the pumping well, in comparison to tracer m-TFMB which had 37 percent tracer recovery for the same flow path. Kelley and Pickens (1986) concluded that analysis of the PFB and SCN breakthrough curves could yield no information towards characterization of transport parameters.

Kelley and Pickens (1986) presented a qualitative analysis of the m-TFMB and p-FB breakthrough curves. They presented a single-porosity interpretation of the m-TFMB breakthrough curve which used a porosity of 0.04, a dispersivity of 1.5 m, and a mass input into the tracer-addition well equal to one half of the actual amount of tracer added. However, this porosity compares poorly with the average value of 0.25 determined from laboratory determinations on two core samples. Using the double-permeability conceptualization, they obtained a reasonable fit to the observed m-TFMB concentrations using both five- and six-aquifer systems. However, the Culebra has not been tested hydraulically using small vertical test intervals that would allow evaluation of the reasonableness of this double-permeability conceptualization. The attempted double-porosity interpretation of the m-TFMB breakthrough curve yielded fracture apertures of 1.6 cm for a matrix-block size of 2 m. These apertures are considered to be much too large to be physically realistic and thus this interpretation is not considered to be credible. Kelley and Pickens (1986) were unable to match the p-FB breakthrough curve using the single-

porosity and double-porosity conceptualizations. They found that the multi-aquifer conceptualization provided an approximate fit to the observed p-FB breakthrough curve.

Kelley and Pickens (1986) concluded that the interpretation of the convergent-flow tracer test conducted at the H-4 hydropad did not provide reliable quantitative estimates of the physical solute-transport parameters for the Culebra. Qualitatively, the observed tracer-breakthrough curves could be simulated by representing the Culebra with a layered system of higher- and lower-permeability units. No evidence was obtained to indicate that transport of the tracers had occurred through fractures.

8.5 Suitability of Tracer Test for Further Analysis

From examination of the breakthrough curves for the four tracers, the following observations suggest that considerable uncertainty exists in the suitability of the data for interpreting transport parameters. These include:

- Sample contamination likely existed early in the tracer test;
- All breakthrough curves for the H-4 tracer test exhibit very erratic concentration levels. (In contrast, breakthrough curves from the other hydropads exhibited, at least approximately, monotonically increasing and decreasing concentrations on the rising and falling limbs, respectively.)
- The time scale of the tracer test (approximately 2 yrs) is so long that even the best tracers (e.g., m-TFMB and PFB) would be expected to undergo significant biodegradation; and
- The pumping-rate history showed many periods of unknown duration with the pump off.

Because of these significant uncertainties in the data, no further quantitative interpretation of the breakthrough curves from the H-4 tracer test was attempted.

8.6 Summary of Results for H-4

A convergent-flow tracer test was performed at the H-4 hydropad. Considerable differences in breakthrough curves was obtained even for tracers injected at the same well. Detailed quantitative interpretations of the tracer test were not possible because of uncertainties in the tracer behavior through degradation and the flow regime due to pumping stoppages.

Qualitative interpretations were conducted on two of the breakthrough curves by Kelley and Pickens (1986). The long transit time between the tracer-addition wells and the pumping well suggests that transport in fractures is not an important mechanism on the two transport paths tested. Single-porosity (matrix) transport through a vertically heterogeneous system is considered to be the most representative conceptualization for the H-4 hydropad.

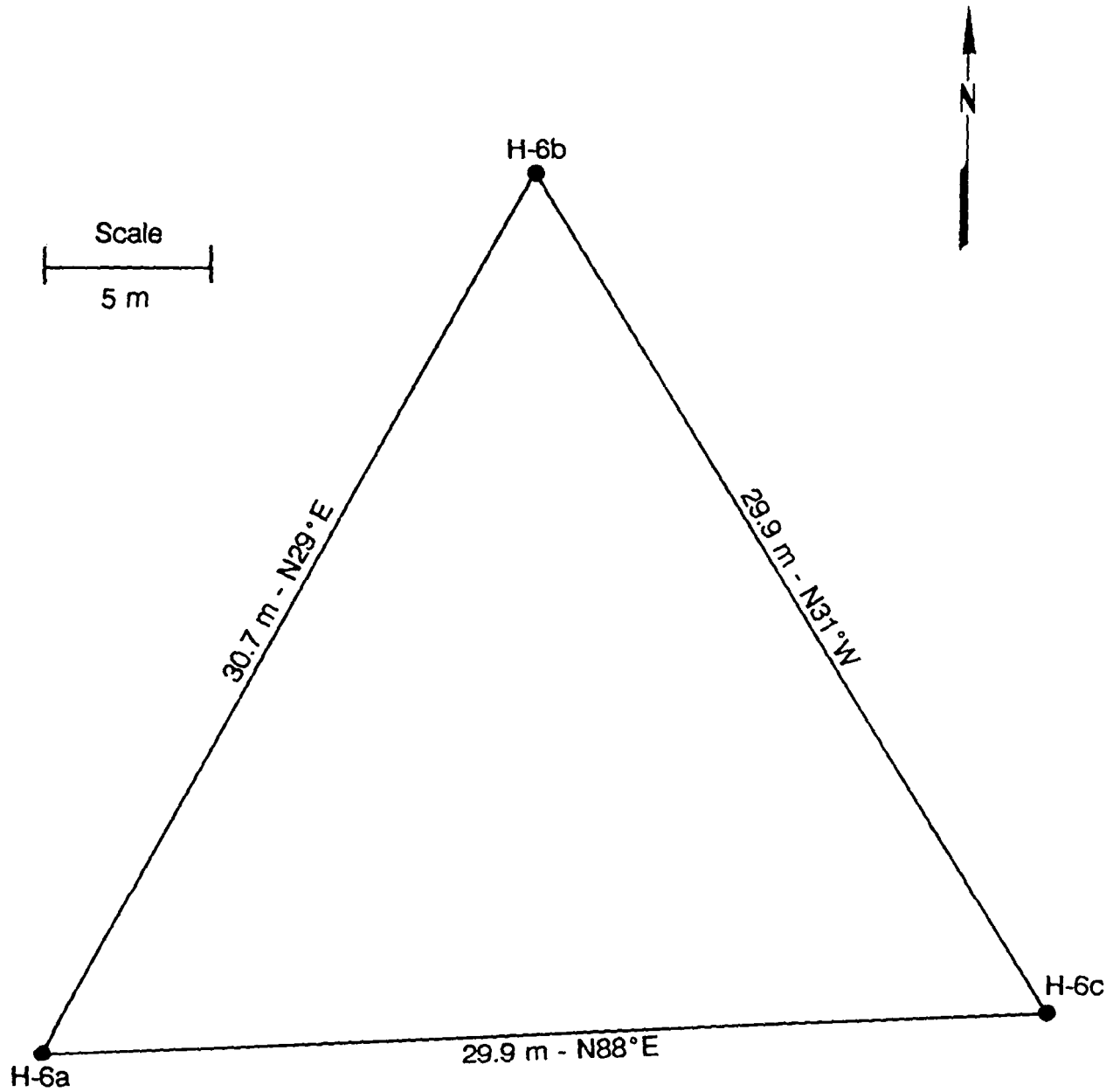
9.0 H-6 HYDROPAD TRACER TESTS

Seven tracer tests have been conducted at the H-6 hydropad. From August 1981 to November 1982, a series of five convergent-flow tracer tests were performed. Two two-well recirculating tracer tests were performed from April to July 1983. The following sections briefly discuss the well configurations, hydropad hydrogeology, histories of the seven tests, suitability of tests for analysis, current analysis of suitable tests, sensitivity analyses, and summary of the test results.

9.1 Well Configurations

The H-6 hydropad is located in the northwest corner of the WIPP site, approximately four kilometers northwest of the Air-Intake Shaft (Figure 1-2). It consists of three wells, H-6a, H-6b, and H-6c, arranged in an approximate equilateral triangle measuring approximately 30 m on each side (Figure 9-1). The hydropad is located in Section 18, Township 22 south, and Range 31 east. The UTM coordinates, ground-surface elevations, and top-of-casing elevations for the H-6 wells are provided in Table 9-1. The relative positions of the wells at the depth of the Culebra dolomite are illustrated in Figure 9-1.

In June and July 1978, H-6a was drilled with a 20-cm (7-7/8-inch) bit to a depth of 144.6 m BGS and cased with 13.97-cm (5-1/2-inch) casing (Dennehy, 1982). It was then deepened to 160.0 m BGS by coring through the Magenta dolomite. The borehole remained in this configuration until January 20, 1981 when it was recompleted by coring through the Culebra interval to a total depth of 194.2 m BGS. A PIP was set at a depth of 181.1 m BGS in the open borehole between the Magenta and Culebra dolomites. The 49.4-m open-hole section of the well has a diameter of 12.1 cm.



NOTE: The borehole-deviation survey did not extend to the center of the Culebra dolomite in borehole H-6a.

Figure 9-1. Plan view of the wells at the H-6 hydropad showing distances between wells at the center of the Culebra.

Table 9-1. UTM Coordinates, Ground-Surface Elevations, and Top-of-Casing Elevations for the H-6 Hydropad Wells

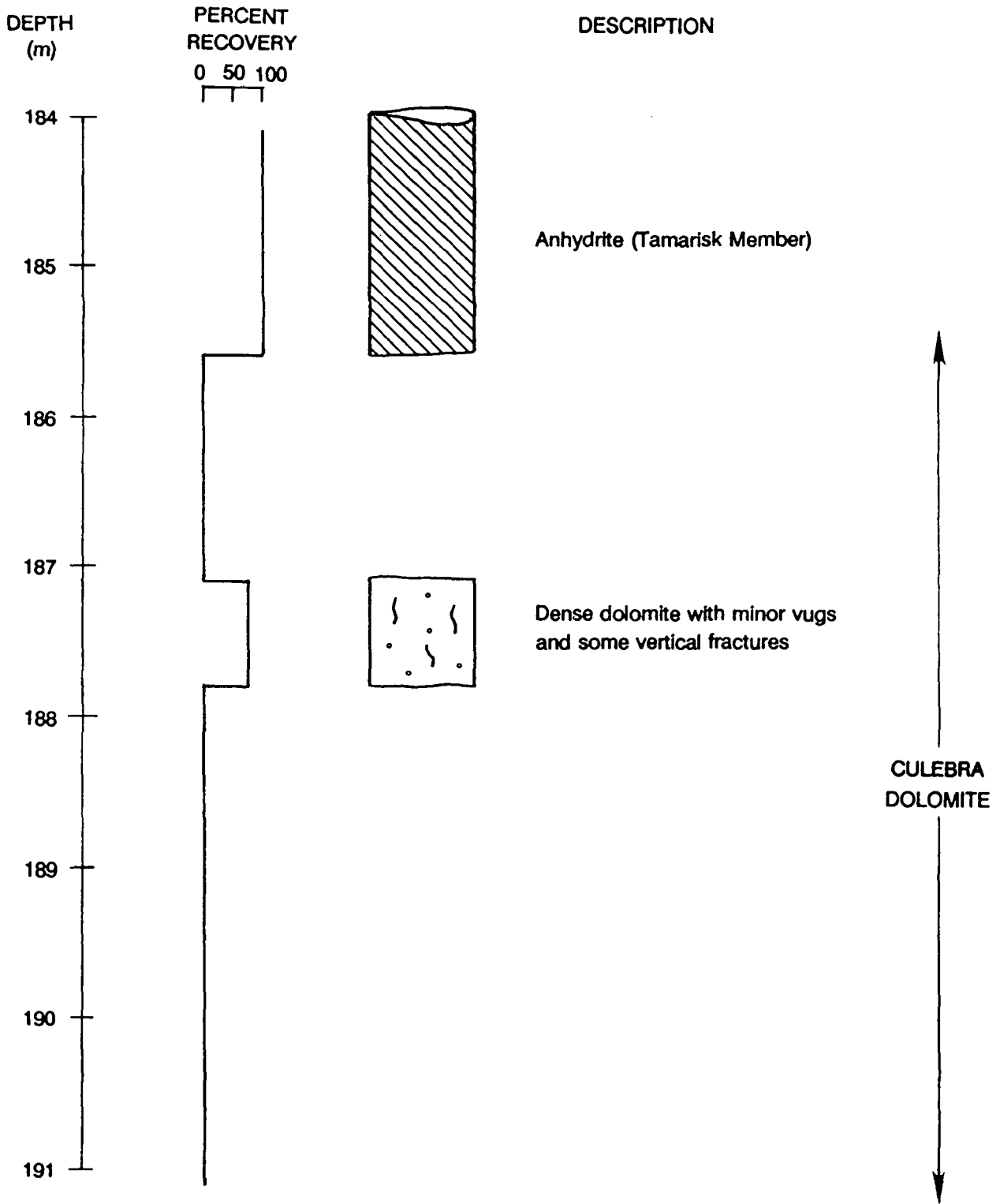
Well	UTM Coordinates		Ground-Surface Elevation (m amsl)	Top-of-Casing Elevation (m amsl)
	m East	m North		
H-6a	610,580	3,584,982	1020.24	1020.50
H-6b	610,594	3,585,008	1020.34	1020.55
H-6c	610,610	3,584,983	1020.45	1020.63

H-6b was drilled and cored in June and July 1978 (Dennehy, 1982). Initially, the borehole was drilled to a depth of 179.8 m BGS using a 20-cm bit and cased with 13.97-cm casing. The well was then cored through the Culebra dolomite to a total depth of 195.1 m BGS using a 12.07-cm (4-3/4-inch) bit. The lower 15.3 m of the well is open hole with a diameter of 12.1 cm.

In June 1978, H-6c was drilled to a depth of 213.1 m BGS using a 20-cm bit and cased with 13.97-cm casing (Dennehy, 1982). It was then cored to a total depth of 225.9 m BGS using a 12.07-cm core bit. The borehole remained in this configuration until May 1981 when it was recompleted. A bridge plug was placed at a depth of 195.4 m BGS to isolate the underlying Rustler-Salado contact. The casing was then perforated across the Culebra interval from 184.1 to 191.1 m BGS using four shots per 0.3 m. The well was in this configuration during the time of the convergent-flow tracer tests and the two-well recirculating tests. In August 1986 the well was again recompleted. A second bridge plug was set between the Magenta and Culebra intervals and the Magenta was perforated from 149.4 to 156.7 m BGS.

9.2 Local Hydrogeology

The Culebra dolomite is approximately 7 m thick at the H-6 hydropad. The Culebra interval was cored in well H-6b with approximately 10 percent recovery. Figure 9-2 shows the results of examination of the core located in the Department of Energy Core Library at the WIPP site. The 0.7 m of core recovered at H-6b is a relatively dense dolomite with vugs and vertical fractures. The poor core recovery suggests a high degree of fracturing, vugs, and/or poor induration due to a high silt content. Kelley and Saulnier (1990) present the results of porosity and permeability measurements on the core recovered at H-6b. The measured porosities range from 0.107 to 0.255 and the gas permeabilities range from 3.9×10^{-17} to 1.7×10^{-15} m².



NOTE: Depths here correspond to depths reported on the core.

Figure 9-2. Results of core examination of the Culebra dolomite from borehole H-6b.

DSTs as well as large- and small-scale pumping tests have been performed in an effort to determine the hydraulic properties of the Culebra dolomite at the H-6 hydropad. Discussions of these tests can be found in Beauheim (1986, 1987c), Gonzalez (1983), Dennehy (1982), and Seward (1982). From hydropad-scale interference pumping tests, Cauffman et al. (1990) estimated an average transmissivity of $3.6 \times 10^{-5} \text{ m}^2/\text{s}$ at the H-6 hydropad.

Hydraulic tests conducted at the H-6 hydropad have determined that horizontal transmissivity is anisotropic at that location. The method of analysis required three wells with sequential pumping from at least two of the wells and monitoring of drawdown in all three wells (Neuman et al., 1984). Gonzalez (1983) presents an anisotropy ratio for the principal horizontal components of transmissivity of 2.1:1 and a principal direction of N29°W at the H-6 hydropad. An orientation of N29.6°W for the principal direction and a ratio of 1.91:1 between the principal transmissivities was reported by Neuman et al. (1984).

9.3 History of the Seven Tracer Tests and Selection of Tracer Tests for Interpretation

A suite of five convergent-flow tracer tests was conducted at the H-6 hydropad from August 1981 to November 1982. In addition, two two-well recirculating tests were conducted from April to July 1983. The purpose of conducting a series of convergent-flow tracer tests was to evaluate Culebra properties (effective porosity and dispersivity) along different travel paths for several pumping conditions (Hydro Geo Chem, 1985). The two-well recirculating tests were conducted to estimate the effects of different flow fields on the estimates of porosity and dispersivity (Hydro Geo Chem, 1985). Full details on the test histories and concentration data for the H-6 tracer tests are reported in Hydro Geo Chem (1985).

9.3.1 Two-Well Recirculating Tracer Tests

The flow paths investigated by the two two-well recirculating tests were H-6c to H-6b and H-6a to H-6b (Hydro Geo Chem, 1985). For these tests, one well served as a withdrawal well and the second well served as an injection well. Discharge from the withdrawal well was continuously reintroduced in the injection well. Suspended sediments were removed from the circulating fluid with paper-filter units.

9.3.1.1 TRACER TEST HISTORIES

Table 9-2 summarizes the pumping and tracer-injection information for the two two-well recirculating tests.

Test #1

Pumping began at 10:50 on April 15, 1983 and ended at 14:50 on May 14, 1983. The average pumping rate was 0.63 L/s. The pumped well was H-6b and the injection well was H-6c. The pump intake was located approximately 164.6 m BTC. Discharge from the withdrawal well was connected, with 3.81-cm (1-1/2-inch) galvanized pipe, to the injection well head. Flow into the injection well was through 3.81-cm (1/2-inch) tubing suspended to a depth roughly corresponding to the water surface in the well. The average tracer-injection rate was 8.7×10^{-4} L/s. The tracers SCN (1.339 kg) and PFB (0.603 kg) were injected into H-6c from 13:47 to 16:19 on April 19, 1983. Formation fluid was used to prepare the tracer solution which was slowly added to the recirculating fluid using a positive-displacement metering pump. The PFB and SCN concentrations observed at the pumping well are shown in Figure 9-3. The times in Figure 9-3 are actual; they have not been corrected to account for the time for the tracers to travel from the injection point down to the Culebra center in the injection well nor to account for the time for the tracers to travel

Table 9-2. Summary of Pumping and Tracer-Injection Information for the Two-Well Recirculating Tracer Tests Conducted at the H-6 Hydropad

	H-6a	H-6b	H-6c	
TEST #1				
Well Type		Pumping	Injection	
Average Pumping Rate		0.63 L/s		
Time Pumping Began		10:50		
Date Pumping Began		04/15/83		
Time Pumping Ended		14:50		
Date Pumping Ended		05/14/83		
Tracers Injected			SCN	PFB
Masses Injected			1.339 kg	0.603 kg
Time Tracers Injected			13:47 to 16:19	
Date Tracers Injected			04/19/83	
Average Tracer-Injection Rate			8.7 x 10 ⁻⁴ L/s	
TEST #2				
Well Type		Injection	Pumping	
Average Pumping Rate			0.14 L/s	
Time Pumping Began			06:51	
Date Pumping Began			06/17/83	
Time Pumping Ended			08:15	
Date Pumping Ended			07/26/83	
Tracer Injected	m-TFMB	p-FB		
Masses Injected	1.0 kg	0.93 kg		
Time Tracer Injected	08:50 to 13:27			
Date Tracer Injected	06/22/83			
Average Tracer-Injection Rate	6.0 x 10 ⁻³ L/s			

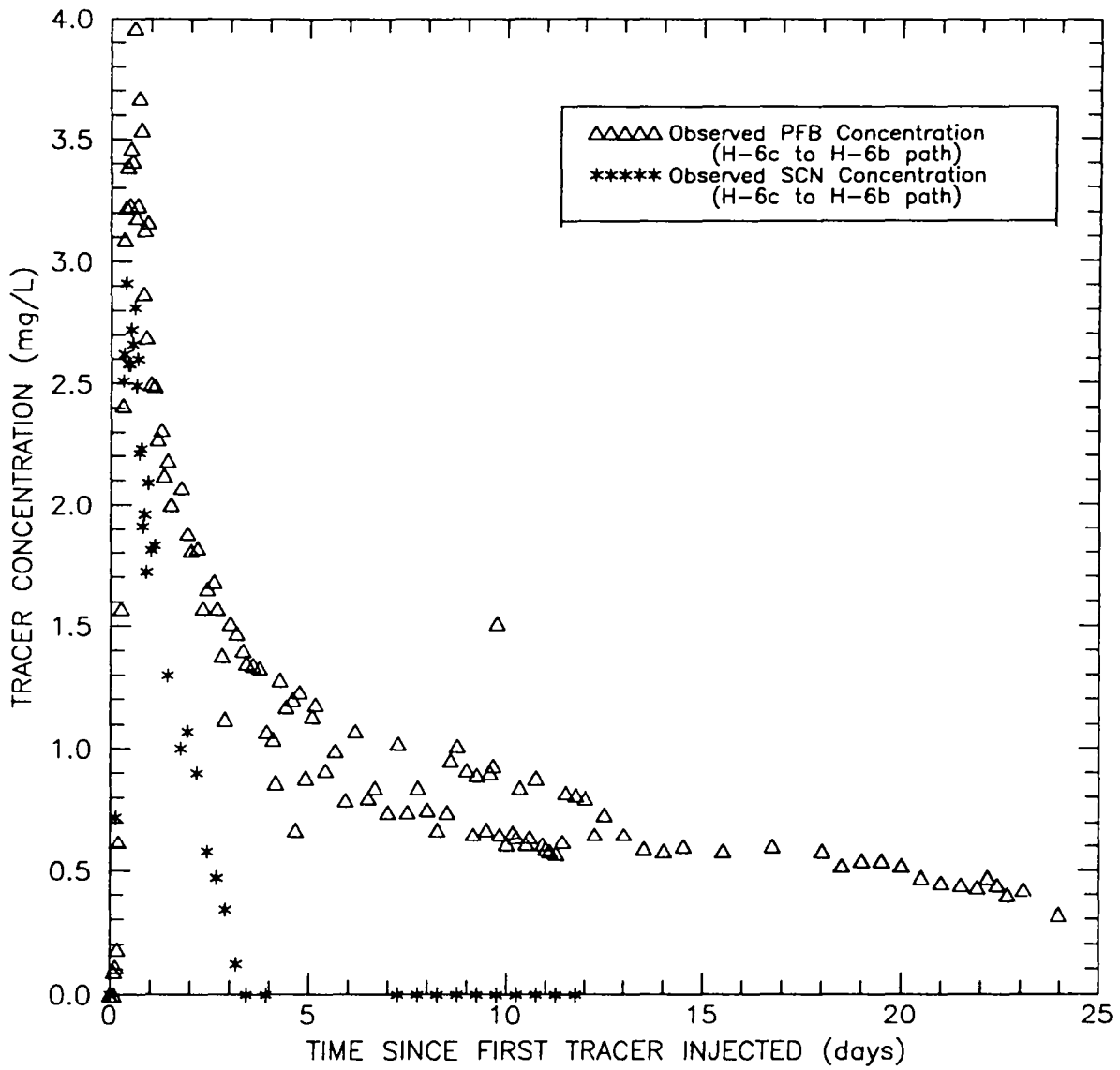


Figure 9-3. Observed PFB and SCN data for two-well recirculating tracer test #1 conducted at the H-6 hydropad.

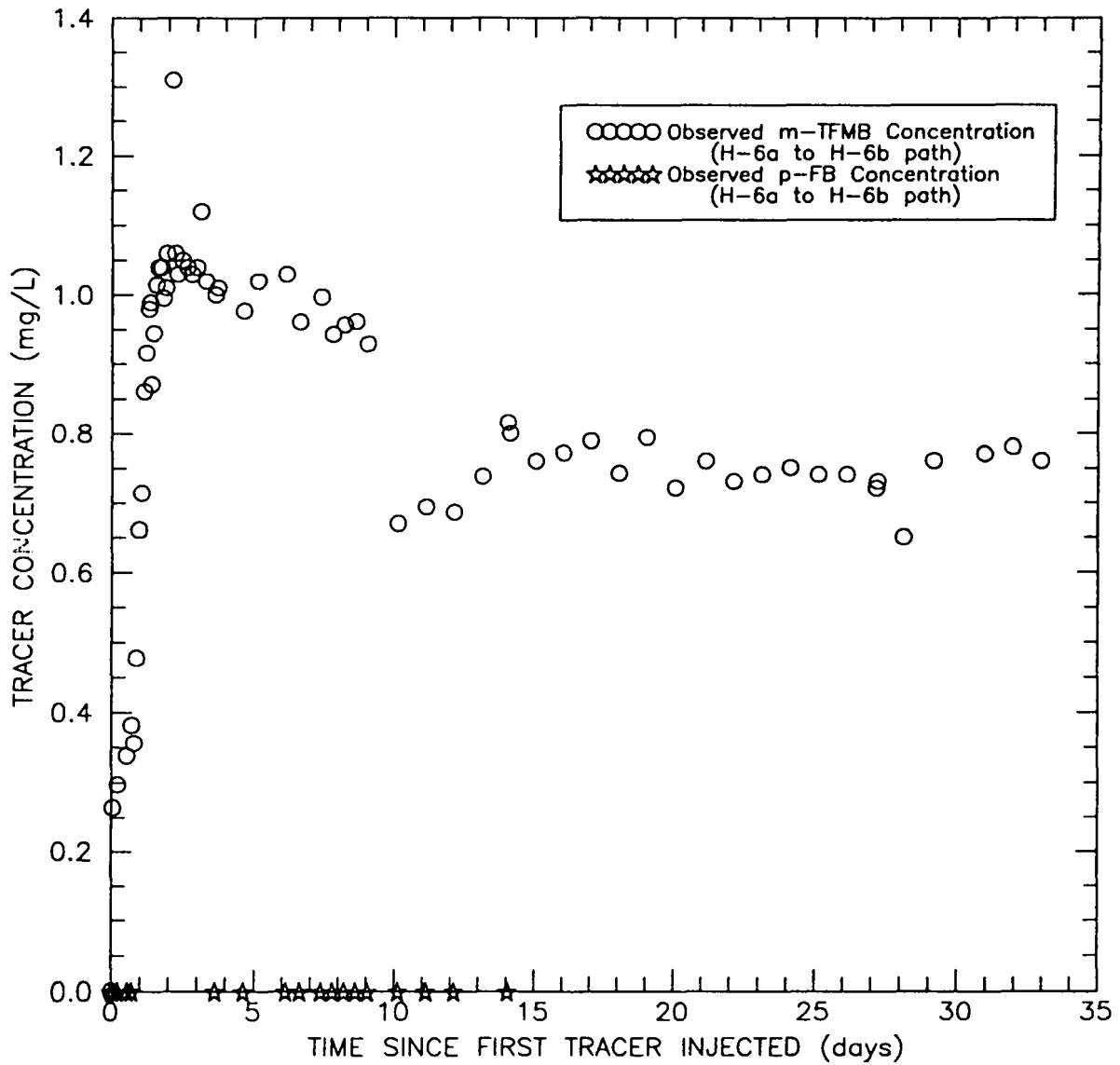
from the Culebra up the pumping well to the sampling point. Appendix E-1 contains the concentration data as reported in Hydro Geo Chem (1985).

Test #2

The withdrawal and injection wells for recirculating test #2 were H-6b and H-6a, respectively. The pumping period lasted from 06:51 on June 17, 1983 to 08:15 on July 26, 1983 at an average rate of 0.14 L/s. The pump intake was located approximately 131 m BTC. The discharge and recirculating line was 3.81-cm galvanized pipe. The 1.27-cm injection tubing in H-6a was suspended to a depth roughly corresponding to the water surface in the well. Injection of 0.93 kg of p-FB and 1.0 kg of m-TFMB occurred on June 22, 1983 from 08:50 to 13:27 at an average rate of 6.0×10^{-3} L/s. The tracer solution was prepared with distilled water. Figure 9-4 shows the concentration data versus actual time for water collected from the pumping well during recirculating test #2. The concentration data, as reported in Hydro Geo Chem (1985), is tabulated in Appendix E-2.

9.3.1.2 SUITABILITY OF TRACER TESTS FOR ANALYSIS

The tracer-concentration data from test #1 shown in Figure 9-3 are not considered interpretable because both PFB and SCN had been used for tracer tests at the H-6 hydropad on two previous occasions. PFB was injected directly into well H-6b on August 23, 1981 and on October 5, 1982 for convergent-flow tracer tests #1 and #4, respectively (see Section 9.3.2.1). SCN was also injected into well H-6b on October 5, 1982, and was pumped from H-6b after it was injected into H-6a on October 27, 1982 for convergent-flow tracer test #5. Therefore, residual PFB and SCN must have remained in the Culebra around well H-6b after the convergent-flow tests, and must have made some contribution to the concentrations measured during recirculating tracer test #1. Because



NOTE: Additional samples where p-FB was identified but not quantifiable due to an interfering compound are indicated in Appendix E-2.

Figure 9-4. Observed m-TFMB and p-FB data for two-well recirculating tracer test #2 conducted at the H-6 hydropad.

the contributions made by the residual tracers cannot be quantified, no defensible interpretation of recirculating tracer test #1 can be performed.

The tracer-concentration data from test #2 shown in Figure 9-4 are also considered uninterpretable for similar reasons. The tracer m-TFMB had been previously injected into well H-6a on August 23, 1981 and on October 27, 1982 for convergent-flow tracer tests #1 and #5, respectively. The tracer p-FB was injected into well H-6b on September 2, 1981 and on September 30, 1982 for convergent-flow tracer tests #2 and #3, respectively, and was pumped from H-6b after it was injected into well H-6c on November 5, 1982 for convergent-flow tracer test #5. Two samples collected from well H-6b on June 17 and 22, 1983, before tracer injection for recirculating tracer test #2 began, showed residual m-TFMB concentrations of 0.229 and 0.307 mg/L, respectively. All p-FB data for test #2 were reported as either none, 0.0, not detectable, or present but not quantifiable because of an interfering compound. Thus, neither the m-TFMB data nor the p-FB data could be reliably interpreted.

9.3.2 Convergent-Flow Tracer Tests

Five convergent-flow tracer tests were performed at the H-6 hydropad from August 1981 to November 1982. The following sections present a brief summary of the pumping and tracer-injection history, discuss the suitability of the tests for analysis, and discuss the test equipment and observed breakthrough curves for the analyzed tests. Detailed descriptions of the convergent-flow tracer tests conducted at the H-6 hydropad are presented in Hydro Geo Chem (1985).

9.3.2.1 PUMPING AND TRACER-INJECTION HISTORY

The convergent-flow tracer tests are referred to as test #1 through test #5. A summary of the pumping and tracer-injection information for the five tests is provided in Table 9-3. The first two tests consisted of tracer injection at two different times while H-6c was continuously pumped during a 23-day period in August and September 1981. The two injections were considered separate tests with injection of tracers into both H-6b and H-6a for test #1 and injection into H-6b only for test #2. During continuous pumping of H-6c in a 15-day period in September and October 1982, tracers were injected into H-6b at two different times. The first injection is referred to as test #3 and the second injection is referred to as test #4. During continuous pumping of H-6b in a 36-day period in October and November 1982, a pulse of tracers was injected into H-6a and H-6c. This last convergent-flow tracer test conducted at the H-6 hydropad is referred to as test #5.

Test #1

The pumping well and rate for test #1 were H-6c and 1.04 L/s, respectively. Pumping for this test started at 10:10 on August 19, 1981 and ended at 07:00 on September 11, 1981. The pumping rate was relatively stable during this period, fluctuating from a measured minimum of 1.01 L/s to a measured maximum of 1.11 L/s. Prior to tracer injection, the pumping well was pumped for four days in an effort to establish a relatively uniform convergent flow field. The periodic measurements of the pumping rate taken during test #1 are presented in Figure 9-5. The tracers m-TFMB and ortho-fluorobenzoate (o-FB) were injected into H-6a and the tracers PFB and meta-fluorobenzoate (m-FB) were injected into H-6b. All tracers were injected simultaneously at 17:36 on August 23, 1981. The total injection time is estimated to be approximately 29 min. The tracer-labeled volume injected into H-6a consisted of 0.953 kg of m-TFMB and 0.525 kg of o-FB mixed with 100 L of formation fluid. A 100 L volume of unmarked formation fluid was injected immediately following tracer injection. The total volume injected (200 L) is about 106 L greater than the downhole system volume (94 L) in H-6a.

Table 9-3. Summary of Pumping and Tracer-Injection Information for the Convergent-Flow Tracer Tests Conducted at the H-6 Hydropad

	<u>H-6a</u>		<u>H-6b</u>		<u>H-6c</u>
TEST #1					
Well Type	Tracer Injection		Tracer Injection		Pumping
Average Pumping Rate					1.04 L/s
Time Pumping Began					10:10
Date Pumping Began					08/19/81
Time Pumping Ended					07:00
Date Pumping Ended					09/11/81
Tracers Injected	m-TFMB	o-FB	PFB	m-FB	
Masses Injected	0.953 kg	0.525 kg	0.894 kg	0.376 kg	
Time Tracers Injected	17:36		17:36		
Date Tracers Injected	08/23/81		08/23/81		
Tracer Volume	100 L		100 L		
Chaser Volume	100 L		100 L		
Downhole System Volume	94 L		80 L		
TEST #2					
Well Type			Tracer Injection		Pumping
Average Pumping Rate					1.04 L/s
Time Pumping Began					10:10
Date Pumping Began					08/19/81
Time Pumping Ended					07:00
Date Pumping Ended					09/11/81
Tracer Injected			p-FB		
Mass Injected			0.569 kg		
Time Tracer Injected			13:00		
Date Tracer Injected			09/02/81		
Tracer Volume			100 L		
Chaser Volume			100 L		
Downhole System Volume			80 L		

Table 9-3. Summary of Pumping and Tracer-Injection Information for the Convergent-Flow Tracer Tests Conducted at the H-6 Hydropad
(cont'd)

	H-6a	H-6b	H-6c
TEST #3			
Well Type		Tracer Injection	Pumping
Average Pumping Rate			0.5 L/s
Time Pumping Began			09:25
Date Pumping Began			09/30/82
Time Pumping Ended			06:00
Date Pumping Ended			10/15/82
Tracers Injected		p-FB	
Masses Injected		1.0 kg	
Time Tracers Injected		09:25	
Date Tracers Injected		09/30/82	
Tracer Volume		100 L	
Chaser Volume		50 L	
Downhole System Volume		80 L	
TEST #4			
Well Type		Tracer Injection	Pumping
Average Pumping Rate			0.5 L/s
Time Pumping Began			09:25
Date Pumping Began			09/30/82
Time Pumping Ended			06:00
Date Pumping Ended			10/15/82
Tracers Injected		PFB SCN	
Masses Injected		1.0 kg 2.0 kg	
Time Tracers Injected		09:50	
Date Tracers Injected		10/05/82	
Tracer Volume		100 L	
Chaser Volume		50 L	
Downhole System Volume		80 L	

Table 9-3. Summary of Pumping and Tracer-Injection Information for the Convergent-Flow Tracer Tests Conducted at the H-6 Hydropad
(cont'd)

	H-6a		H-6b	H-6c
TEST #5				
Well Type	Tracer Injection		Pumping	Tracer Injection
Average Pumping Rate			1.01 L/s	
Time Pumping Began			10:00	
Date Pumping Began			10/24/82	
Time Pumping Ended			18:00	
Date Pumping Ended			11/29/82	
Tracers Injected	SCN	m-TFMB		p-FB
Masses Injected	2.0 kg	1.0 kg		1.0 kg
Time Tracers Injected	14:40			23:30
Date Tracers Injected	10/27/82			11/05/82
Tracer Volume	100 L			100 L
Chaser Volume	200 L			150 L
Downhole System Volume	94 L			102 L

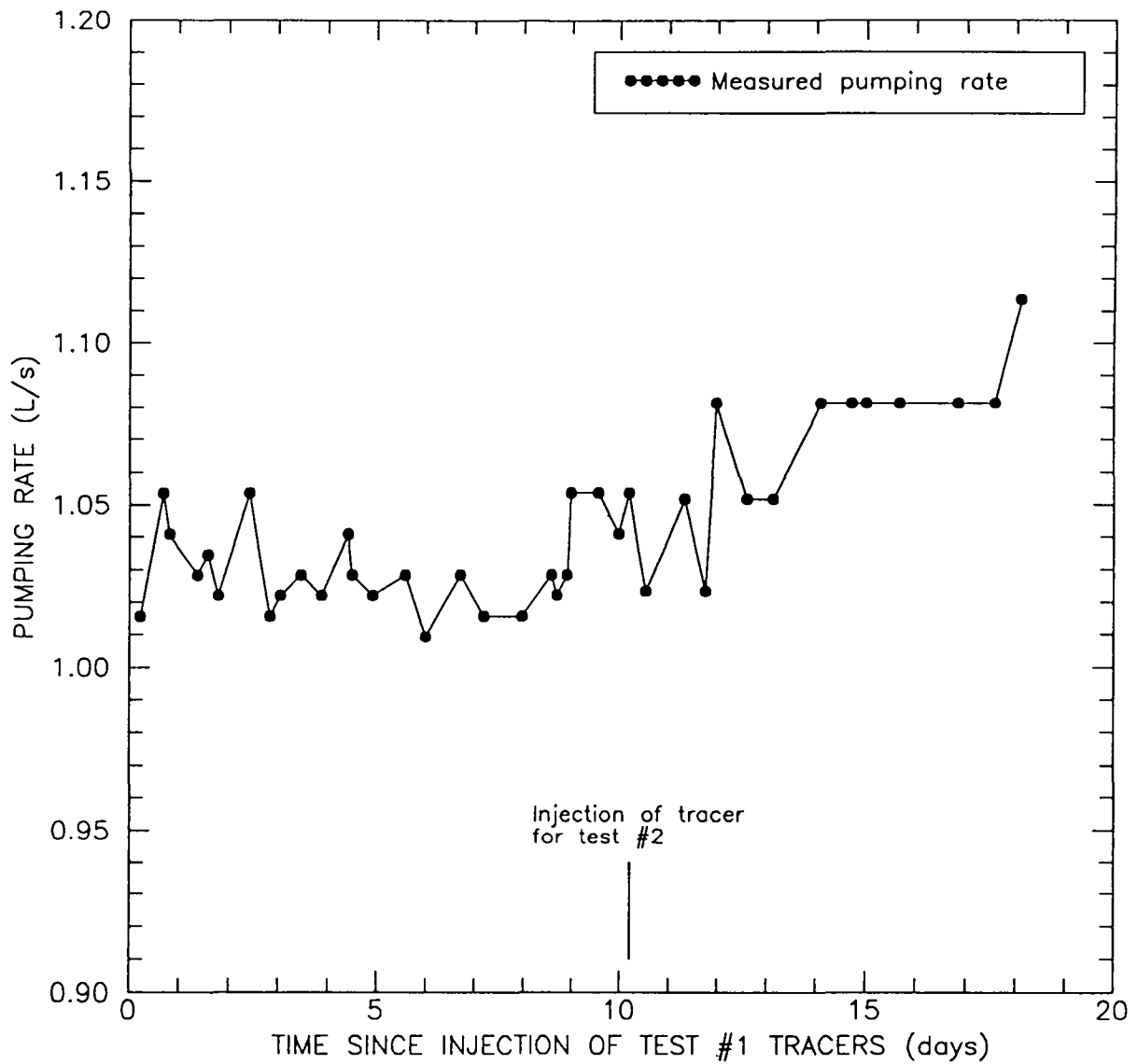


Figure 9-5. Pumping rate at well H-6c during convergent-flow tracer tests #1 and #2 conducted at the H-6 hydropad.

Masses of 0.894 kg of PFB and 0.376 kg of m-FB mixed with 100 L of formation fluid were injected into H-6b. This tracer-labeled slug was followed by the injection of an additional 100 L of formation fluid. The total volume injected was 200 L, 120 L greater than the downhole system volume of 80 L. Figure 9-6 shows the breakthrough curves obtained for PFB, m-TFMB, m-FB, and o-FB from water samples collected at pumping well H-6c. The concentration data reported by Hydro Geo Chem (1985) are provided in Appendix F-1.

Test #2

The pumping history for test #2 is identical to that of test #1 (Figure 9-5). Consequently, pumping well H-6c had been pumped for 14 days prior to tracer injection in well H-6b. The tracer p-FB was injected into well H-6b at 13:00 on September 2, 1981. The total injected volume of 200 L was made up of a tracer volume consisting of 0.569 kg of p-FB mixed with 100 L of formation fluid and a 100-L chaser volume. The total volume of fluid injected during test #2 was 120 L greater than the downhole system volume. No tracer was injected into H-6a during test #2.

After tracer injection into well H-6b during test #1, a sample was collected from that well for tracer analysis (Hydro Geo Chem, 1985). The sampling procedure included the injection of nitrogen gas down one tube fitted inside the well to force a fluid sample to the surface through a second tube. Test #2 was conducted in an effort to determine whether this sampling had affected tracer migration during test #1. Results of analysis of the water sample taken from H-6b after tracer injection were not reported in Hydro Geo Chem (1985). The p-FB breakthrough curve obtained from water samples collected at pumping well H-6c is shown in Figure 9-7 and the concentration data as reported in Hydro Geo Chem (1985) are given in Appendix F-2.

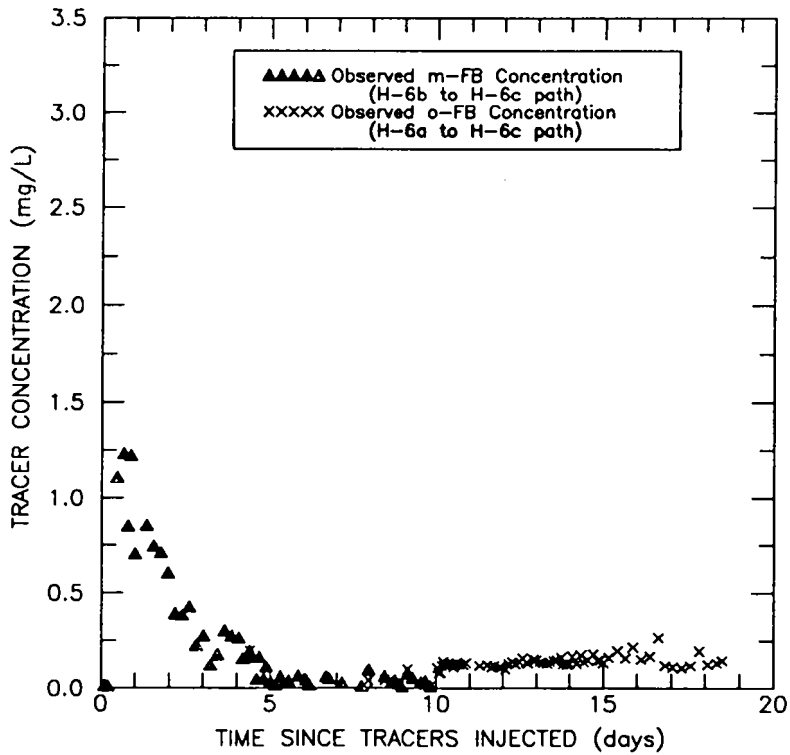
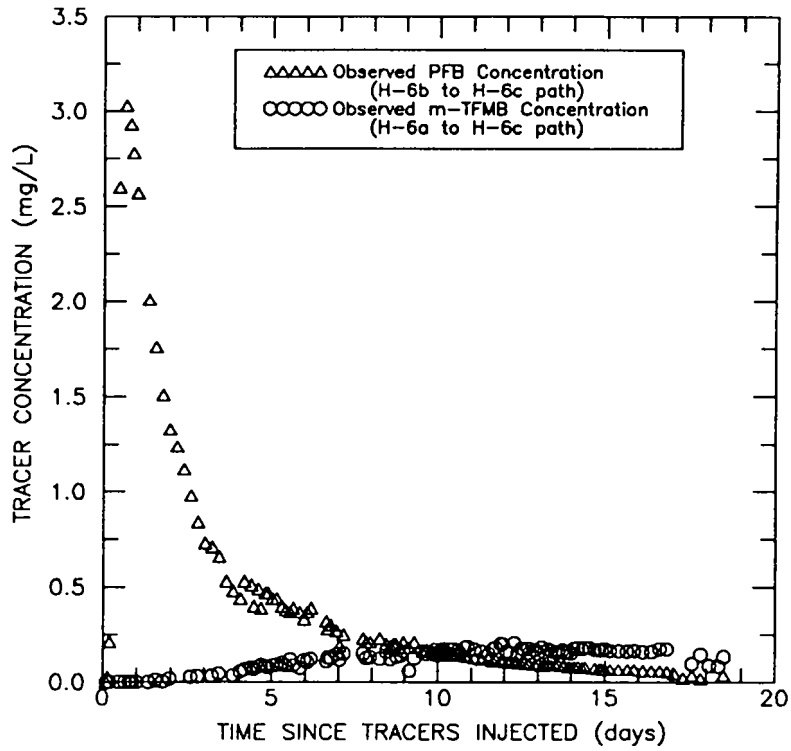


Figure 9-6. Observed PFB, m-TFMB, m-FB, and o-FB data for convergent-flow tracer test #1 conducted at the H-6 hydropad.

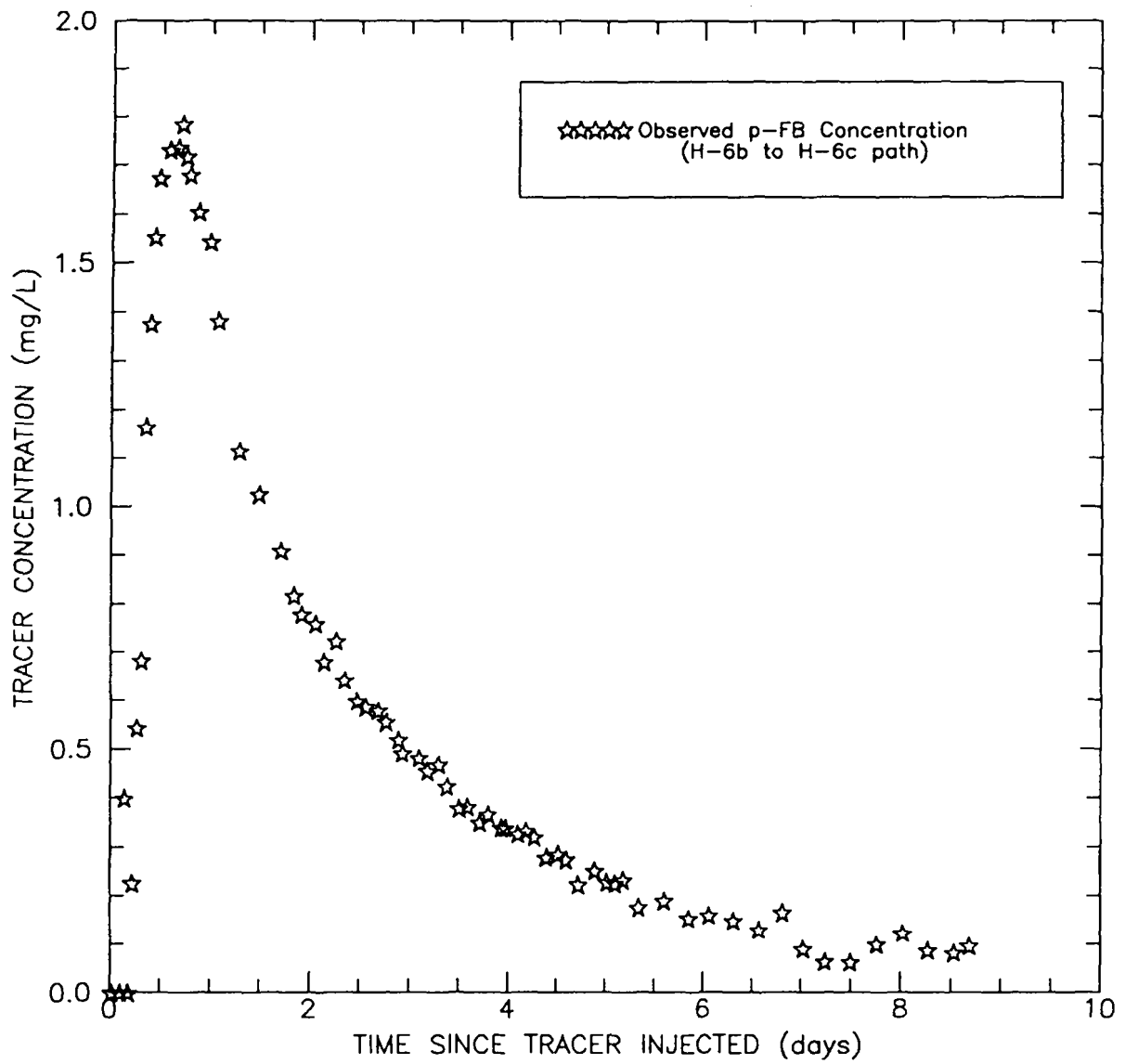


Figure 9-7. Observed p-FB data for convergent-flow tracer test #2 conducted at the H-6 hydropad.

Test #3

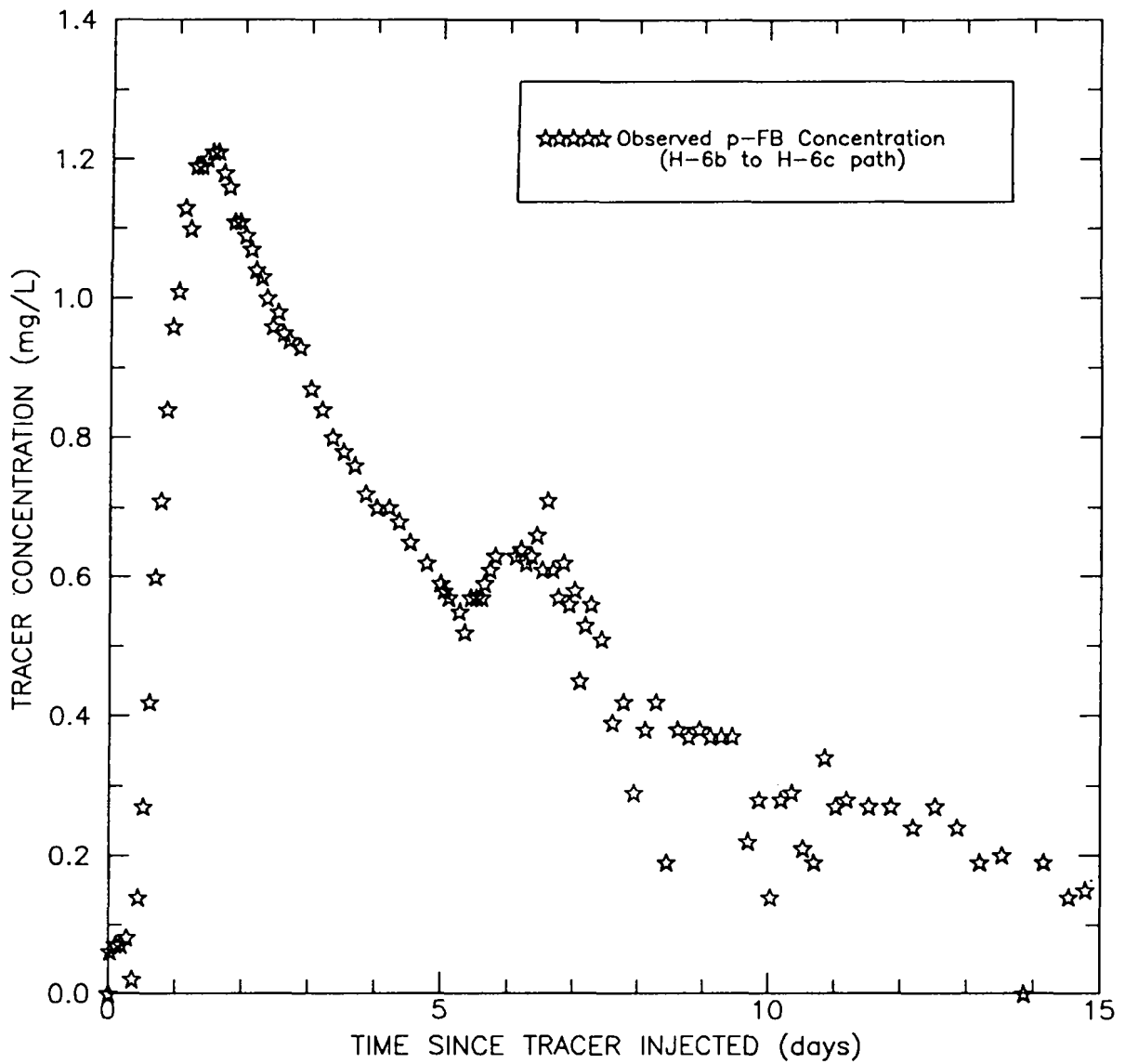
The pumping period for test #3 began at 09:25 on September 30, 1982 and ended at 06:00 on October 15, 1982. The pumping well was H-6c. The pumping rate fluctuated between a low of 0.50 L/s and a high of 0.53 L/s with an average rate of 0.50 L/s. For this test, the tracer p-FB was injected into H-6b immediately after pumping began in H-6c. The volume of tracer fluid consisted of 1.0 kg of p-FB mixed with 100 L of formation fluid. The volume of chaser fluid was 50 L. The downhole system volume was approximately 70 L less than the total injection volume. No tracer was injected into H-6a during test #3. The p-FB concentration data for water samples collected at pumping well H-6c are shown in Figure 9-8 and tabulated in Appendix F-3.

Test #4

The pumping history described for test #3 also applies to test #4. The tracers PFB and SCN were injected into H-6b at 09:50 on October 5, 1982, five days after pumping at the pumping well began. One kilogram of PFB and 2.0 kg of SCN mixed with 100 L of formation fluid made up the tracer-labeled volume. This slug was followed by 50 L of untraced formation fluid. The total volume of fluid injected into H-6b was approximately 70 L greater than the downhole system volume. Tracer was not injected into H-6a during test #4. The breakthrough curves obtained for PFB and SCN from water samples collected at pumping well H-6c are shown in Figure 9-9. Appendix F-4 contains the concentration data as reported in Hydro Geo Chem (1985).

Test #5

The pumping well for test #5 was H-6b. Pumping at this well began at 10:00 on October 24, 1982 and continued until 18:00 on November 29, 1982. The average pumping rate was 1.01 L/s with rates as low as 1.00 L/s and as high as 1.04 L/s. Tracers were injected into both H-6a and H-6c. The tracer volume injected into H-6a consisted of



The secondary peak was caused by delayed flushing of the tracer from the tracer-addition well during test #4.

Figure 9-8. Observed p-FB data for convergent-flow tracer test #3 conducted at the H-6 hydropad.

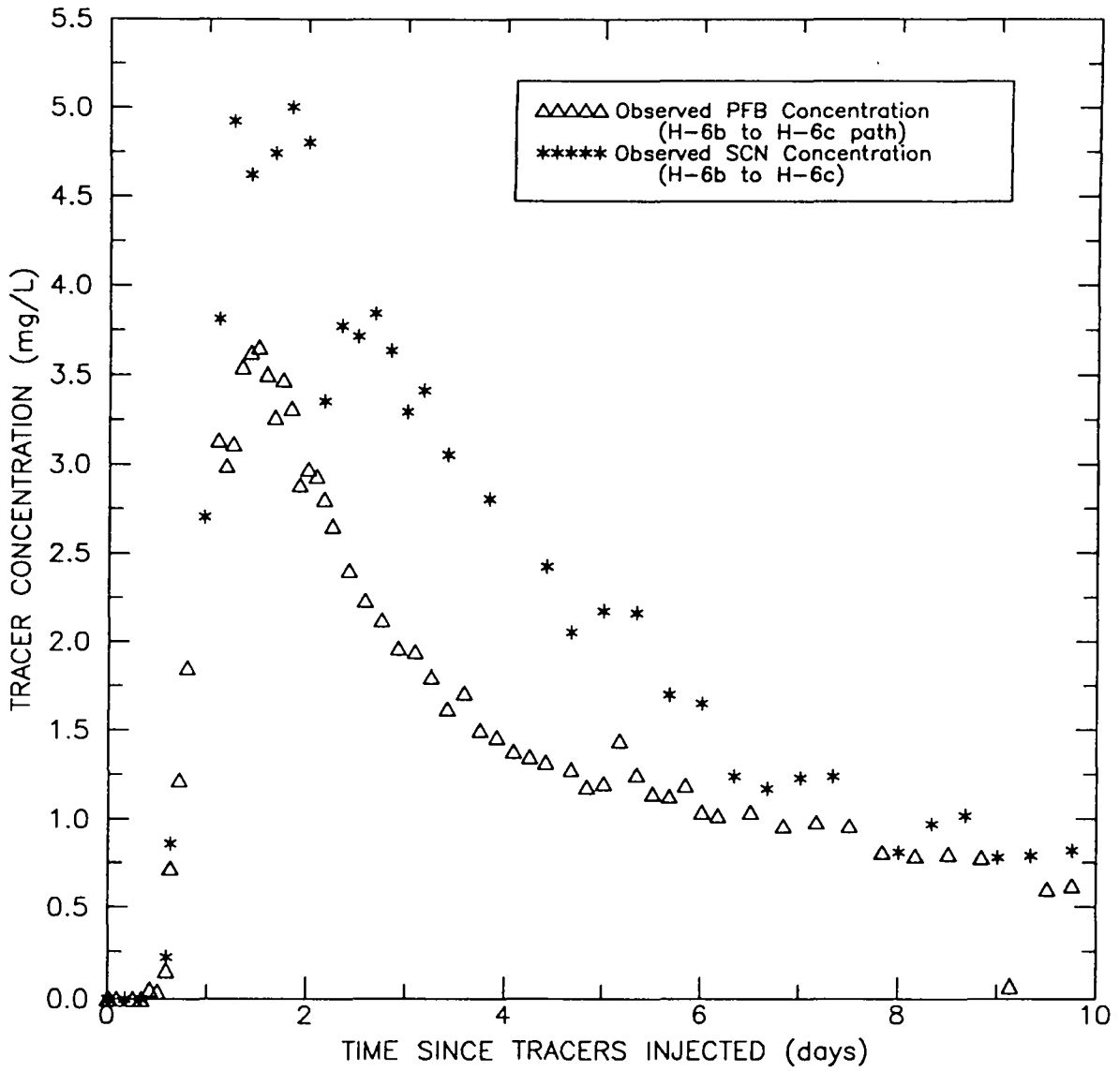
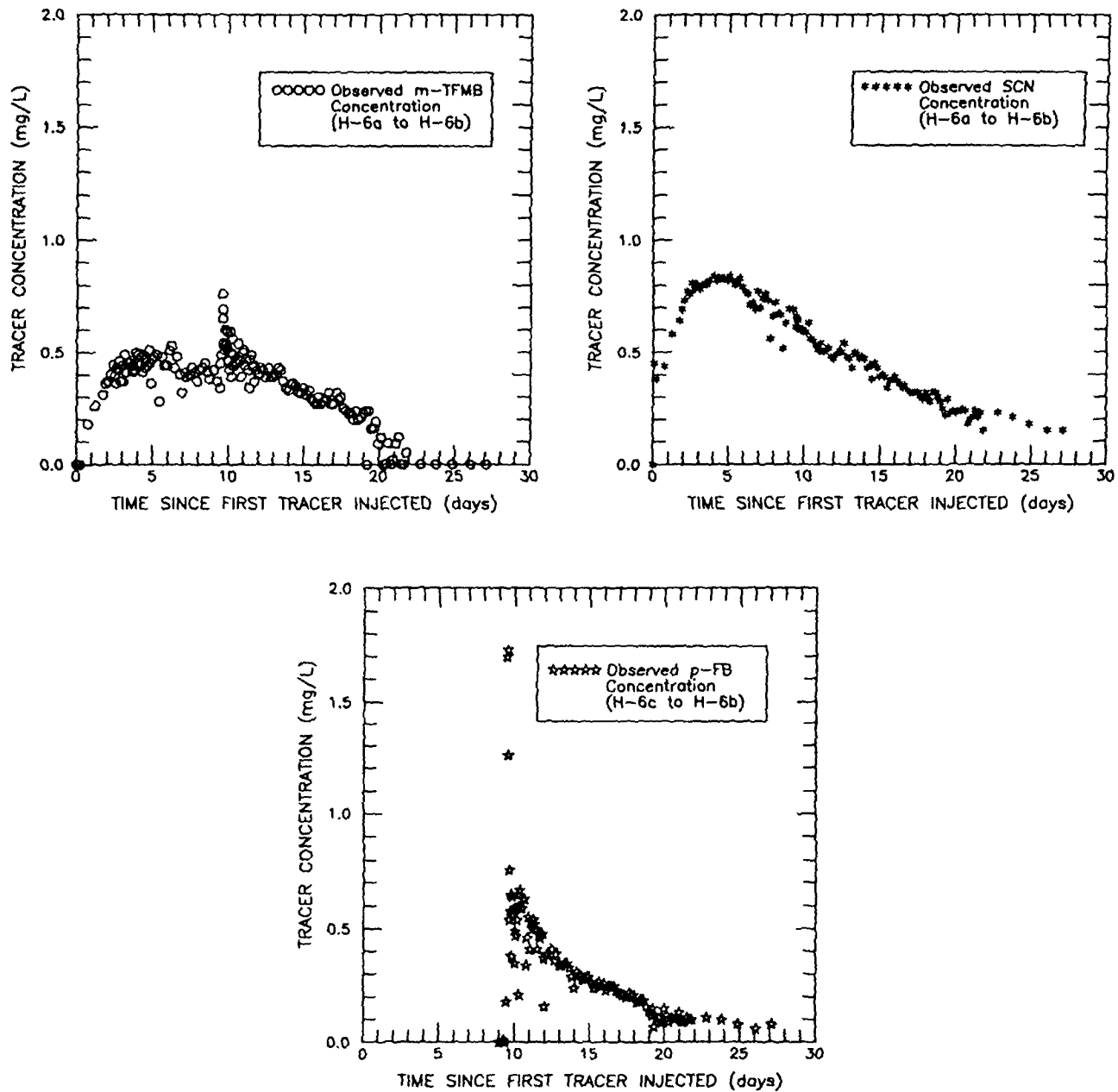


Figure 9-9. Observed PFB and SCN data for convergent-flow tracer test #4 conducted at the H-6 hydropad.

2.0 kg of SCN and 1.0 kg of m-TFMB mixed with 100 L of formation fluid. A 200-L chaser volume was injected following injection of the tracer volume. The total volume of fluid injected (300 L) into H-6a was 206 L greater than the downhole-system volume (94 L). Tracers were injected into H-6a at 14:40 on October 27, 1982, three days after pumping began in H-6b. At 23:30 on November 5, 1982, 1.0 kilogram of p-FB mixed with 100 L of formation fluid was injected into H-6c. The chaser volume was 150 L. A total fluid volume of 250 L, which is 148 L greater than the downhole system volume of 102 L, was injected into H-6c. Tracer injection into H-6c occurred 12 days after pumping began in H-6b, nine days after the first tracer was injection into H-6a. Figure 9-10 shows the m-TFMB, SCN, and p-FB breakthrough curves obtained from water samples collected at pumping well H-6b. The concentration data for test #5 as reported in Hydro Geo Chem (1985) are provided in Appendix F-5.

9.3.2.2 SUITABILITY OF TRACER TESTS FOR ANALYSIS

For tests #3 and #4, the volume of chaser fluid added to the tracer-addition wells after tracer injection was insufficient to flush the tracer from the wells. The use of an insufficient chaser volume results in a very large uncertainty in defining the initial tracer mass in the Culebra. Consequently, the results of these two tests are considered uncertain and, therefore, tests #3 and #4 were not interpreted. In addition, tests #3 and #4 investigated only one travel path (H-6b to H-6c) which had already been investigated in tests #1 and #2 eliminating the benefit of evaluating two independent flow paths during the same test. The breakthrough of p-FB in test #3 exhibits a distinct secondary peak approximately five days after the primary peak (Figure 9-8). The secondary peak was the result of flushing residual p-FB from H-6b out into the Culebra due to the injection of additional tracers into H-6b during test #4. Tracers were injected for test #4 five days after p-FB was injected for test #3.



NOTE: Start of p-FB injection was 9.4 days after start of m-TFMB and SCN injection.

Figure 9-10. Observed m-TFMB, SCN, and p-FB data for convergent-flow tracer test #5 conducted at the H-6 hydropad.

The pumping well for test #5 was H-6b which had previously been used as a tracer-addition well for SCN and p-FB. Also, m-TFMB had previously been injected at H-6a. Therefore, recovery of previously injected tracers could not be avoided. As a result, test #5 was considered unreliable.

Test #5 was the only convergent-flow tracer test that tested the path between H-6a and H-6b. The reported concentration data show that SCN had a relatively high concentration of 0.45 mg/L for the first sample collected from H-6b 1.4 hours after the start of tracer injection. This concentration level appears anomalous considering the time for tracer to travel from the injection point down to the center of the Culebra in the tracer-addition well and from the Culebra up to the sampling point in the pumping well is approximately 0.5 hr. This high initial concentration may represent recovery of SCN that had been injected into H-6b during test #4. The overall breakthrough curve for SCN (Figure 9-10) is well defined, but how much of the tracer came from H-6a and how much was remaining from test #4 is unknown. The breakthrough curve for m-TFMB (Figure 9-10) has an unusual shape that may be related to recovery of m-TFMB injected in previous tracer tests. Qualitatively, it appears that the rate of transport along the H-6a to H-6b path in test #5 is intermediate between the fast rate along the H-6b to H-6c path and the slow rate along the H-6a to H-6c path demonstrated in test #1.

The breakthrough curve for p-FB from H-6c to H-6b in test #5 (Figure 9-10) is qualitatively similar to breakthrough curves from H-6b to H-6c defined in the first four convergent-flow tracer tests at the H-6 hydropad (Figures 9-6, 9-7, 9-8, and 9-9). Noise or scatter in the data may reflect recovery of p-FB injected into the Culebra during earlier tests.

The conditions of tests #1 and #2 provided the best opportunity for obtaining meaningful interpreted results. Only the PFB and m-TFMB breakthrough curves from test #1 were analyzed because, of the six tracers utilized in the convergent-flow tracer tests, only p-FB, PFB and m-TFMB appeared to have behaved conservatively. In field notes,

Hydro Geo Chem report that the other three tracers, o-FB, m-FB, and SCN, showed signs of degradation in laboratory stability tests in time periods of days to tens of days.

In summary, the m-TFMB and PFB breakthrough curves obtained from test #1 and the p-FB breakthrough curve obtained from test #2 were analyzed. The tracer-injection procedures of tests #3 and #4 were deemed to be inadequate and the results were considered to be unreliable. The results of test #5 were questionable because of the potential for recovering tracers injected during previous tests.

9.3.2.3 TEST EQUIPMENT FOR ANALYZED TESTS

Figure 9-11 shows the configuration of the three H-6 hydropad wells during convergent-flow tracer tests #1 and #2. A submersible pump was set in the open casing of H-6c at a depth of about 165 m BGS. Fluid pumped from the well traveled to ground surface through a 3.81-cm (1-1/2-inch) discharge line. The discharge rate was measured through a 2.54-cm (1-inch) in-line totalizing flow meter. In well H-6a, a PIP with 6.03-cm (2-3/8-inch) feed-through tubing was installed above the Culebra interval at a depth of approximately 181.1 m BGS. A 1.27-cm (1/2-inch) injection tube was lowered inside the feed-through tubing to a depth of about 182.9 m. An air-inflatable packer was set in the casing immediately above the Culebra interval in well H-6b. The tracers were injected through 1.27-cm injection tubing fed through the packer. Two additional tubes were installed in H-6b in order to collect a tracer sample after tracer injection.

At each tracer-addition well, the injection tubing was connected to a container located beside the well on an elevated platform. The tracer(s) to be injected were mixed in that container. The injection tubing was clamped shut during mixing and then opened for gravity-driven tracer injection.

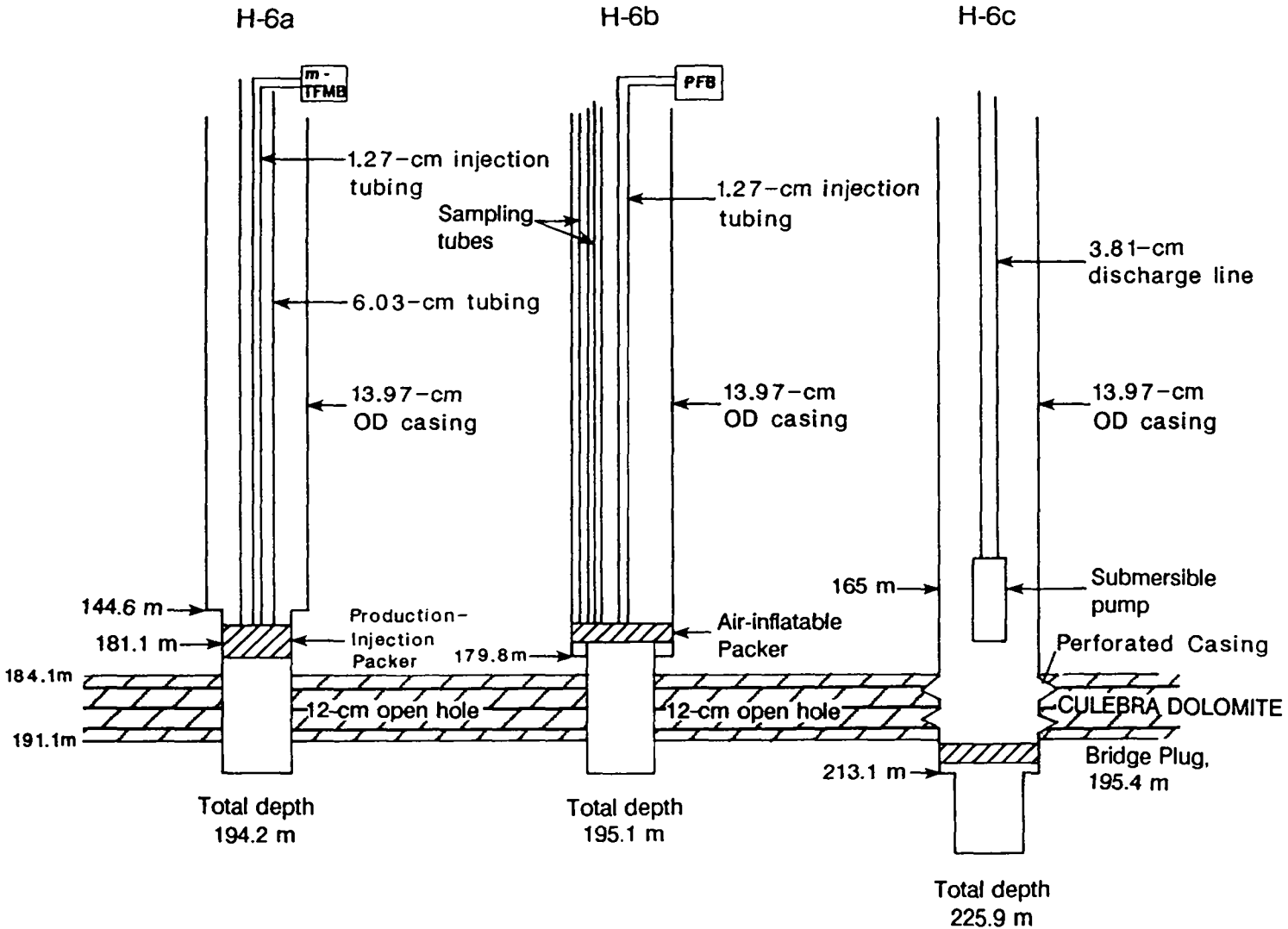


Figure 9-11. Downhole-equipment configurations for convergent-flow tracer tests #1 and #2 at the H-6 hydrograd.

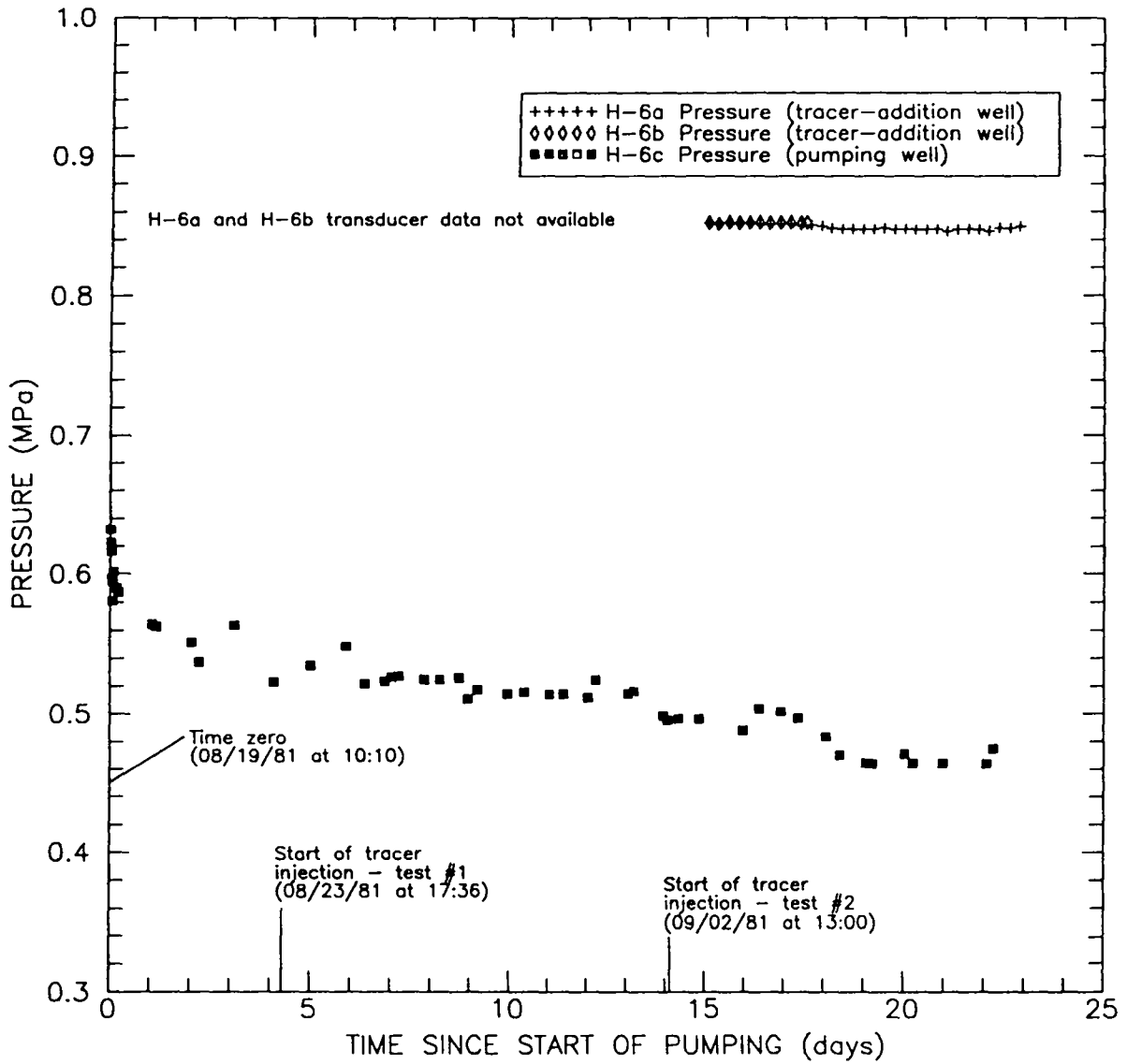
A DAS was used to monitor downhole pressure transducers in the three H-6 hydropad wells during convergent-flow tracer tests #1 and #2. The transducer monitoring pressure in H-6c failed at the beginning of test #1. Water levels were collected manually in H-6c after the transducer failed. Figure 9-12 shows the pressure data for the three H-6 hydropad wells during the first and second convergent-flow tracer tests. Data from the transducers in H-6a and H-6b were not available until approximately 15 days after pumping for the tests began.

Samples were collected at the pumping well using both an automatic sampler and manual sampling methods. Samples were collected in polyethylene bottles from the timer-driven automatic sampler. Manual samples, also collected in polyethylene bottles, were taken through a by-pass valve in the discharge line. Duplicate samples were collected by both methods. The fluid samples collected during tests #1 and #2 were analyzed for tracer content using HPLC techniques (Hydro Geo Chem, 1985). A discussion of the tracer-analysis equipment is given in Hydro Geo Chem (1985).

9.3.2.4 OBSERVED TRACER BREAKTHROUGHS FOR ANALYZED TESTS

Test #1

The breakthrough curves obtained for m-TFMB and PFB from water samples collected at the pumping well are illustrated in Figure 9-6. The concentration data reported by Hydro Geo Chem (1985) and the corrected travel times are presented in Appendix F-1. The corrected travel time accounts for the time required for the tracer to travel from the injection point down to the center of the Culebra in the tracer-addition well and from the Culebra up to the sampling point in the pumping well. The time corrections are noted in Appendix F-1.



H-6a and H-6b pressure data pared for figure clarity.

Figure 9-12. Pressure data for the H-6 hydropad wells during convergent-flow tracer tests #1 and #2.

The tracer PFB was first detected at the pumping well approximately 4 hrs (corrected time) after it had been injected. After about 16 hrs (corrected time), the peak concentration of PFB occurred. The observed recovery of PFB at the pumping well was about 80 percent. It was 37 hrs (corrected time) after injection before the tracer m-TFMB was detected at the pumping well and another 258 hrs before the peak concentration was observed. Twenty percent of the m-TFMB injected into well H-6a was recovered at well H-6c. The peak concentration of m-TFMB is a factor of about 14 less than the peak concentration of PFB. The peak-concentration arrival times differ by a factor of about 19.

Test #2

Figure 9-7 shows the p-FB breakthrough curve and Appendix F-2 contains the concentration data reported by Hydro Geo Chem (1985) and the corrected travel times. The corrected times of first detection and peak-concentration arrival are about 3 and 17 hrs, respectively. Observed recovery of p-FB at the pumping well was about 63 percent.

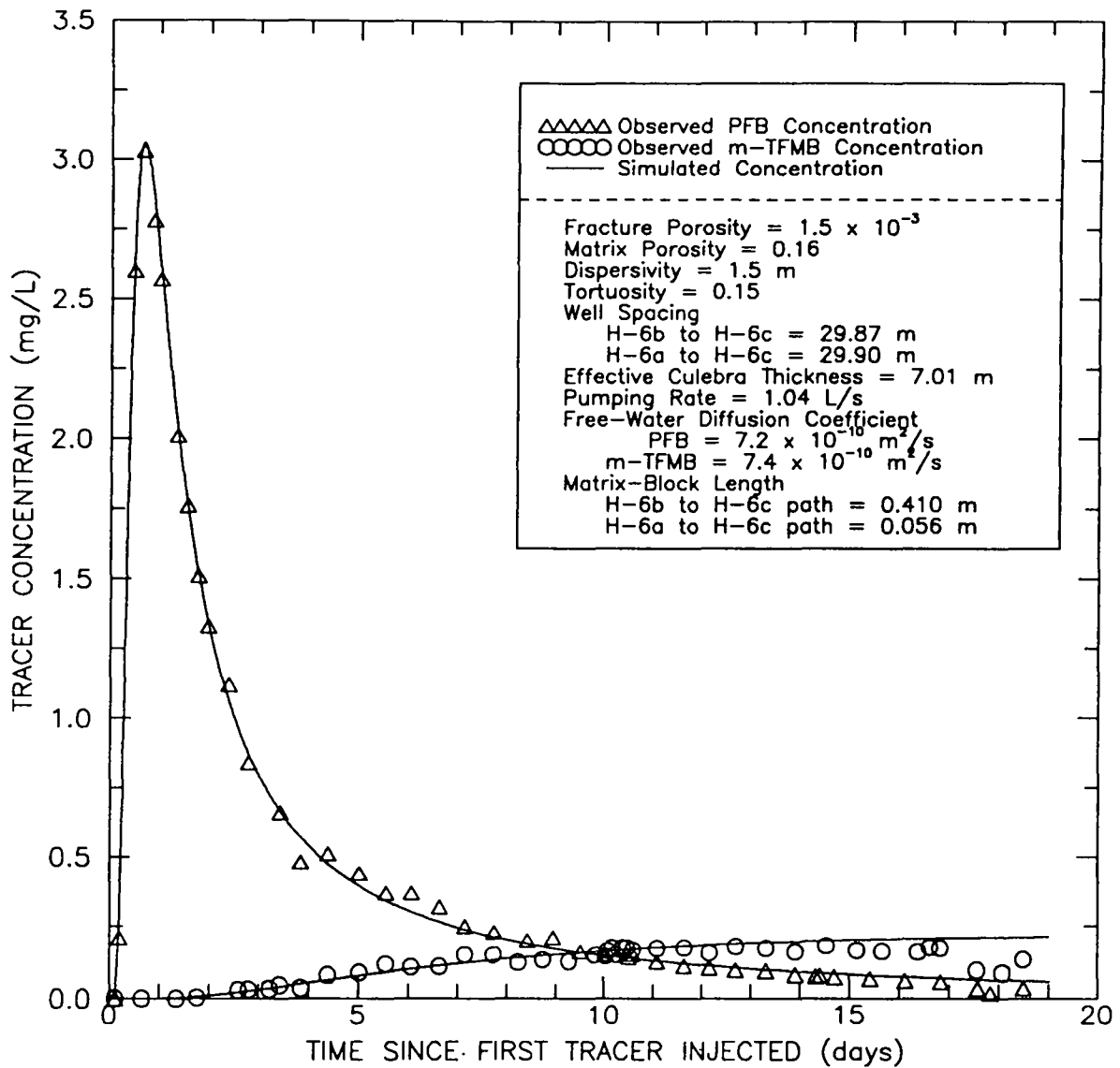
The tracer PFB injected during test #1 and the tracer p-FB injected during test #2 both traveled from well H-6b to H-6c. Theoretically, if the difference in the mass injected is taken into account, the peak-concentration arrival time and peak concentration for these two tracers should have been the same. In actuality, p-FB arrived at the pumping well one hour quicker than did PFB and, correcting for masses injected, the peak concentration of p-FB was a factor of 1.1 less than the peak concentration of PFB. Inherent to this comparison is the assumption of a constant pumping rate. The reduction in arrival time and peak concentration are likely the result of the gradual increase in pumping rate that occurred during test #2 (Figure 9-5).

9.4 Analysis of Tracer-Breakthrough Curves for Convergent-Flow Tracer Test #1

The two test #1 breakthrough curves, like the breakthrough curves from the H-3 test, differ significantly (Figure 9-6). The observed concentrations for PFB, which traveled from H-6b to H-6c, rose rapidly, peaked sharply, and tailed notably. m-TFMB traveled from H-6a to H-6c and had a breakthrough curve that rose gradually, did not have a well-defined peak, and tailed slightly. The breakthrough curves for the H-6 and H-3 tests show similar behavior. However, the tracer PFB broke through rapidly during the H-6 test but gradually during the H-3 test, whereas the tracer m-TFMB broke through gradually during the H-6 test and rapidly during the H-3 test. This comparison demonstrates that the properties of the tracers themselves were not responsible for the different behaviors observed along different flow paths. The heterogeneous- and anisotropic-analysis approaches used to analyze the H-3 tracer test (Section 3.4) were also used to analyze the H-6 tracer test.

9.4.1 Heterogeneous-Analysis Approach

A discussion of the fitting parameters for the heterogeneous-analysis approach can be found in Section 3.4.1. The other input parameters were held constant at values considered to be consistent with the current physical and conceptual understanding of the Culebra (see Section 5.0). The observed PFB and m-TFMB concentrations and the best-fit, heterogeneous simulations are presented in Figure 9-13. The observed and simulated breakthrough curves exhibit an excellent match. The fracture porosity used to generate both simulated curves was 1.5×10^{-3} . The best-fit matrix-block lengths are 0.41 m for the H-6b to H-6c path (PFB breakthrough curve) and 0.06 m for the H-6a to H-6c path (m-TFMB breakthrough curve). A summary of the parameters used in the best-fit, heterogeneous simulations is provided in Table 9-4.



Observed data pared for figure clarity.

Figure 9-13. Observed and best-fit simulated breakthrough curves for H-6 convergent-flow tracer test #1 using the heterogeneous-analysis approach.

Table 9-4. Transport Parameters Used in the Interpretations of H-6 Convergent-Flow Tracer Test #1

Parameter	Heterogeneous-Analysis Approach		Anisotropic-Analysis Approach	
Culebra Thickness	7.0 m			
Well Spacings	29.9 m		H-6b to H-6c	
	29.9 m		H-6a to H-6c	
Free-Water Diffusion Coefficients	7.2 x 10 ⁻¹⁰ m ² /s		PFB	
	7.4 x 10 ⁻¹⁰ m ² /s		m-TFMB	
Longitudinal Dispersivity	1.5 m			
Tortuosity	0.15			
Matrix Porosity	0.16			
Fracture Porosity	1.5 x 10 ⁻³		3.0 x 10 ⁻³	
Matrix-Block Lengths	0.41 m	H-6b to H-6c	0.15 m	H-6b to H-6c
	0.06 m	H-6a to H-6c	0.15 m	H-6b to H-6c
Anisotropy Ratio	1:1		7:1	
Principal-Transmissivity Direction	na		N31° W (parallel to the H-6b to H-6c path)	
na means not applicable				

For the fracture porosity of 1.5×10^{-3} used in the heterogeneous simulations, the inner and outer radii of the tracer-input zones (shown schematically in Figures 3-5 and 3-8) were 0.45 and 1.80 m, respectively, for H-6a and 0.78 and 1.95 m, respectively, for H-6b. The initial mass was distributed over 10 grid blocks at H-6b and 8 grid blocks at H-6a. The paths from H-6b to H-6c and H-6a to H-6c were discretized into 105 and 102 grid blocks, respectively, using grid-block sizes ranging from 0.26 to 0.45 m.

The distribution of mass in the fractures and matrix for the two travel paths and the tracer mass recovered at the pumping well is illustrated in Figure 9-14. For the tracer PFB, the mass in the fractures rapidly declined due to losses to the matrix and to the pumping well. The mass of PFB in the matrix rapidly increased to a peak, then decreased substantially as mass moved from the matrix back into the fractures and traveled to the pumping well. The simulated PFB curve indicates 80 percent recovery at the pumping well which is identical to the estimated mass recovery based on the observed breakthrough curve. The bulk of the unrecovered tracer is located in the matrix at the end of the test. The rapid decline of m-TFMB mass in the fractures is the result of large diffusive losses to the matrix caused by the small matrix-block size (large surface area). The mass of m-TFMB in the matrix reaches a peak and then slowly declines. The decline of m-TFMB mass in the matrix is much less than that of PFB resulting in less m-TFMB recovery at the pumping well. The simulations predicted that 23 percent of the m-TFMB injected into H-6a was recovered at H-6c. At the end of the tracer test, the bulk of the unrecovered tracer is located in the matrix. The simulated mass recovery (23 percent) compares favorably with the mass recovery at the pumping well estimated based on the observed breakthrough curve (20 percent).

9.4.2 Anisotropic-Analysis Approach

Section 3.4.2 discusses the fitting parameters for the anisotropic approach. A fracture porosity of 3.0×10^{-3} , calculated with Equation 5-9, was used in the anisotropic simulations.

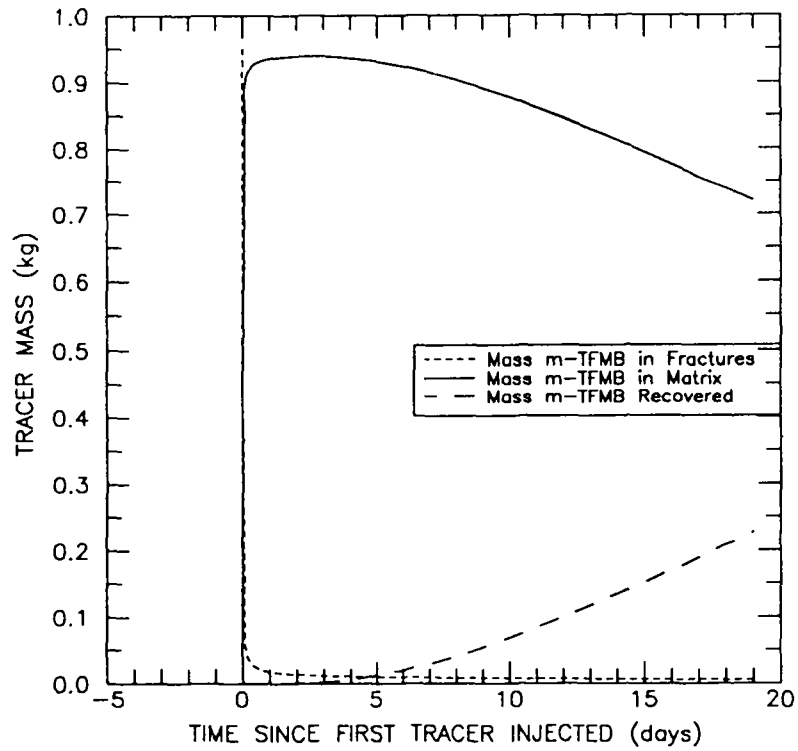
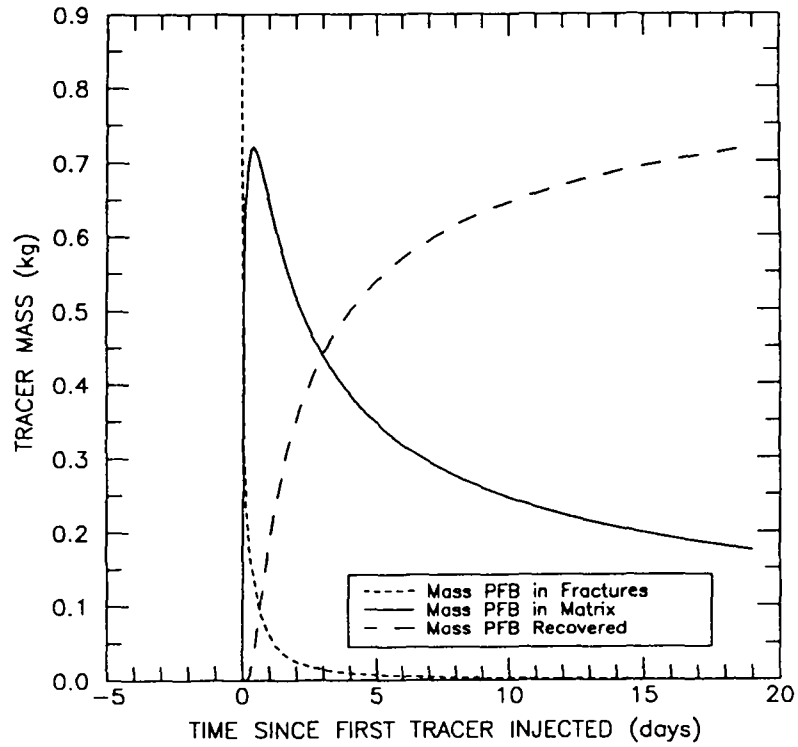


Figure 9-14. Mass distribution in the fractures and matrix and mass recovered at the pumping well for the best-fit heterogeneous simulation of the test #1 tracer-breakthrough curves for the H-6 hydropad.

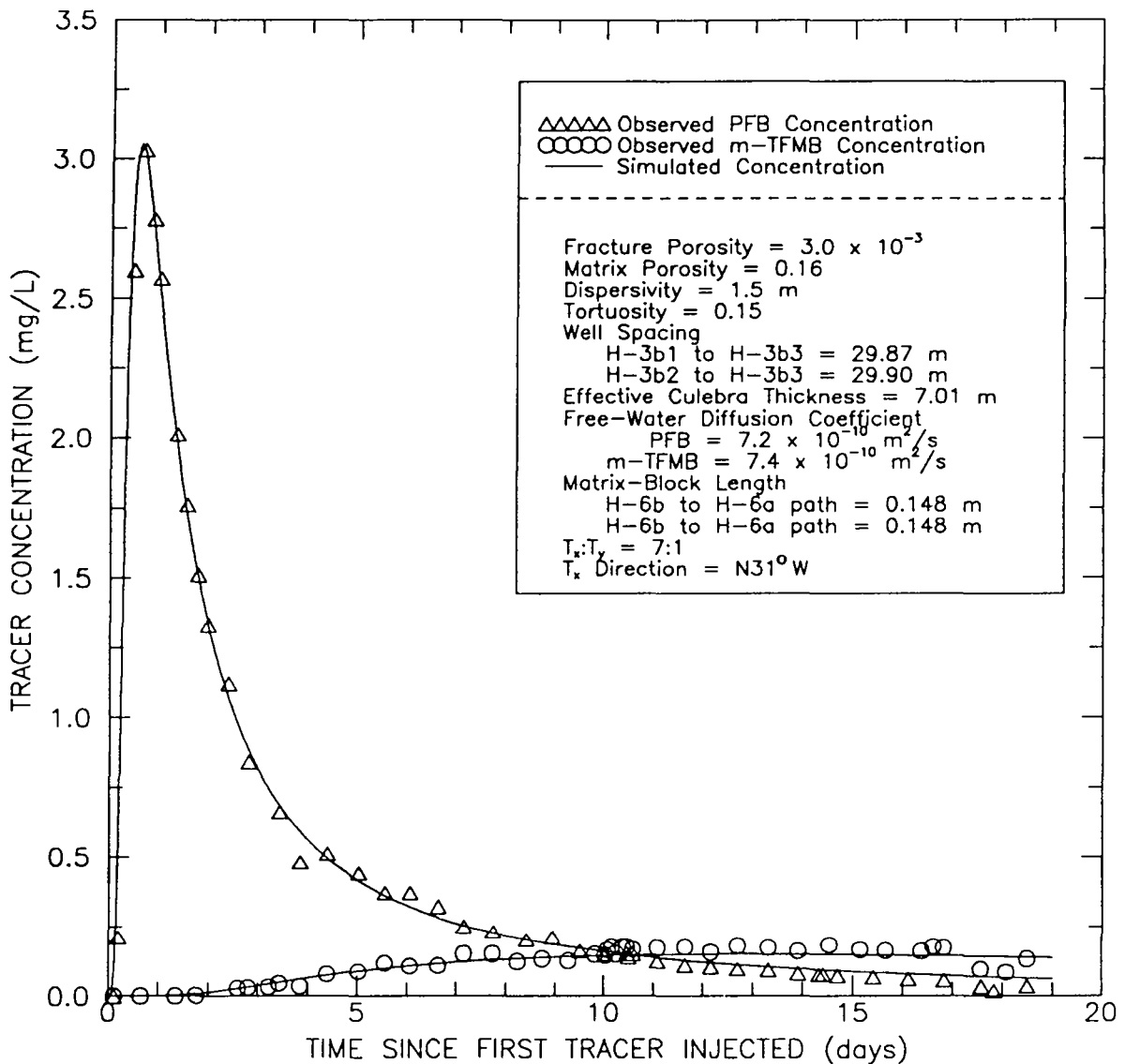
Using this fracture porosity, the calculated inner and outer radii for the tracer-input zones (shown schematically in Figures 3-5 and 3-8) are 0.32 and 1.26 m, respectively, for H-6a and 0.54 and 1.35 m, respectively, for H-6b. The initial tracer mass was distributed over 10 of the 106 grid blocks used to discretize the H-6b to H-6c path and over 8 of the 104 grid blocks used to discretize the H-6a to H-6c path. The grid blocks that discretized the two flow paths ranged in size from 0.26 to 0.32 m.

The best-fit, anisotropic simulations are compared to the observed breakthrough curves in Figure 9-15. The observed and simulated breakthrough curves exhibit an excellent match. An anisotropy ratio of 7:1, a preferred T_x direction of N31°W (aligned parallel to the H-6b to H-6c path), and a matrix-block length of 0.15 m produced the best-fit simulations. The best-fit, anisotropic simulations were generated using the transport parameters given in Table 9-4.

Figure 9-16 provides the distribution of PFB and m-TFMB in the fractures and matrix during the tracer test and the mass of tracers recovered at the pumping well. Comparing this figure to Figure 9-14 shows that the distribution of mass between the matrix and fractures for the anisotropic simulation is very similar to the distribution for the heterogeneous simulation. Based on the simulated results, 83 percent of the PFB injected into H-6b and 19 percent of the m-TFMB injected into H-6a were recovered at the pumping well. The simulated mass recoveries for PFB and m-TFMB compare favorably with the mass recoveries of 80 and 20 percent, respectively, at the pumping well estimated from the observed breakthrough curves.

9.5 Analysis of Tracer-Breakthrough Curve for Convergent-Flow Tracer Test #2

Test #2 investigated only the path from H-6b to H-6c. Assuming isotropic conditions and using fracture porosity and matrix-block length as fitting parameters, the best-fit



Observed data pared for figure clarity.

Figure 9-15. Observed and best-fit simulated breakthrough curves for H-6 convergent-flow tracer test #1 using the anisotropic-analysis approach.

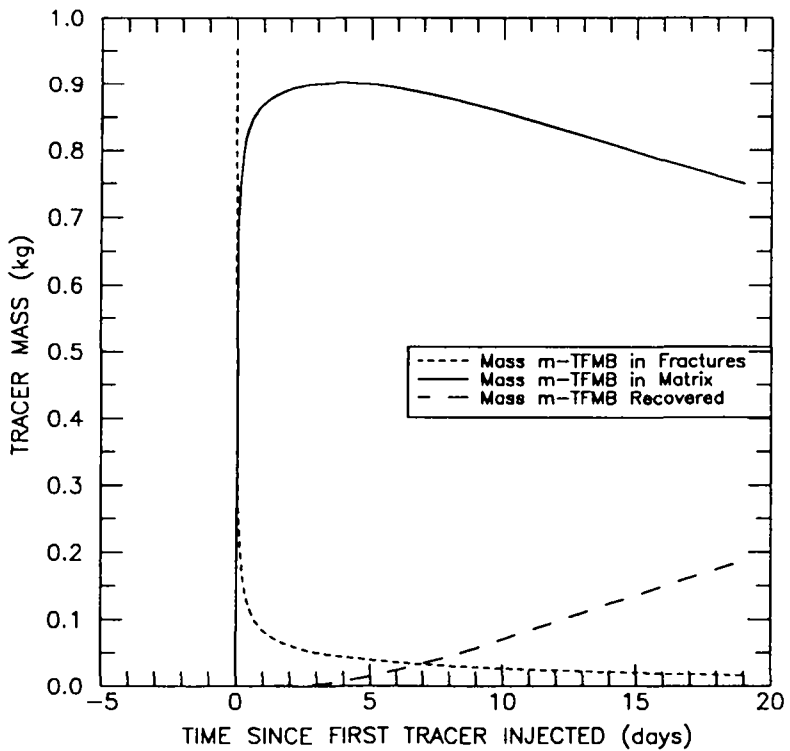
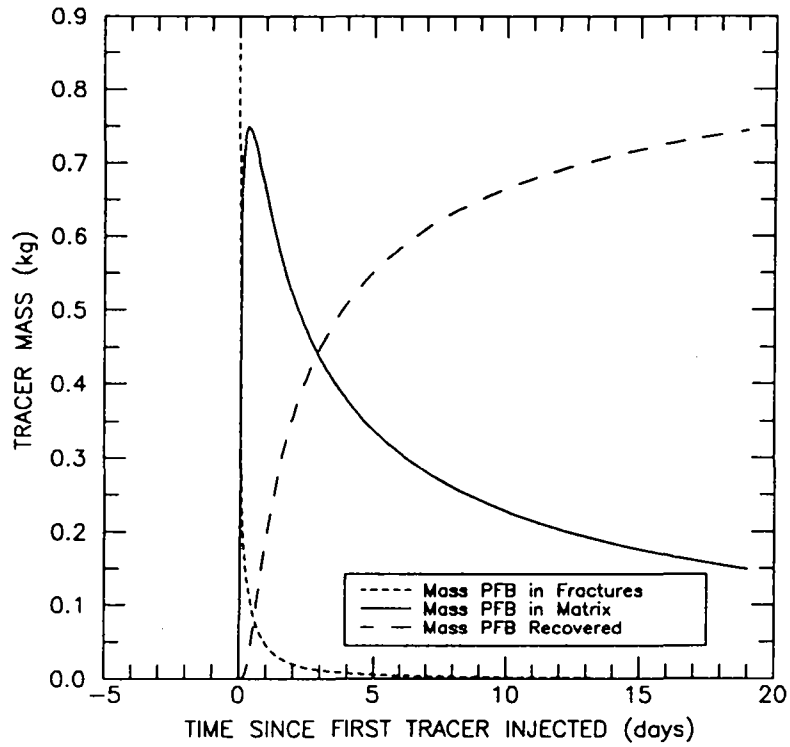


Figure 9-16. Mass distribution in the fractures and matrix and mass recovered at the pumping well for the best-fit anisotropic simulation of the test #1 tracer-breakthrough curves for the H-6 hydropad.

simulation presented in Figure 9-17 was generated. The values for the other input parameters are discussed in Section 5.0. The best-fit fracture porosity was 1.5×10^{-3} and the best-fit matrix-block length was 0.44 m. The transport parameters used in this simulation are presented in Table 9-5. The calculated inner and outer radii for the tracer-input zones (shown schematically in Figures 3-5 and 3-8) are 0.78 and 1.95 m, respectively, for tracer-injection well H-6b. The model discretized the path from H-6b to H-6c into 105 grid blocks and initial mass was distributed in the outer 10 grid blocks. The grid-block discretization for the flow path was identical to that used for test #1.

Theoretically, the best-fit, heterogeneous parameters determined for the test #1 PFB breakthrough curve should be identical to the best-fit parameters for the test #2 curve if the testing conditions were exactly identical. Comparing the results shows that the estimate of fracture porosity is the same but the interpreted matrix-block lengths exhibit a minor difference. The test #1 PFB curve and the test #2 curve were fit with matrix-block lengths of 0.41 and 0.44 m, respectively. The difference in the two block lengths is about 8 percent. The distribution of p-FB between the fractures and matrix during test #2 and the mass of p-FB recovered at the pumping well are illustrated in Figure 9-18. The simulation predicted 69 percent recovery for p-FB which compares well with the estimate of 63 percent recovery based on the observed tracer-breakthrough curve.

9.6 Sensitivity Analyses

The detailed sensitivity analysis on each parameter presented for the H-3 tracer test was not repeated for the H-6 test. For test #1, the base-case conditions were represented by the input parameters for the best-fit, anisotropic simulations. The input parameters for the best-fit heterogeneous simulation of test #2 represented the base-case conditions for the sensitivity analysis of that test. Sensitivity analysis on the H-6 tests focus on the effect of matrix-block length, the effect of anisotropy, and determination of uncertainty in interpreted matrix-block lengths.

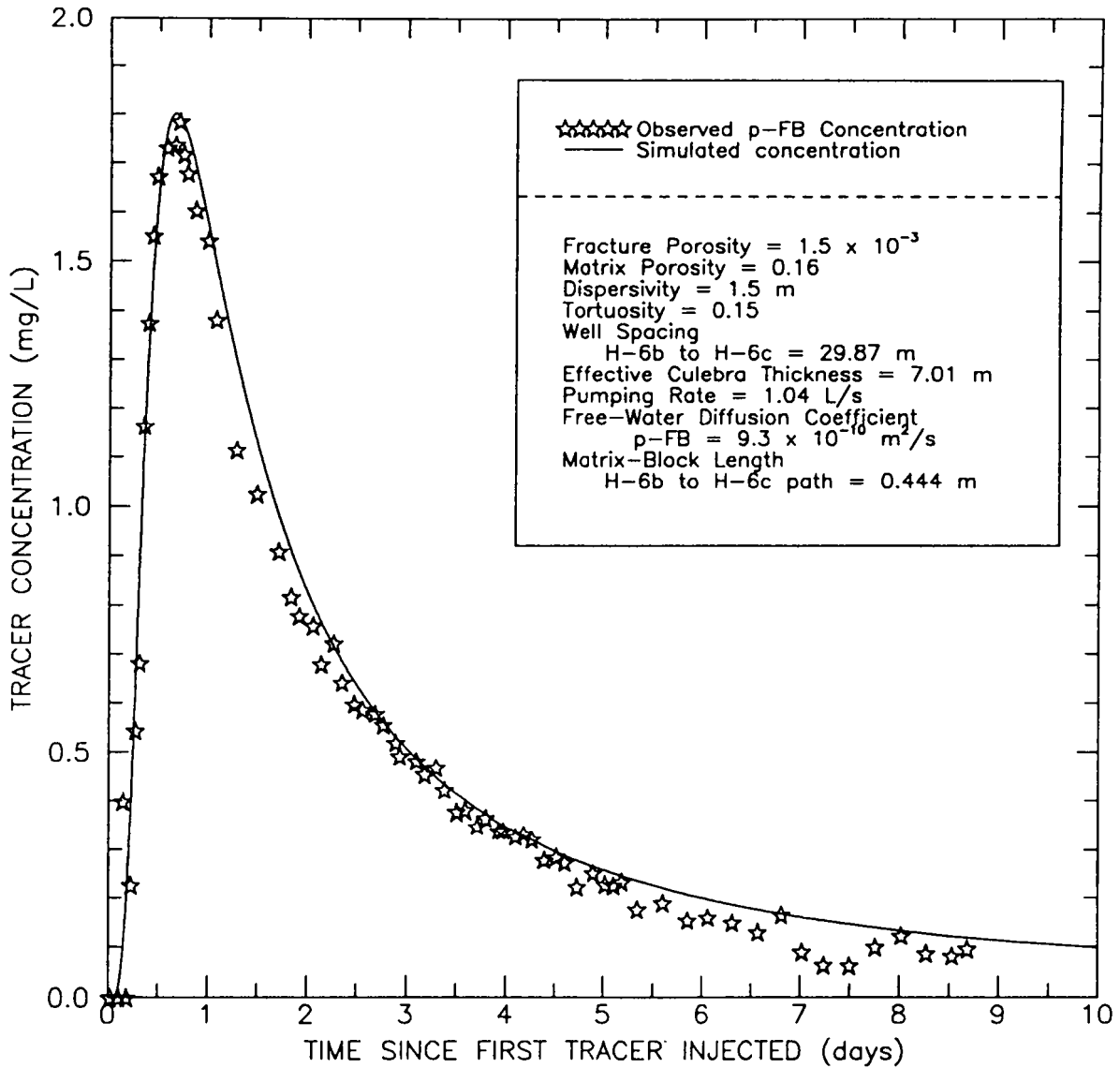


Figure 9-17. Observed and best-fit simulated breakthrough curve for H-6 convergent-flow tracer test #2 using the heterogeneous-analysis approach.

Table 9-5. Transport Parameters Used in the Interpretation of H-6 Convergent-Flow Tracer Test #2

Parameter	Value
Culebra Thickness	7.0 m
Well Spacing	29.9 m
Free-Water Diffusion Coefficient	$9.3 \times 10^{-10} \text{ m}^2/\text{s}$
Longitudinal Dispersivity	1.5 m
Tortuosity	0.15
Matrix Porosity	0.16
Fracture Porosity	1.5×10^{-3}
Matrix-Block Length	0.44 m
Anisotropy Ratio	1:1
Principal-Transmissivity Direction	na

na means not applicable

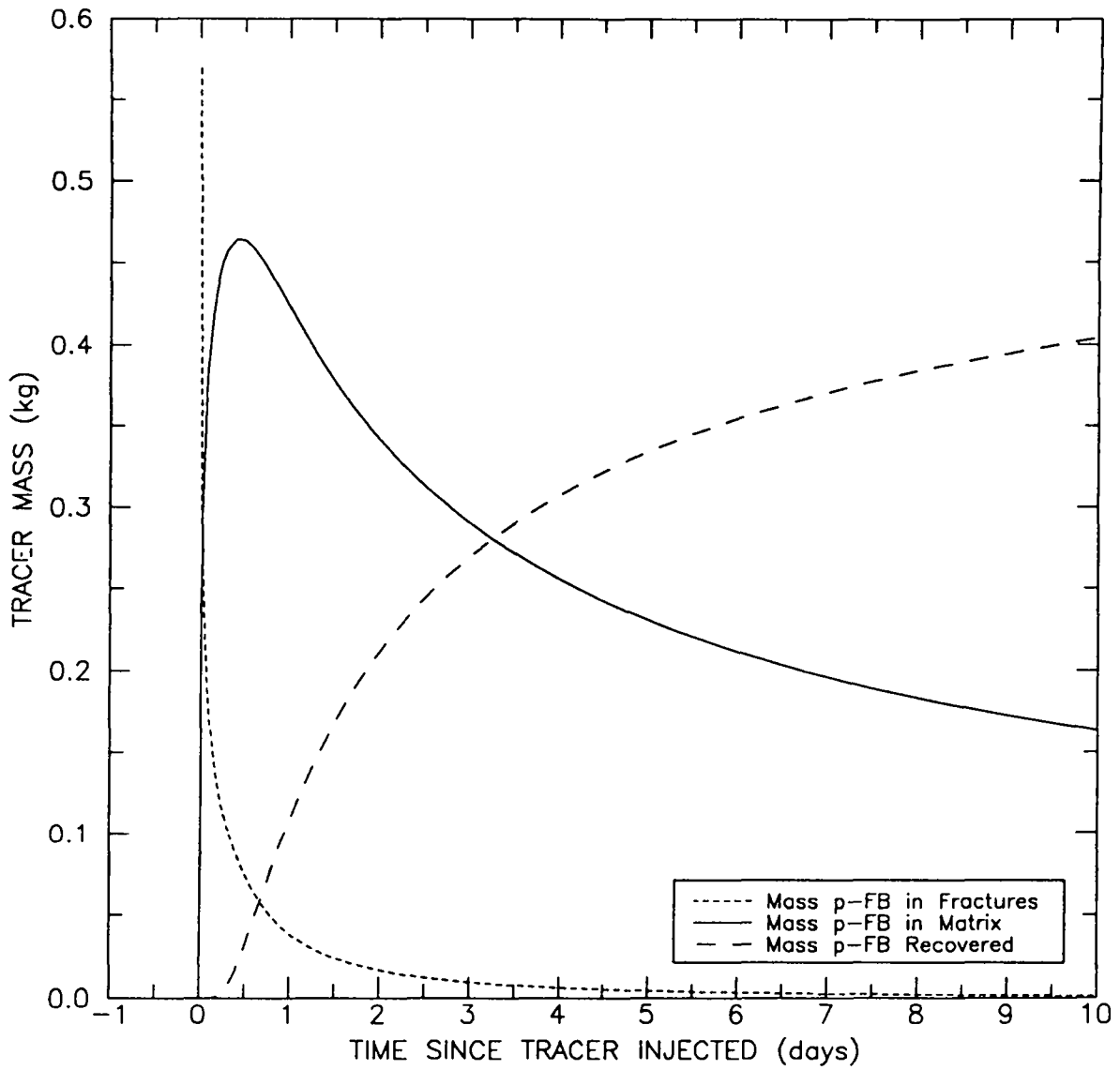
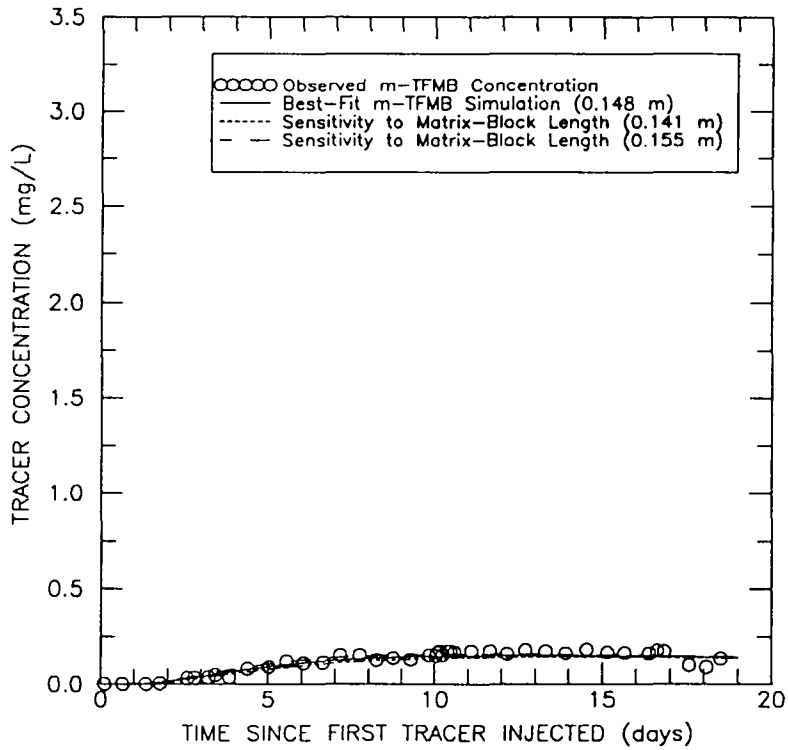
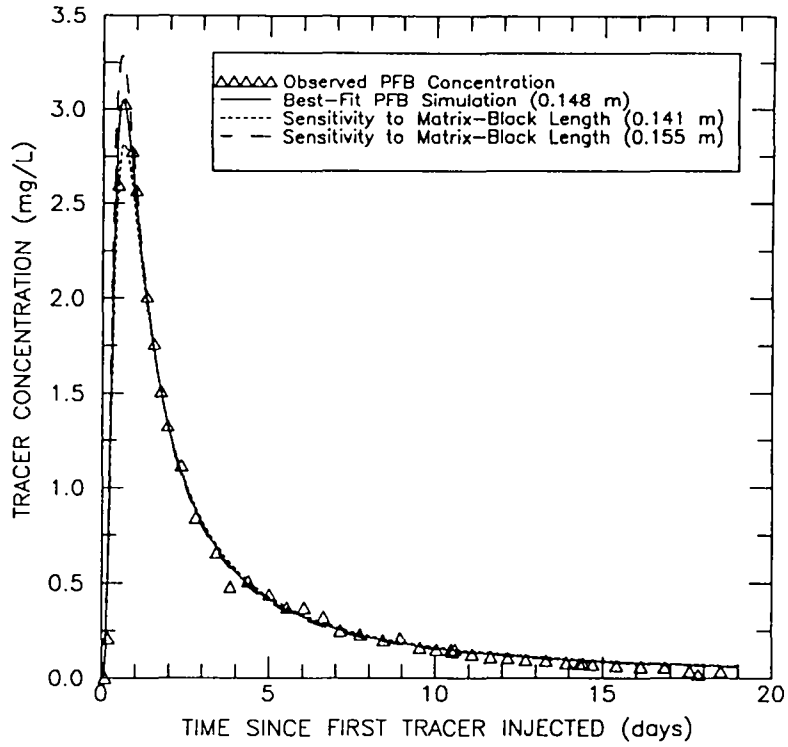


Figure 9-18. Mass distribution in the fractures and matrix and mass recovered at the pumping well for the best-fit heterogeneous simulation of the test #2 tracer-breakthrough curve for the H-6 hydropad.

9.6.1 Effect of Matrix-Block Length

Two matrix-block lengths were considered in the sensitivity analyses; one value five percent above and one value five percent below the base-case value. For test #1, the base-case value was 0.15 m and the two sensitivity values were 0.14 and 0.16 m. The base-case value was 0.44 m for test #2 and the sensitivity values were 0.42 m and 0.47 m. The results of the sensitivity to matrix-block length are illustrated in Figures 9-19 and 9-20 for tests #1 and #2, respectively. For the transport of PFB or p-FB on the path from H-6b to H-6c, small variations in the matrix-block length do not have much effect on the rising and falling limbs of the breakthrough curve but have a significant effect on the peak concentration. The effect of slight variations in matrix-block length for the transport of m-TFMB on the path from H-6a to H-6c is small.

Matrix-block length and tortuosity are related in the independent parameter group referred to as the characteristic matrix-diffusion time (Equation 5-13). Using this relationship, the uncertainty in matrix-block length due to uncertainty in the assigned value for tortuosity can be determined. With all other parameters and the value for the characteristic matrix-diffusion time held constant, Equation 5-13 can be used to calculate the corresponding value of matrix-block length needed to yield identical simulated results. For the best-fit anisotropic simulation, the characteristic matrix-diffusion time is 1.6 yrs for PFB and m-TFMB. Section 5.1.7 discusses an estimated range of 0.027 to 0.38 for tortuosity of the Culebra at the WIPP site. Substituting the end members of this range into Equation 5-13 yields matrix-block lengths of 0.06 m for a tortuosity of 0.027 and 0.24 m for a tortuosity of 0.38, respectively. This exercise indicates that the matrix-block length required to reproduce the best-fit anisotropic simulation ranges from 0.06 to 0.24 m for a tortuosity range of 0.027 to 0.38. Therefore, the uncertainty in the best-fit matrix-block length (0.15 m) for the anisotropic simulation based on uncertainty in the assigned value of 0.15 for tortuosity is -0.09 to +0.09 m.



Observed data pared for figure clarity.

Figure 9-19. Sensitivity to matrix-block length for H-6 convergent-flow tracer test #1.

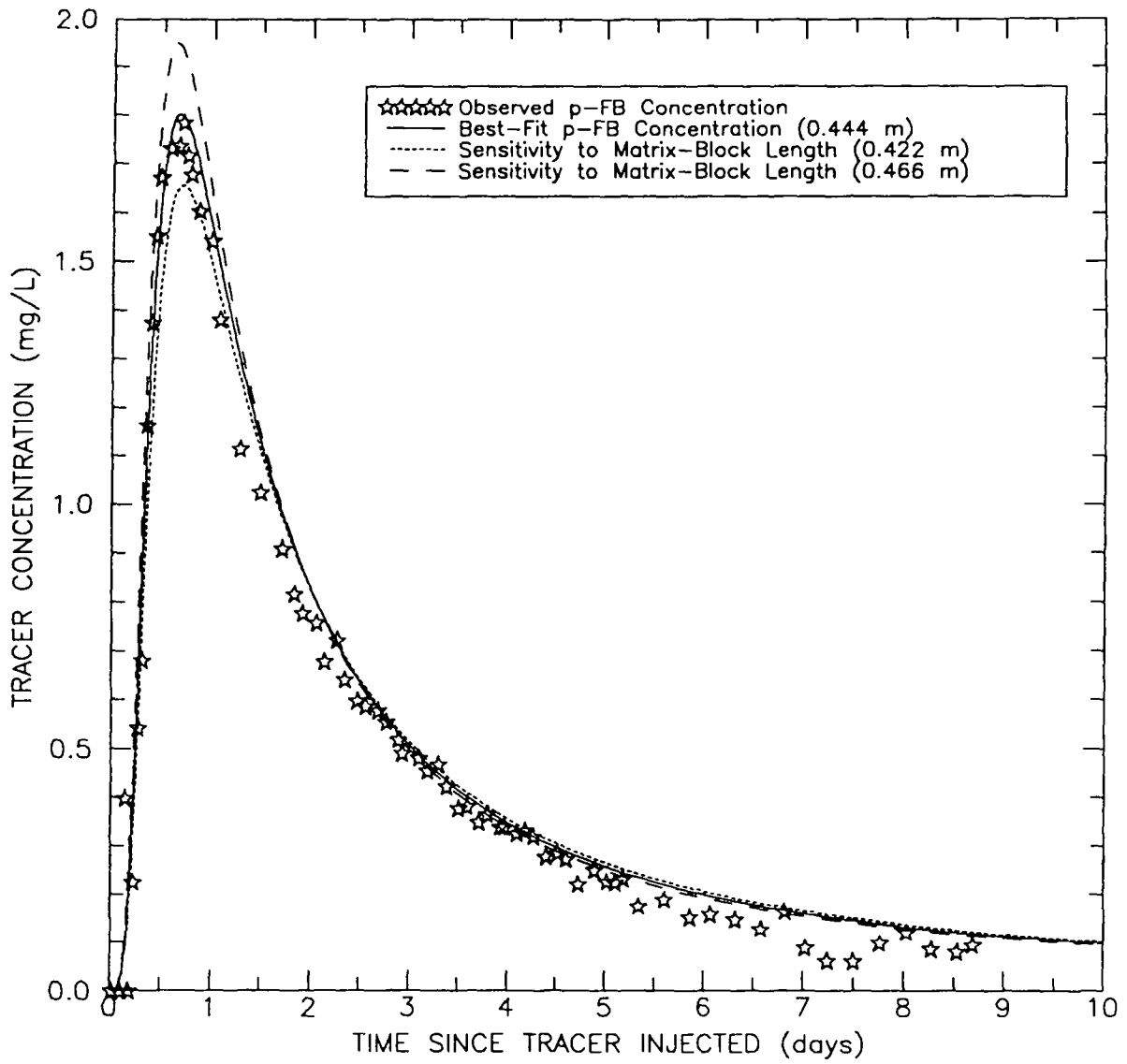


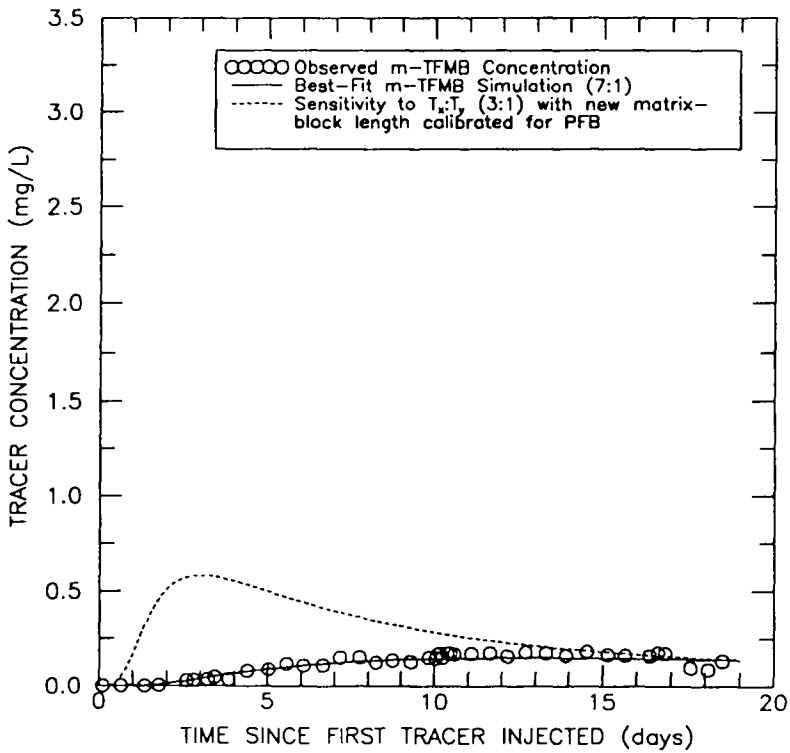
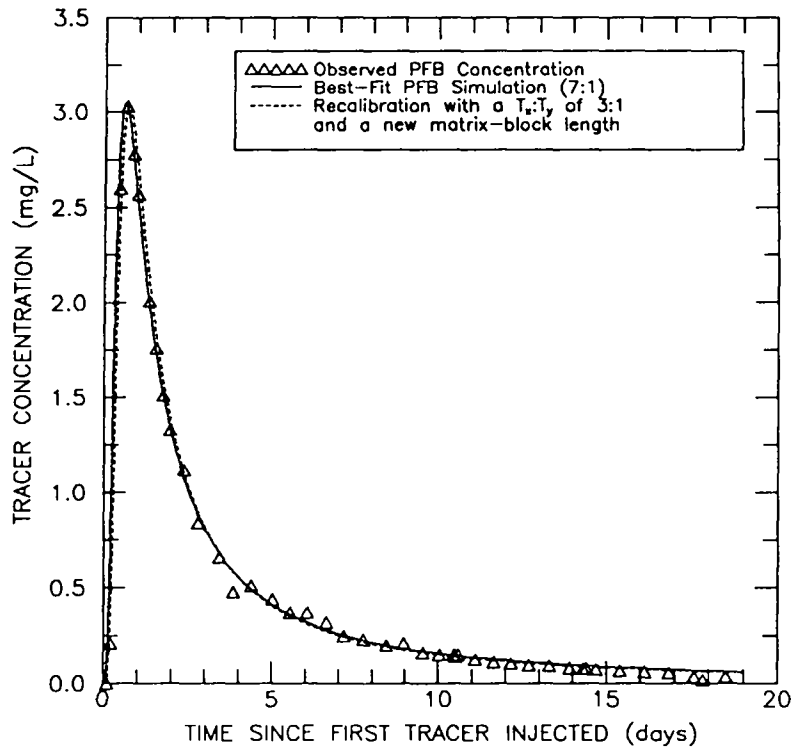
Figure 9-20. Sensitivity to matrix-block length for H-6 convergent-flow tracer test #2.

9.6.2 Effect of Anisotropy Ratio

The approach taken in the investigation of the sensitivity of the H-6 simulations to anisotropy ratio is the same as that described for the H-3 tracer test with PFB substituting for m-TFMB and m-TFMB substituting for PFB in the discussion in Section 7.5.7. For this sensitivity analysis, the best-fit anisotropy ratio is 7:1 and the sensitivity anisotropy ratio is 3:1. Figure 9-21 illustrates that both the PFB and m-TFMB breakthrough curves cannot be matched with a $T_x:T_y$ of 3:1. Through a series of simulations using a range of anisotropy ratios from 3:1 to 10:1, it was concluded that only a $T_x:T_y$ value of 7:1 generates simulated results that match both the PFB and m-TFMB breakthrough curves.

9.6.3 Determination of Maximum and Minimum Matrix-Block Lengths

A set of sensitivity analyses was conducted to estimate the maximum and minimum matrix-block lengths in order to further characterize uncertainty in this important fitted parameter at the H-6 hydropad. In order for the simulation to require a maximum matrix-block length to fit the observed data, the assigned transport parameters must be given values which ensure maximum diffusion of solute from the fractures into the matrix. If diffusive losses are maximized, the surface area available for diffusion must be reduced by increasing the matrix-block length in order to maintain the same breakthrough curve. On the other hand, a combination of assigned parameters which results in less matrix diffusion would need to be counterbalanced by decreasing the matrix-block length and subsequently increasing the surface area available for diffusion of mass from the fractures into the matrix. The degree of increase or decrease in the simulated matrix diffusion was constrained by the end-member values for the fixed transport parameters as discussed in Section 5.0. The sensitivity simulation with parameters assigned to result in maximum matrix diffusion used the maximum values for tortuosity, matrix porosity, well spacing, effective Culebra thickness, free-water diffusion coefficient, and longitudinal dispersivity and the minimum value for pumping rate. Minimizing matrix diffusion was initially simulated by assigning minimum



Observed data pared for figure clarity.

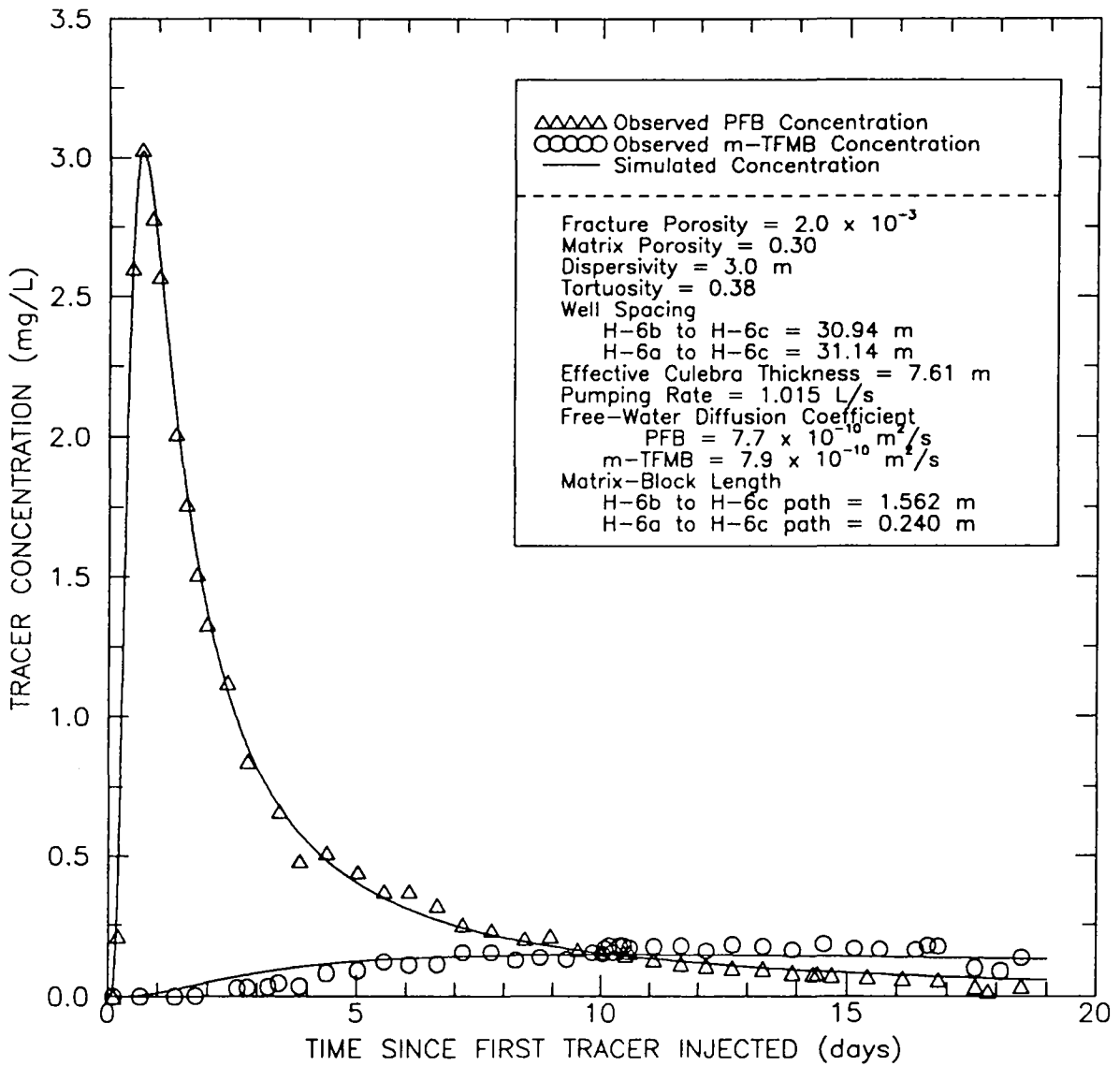
Figure 9-21. Sensitivity to horizontal anisotropy ($T_x:T_y$) for H-6 convergent-flow tracer test #1.

values for tortuosity, matrix porosity, well spacing, effective Culebra thickness, free-water diffusion coefficient, and longitudinal dispersivity and a maximum value for pumping rate. For that combination of parameters, the observed m-TFMB concentration data could not be matched and, therefore, a minimum matrix-block length could not be defined for the path from H-6a to H-6c. A good match between the observed and simulated m-TFMB data required an increase in the matrix porosity from 0.08 to 0.30 and an increase from 2 to 4.5 m in effective Culebra thickness. The values for each parameter used in this sensitivity analysis are summarized in Table 9-6.

The sensitivity interpretations used the heterogeneous-analysis approach since that approach yields the upper bound on the matrix-block length through calibration to the rapid-transport breakthrough curve and the lower bound on the matrix-block length through calibration to the slow-transport breakthrough curve. For both sensitivity simulations (i.e., maximizing and minimizing matrix diffusion), the fitting parameters were fracture porosity and matrix-block length for the rapid-transport breakthrough curve and matrix-block length only for the slow-transport breakthrough curve. The simulated breakthrough curves for the case of maximizing matrix diffusion are compared to the observed breakthrough curves in Figure 9-22. The sensitivity analysis yielded a fracture porosity of 2.0×10^{-3} and matrix-block lengths of 1.56 and 0.24 m for the H-6b to H-6c and the H-6a to H-6c paths, respectively. Using transport parameters that minimized matrix diffusion, the observed PFB and m-TFMB breakthrough curves were matched using a fracture porosity of 2.2×10^{-3} and matrix-block lengths of 0.18 and 0.03 m for the H-6b to H-6c path and the H-6a to H-6c path, respectively (Figure 9-23). In summary, this sensitivity analysis indicated a maximum matrix-block length of 1.56 m and a minimum matrix-block length of 0.03 m at the H-6 hydropad.

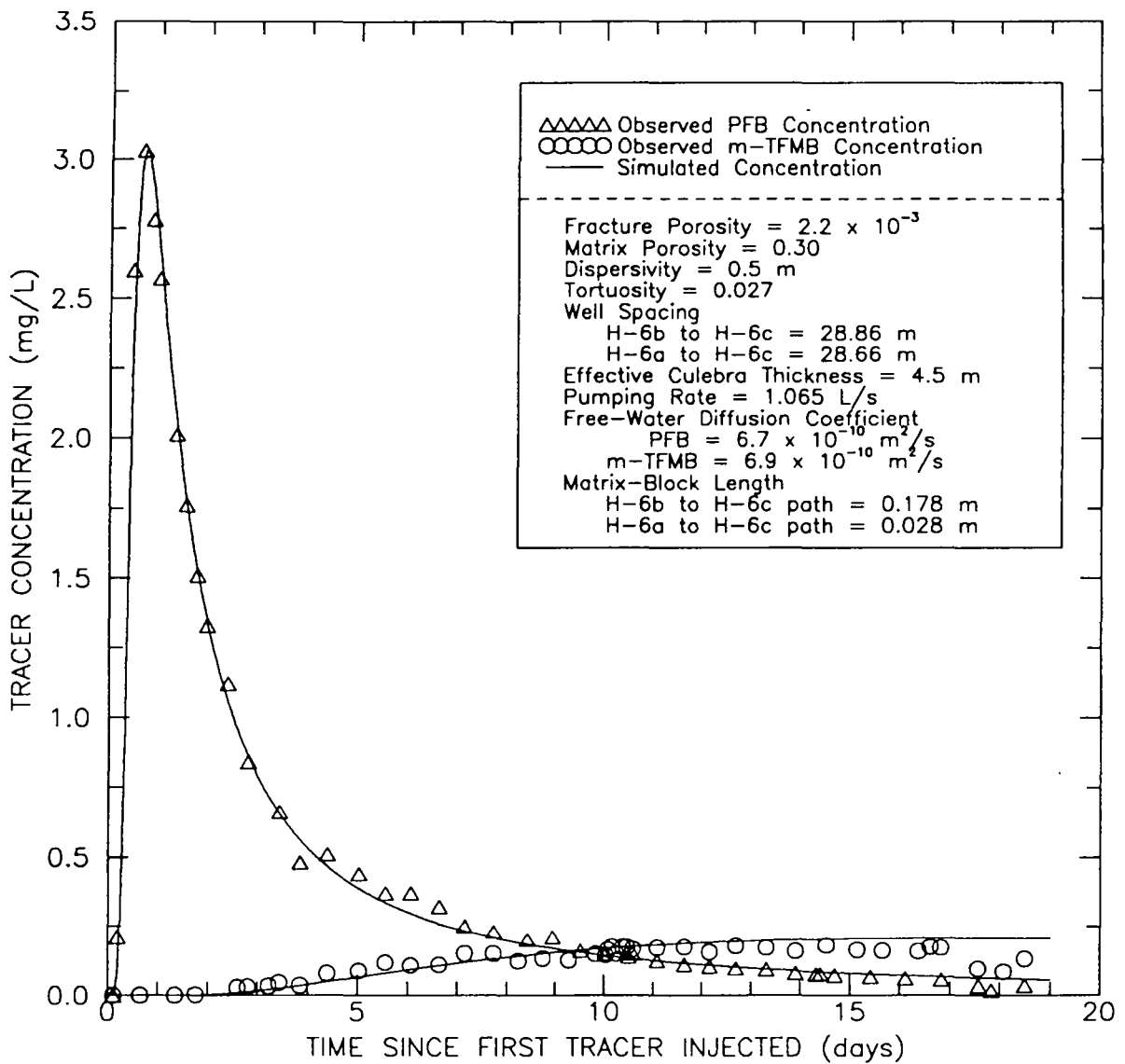
Table 9-6. Transport Parameters Used in the Sensitivity Analysis to Determine the Maximum and Minimum Matrix-Block Lengths at the H-6 Hydropad

Parameter	Sensitivity Analysis to Determine Maximum Matrix-Block Length		Sensitivity Analysis to Determine Minimum Matrix-Block Length	
Effective-Culebra Thickness	7.6 m		4.5 m	
Well Spacings	30.9 m	H-6b to H-6c	28.9 m	H-6b to H-6c
	31.1 m	H-6a to H-6c	28.7 m	H-6a to H-6c
Free-Water Diffusion Coefficients	m-TFMB	$7.9 \times 10^{-10} \text{ m}^2/\text{s}$	m-TFMB	$6.9 \times 10^{-10} \text{ m}^2/\text{s}$
	PFB	$7.7 \times 10^{-10} \text{ m}^2/\text{s}$	PFB	$6.7 \times 10^{-10} \text{ m}^2/\text{s}$
Longitudinal Dispersivity	3.0 m		0.5 m	
Tortuosity	0.38		0.027	
Matrix Porosity	0.30		0.30	
Fracture Porosity	2.0×10^{-3}		2.2×10^{-3}	
Matrix-Block Length	1.56 m	H-6b to H-6c	0.18 m	H-6b to H-6c
	0.24 m	H-6a to H-6c	0.03 m	H-6a to H-6c



Observed data pared for figure clarity.

Figure 9-22. Sensitivity recalibration to observed tracer breakthrough at the H-6 hydropad to obtain maximum matrix-block lengths.



Observed data pared for figure clarity.

Figure 9-23. Sensitivity recalibration to observed tracer breakthrough at the H-6 hydropad to obtain minimum matrix-block lengths.

9.7 Summary of Results for H-6

Five convergent-flow tracer tests and two two-well recirculating tests were conducted at the H-6 hydropad from August 1981 to July 1983. After careful examination of the data collected from all of these tests, it was determined that only the PFB and m-TFMB results from convergent-flow test #1 and the results from convergent-flow test #2 were reliable. The two breakthrough curves from test #1 differ significantly. PFB, which traveled from H-6b to H-6c, broke through rapidly, had a sharp peak concentration, and tailed notably. The breakthrough curve for the tracer that traveled from H-6a to H-6c (m-TFMB) rose gradually and did not produce a well-defined peak. Test #2 also investigated the path from H-6b to H-6c by injecting the tracer p-FB into H-6b and pumping H-6c. Like the PFB breakthrough curve, the p-FB curve rose rapidly, peaked sharply, and tailed significantly. The differences between the test #1 breakthrough curves were interpreted using two approaches. The first approach assumed that heterogeneity between the different flow paths, in the form of matrix-block length (or surface area available for matrix diffusion), could explain the differences. Anisotropy in horizontal transmissivity was used to explain the differences with the second approach. For test #2, where only one path was investigated, the test was interpreted by fitting the observed concentrations with fracture porosity and matrix-block length, assuming isotropic transmissivity.

The matrix-block lengths determined for the paths from H-6b to H-6c and H-6a to H-6c using the heterogeneous approach to analyze the test #1 curves were 0.41 and 0.06 m, respectively. Analysis of the test #2 breakthrough curve yielded a matrix-block length of 0.44 m for the path from H-6b to H-6c. The two matrix-block lengths determined for the H-6b to H-6c path were not identical; they differed by 8 percent and had an average of 0.43 m. The block lengths determined for the two travel paths are consistent with the shapes of the observed breakthrough curves. A larger matrix-block length results in a smaller matrix-surface area and less diffusion of solute from the fractures to the matrix while a smaller matrix-block length results in more matrix diffusion because there is more

matrix-surface area. The fracture porosity determined from the heterogeneous analysis of tests #1 and #2 was 1.5×10^{-3} .

For test #1, an anisotropy ratio of 7:1, a T_x orientation of N31° W (aligned parallel to the H-6b to H-6c path), and a matrix-block length of 0.15 m yielded simulated breakthrough curves that closely matched the observed tracer concentrations. The two matrix-block lengths determined using the heterogeneous-analysis approach bound the length determined using the anisotropic-analysis approach. The interpreted anisotropy ratio of 7:1 is greater than the hydraulic testing based values of 1.91:1 reported by Neuman et al. (1984) and 2.1:1 reported by Gonzalez (1983). The orientation of the maximum principal direction reported here (N31° W or parallel to the path from H-6b to H-6c) is almost identical to the principal-transmissivity directions of N29.6° W reported by Neuman et al. (1984) and N29° W reported by Gonzalez (1983).

Sensitivity analyses were conducted on matrix-block length and anisotropy ratio. For the rapid-transport path (H-6b to H-6c), a slight change in matrix-block length has a significant effect on the peak concentration but little effect on the rising and falling limbs of the breakthrough curve. A slight variation in matrix-block length has a small effect on the m-TFMB breakthrough curve. Examination of a range in anisotropy ratio from 3:1 to 10:1 indicated that both breakthrough curves at the H-6 hydropad could be matched only with a ratio of 7:1. The sensitivity analyses conducted to determine the maximum and minimum matrix-block lengths for the H-6 hydropad yielded high- and low-end values of 1.56 and 0.03 m, respectively. The maximum and minimum matrix-block lengths can be viewed as a measure of the uncertainty in this fitting parameter because the sensitivity analysis included uncertainty in the assigned parameters.

10.0 H-11 HYDROPAD TRACER TEST

A four well convergent-flow tracer test was conducted at the H-11 hydropad from May to July 1988. Discussed in the follow sections are the well configurations, hydropad hydrogeology, tracer-test history, analysis of the tracer test, sensitivity analyses, and a summary of the results.

10.1 Well Configurations

The H-11 hydropad, located in the southeast portion of the WIPP site (Figure 1-2), consists of four wells, H-11b1, H-11b2, H-11b3, and H-11b4, completed to the Rustler Formation. Three of the wells, H-11b1, H-11b2, and H-11b3, are arranged in an approximate equilateral triangle with about 22-m sides (Figure 10-1). The fourth well, H-11b4, is positioned about 43 m to the west of the triangle. All four wells are located in Section 33, Township 22 south, and Range 31 east. The UTM coordinates, ground-surface elevations, and top-of-casing elevations for the H-11 hydropad wells are summarized in Table 10-1. The relative positions of the wells at the depth of the Culebra dolomite are illustrated in Figure 10-1.

H-11b1 was drilled and cored in August 1983 (Mercer, 1990). The well was drilled to a depth of 213.4 m BGS with a 20-cm (7-7/8-inch) bit and cored to a depth of 239.3 m BGS with a 12.07-cm (4-3/4-inch) bit. After coring, the cored section of the borehole to a depth of 223.4 m was reamed to a diameter of 20 cm. The borehole was then cased with 13.97-cm (5-1/2-inch) casing that was set and cemented from the surface to 223.1 m BGS. A 12.07-cm bit was then used to drill out the cement and clean the hole from 223.1 m BGS to the total depth of 239.3 m BGS.

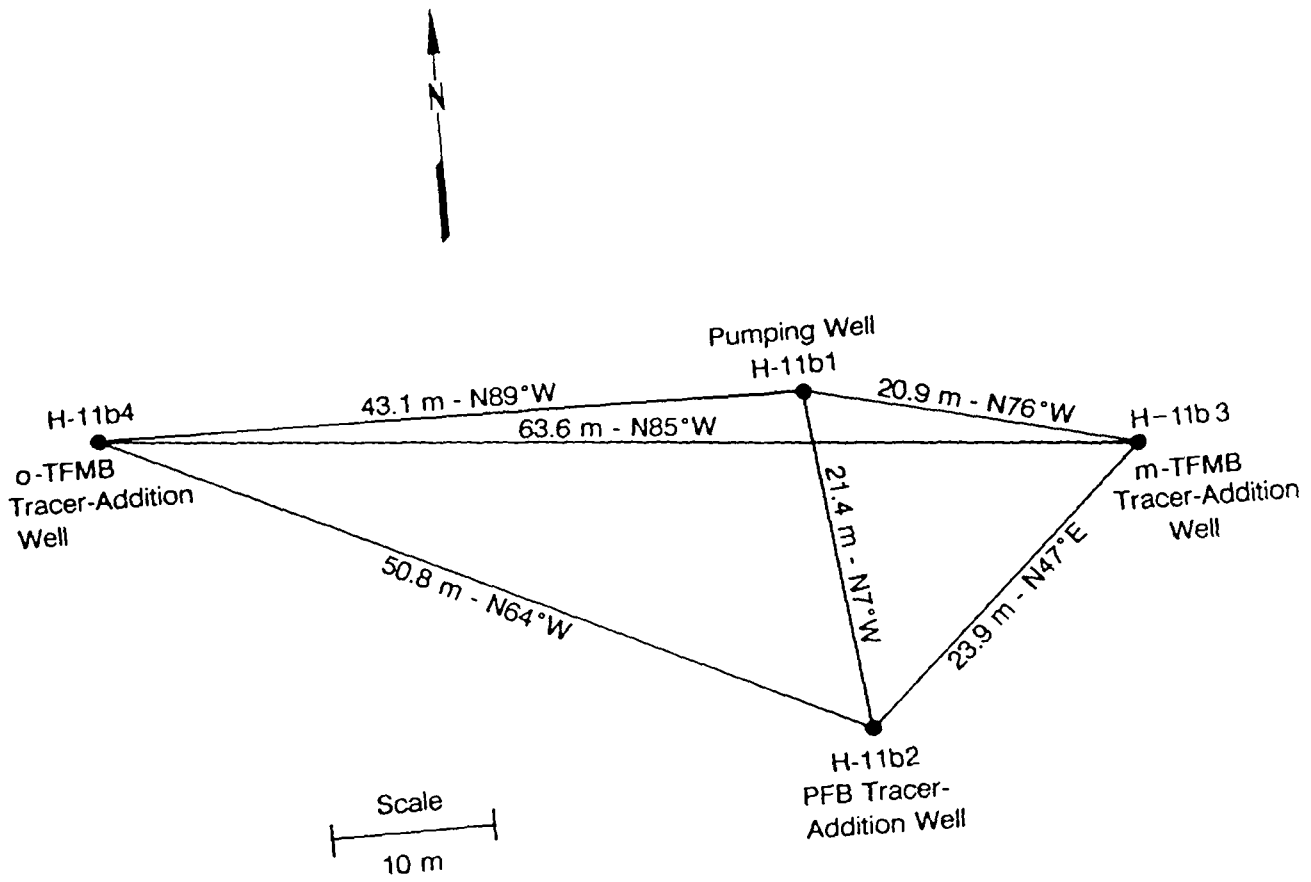


Figure 10-1. Plan view of the wells at the H-11 hydropad showing distances between wells at the center of the Culebra.

Table 10-1. UTM Coordinates, Ground-Surface Elevations, and Top-of-Casing Elevations for the H-11 Hydropad Wells

Well	UTM Coordinates		Ground-Surface Elevation (m amsl)	Top-of-Casing Elevation (m amsl)
	m East	m North		
H-11b1	615,346	3,579,130	1039.67	1039.87
H-11b2	315,348	3,579,107	1039.73	1039.88
H-11b3	615,367	3,579,127	1039.98	1040.12
H-11b4	315,301	3,579,131	1039.37	1039.65

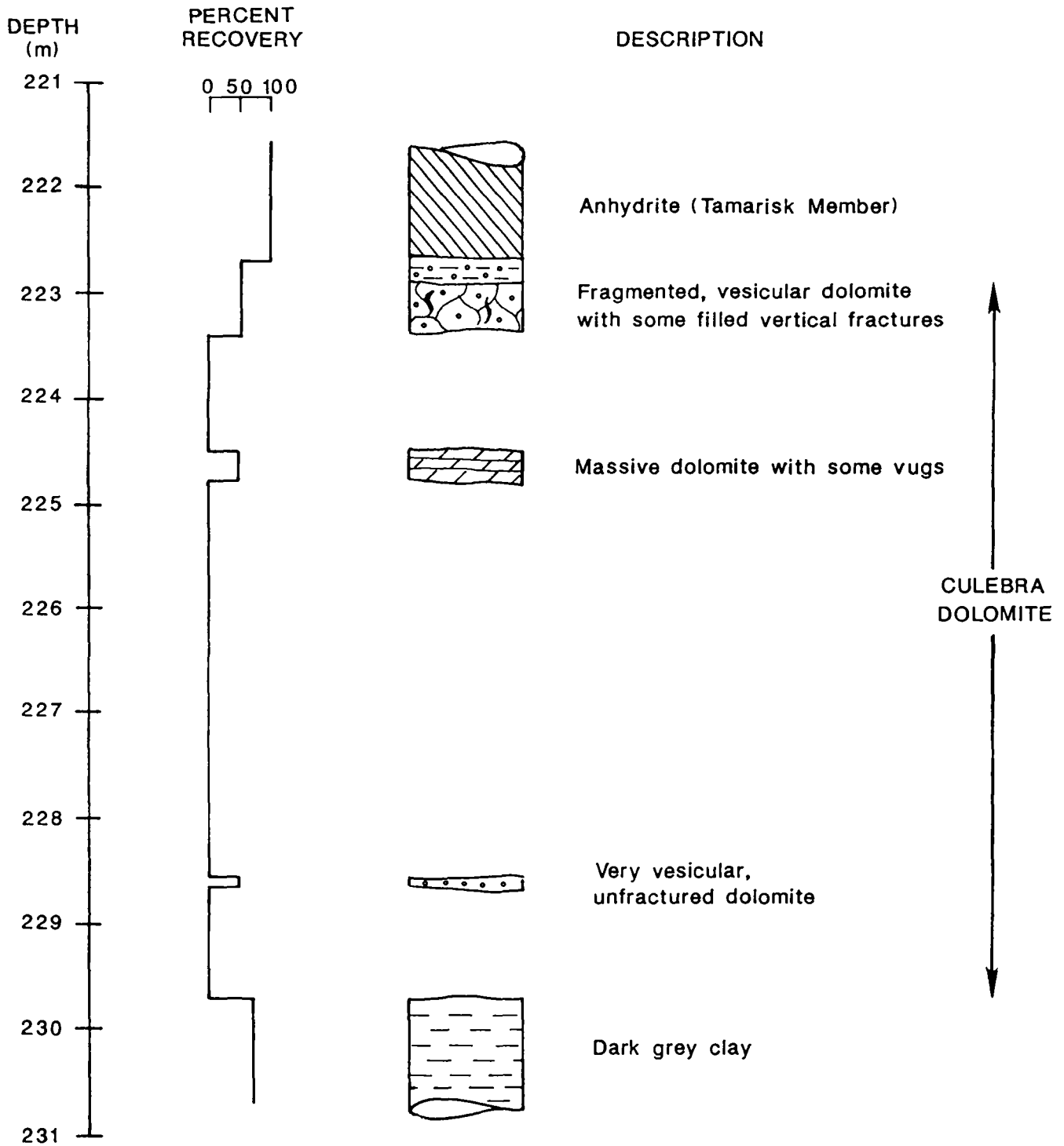
H-11b2 was drilled and cored to a total depth of 236.5 m BGS in November 1983 (Mercer, 1990). After coring, the cored section of the borehole to a depth of 223.7 m was reamed to a diameter of 20 cm and 13.97-cm casing was set and cemented from the surface to 223.5 m BGS. The cement fill was drilled out and the hole was cleaned from 223.5 m BGS to the total depth using a 12.07-cm bit. H-11b2 is completed open hole (12.1-cm diameter) from 223.5 to 236.5 m BGS.

H-11b3 was drilled to 18.3 m and cored from 18.3 m to the total depth of 240.4 m BGS in December 1983 and January 1984 (Mercer, 1990). After coring at a diameter of 12.07 cm, the borehole was reamed to a diameter of 20 cm to 223.7 m and 13.97-cm casing was set and cemented from the surface to 223.4 m BGS. The cement fill was then drilled out and the borehole was cleaned using a 12.07-cm bit. The lower 16.5 m of H-11b3 is completed open hole and has a diameter of 12.1 cm.

H-11b4, constructed in February and March 1988, was initially drilled with a 20-cm bit to a depth of 217.6 m BGS and cased with 13.97-cm casing that was set and cemented from the surface to 217.6 m BGS (Mercer, 1990). The cement plug was then drilled out and the borehole was cored through the Culebra interval to a total depth of 233.2 m BGS using a 11.43-cm (4-1/2-inch) core bit. After coring, the 15.5 m open-hole section of the borehole was reamed to a diameter of 12.1 cm.

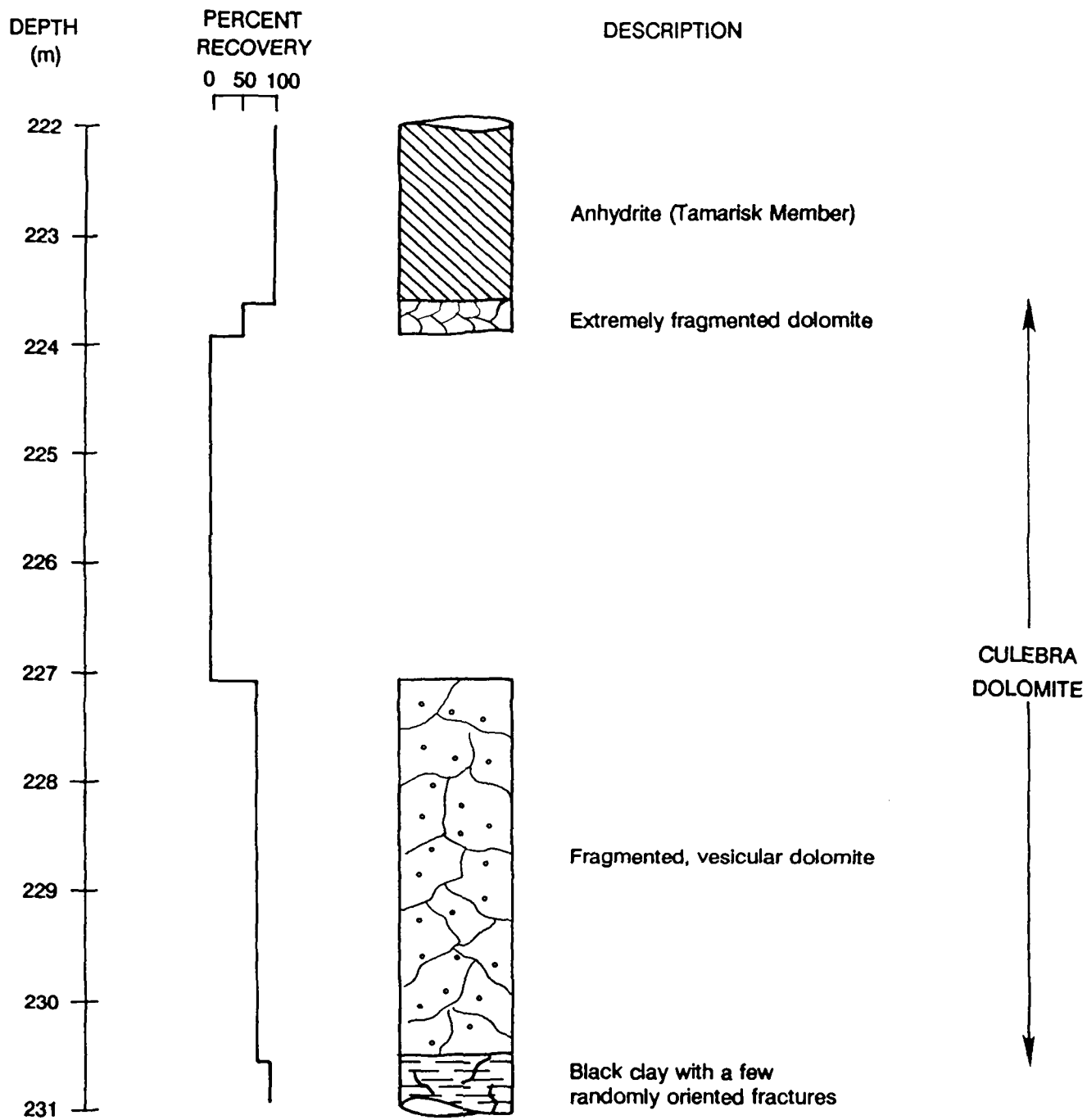
10.2 Local Hydrogeology

The Culebra is a 7.0 to 7.9-m thick massive to vuggy, argillaceous dolomite with varying amounts of silt at the H-11 hydropad. The Culebra interval was cored in wells H-11b1, H-11b2, H-11b3, and H-11b4. Core recovery at the first three wells was poor. Based on an examination of the H-11 core located in the Department of Energy Core Library at the WIPP site, Figures 10-2 through 10-5 were created. Core recovery of



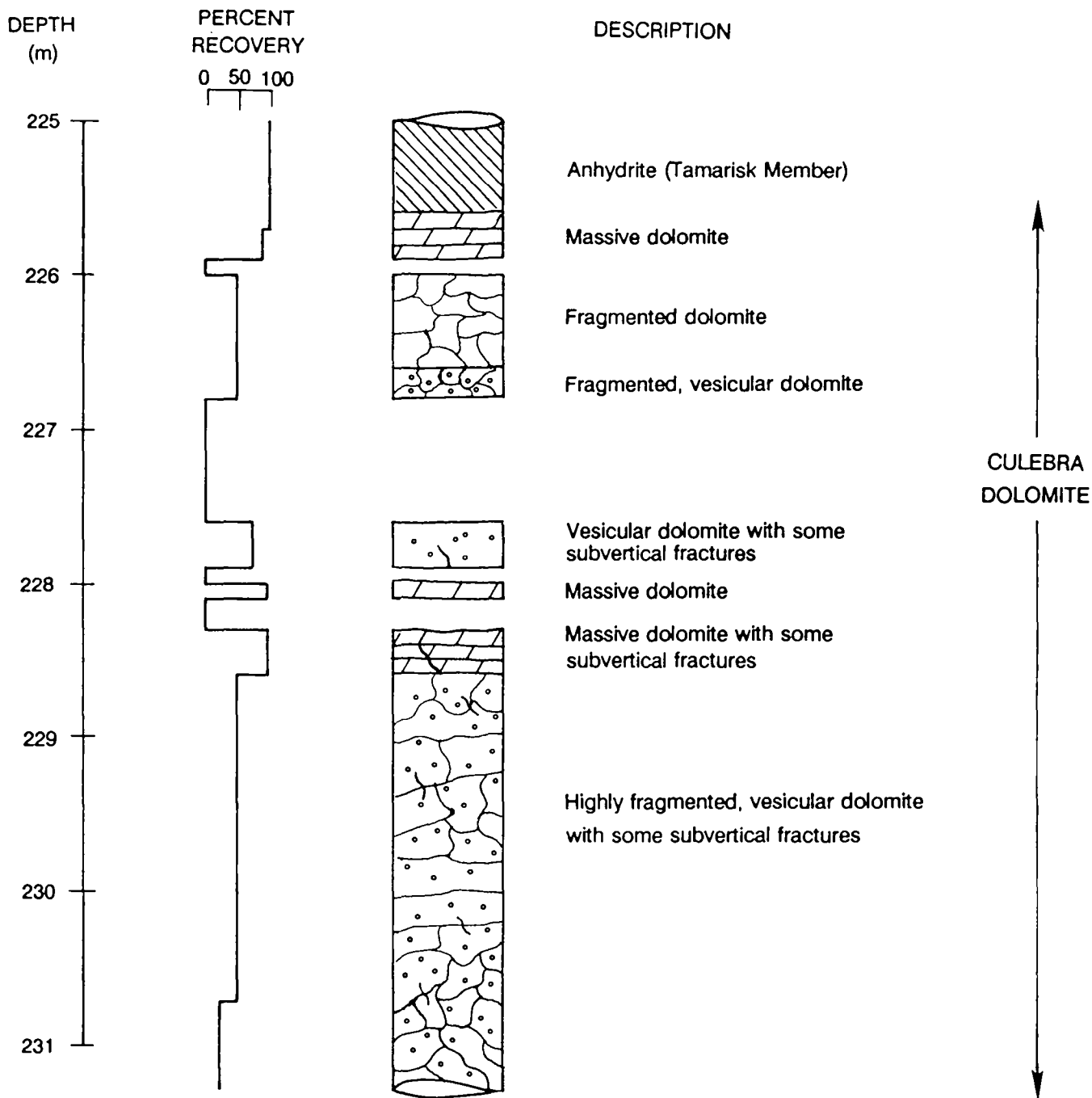
NOTE: Depths here correspond to depths reported on core.

Figure 10-2. Results of core examination of the Culebra dolomite from borehole H-11b1.



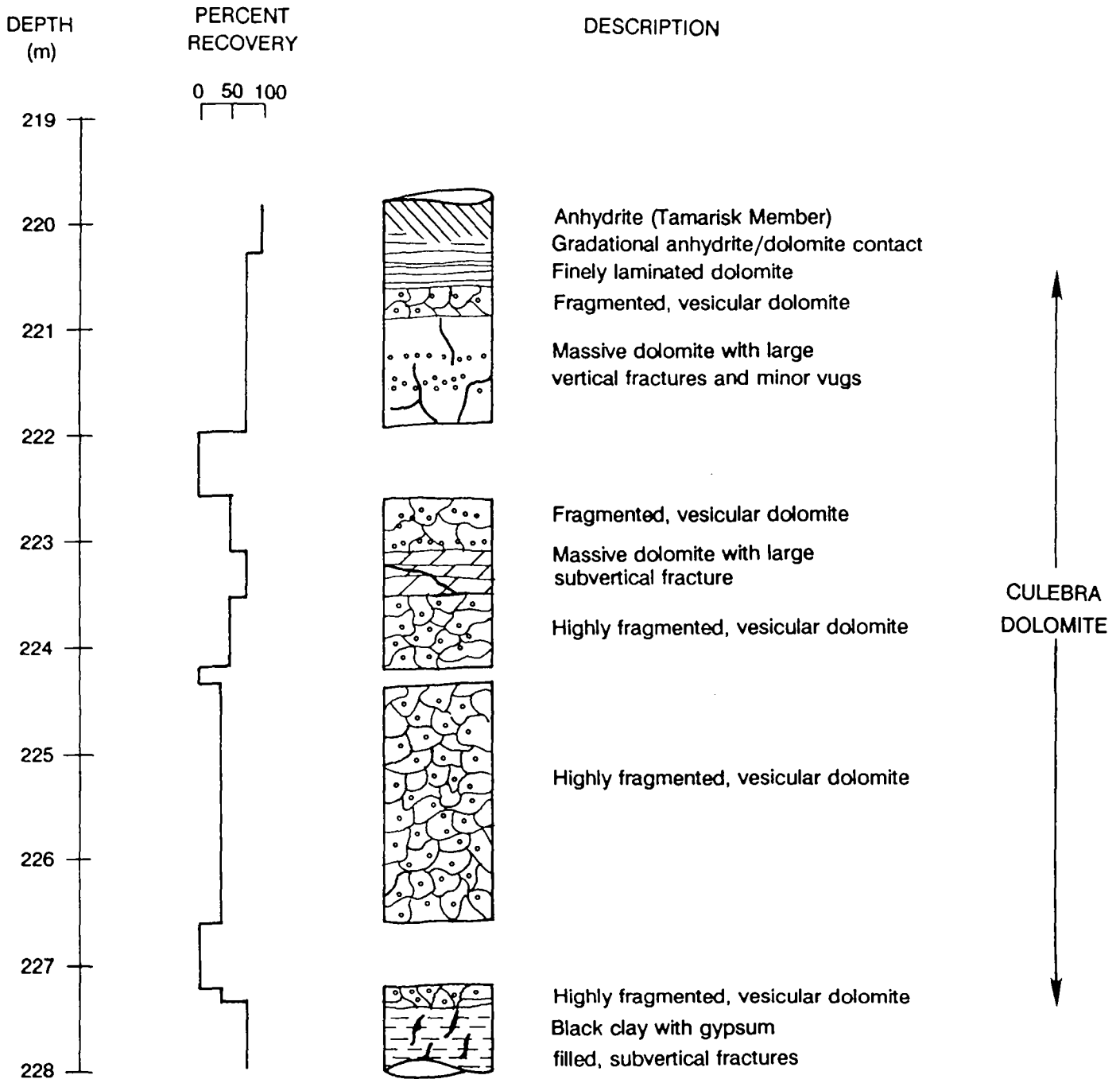
NOTE: Depths here correspond to depths reported on the core.

Figure 10-3. Results of core examination of the Culebra dolomite from borehole H-11b2.



NOTE: Depths here correspond to depths reported on the core.

Figure 10-4. Results of core examination of the Culebra dolomite from borehole H-11b3.



NOTE: Depths here correspond to depths reported on the core.

Figure 10-5. Results of core examination of the Culebra dolomite from borehole H-11b4.

approximately 15 percent at H-11b1, 40 percent at H-11b2 and H-11b3, and 80 percent at H-11b4 suggests a high degree of fracturing, vugs, and/or poor induration due to a high silt content. The majority of the recovered core is fragmented and highly vesicular with abundant open fractures.

In an effort to determine the hydraulic properties of the Culebra dolomite at the H-11 hydropad, both pumping tests and slug tests have been conducted at that site. A discussion of some of these tests can be found in Beauheim (1989) and Saulnier (1987). Using data from these tests, Cauffman et al. (1990) estimated an average transmissivity of $3.1 \times 10^{-5} \text{ m}^2/\text{s}$ for the Culebra dolomite at the H-11 hydropad.

The Culebra dolomite at the H-11 hydropad was hydrologically evaluated in 1984 and 1985 with a series of pumping tests. Each of the three wells (H-11b4 had not been drilled at this time) was pumped for a period ranging from 12 to 21 hrs. The fluid-pressure responses were monitored in the two non-pumping wells. Saulnier (1987) analyzed these tests using the method of Hantush (1966) to determine the degree of anisotropy at the H-11 hydropad. He calculated a ratio of maximum to minimum transmissivity vectors of 1.6:1 with the average maximum transmissivity vector oriented N84.2°E and the average minimum transmissivity vector oriented N5.8°W. The ranges of the maximum and minimum principal directions determined by Saulnier (1987) are illustrated in Figure 5-4. Interpretation of the 1984 and 1985 pumping tests indicated that the Culebra behaves as a double-porosity medium at the H-11 hydropad (Saulnier, 1987).

Two observations suggest that well H-11b2 may not be as well connected hydraulically to the Culebra as the other three wells at the H-11 hydropad. First, well-development pumping was performed in the wells at the H-11 hydropad in late 1987 and early 1988 in preparation for the H-11 multipad pumping and convergent-flow tracer tests. Well H-11b2 was initially intended to be the pumping well for the test but, perhaps because of problems with infilling of material from below the Culebra interval, it could not sustain the designed pumping rate of 0.32 to 0.38 L/s. In comparison, wells H-11b1, H-11b3, and

H-11b4 were capable of sustaining pumping rates greater than 0.38 L/s. Second, during tracer injection to wells H-11b2, H-11b3, and H-11b4, the observed pressure increase in well H-11b2 (0.942 MPa) was higher than in H-11b3 (0.011 MPa) or H-11b4 (0.028 MPa). The observations at H-11b2 of this higher pressure during tracer injection and the inability to sustain a 0.38 L/s pumping rate suggest that H-11b2 is not as well connected hydraulically to the Culebra as the other wells. It is not known whether these observations are a consequence of reduced fracturing locally at the H-11b2 location or possible clogging of fractures immediately surrounding the well during the drilling and/or well cleaning and development operations.

10.3 Tracer-Test History

A convergent-flow tracer test was conducted at the H-11 hydropad from May 1988 to July 1988. The following sections briefly discuss the pumping and tracer-injection history, test equipment, and observed tracer-breakthrough curves. Full details on the H-11 tracer test including tabulated data for pumping rates, fluid pressures in wells, and tracer concentrations are reported in Stensrud et al. (1990).

10.3.1 Pumping and Tracer-Injection History

Pumping for the H-11 tracer test began at 09:00 on May 5, 1988 and continued for 63 days until 09:00 on July 7, 1988. The pumping well was H-11b1. The initial pumping rate of 0.40 L/s gradually declined to 0.38 L/s. The average pumping rate during the time of tracer migration to the pumping well was 0.38 L/s. The pump shut down from 12:50 to 14:01 on May 12, 1988 (prior to tracer injection) and again from 16:51 to 18:40 on July 3, 1988 (after tracer injection). A total of about 2.07×10^6 L of fluid were pumped from H-11b1. Periodic measurements of the pumping rate taken during the tracer test yield

the pumping record presented in Figure 10-6. The pumping information is summarized in Table 10-2.

Tracers were injected into wells H-11b2, H-11b3, and H-11b4 on May 14, 1988. The tracer slug injected into H-11b2 consisted of 1.997 kg of PFB mixed with 189 L of formation fluid. A 188 L chaser volume was injected immediately after the tracer volume. Injection of the tracer volume began at 11:00 and injection of the chaser volume ended at 12:34. The total volume injected into H-11b2 was 377 L, about 316 L greater than the downhole system volume of 61 L. Injection of the tracer and chaser solutions into H-11b3 took place from 13:30 to 15:04. The tracer-labeled slug consisted of 1.993 kg of m-TFMB mixed with 189 L of formation fluid and the unlabeled volume consisted of 373 L of formation fluid. The downhole system volume in H-11b3 is 150 L, about 412 L less than the total injected volume of 562 L. The tracer injected into H-11b4 was 2.898 kg of ortho-trifluoromethylbenzoate (o-TFMB). The tracer and chaser slugs were 189 and 187 L, respectively, for a total injected volume of 376 L. The downhole system volume (44 L) was about 332 L less than the volume injected. The total injection period was from 16:00 to 17:03. Table 10-2 summarizes tracer-injection information for the H-11 tracer test.

10.3.2 Test Equipment

Figure 10-7 shows the configuration of pumping well H-11b1 during the convergent-flow tracer test. A submersible pump was installed in H-11b1 below an air-inflatable sliding-end packer. The packer was set in the casing approximately 3.0 m above the Culebra interval. The pump intake was located about 221.4 m BTC. A 3.81-cm (1-1/2-inch) discharge pipe extended through the packer to the ground surface. Three downhole pressure transducers were attached to the discharge pipe. Two transducers monitored the fluid pressure in the interval below the packer through a feed-through plug. A third transducer monitored the fluid pressure in the annulus above the packer.

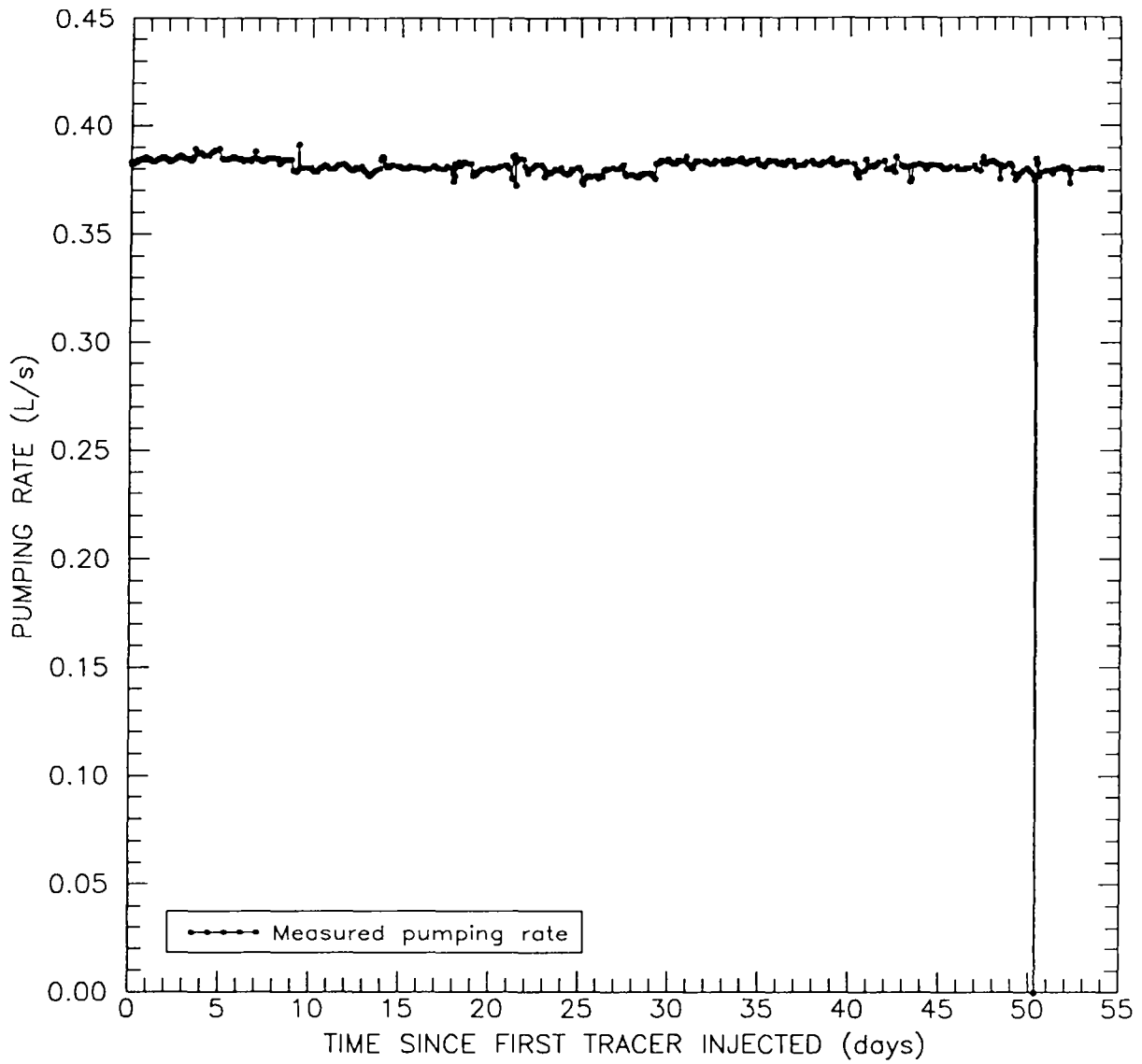
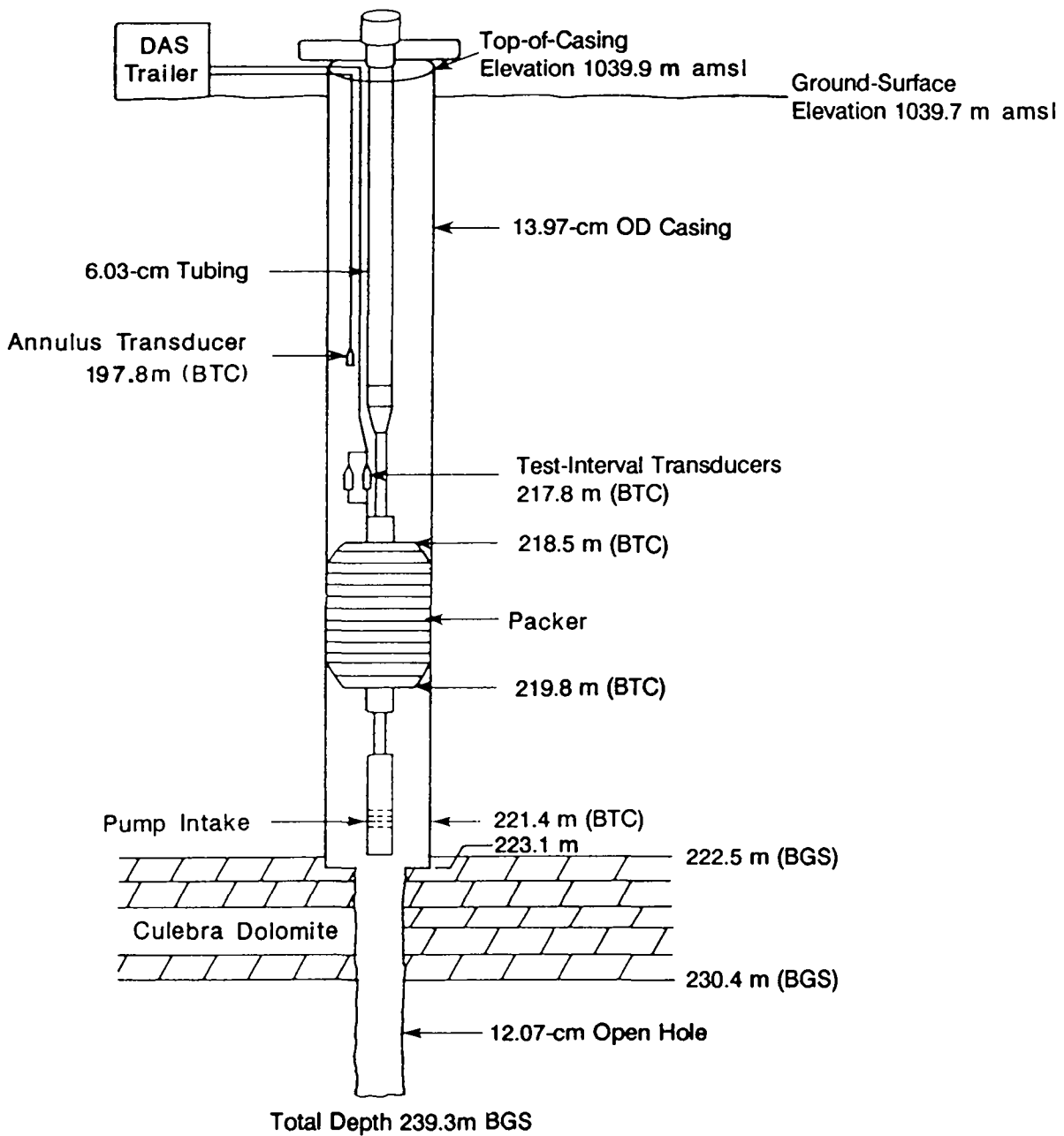


Figure 10-6. Pumping rate at well H-11b1 during the convergent-flow tracer test conducted at the H-11 hydropad.

Table 10-2. Summary of Pumping and Tracer-Injection Information for the Convergent-Flow Tracer Test Conducted at the H-11 Hydropad

	<u>H-11b1</u>	<u>H-11b2</u>	<u>H-11b3</u>	<u>H-11b4</u>
Well Type	Pumping	Tracer Injection	Tracer Injection	Tracer Injection
Average Pumping Rate	0.38 L/s			
Time Pumping Began	09:00			
Date Pumping Began	05/05/88			
Time Pumping Ended	09:00			
Date Pumping Ended	07/07/88			
Tracer Injected		PFB	m-TFMB	o-TFMB
Mass Injected		1.997 kg	1.993 kg	2.898 kg
Time Tracer Injected		11:00 to 12:34	13:30 to 15:04	16:00 to 17:03
Date Tracer Injected		05/14/88	05/14/88	05/14/88
Tracer Volume		189 L	189 L	189 L
Chaser Volume		188 L	373 L	187 L
Downhole System Volume		61 L	150 L	44 L

PUMPING WELL H-11b1



NOTE:

BGS = Below Ground Surface

BTC = Below Top of Casing

Figure 10-7. Downhole-equipment configuration for pumping well H-11b1 during the convergent-flow tracer test conducted at the H-11 hydropad (after Stensrud et al., 1990).

The downhole-equipment assemblies for the three tracer-addition wells were identical and are illustrated in Figure 10-8. An 11.43-cm (4-1/2-inch) inflatable packer and a 3.81-cm (1-1/2-inch) minipacker, installed in the mandrel of the inflatable packer, were set approximately 0.61 m above the bottom of the casing. The minipacker was used to control injection. Due to borehole conditions, the packers were placed higher in H-11b2 than in H-11b3 and H-11b4. The injection tubing located below the packers had a 9.53-cm (3-3/4-inch) outside diameter and four 1.91-cm perforations every 0.61 m. The purpose of the perforations was to enable uniform distribution of the tracer over the entire Culebra interval. Tracer was delivered to the packer assembly through 1.27-cm (1/2-inch) tubing. The packer and minipacker were equipped with feed-through plugs for the inflation and transducer lines. Fluid pressures above and below the packers were measured with downhole-pressure transducers. Additional discussion of this assembly can be found in Stensrud et al. (1990). The depths of the packer and tracer-injection ports in the three tracer-injection wells are summarized in Table 10-3.

A DAS was used to monitor the fluid pressures in the four H-11 hydropad wells during the tracer test. The DAS used nine downhole pressure transducers, three in H-11b1 and two in each of the wells H-11b2, H-11b3, and H-11b4, to monitor pressure changes. In the three tracer-addition wells, pressure data were collected for the regions above and below the packers. Pressures in the test interval and in the annulus above the packer were measured in H-11b1. The pressure data are shown in Figure 10-9 and tabulated in Stensrud et al. (1990).

The tracer solution was mixed in a storage tank located on the surface near the injection well. Attached to this tank was a small circulating pump used to mix the tracer solution in an effort to maintain a uniform tracer concentration during injection. A second tank held the chaser solution. To prevent air from entering the injection line, the two tanks were linked with tubes and valves. Gravity flow was used for injection of both the tracer and chaser fluids.

10-16

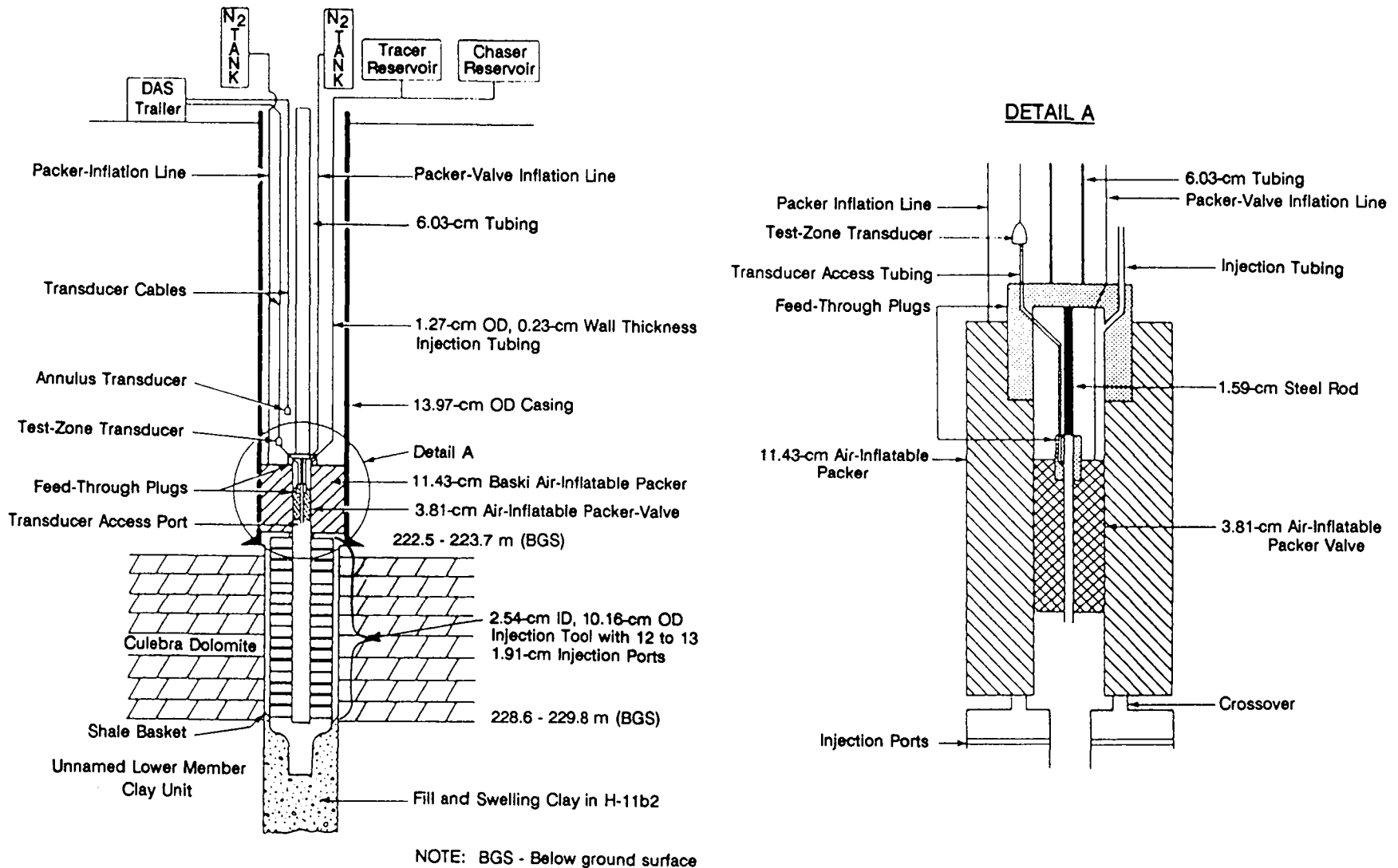
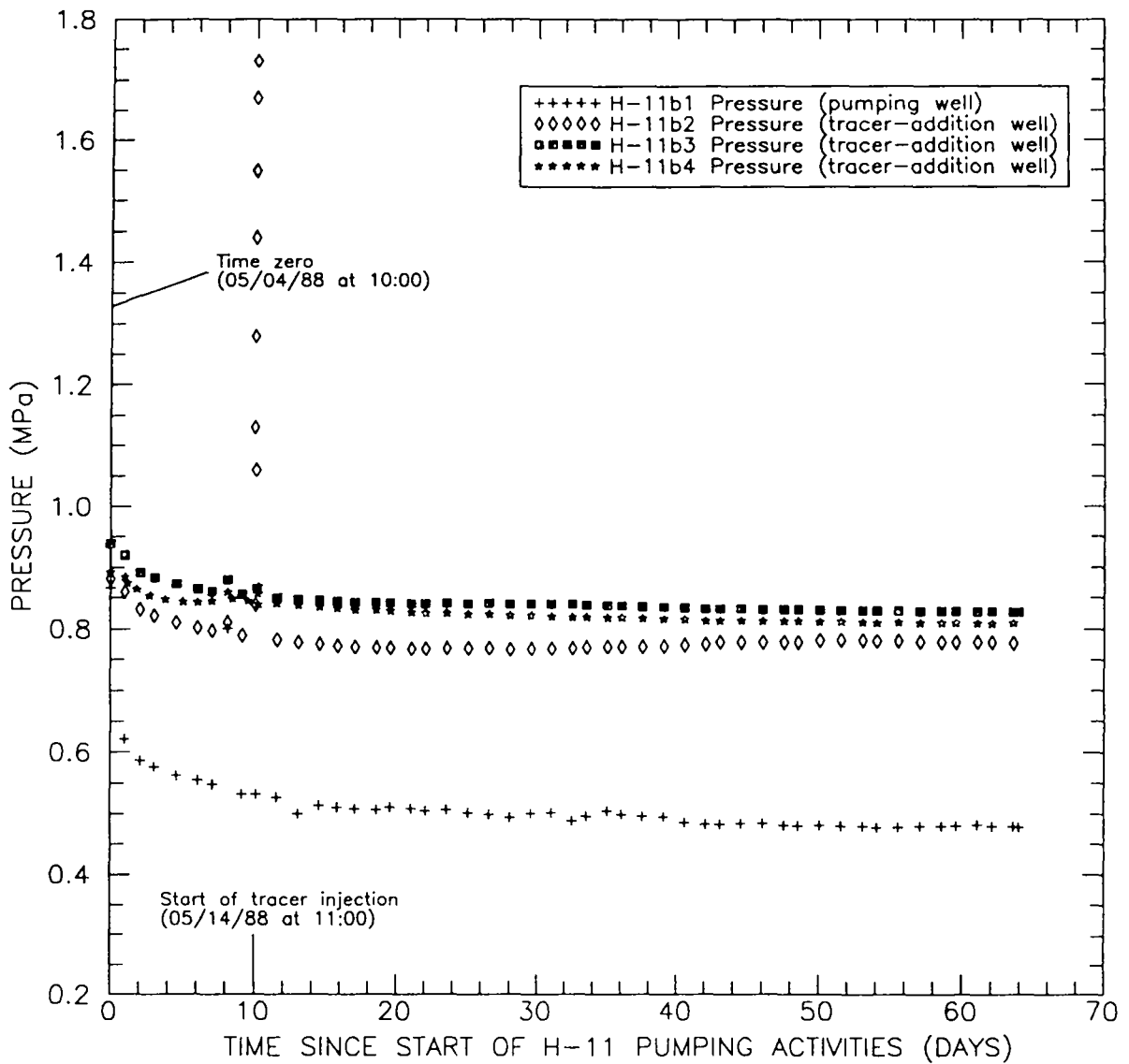


Figure 10-8. Schematic illustration of the tracer-injection system used in H-11b2, H-11b3, and H-11b4 during the convergent-flow tracer test conducted at the H-11 hydropad (after Stensrud et al., 1990).

Table 10-3. Depths of the Packers and Tracer-Injection Ports in the Three Tracer-Addition Wells for the H-11 Convergent-Flow Tracer Test

Well	Packer Depth (m BTC)	Injection-Port Depths (m BTC)
H-11b2	220.0 - 220.9	223.9 - 230.6
H-11b3	221.7 - 222.7	223.5 - 230.2
H-11b4	219.2 - 220.2	221.0 - 227.7



Observed data pared for figure clarity.

Figure 10-9. Pressure data for the H-11 hydropad wells during the convergent-flow tracer test.

Fluid samples were manually collected from the H-11b1 discharge line. The samples were stored in 118.28-mL bottles capped with aluminum foil and sealed. Samples were stored under refrigerated conditions at the H-11 hydropad and shipped in chilled containers to a laboratory for analysis. HPLC methods were used to analyze the samples for tracer concentrations. A complete description of the tracer-analysis technique can be found in Stensrud et al. (1990).

10.3.3 Observed Tracer Breakthrough

The concentrations of m-TFMB, PFB, and o-TFMB determined for fluid collected at the pumping well are illustrated in Figure 10-10. Appendix G contains the concentration data and corrected travel times. The times are corrected to account for the tracer traveling from the injection point down to the Culebra center in the injection well and to account for tracer traveling from the Culebra up to the sampling point in the pumping well. The time corrections are noted in Appendix G.

The first tracer to reach the pumping well was m-TFMB, detected about 1 hr (corrected time) after it was injected. The peak concentration of m-TFMB occurred about 8 hrs (corrected time) after injection. An estimate of 74 percent recovery for m-TFMB was made based on integration of the observed breakthrough curve. For the tracer PFB, the corrected times of first detection and peak concentration are approximately 16 hrs and 6 days, respectively. Integration of the observed PFB breakthrough curve yields a recovery estimate of 64 percent. o-TFMB was first detected at the pumping well about 4 days (corrected time) after it was injected. The peak concentration of o-TFMB occurred 20 days later. About 31 percent of the tracer o-TFMB injected into H-11b4 was recovered at H-11b1. The peak concentration of m-TFMB is about a factor of five greater than the peak concentration of PFB and about a factor of 11 greater than the peak concentration of o-TFMB. The difference between the peak concentrations of PFB and o-TFMB is about a factor of two. The peak concentration of m-TFMB was observed at the pumping well a

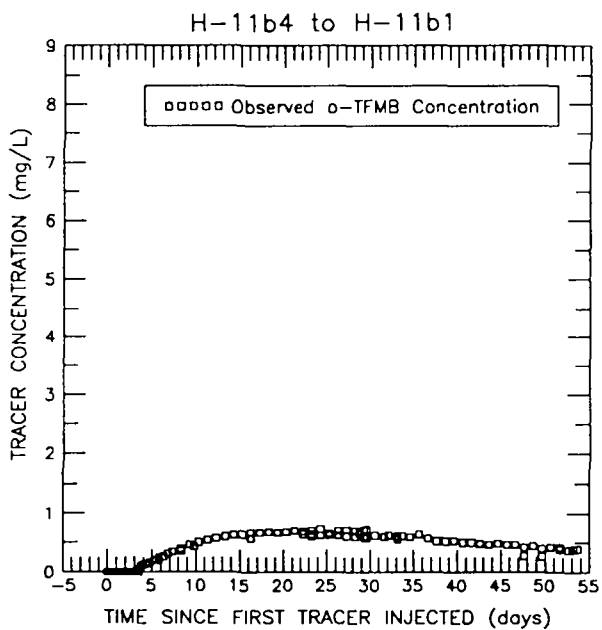
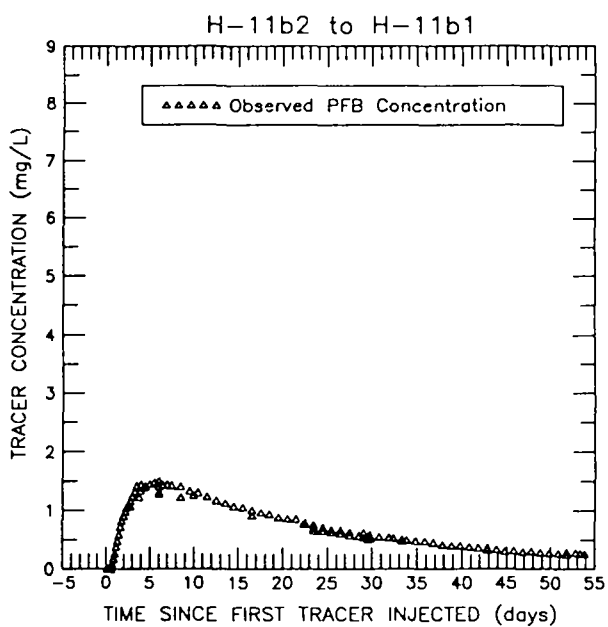
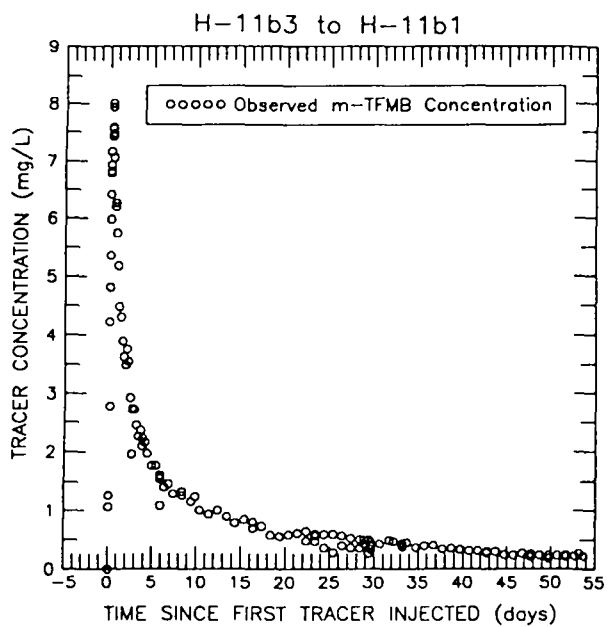


Figure 10-10. Observed m-TFMB, PFB, and o-TFMB data for the convergent-flow tracer test conducted at the H-11 hydropad.

factor of 18 faster than the peak concentration of PFB and a factor of 73 faster than the peak concentration of o-TFMB. The peak-concentration arrival times of PFB and o-TFMB differ by about a factor of four.

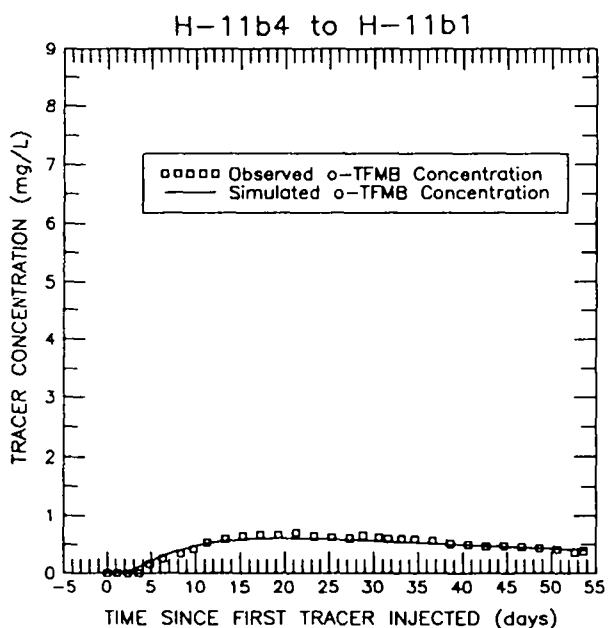
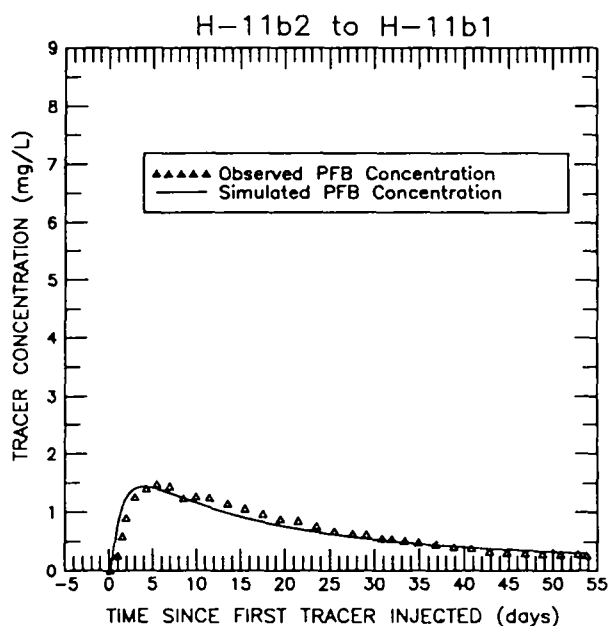
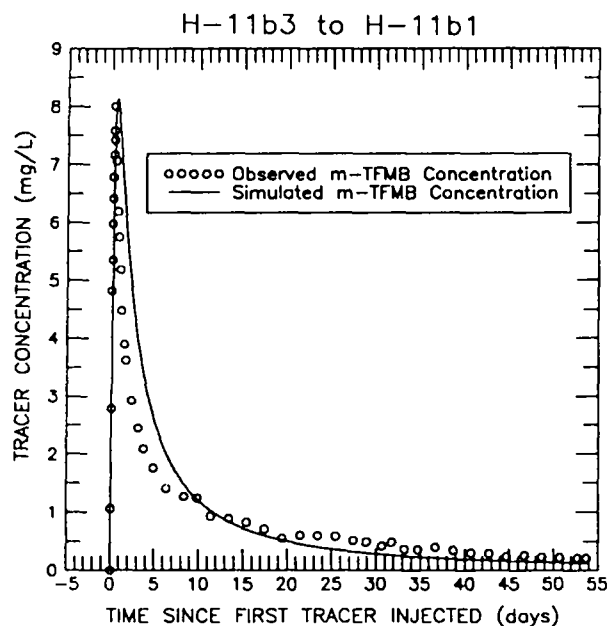
As discussed in Section 10.2, H-11b2 may not be as well connected hydraulically to the Culebra as the other three wells at the H-11 hydropad. Poor connection between H-11b2 and the formation may have influenced the transport of PFB from H-11b2 to H-11b1.

10.4 Analysis of Tracer-Breakthrough Curves

The heterogeneous- and anisotropic-analysis approaches used to analyze the H-3 tracer test and H-6 tracer test #1 were also used to analyze the H-11 tracer test. These two approaches are discussed in Section 3.4. The parameters used to fit the simulated data to the observed breakthrough curves are discussed in Section 3.4.1 for the heterogeneous-analysis approach and in Section 3.4.2 for the anisotropic-analysis approach.

10.4.1 Heterogeneous-Analysis Approach

Calibrating to the rapid-transport breakthrough curve (m-TFMB) yielded a best-fit fracture porosity of 5.0×10^{-4} and a matrix-block length of 0.32 m for the path from H-11b3 to H-11b1. Maintaining this fracture porosity, the PFB and o-TFMB breakthrough curves were matched using matrix-block lengths of 0.13 and 0.29 m, respectively. A comparison of the observed and simulated breakthrough curves for the three tracers is provided in Figure 10-11. The input parameters used in the best-fit, heterogeneous simulations are summarized in Table 10-4. Using a fracture porosity of 5.0×10^{-4} , the inner and outer radii of the tracer-input zones (shown schematically in Figures 3-5 and 3-8) are 3.30 and 5.10 m, respectively, for H-11b2, 4.35 and 5.80 m, respectively, for H-11b3, and 3.60 and 5.40 m,



SIMULATION PARAMETERS

Fracture Porosity = 5.0×10^{-4}
 Matrix Porosity = 0.16
 Dispersivity = 1.5 m
 Tortuosity = 0.11
 Pumping Rate = 0.38 L/s
 Thickness = 7.62 m
 Well Spacing
 b3 to b1 = 20.9 m
 b2 to b1 = 21.4 m
 b4 to b1 = 43.1 m
 Free-Water Diffusion Coefficient
 m-TFMB = $7.4 \times 10^{-10} \text{ m}^2/\text{s}$
 PFB = $7.2 \times 10^{-10} \text{ m}^2/\text{s}$
 o-TFMB = $7.4 \times 10^{-10} \text{ m}^2/\text{s}$
 Matrix-Block Lengths
 b3 to b1 path = 0.317 m
 b2 to b1 path = 0.127 m
 b4 to b1 path = 0.289 m

Observed data pared for figure clarity.

Figure 10-11. Observed and best-fit simulated breakthrough curves for the H-11 convergent-flow tracer test using the heterogeneous-analysis approach.

Table 10-4. Transport Parameters Used in the Interpretations of the H-11 Convergent-Flow Tracer Test

Parameter	Heterogeneous-Analysis Approach		Anisotropic-Analysis Approach	
Culebra Thickness			7.6 m	
Well Spacings	20.9 m		H-11b3 to H-11b1	
	21.4 m		H-11b2 to H-11b1	
	43.1 m		H-11b4 to H-11b1	
Free-Water Diffusion Coefficients	$7.4 \times 10^{-10} \text{ m}^2/\text{s}$		m-TFMB	
	$7.2 \times 10^{-10} \text{ m}^2/\text{s}$		PFB	
	$7.4 \times 10^{-10} \text{ m}^2/\text{s}$		o-TFMB	
Longitudinal Dispersivity			1.5 m	
Tortuosity			0.11	
Matrix Porosity			0.16	
Fracture Porosity	5.0×10^{-4}		1.0×10^{-3}	
Matrix-Block Lengths	0.32 m	H-11b3 to H-11b1	0.19 m	H-11b3 to H-11b1
	0.13 m	H-11b2 to H-11b1	0.19 m	H-11b2 to H-11b1
	0.29 m	H-11b4 to H-11b1	0.19 m	H-11b4 to H-11b1
Anisotropy Ratio	1:1		3:1	
Principal-Transmissivity Direction	na		N72°W (4 degrees clockwise from the H-11b3 to H-11b1 path)	
na means not applicable				

respectively, for H-11b4. The H-11b3 to H-11b1 path was discretized into 89 grid blocks ranging in size from 0.29 to 0.34 m with the outer 40 blocks containing initial tracer. The H-11b2 to H-11b1 path was modeled with 87 grid blocks ranging in size from 0.29 to 0.34 m and initial mass was distributed into 34 grid blocks. For the path from H-11b4 to H-11b1, 162 grid blocks ranging in size from 0.27 to 0.34 m were used with initial mass in 36 grid blocks.

The time to displace m-TFMB from the H-11b3 borehole was about 57 minutes. First detection of m-TFMB at the pumping well occurred about 80 minutes after the tracer was emplaced in the Culebra. From the time of tracer emplacement to arrival of the peak concentration at the pumping well was about 7.8 hrs. Development of the input distribution for m-TFMB assumed that the time of tracer injection was relatively short compared to the time for the tracer to migrate from the injection well to the pumping well. For the H-11b3 to H-11b1 path, this assumption is satisfied when the injection time is compared to the arrival time of the peak concentration but is violated when the injection time is compared to the time of first tracer detection. The latter comparison, however, is not appropriate since the first arrival of detectable tracer at the pumping well is caused by dispersion and diffusion in addition to advection. Therefore, the assumption of an initial circular ring of tracer surrounding H-11b3 is considered a reasonable approximation for modeling purposes.

The path from H-11b3 to H-11b1 is oriented N76° W and the path from H-11b4 to H-11b1 is oriented N89° W. The difference in these orientations is 13 degrees (Figure 10-1). Because the two paths are oriented similarly, the breakthrough curves for the tracers traveling these two paths (m-TFMB and o-TFMB) might be expected to be similar. Examination of Figure 10-10 reveals very different breakthrough characteristics. The breakthrough curve for m-TFMB, which traveled 20.9 m from H-11b3 to H-11b1, peaked quickly and sharply. A very broad breakthrough curve with low concentrations was obtained for o-TFMB which traveled from H-11b4 to H-11b1, a distance of 43.1 m. The difference in the two breakthrough curves can be accounted for by the difference in the lengths of the travel paths, 20.9 m versus 43.1 m. The longer path from H-11b4 to H-11b1 resulted in

lower ground-water velocities in the vicinity of the tracer-addition well and greater residence time for the tracer. Consequently, diffusion of the tracer from the fracture to the matrix was greater and the amount of tracer reaching the pumping well was less during the period of the test. Because this effect was anticipated, the mass of o-TFMB injected into H-11b4 (2.898 kg) was one and a half times greater than the mass injected into the other two wells. Even with a higher injected mass, the observed o-TFMB concentrations were very low, almost at the detection limit. The conclusion that the difference in the m-TFMB and o-TFMB breakthrough curves is almost solely the consequence of the travel length is supported by the matrix-block lengths determined with the heterogeneous analysis. The matrix-block length estimated for the path from H-11b3 to H-11b1 is 0.32 m while the length estimated for the H-11b4 to H-11b1 path is 0.29 m. The two lengths differ by 10 percent. The difference in the matrix-block lengths can be attributed to the fact that the orientations of the two travel paths are not identical.

The distributions of tracer masses in the fractures and matrix for the three travel paths and the tracer masses recovered at the pumping well are illustrated in Figure 10-12. For the path from H-11b3 to H-11b1, m-TFMB is rapidly depleted from the fracture as a result of diffusion into the matrix and substantial tracer recovery at the pumping well. With time, m-TFMB is also depleted from the matrix and is recovered at the pumping well. The rapid decline of PFB from the fractures during the early portion of the test was due to large diffusive losses to the matrix and some losses to the pumping well. PFB was also depleted from the matrix with time but not to the same degree as m-TFMB. This, along with the shape of the breakthrough curves, indicates that matrix participation was greater along the path from H-11b2 to H-11b1 than along the H-11b3 to H-11b1 path. Considerable reduction in the mass of o-TFMB in the fractures occurred before the tracer was observed at the pumping well as a result of diffusion into the matrix. The bulk of the tracers not recovered (approximately 19 percent for m-TFMB, 37 percent for PFB, and 70 percent for o-TFMB) were located in the matrix at the end of the tracer test. The simulations using the heterogeneous-analysis approach yielded 81 percent recovery for m-TFMB, 63 percent

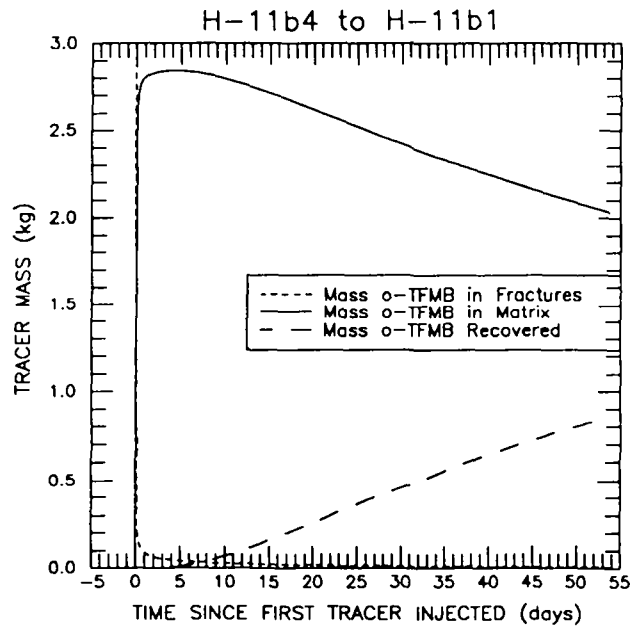
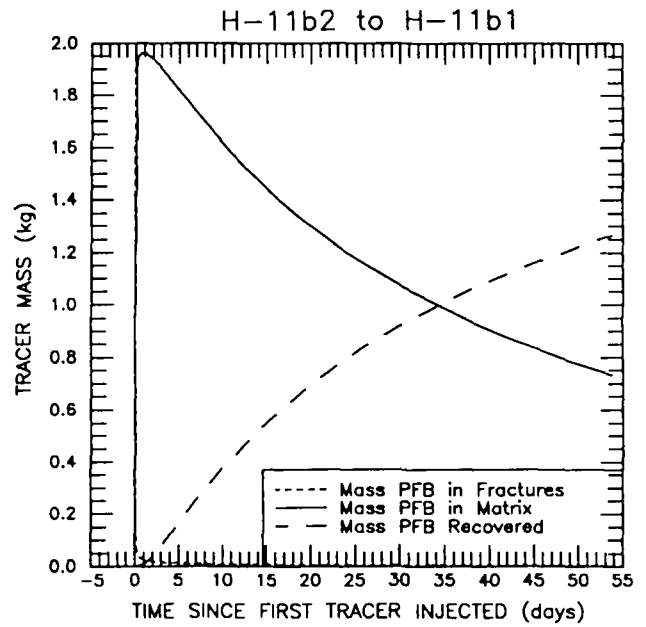
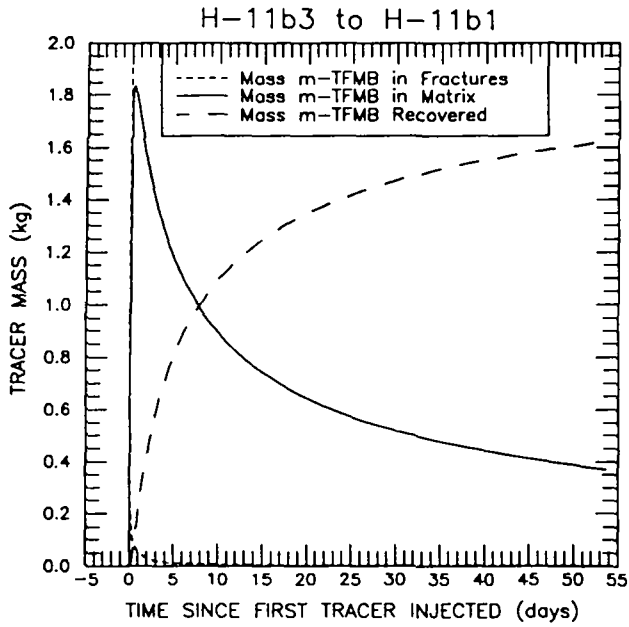


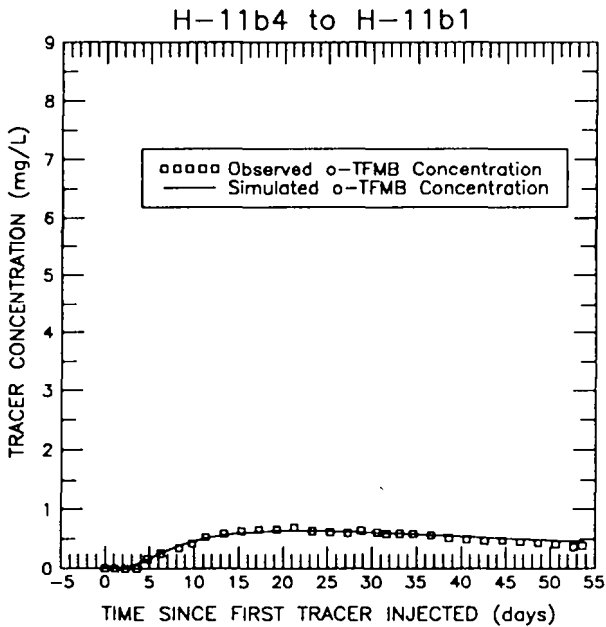
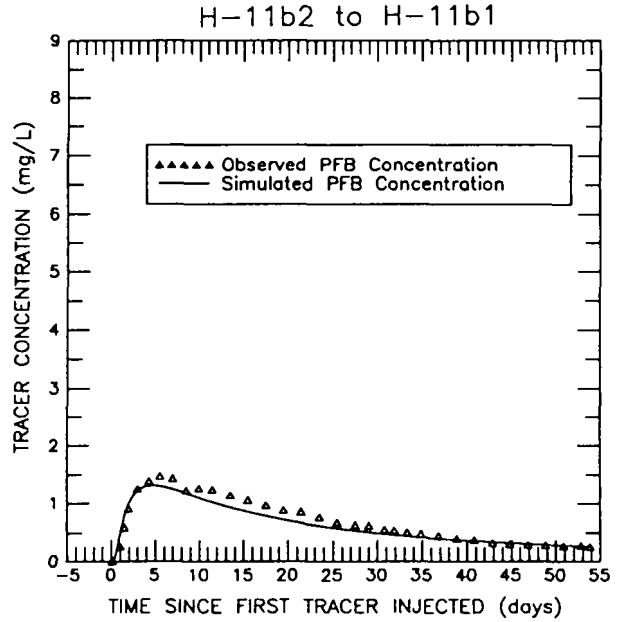
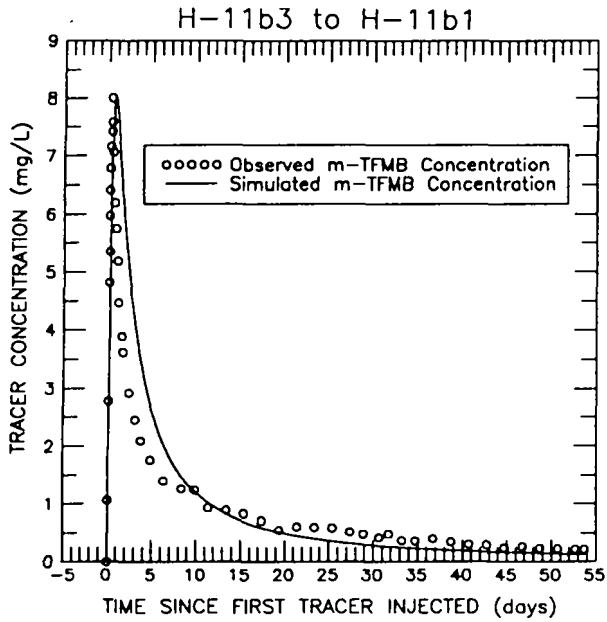
Figure 10-12. Mass distribution in the fractures and matrix and mass recovered at the pumping well for the best-fit heterogeneous simulation of the tracer-breakthrough curves for the H-11 hydropad.

recovery for PFB, and 30 percent recovery for o-TFMB. The estimated amount of mass recovery based on the observed breakthrough curves was 74 percent for m-TFMB, 64 percent for PFB, and 31 percent for o-TFMB. The simulated recovery for m-TFMB was slightly higher than the observed m-TFMB recovery. The agreement between simulated and observed recovery for PFB and o-TFMB was excellent.

10.4.2 Anisotropic-Analysis Approach

An anisotropy ratio of 3:1, a T_x direction oriented N72° W (four degrees clockwise from the H-11b3 to H-11b1 path), and a matrix-block length of 0.19 m generated simulated breakthrough curves that best fit the observed tracer concentrations using the anisotropic-analysis approach (Figure 10-13). The fracture porosity used for the anisotropic simulations was the estimated value of 1.0×10^{-3} calculated with Equation 5-9. The inner and outer radii of the tracer-input zones (shown schematically in Figures 3-5 and 3-8) calculated with this fracture porosity are 2.40 and 3.60 m, respectively, for H-11b2, 3.00 and 4.20 m, respectively, for H-11b3, and 2.40 and 3.90 m, respectively, for H-11b4. Initial masses of the tracers were distributed over 28 grid blocks at H-11b3, 24 grid blocks at H-11b2, and 26 grid blocks at H-11b4. The paths from H-11b3 to H-11b1, H-11b2 to H-11b1, and H-11b4 to H-11b1 were discretized with 82, 82, and 157 grid blocks, respectively, ranging in size from 0.27 to 0.34 m. The input parameters for these simulations are summarized in Table 10-4.

The distributions of tracer masses between the fractures and matrix for the anisotropic simulations (Figure 10-14) are similar to the distributions determined from the heterogeneous simulations (Figure 10-12). In both cases, the masses of tracers in the fractures rapidly declined along all three flow paths. For the rapid-transport path from H-11b3 to H-11b1, the decline was due to two processes: mass diffusion from the fractures to the matrix and substantial mass recovery at the pumping well. For o-TFMB, which traveled from H-11b4 to H-11b1, the rapid decline of mass in the fractures was due to substantial diffusive losses to the matrix. The decline of PFB in the fractures for the H-11b2



SIMULATION PARAMETERS

Fracture Porosity = 1.0×10^{-3}
 Matrix Porosity = 0.16
 Dispersivity = 1.5 m
 Tortuosity = 0.11
 Thickness = 7.62 m

Well Spacing
 b3 to b1 = 20.9 m
 b2 to b1 = 21.4 m
 b4 to b1 = 43.1 m

Free-Water Diffusion Coefficient
 m-TFMB = $7.4 \times 10^{-10} \text{ m}^2/\text{s}$
 PFB = $7.2 \times 10^{-10} \text{ m}^2/\text{s}$
 o-TFMB = $7.4 \times 10^{-10} \text{ m}^2/\text{s}$

Matrix-Block Lengths
 b3 to b1 path = 0.192 m
 b2 to b1 path = 0.192 m
 b4 to b1 path = 0.192 m

$T_x:T_y = 3:1$
 T_x Orientation = N72°W

Observed data pared for figure clarity.

Figure 10-13. Observed and best-fit simulated breakthrough curves for the H-11 convergent-flow tracer test using the anisotropic-analysis approach.

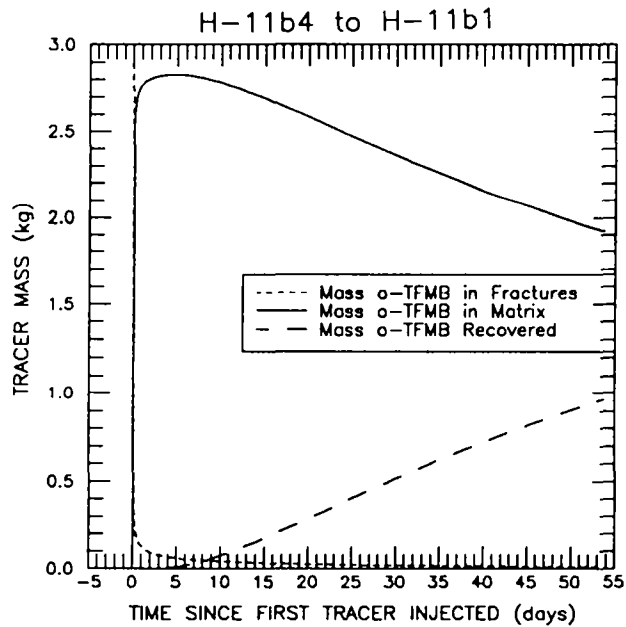
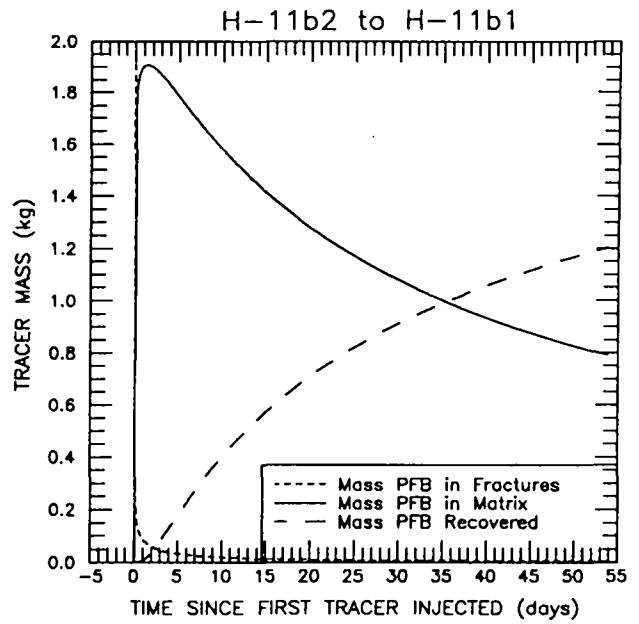
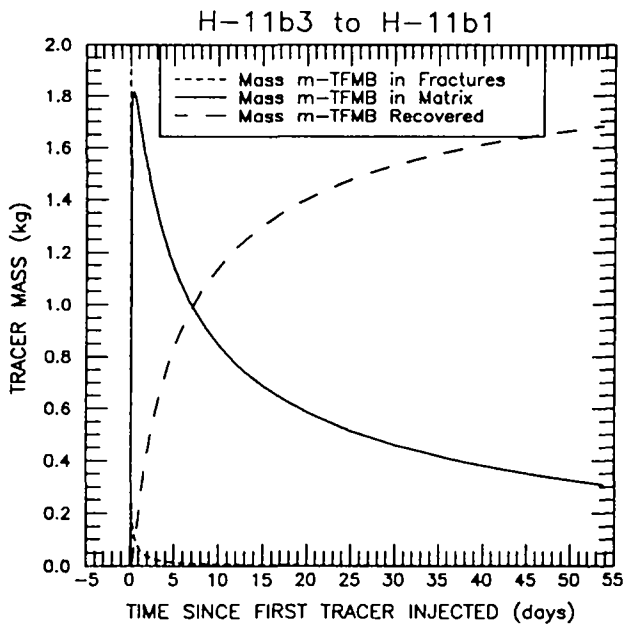


Figure 10-14. Mass distribution in the fractures and matrix and mass recovered at the pumping well for the best-fit anisotropic simulation of the tracer-breakthrough curves for the H-11 hydrograd.

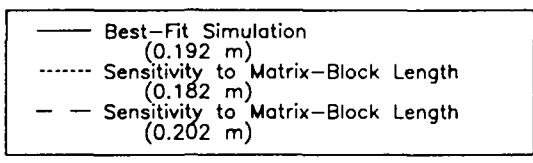
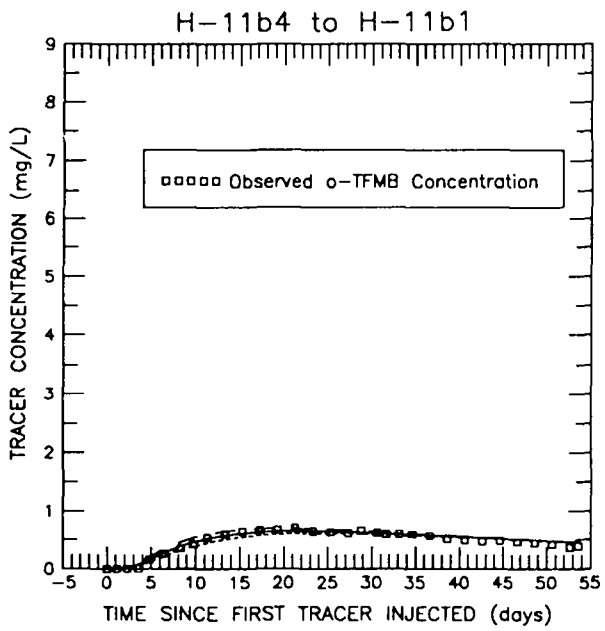
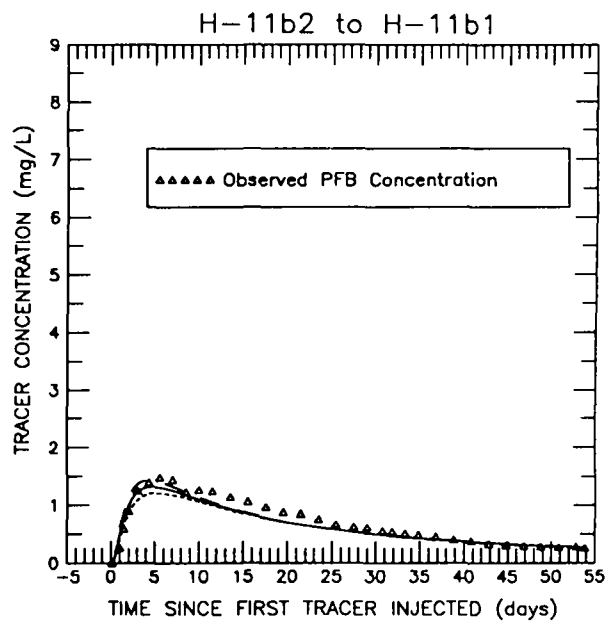
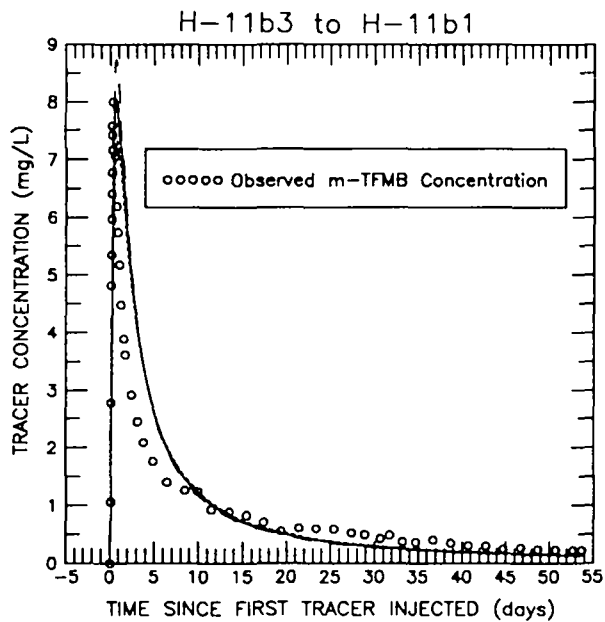
to H-11b1 path was the result of a combination of diffusion into the matrix and tracer recovery at the pumping well. For all three travel paths, the amount of mass in the matrix peaked and then declined. These declines were the result of diffusion from the matrix to the fractures as mass was further depleted from the fractures by tracer recovery at the pumping well. The degree of mass depletion from the matrix correlates to the amount of tracer recovery. The tracer showing the greatest degree of mass depletion from the matrix (m-TFMB) also showed the highest recovery at the pumping well (Figure 10-14). Tracer recoveries for the anisotropic simulations were 84 percent for m-TFMB, 60 percent for PFB, and 33 percent for o-TFMB which compare favorably with the observed recoveries of 74, 64, and 31 percent, respectively.

10.5 Sensitivity Analyses

Sensitivity analyses examined the effect of matrix-block length and anisotropy ratio on the simulated breakthrough curves from the H-11 tracer test. In addition, the minimum and maximum matrix-block lengths for the three transport paths were defined to provide insight into the uncertainty in that important fitting parameter. The detailed sensitivity analysis presented for the H-3 tracer test was not repeated for the H-11 test. The base-case parameters for the matrix-block length and anisotropy ratio sensitivity analyses were the input parameters for the best-fit, anisotropic simulations.

10.5.1 Effect of Matrix-Block Length

The sensitivity to matrix-block length considered lengths five percent higher (0.20 m) and five percent lower (0.18 m) than the base-case length of 0.19 m. The results of this sensitivity analysis are presented in Figure 10-15. For the H-11b3 to H-11b1 path, matrix-block length has a substantial effect on the peak concentration but little effect on the rising and falling limbs of the breakthrough curve. Changing the matrix-block length by 5 percent



Observed data pared for figure clarity.

Figure 10-15. Sensitivity to matrix-block length for the H-11 convergent-flow tracer test.

changed the peak concentration by 9 percent. Varying the matrix-block length by 5 percent has a small effect on the peak concentration for the H-11b2 to H-11b1 path but, again, little effect on the rising and falling limbs of the breakthrough curve. The breakthrough curve for the path from H-11b4 to H-11b1 is not noticeably affected by the small changes in matrix-block length considered here. In summary, changing the matrix-block length has the greatest effect on the path that has the least matrix participation and the least effect on the path that has the greatest matrix participation.

Matrix-block length and tortuosity are related in the independent parameter group referred to as the characteristic matrix-diffusion time (Equation 5-13). Using this relationship, the uncertainty in matrix-block length due to uncertainty in the assigned value for tortuosity can be determined. With all other parameters and the value for the characteristic matrix-diffusion time held constant, Equation 5-13 can be used to calculate the corresponding value of matrix-block length needed to yield identical simulated results. For the best-fit anisotropic simulation, the characteristic matrix-diffusion times are 3.6, 3.7, and 3.6 yrs for m-TFMB, PFB, and o-TFMB, respectively. Section 5.1.7 discusses an estimated range of 0.027 to 0.38 for tortuosity of the Culebra at the WIPP site. Substituting the end members of this range into Equation 5-13 yields matrix-block lengths of 0.10 m for a tortuosity of 0.027 and 0.36 m for a tortuosity of 0.38. This exercise indicates that the matrix-block length required to reproduce the best-fit anisotropic simulation ranges from 0.10 to 0.36 m for a tortuosity range of 0.027 to 0.38, respectively. Therefore, the uncertainty in the best-fit matrix-block length (0.19 m) for the anisotropic simulation based on uncertainty in the assigned value of 0.11 for tortuosity is -0.09 to +0.17 m.

10.5.2 Effect of Anisotropy Ratio

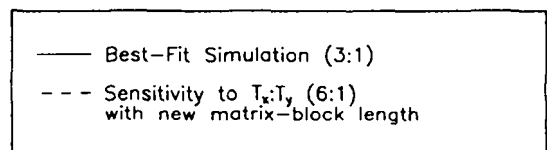
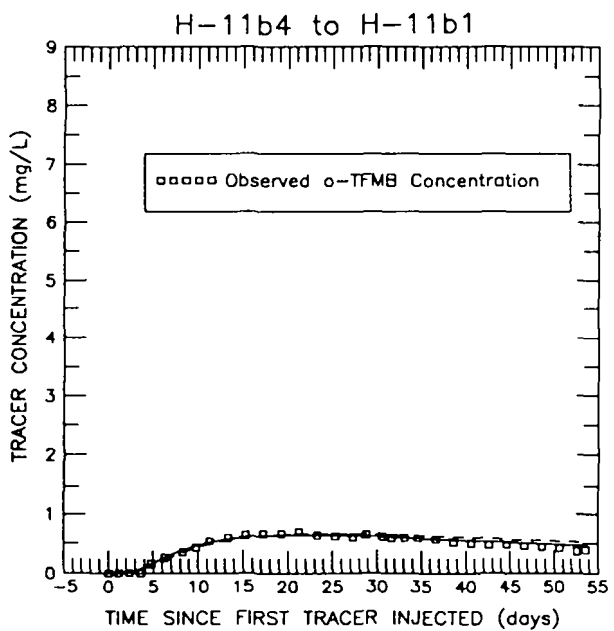
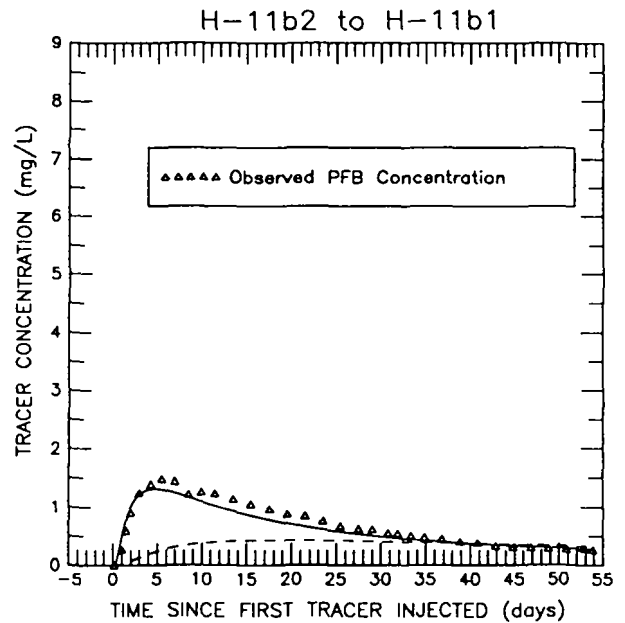
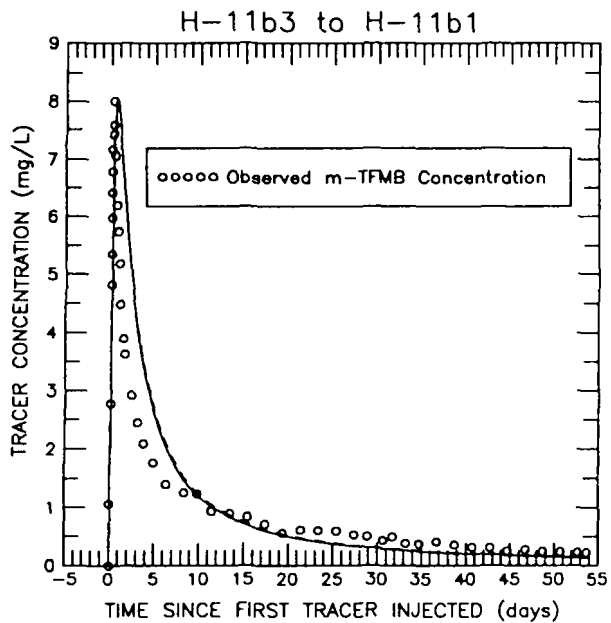
The approach used to investigate the sensitivity to anisotropy ratio was the same as that described in Section 7.5.7 for the H-3 tracer test. The anisotropy ratio was changed and recalibration of the rapid-transport breakthrough curve, using matrix-block length, was

conducted. The two other breakthrough curves were then simulated using the new anisotropy ratio and matrix-block length. An anisotropy ratio of 6:1 was considered in the sensitivity calculations along with a new orientation of the T_x direction. The new orientation was $N76^\circ W$ (parallel to the H-11b3 to H-11b1 path). The results of this sensitivity analysis show that the m-TFMB and o-TFMB breakthrough curves were closely matched but the simulated PFB curve did not fit the observed data (Figure 10-16). The paths from H-11b3 to H-11b1 and H-11b4 to H-11b1 have approximately the same orientation and, therefore, the transport behavior along these two paths is very similar. Consequently, any transport parameters yielding simulations that closely match the observed data for one path will also produce results that closely match the observed data for the other path. For any reasonable anisotropy ratio, a matrix-block length can be found that will yield simulated results that match the observed m-TFMB and o-TFMB breakthrough curves. However, investigating anisotropy ratios ranging from 2.5:1 to 6:1 indicated that only one $T_x:T_y$ value (3:1) gives simulated breakthrough curves that fit all three of the observed breakthrough curves.

The best-fit anisotropic simulations used a T_x direction oriented $N72^\circ W$ (4 degrees clockwise from the H-11b3 to H-11b1 path). Investigation of orientations ranging from $N76^\circ W$ to $N64^\circ W$ indicated that changing the orientation results in a poorer fit between the observed and simulated data.

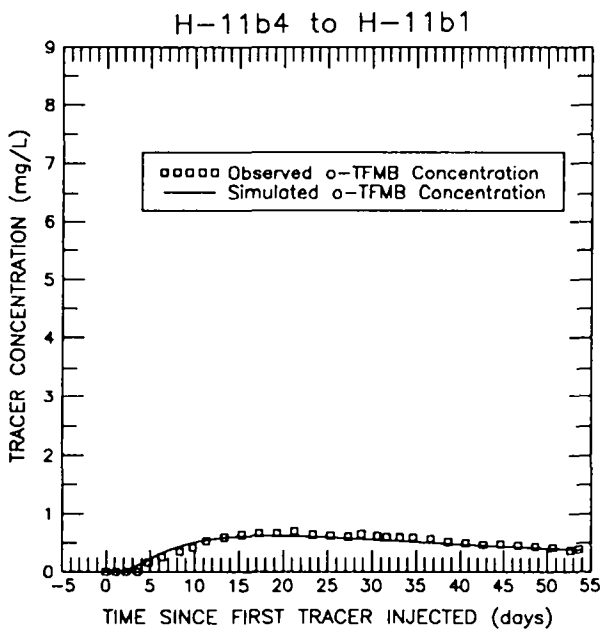
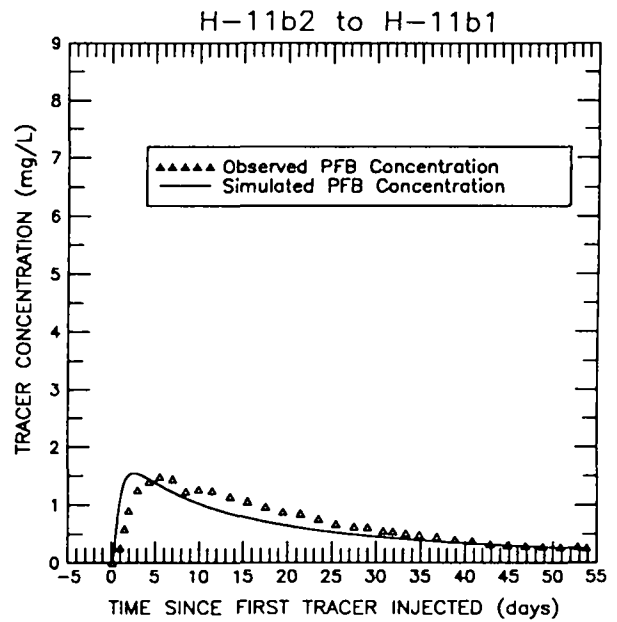
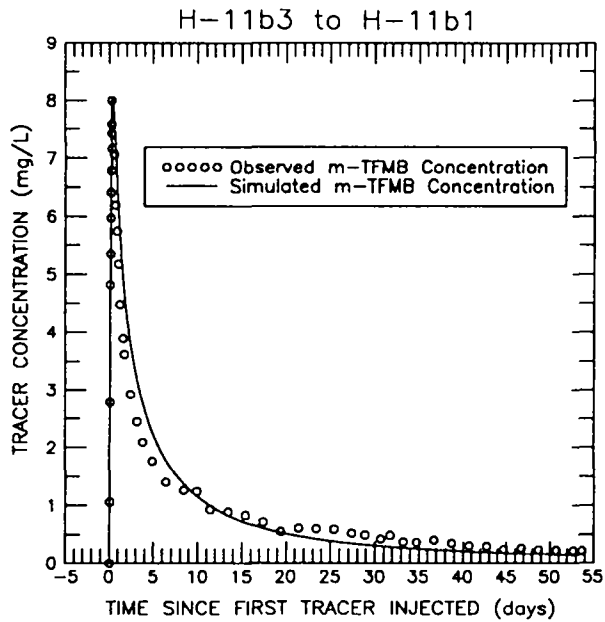
10.5.3 Determination of Maximum and Minimum Matrix-Block Lengths

A sensitivity analysis designed to determine the maximum and minimum matrix-block lengths was also conducted for the H-11 tracer test. This exercise provided further characterization of the uncertainty in the fitted values of matrix-block length. Assigning model-input parameters in such a way that maximizes diffusive losses from the fractures to the matrix yielded a fracture porosity of 2.0×10^{-4} and maximum matrix-block lengths of 1.07 m for the H-11b3 to H-11b1 path, 0.52 m for the H-11b2 to H-11b1 path, and 1.20 m for the H-11b4 to H-11b1 path (Figure 10-17). This simulation used maximum values for



Observed data pared for figure clarity.

Figure 10-16. Sensitivity to horizontal anisotropy ($T_x:T_y$) for the H-11 convergent-flow tracer test.



SIMULATION PARAMETERS	
Fracture Porosity	= 2.0×10^{-4}
Matrix Porosity	= 0.30
Dispersivity	= 0.5 m
Tortuosity	= 0.38
Pumping Rate	= 0.3775 L/s
Thickness	= 8.22 m
Well Spacing	
b3 to b1	= 21.34 m
b2 to b1	= 21.84 m
b4 to b1	= 43.54 m
Free-Water Diffusion Coefficient	
m-TFMB	= $7.9 \times 10^{-10} \text{ m}^2/\text{s}$
PFB	= $7.7 \times 10^{-10} \text{ m}^2/\text{s}$
o-TFMB	= $7.9 \times 10^{-10} \text{ m}^2/\text{s}$
Matrix-Block Lengths	
b3 to b1 path	= 1.070 m
b2 to b1 path	= 0.516 m
b4 to b1 path	= 1.200 m

Observed data pared for figure clarity.

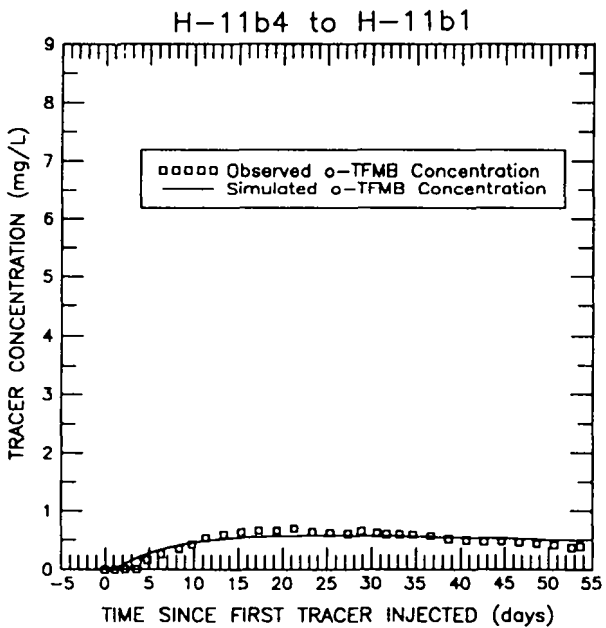
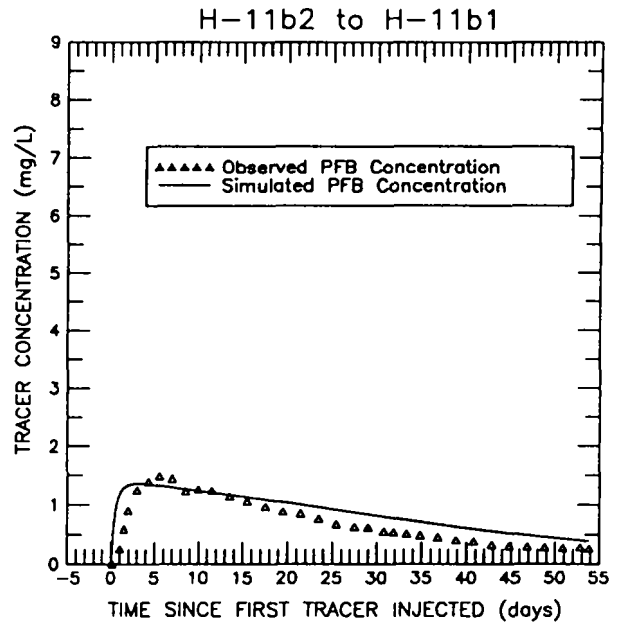
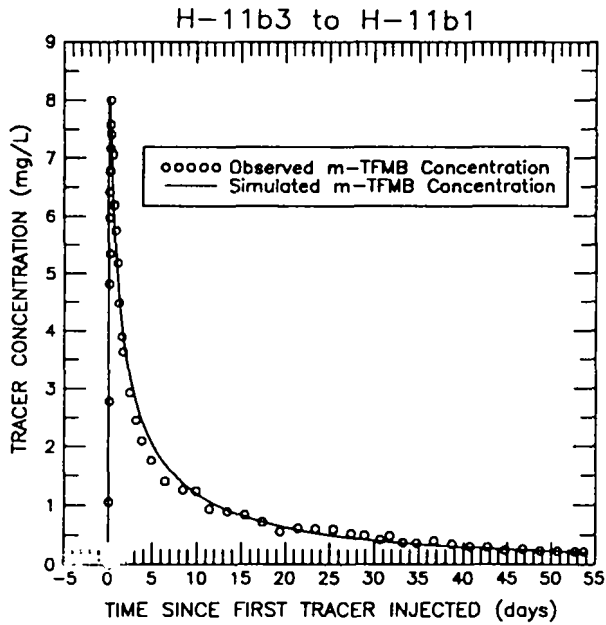
Figure 10-17. Sensitivity recalibration to observed tracer breakthrough at the H-11 hydropad to obtain maximum matrix-block lengths.

tortuosity, matrix porosity, well spacing, effective Culebra thickness, and free-water diffusion coefficient, and minimum values for longitudinal dispersivity and pumping rate. For a combination of parameters that minimized matrix diffusion (i.e., minimum values for tortuosity, matrix porosity, well spacing, effective Culebra thickness, and free-water diffusion coefficient and maximum values for longitudinal dispersivity and pumping rate), the observed PFB and o-TFMB concentration data could not be matched and, therefore, a minimum matrix-block length could not be defined for the H-11b2 to H-11b1 and H-11b4 to H-11b1 paths. To match the observed PFB and o-TFMB data with the simulations, the matrix porosity had to be increased from its minimum value (0.08) to its maximum value (0.30). This recalibration yielded minimum matrix-block lengths of 0.05 m for the path from H-11b3 to H-11b1, 0.02 m for the path from H-11b2 to H-11b1, and 0.05 m for the path from H-11b4 to H-11b1 (Figure 10-18). A fracture porosity of 8.0×10^{-4} was used for these simulations. The parameters used for these sensitivities are summarized in Table 10-5.

10.6 Summary of Results for H-11

The three breakthrough curves from the H-11 convergent-flow tracer test differ significantly. The difference between the m-TFMB and PFB breakthrough curves can be explained by differences in the transport behavior along their respective travel paths due to heterogeneity between the two paths or to horizontal anisotropy in transmissivity. The difference between the m-TFMB and o-TFMB breakthrough curves can be explained principally by the difference in the distances that the tracers had to travel (20.9 m versus 43.1 m).

Simulation of the breakthrough curves using the heterogeneous-analysis approach yielded a fracture porosity of 5.0×10^{-4} and matrix-block lengths of 0.32 m for the H-11b3 to H-11b1 path, 0.13 m for the path from H-11b2 to H-11b1, and 0.29 m for the H-11b4 to H-11b1 path. Using the anisotropic-analysis approach, the observed tracer concentrations were best fit with a fracture porosity of 1.0×10^{-3} , an anisotropy ratio of 3:1, a T_x direction



SIMULATION PARAMETERS

Fracture Porosity = 8.0×10^{-4}
 Matrix Porosity = 0.30
 Dispersivity = 3.0 m
 Tortuosity = 0.027
 Pumping Rate = 0.3875 L/s
 Thickness = 2.0 m
 Well Spacing
 b3 to b1 = 20.46 m
 b2 to b1 = 20.96 m
 b4 to b1 = 42.66 m
 Free-Water Diffusion Coefficient
 m-TFMB = $6.9 \times 10^{-10} \text{ m}^2/\text{s}$
 PFB = $6.7 \times 10^{-10} \text{ m}^2/\text{s}$
 o-TFMB = $6.9 \times 10^{-10} \text{ m}^2/\text{s}$
 Matrix-Block Lengths
 b3 to b1 path = 0.0504 m
 b2 to b1 path = 0.0200 m
 b4 to b1 path = 0.0530 m

Observed data pared for figure clarity.

Figure 10-18. Sensitivity recalibration to observed tracer breakthrough at the H-11 hydropad to obtain minimum matrix-block lengths.

Table 10-5. Transport Parameters Used in the Sensitivity Analysis to Determine the Maximum and Minimum Matrix-Block Lengths at the H-11 Hydropad

<u>Parameter</u>	<u>Sensitivity Analysis to Determine Maximum Matrix-Block Length</u>	<u>Sensitivity Analysis to Determine Minimum Matrix-Block Length</u>
Effective-Culebra Thickness	8.22 m	2.0 m
Pumping Rate	0.3775 L/s	0.3875 L/s
Well Spacings	21.3 m H-11b3 to H-11b1 21.8 m H-11b2 to H-11b1 43.5 m H-11b4 to H-11b1	20.5 m H-11b3 to H-11b1 21.0 m H-11b2 to H-11b1 42.7 m H-11b4 to H-11b1
Free-Water Diffusion Coefficients	m-TFMB $7.9 \times 10^{-10} \text{ m}^2/\text{s}$ PFB $7.7 \times 10^{-10} \text{ m}^2/\text{s}$ o-TFMB $7.9 \times 10^{-10} \text{ m}^2/\text{s}$	m-TFMB $6.9 \times 10^{-10} \text{ m}^2/\text{s}$ PFB $6.7 \times 10^{-10} \text{ m}^2/\text{s}$ o-TFMB $6.9 \times 10^{-10} \text{ m}^2/\text{s}$
Longitudinal Dispersivity	0.5 m	3.0 m
Tortuosity	0.38	0.027
Matrix Porosity	0.30	0.30
Fracture Porosity	2.0×10^{-4}	8.0×10^{-4}
Matrix-Block Length	1.07 m H-11b3 to H-11b1 0.52 m H-11b2 to H-11b1 1.20 m H-11b4 to H-11b1	0.05 m H-11b3 to H-11b1 0.02 m H-11b2 to H-11b1 0.05 m H-11b4 to H-11b1

of $N72^{\circ}W$ (four degrees clockwise from the H-11b3 to H-11b1 path), and a matrix-block length of 0.19 m. The matrix-block length determined with the anisotropic-analysis approach is bounded by the lengths determined with the heterogeneous approach. The anisotropy ratio determined with this analysis is greater than the hydraulic testing based value of 1.6:1 reported by Saulnier (1987). The T_x direction of $N72^{\circ}W$ reported here is 23.8 degrees clockwise from the average direction of $N84.2^{\circ}E$ reported by Saulnier (1987) but is within the range of directions that he reported.

Sensitivity analyses were conducted on matrix-block length and anisotropy ratio. Matrix-block length was determined to be a more sensitive parameter for the path with less matrix participation and a less sensitive parameter for the path with greater matrix participation. The simulations examining sensitivity to anisotropy ratio indicated that the observed m-TFMB and o-TFMB data can be matched with anisotropy ratios ranging from 1:1 to 20:1 but all three of the observed breakthrough curves could be matched only with an anisotropy ratio of 3:1 combined with a principal-transmissivity direction of $N72^{\circ}W$. The sensitivity analysis conducted to determine the maximum and minimum matrix-block lengths for the H-11 hydropad yielded a high-end value of 1.20 m and a low-end value of 0.02 m. This sensitivity included the uncertainty in the assigned parameters and, therefore, the determined maximum and minimum matrix-block lengths can be viewed as a measure of the uncertainty in that parameter.

11.0 COMPARISON OF SINGLE- AND DOUBLE-POROSITY TRANSPORT CONCEPTUALIZATIONS FOR THE H-3, H-6, AND H-11 TRACER TESTS

Simulations were conducted using SWIFT II with single-porosity conceptualizations to evaluate whether or not single-porosity, fracture-only or single-porosity, matrix-only models could adequately simulate the tracer-breakthrough curves for the H-3, H-6, and H-11 hydropads. The parameters controlling single-porosity transport are porosity, longitudinal dispersivity, effective aquifer thickness, well spacing, and pumping rate. Although tortuosity and free-water diffusion coefficient are important parameters in double-porosity transport, the values for these parameters are irrelevant in the single-porosity model because of the dominance of mechanical dispersion (longitudinal dispersivity multiplied by pore-water velocity) in comparison to diffusion. Two criteria were used in an attempt to match the observed tracer-breakthrough curves using a single-porosity approach. The first single-porosity system used the arrival time for the peak concentration for the rapid-transport travel path as the matching criterion. A porosity representative of fractures only was necessary to satisfy this criterion. The second single-porosity system used the magnitude of the peak concentration observed for each flow path at the hydropad as the matching criterion. Porosities representative of the rock matrix were utilized for this fitting exercise. Adjustments of each transport input parameter were made to maximize the possibility of fitting the observed data using a single-porosity conceptualization, however, these adjustments were limited to the range for each parameter as discussed in Section 5.0.

The time to peak concentration for the m-TFMB breakthrough curve observed at the H-3 hydropad can be matched using a single-porosity, fracture-only system with a porosity of 2.0×10^{-3} (Figure 11-1). This porosity is equal to the initial estimate of the fracture porosity calculated using Equation 5-9. The Culebra thickness, well spacing, longitudinal dispersivity, and pumping rate for this simulation are summarized in Table 11-1. Although the time to reach the peak m-TFMB concentration was matched by the single-porosity, fracture-only simulation, the predicted peak concentration was a factor of 9.5 greater than

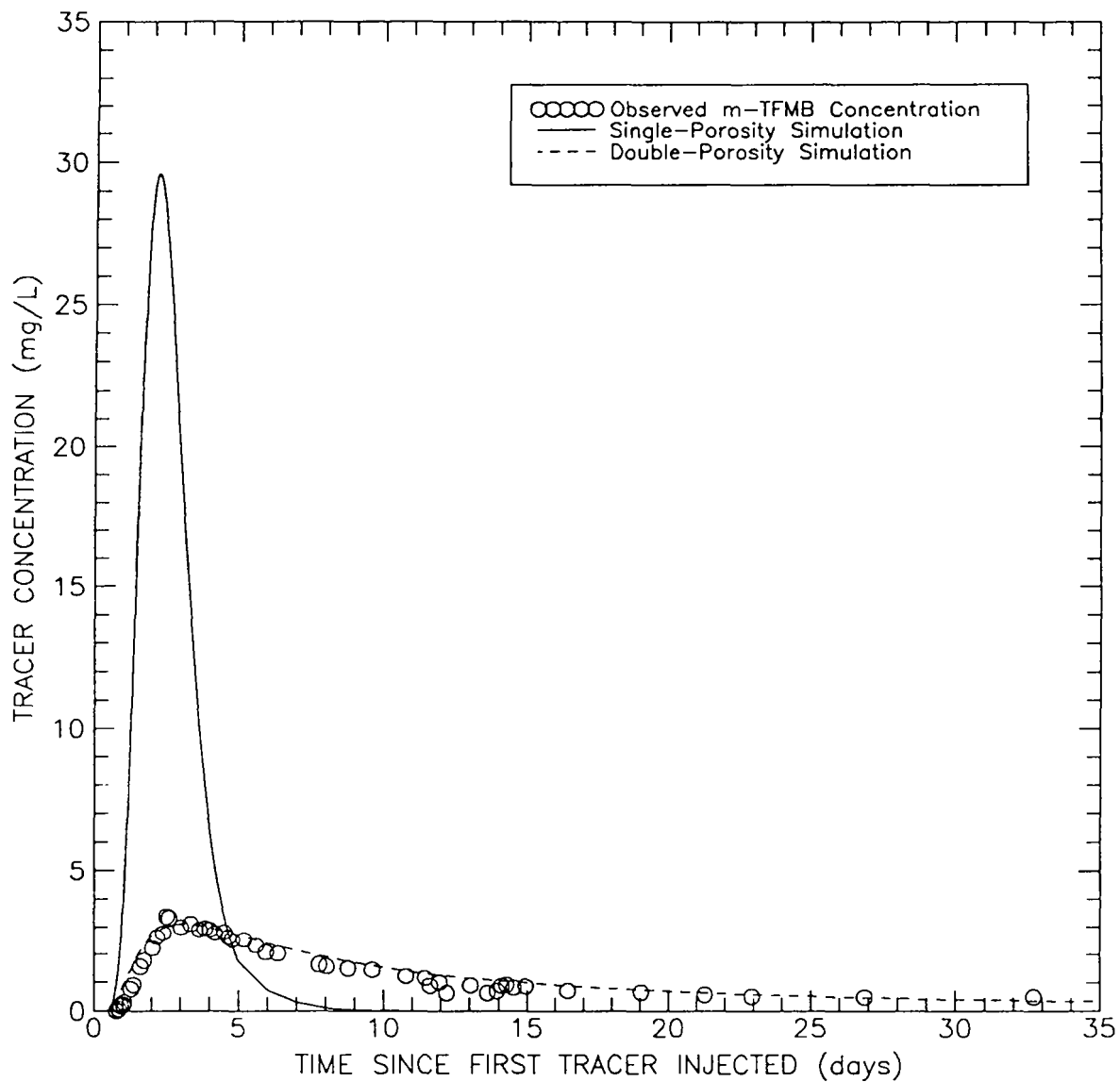


Figure 11-1. Single-porosity, fracture-system simulation of the m-TFMB breakthrough curve at the H-3 hydropad.

Table 11-1. Transport Parameters for Attempted Single-Porosity Interpretations of the H-3 Convergent-Flow Tracer Test

	Peak-Concentration Arrival-Time Case (Fracture Only)	Peak-Concentration Case (Matrix Only)	
	<u>m-TFMB Breakthrough Curve</u>	<u>m-TFMB Breakthrough Curve</u>	<u>PFB Breakthrough Curve</u>
Porosity	2.0 x 10 ⁻³	0.08	0.17
Longitudinal Dispersivity	1.5 m	1.7 m	3.0 m
Culebra Thickness	7.21 m	2.0 m	7.62 m
Well Spacing	30.7 m	30.3 m	26.4 m
Pumping Rate	0.19 L/s	0.195 L/s	0.195 L/s

the observed peak concentration. The best-fit, double-porosity simulation using the anisotropic-analysis approach is also shown on Figure 11-1. Unlike the single-porosity, fracture-only simulation, the double-porosity simulation matched both the peak-concentration arrival time and the peak concentration. The best attempted matches to the observed m-TFMB and PFB peak concentrations at the H-3 hydropad using a single-porosity, matrix-only conceptualization and the best-fit, double-porosity simulations are illustrated in Figure 11-2. The values for the transport parameters used in the single-porosity, matrix-only simulations are summarized on Table 11-1. For the single-porosity, matrix-only simulations, the predicted time to reach peak concentration was a factor of 5.5 longer than the observed time for the m-TFMB breakthrough curve and a factor of 4.3 longer than the observed time for the PFB breakthrough curve. The m-TFMB breakthrough curve produced by the single-porosity, matrix-only simulation was more symmetric (i.e., less late-time tailing) with respect to the rising and falling limbs, than is the observed breakthrough curve.

The time to reach the peak PFB concentration for test #1 at the H-6 hydropad was matched using a porosity of 3.0×10^{-3} with a single-porosity, fracture-only conceptualization. The results of this simulation and the best-fit, double-porosity simulation are illustrated in Figure 11-3. The transport parameters used are summarized in Table 11-2. The single-porosity, fracture-only simulation yielded a peak concentration that was a factor of 6.3 greater than the observed peak concentration and a breakthrough curve having nearly symmetrical rising and falling limbs and essentially no tailing. The maximum concentrations of PFB and m-TFMB observed at the H-6 hydropad were matched using single-porosity, matrix-only conceptualizations with the parameters summarized in Table 11-2. Although the magnitudes of the peak concentrations were matched with the single-porosity, matrix-only simulations, the simulated time to reach the peak was a factor of 5.4 greater than the observed time for the PFB breakthrough curve and a factor of 3.2 greater than the observed time for the m-TFMB breakthrough curve. A comparison of the observed data, single-porosity, matrix-only results, and best-fit, double-porosity results is given in Figure 11-4.

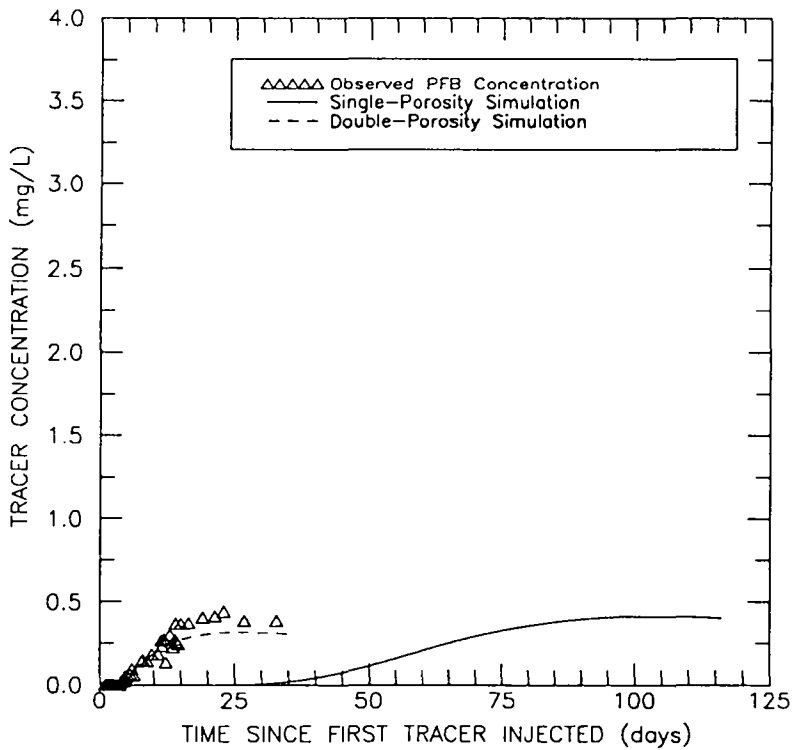
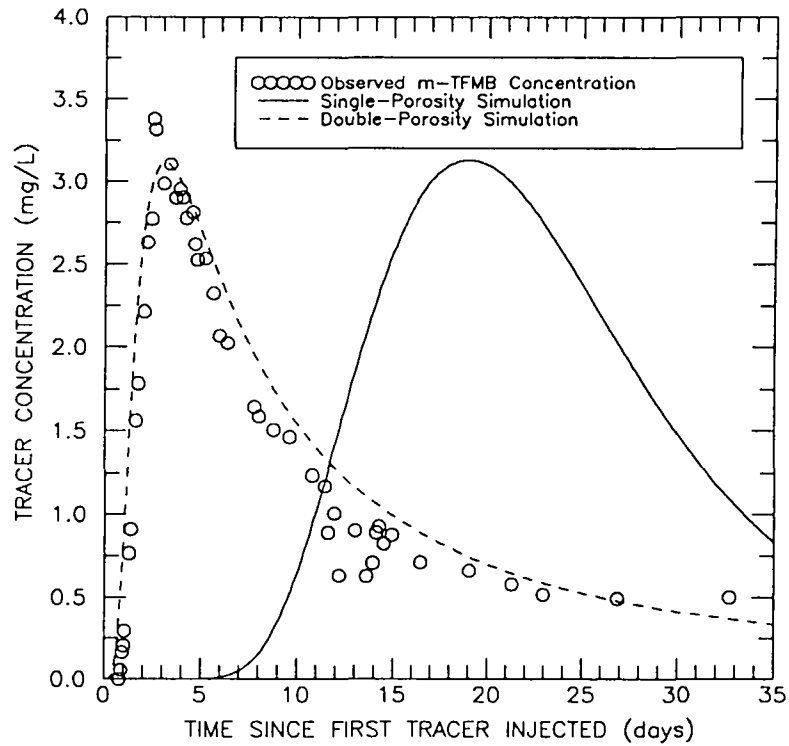
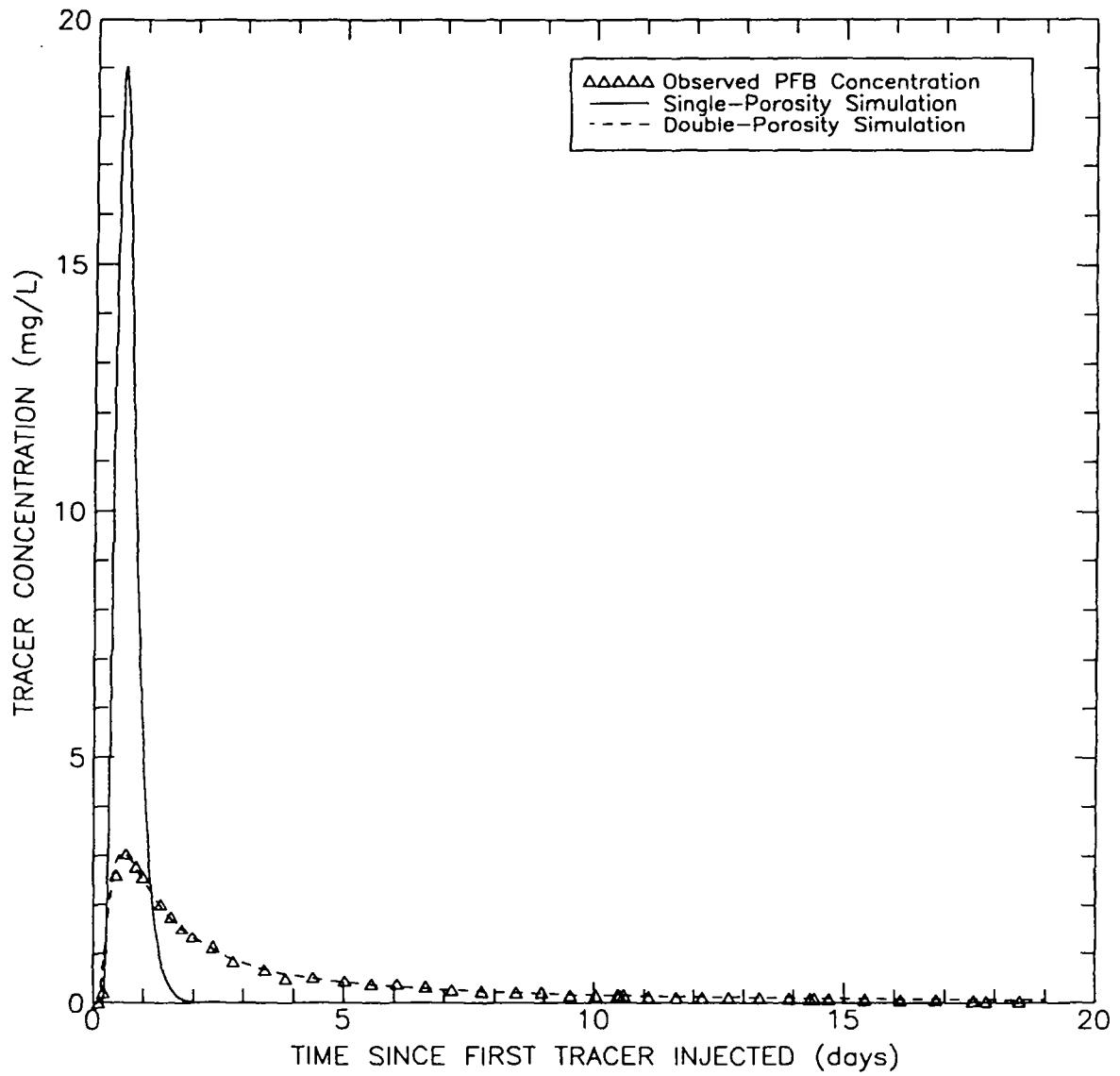


Figure 11-2. Single-porosity, matrix-system simulations of the m-TFMB and PFB breakthrough curves at the H-3 hydropad.

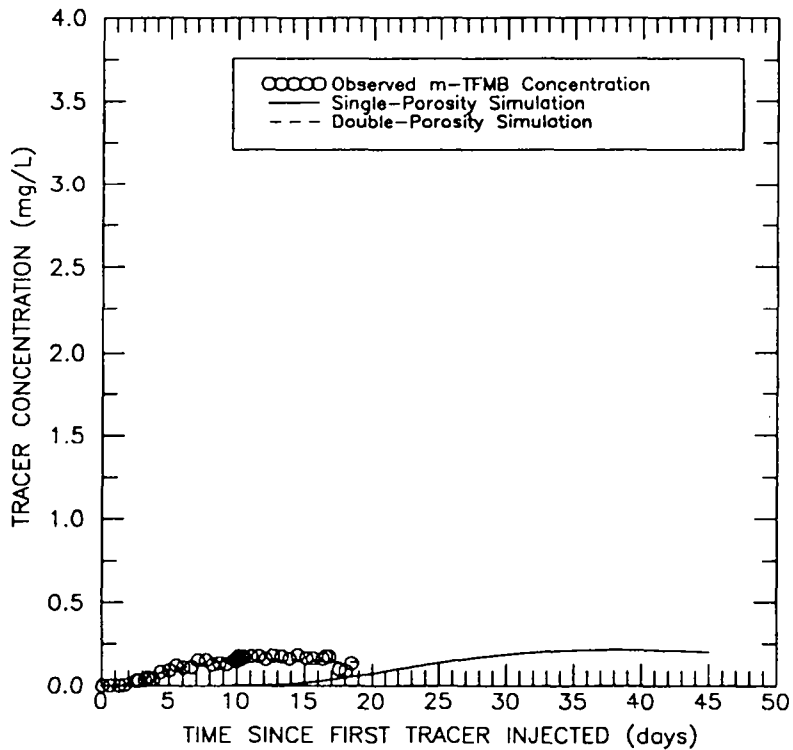
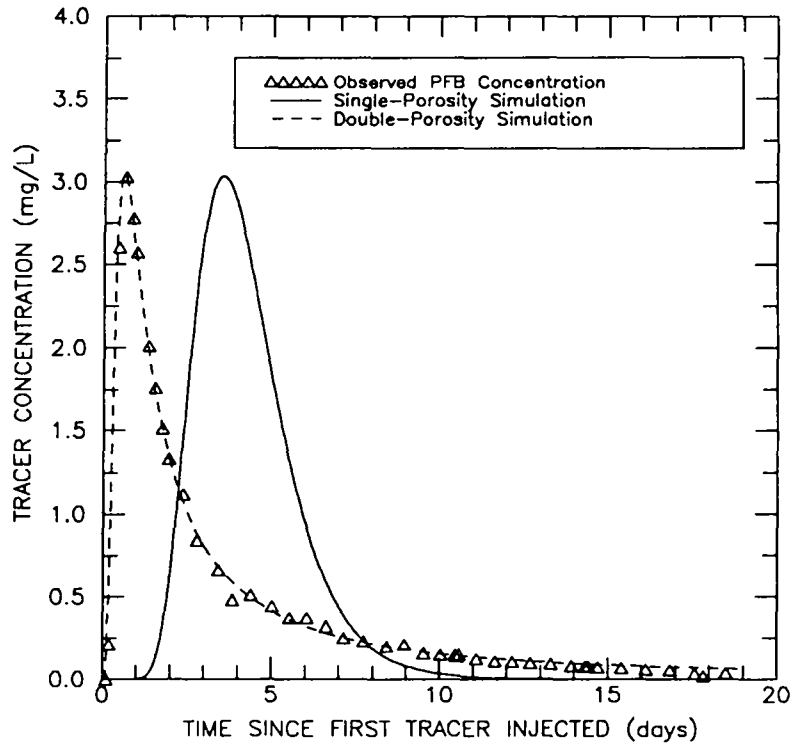


Observed data pared for figure clarity.

Figure 11-3. Single-porosity, fracture-system simulation of the PFB breakthrough curve at the H-6 hydrograd.

Table 11-2. Transport Parameters for Attempted Single-Porosity Interpretations of H-6 Convergent-Flow Tracer Test #1

	Peak-Concentration Arrival-Time Case (Fracture Only)	Peak-Concentration Case (Matrix Only)	
	<u>PFB Breakthrough Curve</u>	<u>PFB Breakthrough Curve</u>	<u>m-TFMB Breakthrough Curve</u>
Porosity	3.0 x 10 ⁻³	0.08	0.22
Longitudinal Dispersivity	1.5 m	1.35 m	3.0 m
Culebra Thickness	7.01 m	2.0 m	7.61 m
Well Spacing	29.9 m	28.9 m	31.1 m
Pumping Rate	1.04 L/s	1.065 L/s	1.065 L/s

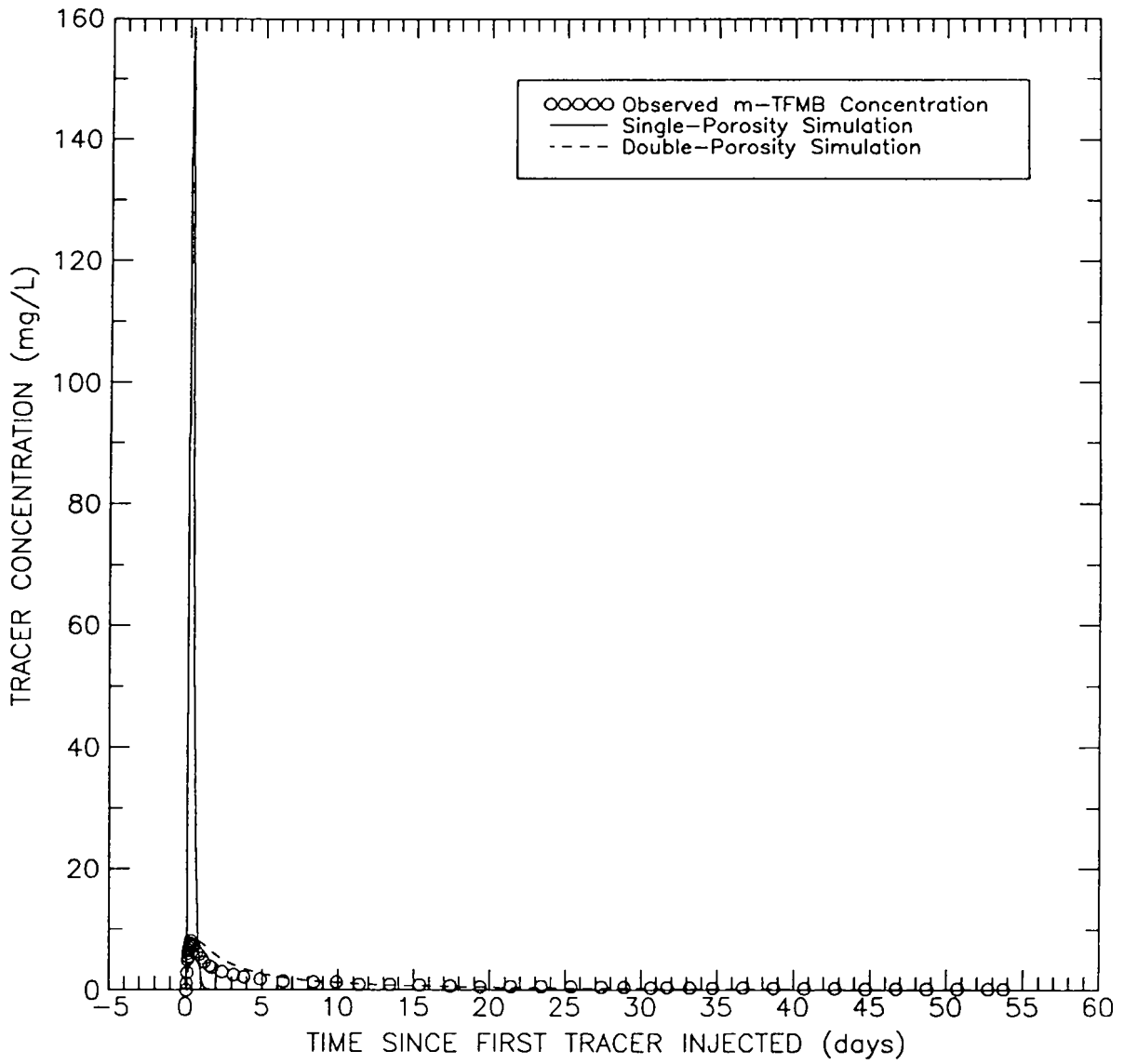


Observed data pared for figure clarity.

Figure 11-4. Single-porosity, matrix-system simulations of the PFB and m-TFMB breakthrough curves at the H-6 hydropad.

The single-porosity, fracture-only simulation yielding the closest match to the arrival time of the peak m-TFMB concentration at the H-11 hydropad required a porosity equal to the estimated fracture porosity of 1.0×10^{-3} calculated with Equation 5-9. This simulation, the best-fit, double-porosity simulation, and the observed m-TFMB data are illustrated in Figure 11-5. The single-porosity, fracture-only parameters are summarized in Table 11-3. Striking differences between the single-porosity, fracture-only simulation and the observed data are the absence of tailing in the simulated breakthrough curve and the presence of significant tailing in the observed data, and the magnitude of the peak concentration. The peak concentration simulated using the single-porosity, fracture-only model is a factor of 19.8 higher than the observed peak concentration. The single-porosity, matrix-only simulations yielding the closest match to the observed magnitudes of the m-TFMB, PFB, and o-TFMB peak concentrations are presented in Figure 11-6 along with the best-fit, double-porosity simulations for each breakthrough curve. In each case, the single-porosity, matrix-only model produced breakthrough curves that peaked later and had less tailing than the observed curves. For the m-TFMB, PFB, and o-TFMB breakthrough curves the single-porosity, matrix-only model yielded peak-concentration arrival times that were factors of 13.5, 4.5, and 5.2, respectively, later than the observed peak-concentration arrival times. Table 11-3 contains the values of the transport parameters used for the single-porosity, matrix-only simulations.

In summary, satisfactory comparisons between the observed and calculated breakthrough curves for the H-3, H-6, and H-11 tracer tests were not possible using either single-porosity, fracture-only or single-porosity, matrix-only conceptualizations with the objective of fitting either the arrival time of the peak concentration or the peak concentration, respectively, using values for the transport parameters that fall within the ranges discussed in Section 5.0. The single-porosity simulations could match either the peak-concentration arrival time or the peak concentration but not both. A match to the peak-concentration arrival time yielded peak concentrations that were factors of 6.3 to 19.8 larger than the observed peak concentration. Simulations that matched the peak

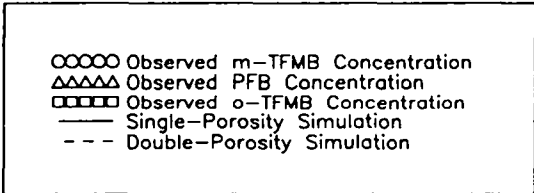
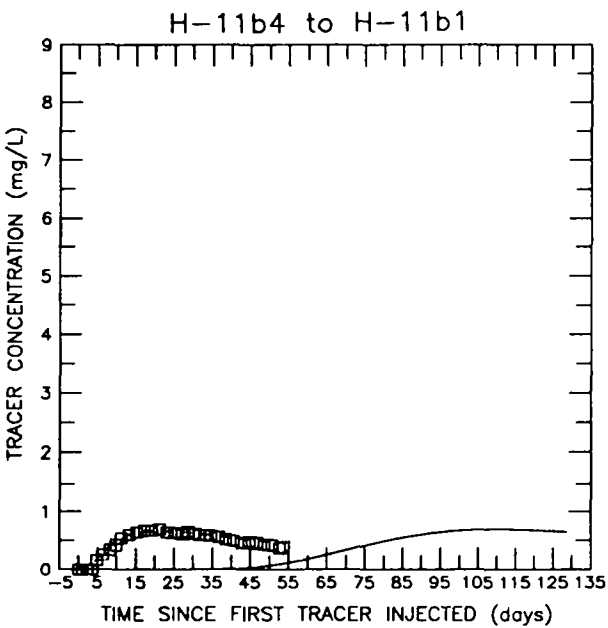
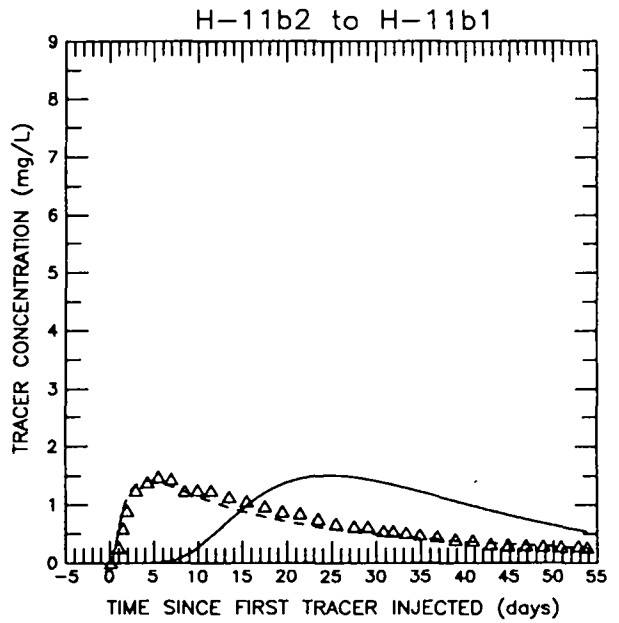
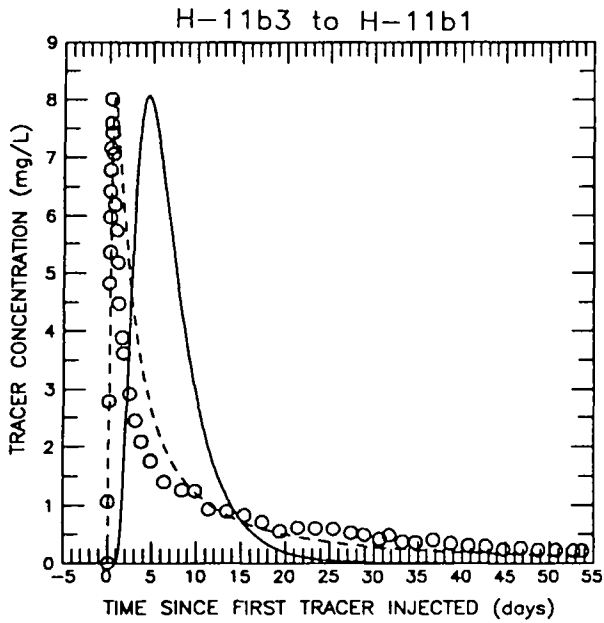


Observed data pared for figure clarity.

Figure 11-5. Single-porosity, fracture-system simulation of the m-TFMB breakthrough curve at the H-11 hydropad.

Table 11-3. Transport Parameters for Attempted Single-Porosity Interpretations of the H-11 Convergent-Flow Tracer Test

	Peak-Concentration Arrival-Time Case (Fracture Only)	Peak-Concentration Case (Matrix Only)		
	m-TFMB Breakthrough Curve	m-TFMB Breakthrough Curve	PFB Breakthrough Curve	o-TFMB Breakthrough Curve
Porosity	1.0×10^{-3}	0.082	0.11	0.10
Longitudinal Dispersivity	1.5 m	3.0 m	3.0 m	3.0 m
Culebra Thickness	7.62 m	2.0 m	8.22 m	8.22 m
Well Spacing	20.9 m	20.5 m	20.96 m	42.7 m
Pumping Rate	0.38 L/s	0.3875 L/s	0.3875 L/s	0.3875 L/s



Observed data pared for figure clarity.

Figure 11-6. Single-porosity, matrix system simulations of the m-TFMB, PFB, and o-TFMB breakthrough curves at the H-11 hydropad.

concentrations produced peak arrival times that were factors of 3.2 to 13.5 later than the observed data. In addition, the rising and falling limbs of the breakthrough curves produced by the single-porosity simulations were more symmetrical than those of the observed data and the degree of tailing of the simulated breakthrough curves was significantly less than the observed tailing. The inability of the model to reproduce the observed breakthrough curves using a single-porosity conceptualization indicates that transport in the Culebra at the H-3, H-6, and H-11 hydropads cannot be adequately represented by a system of fractures only or matrix only. Using a double-porosity conceptualization, on the other hand, yielded simulated breakthrough curves that closely fit both the arrival time and concentration of the tracer peak as well as the general characteristics of the observed breakthrough curves.

12.0 SUMMARY AND CONCLUSIONS

The results of this tracer-test interpretation study are intended to provide quantification of transport processes and parameters in support of performance-assessment calculations for the WIPP repository being performed by Sandia National Laboratories. This section provides a summary of the results of the tracer tests and their interpretations, presents key conclusions, and discusses the implications of the results of this study for regional-scale transport simulations.

12.1 Summary

Tracer tests have been conducted in the Culebra Dolomite Member of the Rustler Formation at the H-2, H-3, H-4, H-6, and H-11 hydropads. The objective of the tracer-test interpretations was to evaluate quantitatively the physical solute-transport parameters of the Culebra dolomite at these hydropad locations. Two-well recirculating tracer tests were conducted at the H-2 and H-6 hydropads and convergent-flow tracer tests were conducted at the H-3, H-4, H-6, and H-11 hydropads. A previous interpretation of the H-2 tracer tests is presented in Hydro Geo Chem (1986). The convergent-flow tracer tests conducted at the H-3 and H-4 hydropads have also been previously interpreted in Kelley and Pickens (1986). Examination of the tracer tests conducted at the H-2 and H-4 hydropads and five of the seven tracer tests conducted at the H-6 hydropad indicated that the data were unsuitable for further quantitative analyses because of factors such as tracer degradation, insufficient flushing of the tracer from the tracer-addition wells, and equipment failure. Some of these tests do provide important qualitative information about transport processes in the Culebra dolomite. Tests analyzed and discussed in detail in this report are the convergent-flow tracer test conducted at the H-3 hydropad, the first two convergent-flow tracer tests conducted at the H-6 hydropad, and the convergent-flow tracer test conducted at the H-11 hydropad.

Hydro Geo Chem (1986) reported that quantitative evaluation of formation properties from the PFB breakthrough curve obtained from the H-2 two-well recirculating tracer tests was not possible. They interpreted the SCN breakthrough curve using the Grove and Beetem (1971) model that assumes a one-dimensional single-porosity, homogeneous porous medium. Although the comparison between the model and observed breakthrough curves was relatively poor, they estimated a range of 0.11 to 0.19 for effective porosity and a range of 4.9 to 5.5 m for dispersivity. Examination of the travel times for the tracers in the H-2 tests suggests that transport has occurred under single-porosity, matrix-only conditions.

The convergent-flow tracer tests conducted at the H-3 and H-4 hydropads were previously interpreted by Kelley and Pickens (1986). For the H-3 hydropad, they selected a double-porosity conceptualization consisting of an idealized homogeneous system of three intersecting, orthogonal sets of parallel fractures as suitable for simulating the tracer-breakthrough curves. They reported a fracture porosity of 1.9×10^{-3} , matrix-block lengths of 1.2 and 2.1 m for tortuosities of 0.15 and 0.45, respectively, for the H-3b1 to H-3b3 path, and matrix-block lengths of 0.25 and 0.44 m for tortuosities of 0.15 and 0.45, respectively, for the H-3b2 to H-3b3 path. Tortuosity values for these interpretations were selected based on literature values. Subsequent core measurements indicated that only the simulations using a tortuosity of 0.15 are realistic for the H-3 hydropad. Kelley and Pickens (1986) concluded that the interpretation of the convergent-flow tracer test conducted at the H-4 hydropad did not provide reliable quantitative estimates of the physical solute-transport parameters for the Culebra. Qualitatively, the observed tracer-breakthrough curves could possibly be simulated by representing the Culebra with a layered-porous-media system of higher- and lower-permeability units. No evidence was obtained to indicate that transport of the tracers had occurred through fractures at the H-4 hydropad.

The transport parameters used in the tracer-test interpretations presented in this report were determined based on the current physical and conceptual understanding of the Culebra dolomite. Values for the input parameters affecting tracer transport were assigned

based on data from laboratory experiments conducted on Culebra core collected across the WIPP site and scientific judgement. A range of measured or estimated values and the measurement and/or calculated uncertainty for the values was developed to define a potential range for each transport parameter. Transport of the tracers from the tracer-addition wells to the pumping wells was analyzed using the finite-difference model SWIFT II.

Prior to analyzing the tracer-breakthrough curves, the appropriate governing processes had to be estimated using the information base for the specific hydropads. At the H-3, H-6, and H-11 hydropads, the characteristics of the tracer-breakthrough curves and hydraulic-test responses suggested that a double-porosity conceptualization of the Culebra dolomite could be appropriate. In the tracer tests, these characteristics include the very rapid breakthrough and strong tailing that occurred on one flow path at each hydropad. In the hydraulic tests, these characteristics include a distinct shift in the pressure curve, accompanied by a minimum in the pressure-derivative curve, indicative of the change from early-time, fracture-dominated response to late-time, matrix-dominated response. The double-porosity conceptualization assumed three intersecting, orthogonal sets of parallel fractures. With this conceptualization, the fractures represent the principal-transport medium and the matrix provides the bulk of the solute-storage capability. The double-porosity model considered advective-dispersive transport in the fractures and diffusive transport in the matrix.

Major differences were observed in the breakthrough curves at the individual hydropads. Two approaches were considered to explain those differences. The first was the heterogeneous-analysis approach, which assumed that the differences resulted from heterogeneity between the different flow paths at the individual hydropads. The heterogeneity considered was matrix-block length, which is also a measure of fracture spacing. The second was the anisotropic-analysis approach, which assumed that anisotropy in the horizontal transmissivity caused the differences in the tracer-breakthrough characteristics. The existence of anisotropy implies that directional fracture/matrix

properties are present at the H-3, H-6, and H-11 hydropads and that preferred fracture orientations result in more direct transport along one flow path. In summary, the heterogeneous-analysis approach examines a physical scenario which assumes that all of the differences in the breakthrough curves are due to the different surface area available for diffusion (i.e., greater for small matrix-block size and smaller for large matrix-block size) whereas the anisotropic-analysis approach assumes that all of the difference is due to differences in fluid flux along each path (which affects both the advective-transport rate and the time available for diffusion). Actual solute transport was most likely a combination of heterogeneous and anisotropic effects. However, the analyses presented in this report investigated only the two idealized cases.

Table 12-1 summarizes the best-fit, double-porosity, fitted parameters determined from analysis of the H-3, H-6, and H-11 tracer tests. Because the fitting parameters are not known to a high degree of certainty, the values reported in Table 12-1 are rounded to a smaller number of significant figures than the value actually used in the simulations. Results using the heterogeneous-analysis approach yielded fracture porosities ranging from 5.0×10^{-4} to 1.5×10^{-3} with an arithmetic average of 1.1×10^{-3} and matrix-block lengths ranging from 0.06 to 1.23 m with an arithmetic average of 0.39 m. The lowest fracture porosity was at the H-11 hydropad and the highest was at the H-6 hydropad. The largest and smallest matrix-block lengths were determined for the H-3 and H-6 hydropads, respectively. Fracture porosities of 2.0×10^{-3} for the H-3 hydropad, 3.0×10^{-3} for the H-6 hydropad, and 1.0×10^{-3} for the H-11 hydropad were used for the anisotropic-analysis approach. The calibrated matrix-block lengths with this approach were 0.48, 0.15 and 0.19 m for the H-3, H-6, and H-11 hydropads, respectively, with an average of 0.27 m. For all hydropads, the best-fit, anisotropic matrix-block length was within the range determined by the heterogeneous-analysis approach. The highest anisotropy ratio (7:1) was calculated for the H-6 hydropad and the lowest (3:1) for the H-11 hydropad. For the H-3 and H-6 hydropads, the orientations of the principal-transmissivity vectors were determined to be N57°E and N31°W, respectively (parallel to the fracture-controlled transport paths). The calculated

Table 12-1. Summary of Best-Fit, Double-Porosity, Fitted Parameters from Interpretation of the Tracer Tests at the H-3, H-6, and H-11 Hydropads

<u>Test and Path</u>	<u>Heterogeneous</u>		<u>Anisotropic</u>			
	<u>Fracture Porosity</u>	<u>Matrix-Block Length</u>	<u>Fracture Porosity</u>	<u>Matrix-Block Length</u>	<u>T_x:T_y</u>	<u>Principal Direction</u>
H-3 TEST						
H-3b1 to H-3b3	1.2 x 10 ⁻³	1.23 m	2.0 x 10 ⁻³	0.48 m	6:1	N57° E
H-3b2 to H-3b3	1.2 x 10 ⁻³	0.23 m	2.0 x 10 ⁻³	0.48 m	6:1	N57° E
H-6 TEST #1						
H-6b to H-6c	1.5 x 10 ⁻³	0.41 m	3.0 x 10 ⁻³	0.15 m	7:1	N31° W
H-6a to H-6c	1.5 x 10 ⁻³	0.06 m	3.0 x 10 ⁻³	0.15 m	7:1	N31° W
H-6 TEST #2						
H-6b to H-6c	1.5 x 10 ⁻³	0.44 m	na	na	na	na
H-11 TEST						
H-11b3 to H-11b1	5.0 x 10 ⁻⁴	0.32 m	1.0 x 10 ⁻³	0.19 m	3:1	N72° W
H-11b2 to H-11b1	5.0 x 10 ⁻⁴	0.13 m	1.0 x 10 ⁻³	0.19 m	3:1	N72° W
H-11b4 to H-11b1	5.0 x 10 ⁻⁴	0.29 m	1.0 x 10 ⁻³	0.19 m	3:1	N72° W
na means not applicable						

principal direction was oriented N72° W (4 degrees clockwise from the fracture-controlled transport path) at the H-11 hydropad.

Interpretations of the tracer-breakthrough curves using the anisotropic-analysis approach indicate that the rapid transport paths (H-3b1 to H-3b3, H-6b to H-6c, and H-11b3 to H-11b1) are aligned parallel to the major axis of transmissivity at the H-3 and H-6 hydropads and nearly parallel to the major axis at the H-11 hydropad. Sensitivity analyses indicated that T_x orientation is a very sensitive parameter. Small deviations in the best-fit orientation significantly degraded the match between the simulated and observed breakthrough curves. This suggests confidence in the best-fit orientations. At the H-6 hydropad, the T_x orientation (N31° W) determined through analysis of the tracer test is almost identical to the orientations of N29° W (Gonzalez, 1983) and N29.6° W (Neuman et al., 1984) determined through analysis of hydraulic-test data. The T_x direction of N72° W reported from the anisotropic-analysis interpretation of the tracer test conducted at the H-11 hydropad falls within the wide range that Saulnier (1987) developed based on interpretations of hydraulic-test data. In summary, the good agreement between the T_x orientations determined from analysis of the tracer tests and the orientations reported by Gonzalez (1983), Neuman et al. (1984), and Saulnier (1987) based on interpretations of hydraulic-test data, and the sensitivity of the simulated curves to T_x direction support the best-fit orientations reported here.

The anisotropy ratios yielded by interpretation of the tracer test using the anisotropic-analysis approach were 6:1 at the H-3 hydropad, 7:1 at the H-6 hydropad, and 3:1 at the H-11 hydropad. The interpreted anisotropy ratio at the H-6 hydropad is greater than the hydraulic testing based values of 1.91:1 reported by Neuman et al. (1984) and 2.1:1 reported by Gonzalez (1983). The anisotropy ratio of 1.6:1 estimated by Saulnier (1987) based on hydraulic-testing data is lower than the ratio of 3:1 determined based on analysis of the H-11 tracer test. The anisotropy ratio determined from hydraulic testing is expected to differ from that interpreted from fitting of the tracer-breakthrough curves because of the different scales tested. Evaluation of the hydraulic tests utilize pressure data based on

stressing the Culebra to distances on the order of 100's to 1000's of meters whereas the evaluation of tracer tests utilize data based on tracer transport along distances from 21 to 43 m.

Using the H-3 tracer test, sensitivity analyses were conducted on the parameters tortuosity, matrix porosity, longitudinal dispersivity, and fracture porosity. The upper and lower bounds estimated from measured tortuosity and matrix-porosity values from Culebra core were examined by the sensitivity analysis and indicated that model results for both flow paths are very sensitive to these two parameters. The effect of increasing tortuosity and increasing matrix porosity is to increase diffusive losses from the fractures to the matrix. For the fracture-controlled path, increasing longitudinal dispersivity results in less mass loss to the matrix and decreasing dispersivity causes a reduction in the influence of hydrodynamic-dispersive transport. Both effects yield higher peak concentrations at the pumping well. Increasing dispersivity decreases the amount of mass lost to the matrix and reducing dispersivity increases diffusive losses to the matrix along the slow-transport path. In a double-porosity system, an increase in fracture porosity results in a corresponding decrease in ground-water velocity within the fracture system under the same pumping rate. Therefore, the residence time in the fractures is increased allowing greater diffusive losses to the matrix. The effect of fracture porosity on breakthrough concentration is more evident along the fracture-dominated transport path than along the slow transport path.

Sensitivity analyses were conducted for all three of the analyzed tracer tests to examine the effects of matrix-block length and anisotropy ratio on simulated results. Matrix-block length controls both the matrix-surface-area-to-volume ratio and the total number of fractures in a given model volume and, therefore, has a large impact on solute diffusion between fractures and matrix. The purpose of the analysis of sensitivity to anisotropy ratio was to determine whether there was more than one $T_x:T_y$ and T_x direction that would yield model simulations that matched all of the observed breakthrough curves at an individual hydropad. The conclusion from this analysis was that only one combination of anisotropy

ratio and principal T_x direction at each hydropad will give simulated results that match all of the observed tracer-breakthrough curves.

Sensitivity analyses were also conducted to estimate the maximum and minimum matrix-block lengths at the H-3, H-6, and H-11 hydropads in order to estimate the uncertainty in this important fitted parameter. For the simulation to require a maximum matrix-block length to fit the observed data, the other transport parameters must be assigned values that ensure maximum diffusive loss from the fracture into the matrix. For the simulation to require a minimum matrix-block length to fit the observed data, the other transport parameters must be assigned values that ensure minimal diffusive loss from the fractures into the matrix, yet still produce a reasonable match between observed and simulated breakthrough. The heterogeneous-analysis approach was used for this series of sensitivity analyses since that approach yields an upper bound for the matrix-block length through calibration to the fracture-controlled breakthrough curve and a lower bound for the matrix-block length through calibration to the slow breakthrough curve. Table 12-2 and Figure 12-1 summarize the best-fit, maximum, and minimum matrix-block lengths for the H-3, H-6, and H-11 hydropads. For H-3, the lowest and highest estimated matrix-block lengths are 0.03 and 3.22 m. The lowest matrix-block length at the H-6 hydropad was 0.03 m and the highest value was 1.56 m. Low and high values of 0.02 and 1.20 m were estimated for matrix-block length at the H-11 hydropad.

Simulations were conducted using a single-porosity model to evaluate whether or not single-porosity, fracture-only or single-porosity, matrix-only conceptualizations could adequately simulate the tracer-breakthrough curves for the H-3, H-6, and H-11 hydropads. The two criteria used for the simulations were (1) the arrival time of the peak concentration for the rapid-transport path and (2) the magnitude of the peak concentration observed for each flow path. For the first criterion porosities representative of fracture-only conditions were necessary and for the second criterion porosities representative of matrix-only conditions were necessary. Each of the parameters controlling single-porosity transport was adjusted within the ranges defined in Section 5.0 until the closest match between the

Table 12-2. Best-Fit, Minimum, and Maximum Matrix-Block Lengths for the H-3, H-6, and H-11 Hydropads

<u>Hydropad</u>	<u>Matrix-Block Length (m)</u>		
	<u>Best-Fit</u>	<u>Minimum</u>	<u>Maximum</u>
H-3	0.23 - 1.23	0.03 - 0.20	0.75 - 3.22
H-6	0.06 - 0.44	0.03 - 0.18	0.24 - 1.56
H-11	0.13 - 0.32	0.02 - 0.05	0.52 - 1.20

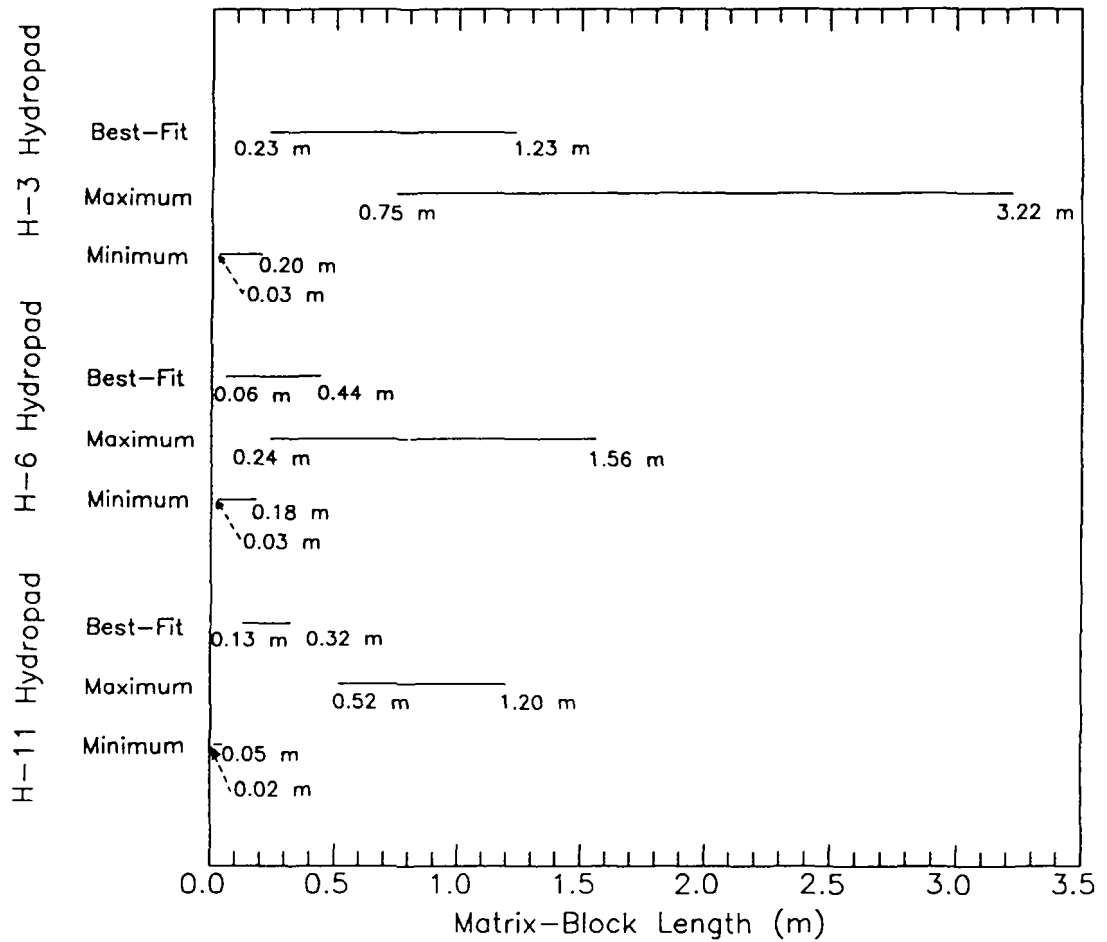


Figure 12-1. Summary of ranges of best-fit, maximum, and minimum matrix-block lengths for the H-3, H-6, and H-11 hydropads using the heterogeneous-analysis approach.

simulated and observed data was obtained. The single-porosity simulations could match either the peak-concentration arrival time or the peak concentration, but not both. Fracture-only simulations matching the peak-concentration arrival time yielded peak concentrations ranging from a factor of 6.3 to a factor of 19.8 higher than the observed peak concentration. Arrival of the peak tracer concentration by factors of 3.2 to 13.5 later than the observed peak were obtained with matrix-only simulations that matched to peak concentration. In addition, the overall shapes of the breakthrough curves generated with the single-porosity models did not match those of the observed breakthrough curves. The inability of the model to reproduce the observed breakthrough curves using either single-porosity, fracture-only or single-porosity, matrix-only conceptualizations indicates that transport in the Culebra cannot be adequately represented by a system of fractures only or matrix only at the H-3, H-6, and H-11 hydropads.

12.2 Conclusions

The main conclusions of this report are:

- Evaluation of pumping and tracer tests for the H-3, H-6, and H-11 hydropads indicates that the Culebra dolomite can be represented as a double-porosity medium at those locations. The identification of double-porosity transport behavior is consistent with other observations of the physical characteristics of the Culebra in the WIPP-site region including the presence of fractures in outcrops, shafts, and core samples and the presence of relatively large matrix porosities.
- Single-porosity, fracture-only and single-porosity, matrix-only conceptualizations were determined to be unsuitable for simulating the observed breakthrough curves at the H-3, H-6, and H-11 hydropads. Single-porosity conceptualizations were unable to reproduce the observed

breakthrough curves indicating that the Culebra at these hydropads could not be represented by a system of fractures only or matrix only.

- Single-porosity, matrix-only transport is considered to be the most representative conceptualization for the H-2 hydropad based on the large observed transport times between H-2 hydropad wells. Single-porosity, matrix-only transport through a vertically heterogeneous system is considered to be the most representative conceptualization for the H-4 hydropad based on a comparison of simulations that used different system conceptualizations.
- The breakthrough curves for the convergent-flow tracer tests conducted at the H-3, H-6, and H-11 hydropads were fit equally well using two different interpretation approaches: a heterogeneous-analysis approach relying upon physical differences between the travel paths to account for variations in breakthrough curves and an anisotropic-analysis approach which assumes that anisotropy in the horizontal transmissivity could account for the differences. Calibration to the observed breakthrough curves for the heterogeneous-analysis approach was conducted using fracture porosity and matrix-block length as the fitting parameters. Results indicated fracture porosities of 1.2×10^{-3} , 1.5×10^{-3} , and 5.0×10^{-4} at the H-3, H-6, and H-11 hydropads, respectively, with an arithmetic average of 1.1×10^{-3} . The determined matrix-block lengths were 1.23 and 0.23 m at the H-3 hydropad; 0.41, 0.06, and 0.44 m at the H-6 hydropad; and 0.32, 0.13, and 0.29 m at the H-11 hydropad. The arithmetic-average matrix-block length was 0.39 m. The fracture porosities used with the anisotropic-analysis approach were 2.0×10^{-3} for the H-3 hydropad, 3.0×10^{-3} for the H-6 hydropad, and 1.0×10^{-3} for the H-11 hydropad. The fitting parameters for the anisotropic simulations were horizontal anisotropy, which includes anisotropy ratio and orientation of the principal-transmissivity direction, and matrix-block length. The calibrated matrix-block lengths with this approach were 0.48, 0.15, and 0.19 m for the

H-3, H-6, and H-11 hydropads, respectively, with an average of 0.27 m. In all cases, the matrix-block length from the anisotropic interpretations lies within the range of matrix-block lengths determined by the heterogeneous-analysis approach. Anisotropy ratios of 6:1, 7:1, and 3:1 were determined for the H-3, H-6, and H-11 hydropads, respectively. The fitted parameters for the best-fit double-porosity simulations are summarized in Table 12-1.

- The parameters characterizing the transport properties for the Culebra at the hydropads where tracer tests have been performed are not known perfectly. Ranges of values for the parameters affecting tracer transport were assigned based on data from laboratory experiments conducted on Culebra core collected across the WIPP site and scientific judgement. Measurement and/or calculated uncertainties in the parameters were also defined. The ranges of potential values developed for the Culebra parameters that apply to the regional scale were 0.027 to 0.38 for matrix tortuosity, 0.08 to 0.30 for matrix porosity, and 2.0 to 8.2 m for the effective Culebra thickness.
- Sensitivity analyses illustrated that only one anisotropy ratio and T_x orientation at each hydropad would yield simulated results that match all of the observed tracer-breakthrough curves. The orientation of the principal transmissivity direction was determined to be parallel to the fracture-controlled transport path or N57°E and N31°W for the H-3 and H-6 hydropads, respectively, and four degrees clockwise from the fracture-controlled transport path or N72°W at the H-11 hydropad.
- Sensitivity analyses conducted to determine minimum and maximum matrix-block lengths provided a measure of the uncertainty in this important fitted parameter. These sensitivity analyses yielded a low-end value of 0.03 m and a high-end value of 3.22 m at the H-3 hydropad, a low-end value of 0.03 m and a high-end value of 1.56 m at the H-6 hydropad, and a low-end value of

0.02 m and a high-end value of 1.20 m for the H-11 hydropad. The range of matrix-block lengths when one considers all tests is from 0.02 to 3.22 m. The interpreted best-fit and range of matrix-block lengths are summarized in Table 12-2 and Figure 12-1.

- Diffusion of solutes from the fractures to the matrix is an important process during transport in the Culebra. The large solute-storage capacity provided by the relatively high matrix porosity (estimated range of 0.08 to 0.30) is a key factor in the importance of the matrix-diffusion process in the Culebra at the WIPP site.
- Sensitivity analyses on effective Culebra thickness showed that the assumed transport thickness impacts the value of fracture porosity, matrix porosity, and matrix-block length required to simulate the observed breakthrough curves. Evaluation of the impact of this type of vertical heterogeneity on transport in the Culebra would benefit from further field testing at existing hydropads. One field test could include pumping a well while simultaneously conducting a spinner flowmeter to delineate levels at which the bulk of flow is occurring into the borehole. A second technique might involve injecting different tracers into different vertically isolated intervals of the tracer-addition wells during a convergent-flow tracer test.
- Although the observed tracer-test behavior has been successfully simulated using the double-porosity transport model, other conceptualizations for physical transport are possible. For example, advective transport through a heterogeneous medium, through variable-aperture fractures, or through networks of discrete fractures are alternative models that should be assessed. Some combination of these forms of advective transport combined with matrix diffusion should also be considered. While these alternative models could be applied to the existing tracer-test data sets, the limited number of tracer travel

paths in a single convergent-flow test and the limitation of only a single pumping rate and well at each hydropad most likely preclude the possibility for differentiating between alternative transport models with the existing tracer-test data.

12.3 Implications for Regional-Scale Transport Calculations

Double-porosity transport parameters have been interpreted for the Culebra dolomite at the scale of tens of meters from tracer tests performed at the H-3, H-6, and H-11 hydropads. In an attempt to identify any correlation between hydrologic and double-porosity transport parameters, Table 12-3 summarizes transmissivities, fracture porosities, and average matrix-block sizes for the three hydropads. Interestingly, all of these interpreted parameters show a relatively small degree of variation. The H-3 hydropad exhibits the lowest transmissivity and largest matrix-block length (fracture spacing) and the H-6 and H-11 hydropads exhibit approximately equal transmissivities, which are about an order of magnitude higher than at H-3, and approximately equal matrix-block lengths which are about a factor of three smaller than at H-3. From this limited data base it appears that the matrix-block length (fracture spacing) decreases with increasing transmissivity. No apparent trend between transmissivity and fracture porosity is evident from the data available. Because no strong correlation exists between matrix-block length and transmissivity or between fracture porosity and transmissivity there is, at present, no mechanism for extrapolating these parameters over the WIPP-site region using the widely distributed transmissivity data base currently available for the site.

The Culebra is expected to exhibit heterogeneity in properties along the estimated offsite pathway from above the waste panels to the southern WIPP-site boundary as shown in Figure 2-7. Transmissivity of the Culebra dolomite has been estimated from field hydraulic testing at four locations along this pathway (H-1, H-3, H-11, and DOE-1) and ranges from $9.4 \times 10^{-7} \text{ m}^2/\text{s}$ at H-1 to $3.1 \times 10^{-5} \text{ m}^2/\text{s}$ at H-11 (Cauffman et al., 1990).

Table 12-3. Summary of Transmissivities, Fracture Porosities, and Matrix-Block Lengths for the H-3, H-6, and H-11 Hydropads

<u>Hydropad</u>	<u>Transmissivity</u>	<u>Heterogeneous</u>		<u>Anisotropic</u>	
		<u>Fracture Porosity</u>	<u>Average Matrix-Block Length</u>	<u>Fracture Porosity</u>	<u>Matrix-Block Length</u>
H-3	$2.5 \times 10^{-6} \text{ m}^2/\text{s}$	1.2×10^{-3}	0.73 m	2.0×10^{-3}	0.48 m
H-6	$3.5 \times 10^{-5} \text{ m}^2/\text{s}$	1.5×10^{-3}	0.24 m	3.0×10^{-3}	0.15 m
H-11	$3.1 \times 10^{-5} \text{ m}^2/\text{s}$	5.0×10^{-4}	0.24 m	1.0×10^{-3}	0.19 m

Hydraulic responses observed during testing indicate apparent single-porosity, matrix-only behavior at H-1 and double-porosity behavior at H-3, H-11, and DOE-1 (Beauheim, 1987a, 1987b; 1989). As shown in Figure 2-7, H-1 is located above the northern edge of the northwestern portion of the waste-panel region. Hydropad H-2, located about 0.8 km west of H-1, has an average Culebra transmissivity of $6.3 \times 10^{-7} \text{ m}^2/\text{s}$. At the H-2 hydropad, single-porosity hydraulic and transport behavior have been observed. Because of the similarity in transmissivity at H-1 and the H-2 hydropad, it is expected that flow and transport in a porous-medium system exists in the Culebra above some of the waste-panel region. Because hydropad H-3 is located about 0.2 km south of the southern boundary of the waste-panel region, double-porosity flow and transport also may exist over the southern portion of the waste-panel area.

The potential ranges of transmissivities, matrix-block lengths, and fracture porosities along the offsite pathway to the southern WIPP-site boundary could be larger than those interpreted at the H-3 and H-11 hydropads. Transport characteristics have been determined from tracer tests at only two locations (i.e., H-3 and H-11 hydropads) along the offsite transport pathway (Figure 2-7). Only single tracer tests have been performed at these two hydropads, testing two transport paths at the H-3 hydropad and three transport paths at the H-11 hydropad. The model-calibrated transmissivity distribution (Figure 12-2) along the offsite travel path in the Culebra is uncertain as a result of the limited number of boreholes in the southeastern portion of the WIPP site. Reduction in the uncertainties in the flow and transport properties may necessitate the installation and testing of additional boreholes in the Culebra in the southeastern quadrant of the WIPP site and the implementation of additional tracer tests at existing and/or new hydropad sites to further test transport characteristics including vertical heterogeneities in the Culebra. The uncertainty in transmissivity further manifests itself in uncertainty in the Darcy flux in the fractures. The Darcy flux in the fractures is important with respect to transport rates in the fractures and time available for solute diffusion into the matrix.

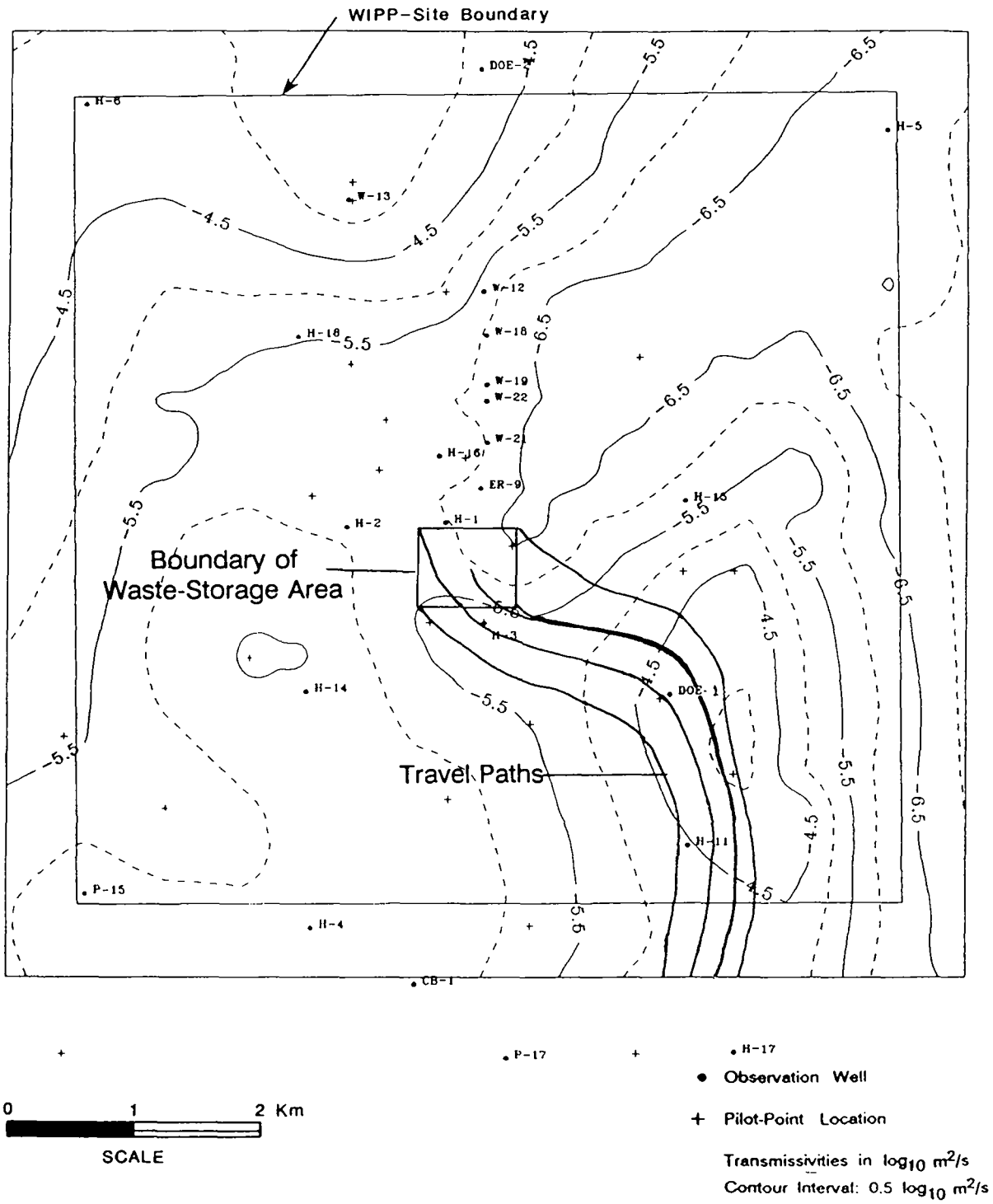


Figure 12-2. Transient calibrated \log_{10} transmissivities within the WIPP-site boundary (from LaVenue et al., 1990).

Little quantitative data are available concerning the geometry and continuity of fractures in the Culebra. Examination of core from the WIPP-site boreholes has revealed that (1) both high-angle and horizontal fractures are present and (2) fractures vary from being open to being partially or fully filled with clay or gypsum. Mapping at the WIPP-site shafts indicates that the fractures are associated with discrete levels within the Culebra. Examination of a Culebra outcrop near the WIPP site shows significant heterogeneity in fracturing both horizontally and vertically. However, the enhanced weathering and differential vertical movements at the outcrop have likely caused fracturing to be much more extensive than at any location within the Culebra along the offsite flow path. These observations suggest that fracturing in the Culebra is heterogeneous at a variety of scales. For the hydropad-scale tracer-test interpretations, it was assumed that there is sufficient uniformity to allow selection of the SWIFT II option utilizing three intersecting fracture sets. One approach for regional-scale transport simulations would be to use a conceptualization consisting of a single set of parallel non-intersecting fractures with fracture spacing equal to the values determined in the hydropad-scale tests. Such an approach has been used by Reeves et al. (1987, 1991) and Lappin et al. (1989, 1990) for transport simulations in the Culebra at the WIPP site. This approach is conservative with respect to the surface area available for matrix diffusion, leading to more rapid offsite contaminant transport.

Both the single-porosity, fracture-only and single-porosity, matrix-only conceptualizations were determined to be unsuitable for simulating tracer tests at the H-3, H-6, and H-11 hydropads (Section 11.0), whereas the double-porosity conceptualization resulted in good agreement between observed and simulated breakthrough curves. Because double-porosity conditions may be present over at least the southern portion of the waste-panel area and because double-porosity conditions likely exist along the offsite transport pathway, a double-porosity conceptualization is the appropriate model for regional-scale transport calculations.

Alternative conceptualizations for transport through the Culebra that could fit the observed data equally as well as a double-porosity conceptualization may be possible.

However, differentiating realistic alternative transport models from unrealistic models can probably not be performed with the existing tracer-test data. In addition, the impacts of such alternative models for regional-scale transport are, at present, unknown. A new series of tracer tests has been proposed that incorporates a large number of travel paths (13), transport under a variety of flow rates, and transport scales that vary by an order of magnitude. This test series will provide the data necessary to rigorously test the viability of the double-porosity model and whether or not alternative transport conceptualizations are realistic for the Culebra dolomite at the WIPP site. This test series will also provide data for a direct examination of scaling effects and vertical heterogeneity. Laboratory column tests currently under development will further examine the matrix-diffusion process that is a critical component of the double-porosity model.

13.0 REFERENCES

- Abelin, H., L. Birgersson, L. Moreno, H. Widén, T. Ågren, and I. Neretnieks. 1991. "A Large-Scale Flow and Tracer Experiment in Granite. 2. Results and Interpretation," *Water Resources Research*. Vol. 27, no. 12, 3119-3135.
- American Society of Mechanical Engineers. 1986. *Quality Assurance Program Requirements for Nuclear Facilities*. ANSI/ASME NQA-1. New York, NY: American Society of Mechanical Engineers.
- Arya, A. 1986. "Dispersion and Reservoir Heterogeneity." PhD dissertation. Austin, TX: University of Texas at Austin.
- Arya, A., T.A. Hewett, R.G. Larson, and L.W. Lake. 1988. "Dispersion and Reservoir Heterogeneity," *SPE Reservoir Engineering*. Vol. 3, no. 1, 140-148.
- Bachman, G.O. 1980. *Regional Geology and Cenozoic History of Pecos Region, South-Eastern New Mexico*. Open-File Report 80-1099. Denver, CO: U.S. Geological Survey.
- Bachman, G.O. 1985. *Assessment of Near-Surface Dissolution at and Near the Waste Isolation Pilot Plant (WIPP), Southeastern New Mexico*. SAND84-7178. Albuquerque, NM: Sandia National Laboratories.
- Bachman, G.O. 1987. *Karst in Evaporites in Southeastern New Mexico*. SAND86-7078. Albuquerque, NM: Sandia National Laboratories.
- Barackman, M.L. 1986. "Diverging Flow Tracer Tests in Fractured Granite; Equipment Design and Data Collection." M.S. thesis. Tucson, AZ: University of Arizona.
- Bear, J. 1972. *Dynamics of Fluids in Porous Media*. New York, NY: American Elsevier Publishing Company.
- Beauheim, R.L. 1986. *Hydraulic-Test Interpretations for Well DOE-2 at the Waste Isolation Pilot Plant (WIPP) Site*. SAND86-1364. Albuquerque, NM: Sandia National Laboratories.

- Beauheim, R.L. 1987a. *Interpretations of Single-Well Hydraulic Tests Conducted at and Near the Waste Isolation Pilot Plant (WIPP) Site, 1983-1987*. SAND87-0039. Albuquerque, NM: Sandia National Laboratories.
- Beauheim, R.L. 1987b. *Analysis of Pumping Tests of the Culebra Dolomite Conducted at the H-3 Hydropad at the Waste Isolation Pilot Plant (WIPP) Site*. SAND86-2311. Albuquerque, NM: Sandia National Laboratories.
- Beauheim, R.L. 1987c. *Interpretation of the WIPP-13 Multipad Pumping Test of the Culebra Dolomite at the Waste Isolation Pilot Plant (WIPP) Site*. SAND87-2456. Albuquerque, NM: Sandia National Laboratories.
- Beauheim, R.L. 1989. *Interpretation of H-11b4 Hydraulic Tests and the H-11 Multipad Pumping Test of the Culebra Dolomite at the Waste Isolation Pilot Plant (WIPP) Site*. SAND89-0536. Albuquerque, NM: Sandia National Laboratories.
- Beauheim, R.L., and R.M. Holt. 1990. "Hydrogeology of the WIPP Site," *Geological and Hydrological Studies of Evaporites in the Northern Delaware Basin for the Waste Isolation Pilot Plant (WIPP), New Mexico, GSA Field Trip #14 Guidebook, Geological Society of America 1990 Annual Meeting, Dallas, TX, October 29-November 1, 1990*. Dallas, TX: Dallas Geological Society. 131-179.
- Beauheim, R.L., T.F. Dale, and J.F. Pickens. 1991. *Interpretations of Single-Well Hydraulic Tests of the Rustler Formation Conducted in the Vicinity of the Waste Isolation Pilot Plant Site, 1988-1989*. SAND89-0869. Albuquerque, NM: Sandia National Laboratories.
- Bourdet, D., and A.C. Gringarten. 1980. "Determination of Fissure Volume and Block Size in Fractured Reservoirs by Type-Curve Analysis." *55th Annual Fall Technical Conference and Exhibition, Dallas, TX, September 21-24, 1980*. SPE 9293. Richardson, TX: Society of Petroleum Engineers.
- Bourdet, D., J.A. Ayoub, and Y.M. Pirard. 1989. "Use of Pressure Derivative in Well-Test Interpretation," *SPE Formation Evaluation*. Vol. 4, no. 2, 293-302.
- Bowman, R.S. 1984. "Evaluation of Some New Tracers for Soil Water Studies," *Soil Science Society of America Journal*. Vol. 48, no. 5, 987-993.

- Bowman, R.S., and R.C. Rice. 1986. "Transport of Conservative Tracers in the Field Under Intermittent Flood Irrigation," *Water Resources Research*. Vol. 22, no. 11, 1531-1536.
- Cauffman, T.L., A.M. LaVenue, and J.P. McCord. 1990. *Ground-Water Flow Modeling of the Culebra Dolomite. Volume II: Data Base*. SAND89-7068/2. Albuquerque, NM: Sandia National Laboratories.
- Chaturvedi, L., and J.K. Channell. 1985. *The Rustler Formation as a Transport Medium for Contaminated Groundwater*. EEG-32. Sante Fe, NM: Environmental Evaluation Group.
- Chaturvedi, L., and K. Rehfeldt. 1984. "Groundwater Occurrence and the Dissolution of Salt at the WIPP Radioactive Waste Repository Site," *EOS Transactions, American Geophysical Union*. Vol. 65, no. 31.
- Chen, C.S. 1986. "Solutions for Radionuclide Transport From an Injection Well Into a Single Fracture in a Porous Formation," *Water Resources Research*. Vol. 22, no. 4, 508-518.
- Cooper, J.B., and V.M. Glanzman. 1971. *Geohydrology of Project Gnome Site, Eddy County, New Mexico*. Geological Survey Professional Paper 712-A. Washington DC: U.S. Government Printing Office.
- de Marsily, G. 1986. *Quantitative Hydrogeology: Groundwater Hydrology for Engineers*. Orlando, FL: Academic Press, Inc.
- Deal, D.E., R.J. Abitz, D.S. Belski, J.B. Clark, M.E. Crawley, and M.L. Martin. 1991. *Brine Sampling and Evaluation Program. 1989 Report*. DOE-WIPP-91-009. Carlsbad, NM: Westinghouse Electric Corporation.
- Dennehy, K.F. 1982. *Results of Hydrologic Tests and Water-Chemistry Analyses, Wells H-6A, H-6B, and H-6C, at the Proposed Waste Isolation Pilot Plant Site, Southeastern New Mexico*. Water-Resources Investigations 82-8. Albuquerque, NM: U.S. Geological Survey.
- Domenico, P.A. 1972. *Concepts and Models in Groundwater Hydrology*. New York, NY: McGraw-Hill Book Co.

- Dykhuizen, R.C., and W.H. Casey. 1989. *An Analysis of Solute Diffusion in the Culebra Dolomite*. SAND89-0750. Albuquerque, NM: Sandia National Laboratories.
- Finley, N.C., and M. Reeves. 1981. *SWIFT Self-Teaching Curriculum: Illustrative Problems to Supplement the User's Manual for the Sandia Waste-Isolation Flow and Transport Model (SWIFT)*. SAND81-0410, NUREG/CR-1968. Albuquerque, NM: Sandia National Laboratories.
- Gelhar, L.W., A. Mantoglou, C. Welty, and K.R. Rehfeldt. 1985. *A Review of Field-Scale Physical Solute Transport Processes in Saturated and Unsaturated Porous Media*. EPRI EA-4190. Palo Alto, CA: Electric Power Research Institute.
- Gonzalez, D.D. 1983. *Groundwater Flow in the Rustler Formation, Waste Isolation Pilot Plant (WIPP), Southeast New Mexico (SENM): Interim Report*. SAND82-1012. Albuquerque, NM: Sandia National Laboratories.
- Grove, D.B., and W.A. Beetem. 1971. "Porosity and Dispersion Constant Calculations for a Fractured Carbonate Aquifer Using the Two Well Tracer Method," *Water Resources Research*. Vol. 7, no. 1, 128-134.
- Guvanasen, V., and V.M. Guvanasen. 1987. "An Approximate Semianalytical Solution for Tracer Injection Tests in a Confined Aquifer With a Radially Converging Flow Field and Finite Volume of Tracer and Chase Fluid," *Water Resources Research*. Vol. 23, no. 8, 1607-1619.
- Hantush, M.S. 1966. "Analysis of Data from Pumping Tests in Anisotropic Aquifers," *Journal of Geophysical Research*. Vol. 71, no. 2, 421-426.
- Holt, R.M., and D.W. Powers. 1984. *Geotechnical Activities in the Waste Handling Shaft, Waste Isolation Pilot Plant (WIPP) Project, Southeastern New Mexico*. WTSD-TME-038. Carlsbad, NM: U.S. Department of Energy, Waste Isolation Pilot Plant.
- Holt, R.M., and D.W. Powers. 1986. *Geotechnical Activities in the Exhaust Shaft*. DOE-WIPP-86-008. Carlsbad, NM: U.S. Department of Energy.

- Holt, R.M., and D.W. Powers. 1988. *Facies Variability and Post-Depositional Alteration Within the Rustler Formation in the Vicinity of the Waste Isolation Pilot Plant, Southeastern New Mexico*. DOE-WIPP-88-04. Carlsbad, NM: Westinghouse Electric Corporation.
- Holt, R.M., and D.W. Powers. 1990a. "Halite Sequences Within the Late Permian Salado Formation in the Vicinity of the Waste Isolation Pilot Plant," *Geological and Hydrological Studies of Evaporites in the Northern Delaware Basin for the Waste Isolation Pilot Plant (WIPP), New Mexico, Field Trip #14 Guidebook, Geological Society of America 1990 Annual Meeting, Dallas, TX, October 29-November 1, 1990*. Dallas, TX: Dallas Geological Society. 45-78.
- Holt, R.M., and D.W. Powers. 1990b. *Geologic Mapping of the Air Intake Shaft at the Waste Isolation Pilot Plant*. DOE/WIPP-90-051. Carlsbad, NM: Westinghouse Electric Corporation.
- Hydro Geo Chem, Inc. 1985. *WIPP Hydrology Program, Waste Isolation Pilot Plant, SENM, Hydrologic Data Report #1*. SAND85-7206. Albuquerque, NM: Sandia National Laboratories.
- Hydro Geo Chem, Inc. 1986. *Two-Well Recirculation Tracer Tests at the H-2 Hydropad, Waste Isolation Pilot Plant (WIPP), Southeastern New Mexico*. SAND86-7092. Albuquerque, NM: Sandia National Laboratories.
- INTERA Technologies, Inc. 1986. *WIPP Hydrology Program, Waste Isolation Pilot Plant, Southeastern New Mexico, Hydrologic Data Report #3*. SAND86-7109. Albuquerque, NM: Sandia National Laboratories.
- Izette, G.A., and R.E. Wilcox. 1982. *Map Showing Localities and Inferred Distributions of the Huckleberry Ridge, Mesa Falls, and Lava Creek Ash Beds (Pearlette Family Ash Beds) of Pleistocene Age in the Western United States and Southern Canada*. Miscellaneous Investigations Series Map I-1325. Washington DC: U.S. Geological Survey.
- Johns, R.A., and P.V. Roberts. 1991. "A Solute Transport Model for Channelized Flow in a Fracture," *Water Resources Research*. Vol. 27, no. 8, 1797-1808.

- Jones, C.L. 1975. *Potash Resources in Part of Los Medaños Area of Eddy and Lea Counties, New Mexico*. Open-File Report 75-407. Denver, CO: U.S. Geological Survey.
- Jones, C.L., M.E. Cooley, and G.O. Bachman. 1973. *Salt Deposits of Los Medaños Area, Eddy and Lea Counties, New Mexico*. USGS Open-File Report 4339-7. Albuquerque, NM: U.S. Geological Survey.
- Katsube, T.J., T.W. Melnyk, and J.P. Hume. 1986. *Pore Structure from Diffusion in Granitic Rocks*. Technical Report TR-381. Pinawa, Manitoba: Atomic Energy of Canada Ltd.
- Kelley, V.A., and J.F. Pickens. 1986. *Interpretation of the Convergent-Flow Tracer Tests Conducted in the Culebra Dolomite at the H-3 and H-4 Hydropads at the Waste Isolation Pilot Plant (WIPP) Site*. SAND86-7161. Albuquerque, NM: Sandia National Laboratories.
- Kelley, V.A., and G.J. Saulnier, Jr. 1990. *Core Analyses for Selected Samples From the Culebra Dolomite at the Waste Isolation Pilot Plant (WIPP) Site*. SAND90-7011. Albuquerque, NM: Sandia National Laboratories.
- Klinkenberg, L.J. 1951. "Analogy Between Diffusion and Electrical Conductivity in Porous Rocks," *Bulletin of the Geological Society of America*. Vol. 62, 559-564.
- Lallemand-Barrès, A., and P. Peaudecerf. 1978. "Recherche des Relations Entre les Valeurs Mesurées de la Dispersivité Macroscopique d'un Milieu Aquifère, Ses Autres Caractéristiques et les Conditions de Mesure," *Bulletin du B.R.G.M. (Deuxième Série)*. Section III, no. 4, 277-284.
- Lambert, S.J. 1987. *Feasibility Study: Applicability of Geochronologic Methods Involving Radiocarbon and Other Nuclides to the Groundwater Hydrology of the Rustler Formation, Southeastern New Mexico*. SAND86-1054. Albuquerque, NM: Sandia National Laboratories.
- Lambert, S.J., and D.M. Harvey. 1987. *Stable-Isotope Geochemistry of Groundwaters in the Delaware Basin of Southeastern New Mexico*. SAND87-0138. Albuquerque, NM: Sandia National Laboratories.

- Lappin, A.R., R.L. Hunter, D.P. Garber, and P.B. Davies, eds. 1989. *Systems Analysis, Long-Term Radionuclide Transport, and Dose Assessments, Waste Isolation Pilot Plant, (WIPP), Southeastern New Mexico; March 1989*. SAND89-0462. Albuquerque, NM: Sandia National Laboratories.
- Lappin, A.R., R.L. Hunter, P.B. Davies, D.J. Borns, M. Reeves, J.F. Pickens, and H.J. Iuzzolino. 1990. *Systems Analysis, Long-Term Radionuclide Transport, and Dose Assessments, Waste Isolation Pilot Plant (WIPP), Southeastern New Mexico; September 1989*. SAND89-1996. Albuquerque, NM: Sandia National Laboratories.
- LaVenue, A.M., T.L. Cauffman, and J.F. Pickens. 1990. *Ground-Water Flow Modeling of the Culebra Dolomite. Volume I: Model Calibration*. SAND89-7068/1. Albuquerque, NM: Sandia National Laboratories.
- Lowenstein, T.K. 1987. *Post Burial Alteration of the Permian Rustler Formation Evaporites, WIPP Site, New Mexico: Textural, Stratigraphic and Chemical Evidence*. EEG-36. Sante Fe, NM: Environmental Evaluation Group.
- Mercer, J.W. 1983. *Geohydrology of the Proposed Waste Isolation Pilot Plant Site, Los Medanos Area, Southeastern New Mexico*. Water-Resources Investigations Report 83-4016. Albuquerque, NM: U.S. Geological Survey.
- Mercer, J.W. 1990. *Basic Data Report for Drillholes at the H-11 Complex (Waste Isolation Pilot Plant-WIPP)*. SAND89-0200. Albuquerque, NM: Sandia National Laboratories.
- Mercer, J.W., and B.R. Orr. 1979. *Interim Data Report on the Geohydrology of the Proposed Waste Isolation Pilot Plant Site Southeast New Mexico*. Water-Resources Investigations 79-98. Albuquerque, NM: U.S. Geological Survey.
- Mercer, J.W., P. Davis, K.F. Dennehy, and C.L. Goetz. 1981. *Results of Hydrologic Tests and Water-Chemistry Analyses, Wells H-4A, H-4B, and H-4C at the Proposed Waste Isolation Pilot Plant Site, Southeastern New Mexico*. Water-Resources Investigations 81-36. Albuquerque, NM: U.S. Geological Survey.

- Moench, A.F. 1987. "Radial Dispersion in a Double-Porosity System with Fracture Skin," *Proceedings: Twelfth Workshop Geothermal Reservoir Engineering*. Stanford University. (Copy on file at the Waste Management and Transportation Library, Sandia National Laboratories, Albuquerque, NM.)
- Moreno, L., and C.F. Tsang. 1991. "Multiple-Peak Response to Tracer Injection Tests in Single Fractures: A Numerical Study," *Water Resources Research*. Vol. 27, no. 8, 2143-2150.
- Moreno, L., Y.W. Tsang, C.F. Tsang, F.V. Hale, and I. Neretnieks. 1988. "Flow and Tracer Transport in a Single Fracture: A Stochastic Model and Its Relation to Some Field Observations," *Water Resources Research*. Vol. 24, no. 12, 2033-2048.
- Moreno, L., C.F. Tsang, Y. Tsang, and I. Neretnieks. 1990. "Some Anomalous Features of Flow and Solute Transport Arising From Fracture Aperture Variability," *Water Resources Research*. Vol. 26, no. 10, 2377-2391.
- Neuman, S.P. 1990. "Universal Scaling of Hydraulic Conductivities and Dispersivities in Geologic Media," *Water Resources Research*. Vol. 26, no. 8, 1749-1758.
- Neuman, S.P., G.R. Walter, H.W. Bentley, J.J. Ward, and D.D. Gonzalez. 1984. "Determination of Horizontal Aquifer Anisotropy with Three Wells," *Ground Water*. Vol. 22, no. 1, 66-72.
- Papadopoulos, I.S. 1967. "Nonsteady Flow to a Well in an Infinite Anisotropic Aquifer," *Hydrology of Fractured Rocks, 1965 Proceedings*. International Association of Scientific Hydrology. Vol. 1, 21-31.
- Pickens, J.F., and G.E. Grisak. 1981a. "Scale-Dependent Dispersion in a Stratified Granular Aquifer," *Water Resources Research*. Vol. 17, no. 4, 1191-1211.
- Pickens, J.F., and G.E. Grisak. 1981b. "Modeling of Scale-Dependent Dispersion in Hydrogeologic Systems," *Water Resources Research*. Vol. 17, no. 6, 1701-1711.

- Powers, D.W., and R.M. Holt. 1984. "Depositional Environments and Dissolution in the Rustler Formation (Permian), Southeastern New Mexico." *Abstracts with Programs, The Geological Society of America, 97th Annual Meeting, Reno, NV, November 5-8, 1984*. Vol. 16, no. 6, 627.
- Powers, D.W., S.J. Lambert, S-E. Shaffer, L.R. Hill, and W.D. Weart, eds. 1978. *Geological Characterization Report, Waste Isolation Pilot Plant (WIPP) Site, Southeastern New Mexico*. Vols. 1-2. SAND78-1596. Albuquerque, NM: Sandia National Laboratories.
- Reeves, M., D.S. Ward, N.D. Johns, and R.M. Cranwell. 1986a. *Theory and Implementation for SWIFT II, the Sandia Waste-Isolation Flow and Transport Model for Fractured Media, Release 4.84*. SAND83-1159, NUREG/CR-3328. Albuquerque, NM: Sandia National Laboratories.
- Reeves, M., D.S. Ward, N.D. Johns, and R.M. Cranwell. 1986b. *Data Input Guide for SWIFT II, The Sandia Waste-Isolation Flow and Transport Model for Fractured Media, Release 4.84*. SAND83-0242, NUREG/CR-3162. Albuquerque, NM: Sandia National Laboratories.
- Reeves, M., D.S. Ward, P.A. Davis, and E.J. Bonano. 1986c. *SWIFT II Self-Teaching Curriculum: Illustrative Problems for the Sandia Waste-Isolation Flow and Transport Model for Fractured Media*. SAND84-1586, NUREG/CR-3925. Albuquerque, NM: Sandia National Laboratories.
- Reeves, M., V.A. Kelley, and J.F. Pickens. 1987. *Regional Double-Porosity Solute Transport in the Culebra Dolomite: An Analysis of Parameter Sensitivity and Importance at the Waste Isolation Pilot Plant (WIPP) Site*. SAND87-7105. Albuquerque, NM: Sandia National Laboratories.
- Reeves, M., G.A. Freeze, V.A. Kelley, J.F. Pickens, and D.T. Upton. 1991. *Regional Double-Porosity Solute Transport in the Culebra Dolomite Under Brine-Reservoir-Breach Release Conditions: An Analysis of Parameter Sensitivity and Importance*. SAND89-7069. Albuquerque, NM: Sandia National Laboratories.

- Robinson, T.W., and W.B. Lang. 1938. *Geology and Ground-Water Conditions of the Pecos River Valley in the Vicinity of Laguna Grande de la Sal, New Mexico*. 12th and 13th Biennial Reports of the State Engineer of New Mexico. Sante Fe, NM: State Engineer.
- Russell, A.D., and G.M. Thompson. 1981. "Fluorocarbon Enrichment of Ground Water," *EOS Transactions, American Geophysical Union*. Vol. 62, no. 45, 866.
- Saulnier, G.J., Jr. 1987. *Analysis of Pumping Tests of the Culebra Dolomite Conducted at the H-11 Hydropad at the Waste Isolation Pilot Plant (WIPP) Site*. SAND87-7124. Albuquerque, NM: Sandia National Laboratories.
- Saulnier, G.J., Jr., G.A. Freeze, and W.A. Stensrud. 1987. *WIPP Hydrology Program Waste Isolation Pilot Plant, Southeastern New Mexico, Hydrologic Data Report #4*. SAND86-7166. Albuquerque, NM: Sandia National Laboratories.
- Seward, P.D. 1982. *Abridged Borehole Histories for the Waste Isolation Pilot Plant (WIPP) Studies*. SAND82-0080. Albuquerque, NM: Sandia National Laboratories.
- Shapiro, A.M., and J.R. Nicholas. 1989. "Assessing the Validity of the Channel Model of Fracture Aperture Under Field Conditions," *Water Resources Research*. Vol. 25, no. 5, 817-828.
- Snyder, R.P. 1985. *Dissolution of Halite and Gypsum, and Hydration of Anhydrite to Gypsum, Rustler Formation, in the Vicinity of the Waste Isolation Pilot Plant, Southeastern New Mexico*. Open-File Report 85-229. Denver, CO: U.S. Geologic Survey.
- Stensrud, W.A., M.A. Bame, K.D. Lantz, J.B. Palmer, and G.J. Saulnier, Jr. 1988. *WIPP Hydrology Program, Waste Isolation Pilot Plant, Southeastern New Mexico, Hydrologic Data Report #7*. SAND88-7014. Albuquerque, NM: Sandia National Laboratories.
- Stensrud, W.A., M.A. Bame, K.D. Lantz, J.B. Palmer, and G.J. Saulnier, Jr. 1990. *WIPP Hydrology Program, Waste Isolation Pilot Plant, Southeastern New Mexico, Hydrologic Data Report #8*. SAND89-7056. Albuquerque, NM: Sandia National Laboratories.

- Stetzenbach, K.J., S.L. Jensen, and G.M. Thompson. 1982. "Trace Enrichment of Fluorinated Organic Acids Used as Ground-Water Tracers by Liquid Chromatography," *Environmental Science and Technology*. Vol. 16, no. 5, 250-254.
- Tang, D.H., E.O. Frind, and E.A. Sudicky. 1981. "Contaminant Transport in Fractured Porous Media: Analytical Solution for a Single Fracture," *Water Resources Research*. Vol. 17, no. 3, 555-564.
- Thompson, G.M., and K.J. Stetzenbach. 1980. "Assessment and Advances in Tracers Technology." Topical report to the Nuclear Regulatory Commission. (Copy on file at the Waste Management and Transportation Library, Sandia National Laboratories, Albuquerque, NM.)
- Tsang, Y.W., and C.F. Tsang. 1987. "Channel Model of Flow Through Fractured Media," *Water Resources Research*. Vol. 23, no. 3, 467-479.
- Tsang, Y.W., C.F. Tsang, I. Neretnieks, and L. Moreno. 1988. "Flow and Tracer Transport in Fractured Media: A Variable Aperture Channel Model and Its Properties," *Water Resources Research*. Vol. 24, no. 12, 2049-2060.
- U.S. Nuclear Regulatory Commission. 1977. "Quality Assurance Criteria for Nuclear Power Plants and Fuel Reprocessing Plants," *Code of Federal Regulations 10, Part 50, Appendix B*. Washington, DC: Superintendent of Documents, U.S. Government Printing Office. (Copy on file in the Law Library, University of New Mexico, Albuquerque, NM.)
- Van Golf-Racht, T.D. 1982. *Fundamentals of Fractured Reservoir Engineering*. Developments in Petroleum Science 12. New York: Elsevier Science Publishers.
- Vine, J.D. 1963. *Surface Geology of the Nash Draw Quadrangle, Eddy County, New Mexico*. Geological Survey Bulletin 1141-B. Washington, DC: U.S. Government Printing Office.
- Walter, G.R. 1982. *Theoretical and Experimental Determination of Matrix Diffusion and Related Solute Transport Properties of Fractured Tuffs From the Nevada Test Site*. LA-9471-MS. Los Alamos, NM: Los Alamos National Laboratories.

- Ward, D.S., M. Reeves, and L.E. Duda. 1984. *Verification and Field Comparison of the Sandia Waste-Isolation Flow and Transport Model (SWIFT)*. SAND83-1154, NUREG/CR-3316. Albuquerque, NM: Sandia National Laboratories.
- Webster, D.S., J.F. Proctor, and I.W. Marine. 1970. *Two-Well Tracer Test in Fractured Crystalline Rock*. Geological Survey Water-Supply Paper 1544-I. Washington, DC: U.S. Government Printing Office.
- Welty, C., and L.W. Gelhar. 1989. *Evaluation of Longitudinal Dispersivity from Tracer Test Data*. Report Number 320. Cambridge, MA: Massachusetts Institute of Technology, Department of Civil Engineering, Ralph M. Parsons Laboratory for Water Resources and Hydrodynamics. (Copy on file at the Waste Management and Transportation Library, Sandia National Laboratories, Albuquerque, NM.)

**APPENDIX A: REVIEW OF CHEMICAL AND BIOLOGICAL ACTIVITY
OF FLUORINATED ACIDS USED AS TRACERS**

BY

K.J. STETZENBACH AND L.D. STETZENBACH

REVIEW OF CHEMICAL AND BIOLOGICAL ACTIVITY
OF FLUORINATED ACIDS USED AS TRACERS

by

Klaus J. Stetzenbach, Ph.D.*
Analytical Chemist
Assistant Director, University Analytical Center
University of Arizona, Tucson

and

Linda D. Stetzenbach, Ph.D.**
Environmental Microbiologist
Research Associate, University of Arizona, Tucson

October, 1986

* Current location: Director, Physical Science Division,
Harry Reid Center for Environmental Studies,
University of Nevada, Las Vegas.

** Current location: Biological Science Division,
Harry Reid Center for Environmental Studies,
University of Nevada, Las Vegas.

TABLE OF CONTENTS

Executive Summary	1
Chemical Stability	2
Biodegradation	3
Degradation in the Subsurface	6
Degradation Studies of Haloaromatic Compounds used as Tracers	8
Sorption Studies of Tracers	10
Thiocyanate	12
Other Fluorinated Tracers	13
Other Aromatic Acids	14
List of Abbreviations	15
Recommendations	16
References	18

EXECUTIVE SUMMARY

The tracers have been reviewed in this report for their suitability in long term (1 to 1.5 years) tests with respect to sorption and degradation.

Chemical degradation does not appear to be a problem for the fluorinated organic acids.

Thiocyanate may decompose in the aquifer.

Biodegradation may affect all the tracers reviewed.

The perfluorinated compounds have a very low probability of being affected by biodegradation.

All of the polyfluorinated aromatic tracers should be able to be used at least once in a new area.

Tracer test of 500 days should be possible with PFBA.

The use of more than one tracer (of the similar chemical structure) at the same time may increase the chances for biodegradation.

CHEMICAL STABILITY

The long term chemical stability of aromatic acids, especially halogenated ones is quite good. Aromatic compounds that have halogen atoms attached to the ring, have short and therefore strong bonds between the carbon and halide atom. Carbon - fluorine bonds are the shortest of the carbon halide bonds and are therefore expected to be the strongest and least reactive. As a general rule, it can be stated that more halogen atoms on a molecule, especially fluorine, further increase their stability. Teflon is an example of a perfluorinated compounds that is virtually resistant to all chemical attack. The acid functional group (carboxyl group), is completely oxidized, difficult to reduce and does not undergo other reactions in aqueous (ground water) solutions. I would not expect there to be any chemicals in the ground water that can readily react with the fluorinated organic compounds. The reactivity of the tracers in the subsurface is limited to adsorption or chemisorption to the aquifer materials or biodegradation.

Adsorption is a readily reversible reaction that delays the tracer's breakthrough time with respect to water moving between the same points. All of the tracer can be eventually recovered. Chemisorption of a tracer is not readily reversible and does not retard the rate of movement of the tracer through the subsurface. It does however reduce the amount of tracer that can be recovered. It is possible for all the tracer to be lost to this process.

BIODEGRADATION

Microorganisms are capable of degrading aromatic hydrocarbons and the aromatic fraction can be used to sustain bacterial growth. Utilization of organic compounds occurs via catabolic pathways catalyzed by a series of enzymes. The product formed may then be utilized by another population of bacteria or the resulting compounds may be resistant to further degradation.

Environmental factors that affect the rate and extent of biodegradation of a chemical tracer are its concentration, the population of microorganisms, presence of other nutrients (including trace metals), dissolved oxygen, pH, temperature salinity and contact time. Another factor that may affect degradation is prior exposure of the microbial population to the tracer or to a similar compound. One must be careful about assumptions made because of similarities between two chemicals or environmental conditions. Differences such as positional isomers, type of halogen or activity of the microbial population may alter the expected results.

The fluorinated aromatic acid tracers have pK values of 4.5 or less, making them anions at normal ground water^a pH. Ionized compounds are not able to pass through the microbial cell membrane and therefore are not generally utilized. Some bacteria however have acquired or can acquire the ability to transport such compounds as the result of mutations. It is possible then, during extended tracer tests of 7 to 30 days to lose a small percentage of tracer as the result of bacterial activity. During long tracer tests (1 to 1.5 years) all of the tracer may be degraded.

The success of microbial degradation is also related to previous and/or low level chronic exposure to the compound. Chronic sublethal exposure may increase the tolerance of microorganisms and allow for adaptation of the biological community. The microbial population would then more rapidly respond to the presence of that and/or similar compounds, produce the necessary enzymes, and degradation rates would increase. If the compound is chemically analogous to a natural substrate a similar situation may occur with the microbial population readily producing enzymes necessary for degradation. Some chemicals can also act as initiators. These compounds may or may not be degraded in the process, but their presence gives bacteria the ability to degrade compounds of similar chemical structure. Without the presence of the initiator degradation may not take place.

The concentration of the organic compound is also important in determining the rate of biodegradation. Mineralization rates have been shown to be directly proportional to the concentration of the compound over a wide concentration range. The compound may also be in a concentration too low for degradation to occur. The lowest concentration of a compound that will support microbial growth is termed the threshold. At concentrations too low, degradation produces only enough energy for maintenance of the microbial population and growth is absent. Under these conditions degradation rates are retarded due to lack of an actively growing population. At higher concentrations, diffusion provides molecules to the cell surfaces at a rate sufficient to meet the need of energy of maintenance and cell growth. The microbial population is stimulated and the number of microbes increase with

time and degradation rates are enhanced. Thresholds vary with the microbial population involved. If the population is oligotrophic in nature (grows and survives in an environment with a low concentration of available carbon) a lower threshold may exist.

Temperature also influences the rates of degradation. Microbes have maximal and minimal temperature ranges for survival and optimal temperatures of substrate utilization. Rates of degradation decrease with decreases in temperature below the optimal growth temperature as growth rates are retarded.

Chemical interactions of clay with ions and organic compounds also affect microbial growth and therefore activity. The sorption of compounds to suspended organic matter, soil, and sediments as well as the presence of trace elements may result in binding within the clay lattice. These compounds would then be unavailable to the microbial cell and would not be degraded.

The presence of readily utilizable carbon sources also may have an effect of the transformation of a compound. Increased degradation of phenols with the addition of natural substrates (amino acids, carbohydrates, or fatty acids) has been demonstrated.

DEGRADATION in the SUBSURFACE

Extensive literature is available on the biodegradation of halo substituted aromatic compounds, showing that these compounds can be degraded by bacteria. However, these experimental results were obtained with laboratory cultures of bacteria that had been specifically grown for these purposes.

Soil contains approximately 10^7 - 10^9 microorganisms/gram dry weight of soil with numbers typically higher in soils than in fresh water and marine habitats. This may be due to the increased availability of nutrients adsorbed onto surfaces and the presence of molecular oxygen within the interstitial spaces of the soil matrix. The predominant bacterial genera in soils are Pseudomonas, Flavobacterium, Argobacterium, Arthrobacter, Alcaligenes, Bacillus, and Clostridium. Other genera readily isolated from soil include Mycobacterium, Corynebacterium, and Micrococcus. These ten genera are also among those demonstrating the ability to biodegrade contaminant hydrocarbons. The bacterial populations identified in water from deep ground water wells consist of many of these same genera. The activity of bacteria in situ in deep aquifers, however has not been adequately studied and degradation rates of tracers then is difficult to predict. It may not be valid to draw parallel conclusions on degradation of tracers in situ with results obtained in the laboratory. Further, it may also not be valid to conclude that bacterial activity in deep aquifers is the same as that in soils.

It also needs to be pointed out that the bacterial populations found in soils may be much more diverse than deep aquifer

flora. Increased diversity enhances the likelihood of a population able to degrade the tracer compounds. It must also be stated that in degradation studies with pesticides, degradation is almost always more rapid in the field than in the laboratory.

DEGRADATION STUDIES of HALOAROMATIC COMPOUNDS used as TRACERS

No references were found about the biodegradation of fluorinated benzoic acids in soils or aquifers except for experiments conducted at the University of Arizona and the Water Conservation Laboratory in Phoenix. However, numerous references of laboratory studies concerning the biodegradation of similar chemicals such as ortho-, meta- and para-chlorobenzoic acids show that they are degraded by soil microorganisms in >64, 32 and 64 days respectively. An experiment reported by Thompson and Stetzenbach showed that o-, m-, and p-fluorobenzoic acids degraded in 31, <30 and 13 days respectively. Polyfluoro substituted compounds used in the same experiment showed no degradation during this 30 day period. Of the polyfluorinated compounds, m-trifluoromethylbenzoic acid (m-TFMBA) and tetrafluorophthalic acid (TFPA) showed no degradation for at least 6 months and pentafluorobenzoic acid (PFBA) remained unchanged for at least 2 years. Follow-up experiments performed by Barackman with waters that had been in contact with benzoate and fluorinated benzoic acids for four years produced no degradation of PFBA, o-TFMBA and m-TFMBA after 30 days.

PFBA and m-TFMBA were also used as tracers in trench infiltration studies on Mt. Lemmon Arizona at an elevation of 9,000 feet with 40 inches of annual precipitation. While these studies cannot be used to obtain quantitative information about degradation of the tracers, they do show that they were still present in detectable amounts more than two years after being placed in the trenches in a moist but unsaturated environment.

Bowman's works of 1984 and 1986 tend to confuse the issue of biodegradation. In initial soil column studies with several fluorinated acids (PFBA, o-TFMBA, m-TFMBA, o-FBA, m-FBA, p-FBA and DFBA) all showed 100% recovery. In a 1984 study with PFBA, DFBA, m-TFMBA and o-TFMBA, only m-TFMBA had less than full recovery. A 1986 study resulted in less than 100% recovery for o- and m-fluorobenzoic acid and m-TFMBA. In all three studies, PFBA and DFBA had 100% recovery. The lack of recovery is suspected to be due to biodegradation rather than chemisorption.

SORPTION STUDIES of TRACERS

A number of sorption studies have been performed with fluorinated organic acids. Some sorption information has also been obtained as a result of degradation studies. The per-fluorinated compounds (PFBA and TFPA) and m-TFMBA did not show any sorption during the degradation studies performed by Thompson and K. Stetzenbach. With the other acids, the experimental design did not allow differentiation between sorption or degradation. Experiments performed by K. Stetzenbach in support of a tracing test in a coal seam showed that only PFBA did not sorb on what is essentially an organic surface (even Iodide sorbed under these conditions). However, it is highly unlikely that such a surface would be encountered at the WIPP site. Bowman, in his numerous soil experiments, did not report any retardation with PFBA, m-TFMBA, o-TFMBA, DFBA or the monofluoro substituted compounds.

Another sorption study by K. Stetzenbach on sand, weathered granite and unweathered granite showed that PFBA, DFBA, m-TFMBA and TFPA were not sorbed. Both o-TFBA and SCN showed sorption. The table below lists the % recovery after 12 to 24 hours. (This experiment was done rapidly to ensure that degradation was not responsible for any losses.)

SORPTION STUDIES ON SAND AND GRANITE

Percent Recovery

	<u>SAND</u>	<u>GRANITE</u> weathered	unweathered
SCN	89	95	181
PFBA	102	100	100
TFPA	106	119	---
m-TFMBA	98	99	100
DFBA	100	106	100
o-TFMBA	96	97	94

SURFACE AREAS:

SAND	0.76 m ² /g
WEATHERED GRANITE	2.98 m ² /g
UNWEATHERED GRANITE	0.65 m ² /g

All tracer concentrations were between 1 and 2 ppm.

THIOCYANATE

Thiocyanate is an inorganic anion that occurs in industrial wastes and as a natural product mainly due to the activity of an enzyme called rhodanese. This enzyme is found in soil bacteria. Reports of thiocyanate (SCN) being used as a tracer go back to the 1950s. Thiocyanate is called a pseudohalide because its chemical behavior is similar to the halide ions. It would therefore be expected to behave in a manner not unlike chloride and bromide in an aquifer. While SCN does not sorb to most aquifer materials its recovery is seldom 100%. But, it is usually high enough that the loss is not considered to be a serious problem. According to Thompson one can always expect to lose at least 5% of the SCN in a tracer test. Bowman, in his soil tracing tests, showed significantly higher losses, which he attributed to chemical or biological degradation, but there was no retardation.

It is my opinion that in aquifers that do not have high levels of bacteria the thiocyanate loss is due to chemisorption. In soils that have been in contact with vegetation and manmade chemicals it is highly likely that the SCN is lost due to bacterial activity. Relatively simple experiments could be designed to prove or disprove this hypothesis.

I believe that thiocyanate is not a good long term tracer because of the chemisorption problem.

OTHER FLUORINATED TRACERS

Another group of chemicals that have a high potential as ground water tracers are three perfluorinated aliphatic acids. The three acids are trifluoroacetic acid, pentafluoropropionic acid and heptafluorobutyric acid. They are extremely strong acids, so they are always ionized in water above pH 2. They are highly resistant to chemical and microbial attack because they are perfluorinated and trifluoroacetic acid is readily available at low cost. Their major drawback is that there is no simple, highly sensitive analytical method to measure them in water. At present, the best method requires lengthy derivitization and analysis by costly GC/MS instrumentation. Ground waters that have high chloride (or other halide) content further complicate the analytical procedure. At higher concentrations these acids can be detected with less sophisticated procedures, but the high levels of tracer required may pose other problems such as high cost and chemical reactions at the injection site.

Thompson and K. Stetzenbach used the perfluorinated aliphatic acids as tracers in the experimental waste isolation trenches on Mt. Lemmon Arizona. The tracers were used to monitor the movement of water through and around the trenches. The experimental design does not allow for quantitative statements about sorption or degradation. However, the tracers could still be detected in the trenches more than two years after the start of the experiment, suggesting that neither chemical reactions nor biodegradation was removing them.

OTHER AROMATIC ACIDS

Fluorocinnamic acids and 5-fluorosallylic acid are potentially useful tracers. These compounds are expensive, but significant price reductions could be had with large quantity orders. None of these compounds has been studied as to their sorption or degradation. But, they are similar to the fluorinated aromatic acids. Their greatest advantage over the other aromatic tracers is their analytical sensitivity. They can be detected (in laboratory tests) at concentrations that are two to three orders of magnitude lower than the other fluorinated aromatic acids. This means that a test requiring 1Kg of PFBA could be done with 1g of FSA.

The potential is there, but extensive testing must still be done before they can be used in a tracing test.

LIST of ABBREVIATIONS

AROMATIC FLUORINATED ACIDS

PFBA (a perfluorinated acid)	Pentafluorobenzoic acid
TFPA (a perfluorinated acid)	Tetrafluorophthalic acid
m-TFMBA	meta-trifluoromethylbenzoic acid
DFBA	2,6-Difluorobenzoic acid
o-FBA (a monofluoro acid)	ortho-fluorobenzoic acid
m-FBA (a monofluoro acid)	meta-fluorobenzoic acid
p-FBA (a monofluoro acid)	para-fluorobenzoic acid
FSA	5-fluorosalicylic acid
	fluorocinnamic acids

ALIPHATIC FLUORINATED ACIDS

TFA (a perfluorinated acid)	Trifluoroacetic acid
PFPP (a perfluorinated acid)	Pentafluoropropionic acid
HFB (a perfluorinated acid)	Heptafluorobutyric acid

RECOMMENDATIONS
(aromatic fluorinated acids)

Pentafluorobenzoic acid

Pentafluorobenzoic acid is a perfluorinated aromatic acid that has been tested extensively for biodegradation and sorption in laboratory experiments, column studies and in the field. In no case has there been any degradation or sorption (compared to bromide) of this acid. In chromatographic experiments this acid exhibits anionic exclusion properties. I would expect this compound to be a good tracer for a long term (1 to 1.5 years) tracer test at the WIPP site.

TETRAFLUOROPHTHALIC ACID

This is another perfluorinated acid but, unlike PFBA, it has not been tested sufficiently. However, like PFBA it should be stable and nonsorbing. My only concern with this compound is that with its dicarboxylic acid functional group it may be more susceptible to biodegradation than the monofunctional PFBA. It is also more expensive than PFBA.

META-TRIFLUOROMETHYLBENZOIC ACID

This acid has been the most widely tested and used of the fluorinated acids. It has been added to drilling mud, used in concentrated brines, the waste isolation trench experiments (see text) and numerous other tests. Experiments conducted at the University of Arizona indicated no sorption and resistance to biodegradation for at least 6 months to one year. Experiments at the Soil Conservation Laboratory in Phoenix point towards much earlier biodegradation, especially when this tracer has been used before on or near the same plot.

DIFLUOROBENZOIC ACID

This acid has been used by Bowman in several experiments with 100% recovery in his reported studies.

ORTHO-TRIFLUOROMETHYLBENZOIC ACID

This acid has not been tested as extensively as the m-TFMBA. It has been used by Bowman and Barackman with good results. Only short term (30 to 100 days) stability data is available.

PARA-FLUOROBENZOIC ACID

Being a monofluoro compound, it will not be as inert as the polyfluorinated compounds.

META-FLUOROBENZOIC ACID

This compound lacks the stability necessary for long term tracer tests.

ORTHO-FLUOROBENZOIC ACID

This compound lacks the stability necessary for long term tracer tests.

SORPTION

Before tracing tests are conducted at the WIPP site relatively simple and inexpensive sorption tests should be conducted with all potential tracers on as many types of aquifer materials as possible. These tests do not require much time and will result in data that no literature review or expert opinion can provide.

DEGRADATION

Since it not be practical to conduct long term degradation studies prior to the tracing tests, I believe it is necessary to conduct them simultaneously. The polyfluorinated aromatic compounds can be used at least once in an area that has had no contact with these types of tracers or similar compounds. The use of multiple tracers, related chemically, during the same test may cause degradation of one or more of the tracers.

TRACER MIXING

The mixing of the tracer solution in the borehole is an extremely important aspect of a tracing test that is almost always overlooked. For plug injections, solutions of tracer are kept small and highly concentrated. These solutions, which are more dense than the water into which they are poured, always sink to the bottom of the borehole with virtually no mixing. Even with sophisticated injection equipment it cannot be assumed that the tracer solution will mix with the water and provide a uniform injection concentration.

REFERENCES

- Gibson, David T. (ed.) 1984. Microbial Degradation of Organic Compounds.
- Stetzenbach, Linda D. 1986. The Degradation and Utilization of Polycyclic Aromatic Hydrocarbons. Ph.D. Dissertation. University of Arizona, Tucson.
- Stetzenbach, Linda D., Lee M. Kelley, and Norval A. Sinclair. 1986. Isolation, Identification, and Growth of Well-Water Bacteria. Groundwater. 24:6-10.
- Barackman, Martin L. 1986. Diverging Flow Tracer Test in Fractured Granite; Equipment Design and Data Collection. MS Thesis. University of Arizona, Tucson.
- Stetzenbach, Klaus J. 1980 - 1984 Unpublished Data, University of Arizona, Tucson.
- McCray, J. G., Nowatzki, E. A., Stetzenbach, K. J., and Armstrong, G. 1985. Low-Level Nuclear Waste Shallow Land Burial Trench Isolation. Final Report to NRC. NUREG/CR-4194.
- Bowman, R. S. Evaluation of some new Tracers for Soil Water Studies. Soil Sci. Soc. Am. J., 48, 987-993, 1984a.
- Bowman, R. S. and Rice, R. C. Transport of Conservative Tracers in the Field under Intermittent Flood Irrigation. Water Resources Research, 22, 1531-1536, 1986.
- Thompson, G. M. and Stetzenbach, K. J. Assessment and Advances in Tracer Technology. Report to NRC. 1980.

**APPENDIX B: TABULATED TRACER-CONCENTRATION DATA
FROM TWO-WELL RECIRCULATING TRACER TEST #2 CONDUCTED
AT THE H-2 HYDROPAD**

TIME SINCE PUMPING FOR TEST #2 BEGAN ^a (days)	PFB CONCENTRATION (mg/L)	SCN CONCENTRATION (mg/L)
3	0.32	
8	0.21	
14	0.33	
18	1.26	
23	3.71	
25	5.09	
28	2.56	
29	7.11	
32	3.62	
35	9.12	
37	10.05	
39	11.36	
41	11.36	
42	9.	
43	10.4	
44	11.08	
45	10.7	
46	10.	
47	9.51	
48	8.85	
49	6.4	
54	8.19	
57	7.4	
60	5.64	
65	3.92	
70	3.28	
73	2.23	

TIME SINCE PUMPING FOR TEST #2 BEGAN ^a (days)	PFB CONCENTRATION (mg/L)	SCN CONCENTRATION (mg/L)
77		0.012
78		0.018
79		0.024
80		0.03
81		0.041
82		0.055
84		0.076
85		0.095
86		0.142
87		0.245
88		0.228
89		0.343
90	0.7	0.371
93		0.576
94		0.624
95	0.4	0.661
98		0.866
99		1.39
100	0.5	1.63
101		1.68
102		1.82
106	0.29	1.99
107		2.61
108		2.74
109	0.24	2.89
111		3.33
113		3.45

TIME SINCE PUMPING FOR TEST #2 BEGAN ^a (days)	PFB CONCENTRATION (mg/L)	SCN CONCENTRATION (mg/L)
114		3.49
115	0.19	3.67
116		3.76
117		3.16
118		3.72
120		4.26
121	0.2	4.41
122		4.41
125		3.52
127		4.55
128		4.54
129		4.65
133		4.8
134		4.91
135		4.88
136	0.13	4.97
139		5.12
140		4.76
143		5.41
144		4.61
145		3.79
146		4.59
148		5.84
149		5.62
151		6.02
152		5.96
153		6.12

TIME SINCE PUMPING FOR TEST #2 BEGAN ^a (days)	PFB CONCENTRATION (mg/L)	SCN CONCENTRATION (mg/L)
154		6.26
155		6.06
156	0.3	5.8
157		6.12
160		5.42
161		6.6
162		6.57
163		6.8
165		5.31
166	0.2	6.65
168		6.76
169		7.38
170		7.53
172		7.54
174		7.49
175		7.72
177		8.07
181		7.94
182		8.23
184		7.75
185		7.98
188		6.94
189		7.89
191		7.42
193		6.66
197		10.31
198		10.38

TIME SINCE PUMPING FOR TEST #2 BEGAN ^a (days)	PFB CONCENTRATION (mg/L)	SCN CONCENTRATION (mg/L)
199		10.31
200		10.36
204		10.26
205		10.49
206		10.71
207		11.14
208		7.09
210		12.11
211		9.04
212		11.89
213		12.24
214		12.31
220		12.47
221		12.6
223		12.6
225		12.55
226		12.51
228		12.63
229		12.25
233		12.39
234		12.63
235		12.7
238		12.59
239		12.28
242		12.31
245		12.34
246		12.43

TIME SINCE PUMPING FOR TEST #2 BEGAN ^a (days)	PFB CONCENTRATION (mg/L)	SCN CONCENTRATION (mg/L)
247		12.59
248		13
249		12.88
251		12.84
253		7.81
254		10.23
258		12.39
259		12.35
260		12.33
262		12.23
263		12.2
264		12.6
268		11.26
269		8.82
272		10.21
273		10.83
274		11.11

^a Tracer injection for recirculation test #2 began July 10, 1980.

**APPENDIX C: TABULATED TRACER-CONCENTRATION DATA
FROM THE CONVERGENT-FLOW TRACER TEST CONDUCTED
AT THE H-3 HYDROPAD**

TIME SINCE FIRST TRACER INJECTED ^a (hrs)	CORRECTED TIME FOR PFB ^b (days)	PFB CONCENTRATION (mg/L)	CORRECTED TIME FOR m-TFMB ^c (days)	m-TFMB CONCENTRATION (mg/L)
-2.50	-0.171	0.000	-0.208	0.000
0.00	-0.067	0.000	-0.104	0.000
21.25	0.819	0.000	0.781	0.000
23.25	0.902	0.000	0.865	0.056
24.95	0.973	0.000	0.935	0.167
26.75	1.048	0.000	1.010	0.207
27.75	1.090	0.000	1.052	0.295
33.25	1.319	0.000	1.281	0.765
35.25	1.402	0.000	1.365	0.908
41.25	1.652	0.000	1.615	1.562
44.25	1.777	0.000	1.740	1.782
51.25	2.069	0.000	2.031	2.216
55.25	2.235	0.000	2.198	2.634
60.25	2.444	0.000	2.406	2.773
63.25	2.569	0.000	2.531	3.379
65.25	2.652	0.000	2.615	3.315
75.25	3.069	0.000	3.031	2.986
83.25	3.402	0.000	3.365	3.107
90.25	3.694	0.000	3.656	2.901
95.25	3.902	0.020	3.865	2.952
99.25	4.069	0.020	4.031	2.903
103.25	4.235	0.020	4.198	2.776
111.25	4.569	0.025	4.531	2.811
114.25	4.694	0.051	4.656	2.623
117.25	4.819	0.043	4.781	2.525
127.25	5.235	0.055	5.198	2.532
137.25	5.652	0.065	5.615	2.324
145.25	5.985	0.095	5.948	2.067
155.25	6.402	0.057	6.365	2.024

TIME SINCE FIRST TRACER INJECTED ^a (hrs)	CORRECTED TIME FOR PFB ^b (days)	PFB CONCENTRATION (mg/L)	CORRECTED TIME FOR m-TFMB ^c (days)	m-TFMB CONCENTRATION (mg/L)
189.25	7.819	0.143	7.781	1.645
195.25	8.069	0.148	8.031	1.587
213.25	8.819	0.141	8.781	1.506
233.25	9.652	0.183	9.615	1.463
261.25	10.819	0.183	10.781	1.237
277.25	11.485	0.267	11.448	1.173
281.25	11.652	0.233	11.615	0.888
289.25	11.985	0.277	11.948	1.005
295.25	12.235	0.133	12.198	0.633
315.25	13.069	0.301	13.031	0.901
329.25	13.652	0.226	13.615	0.629
337.25	13.985	0.270	13.948	0.708
341.25	14.152	0.371	14.115	0.888
345.25	14.319	0.256	14.281	0.925
351.25	14.569	0.244	14.531	0.821
361.25	14.985	0.370	14.948	0.873
397.25	16.485	0.375	16.448	0.712
459.25	19.069	0.407	19.031	0.662
513.25	21.319	0.415	21.281	0.579
553.25	22.985	0.444	22.948	0.516
647.25	26.902	0.391	26.865	0.491
787.25	32.735	0.391	32.698	0.499

^a PFB was injected at 12:45 on May 9, 1984.

m-TFMB was injected at 13:55 on May 9, 1984.

^b The time correction for PFB is 94 minutes.

^c The time correction for m-TFMB is 150 minutes.

**APPENDIX D: TABULATED TRACER-CONCENTRATION DATA
FROM THE CONVERGENT-FLOW TRACER TEST CONDUCTED
AT THE H-4 HYDROPAD**

TIME SINCE TRACERS INJECTED INTO H-4a ^a (days)	PFB CONC. ($\mu\text{g/L}$)	p-FB CONC. ($\mu\text{g/L}$)	TIME SINCE TRACERS INJECTED INTO H-4b ^b (days)	m-TFMB CONC. ($\mu\text{g/L}$)	SCN CONC. ($\mu\text{g/L}$)
2.13	51	24	3.38	0	
2.92	0	6.9	8.13	0	
3.19	955	167	11.30	0	
3.42	543	123	12.08	29	
3.88	128	198	12.36	20	
3.88	0	0	12.58	43	
4.88	0	14	13.04	26	
6.12	0	0	13.04	429	
6.23	0	0	14.04	53	
7.00	0	0	15.28	0	
8.00	0	0	15.39	0	
10.19	0	0	16.17	0	
13.75	0	0	17.17	0	
16.00	0	0	19.35	0	
19.25	0	0	22.92	0	
19.50	0	0	25.17	0	
19.75	0	0	28.42	0	
23.00	0	0	28.67	0	
28.25	0	0	28.92	0	
33.75	0	0	32.17	0	
41.25	0	0	37.42	0	
44.44	0	0	42.92	0	
47.98	0	0	50.42	0	
78.50	0	0	53.60	0	
83.83	0	0	57.15	0	

TIME SINCE TRACERS INJECTED INTO H-4a ^a (days)	PFB CONC. ($\mu\text{g/L}$)	p-FB CONC. ($\mu\text{g/L}$)	TIME SINCE TRACERS INJECTED INTO H-4b ^b (days)	m-TFMB CONC. ($\mu\text{g/L}$)	SCN CONC. ($\mu\text{g/L}$)
88.96	0	0	87.67	0	
103.33	0	0	93.00	0	
111.10	0	0	98.13	0	
120.33	0	0	112.50	0	
126.67	0	0	120.26	0	
132.00	0	0	129.50	0	
137.33	0	0	135.83	0	
150.63	0	0	141.17	0	
158.25	0	0	146.50	0	
169.00	0	0	159.79	0	
184.91	0	0	167.42	0	
207.05	0	0	178.17	0	
222.85	0	0	194.08	0	
238.08	0	0	216.22	0	
244.20	0	0	232.02	0	
253.04	0	0	247.25	0	
255.83	0	0	253.36	0	
265.27	0	0	262.21	78	
271.90	0	0	265.00	116	
277.19	0	0	270.01		0.0278
278.86	0	0	274.44	80	
280.86	0	0	279.00		0.0245
282.87	0	0	280.13		0.0484
289.25	0	0	281.06	135	0.105
296.97	0	0	282.13		0.0844

TIME SINCE TRACERS INJECTED INTO H-4a ^a (days)	PFB CONC. ($\mu\text{g/L}$)	p-FB CONC. ($\mu\text{g/L}$)	TIME SINCE TRACERS INJECTED INTO H-4b ^b (days)	m-TFMB CONC. ($\mu\text{g/L}$)	SCN CONC. ($\mu\text{g/L}$)
297.17	0	0	284.35		0.0726
299.15	0	0	285.00		0.0713
307.08	0	0	286.35	243	0.123
310.32	0	0	287.19		0.0989
313.04	0	0	288.03	214	0.116
319.10	0	0	289.13		0.148
321.13	0	0	290.03	158	
324.08	0	0	292.03	231	0.129
328.11	0	0	293.00		0.149
333.10	0	0	296.33		0.143
339.06	0	0	297.33		0.172
341.80	0	0	298.42	248	0.107
345.07	0	0	306.14	211	0.173
346.91	0	0	306.33	298	0.193
348.89	0	0	307.10		0.185
359.00	0	0	308.31	331	0.328
363.88	0	0	316.25	289	0.109
375.12	0	0	316.25		0.402
379.02	0	0	319.48	210	
381.10	0	0	321.13		0.193
385.10	0	0	322.21	219	0.162
387.92	0	0	323.21		0.303
390.17	0	36	325.33		0.113
396.06	0	35	328.26	319	0.186
404.04	0	45	329.38		0.274

TIME SINCE TRACERS INJECTED INTO H-4a ^a (days)	PFB CONC. ($\mu\text{g/L}$)	p-FB CONC. ($\mu\text{g/L}$)	TIME SINCE TRACERS INJECTED INTO H-4b ^b (days)	m-TFMB CONC. ($\mu\text{g/L}$)	SCN CONC. ($\mu\text{g/L}$)
409.06	0	60	330.29	542	0.180
416.20	0	46	331.29		0.191
422.98	0	45	332.38		0.193
434.93	0	78	333.25	226	
458.03	0	83	334.10		0.203
471.92	0	47	335.35		0.136
499.92	0	49	337.28	176	0.0674
501.08	48	75	338.19		0.0559
501.95	41	78	339.19		0.0726
503.10	44	101	342.27	327	0.072
504.04	50	100	345.00		0.123
507.00	54	94	348.23	490	0.167
510.10	53	101	350.31		0.142
514.08	47	142	350.97	537	0.168
517.17	45	60	352.10		0.195
522.10	49	101	354.23	321	0.064
523.85	43	91	355.08		0.145
526.90	28	66	356.08	180	0.0445
530.21	46	105	358.05	203	0.0482
536.06	tr	120	358.06		0.0465
543.94	tr	65	362.38		0.0384
556.10	16	106	366.02		0.171
558.88	46	103	368.17	570	0.0584
560.88	14	59	369.17		0.0962
565.02	35	12	370.27		0.113

TIME SINCE TRACERS INJECTED INTO H-4a ^a (days)	PFB CONC. ($\mu\text{g/L}$)	p-FB CONC. ($\mu\text{g/L}$)	TIME SINCE TRACERS INJECTED INTO H-4b ^b (days)	m-TFMB CONC. ($\mu\text{g/L}$)	SCN CONC. ($\mu\text{g/L}$)
571.15	44	99	373.05	556	0.0688
573.17	31	99	375.08		0.100
576.92	26		384.28	418	
579.83	33	137.0	388.19	723	
585.98	51	7.0	390.27	131	
592.00	48	160.0	394.27	562	
609.04	tr	109.0	397.09	716	
631.90	45	119.0	399.33	626	
672.10	50	108.0	405.23	624	
			413.20	606	
			418.23	693	
			425.36	619	
			432.15	492	
			442.85	469	
			467.20	368	
			481.09	351	
			509.09	447	
			510.25	304	
			511.12	329	
			512.27	342	
			513.21	343	
			516.17	354	
			519.27	342	
			523.25	330	
			526.33	310	

TIME SINCE TRACERS INJECTED INTO H-4a ^a (days)	PFB CONC. ($\mu\text{g/L}$)	p-FB CONC. ($\mu\text{g/L}$)	TIME SINCE TRACERS INJECTED INTO H-4b ^b (days)	m-TFMB CONC. ($\mu\text{g/L}$)	SCN CONC. ($\mu\text{g/L}$)
			531.27	321	
			533.02	322	
			534.27	161	
			536.06	209	
			539.38	265	
			545.23	297	
			553.10	132	
			565.27	259	
			568.04	249	
			570.04	230	
			574.19	195	
			580.31	204	
			582.33	380	
			586.08	153	
			589.00	134	
			595.15	173	
			601.17	209	
			618.21	123	
			641.06	105	
			681.27	95	

^a The tracers PFB and p-FB were injected into H-4a at 12:00 on November 5, 1982.

^b The tracers m-TFMB and SCN were injected into H-4b at 07:53 on October 27, 1982.

tr means trace of tracer detected

**APPENDIX E-1: TABULATED TRACER-CONCENTRATION DATA
FROM TWO-WELL RECIRCULATING TRACER TEST #1 AT THE H-6 HYDROPAD**

TIME SINCE TRACER INJECTION (days)	SCN CONCENTRATION (mg/L)	PFB CONCENTRATION (mg/L)
0.09		0.09
0.09		0.00
0.13	0.72	0.11
0.18		0.18
0.22		0.62
0.26		1.57
0.30	2.51	2.41
0.34	2.62	3.09
0.38	2.91	3.22
0.43	2.58	3.39
0.47	2.58	3.23
0.51	2.72	3.46
0.55	2.66	3.41
0.59	2.81	3.96
0.63	2.49	3.18
0.68	2.60	3.23
0.72	2.21	3.67
0.76	2.23	3.54
0.80	1.91	2.87
0.84	1.96	3.13
0.88	1.72	2.69
0.93	2.09	3.16
1.01	1.81	2.50
1.09	1.83	2.49
1.18		2.27
1.26		2.31
1.34		2.12

<u>TIME SINCE TRACER INJECTION (days)</u>	<u>SCN CONCENTRATION (mg/L)</u>	<u>PFB CONCENTRATION (mg/L)</u>
1.43	1.30	2.18
1.51		2.00
1.76	1.00	2.07
1.93	1.07	1.88
2.01		1.81
2.18	0.90	1.82
2.30		1.57
2.43	0.58	1.65
2.59		1.68
2.68	0.47	1.57
2.80		1.38
2.88	0.34	1.12
3.01		1.51
3.18	0.12	1.47
3.34		1.40
3.43	0.00	1.35
3.59		1.34
3.76		1.33
3.93	0.00	1.07
4.09		1.04
4.18		0.86
4.26		1.28
4.43		1.17
4.59		1.20
4.68		0.67
4.76		1.23
4.93		0.88

<u>TIME SINCE TRACER INJECTION (days)</u>	<u>SCN CONCENTRATION (mg/L)</u>	<u>PFB CONCENTRATION (mg/L)</u>
5.09		1.13
5.18		1.18
5.43		0.91
5.68		0.99
5.93		0.79
6.18		1.07
6.51		0.80
6.68		0.84
7.01		0.74
7.26	0.00	1.02
7.51		0.74
7.76	0.00	0.84
8.01		0.75
8.26	0.00	0.67
8.51		0.74
8.59		0.95
8.76	0.00	1.01
9.01		0.91
9.18		0.65
9.26	0.00	0.89
9.51		0.67
9.59		0.90
9.68		0.93
9.76	0.00	1.51
9.84		0.65
10.01		0.61
10.18		0.66

TIME SINCE TRACER INJECTION (days)	SCN CONCENTRATION (mg/L)	PFB CONCENTRATION (mg/L)
10.26	0.00	0.64
10.34		0.84
10.51		0.61
10.59		0.64
10.76	0.00	0.88
10.93		0.61
11.01		0.59
11.09		0.58
11.26	0.00	0.57
11.43		0.62
11.51		0.82
11.76	0.00	0.81
12.01		0.80
12.26		0.65
12.51		0.73
13.01		0.65
13.51		0.59
14.01		0.58
14.51		0.60
15.51		0.58
16.76		0.60
18.01		0.58
18.51		0.52
19.01		0.54
19.51		0.54
20.01		0.52
20.51		0.47

<u>TIME SINCE TRACER INJECTION (days)</u>	<u>SCN CONCENTRATION (mg/L)</u>	<u>PFB CONCENTRATION (mg/L)</u>
21.01		0.45
21.51		0.44
21.93		0.43
22.18		0.47
22.43		0.44
22.68		0.40
23.09		0.42
23.97		0.32

**APPENDIX E-2: TABULATED TRACER-CONCENTRATION DATA
FROM TWO-WELL RECIRCULATING TRACER TEST #2 AT THE H-6 HYDROPAD**

TIME SINCE TRACER INJECTION (days)	m-TFMB CONCENTRATION (mg/L)	p-FB CONCENTRATION (mg/L)
0.05	0.264	none
0.22	0.297	none
0.55	0.338	none
0.72	0.382	none
0.80	0.356	nq
0.88	0.478	nq
0.97	0.661	nq
1.05	0.714	nq
1.13	0.861	nq
1.22	0.916	nq
1.30	0.980	nq
1.34	0.989	nq
1.38	0.871	nq
1.47	0.945	nq
1.55	1.015	nq
1.63	1.04	nq
1.72	1.04	nq
1.80	0.995	nq
1.88	1.01	nq
1.92	1.06	nq
2.13	1.31	nq
2.22	1.06	nq
2.30	1.03	nq
2.47	1.05	nq
2.63	1.04	nq
2.80	1.03	nq
2.97	1.04	nq

TIME SINCE TRACER INJECTION (days)	m-TFMB CONCENTRATION (mg/L)	p-FB CONCENTRATION (mg/L)
3.13	1.12	nq
3.30	1.02	nq
3.63	1.00	0.0
3.72	1.01	nq
4.63	0.977	0.0
5.13	1.02	nq
6.13	1.03	0.0
6.63	0.961	0.0
7.38	0.997	0.0
7.80	0.943	0.0
8.22	0.957	0.0
8.63	0.962	0.0
9.05	0.929	0.0
10.13	0.670	0.0
11.13	0.694	0.0
12.13	0.686	0.0
13.13	0.738	nq
14.05	0.816	0.0
14.13	0.800	na
15.05	0.760	na
16.05	0.772	na
17.05	0.789	na
18.05	0.742	na
19.05	0.794	na
20.05	0.721	na
21.13	0.76	na
22.13	0.73	na

<u>TIME SINCE TRACER INJECTION (days)</u>	<u>m-TFMB CONCENTRATION (mg/L)</u>	<u>p-FB CONCENTRATION (mg/L)</u>
23.13	0.74	na
24.13	0.75	na
25.13	0.74	nd
26.13	0.74	nd
27.05	na	nd
27.17	0.72	nd
27.21	0.73	nd
27.26	na	nd
27.42	na	nd
27.51	na	nd
27.59	na	nq
27.76	na	nd
27.92	na	nd
28.09	na	nd
28.13	0.65	nd
28.34	na	nd
28.42	na	nd
28.67	na	0.05 ?
28.92	na	nd
29.09	na	nd
29.17	0.76	nq
29.26	na	nd
29.42	na	nd
29.59	na	nd
29.67	na	nd
29.92	na	nd
30.01	na	nd

<u>TIME SINCE TRACER INJECTION (days)</u>	<u>m-TFMB CONCENTRATION (mg/L)</u>	<u>p-FB CONCENTRATION (mg/L)</u>
30.22	0.66	nd
30.30	na	nd
30.55	na	nd
30.97	0.77	nd
31.22	na	nd
31.47	na	nd
31.97	0.78	nd
32.22	na	nd
32.47	na	nd
32.97	0.76	nq
33.30	na	nd

nq p-FB present but not quantifiable due to an interfering compound
na not analyzed
nd not detected

**APPENDIX F-1: TABULATED TRACER-CONCENTRATION DATA
FROM CONVERGENT-FLOW TRACER TEST #1 CONDUCTED
AT THE H-6 HYDROPAD**

<u>TIME SINCE TRACERS INJECTED ^a</u> <u>(hrs)</u>	<u>CORRECTED TIME FOR m-TFMB AND o-FB ^b</u> <u>(days)</u>	<u>m-TFMB CONC.</u> <u>(mg/L)</u>	<u>o-FB CONC.</u> <u>(mg/L)</u>	<u>CORRECTED TIME FOR PFB AND m-FB ^c</u> <u>(days)</u>	<u>PFB CONC.</u> <u>(mg/L)</u>	<u>m-FB CONC.</u> <u>(mg/L)</u>
3.16	0.107	0.000		0.109	0.000	0.015
4.16	0.148	0.000		0.150	0.026	
5.16	0.190	0.000		0.192	0.210	0.012
11.65	0.460	0.000		0.463	2.600	1.109
16.24	0.652	0.000		0.654	3.029	1.232
19.41	0.784	0.000		0.786	2.930	0.852
21.38	0.866	0.000		0.868	2.780	1.222
24.39	0.991	0.000		0.993	2.570	0.703
32.91	1.346	0.000		1.348	2.010	0.854
37.91	1.555	0.010		1.557	1.760	0.743
42.94	1.764	0.003		1.766	1.510	0.710
47.94	1.973	0.018		1.975	1.330	0.605
52.91	2.180			2.182	1.240	0.389
57.91	2.388			2.390	1.120	0.380
62.91	2.596	0.028		2.598	0.980	0.425
67.91	2.805	0.030		2.807	0.840	0.224
72.96	3.015			3.017	0.730	0.275
77.91	3.221	0.033		3.223	0.710	0.120
82.91	3.430	0.045		3.432	0.660	0.178
87.91	3.638			3.640	0.530	0.302
92.91	3.846	0.035		3.848	0.480	0.275
97.91	4.055	0.054		4.057	0.440	0.265
100.91	4.180	0.066		4.182	0.530	0.157
105.91	4.388	0.078	0.194	4.390	0.510	0.194
107.91	4.471	0.068		4.473	0.400	0.164
110.91	4.596	0.079		4.598	0.490	0.047
112.91	4.680	0.089		4.682	0.390	0.164
115.91	4.805	0.082		4.807	0.470	0.049

<u>TIME SINCE TRACERS INJECTED ^a</u> <u>(hrs)</u>	<u>CORRECTED TIME FOR m-TFMB AND o-FB ^b</u> <u>(days)</u>	<u>m-TFMB CONC.</u> <u>(mg/L)</u>	<u>o-FB CONC.</u> <u>(mg/L)</u>	<u>CORRECTED TIME FOR PFB AND m-FB ^c</u> <u>(days)</u>	<u>PFB CONC.</u> <u>(mg/L)</u>	<u>m-FB CONC.</u> <u>(mg/L)</u>
117.88	4.887	0.076		4.889	0.470	0.114
121.16	5.023	0.087		5.025	0.440	0.034
124.16	5.148	0.090		5.150	0.440	0.016
127.91	5.305	0.099		5.307	0.400	0.060
130.41	5.409	0.087		5.411	0.380	0.028
133.91	5.555	0.117		5.557	0.370	0.039
135.91	5.638	0.086		5.640	0.390	
140.91	5.846	0.072		5.848	0.370	0.063
143.91	5.971	0.114		5.973	0.330	
146.16	6.065	0.106		6.067	0.370	0.045
148.66	6.169	0.121		6.171	0.390	0.017
159.91	6.638	0.109		6.640	0.320	
160.91	6.680	0.130		6.682	0.280	0.061
162.93	6.764	0.126		6.766	0.300	0.050
167.21	6.942	0.146		6.944	0.270	
169.41	7.034	0.117		7.036	0.190	
172.41	7.159	0.150		7.161	0.250	0.026
186.41	7.742	0.150		7.744	0.230	0.011
188.41	7.825	0.126		7.828	0.210	
191.41	7.950	0.131	0.040	7.953	0.210	0.098
198.41	8.242	0.123		8.244	0.230	
202.91	8.430	0.160	0.041	8.432	0.200	0.061
205.91	8.555	0.119		8.557	0.190	
208.48	8.662	0.169		8.664	0.200	0.032
210.44	8.743	0.133		8.745	0.200	0.042
213.54	8.873	0.140		8.875	0.180	0.024
215.46	8.953	0.161		8.955	0.210	0.008
219.91	9.138	0.059	0.097	9.140	0.180	0.079

<u>TIME SINCE TRACERS INJECTED ^a</u> <u>(hrs)</u>	<u>CORRECTED TIME FOR m-TFMB AND o-FB ^b</u> <u>(days)</u>	<u>m-TFMB CONC.</u> <u>(mg/L)</u>	<u>o-FB CONC.</u> <u>(mg/L)</u>	<u>CORRECTED TIME FOR PFB AND m-FB ^c</u> <u>(days)</u>	<u>PFB CONC.</u> <u>(mg/L)</u>	<u>m-FB CONC.</u> <u>(mg/L)</u>
223.41	9.284	0.126		9.286	0.210	0.054
229.24	9.527	0.163		9.529	0.160	0.031
232.41	9.659	0.146	0.017	9.661	0.170	0.036
236.41	9.825	0.148	0.011	9.828	0.160	0.011
238.41	9.909	0.170		9.911	0.159	
239.41	9.950	0.150		9.953	0.160	
240.41	9.992	0.156		9.994	0.156	
241.41	10.034	0.145	0.105	10.036	0.150	
242.41	10.075	0.165	0.080	10.078	0.139	
243.41	10.117		0.084	10.119	0.141	
244.41	10.159	0.174	0.117	10.161	0.160	
245.41	10.200		0.142	10.203	0.147	
246.41	10.242	0.150	0.127	10.244	0.150	
247.41	10.284		0.120	10.286	0.141	
249.66	10.378	0.174	0.134	10.380	0.150	
251.66	10.461	0.174	0.130	10.463	0.150	
252.66	10.503		0.108	10.506	0.138	
253.66	10.545		0.176	10.588	0.150	
254.66	10.586	0.167	0.134	10.671	0.140	
256.66	10.669	0.150	0.126	10.800	0.140	
259.74	10.798	0.182	0.124	10.883	0.133	
261.74	10.881	0.187	0.134	11.091	0.124	
266.74	11.089	0.172		11.300	0.120	
271.74	11.298	0.161	0.120	11.522	0.123	
277.08	11.520	0.147	0.123	11.647	0.110	
280.08	11.645	0.174	0.110	11.730	0.119	
282.08	11.728	0.181	0.119	11.869	0.112	
285.41	11.867	0.202	0.112	11.953	0.108	

<u>TIME SINCE TRACERS INJECTED ^a</u> <u>(hrs)</u>	<u>CORRECTED TIME FOR m-TFMB AND o-FB ^b</u> <u>(days)</u>	<u>m-TFMB CONC.</u> <u>(mg/L)</u>	<u>o-FB CONC.</u> <u>(mg/L)</u>	<u>CORRECTED TIME FOR PFB AND m-FB ^c</u> <u>(days)</u>	<u>PFB CONC.</u> <u>(mg/L)</u>	<u>m-FB CONC.</u> <u>(mg/L)</u>
287.41	11.950	0.201	0.108	12.078	0.105	
290.41	12.075	0.162	0.098	12.161	0.104	
292.41	12.159	0.156	0.128	12.286	0.103	
295.41	12.284	0.207	0.138	12.369	0.106	
297.41	12.367	0.147	0.127	12.494	0.100	
300.41	12.492	0.178	0.140	12.578	0.100	
302.41	12.575	0.171	0.159	12.703	0.096	
305.41	12.700	0.178	0.135	12.744	0.098	
306.41	12.742	0.154	0.131	12.911	0.093	
310.41	12.909	0.170	0.151	12.994	0.095	
312.41	12.992	0.153	0.150	13.109	0.084	
315.16	13.107	0.184	0.139	13.192	0.093	
317.16	13.190	0.159	0.133	13.317	0.093	
320.16	13.315	0.172	0.129	13.400	0.089	
322.16	13.398	0.165	0.140	13.525	0.089	
325.16	13.523	0.157	0.145	13.609	0.092	
327.16	13.607	0.161	0.149	13.744	0.086	
330.41	13.742	0.169	0.162	13.786	0.088	
331.41	13.784	0.156	0.127	13.911	0.080	
334.41	13.909	0.160	0.123	13.994	0.077	
336.41	13.992	0.153	0.129	14.078	0.083	
338.41	14.075	0.177	0.167	14.203	0.082	
341.41	14.200	0.180	0.130	14.328	0.076	
344.41	14.325	0.172	0.176	14.411	0.077	
346.41	14.409	0.181	0.139	14.536		
349.41	14.534	0.181	0.148	14.703	0.072	
353.41	14.700	0.169	0.178	14.828	0.068	
356.41	14.825	0.171	0.147	14.911	0.068	

<u>TIME SINCE TRACERS INJECTED ^a</u> <u>(hrs)</u>	<u>CORRECTED TIME FOR m-TFMB AND o-FB ^b</u> <u>(days)</u>	<u>m-TFMB CONC.</u> <u>(mg/L)</u>	<u>o-FB CONC.</u> <u>(mg/L)</u>	<u>CORRECTED TIME FOR PFB AND m-FB ^c</u> <u>(days)</u>	<u>PFB CONC.</u> <u>(mg/L)</u>	<u>m-FB CONC.</u> <u>(mg/L)</u>
358.41	14.909	0.167	0.150	14.994	0.066	
360.41	14.992	0.174	0.133	15.150	0.064	
364.16	15.148	0.165	0.162	15.411	0.066	
370.41	15.409	0.163	0.195	15.661	0.065	
376.41	15.659	0.161	0.158	15.869	0.064	
381.41	15.867	0.164	0.216	16.119	0.060	
387.41	16.117	0.157	0.152	16.380	0.059	
393.66	16.378	0.159	0.170	16.619	0.059	
399.41	16.617	0.175	0.265	16.828	0.056	
404.41	16.825	0.167	0.118	17.046	0.046	
409.66	17.044		0.111	17.307	0.021	
415.91	17.305	0.096	0.105	17.567	0.034	
422.16	17.565	0.145	0.120	17.828	0.018	
428.41	17.825	0.086	0.195	18.078		
434.41	18.075	0.083	0.126	18.338		
440.66	18.336	0.132	0.133	18.494	0.035	
444.41	18.492		0.145			

^a All tracers were injected at 17:36 on August 23, 1981.

^b The time correction for m-TFMB and o-FB is 36 minutes.

^c The time correction for PFB and m-FB is 33 minutes.

**APPENDIX F-2: TABULATED TRACER-CONCENTRATION DATA
FROM CONVERGENT-FLOW TRACER TEST #2 CONDUCTED
AT THE H-6 HYDROPAD**

<u>TIME SINCE TRACER INJECTED ^a</u> (hrs)	<u>CORRECTED TIME ^b</u> (days)	<u>p-FB CONCENTRATION</u> (mg/L)
1.00	0.019	0.000
3.00	0.102	0.000
4.00	0.144	0.399
5.00	0.185	0.000
6.00	0.227	0.226
7.00	0.269	0.543
8.00	0.310	0.681
9.00	0.352	1.164
10.00	0.394	1.375
11.00	0.435	1.552
12.00	0.477	1.672
14.25	0.571	1.730
16.25	0.654	1.736
17.25	0.696	1.784
18.25	0.738	1.716
19.25	0.779	1.678
21.25	0.863	1.603
24.33	0.991	1.542
26.33	1.074	1.381
31.33	1.283	1.114
36.33	1.491	1.024
41.67	1.713	0.908
44.67	1.838	0.816
46.67	1.922	0.777
50.00	2.060	0.757
52.00	2.144	0.679
55.00	2.269	0.721

F2-3

TIME SINCE TRACER INJECTED ^a (hrs)	CORRECTED TIME ^b (days)	p-FB CONCENTRATION (mg/L)
57.00	2.352	0.641
60.00	2.477	0.598
62.00	2.560	0.586
65.00	2.685	0.578
67.00	2.769	0.555
70.00	2.894	0.519
71.00	2.935	0.491
75.00	3.102	0.481
77.00	3.185	0.454
79.75	3.300	0.468
81.75	3.383	0.423
84.75	3.508	0.378
86.75	3.592	0.381
89.75	3.717	0.349
91.75	3.800	0.366
95.00	3.935	0.339
96.00	3.977	0.339
99.00	4.102	0.326
101.00	4.185	0.332
103.00	4.269	0.320
106.00	4.394	0.279
109.00	4.519	0.285
111.00	4.602	0.273
114.00	4.727	0.222
118.00	4.894	0.251
121.00	5.019	0.227
123.00	5.102	0.225

TIME SINCE TRACER INJECTED ^a (hrs)	CORRECTED TIME ^b (days)	p-FB CONCENTRATION (mg/L)
125.00	5.185	0.232
128.75	5.342	0.176
135.00	5.602	0.190
141.00	5.852	0.154
146.00	6.060	0.160
152.00	6.310	0.149
158.25	6.571	0.130
164.00	6.810	0.165
169.00	7.019	0.089
174.25	7.238	0.063
180.50	7.498	0.062
186.75	7.758	0.099
193.00	8.019	0.122
199.00	8.269	0.086
205.25	8.529	0.081
209.00	8.685	0.095

^a p-FB was injected at 13:00 on September 2, 1981.

^b The time correction for p-FB is 33 minutes.

**APPENDIX F-3: TABULATED TRACER-CONCENTRATION DATA
FROM CONVERGENT-FLOW TRACER TEST #3 CONDUCTED
AT THE H-6 HYDROPAD**

F3-2

<u>TIME SINCE TRACER INJECTION</u> <u>(days)</u>	<u>p-FB CONCENTRATION</u> <u>(mg/L)</u>
0.02	0.06
0.11	0.07
0.19	0.07
0.27	0.08
0.36	0.02
0.44	0.14
0.52	0.27
0.61	0.42
0.69	0.60
0.77	0.71
0.86	0.84
0.94	0.96
1.02	1.01
1.11	1.13
1.19	1.10
1.27	1.19
1.36	1.19
1.44	1.20
1.52	1.21
1.61	1.21
1.69	1.18
1.77	1.16
1.86	1.11
1.94	1.11
2.02	1.09
2.11	1.07
2.19	1.04

TIME SINCE TRACER INJECTION
(days)

p-FB CONCENTRATION
(mg/L)

2.27	1.03
2.36	1.00
2.44	0.96
2.52	0.98
2.61	0.95
2.69	0.94
2.86	0.93
3.02	0.87
3.19	0.84
3.36	0.80
3.52	0.78
3.69	0.76
3.86	0.72
4.02	0.70
4.21	0.70
4.36	0.68
4.52	0.65
4.77	0.62
4.98	0.59
5.03	0.58
5.11	0.57
5.19	na
5.27	0.55
5.36	0.52
5.44	0.57
5.52	0.57
5.61	0.57

TIME SINCE TRACER INJECTION (days)	p-FB CONCENTRATION (mg/L)
5.65	0.59
5.73	0.61
5.82	0.63
5.98	na
6.12	0.63
6.20	0.64
6.27	0.62
6.36	0.63
6.44	0.66
6.52	0.61
6.61	0.71
6.69	0.61
6.77	0.57
6.86	0.62
6.94	0.56
7.02	0.58
7.11	0.45
7.19	0.53
7.27	0.56
7.36	na
7.44	0.51
7.52	na
7.61	0.39
7.69	na
7.77	0.42
7.86	na
7.94	0.29

TIME SINCE TRACER INJECTION (days)	p-FB CONCENTRATION (mg/L)
8.02	na
8.11	0.38
8.19	na
8.27	0.42
8.44	0.19
8.61	0.38
8.77	0.37
8.86	na
8.94	0.38
9.11	0.37
9.27	0.37
9.44	0.37
9.69	0.22
9.86	0.28
10.02	0.14
10.19	0.28
10.36	0.29
10.52	0.21
10.69	0.19
10.86	0.34
11.02	0.27
11.19	0.28
11.36	na
11.52	0.27
11.69	na
11.86	0.27
12.02	na

<u>TIME SINCE TRACER INJECTION</u> <u>(days)</u>	<u>p-FB CONCENTRATION</u> <u>(mg/L)</u>
12.19	0.24
12.36	na
12.52	0.27
12.86	0.24
13.02	na
13.19	0.19
13.36	na
13.52	0.20
13.69	na
13.86	0.00
14.02	na
14.15	0.19
14.36	na
14.52	0.14
14.77	0.15

na not analyzed

**APPENDIX F-4: TABULATED TRACER-CONCENTRATION DATA
FROM CONVERGENT-FLOW TRACER TEST #4 CONDUCTED
AT THE H-6 HYDROPAD**

<u>TIME SINCE TRACER INJECTION (days)</u>	<u>PFB CONCENTRATION (mg/L)</u>	<u>SCN CONCENTRATION (mg/L)</u>
0.02	0.00	0.00
0.09	0.00	na
0.17	na	0.00
0.26	0.00	na
0.34	0.00	0.00
0.42	0.05	na
0.51	0.04	na
0.59	0.15	0.22
0.63	0.72	0.86
0.72	1.22	na
0.80	1.85	na
0.97	na	2.70
1.10	3.13	3.81
1.18	2.99	na
1.26	3.11	4.92
1.34	3.54	na
1.42	3.62	4.62
1.51	3.65	na
1.59	3.50	na
1.67	3.26	4.74
1.76	3.47	na
1.84	3.31	5.00
1.92	2.88	na
2.01	2.97	4.80
2.09	2.93	na
2.17	2.80	3.35
2.26	2.65	na

<u>TIME SINCE TRACER INJECTION (days)</u>	<u>PFB CONCENTRATION (mg/L)</u>	<u>SCN CONCENTRATION (mg/L)</u>
2.34	na	3.77
2.42	2.40	na
2.51	na	3.71
2.59	2.23	na
2.67	na	3.84
2.76	2.12	na
2.84	na	3.63
2.92	1.96	na
3.01	na	3.29
3.09	1.94	na
3.17	na	3.41
3.26	1.80	na
3.42	1.62	3.05
3.59	1.71	na
3.76	1.50	na
3.84	na	2.80
3.92	1.46	na
4.09	1.38	na
4.26	1.35	na
4.42	1.32	2.42
4.67	1.28	2.05
4.84	1.18	na
5.01	1.20	2.17
5.17	1.44	na
5.34	1.25	2.16
5.51	1.14	na
5.67	1.13	1.70

TIME SINCE TRACER INJECTION (days)	PFB CONCENTRATION (mg/L)	SCN CONCENTRATION (mg/L)
5.84	1.19	na
6.01	1.04	1.65
6.17	1.02	na
6.34	na	1.24
6.51	1.04	na
6.67	na	1.17
6.84	0.96	na
7.01	na	1.23
7.17	0.98	na
7.34	na	1.24
7.51	0.96	na
7.84	0.81	na
8.01	na	0.81
8.17	0.79	na
8.34	na	0.97
8.51	0.80	na
8.67	na	1.02
8.84	0.78	na
9.01	na	0.78
9.13	0.07	na
9.34	na	0.79
9.51	0.60	na
9.76	0.62	0.82

na not analyzed

**APPENDIX F-5: TABULATED TRACER-CONCENTRATION DATA
FROM CONVERGENT-FLOW TRACER TEST #5 CONDUCTED
AT THE H-6 HYDROPAD**

<u>TIME SINCE TRACER INJECTION (days)</u>	<u>p-FB CONC. (mg/L)</u>	<u>m-TFMB CONC. (mg/L)</u>	<u>SCN CONC. (mg/L)</u>
0.06		0.00	0.45
0.23		0.00	0.38
0.73		0.18	0.44
1.23		0.26	0.58
1.73		0.31	0.64
1.89		0.36	0.69
2.06		0.37	0.73
2.23		0.40	0.77
2.39		0.44	0.76
2.48		0.39	na
2.56		0.36	0.81
2.64		0.43	na
2.73		0.42	0.78
2.81		0.46	na
2.89		0.37	0.80
2.93		0.37	na
2.98		0.44	na
3.06		0.37	0.78
3.14		0.49	na
3.23		0.41	0.80
3.31		0.45	na
3.39		0.45	0.81
3.48		0.45	na
3.56		0.46	0.80
3.64		0.41	na
3.73		0.44	0.82
3.81		0.42	na

<u>TIME SINCE TRACER INJECTION (days)</u>	<u>p-FB CONC. (mg/L)</u>	<u>m-TFMB CONC. (mg/L)</u>	<u>SCN CONC. (mg/L)</u>
3.89		0.50	na
3.98		0.45	na
4.06		0.49	0.84
4.14		0.44	na
4.23		0.48	0.82
4.31		0.41	na
4.39		0.49	0.83
4.48		0.43	na
4.56		0.47	0.83
4.64		0.44	na
4.73		0.51	0.83
4.81		0.45	na
4.89		0.36	0.82
4.98		0.47	na
5.10		0.48	0.84
5.26		0.49	0.82
5.43		0.28	0.80
5.60		0.48	0.81
5.76		0.44	0.83
5.93		0.44	0.79
6.10		0.51	0.77
6.26		0.53	0.76
6.43		0.43	0.71
6.60		0.48	0.72
6.76		0.40	0.69
6.93		0.32	0.77
7.10		0.41	0.70

<u>TIME SINCE TRACER INJECTION (days)</u>	<u>p-FB CONC. (mg/L)</u>	<u>m-TFMB CONC. (mg/L)</u>	<u>SCN CONC. (mg/L)</u>
7.26		0.39	0.74
7.43		0.40	0.76
7.60		0.43	0.73
7.76		0.41	0.56
7.93		0.37	0.66
8.10		0.42	0.72
8.26		0.43	0.67
8.43		0.45	0.67
8.60		0.41	0.52
8.76		0.38	0.63
9.01	0.00	0.42	0.69
9.28	0.01	0.37	0.69
9.43	0.00	0.34	0.61
9.47	0.18	0.45	0.66
9.51	1.70	0.49	0.65
9.56	1.73	0.76	0.64
9.60	1.26	0.65	0.61
9.64	0.76	0.69	na
9.68	0.54	0.54	na
9.72	0.58	0.51	na
9.76	0.65	0.60	0.60
9.81	0.38	0.53	na
9.85	0.64	0.54	na
9.89	0.58	0.59	0.60
9.93	0.56	0.52	0.59
9.97	0.59	0.46	na
10.01	0.35	0.46	na

<u>TIME SINCE TRACER INJECTION (days)</u>	<u>p-FB CONC. (mg/L)</u>	<u>m-TFMB CONC. (mg/L)</u>	<u>SCN CONC. (mg/L)</u>
10.06	0.49	0.42	na
10.10	0.47	0.59	0.59
10.14	0.59	0.50	na
10.18	0.54	0.39	na
10.22	0.65	0.56	na
10.26	0.60	0.44	0.63
10.31	0.21	0.49	na
10.35	0.67	0.44	na
10.43	0.59	0.46	0.56
10.51	0.59	0.45	na
10.60	0.63	0.47	0.55
10.68	0.63	0.54	na
10.76	0.34	0.46	0.53
10.85	0.46	0.39	na
10.93	0.55	0.50	0.51
11.01	0.41	0.51	na
11.10	0.53	0.44	0.54
11.18	0.50	0.47	na
11.26	0.54	0.42	0.50
11.35	0.52	0.34	na
11.43	0.50	0.47	0.51
11.51	0.41	0.49	na
11.60	0.48	0.44	0.52
11.68	0.47	0.44	na
11.76	0.46	0.37	0.48
11.85	0.48	0.42	na
11.93	0.37	0.40	0.47

<u>TIME SINCE TRACER INJECTION (days)</u>	<u>p-FB CONC. (mg/L)</u>	<u>m-TFMB CONC. (mg/L)</u>	<u>SCN CONC. (mg/L)</u>
12.01	0.16	0.40	na
12.14	0.39	0.43	0.49
12.31	0.39	0.42	0.51
12.47	0.41	0.39	0.50
12.64	0.36	0.43	0.54
12.81	0.39	0.39	0.48
12.97	0.34	0.39	0.47
13.14	0.34	0.40	0.43
13.31	0.35	0.43	0.50
13.47	0.35	0.42	0.49
13.64	0.33	0.37	0.47
13.81	0.29	0.34	0.48
13.97	0.24	0.33	0.47
14.14	0.31	0.36	0.43
14.31	0.30	0.36	0.44
14.47	0.28	0.35	0.38
14.64	0.28	0.32	0.45
14.81	0.29	0.32	0.43
14.97	0.29	0.34	0.39
15.14	0.27	0.31	0.40
15.31	0.24	0.33	0.39
15.47	0.26	0.29	0.34
15.64	0.27	0.28	0.37
15.81	0.25	0.27	0.38
15.97	0.26	0.30	0.39
16.14	0.23	0.27	0.37
16.31	0.25	0.28	0.36

<u>TIME SINCE TRACER INJECTION (days)</u>	<u>p-FB CONC. (mg/L)</u>	<u>m-TFMB CONC. (mg/L)</u>	<u>SCN CONC. (mg/L)</u>
16.47	0.25	0.29	0.34
16.64	0.25	0.32	0.35
16.81	0.23	0.27	0.33
16.97	0.22	0.27	0.32
17.14	0.21	0.32	0.32
17.31	0.21	0.29	0.32
17.47	0.20	0.30	0.32
17.64	0.22	0.25	0.30
17.81	0.21	0.24	0.29
17.97	0.21	0.23	0.32
18.14	0.18	0.23	0.30
18.31	0.18	0.20	0.28
18.47	0.19	0.24	0.32
18.64	0.19	0.20	0.32
18.81	0.16	0.21	0.30
18.97	0.14	0.23	0.28
19.14	0.12	0.24	0.25
19.22	0.15	0.00	na
19.31	0.07	0.24	0.22
19.47	0.10	0.16	0.29
19.64	0.11	0.16	0.23
19.81	0.09	0.19	0.24
19.97	0.15	0.09	0.23
20.14	0.12	0.12	0.24
20.31	0.09	0.00	0.24
20.47	0.11	0.00	0.25
20.64	0.10	0.09	0.24

<u>TIME SINCE TRACER INJECTION (days)</u>	<u>p-FB CONC. (mg/L)</u>	<u>m-TFMB CONC. (mg/L)</u>	<u>SCN CONC. (mg/L)</u>
20.81	0.11	0.00	0.18
20.97	0.13	0.02	0.20
21.14	0.09	0.09	0.21
21.31	0.09	0.12	0.24
21.47	0.11	0.00	0.21
21.64	0.10	0.00	0.23
21.81	0.10	0.05	0.15
22.78	0.11	0.00	0.23
23.80	0.10	0.00	0.21
24.89	0.08	0.00	0.18
26.07	0.06	0.00	0.15
27.11	0.08	0.00	0.15

na not analyzed

**APPENDIX G: TABULATED TRACER-CONCENTRATION DATA
FROM THE CONVERGENT-FLOW TRACER TEST CONDUCTED
AT THE H-11 HYDROPAD**

<u>TIME SINCE FIRST TRACER INJECTED ^a (hrs)</u>	<u>CORRECTED TIME FOR m-TFMB ^c (days)</u>	<u>m-TFMB CONC. (mg/L)</u>	<u>CORRECTED TIME FOR PFB ^b (days)</u>	<u>PFB CONC. (mg/L)</u>	<u>CORRECTED TIME FOR o-TFMB ^d (days)</u>	<u>o-TFMB CONC. (mg/L)</u>
4.50	0.03	0.00	0.14	0.00	-0.06	0.00
5.00	0.06	1.06	0.16	0.00	-0.04	0.00
5.50	0.08	1.26	0.18	0.00	-0.02	0.00
6.00	0.10	2.78	0.20	0.00	0.01	0.00
6.50	0.12	4.23	0.22	0.00	0.03	0.00
6.50	0.12	4.81	0.22	0.00	0.03	0.00
6.50	0.12	4.82	0.22	0.00	0.03	0.00
7.50	0.16	5.35	0.26	0.00	0.07	0.00
8.00	0.18	5.97	0.28	0.00	0.09	0.00
8.50	0.20	6.41	0.30	0.00	0.11	0.00
9.00	0.22	6.78	0.32	0.00	0.13	0.00
9.50	0.24	6.81	0.34	0.00	0.15	0.00
10.00	0.26	6.93	0.36	0.00	0.17	0.00
10.50	0.28	7.16	0.39	0.00	0.19	0.00
11.00	0.31	7.58	0.41	0.00	0.21	0.00
11.50	0.33	7.93	0.43	0.00	0.23	0.00
11.50	0.33	8.00	0.43	0.00	0.23	0.00
12.00	0.35	7.42	0.45	0.00	0.26	0.00
12.50	0.37	7.56	0.47	0.00	0.28	0.00
13.00	0.39	7.42	0.49	0.00	0.30	0.00
14.00	0.43	7.46	0.53	0.00	0.34	0.00
15.00	0.47	7.47	0.57	0.00	0.38	0.00
17.00	0.56	7.06	0.66	0.07	0.46	0.00
21.00	0.72	6.19	0.82	0.16	0.63	0.00
21.50	0.74	6.26	0.84	0.17	0.65	0.00
25.00	0.89	5.74	0.99	0.26	0.80	0.00
29.00	1.06	5.18	1.16	0.38	0.96	0.00
33.00	1.22	4.48	1.32	0.48	1.13	0.00

<u>TIME SINCE FIRST TRACER INJECTED ^a (hrs)</u>	<u>CORRECTED TIME FOR m-TFMB ^c (days)</u>	<u>m-TFMB CONC. (mg/L)</u>	<u>CORRECTED TIME FOR PFB ^b (days)</u>	<u>PFB CONC. (mg/L)</u>	<u>CORRECTED TIME FOR o-TFMB ^d (days)</u>	<u>o-TFMB CONC. (mg/L)</u>
37.00	1.39	4.31	1.49	0.59	1.30	0.00
41.00	1.56	3.89	1.66	0.72	1.46	0.00
45.00	1.72	3.62	1.82	0.81	1.63	0.00
49.00	1.89	3.48	1.99	0.90	1.80	0.00
53.00	2.06	3.75	2.16	0.98	1.96	0.00
57.00	2.22	3.54	2.32	1.05	2.13	0.00
61.00	2.39	2.92	2.49	1.10	2.30	0.00
67.00	2.64	1.96	2.74	1.17	2.55	0.00
67.00	2.64	2.74	2.74	1.07	2.55	0.00
73.00	2.89	2.72	2.99	1.25	2.80	0.00
79.00	3.14	2.45	3.24	1.33	3.05	0.00
85.00	3.39	2.26	3.49	1.42	3.30	0.00
91.00	3.64	2.36	3.74	1.23	3.55	0.00
95.00	3.81	2.09	3.91	1.34	3.71	0.06
97.00	3.89	2.23	3.99	1.44	3.80	0.11
103.00	4.14	2.16	4.24	1.39	4.05	0.12
109.00	4.39	1.97	4.49	1.42	4.30	0.13
121.00	4.89	1.76	4.99	1.46	4.80	0.16
133.00	5.39	1.76	5.49	1.48	5.30	0.20
145.00	5.89	1.54	5.99	1.50	5.80	0.24
145.00	5.89	1.58	5.99	1.32	5.80	0.21
145.00	5.89	1.08	5.99	1.29	5.80	0.20
145.00	5.89	1.60	5.99	1.42	5.80	0.22
157.00	6.39	1.40	6.49	1.44	6.30	0.26
169.00	6.89	1.46	6.99	1.44	6.80	0.31
181.00	7.39	1.28	7.49	1.43	7.30	0.34
205.00	8.39	1.33	8.49	1.41	8.30	0.40
205.00	8.39	1.26	8.49	1.23	8.30	0.35

<u>TIME SINCE FIRST TRACER INJECTED ^a (hrs)</u>	<u>CORRECTED TIME FOR m-TFMB ^c (days)</u>	<u>m-TFMB CONC. (mg/L)</u>	<u>CORRECTED TIME FOR PFB ^b (days)</u>	<u>PFB CONC. (mg/L)</u>	<u>CORRECTED TIME FOR o-TFMB ^d (days)</u>	<u>o-TFMB CONC. (mg/L)</u>
229.00	9.39	1.15	9.49	1.34	9.30	0.46
241.00	9.89	1.24	9.99	1.26	9.80	0.43
253.00	10.39	1.00	10.49	1.31	10.30	0.50
277.00	11.39	0.93	11.49	1.24	11.30	0.54
301.00	12.39	1.00	12.49	1.19	12.30	0.57
326.00	13.43	0.89	13.53	1.14	13.34	0.60
349.00	14.39	0.78	14.49	1.08	14.30	0.63
373.00	15.39	0.83	15.49	1.06	15.30	0.64
397.00	16.39	0.68	16.49	1.01	16.30	0.67
397.00	16.39	0.78	16.49	0.91	16.30	0.57
421.00	17.39	0.71	17.49	0.97	17.30	0.67
445.00	18.39	0.57	18.49	0.94	18.30	0.68
469.00	19.39	0.55	19.49	0.88	19.30	0.67
493.00	20.39	0.58	20.49	0.86	20.30	0.68
517.00	21.39	0.61	21.49	0.85	21.30	0.70
541.00	22.39	0.47	22.49	0.79	22.30	0.69
541.00	22.39	0.64	22.49	0.76	22.30	0.64
565.00	23.39	0.46	23.49	0.65	23.30	0.70
565.00	23.39	0.56	23.49	0.69	23.30	0.61
565.00	23.39	0.57	23.49	0.69	23.30	0.64
565.00	23.39	0.60	23.49	0.76	23.30	0.64
589.00	24.39	0.35	24.49	0.65	24.30	0.73
589.00	24.39	0.59	24.49	0.71	24.30	0.63
613.00	25.39	0.27	25.49	0.63	25.30	0.66
613.00	25.39	0.59	25.49	0.67	25.30	0.63
637.00	26.39	0.39	26.49	0.61	26.30	0.70
637.00	26.39	0.56	26.49	0.66	26.30	0.63
661.00	27.39	0.35	27.49	0.58	27.30	0.71

TIME SINCE FIRST TRACER INJECTED ^a (hrs)	CORRECTED TIME FOR m-TFMB ^c (days)	m-TFMB CONC. (mg/L)	CORRECTED TIME FOR PFB ^b (days)	PFB CONC. (mg/L)	CORRECTED TIME FOR o-TFMB ^d (days)	o-TFMB CONC. (mg/L)
661.00	27.39	0.52	27.49	0.63	27.30	0.61
685.00	28.39	0.34	28.49	0.56	28.30	0.70
685.00	28.39	0.50	28.49	0.57	28.30	0.60
697.00	28.89	0.42	28.99	0.54	28.80	0.69
697.00	28.89	0.49	28.99	0.62	28.80	0.65
709.00	29.39	0.26	29.49	0.51	29.30	0.71
709.00	29.39	0.49	29.49	0.56	29.30	0.58
715.00	29.64	0.32	29.74	0.54	29.55	0.72
715.00	29.64	0.45	29.74	0.58	29.55	0.59
715.00	29.64	0.40	29.74	0.52	29.55	0.57
739.50	30.66	0.42	30.76	0.55	30.57	0.62
765.00	31.72	0.48	31.82	0.54	31.63	0.60
777.00	32.22	0.46	32.32	0.53	32.13	0.62
801.00	33.22	0.43	33.32	0.51	33.13	0.61
801.00	33.22	0.41	33.32	0.51	33.13	0.58
801.00	33.22	0.41	33.32	0.48	33.13	0.55
801.00	33.22	0.37	33.32	0.51	33.13	0.60
813.00	33.72	0.44	33.82	0.50	33.63	0.61
837.00	34.72	0.36	34.82	0.48	34.63	0.59
861.00	35.72	0.39	35.82	0.47	35.63	0.64
885.00	36.72	0.40	36.82	0.45	36.63	0.57
909.00	37.72	0.33	37.82	0.41	37.63	0.52
933.00	38.72	0.34	38.82	0.40	38.63	0.52
957.00	39.72	0.32	39.82	0.40	39.63	0.53
981.00	40.72	0.30	40.82	0.38	40.63	0.50
1005.00	41.72	0.30	41.82	0.36	41.63	0.50
1029.00	42.72	0.29	42.82	0.36	42.63	0.48
1029.00	42.72	0.27	42.82	0.34	42.63	0.47

<u>TIME SINCE FIRST TRACER INJECTED ^a (hrs)</u>	<u>CORRECTED TIME FOR m-TFMB ^c (days)</u>	<u>m-TFMB CONC. (mg/L)</u>	<u>CORRECTED TIME FOR PFB ^b (days)</u>	<u>PFB CONC. (mg/L)</u>	<u>CORRECTED TIME FOR o-TFMB ^d (days)</u>	<u>o-TFMB CONC. (mg/L)</u>
1029.00	42.72	0.29	42.82	0.32	42.63	0.47
1053.00	43.72	0.29	43.82	0.33	43.63	0.46
1077.00	44.72	0.24	44.82	0.30	44.63	0.48
1101.00	45.72	0.23	45.82	0.31	45.63	0.46
1125.00	46.72	0.26	46.82	0.29	46.63	0.46
1149.00	47.72	0.25	47.82	0.30	47.63	0.27
1149.00	47.72	0.20	47.82	0.30	47.63	0.42
1173.00	48.72	0.23	48.82	0.28	48.63	0.44
1197.00	49.72	0.22	49.82	0.27	49.63	0.26
1197.00	49.72	0.17	49.82	0.27	49.63	0.40
1221.00	50.72	0.22	50.82	0.27	50.63	0.42
1245.00	51.72	0.20	51.82	0.25	51.63	0.42
1245.00	51.72	0.23	51.82	0.29	51.63	0.38
1269.00	52.72	0.21	52.82	0.28	52.63	0.37
1281.00	53.22	0.26	53.32	0.27	53.13	0.38
1293.00	53.72	0.21	53.82	0.26	53.63	0.39

- ^a PFB was injected at 11:00 on May 14, 1989.
m-TFMB was injected at 13:30 on May 14, 1989.
o-TFMB was injected at 16:00 on May 14, 1989.
- ^b The time correction for PFB is 75 minutes.
- ^c The time correction for m-TFMB is 70 minutes.
- ^d The time correction for o-TFMB is 52 minutes.

DISTRIBUTION

Federal Agencies

US Department of Energy, (5)
Office of Civilian Radioactive Waste
Management

Attn: Deputy Director, RW-2
Associate Director, RW-10
Office of Program
Administration and
Resources Management
Associate Director, RW-20
Office of Facilities
Siting and Development
Associate Director, RW-30
Office of Systems
Integration and
Regulations
Associate Director, RW-40
Office of External
Relations and Policy

Forrestal Building
Washington, DC 20585

US Department of Energy (4)
WIPP Project Integration Office

Attn: W.J. Arthur III
L.W. Gage
P.J. Higgins
D.A. Olona
PO Box 5400
Albuquerque, NM 87115-5400

US Department of Energy
Attn: National Atomic Museum Library
Albuquerque Operations Office
PO Box 5400
Albuquerque, NM 87185-5400

US Department of Energy (4)
WIPP Project Site Office (Carlsbad)

Attn: R. Becker
V. Daub
J. Lippis
J.A. Mewhinney
R. Batra

PO Box 3090
Carlsbad, NM 88221

US Department of Energy
Research & Waste Management Division

Attn: Director
PO Box E
Oak Ridge, TN 37831

US Department of Energy

Attn: E. Young
Room E-178
GAO/RCED/GTN
Washington, DC 20545

US Department of Energy
Office of Environmental Restoration
and Waste Management

Attn: J. Lytle, EM-30 (Trevion II)
Washington, DC 20585-0002

US Department of Energy (3)
Office of Environmental Restoration
and Waste Management

Attn: M. Frei, EM-34 (Trevion II)
Washington, DC 20585-0002

US Department of Energy
Office of Environmental Restoration
and Waste Management

Attn: S. Schneider, EM-342
(Trevion II)
Washington, DC 20585-0002

US Department of Energy (3)
Office of Environment, Safety
and Health

Attn: C. Borgstrom, EH-25
R. Pelletier, EH-231
Washington, DC 20585

US Department of Energy (2)

Idaho Operations Office
Fuel Processing and Waste
Management Division

785 DOE Place
Idaho Falls, ID 83402

US Environmental Protection
Agency (2)

Radiation Programs (ANR-460)
Attn: R. Guimond
Washington, DC 20460

US Geological Survey (2)

Water Resources Division
Attn: R. Livingston
Suite 200

4501 Indian School, NE
Albuquerque, NM 87110

US Nuclear Regulatory Commission
Attn: H. Marson
Mail Stop 623SS
Washington, DC 20555

Boards

Defense Nuclear Facilities Safety
Board
Attn: D. Winters
Suite 700
625 Indiana Ave., NW
Washington, DC 20004

Nuclear Waste Technical Review
Board (2)
Attn: D.A. Deere
S.J.S. Parry
Suite 910
1100 Wilson Blvd.
Arlington, VA 22209-2297

Advisory Committee on Nuclear Waste
Nuclear Regulatory Commission
Attn: R. Major
7920 Norfolk Ave.
Bethesda, MD 20814

State Agencies

Environmental Evaluation Group (3)
Attn: Library
Suite F-2
7007 Wyoming, NE
Albuquerque, NM 87109

NM Bureau of Mines and Mineral
Resources
Socorro, NM 87801

NM Energy, Minerals, and Natural
Resources Department
Attn: Library
2040 S. Pacheco
Santa Fe, NM 87505

NM Environment Department (3)
Secretary of the Environment
Attn: J. Espinosa
1190 St. Francis Drive
Santa Fe, NM 87503-0968

NM Environment Department
WIPP Project Site
Attn: P. McCasland
PO Box 3090
Carlsbad, NM 88221

Laboratories/Corporations

Battelle Pacific Northwest
Laboratories (2)
Attn: H.C. Burkholder, P7-41
R.E. Westerman, P8-37
Battelle Blvd.
Richland, WA 99352

National Ground Water Information
Center
Attn: J. Bix
6375 Riverside Dr.
Dublin, OH 43017

Savannah River Laboratory (3)
Attn: N. Bibler
M.J. Plodinec
G.G. Wicks
Aiken, SC 29801

Golder Associates (3)
Attn: T.W. Doe
C. Voss
M. Kenrick
4104 148th Ave., NE
Redmond, WA 98052

INTERA Inc. (21)
Attn: G.E. Grisak
J.F. Pickens (5)
G.J. Saulnier
J.D. Avis
G.A. Freeze
M. Reeves
T.L. Cauffman (5)
V.A. Kelley (5)
Library
Suite 300
6850 Austin Center Blvd.
Austin, TX 78731

INTERA Inc. (5)
Attn: D.T. Upton
A.M. LaVenue
8100 Mountain Rd. Pl., NE
Albuquerque, NM 87110

INTERA Inc. (5)
Attn: W. Stensrud
M.D. Fort
R.A. Roberts
J.B. Palmer
T.F. Dale
PO Box 2123
Carlsbad, NM 88221

IT Corporation (2)
Attn: D. Deal
PO Box 2078
Carlsbad, NM 88221

IT Corporation (3)
Attn: R.F. McKinney
M.E. Crawley
J. Myers
Suite 700
5301 Central, NE
Albuquerque, NM 87108

Los Alamos National Laboratory
Attn: B. Erdal, CNC-11
PO Box 1663
Los Alamos, NM 87544

RE/SPEC, Inc.
Attn: W. Coons
Suite 300
4775 Indian School, NE
Albuquerque, NM 87110-3927

RE/SPEC, Inc.
Attn: J.L. Ratigan
PO Box 725
Rapid City, SD 57709

Southwest Research Institute (2)
Center for Nuclear Waste
Regulatory Analysis
Attn: P.K. Nair
6220 Culebra Road
San Antonio, TX 78228-0510

SAIC
Attn: G. Dymmel
101 Convention Center Dr.
Las Vegas, NV 89109

SAIC
Attn: H.R. Pratt,
10260 Campus Point Dr.
San Diego, CA 92121

SAIC (2)
Attn: M. Davis
J. Tollison
2109 Air Park Rd., SE
Albuquerque, NM 87106

S.S. Papadopulos and Associates, Inc.
Attn: J.W. Anthony
12596 W. Bayard Ave.
Suite 290
Lakewood, CO 80228

Tech Repts Inc. (3)
Attn: J. Chapman
R. Jones
E. Lorusso
5000 Marble, NE
Albuquerque, NM 87110

Westinghouse Electric Corporation (7)
Attn: Library
C. Cox
L. Fitch
R. Kehrman
L. Trego
M. Leroch (2)
PO Box 2078
Carlsbad, NM 88221

Universities

New Mexico Tech (4)
Department of Geoscience
Attn: J.L. Wilson
F. Phillips
C.S. Chen
R.S. Bowman
Socorro, NM 87801

Stanford University
Department of Applied Earth Sciences
Attn: S.M. Gorelick
Stanford, CA 94305

Texas A&M University
Department of Geology
Attn: P.A. Domenico
College Station, TX 77843

University of Arizona
Department of Hydrology
Attn: S.P. Neuman
Tucson, AZ 85721

University of California (4)
Lawrence Berkeley Laboratory
Earth Sciences Division
Attn: K. Karasaki
C.F. Tsang
J.C.S. Long
Y.W. Tsang
1 Cyclotron Road
Berkeley, CA 94720

University of Kansas
Kansas Geological Survey
Attn: J. Butler
1930 Constant Ave., Campus West
Lawrence, KS 66046

University of New Mexico (2)
Geology Department
Attn: M. Campana
Library
Albuquerque, NM 87131

University of Texas at Austin
Center for Petroleum and Geosystems
Engineering
Attn: G.A. Pope
CPE2.502
Austin, TX 78712

University of Virginia
Department of Environmental Sciences
Attn: G.M. Hornberger
Clark Hall
Charlottesville, VA 22903

University of Washington
Attn: G.R. Heath
College of Ocean
and Fishery Sciences
583 Henderson Hall
Seattle, WA 98195

University of Wisconsin-Madison (2)
Department of Geology and Geophysics
Attn: H.F. Wang
J.M. Bahr
1215 W. Dayton St.
Madison, WI 53706

Individuals

P. Drez
8816 Cherry Hills Rd., NE
Albuquerque, NM 87111

D.W. Powers
Star Route Box 87
Anthony, TX 79821

Libraries

Thomas Brannigan Library
Attn: D. Dresp
106 W. Hadley St.
Las Cruces, NM 88001

Hobbs Public Library
Attn: M. Lewis
509 N. Ship St.
Hobbs, NM 88248

New Mexico State Library
Attn: N. McCallan
325 Don Gaspar
Santa Fe, NM 87503

New Mexico Tech
Martin Speere Memorial Library
Campus Street
Socorro, NM 87810

New Mexico Junior College
Pannell Library
Attn: R. Hill
Lovington Highway
Hobbs, NM 88240

WIPP Public Reading Room
Carlsbad Public Library
Attn: Director
101 S. Halagueno St.
Carlsbad, NM 88220

Government Publications Department
General Library
University of New Mexico
Albuquerque, NM 87131

National Academy of Sciences, WIPP Panel

Charles Fairhurst, Chairman
Department of Civil and
Mineral Engineering
University of Minnesota
500 Pillsbury Dr., SE
Minneapolis, MN 55455-0220

Howard Adler
Oak Ridge Associated Universities
Medical Sciences Division
PO Box 117
Oak Ridge, TN 37831-0117

John D. Bredehoeft
Western Region Hydrologist
Water Resources Division
US Geological Survey (M/S 439)
345 Middlefield Road
Menlo Park, CA 94025

Fred M. Ernsberger
250 Old Mill Road
Pittsburgh, PA 15238

Rodney C. Ewing
Department of Geology
University of New Mexico
Albuquerque, NM 87131

B. John Garrick
PLG, Inc.
Suite 400
4590 MacArthur Blvd.
Newport Beach, CA 92660-2027

Leonard F. Konikow
US Geological Survey
431 National Center
Reston, VA 22092

Jeremiah O'Driscoll
Jody Incorporated
505 Valley Hill Drive
Atlanta, GA 30350

Christopher G. Whipple
Clement International
Suite 1380
160 Spear St.
San Francisco, CA 94105

Peter B. Myers
National Academy of Sciences
Board on Radioactive
Waste Management
2101 Constitution Ave.
Washington, DC 20418

Ina Alterman
Board on Radioactive
Waste Management
GF456
2101 Constitution Ave.
Washington, DC 20418

Foreign Addresses

Studiecentrum Voor Kernenergie
Centre D'Energie Nucleaire
Attn: A. Bonne
SCK/CEN
Boeretang 200
B-2400 Mol, BELGIUM

Atomic Energy Control Board
Waste Management Division
Attn: D. Metcalfe
PO Box 1046, Station 'B'
Ottawa, Ontario
K1P 5S9 CANADA

Atomic Energy of Canada, Ltd. (3)
Whiteshell Research Estab.
Attn: B. Goodwin
M. Stevens
D. Wushke
Pinewa, Manitoba, CANADA ROE 1L0

Environment Canada
National Water Research Institute
Canada Centre for Inland Lakes
Attn: K.S. Novakowski
867 Lakeshore Road
PO Box 5050
Burlington, Ontario
L7R 4A6 CANADA

Technical Research Center of Finland
Nuclear Engineering Laboratory
Attn: V. Taivassalo
PO Box 169
SF-00181 Helsinki, FINLAND

Technical Research Center of Finland
Nuclear Engineering Laboratory
Attn: A. Hautajarvi
PO Box 208
SF-02151 Espoo, FINLAND

Agence Nationale pour la Gestion des
Déchets Radioactifs (2)
Attn: L. Dewiere
F. Chenevier
Route du Panorama Robert Schuman
B.P. 38
92266 Fontenay-aux-Roses
Cedex, FRANCE

Bureau de Recherches Geologiques et
Minieres
Attn: J.P. Sauty
Underground Storage Department
Avenue de Concyr, B.P. 6009
F-45060 Orleans, Cedex 2 FRANCE

Ghislain de Marsily
Lab. Géologie Appliqué
Tour 26, 5 étage
4 Place Jussieu
F-75252 Paris Cedex 05
FRANCE

École des Mines
Attn: P. Goblet
35, Rue Saint-Honoré
F-77305 Fontainebleau, FRANCE

Francois Chenevier, Director (2)
ANDRA
Route du Panorama Robert Schumann
B.P.38
92266 Fontenay-aux-Roses Cedex
FRANCE

Jean-Pierre Olivier
OECD Nuclear Energy Agency
Division of Radiation Protection
and Waste Management
38, Boulevard Suchet
75016 Paris, FRANCE

Claude Sombret
Centre D'Etudes Nucleaires
De La Vallee Rhone
CEN/VALRHO
S.D.H.A. BP 171
30205 Bagnols-Sur-Geze, FRANCE

Golder Associates Umwelt Technik
Attn: L. Ostrowski
Im Werder 4
D-3100 Celle, GERMANY

Bundesministerium fur Forschung und
Technologie
Postfach 200 706
5300 Bonn 2, GERMANY

Gesellschaft fur Reaktorsicherheit
(GRS) (2)
Attn: B. Baltes
W. Muller
Schwertnergasse 1
D-5000 Cologne, GERMANY

Bundesanstalt fur Geowissenschaften
und Rohstoffe
Attn: M. Langer
Postfach 510 153
3000 Hanover 51, GERMANY

Hahn-Meitner-Institut fur
Kernforschung
Attn: W. Lutze
Glienicke Strasse 100
100 Berlin 39, GERMANY

Institut fur Tieflagerung (2)
Attn: K. Kuhn
Theodor-Heuss-Strasse 4
D-3300 Braunschweig, GERMANY

Physikalisch-Technische Bundesanstalt
Attn: P. Brenneke
Postfach 3345
D-3300 Braunschweig, GERMANY

Japan Atomic Energy Research
Institute (2)
Attn: S. Tashiro
H. Kimura
Tokai-Mura, Naka-Gun
Ibaraki-Ken
319-11, JAPAN

National Institute of Public Health
and Environmental Protection
Attn: S.M. Hassanizadeh
Atonie von Leeuwenhoeklaan 9
PO Box 1
3720 BA Bilthoven, THE NETHERLANDS

Netherlands Energy Research
Foundation ECN
Attn: L.H. Vons
3 Westerduinweg
PO Box 1
1755 ZG Petten, THE NETHERLANDS

Universidad Politécnic de Valencia
Departamento de Ingenieria Hidráulica
y Medio Ambiente
Attn: J. Jaime Gómez-Hernández
46071 Valencia, SPAIN

Universidad Politécnic de Cataluña
Attn: J. Carrera
E.T.S.I.C.
Camino Jordi Girona Salgado, 31
0834 Barcelona, SPAIN

Royal Institute of Technology
Dept. of Chemical Engineering
Attn: I. Neretnieks
S-100 44 Stockholm, SWEDEN

Kemakta Konsult AB
Attn: L. Birgersson
Pipersgatan 27
S-112 28 Stockholm, SWEDEN

Geosigma AB
Attn: P. Andersson
PO Box 894
S-751 08 Uppsala, SWEDEN

Conterra AB
Attn: A. Winberg
Krokslättis Fabriker 30
S-413 37 Mölndal, SWEDEN

Statens Karnkraftinspektion (2)
Attn: B. Dverstorp
J. Andersson
Box 27106
S-102 52 Stockholm, SWEDEN

Svensk Kärnbränslefordöring AB
Attn: F. Karlsson
Project KBS
Kärnbränslesakerhet
Box 5864
10248 Stockholm, SWEDEN

Svensk Kärnbränslehantering AB
Attn: K.-E. Almén
Box 5864
S-102 48 Stockholm, SWEDEN

Colenco Ltd.
Attn: S. Löw
Mellingerstrasse 207
CH-5405 Baden, SWITZERLAND

SolExperts Ltd.
Attn: E. Wyss
Ifangstrasse 12
CH-8603 Schwerzenbach, SWITZERLAND

Nationale Genossenschaft für die
Lagerung Radioaktiver Abfälle (2)
Attn: S. Vomvoris
P. Zuidema
Hardstrasse 73
CH-5430 Wettingen, SWITZERLAND

Intera Sciences
Attn: M.D. Impey
Chiltern House
45 Station Road
Henley-on-Thames, Oxfordshire
RG9 1AT, UNITED KINGDOM

Golder Associates
Attn: J.H. Black
Landmere Lane, Edwalton
Nottingham
NG12 4DE, UNITED KINGDOM

D.R. Knowles
British Nuclear Fuels, plc
Risley, Warrington, Cheshire WA3 6AS
1002607 UNITED KINGDOM

AEA Technology
Attn: J.H. Rees
D5W/29 Culham Laboratory
Abington, Oxfordshire OX14 3DB
UNITED KINGDOM

AEA Technology
Attn: W.R. Rodwell
O44/A31 Winfrith Technical Centre
Dorchester, Dorset DT2 8DH
UNITED KINGDOM

AEA Technology
Attn: J.E. Tinson
B4244 Harwell Laboratory
Didcot, Oxfordshire OX11 0RA
UNITED KINGDOM

Sandia Internal

1502	J.C. Cummings
6000	D.L. Hartley
6119	E.D. Gorham
6119	R.L. Beauheim (10)
6119	P.B. Davies (10)
6119	Staff (15)
6121	J.R. Tillerson
6121	F.D. Hansen (2)
6121	Staff (7)
6300	D.E. Miller
6302	T.E. Blejwas, Acting
6303	W.D. Weart
6303	S.Y. Pickering
6341	A.L. Stevens
6341	Staff (6)
6341	WIPP Central Files (10)
6342	D.R. Anderson
6342	Staff (20)
6343	T.M. Schultheis
6343	Staff (2)
6345	R.C. Lincoln
6345	Staff (9)
6347	D.R. Schafer
7141	S.A. Landenberger (5)
7151	G.C. Claycomb
7613-2	Document Control (10) for DOE/OSTI
8523-2	Central Technical Files
9300	J.E. Powell

THIS PAGE INTENTIONALLY LEFT BLANK